

AJNR

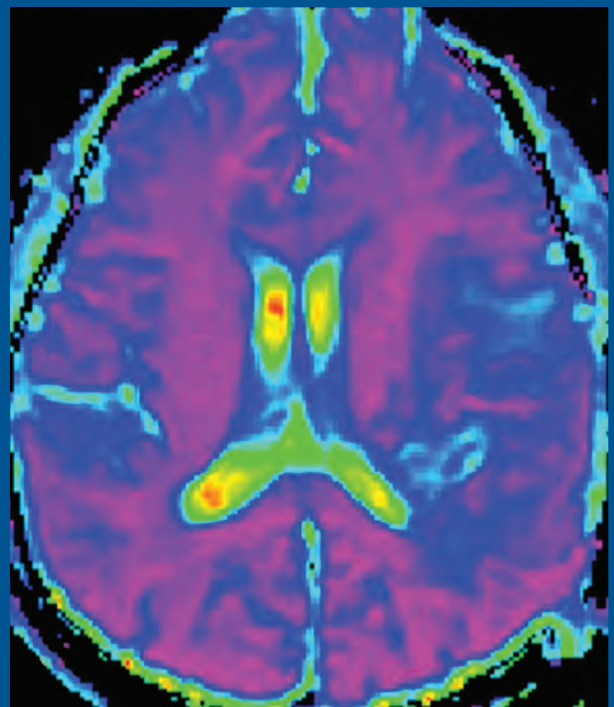
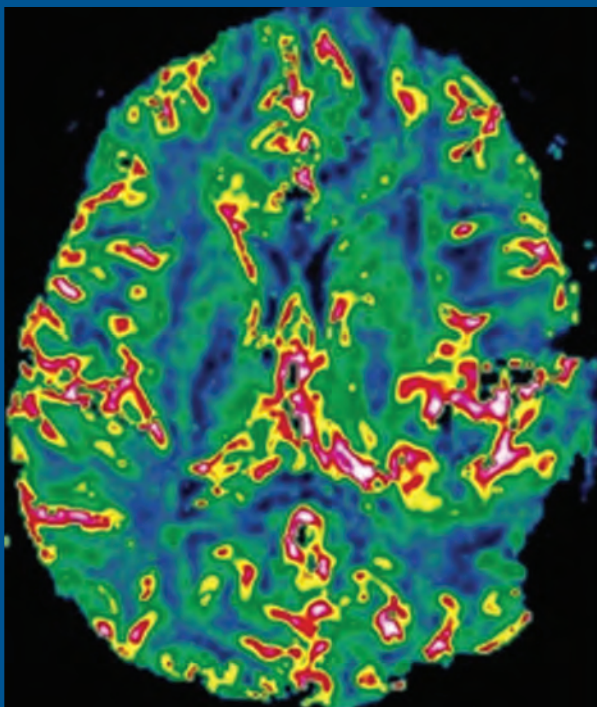
AMERICAN JOURNAL OF NEURORADIOLOGY

MARCH 2014
VOLUME 35
NUMBER 3
WWW.AJNR.ORG

THE JOURNAL OF DIAGNOSTIC AND
INTERVENTIONAL NEURORADIOLOGY

Neuroimaging of rapidly progressing dementias
Treatment complications of Solitaire
and Merci devices
CTA of carotid blowout

Official Journal ASNR • ASFNR • ASHNR • ASPNR • ASSR





MicroVention
TERUMO

Dedicated to the development

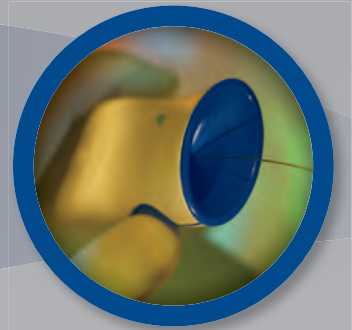
The MicroVention family of neuroendovascular products:

DELIVERY & DETACHMENT SYSTEMS

V-Trak

**V-Trak
Soft**

V-Grip



ACCESS PRODUCTS

Traxcess
Guidewire

Chaperon
Guiding Catheter

Headway
Microcatheter

**Headway
Duo!**
microcatheter

Scepter
*Occlusion Balloon
Catheter*



microvention.com

MICROVENTION, Headway, Chaperon, Traxcess, HydroFrame, HydroFill, HydroSoft, VFC, MicroPlex, Cosmos, HyperSoft, Scepter C, Scepter XC, V-Trak and V-Grip are registered trademarks of MicroVention, Inc. Scientific and clinical data related to this document are on file at MicroVention, Inc. Refer to Instructions for Use for additional information. Federal (USA) law restricts this device for sale by or on the order of a physician. © 2014 MicroVention, Inc. 2/14



0297

of innovative endovascular technologies



HYDROGEL COIL PRODUCTS

HydroFrame[®]
HydroCoil[®] Embolic System

HydroSoft[®]
HydroCoil[®] Embolic System

HydroFill[®]
HydroCoil[®] Embolic System



PLATINUM COIL PRODUCTS

MICROPLEX[®]
coil system

COSMOS[®]
complex coil

VFC[®]
Versatile Range Fill Coil

HYPERSOFT[®]
finishing coil



Introducing...

HyperSoft[®] **3D**
complex coil

The softness of the HyperSoft[®] Coil available in Complex Form!

Now you can Frame, Fill and Finish with the softness you need to match almost any aneurysm morphology.

MicroVention, Inc.
Worldwide Headquarters

1311 Valencia Avenue
Tustin, CA 92780 USA

MicroVention UK Limited

MicroVention Europe, S.A.R.L.

MicroVention Deutschland GmbH

PH +1.714.247.8000

PH +44 (0) 191 258 6777

PH +33 (1) 39 21 77 46

PH +49 211 210 798-0

ASNR 52ND ANNUAL MEETING & THE FOUNDATION OF THE ASNR SYMPOSIUM 2014

MAY 17-22 | Montreal ■ Palais des congrés de Montreal

ASNR 2014 PROGRAM CHAIR/PRESIDENT-ELECT - Gordon K. Sze, MD, FACR

THE FOUNDATION OF THE ASNR



The Foundation of the ASNR Symposium 2014: Inflammatory and Infectious Diseases of the CNS

SYMPOSIUM 2014:

- The Role of Inflammation and Infections in Stroke, Seizures, White Matter Diseases, etc.
- Advanced Imaging Techniques in the Evaluation of Inflammatory CNS Diseases
- Infectious Agents for Human Good: Oncolytic Viruses, Viral Vector Gene Therapy and Advanced Imaging

ADDITIONAL NEW EDUCATIONAL COURSE PROGRAM IN 2014 (concurrent program with the Symposium 2014): Inflammatory and Infectious Diseases

EDUCATIONAL COURSE 2014: with world class speakers including

- Anne G. Osborn, MD, Thomas P. Naidich, MD, Donald Resnick, MD, James G. Smirniotopoulos, MD, Jeffrey S. Ross, MD, Kelly K. Koeller, MD, FACR, David M. Yousem, MD, MBA, Laurie A. Loevner, MD, Peter M. Som, MD, Patricia A. Hudgins, MD, Robert D. Zimmerman MD, FACR, Hugh D. Curtin, MD, M. Judith Donovan Post, MD, FACR, and More...

JUST ADDED... ASNR Introduces Study Groups and Workshops, please visit the ASNR website for more information

- The study groups target areas of critical importance to the field of neuroradiology and are composed of neuroradiologists, neuroscientists, and investigators from associated disciplines, who are united in their interest in higher level, sophisticated investigations of these target areas.
- The workshops are intended to provide a hands-on experience that allows participants to translate knowledge learned at the ASNR meeting into direct experience that will enable them to perform these studies when they return to their practices.

ANNUAL MEETING:

- One-day **MINI SYMPOSIUM** on **TUMORS** - Organized by Girish M. Fatterpekar, MD, MBBS, DNB, Whitney B. Pope, MD, PhD and Gordon K. Sze, MD, FACR
- One-day **MINI SYMPOSIUM** on **STROKE** - Organized by Pina C. Sanelli, MD, MPH and Max Wintermark, MD
- Nobel Prize Laureate, Stanley Prusiner, MD, Keynote Speaker, on Prions and Alzheimer's Disease, Parkinson's Disease, and Other Neurodegenerative Disorders
- More "Hands-On" Experience Applicable to Your Practices
- Young Professionals Programming
- Expanded Self-Assessment Module (SAM) Session Programming Throughout the Week

PROGRAMMING DEVELOPED IN COOPERATION WITH THE...

- American Society of Functional Neuroradiology (ASFNR) David J. Mikulis, MD
- American Society of Head and Neck Radiology (ASHNR) Yoshimi Anzai, MD, MPH
- American Society of Pediatric Neuroradiology (ASPNR) Richard L. Robertson, MD
- American Society of Spine Radiology (ASSR) Meng Law, MD, MBBS, FRACR
- Society of NeuroInterventional Surgery (SNIS) Peter A. Rasmussen, MD



ASFNR ASHNR ASPNR ASSR SNIS

TO REQUEST PROGRAMMING AND REGISTRATION MATERIALS FOR THE ASNR 52ND ANNUAL MEETING, CONTACT:

ASNR 52ND ANNUAL MEETING

c/o American Society of Neuroradiology
800 Enterprise Drive, Suite 205
Oak Brook, Illinois 60523-4216

Phone: 630-574-0220
Fax: 630-574-0661
Email: meetings@asnr.org
Website: www.asnr.org/2014



Scan Now
to visit our website

AJNR

AMERICAN JOURNAL OF NEURORADIOLOGY

MARCH 2014
VOLUME 35
NUMBER 3
WWW.AJNR.ORG

Publication Preview at www.ajnr.org features articles released in advance of print. Visit www.ajnrblog.org to comment on AJNR content and chat with colleagues and AJNR's News Digest at <http://ajnrndigest.org> to read the stories behind the latest research in neuroimaging.

EDITORIALS

PERSPECTIVES

- 413 **Cold and Hot** *M. Castillo*

EDITORIALS

- 414 **Stretch-Resistant Coils for Intracranial Aneurysms: One Step Forward or Two Steps Back?** *W.J. van Rooij and M. Sluzewski*
- 416 **Will A Randomized Trial of Unruptured Brain Arteriovenous Malformations Change Our Clinical Practice?** *L. Pierot, J. Fiehler, C. Cognard, M. Söderman, and L. Spelle*

REVIEW ARTICLES

- 418 **Neuroimaging of Rapidly Progressive Dementias, Part 1: Neurodegenerative Etiologies** *A.J. Degnan and L.M. Levy*
- 424 **Neuroimaging of Rapidly Progressive Dementias, Part 2: Prion, Inflammatory, Neoplastic, and Other Etiologies** *A.J. Degnan and L.M. Levy*

EXPEDITED PUBLICATION

- 432 **WEB-DL Endovascular Treatment of Wide-Neck Bifurcation Aneurysms: Short- and Midterm Results in a European Study** *B. Lubicz, J. Klisch, J.-Y. Gauvrit, I. Szikora, M. Leonardi, T. Liebig, N.P. Nuzzi, E. Boccardi, F.D. Paola, M. Holtmannspötter, W. Weber, E. Calgiari, V. Sychra, B. Mine, and L. Pierot*

METHODOLOGIC PERSPECTIVES

- 439 **Utility of Diffusion Tensor Imaging in Evaluation of the Peritumoral Region in Patients with Primary and Metastatic Brain Tumors** *E.J. Sternberg, M.L. Lipton, and J. Burns*

PATIENT SAFETY

- 445 **Acute Intracranial Hemorrhage in CT: Benefits of Sinogram-Affirmed Iterative Reconstruction Techniques** *B. Bodelle, E. Klein, N.N.N. Naguib, R.W. Bauer, J.M. Kerl, F. Al-Butmeh, J.L. Wichmann, H. Ackermann, T. Lehnert, T.J. Vogl, and B. Schulz*
- 450 **Improved Quality and Diagnostic Confidence Achieved by Use of Dose-Reduced Gadolinium Blood-Pool Agents for Time-Resolved Intracranial MR Angiography** *S. Dehkharghani, J. Kang, and A.M. Saindane*

GENETICS VIGNETTE

- 457 **Genetics of Alzheimer Disease** *A.T. Rao, A.J. Degnan, and L.M. Levy*

 Indicates Editor's Choices selection

 Indicates Fellows' Journal Club selection

 Indicates open access to non-subscribers at www.ajnr.org

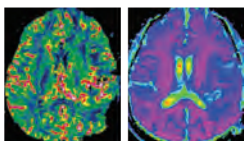
 Indicates article with supplemental on-line table

 Indicates article with supplemental on-line photo

 Indicates article with supplemental on-line video

 Indicates Evidence-Based Medicine Level 1

 Indicates Evidence-Based Medicine Level 2



Perfusion and D map obtained using intravoxel incoherent motion in recurrent tumor.

Go Green!

AJNR urges American Society of Neuroradiology members to reduce their environmental footprint by voluntarily suspending their print subscription.

The savings in paper, printing, transportation, and postage not only help members cut down on clutter, but go to fund new electronic enhancements and expanded content.

The digital edition of *AJNR* presents the print version in its entirety, along with extra features including:

- Publication Preview
- Case of the Week
- Podcasts
- Special Collections
- The *AJNR* Blog
- Weekly Poll

It also **reaches subscribers much faster than print**. An **electronic table of contents** will be sent directly to your mailbox to notify you as soon as it publishes.

Readers can **search, reference, and bookmark** current and archived content 24 hours a day on www.ajnr.org, rather than thumb through stacks of accumulated paper issues for articles and images they need.



<http://www.ajnr.org/cgi/feedback>

ASNR members who wish to opt out of print can do so by using the Feedback form on the *AJNR* Website (<http://www.ajnr.org/cgi/feedback>). Just type "Go Green" in the subject line to stop print and spare our ecosystem.

BRAIN

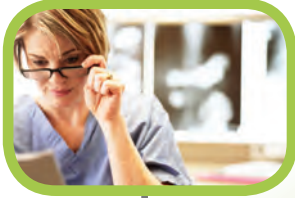
-   459 **Appropriate Use of CT Perfusion following Aneurysmal Subarachnoid Hemorrhage: A Bayesian Analysis Approach** *R.P. Killeen, A. Gupta, H. Delaney, C.E. Johnson, A.J. Tsiouris, J. Comunale, M.E. Fink, H.S. Mangat, A.Z. Segal, A.I. Mushlin, and P.C. Sanelli*
- 466 **Long Insular Artery Infarction: Characteristics of a Previously Unrecognized Entity** *A. Tamura, T. Kasai, K. Akazawa, Y. Nagakane, T. Yoshida, Y. Fujiwara, N. Kuriyama, K. Yamada, T. Mizuno, and M. Nakagawa*
-  472 **Toward Patient-Tailored Perfusion Thresholds for Prediction of Stroke Outcome** *A. Eilaghi, C.D. d'Esterre, T.Y. Lee, R. Jakubovic, J. Brooks, R.T.-K. Liu, L. Zhang, R.H. Swartz, and R.I. Aviv*
-  478 **Pretreatment Advanced Imaging in Patients with Stroke Treated with IV Thrombolysis: Evaluation of a Multihospital Data Base** *J.S. McDonald, J. Fan, D.F. Kallmes, and H.J. Cloft*
-  482 **Arterial Spin-Labeling Assessment of Normalized Vascular Intratumoral Signal Intensity as a Predictor of Histologic Grade of Astrocytic Neoplasms** *J. Furtner, V. Schöpf, K. Schewzow, G. Kasprian, M. Weber, R. Woitek, U. Asenbaum, M. Preusser, C. Marosi, J.A. Hainfellner, G. Widhalm, S. Wolfsberger, and D. Prayer*
-  490 **Histogram Analysis of Intravoxel Incoherent Motion for Differentiating Recurrent Tumor from Treatment Effect in Patients with Glioblastoma: Initial Clinical Experience** *H.S. Kim, C.H. Suh, N. Kim, C.-G. Choi, and S.J. Kim*
- 498 **Semiautomated Volumetric Measurement on Postcontrast MR Imaging for Analysis of Recurrent and Residual Disease in Glioblastoma Multiforme** *D.S. Chow, J. Qi, X. Guo, V.Z. Miloushev, F.M. Iwamoto, J.N. Bruce, A.B. Lassman, L.H. Schwartz, A. Lignelli, B. Zhao, and C.G. Filippi*
-     504 **Evaluation of Common Structural Brain Changes in Aging and Alzheimer Disease with the Use of an MRI-Based Brain Atrophy and Lesion Index: A Comparison Between T1WI and T2WI at 1.5T and 3T** *H. Guo, X. Song, R. Vandorpe, Y. Zhang, W. Chen, N. Zhang, M.H. Schmidt, and K. Rockwood, for the Alzheimer's Disease Neuroimaging Initiative*
-   513 **Volumetric Assessment of Optic Nerve Sheath and Hypophysis in Idiopathic Intracranial Hypertension** *J. Hoffmann, C. Schmidt, H. Kunte, R. Klingebiel, L. Harms, H.-J. Huppertz, L. Lüdemann, and E. Wiener*
- 519 **Accuracy of Postcontrast 3D Turbo Spin-Echo MR Sequence for the Detection of Enhanced Inflammatory Lesions in Patients with Multiple Sclerosis** *J. Hodel, O. Outteryck, E. Ryo, A.-L. Bocher, O. Lambert, D. Chéchin, H. Zéphir, A. Lacour, J.-P. Pruvo, P. Vermersch, and X. Leclerc*

INTERVENTIONAL *Published in collaboration with Interventional Neuroradiology*

-   524 **Complications of Endovascular Treatment for Acute Stroke in the SWIFT Trial with Solitaire and Merci Devices** *P.T. Akins, A.P. Amar, R.S. Pakbaz, and J.D. Fields, on behalf of the SWIFT Investigators*
-  529 **Endovascular Treatment of Middle Cerebral Artery Aneurysms with Flow Modification with the Use of the Pipeline Embolization Device** *K. Yavuz, S. Geyik, I. Saatci, and H.S. Cekirge*
-   536 **Mind the Gap: Impact of Computational Fluid Dynamics Solution Strategy on Prediction of Intracranial Aneurysm Hemodynamics and Rupture Status Indicators** *K. Valen-Sendstad and D.A. Steinman*

COMMENTARY

- 544 **Resolving the Issue of Resolution** *Y. Ventikos*
-  546 **Coiling of Large and Giant Aneurysms: Complications and Long-Term Results of 334 Cases** *N. Chalouhi, S. Tjoumakaris, L.F. Gonzalez, A.S. Dumont, R.M. Starke, D. Hasan, C. Wu, S. Singhal, L.A. Moukartzel, R. Rosenwasser, and P. Jabbour*



Simplify the MOC Process



Manage your CME Credits Online

CMEgateway.org

Available to Members of Participating Societies

American Board of Radiology (ABR)
American College of Radiology (ACR)
American Roentgen Ray Society (ARRS)
American Society of Neuroradiology (ASNR)
Commission on Accreditation of Medical
Physics Educational Programs, Inc. (CAMPEP)
Radiological Society of North America (RSNA)
Society of Interventional Radiology (SIR)
SNM
The Society for Pediatric Radiology (SPR)

It's Easy and Free!

Log on to CME Gateway to:

- View or print reports of your CME credits from multiple societies from a single access point.
- Print an aggregated report or certificate from each participating organization.
- Link to SAMs and other tools to help with maintenance of certification.

American Board of Radiology (ABR) participation!

By activating ABR in your organizational profile, your MOC-fulfilling CME and SAM credits can be transferred to your own personalized database on the ABR Web site.

Sign Up Today!

go to CMEgateway.org

- 553 **Socioeconomic Disparities in the Utilization of Mechanical Thrombectomy for Acute Ischemic Stroke in US Hospitals** W. Brinjikji, A.A. Rabinstein, J.S. McDonald, and H.J. Cloft

EXTRACRANIAL VASCULAR

- 557 **Intraplaque High-Intensity Signal on 3D Time-of-Flight MR Angiography Is Strongly Associated with Symptomatic Carotid Artery Stenosis** A. Gupta, H. Baradaran, H. Kamel, A. Mangla, A. Pandya, V. Fodera, A. Dunning, and P.C. Sanelli
-  562 **CT Angiography Findings in Carotid Blowout Syndrome and Its Role as a Predictor of 1-Year Survival** C.-W. Lee, C.-Y. Yang, Y.-F. Chen, A. Huang, Y.-H. Wang, and H.-M. Liu
- 568 **Multilevel Assessment of Atherosclerotic Extent Using a 40-Section Multidetector Scanner after Transient Ischemic Attack or Ischemic Stroke** L. Mechtouff, L. Bousset, S. Cakmak, J.-L. Lamboley, M. Bourhis, N. Boublay, A.-M. Schott, L. Derex, T.-H. Cho, N. Nighoghossian, and P.C. Douek

HEAD & NECK

- 573 **Clinical Significance of Trochlear Calcifications in the Orbit** K. Buch, R.N. Nadgir, A.D. Tannenbaum, A. Ozonoff, A. Fujita, and O. Sakai
- 578 **Prevalence of the Polar Vessel Sign in Parathyroid Adenomas on the Arterial Phase of 4D CT** M. Bahl, M. Muzaffar, G. Vij, J.A. Sosa, K. Roy Choudhury, and J.K. Hoang
-  582 **Combination Therapy Consisting of Ethanol and Radiofrequency Ablation for Predominantly Cystic Thyroid Nodules** H.M. Yoon, J.H. Baek, J.H. Lee, E.J. Ha, J.K. Kim, J.H. Yoon, and W.B. Kim

PEDIATRICS

-   587 **Left Hemisphere Diffusivity of the Arcuate Fasciculus: Influences of Autism Spectrum Disorder and Language Impairment** T.P.L. Roberts, K. Heiken, D. Zarnow, J. Dell, L. Nagae, L. Blaskey, C. Solot, S.E. Levy, J.I. Berman, and J.C. Edgar
-  593 **Regional Cerebral Blood Flow in Children From 3 to 5 Months of Age** A.F. Duncan, A. Caprihan, E.Q. Montague, J. Lowe, R. Schrader, and J.P. Phillips
- 599 **Brain MRI Measurements at a Term-Equivalent Age and Their Relationship to Neurodevelopmental Outcomes** H.W. Park, H.-K. Yoon, S.B. Han, B.S. Lee, I.Y. Sung, K.S. Kim, and E.A. Kim
- 604 **CT and MRI of Pediatric Skull Lesions with Fluid-Fluid Levels** S.A. Nabavizadeh, L.T. Bilaniuk, T. Feygin, K.V. Shekdar, R.A. Zimmerman, and A. Vossough

SPINE

- 609 **Frequency of Discordance between Facet Joint Activity on Technetium Tc99m Methylene Diphosphonate SPECT/CT and Selection for Percutaneous Treatment at a Large Multispecialty Institution** V.T. Lehman, R.C. Murphy, T.J. Kaufmann, F.E. Diehn, N.S. Murthy, J.T. Wald, K.R. Thielen, K.K. Amrami, J.M. Morris, and T.P. Maus

ONLINE FEATURES (www.ajnr.org)

LETTERS

- E3 **Comment on “Reproducibility of Cerebrospinal Venous Blood Flow and Vessel Anatomy with the Use of Phase Contrast–Vastly Undersampled Isotropic Projection Reconstruction and Contrast-Enhanced MRA”** F. Sisini, A. Taibi, M. Gambaccini, E. Menegatti, and P. Zamboni

BOOK REVIEWS R.M. Quencer, Section Editor

Please visit www.ajnrblog.org to read and comment on Book Reviews.

Letter from the President-Elect – Search for New *AJNR* Editor

In June, 2015, Mauricio Castillo, MD, FACR, will complete an eight-year term as the Editor-in-Chief of the *AJNR*. He follows a short list of illustrious neuroradiologists, from Dr. Juan Taveras to Dr. Michael Huckman to Dr. Robert Quencer to Dr. Robert Grossman.

One only has to pick up any random issue of the *AJNR* to realize what a tremendous mark Mauricio has made on the journal. His imprint starts on the first page of content with his column, Perspectives. Probing, erudite, at times very witty, and always brilliant, Mauricio turns out a monthly commentary on the state of neuroradiology, the state of our profession, and, at times, the state of the world. His references and quotations demonstrate a mind not only scientific and exacting but also knowledgeable in realms far beyond medicine.

Having worked with Mauricio very closely at the ASNR for the past two years, I can also attest to the fact that Mauricio is totally dedicated to the journal. At times, it seemed his reason for being. And the journal has benefitted immensely, in turn. From its look to its organization to the quality of the articles, Mauricio has brought the journal into the forefront of all radiology journals and it now ranks #2 in Impact Factor of all radiology journals. *AJNR* is the premier clinical neuroimaging journal with the highest circulation among all imaging-related subspecialty journals, publishing about 350 articles in 12 issues per year. It receives over 1400 original submissions annually and its Web site is accessed over 10 million times a year. In addition to the print version of the Journal, Mauricio also initiated its biannual Special Collections and monthly *AJNR* Digest. Other electronic activities which he began include its popular Case Collection (Case of the Week, Case of the Month, Classic Case, and Clinical Correlation), podcasts (editor's and fellows' journal club selections, traveling journal club, and Special Collections), and Fellows' Portal. With his international background, Mauricio has also been the ideal person to spread the word of the *AJNR* across the world. Finally, he has done all this and kept the journal in sound financial health through a period of difficult economic times.

Mauricio took over leadership of the journal at a time when the concept of the journal was beginning to enter a state of flux. One only has to look at your neighborhood newsstand to realize that this has been a time when many publications have been unable to adjust and have disappeared. In the past eight years, the demands on the journal have changed. Our current expectations are for instant gratification, not a lag time before publication. We require our information in more bite-size pieces, directed at us and easily accessible.

The new editor will face an even more rapidly evolving world. What is the future of radiology journals? We know that the *AJNR* will survive but in what form? What will be the best digital format? There will be an increased demand for electronic access and a further migration to tablets and smartphones. Preserving the brand of the *AJNR* will become more challenging. While in the past, publication was the end point, increasingly, publication today is the starting point, the beginning of an interactive discussion. How will this impact on the financial state of the journal, with decreasing print advertising? How will the *AJNR* respond to the demands of social media?

To assist the Executive Committee in the search for a new editor in these changing times, I will chair a search committee comprised, in part, of Tina Young-Poussaint, Chair of the Publications Committee, Laurie Lovner, Vice-President, Howard Rowley, Robert Quencer, Robert D. Zimmerman, James Barkovich, Tabbasum Kennedy, and some of the Senior Editors of the *AJNR*, Harry J. Cloft, Nancy Fischbein, Pamela W. Schaefer, Jody Tanabe, and Charles M. Strother, as well as James Gantenberg, Karen Halm, and Angelo Artemakis from the ASNR headquarters. The appointment of the new Editor-in-Chief will be announced in the spring of 2015.

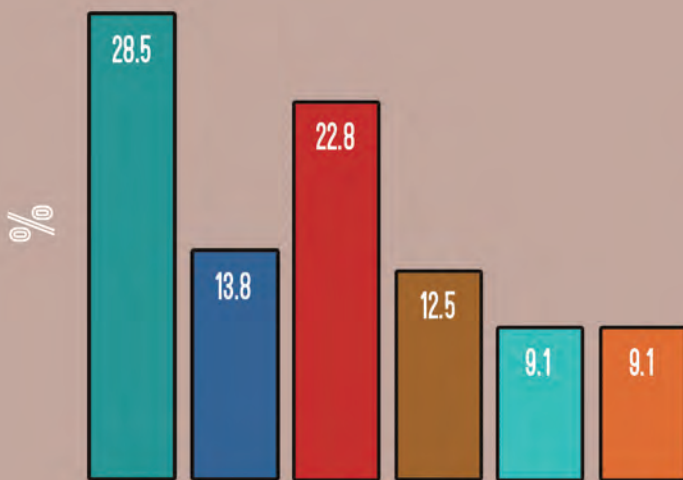
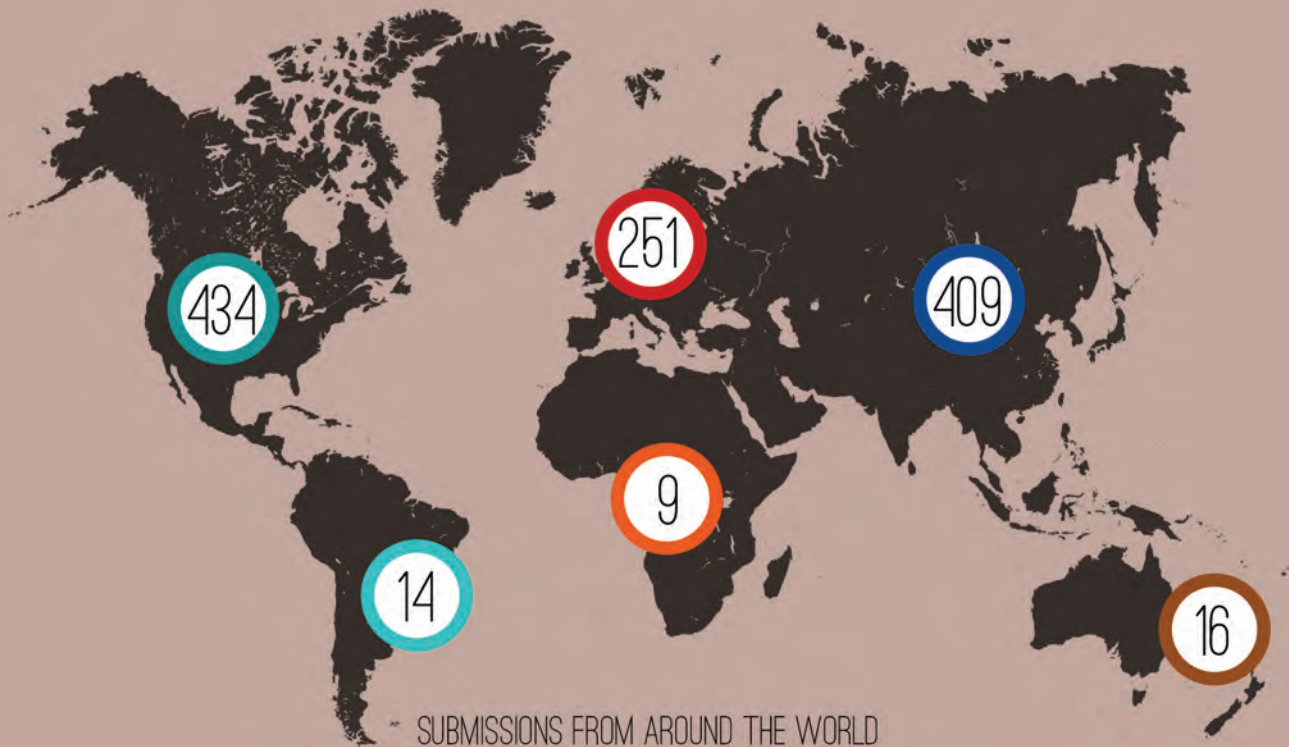
All interested physicians are invited to send their curriculum vitae and an introductory letter of intent to Dr. Gordon Sze, American Society of Neuroradiology, 800 Enterprise Drive, Suite 205, Oak Brook, IL, 60523 and via email to gordon.sze@yale.edu and jgantenberg@asnr.org. In addition, we welcome nominations of candidates from the ASNR membership. The deadline for receipt of submissions is August 1, 2014 but earlier submissions are welcome. A position description for the *AJNR* Editor and basic qualifications are posted at: www.ajnr.org/site/misc/eic-search-2015.xhtml.

Gordon Sze, MD, FACR
Chair, Editor-in-Chief Search Committee
President-Elect
American Society of Neuroradiology

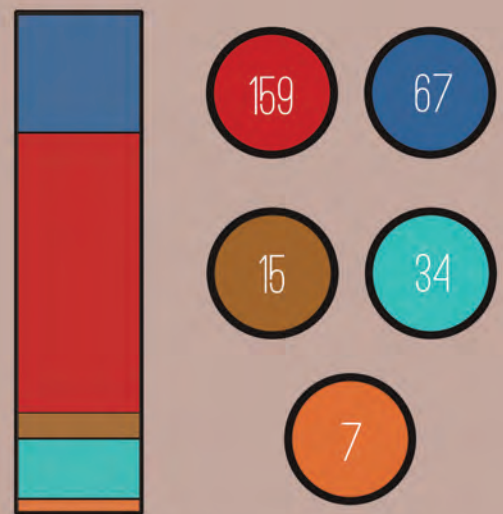
PUBLICATION METRICS

AMERICAN JOURNAL OF NEURORADIOLOGY

AN INTERNATIONAL JOURNAL



ACCEPTANCE RATE BY CONTINENT



INTERNATIONAL READERSHIP BY CONTINENT

MANUSCRIPT DATA

ORIGINAL RESEARCH & CLINICAL REPORT SUBMISSIONS
JANUARY 1, 2013 - DECEMBER 31, 2013

SUBSCRIBER DATA

PERSONAL NON-MEMBER SUBSCRIBERS
JANUARY 21, 2014

MAP BY
VECTORWORLDMAP.COM
Version 2.1
COPYRIGHT 2009, Graphics Factory CC

This map may be freely used for any purpose. This map may be modified and redistributed. If redistributed as is, we require that this copyright notice is redistributed with the map.

Official Journal:

American Society of Neuroradiology
American Society of Functional Neuroradiology
American Society of Head and Neck Radiology
American Society of Pediatric Neuroradiology
American Society of Spine Radiology

EDITOR-IN-CHIEF

Mauricio Castillo, MD

Professor of Radiology and Chief, Division of Neuroradiology, University of North Carolina, School of Medicine, Chapel Hill, North Carolina

SENIOR EDITORS

Harry J. Cloft, MD, PhD

Professor of Radiology and Neurosurgery, Department of Radiology, Mayo Clinic College of Medicine, Rochester, Minnesota

Nancy J. Fischbein, MD

Professor of Radiology, Otolaryngology-Head and Neck Surgery, Neurology, and Neurosurgery and Chief, Head and Neck Radiology, Department of Radiology, Stanford University Medical Center, Stanford, California

Jeffrey S. Ross, MD

Staff Neuroradiologist, Barrow Neurological Institute, St. Joseph's Hospital, Phoenix, Arizona

Pamela W. Schaefer, MD

Clinical Director of MRI and Associate Director of Neuroradiology, Massachusetts General Hospital, Boston, Massachusetts, and Associate Professor, Radiology, Harvard Medical School, Cambridge, Massachusetts

Charles M. Strother, MD

Professor of Radiology, Emeritus, University of Wisconsin, Madison, Wisconsin

Jody Tanabe, MD

Professor of Radiology and Psychiatry, Chief of Neuroradiology, University of Colorado, Denver, Colorado

EDITORIAL BOARD

Ashley H. Aiken, *Atlanta, Georgia*
A. James Barkovich, *San Francisco, California*
Walter S. Bartynski, *Charleston, South Carolina*
Barton F. Branstetter IV, *Pittsburgh, Pennsylvania*
Jonathan L. Brisman, *Lake Success, New York*
Julie Bykowski, *San Diego, California*
Donald W. Chakeres, *Columbus, Ohio*
Alessandro Cianfoni, *Lugano, Switzerland*
Colin Derdeyn, *St. Louis, Missouri*
Rahul S. Desikan, *San Diego, California*
Richard du Mesnil de Rochemont, *Frankfurt, Germany*
Clifford J. Eskey, *Hanover, New Hampshire*
Massimo Filippi, *Milan, Italy*
David Fiorella, *Cleveland, Ohio*
Allan J. Fox, *Toronto, Ontario, Canada*
Christine M. Glastonbury, *San Francisco, California*

John L. Go, *Los Angeles, California*
Wan-Yuo Guo, *Taipei, Taiwan*
Rakesh K. Gupta, *Lucknow, India*
Lotfi Hacein-Bey, *Sacramento, California*
David B. Hackney, *Boston, Massachusetts*
Christopher P. Hess, *San Francisco, California*
Andrei Holodny, *New York, New York*
Benjamin Huang, *Chapel Hill, North Carolina*
Thierry A.G.M. Huisman, *Baltimore, Maryland*
George J. Hunter, *Boston, Massachusetts*
Mahesh V. Jayaraman, *Providence, Rhode Island*
Valerie Jewells, *Chapel Hill, North Carolina*
Timothy J. Kaufmann, *Rochester, Minnesota*
Kenneth F. Layton, *Dallas, Texas*
Ting-Yim Lee, *London, Ontario, Canada*
Michael M. Lell, *Erlangen, Germany*
Michael Lev, *Boston, Massachusetts*
Karl-Olof Lovblad, *Geneva, Switzerland*
Lisa H. Lowe, *Kansas City, Missouri*
Franklin A. Marden, *Chicago, Illinois*
M. Gisele Matheus, *Charleston, South Carolina*
Joseph C. McGowan, *Merion Station, Pennsylvania*
Kevin R. Moore, *Salt Lake City, Utah*
Christopher J. Moran, *St. Louis, Missouri*
Takahisa Mori, *Kamakura City, Japan*

Suresh Mukherji, *Ann Arbor, Michigan*
Amanda Murphy, *Toronto, Ontario, Canada*
Alexander J. Nemeth, *Chicago, Illinois*
Laurent Pierot, *Reims, France*
Jay J. Pillai, *Baltimore, Maryland*
Whitney B. Pope, *Los Angeles, California*
M. Judith Donovan Post, *Miami, Florida*
Tina Young Poussaint, *Boston, Massachusetts*
Joana Ramalho, *Lisbon, Portugal*
Otto Rapalino, *Boston, Massachusetts*
Álex Rovira-Cañellas, *Barcelona, Spain*
Paul M. Ruggieri, *Cleveland, Ohio*
Zoran Rumboldt, *Charleston, South Carolina*
Amit M. Saindane, *Atlanta, Georgia*
Erin Simon Schwartz, *Philadelphia, Pennsylvania*
Aseem Sharma, *St. Louis, Missouri*
J. Keith Smith, *Chapel Hill, North Carolina*
Maria Vittoria Spampinato, *Charleston, South Carolina*
Gordon K. Sze, *New Haven, Connecticut*
Krishnamoorthy Thamburaj, *Hershey, Pennsylvania*
Kent R. Thielen, *Rochester, Minnesota*
Cheng Hong Toh, *Taipei, Taiwan*
Thomas A. Tomsick, *Cincinnati, Ohio*
Aquila S. Turk, *Charleston, South Carolina*
Willem Jan van Rooij, *Tilburg, Netherlands*
Arastoo Vossough, *Philadelphia, Pennsylvania*
Elysa Widjaja, *Toronto, Ontario, Canada*
Max Wintermark, *Charlottesville, Virginia*
Ronald L. Wolf, *Philadelphia, Pennsylvania*
Kei Yamada, *Kyoto, Japan*

EDITORIAL FELLOW

Falgun H. Chokshi, *Atlanta, Georgia*

YOUNG PROFESSIONALS ADVISORY COMMITTEE

Asim K. Bag, *Birmingham, Alabama*
Anna E. Nidecker, *Sacramento, California*
Peter Yi Shen, *Sacramento, California*

HEALTH CARE AND SOCIOECONOMICS EDITOR

Pina C. Sanelli, *New York, New York*

Founding Editor

Juan M. Taveras

Editors Emeriti

Robert I. Grossman, Michael S. Huckman,
Robert M. Quencer

Special Consultants to the Editor

Sandy Cheng-Yu Chen, Girish Fatterpekar,
Ryan Fitzgerald, Yvonne Lui,
Louise M. Henderson, Greg Zaharchuk

INR Liaisons

Timo Krings, Karel terBrugge

Managing Editor

Karen Halm

Electronic Publications Manager

Jason Gantenberg

Editorial Assistant

Mary Harder

Executive Director, ASNR

James B. Gantenberg

Director of Communications, ASNR

Angelo Artemakis

AJNR (Am J Neuroradiol ISSN 0195-6108) is a journal published monthly, owned and published by the American Society of Neuroradiology (ASNR), 800 Enterprise Drive, Suite 205, Oak Brook, IL 60523. Annual dues for the ASNR include \$170.00 for journal subscription. The journal is printed by Cadmus Journal Services, 5457 Twin Knolls Road, Suite 200, Columbia, MD 21045; Periodicals postage paid at Oak Brook, IL and additional mailing offices. Printed in the U.S.A. POSTMASTER: Please send address changes to American Journal of Neuroradiology, P.O. Box 3000, Denville, NJ 07834, U.S.A. Subscription rates: nonmember \$370 (\$440 foreign) print and online, \$300 online only; institutions \$430 (\$495 foreign) print and basic online, \$850 (\$915 foreign) print and extended online, \$355 online only (basic), extended online \$770; single copies are \$35 each (\$40 foreign). Indexed by PubMed/Medline, BIOSIS Previews, Current Contents (Clinical Medicine and Life Sciences), EMBASE, Google Scholar, HighWire Press, Q-Sensei, RefSeek, Science Citation Index, and SCI Expanded. Copyright © American Society of Neuroradiology.



Cold and Hot

M. Castillo, *Editor-in-Chief*

Most healthy human beings maintain a core temperature of 37.0°C (98.6°F) regardless of surrounding environmental conditions. Of course, our temperature normally varies slightly throughout the day and night, and this depends on when, how, and where one measures it. Normal human temperature fluctuations tend to be of about 0.5°C up or down. A healthy human being is said to be “normothermic” or “euthermic.”¹ Our temperature fluctuates with the circadian cycle as in all other living organisms (circadian rhythms occur in 24-hour cycles [circa = around and dian = day]), and in this way, our bodies can keep track of the duration of normal days over our life span.²

The circadian clock is regulated mostly by daylight, and when in dark and/or cold environments, organisms compensate by altering their temperatures. Retinal stimulation by daylight is directly transmitted to the suprachiasmatic nuclei in the hypothalamus, which regulates temperature.³ When our temperature increases, hypothalamic neurons induce sweating and cutaneous vasodilation to dissipate heat. When we get cold, the hypothalamus does the opposite and induces shivering that increases heat production. Thirst is also controlled by the hypothalamus, so if our temperature increases, we lose fluids and increase our serum sodium level. Osmotic receptors in the supraoptic nuclei not only tell our cerebral cortex that we need to drink water but stimulate the neurohypophysis to produce an antidiuretic hormone that directly acts on the renal glomeruli, increasing water reabsorption.* Thirst control involves the fore- and hindbrain (especially the area postrema). As serum concentration of sodium increases, phylogenetically ancient brain regions (the cingulate gyrus, third ventricle, orbitofrontal regions, thalami, midbrain, and hypothalamus) become activated on fMRI.⁴

Our temperature is lowest about 2–3 hours before waking up, so it is not surprising that during the wee hours of the night we commonly reach for our covers. Conversely, our temperature is higher in the late afternoon (and this is why fever and malaise peak at this time when sick). Sleep deprivation, even short-term, lowers our body temperature, and I remember feeling cold on the days after I had been up all night as an intern and sitting in the sun to warm up. The endogenous substances that most affect our circadian cycle are hormones, and temperature variations induced by them have been used to predict ovulation during the normal menstrual cycle (also called the circamensal cycle [circa = around, mensa = month]). Contraceptives suppress the circamensal cycle and result in elevations of temperature of about 0.5°C throughout the entire month.

*NB: I recommend the following wonderful review dealing with issues related to thirst: McKinley MJ, Johnson AK. *The physiologic regulation of thirst and fluid intake.* *News Physiol Sci* 2004;19:1–6.

<http://dx.doi.org/10.3174/ajnr.A3576>

As mentioned previously, our temperature is highest in the afternoons when it reaches about 37.7°C. Anything above this threshold is considered as fever. Under normal conditions, our bodies are capable of dissipating heat to just about 40.0°C, and above this threshold, one enters the state of hyperthermia and starts to develop severe headache and altered mental status. Severe and prolonged hyperthermia results in a heat stroke. Neurologic abnormalities induced by heat stroke involve the brain (especially the basal ganglia and thalami), cerebellum, anterior horn cells in the spinal cord, and peripheral nerves.⁵ Hemorrhages in the external capsule and medial thalami may occur. In the cerebellum, the Purkinje cells are especially sensitive to heat, and patients with hyperthermia may later develop chronic cerebellar atrophy.⁶

The opposite extreme is hypothermia, which is defined as a drop of 2.0°C in body temperature (we begin to shiver at about 36.0°C). Hypothermia is generally due to exposure to inclement weather or is induced for medical procedures. Protective hypothermia is mainly used for the treatment of neonatal encephalopathy, cardiac arrest, neurogenic fever, and more recently brain and spinal cord trauma. For these conditions, the goal is to reach 33.0°C, with the hope that slowing cellular metabolism will be neuroprotective. Lower temperatures inhibit the influx of ions (noticeably calcium) into cells, avoid oxidative stress, decrease free radical production, and, finally, prevent apoptosis. Cooling may be achieved via invasive means (catheters that pump cold saline solution into veins) or noninvasively (water blankets and cool caps that contain crylon gel at –30°C). Cool caps are used for neonatal encephalopathy but also for less serious problems such as alopecia induced by chemotherapy (in the latter, the cold results in decreased scalp blood flow protecting the hair follicles).⁷ In an intriguing new article published in the *American Journal of Neuroradiology (AJNR)*, the authors used catheters placed in the subarachnoid space of swine to cool down the spinal cord without cooling the entire body.⁸ This and other similar experiments have shown that the technique is feasible and may spare complications induced by whole-body hypothermia.

We humans detect temperature changes due to stimulation of our peripheral thermoreceptors found in the skin and mucosa. These receptors are nerve fibers that work in tandem—that is, when exposed to cold, delta fast-speed fibers fire more than the slower C-fibers that are sensitive to heat, but both work simultaneously and the perception of temperature depends on the proportion of each type of fiber that is activated. These fibers enter the spinal cord and ascend in the spinothalamic tracts to the posterolateral thalamic nuclei. From there, the stimuli reach a collection of organs and nuclei best known as the hypothalamus.

Time for an anecdote: Years ago the Chief of Neurosurgery and I decided to seal a CSF leak due to a previous transsphenoidal pituitary adenoma resection with liquid fibrin glue. Under CT guidance, we proceeded to place a needle through the nose of the patient into the breached sellar floor and started injecting the glue. The patient immediately became severely hypothermic, and a

control CT showed that our needle was too deep and the glue had reached the hypothalamus. The patient spent a week in the intensive care unit, and though he completely recovered, it still gives me goose bumps to think about it.

There is no consensus about the most comfortable temperature. The way we perceive temperature has a lot to do with the humidity accompanying it. For example, if the humidity is 0%, 24°C will feel like 21°C, while with a 100% humidity, 24°C will feel like 27°C. The most comfortable humidity levels are between 40% and 50% (levels also said to prevent upper respiratory tract infections). In places with extreme outside temperature variations, it is recommended that inside temperatures be kept at 21°–23°C (69°–73°F).⁹ In the United States, the Occupational Safety and Health Administration recommends a range of 20.5°–24.5°C (68°–76°F) and humidity between 20% and 60% at workplaces.¹⁰ Another anecdote: Upon arriving in Panama City, my colleague and friend, Dr Ilka Guerrero asked me if I had brought a sweater because the city was about the coldest place on earth. After entering my hotel, I understood what she meant. Air conditioning thermostats were kept at 16°C (62°F). Those of us who grew up elsewhere in warmer latitudes never cease to be amazed by how cold buildings are kept in the United States (they are even colder in the United Kingdom where regulations dictate temperature at the workplace be “reasonable”—that is, 16°C (61°F))¹¹

Cold inside buildings is a luxury, and it has been documented that the most expensive stores (Hermes, 20°C) are kept colder than the least expensive ones (Old Navy, 27°C).¹² Apparently colder spaces encourage us to buy more and also save electricity. We radiologists must work in cold environments because computers and monitors (not to forget the view boxes of the past) generate a lot of heat and reading rooms can only be kept comfortable by lowering the thermostat. Work productivity is better at stable and slightly lower temperatures¹³ but colder temperatures are uncomfortable and the New York Public Library allows their workers to accrue compensatory time when its temperature drops below 20°C (68°F).

It is a common belief that heavier individuals are more sensitive to heat (and conversely will feel cold to the touch), while skinny ones are sensitive to cold (but will be hot to the touch). Subcutaneous fat serves as an insulator, but women, who as a general rule have more of it, are more sensitive to cold than men.¹⁴ Malnourished individuals with little fat may experience hypothermia in temperatures of only 15°–18°C.¹⁵ An intriguing observation is that hot and cold result in nearly identical brain responses. (When ice first arrived in Maconda in Garcia Marquez’s *One Hundred Years of Solitude*, people could not tell if it was hot or cold.) With fMRI, the response to noxious hot and cold stimulation was studied, and it was shown that extreme temperatures both activated similar networks.¹⁶ While this study and others confirm the activation of unified neural networks for different intensities of temperature, other studies show that the perception of pleasantness or unpleasantness associated with temperature changes occurs in different brain regions.¹⁷ More or less neuronal firing in these areas occurs as temperature changes.

Our feeling of well-being is tied to what we believe is a comfortable temperature, and some of our activities are immediately associated with temperature. Reading by a source of warmth such as a fireplace comes to mind except when it comes to *AJNR*, which I think can be read when it is cold or hot.

REFERENCES

1. Human body temperature. http://en.wikipedia.org/wiki/Human_body_temperature. Accessed February 21, 2013
2. Circadian rhythm. http://en.wikipedia.org/wiki/Circadian_rhythm. Accessed February 21, 2013
3. Hypothalamus. <http://www.neuroanatomy.wisc.edu/coursebook/neuro2%282%29.pdf>. Accessed February 21, 2013
4. Denton D, Shade R, Zamariippa F, et al. **Neuroimaging of genesis and satiation of thirst and the interceptor-driven theory of origins of primary consciousness.** *Proc Natl Acad Sci U S A* 1999;96:5304–09
5. McLaughlin CT, Kane AG, Auber AE. **MR imaging of heat stroke: external capsule and thalamic T1 shortening and cerebellar injury.** *AJNR Am J Neuroradiol* 2003;24:1372–75
6. Albukrek D, Bakon M, Moran DS, et al. **Heat stroke-induced cerebellar atrophy: clinical course—CT and MR findings.** *Neuroradiology* 1997;39:195–97
7. Hypothermia cap. http://en.wikipedia.org/wiki/Hypothermia_cap. Accessed February 21, 2013
8. Purdy PD, Navakovic RL, Giles BP, et al. **Spinal cord hypothermia without systemic hypothermia.** *AJNR Am J Neuroradiol* 2013; 34:252–56
9. Canadian Centre for Occupational Health and Safety. Thermal comfort for office work. http://www.ccohs.ca/oshanswers/phys_agents/thermal_comfort.html. Accessed February 21, 2013
10. United States Department of Labor. Office temperature/humidity. http://www.osha.gov/pls/oshaweb/owadisp.show_document?p_table=INTERPRETATIONS&p_id=24602. Accessed February 21, 2013
11. Buettner R. **In New York City, a chilly library has its rewards.** *The New York Times*. http://www.nytimes.com/2010/01/12/nyregion/12libraries.html?_r=0. Accessed March 11, 2013
12. Salkin A. **Shivering for luxury.** *The New York Times*. June 26, 2005. <http://www.nytimes.com/2005/06/26/fashion/sundaystyles/26air.html>. Accessed March 11, 2013
13. Salmon R. **Air-conditioning made this debate possible.** *The New York Times*. <http://www.nytimes.com/roomfordebate/2012/06/21/should-air-conditioning-go-global-or-be-rationed-away/air-conditioning-made-this-debate-possible>. Accessed March 11, 2013
14. Fillingim RB, Maixner W, Kincaid S, et al. **Sex differences in temporal summation but not sensory-discriminative processing of thermal pain.** *Pain* 1998;75:121–27
15. Human biological adaptability: an overview. http://anthro.palomar.edu/adapt/adapt_1.htm. Accessed February 21, 2013
16. Tracey I, Becerra L, Chang I, et al. **Noxious hot and cold stimulation produce common patterns of brain activation in humans: a functional magnetic resonance imaging study.** *Neurosci Lett* 2000; 288:159–62
17. Rolls E, Graberhorst F, Parris BA. **Warm pleasant feelings in the brain.** *Neuroimage* 2008;41:1504–13

EDITORIAL

Stretch-Resistant Coils for Intracranial Aneurysms: One Step Forward or Two Steps Back?

W.J. van Rooij
M. Sluzewski

Endovascular treatment of cerebral aneurysms was boosted by the introduction of the Guglielmi detachable coil system (Boston Scientific, Natick, Massachusetts) in 1991. The concept of

“detachability” made the selective placement of long coils into the lumen of an aneurysm much safer: Inserted coils could be repositioned when needed or even withdrawn and replaced by another coil. When the position of the coil in the aneurysm was satisfactory, the coil could be electrolytically detached. Occasionally, operators experienced unintended unraveling of the primary coil winding, on withdrawal or retrieval of the coil. This unraveling of the proximal part of the coil could occur when the distal part was stuck inside the mesh of previously inserted coils. An unraveled coil cannot be repositioned, and further withdrawal either leads to the removal of the remaining part of the coil or to coil fracture, resulting in thrombogenic coil material left in normal cerebroper-
 etal vessels.

To solve this technical problem of coil unraveling and fracture, manufacturers built in a filament centrally in the primary winding of the coil. The filament was made of nitinol, polyglycolic acid, or polypropylene and was attached to the proximal and distal ends of the coil. These coils were called stretch-resistant (SR) coils. In these SR coils, the force of withdrawal is transmitted by the inner filament and not by the wound coil wire itself. The concept of stretch resistance appealed to many operators and manufacturers, and all manufacturers currently have ranges of SR coils.

However, later it was suggested from clinical and experimental studies^{1,2} that the SR filament had a negative influence on the physical properties of the coil, such as coil softness, shape memory, and flexibility. In the experimental study of Miyachi et al,² various types of SR coils caused hardening and straightening of the last few millimeters of the coil. The straightening phenomenon was due to relative SR line shortening and subsequent condensation of pitches of the first loops at the coil end. Coil tail flexibility was lost, and the SR coil for the last part behaved like a stiff wire. This straightening of the last few centimeters of the coil caused catheter kickback and thus progressive difficulty in inserting the final part of the coil. This technical issue was specific to SR coils and did not occur with standard coils.

When the last part of the coil is straightened and cannot be placed inside the aneurysm, the coil has to be withdrawn. With more manipulation, the risk of complications increases. In addition, the handling drawback of SR coils may also result in placement of fewer coils in comparison with standard coils and thus in lower packing attenuations and possibly more recurrences at follow-up. To test the hypothesis of lower packing attenuations obtained with SR coils by impaired handling, we compared the packing attenuations of 74 aneurysms treated with newly introduced SR Galaxy coils (Codman & Shurtleff, Raynham, Massachusetts) with those of 74 volume-matched aneurysms treated with standard Trufill/Orbit coils (Codman & Shurtleff) (Table). The recently introduced SR Galaxy coils only differ from the standard coils in the presence of the SR filament; all other properties are equal.³ The mean packing of aneurysms treated with standard coils was 29.3%, and the mean packing of aneurysms treated with new SR Galaxy coils was 25.7%. This difference of 3.6 percentage points was statistically significant ($P = .0021$).

The result of this comparison confirmed our personal and subjective experience in the handling properties of the 2 compared coil types. Standard coils produce less catheter kickback, are less stiff, and are easier to deliver. While oversizing of the first coil

Clinical and aneurysm characteristics of 74 aneurysms treated with Galaxy stretch-resistant coils and 74 volume-matched controls treated with standard Trufill/Orbit coils

	Galaxy	Trufill/Orbit	P Value (t test)
No. of aneurysms	74	74	
Women/men	55:19	45:29	
Median age (yr)	57	50.5	
Anterior circulation	63	57	
Posterior circulation	11	17	
Ruptured/unruptured	62/12	58/16	
Procedural morbidity	2	0	
No. of angiographic follow-ups	58	62	
Additional treatment	4	3	
Aneurysm volume (mm ³)			
Mean	110	111	.98
Median	75	74	
SD	110	107	
Aneurysm size (mm)			
Mean	5.8	6.4	
Median	6	6	
Range	3–21	3–18	
Packing attenuation (%)			
Mean	25.7	29.3	.0021
Median	25	28.5	
SD	7.0	6.9	

is mostly possible with standard coils, with the new SR Galaxy coils, undersizing is imperative to accommodate the first coil. The better handling properties of the standard coils, therefore, result in higher packing attenuations. In our view, the importance of packing attenuation is 3-fold: First, the relation of high packing attenuation and stable aneurysm occlusion at follow-up has been firmly established. Therefore, it is sensible to place as many coils as possible in a cerebral aneurysm. Second, packing attenuation is the only objective parameter available in comparing the handling performance of different types of coils. Finally, high packing attenuations reflect the ease of use and therefore safety: When coils can be easily and quickly placed inside an aneurysm, the procedure is effective and safe. On the other hand, when coils are difficult to place with repeated catheter kickbacks, the operator will likely, after a period of several futile attempts, withdraw the final coil resulting in lower packing attenuation and increased risk of complications due to microcatheter manipulations.

Although both experimental and clinical data indicate better handling and thus better obtained packing attenuations for the standard coils, most coils available on the market are stretch-resistant. Apparently, the fear of unintended stretching and unraveling of coils during withdrawal generally outweighs the impaired handling. In balancing the pros and cons of stretch resistance, one should know the frequency and impact of the stretching phenomenon. However, there are no data on the incidence of this technical problem and its clinical implications. In our experience, stretching and unraveling on withdrawal of the standard coils can be largely avoided. First, if friction is encountered during delivery of a coil, it is unsafe to try to force the coil into the aneurysm: The coil may be damaged or kinked. When withdrawal is then necessary, unraveling is likely to occur (forced in = stretched out). Second, if a coil has to be withdrawn, it is better to withdraw the microcatheter first for a few millimeters to align the coil with the catheter without kinking at the tip. Third,

when an aneurysm is completely occluded, it is not necessary to try to force another (“last”) coil in, with subsequent risk of the need for retrieval.

With these technical precautions, unraveling of a coil during withdrawal will be rare. We believe that the drawback of possible coil stretching and unraveling in standard coils without stretch resistance is only a minor clinical issue that is outweighed by the shortcomings of the SR filament in terms of handling, safety, and obtained packing attenuation.

Standard coils are hardly available on the market any more. We plead for a renewed appreciation of the better physical properties of standard coils without SR filaments, so that operators can choose between standard or SR coils in every coil type.

REFERENCES

1. Kwon OK, Han MH, Lee KJ, et al. **Technical problems associated with new designs of Guglielmi detachable coils.** *AJNR Am J Neuro-radiol* 2002;23:1269–75
2. Miyachi S, Izumi T, Matsubara N, et al. **The mechanism of catheter kickback in the final stage of coil embolization for aneurysms: the straightening phenomenon.** *Interv Neuroradiol* 2010;16:353–60
3. Khaldi A, Fargen KM, Waldau B, et al. **The Orbit Galaxy XTRASOFT Coils: a multicenter study of coil safety and efficacy in both ruptured and unruptured cerebral aneurysms.** *J Vasc Interv Neurol* 2012;5:17–21

EDITORIAL

Will A Randomized Trial of Unruptured Brain Arteriovenous Malformations Change Our Clinical Practice?

L. Pierot, J. Fiehler, C. Cognard, M. Söderman, and L. Spelle

A Randomized Trial of Unruptured Brain Arteriovenous malformations (ARUBA) was stopped on April 15, 2013, because of the superiority of the medical management group.¹ We congratulate the ARUBA investigators for designing this trial and being able to include 223 patients.

The ARUBA study was designed to determine whether medical management is superior or noninferior to interventional therapy for the prevention of the composite outcome of death from any cause or symptomatic stroke in the management of unruptured brain arteriovenous malformations (bAVMs), and whether it decreases the risk of death or clinical impairment (modified Rankin Scale score of ≥ 2) at 5-year postrandomization. The evaluation of the interventional treatment efficacy for bAVM was not an aim of the study.

The primary end point (death or symptomatic stroke) was reached in 10% of patients in the medical management group and in 31% in the interventional therapy group (hazard ratio, 0.27). Unfortunately, the causes of death (AVM-related or not) were not given. “Stroke” was defined as “a clinically symptomatic event (any new focal neurologic deficit, seizure, or new-onset headache)

that was associated with imaging findings of hemorrhage or ischemia.”¹ Unfortunately, the respective percentage of patients with new focal neurologic deficit, seizure, or new-onset-headache was not given. Imaging findings were also not precisely described, and the respective number of patients with subarachnoid hemorrhage, intraventricular hemorrhage, and parenchymal hematoma was not given. Ischemic lesions were also not described. Due to the absence of these data, a precise analysis of the primary end point is nearly impossible. Additionally, it is also not possible to correlate the primary end point with the 36-month risk of death and neurologic disability because no specific information was provided. In the limited number of patients (87) with 36 months’ follow-up, the risk of death and neurologic disability (modified Rankin Scale score of ≥ 2) was significantly lower for the medical management (14%) compared with the interventional therapy (39%) group.

Brain AVMs represent a very heterogeneous group with regard to clinical presentation (hemorrhage, seizures, headache, focal neurologic deficit), anatomic characteristics (feeding arteries, nidus, draining veins), and modalities of treatment (surgery, radiation therapy, embolization, or combination of modalities).^{2–4} For unruptured bAVMs, the strategy of treatment is a matter of debate because the balance between therapeutic risks and the risk of natural history is difficult to determine and is dependent on several factors, including the ones mentioned above.^{2,5}

In certain bAVM subgroups with specific anatomic characteristics (ie, deep location or deep venous drainage), the risk of bleeding is higher, thus requiring specific treatment strategies or modalities. However, the clinical outcomes even within a subgroup of patients will vary depending on the treatment strategies used because strategy differs as to the mode of action and complication type and rate.

Indeed, one shortcoming of the study design was inclusion of a heterogeneous population of AVM types and their treatment options. The AVM population included 62% of AVMs smaller than 30 mm; diverse Spetzler-Martin-grade AVMs, including 29% grade 1, 32% grade 2, 28% grade 3, and 10% grade 4; associated aneurysms in 16%; and any deep venous drainage in 33% of cases. Furthermore, the treatment modalities were quite heterogeneous: neurosurgery alone (5%); embolization alone (32%); radiation therapy alone (33%); embolization and neurosurgery (12%); embolization and radiation therapy (16%); and, finally, embolization, neurosurgery, and radiation therapy combined (1%). No details were given regarding the precise modalities of treatment (glue or Onyx [Covidien, Irvine, California] for embolization; gamma knife or linear accelerator for radiation therapy). By study design and due to the relatively small population included in the trial before stopping, subgroup analyses will not be conducted.

Therefore, the ARUBA trial data suggest that in a very heterogeneous population of patients with AVM with a mix of different therapeutic approaches, there is a higher short-term risk of death or stroke. However, the generalizability of ARUBA results is quite debatable.

Thirty-nine active centers recruited 226 patients during 6 years, with an average rate of inclusion of 1 patient/center/year. Among the 39 active sites, 7 (18%) included >10 patients; 7

(18%) included 5–10 patients; and 25 (64%) included <5 patients during the study period. Site selection was based on center experience, with management of at least 10 bAVMs per year. Given that some bAVMs treated in the centers would be ruptured, it is clear that not all unruptured AVMs were included in ARUBA. This assumption is confirmed by the fact that for 177 patients (78% of the total randomized), clinicians selected the treatment outside the randomization process. Finally, the proportion of randomized cases (226) versus screened patients (1740) was quite low (13%), and the specific reasons (and numbers) for noneligibility were not given. The data presented above certainly question the representativeness of the population included in the study.

Data from this study will also impact the physician-patient conversation and patient management. The treating physician will have to report that if untreated, the spontaneous AVM rupture rate is 2.2% per year (in ARUBA) and that the risk progressively increases with time (it is certainly useful to evaluate the risk of bleeding at 10, 20, 30 years, and later). This rate is similar to that previously reported in the literature.^{2,5} They will also have to share the result that when patients with brain AVMs are evaluated as a whole group and with varying treatment modalities, the short-term risk of death and stroke is higher with interventional management than with medical management. Additionally, the physician will have to explain the definition of “stroke” in the ARUBA trial “as any new focal neurologic deficit, seizure, or new-onset headache associated with imaging findings of hemorrhage or infarction.”¹ He or she will also have to explain that the respective percentages of different clinical conditions (headache, seizure, new focal neurologic deficit) are unknown. While some patients might consider a few episodes of seizures or headache an acceptable price for having the AVM cured and suppressing the risk of bleeding, others may be reluctant. Patients should know the rate of death or persistent deficit following either treatment strategy, but this information cannot be gathered from the data presented from the ARUBA study.

Additionally, when a patient seeks information about potential outcomes on the basis of their age, clinical condition, and AVM anatomy, physicians will not be able to give any guidance because a detailed analysis of these variables is not available and will not be conducted. Physicians will also have to explain that the mean follow-up in ARUBA was only 33.3 months, though the goal of any interventional treatment is to prevent the risk of AVM rupture and bleeding for a lifetime.

How should physicians use ARUBA results to make management decision in patients with unruptured brain AVMs? Should they immediately stop any interventional treatment for all patients with unruptured bAVMs? This is certainly not reasonable because the study data are from a heterogeneous pool of patients treated with differing treatment modalities, insufficient precision and analysis of the data, and very limited follow-up. In fact, 5-year follow-up may also be insufficient to evaluate the benefit and role of the interventional therapy option in a life-long threatening condition. The heterogeneity of patients included in the study will unfortunately limit the use of these data in the management (in-

terventional treatment or not) of patients with AVMs because the natural history risk/ therapeutic risk was not evaluated in patients or AVM subgroups (or AVM subgroups). Although it may be easy to decide the medical treatment strategy in a 70-year-old man with a lobar 5-cm AVM with superficial venous drainage and no associated aneurysm, these data do not help identify the best strategy for a 25-year-old woman traveling all over the world and having a deep-located AVM measuring 2-cm with deep venous drainage and an intranidal aneurysm. Additionally, due to the heterogeneity of treatment methods used, ARUBA will also not be helpful in selecting the best strategy if interventional treatment is indicated. Therefore, physicians will have to continue to reinforce their careful decision-making process on the basis of multidisciplinary discussions and a precise analysis of the clinical situation and AVM characteristics.

Finally, ARUBA demonstrates that interventional treatment of brain AVMs is associated with clinical risks that will occur immediately or closely after the treatment and that these risks are higher than those related to the natural history, at least in the following 33 months. We are looking forward to information about the clinical status of the patients 20 or 30 years after medical or interventional treatment. Unfortunately, follow-up of the ARUBA patients is foreseen for only 5 years. Because subgroup analysis related to AVM anatomy or therapeutic modalities will not be conducted in ARUBA, further studies will certainly be useful to determine whether ARUBA results are applicable to all patients with unruptured AVMs, regardless of their age and clinical status, the anatomic characteristics of the lesion, and the modalities of treatment used.

Disclosures: Laurent Pierot—UNRELATED: Consultancy: Codman, Covidien/ev3, MicroVention, Penumbra, Sequent, and Stryker. Jens Fiehler—UNRELATED: Consultancy: Codman, Stryker, MicroVention, Grants/Grants Pending: Covidien,* Stryker,* Payment for Lectures (including service on Speakers Bureaus): Covidien, Stryker, Codman, MicroVention, Penumbra, Travel/Accommodations/Meeting Expenses Unrelated to Activities Listed: Covidien. Christophe Cognard—UNRELATED: Consultancy: Stryker, MicroVention, Codman, Sequent, Covidien/ev3. Michael Söderman—UNRELATED: Consultancy: Covidien/ev3, and Neurovi; his hospital has a research agreement with Philips Healthcare, from which he does not benefit personally. Laurent Spelle—UNRELATED: Consultancy: Stryker, Covidien, Sequent.*Money paid to the institution.

REFERENCES

1. Mohr JP, Parides MK, Stapf C. **Medical management with or without interventional therapy for unruptured brain arteriovenous malformations (ARUBA): a multicenter, non-blinded, randomized trial.** *Lancet* 2013;pii:S0140–6736:62302–08
2. Cognard C, Spelle L, Pierot L. **Pial arteriovenous malformations.** In: Forsting M, Wanke I, eds. *Intracranial Vascular Malformations and Aneurysms*. Berlin, Germany: Springer-Verlag; 2004:39–100
3. Pierot L, Kadziolka K, Litré F, et al. **Combined treatment of brain arteriovenous malformations using Onyx embolization followed by radiosurgery.** *AJNR Am J Neuroradiol* 2013;34:1395–400
4. Pierot L, Cognard C, Herbreteau D, et al. **Endovascular treatment of brain arteriovenous malformations using Onyx: results of a prospective, multicenter, European study.** *Eur Radiol* 2013;23:2838–45
5. Hernesniemi JA, Dashti R, Juvela S, et al. **Natural history of brain arteriovenous malformations: a long-term follow-up study of risk of hemorrhage in 238 patients.** *Neurosurgery* 2008;63:823–29

Neuroimaging of Rapidly Progressive Dementias, Part 1: Neurodegenerative Etiologies

A.J. Degnan and L.M. Levy



ABSTRACT

SUMMARY: Most dementias begin insidiously, developing slowly and generally occurring in the elderly age group. The so-called rapidly progressive dementias constitute a different, diverse collection of conditions, many of which are reversible or treatable. For this reason, prompt identification and assessment of acute and subacute forms of dementia are critical to effective treatment. Numerous other entities within this category of presenile rapid-onset dementias are untreatable such as the prion-related diseases. Neuroimaging aids in the diagnosis and evaluation of many of these rapidly progressive dementias, which include myriad conditions ranging from variations of more common neurodegenerative dementias, such as Alzheimer disease, dementia with Lewy bodies, and frontotemporal dementia; infectious-related dementias such as acquired immune deficiency syndrome dementia; autoimmune and malignancy-related conditions; to toxic and metabolic forms of encephalopathy. This first of a 2-part review will specifically address the ability of MR imaging and ancillary neuroimaging strategies to support the diagnostic evaluation of rapidly progressive dementias due to neurodegenerative causes.

ABBREVIATIONS: AD = Alzheimer disease; CBD = corticobasal degeneration; DLB = dementia with Lewy bodies; HD = Huntington disease; MSA = multiple-system atrophy; PSP = progressive supranuclear palsy

With the increase of the aging population in the United States, the accurate recognition of dementia types is becoming an important clinical topic. Dementia is marked by cognitive decline, loss of normal memory function, and impairment in judgment without disruption of consciousness. Clinical history-taking, laboratory investigation, and imaging studies should be used with the aim of ascertaining dementia diagnoses related to reversible causes and etiologies amenable to treatment and determining the prognosis for irreversible and progressive illnesses. Unlike their more typical counterparts, rapidly progressive dementias are also more frequently atypical and heterogeneous in their clinical presentation, necessitating the use of additional diagnostic measures, including MR imaging, to improve diagnosis when the clinical situation is tenuous.

Thorough clinical evaluation and laboratory investigation are fundamental for ascertaining progressive dementias, especially those of more acute onset and in presenile patients (those younger

than 65 years of age). Laboratory investigations are vital in determining several of the illnesses within the differential diagnosis of a rapid-onset dementia, which, for the purposes of this review, is generally 6 months from onset of symptoms to fulminant dementia. As noted in the differential diagnosis On-line Table, rapidly progressive dementias may present with a wide variety of manifestations and etiologies.

Other forms of rapidly progressive dementia, however, are better characterized by using advanced imaging methods such as MR imaging; 1 study of rapidly progressive dementias noted that MR imaging findings suggested the specific diagnosis in one-third of cases.¹ Several excellent clinical reviews of the subject discuss the features of rapidly progressive dementias with supportive laboratory and clinical evaluations, which are abbreviated in this neuroimaging-focused review.²⁻⁴

Neurodegenerative Dementias

Most dementias in general are neurodegenerative, most commonly of the Alzheimer type, though there is increasing awareness with greater imaging and more thorough investigations of non-Alzheimer disease-related dementias.² A review of cases from a referral center for suspected prion disease showed that neurodegenerative disease makes up the largest portion of nonprion diagnoses.⁴ Conditions within this category generally present with a protracted clinical course of gradual decline in cognitive function. However, genetic variants of several neurodegenerative demen-

From the University of Pittsburgh Medical Center (A.J.D.), Pittsburgh, Pennsylvania; and Department of Radiology (L.M.L.), George Washington University Hospital, Washington, DC.

Please address correspondence to Lucien M. Levy, MD, 901 23rd St NW, Washington, DC 20037; e-mail: llevy@mfa.gwu.edu

Indicates open access to non-subscribers at www.ajnr.org

Indicates article with supplemental on-line table.

<http://dx.doi.org/10.3174/ajnr.A3454>

tias may present much more rapidly than their prototypical presentations.

Early-Onset Alzheimer Disease. Unlike its more common form, early-onset AD is characterized by a much shorter time course and greater anatomic and functional alterations.² Imaging findings in early-onset AD are also slightly different from those in senile AD, with a higher magnitude of atrophy within the occipital and parietal lobes.⁵ This change is in lieu of the stereotypical hippocampal atrophy; however, the imaging findings common in AD in general may be observed in cases of early onset, which are discussed at greater depth elsewhere.⁶ Medial temporal lobe atrophy appears to be a great discriminator of AD versus dementia with Lewy bodies and vascular-related cognitive decline.⁷ Imaging findings within certain subtypes of AD are based on genetic syndromes such as those with a *presenilin-1* mutation that manifests white matter changes (hyperintense on FLAIR) atypical of AD.^{8,9}

In AD, MR spectroscopy may aid in the diagnosis, with a notable decrease in *N*-acetylaspartate and an increase in myo-inositol and choline in patients with AD and those with presymptomatic AD.^{10,11} While it is outside the scope of this review, positron-emission tomography may offer added diagnostic acumen in recognizing AD with the use of the newly FDA-approved florbetapir F18 injection (Amyvid; Eli Lilly, Washington, DC), which specifically binds to β -amyloid.¹² Effort is also being directed at developing appropriate targeted MR imaging contrast agents.

As reviewed at greater length elsewhere, several advanced MR imaging techniques may be useful in making the diagnosis of AD.^{2,13} DTI is the subject of numerous active research studies and beyond the scope of this focused review. In brief, there is some evidence that DTI shows increased diffusivity within the temporal lobe in AD and may aid in differentiating it from other dementias such as dementia with Lewy bodies.¹⁴ Magnetization transfer imaging is one of the latest imaging methods to be applied to AD. Histopathologic information may be inferred from this method in light of the correlation between magnetization transfer ratio and the extent of axonal loss, and these changes may proceed to gross volume loss.²

Dementia with Lewy Bodies. DLB accounts for a small fraction of presenile-onset dementia syndromes, constituting only approximately 4% of presenile dementias, but its rapidity of decline with an average survival of 3 years places it in the differential diagnosis of rapidly progressive dementias.^{2,3,15} Frequently, neurologic symptoms in DLB are nonspecific and analogous to other neurodegenerative diseases. Because findings are nonspecific in DLB (such as atrophy within gray matter of the temporal, parietal, and occipital lobes), conventional MR imaging is of greatest benefit in ruling out other causes of rapidly progressive dementia rather than diagnosing DLB specifically.¹⁶ Relative preservation of the medial temporal lobe has been one of the few consistent findings of volumetric structural studies; another key difference compared with AD is the preservation of the NAA-to-creatine ratios on MR spectroscopy.^{17,18} Recent attempts have been made to differentiate DLB from AD, and one such study has noted a lower fractional anisotropy within the white matter of the postcentral gyrus, which correlated with decreased motor function

clinically.¹⁴ Using DTI, Bozzali et al¹⁹ noted decreased fractional anisotropy in many white matter regions, with relatively modest involvement of the temporal lobe. Another recent study by Burton et al¹⁶ reported reduced amygdala volume as a possible marker of DLB that correlates with the presence of Lewy bodies on pathology. Although outside the scope of this MR imaging–based review, reduced dopamine transporter levels in DLB, as shown with iodine 123 *N*-(3-fluoropropyl)-2 β -carbomethoxy-3 β -(4-iodophenyl)-nortropane SPECT, might assist in the diagnosis of DLB in light of the currently limited role for MR imaging.²⁰

Frontotemporal Dementia. Frontotemporal dementia, albeit generally with quicker symptom progression than AD, is a rarer form of rapidly progressive dementia.³ Moreover, some clinical attributes differentiate it from many other dementias, with a prominence of personality changes and impaired sociability. Imaging can demonstrate the atrophy for which this condition is named in half of the cases, though early phases of this condition may be missed and imaging is used with the primary purpose of excluding other forms of dementia.^{2,21} The “knife edge” sign is one imaging finding supportive of frontotemporal dementia on MR imaging and is described as focal atrophy within the anterior temporal lobe at the level of the temporal horn of the lateral ventricle.^{21,22} One study integrating MR imaging and clinical measures of dementia demonstrated associations between worsening of these rating scales and rates of ventricular expansion and whole-brain volume loss.²³

Corticobasal Degeneration. Because CBD may present clinically with progressive dementia and some of the rare neurologic symptoms seen in Creutzfeldt-Jakob disease, such as alien limb and myoclonus, imaging is essential to distinguish these 2 clinically similar entities.³ Patients with CBD may have atrophy of the caudate nucleus, putamen, and some cortical regions (premotor and superior parietal), usually in an asymmetric pattern (Fig 1).²⁴⁻²⁶ Moreover, cerebral atrophy is substantially greater than that seen in the clinically similar syndrome of progressive supranuclear palsy.²⁵ There may also be increased signal intensity within the subcortical white matter.

Progressive Supranuclear Palsy. PSP, a tauopathy frequently in the same differential diagnosis as CBD, may manifest early with executive dysfunction or subcortical dementia and then progress to involve the classic clinical presentation of supranuclear gaze palsy and motor symptoms.²⁷ Classically described MR imaging findings typical of PSP were reviewed by Stamelou et al²⁸ and include the classic “humming bird” or “penguin” sign (Fig 2).²⁴ These findings are largely related to atrophy within the midbrain, with involvement of the midbrain, pons, thalamus, superior cerebellar peduncle, and striatum; there may be hypointensity of the putamen on T2-weighted sequences.^{25,28} Of clinical importance, midbrain atrophy on MR imaging correlates with motor deficits.²⁹ Commensurate with midbrain atrophy, there may be dilation of the third ventricle.²⁸ There may also be T2-weighted hyperintensity of the tegmentum, corresponding to histopathologic evidence of neuronal degeneration in this region; this sign appears to be very specific, but not present in many cases.³⁰

Because there is much overlap between PSP and CBD visually on conventional MR imaging, many volumetric studies have at-

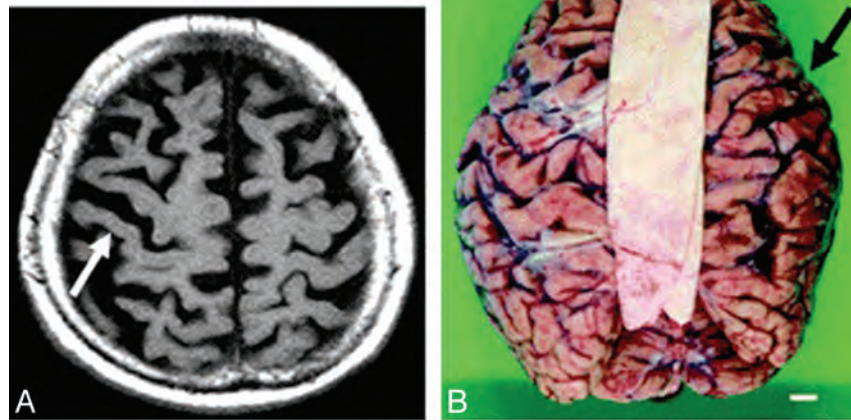


FIG 1. Corticobasal degeneration. Imaging performed in an 84-year-old woman with corticobasal degeneration proved on postmortem examination. A, Axial T2-weighted image shows right-side-dominant atrophy, including the central sulcus (arrow). B, Postmortem examination of this patient's brain shows right-frontal-dominant atrophy (arrow).²⁴

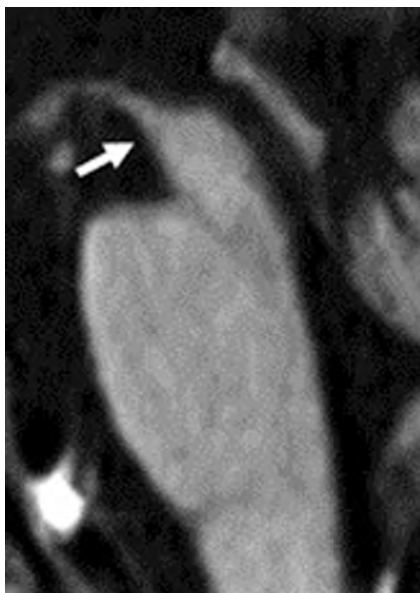


FIG 2. Hummingbird or penguin sign. Imaging performed in a 74-year-old man with PSP. T1-weighted midsagittal image clearly shows atrophy of the midbrain tegmentum (arrow), referred to as the hummingbird or penguin sign. The area of the midbrain tegmentum is 71 mm².²⁴

tempted to delineate differences between the two, particularly noting the lesser involvement of cortical atrophy in PSP.^{25,28,31} Also in the literature are less validated visual findings indicative of PSP; a proposed imaging finding is an abnormal superior profile of the midbrain on sagittal T1 images (Fig 3), in which the normal convex profile of the midbrain becomes flattened or concave, which is akin to the subjective hummingbird sign.³⁰ DWI may demonstrate increased putaminal ADC values, a finding that may aid in differentiating PSP from Parkinson disease.³²

Multiple-System Atrophy. The hallmark feature of this collection of neurodegenerative diseases of unknown cause, multiple-system atrophy, is progressive cerebral atrophy, which has been validated in small groups of patients with serial MR imaging showing rapid atrophy corresponding with the duration of ill-

ness.³³ Atrophic changes are noted by decreased size on conventional imaging and hypointensity on T2-weighted imaging, particularly within the lower brain stem, middle cerebellar peduncles, cerebellum, and putamen.^{26,34} In the pons, there is the classic imaging finding of the “hot cross bun sign” (Fig 4).³⁵⁻³⁷ With this atrophy, there may be a surrounding hyperintense rim seen on T2 images, which may appear before the hot cross bun sign, but it is unfortunately nonspecific, with atrophy being more important in distinguishing MSA from Parkinson disease.^{36,38} T2* gradient-echo signal loss within the dorsolateral putamen reflective of increased iron deposition is highly specific for MSA, but not always present.³⁹ Serial MR imaging has been used to characterize the atrophy noted within the pons, being particularly good at distinguishing MSA and CBD with a 3-fold greater atrophy rate, both of which can be differentiated on this basis from Parkinson dementia and healthy controls.²⁹

DWI may demonstrate increased diffusivity and ADC within the affected middle cerebellar peduncles, and other authors report decreased fractional anisotropy matching this finding.^{34,40-42} Putaminal ADC increases likewise exist in MSA, but not Parkinson disease, and these values also correlate with clinical measures.^{41,43-46} Therefore, DWI and DTI are essential in improving differentiation between MSA and other similar conditions such as PSP and Parkinson disease.

Huntington Disease. Because of the CAG triplet repeat propagated in an autosomal dominant fashion, clinicians diagnose HD on the basis of genetic testing prompted from a family history of early dementia and extrapyramidal symptoms with the hallmark of chorea. Clinically, there is mounting evidence for preclinical cognitive decline preceding any of the motor symptoms of HD.⁴⁷ Classic imaging findings reveal atrophy of the caudate nucleus, with concomitant enlargement of the frontal horns of the lateral ventricles.²⁶ This reduced size of the caudate nucleus has been correlated with cognitive performance and precedes motor symptoms by many years (Fig 5).^{47,48} There may be T2 hyperintensity in the region of the caudate nucleus with this atrophy. Moreover, the basal ganglia may be hypointense on FLAIR and T2-weighted

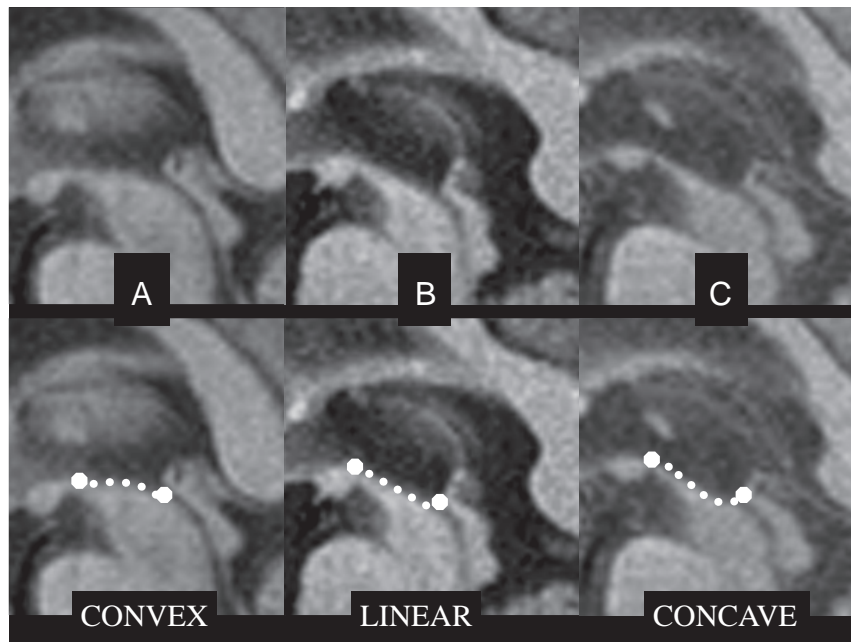


FIG 3. Abnormal superior profile of the midbrain in progressive supranuclear palsy. Top row: midsagittal T1-weighted spin-echo sections in Parkinson disease (A) and PSP (B and C) show the midbrain region. Bottom row: images with outlined profiles of the upper midbrain, which appears convex in A, linear (flat) in B, and concave in C as a result of midbrain atrophy in PSP.³⁰

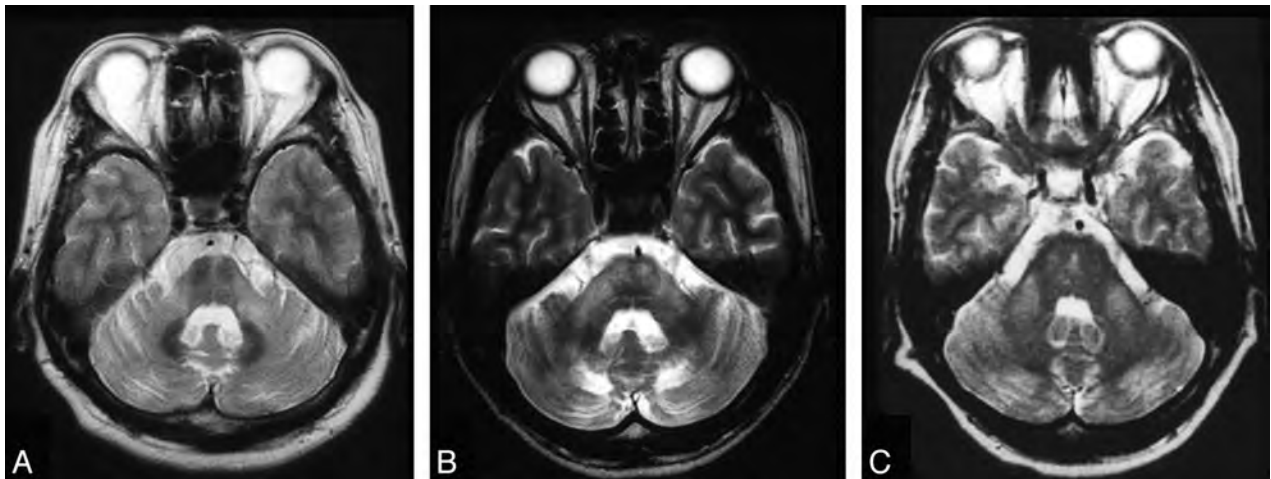


FIG 4. Hot cross bun sign. A 48-year-old woman with spinocerebellar ataxia type 6. T2-weighted fast spin-echo MR image (TR/TE/TI, 3600/102/2 ms) shows bilateral symmetric hyperintensity of atrophic middle cerebellar peduncles. The pons with the “cross sign” and cerebellum are also atrophic, as can be seen in multiple-system atrophy.³⁵

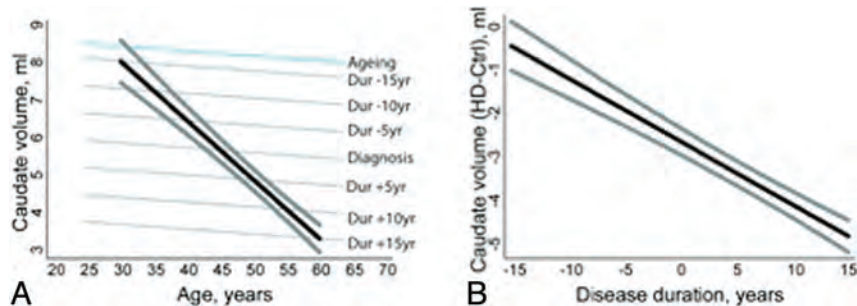


FIG 5. Caudate atrophy in Huntington disease. A, Illustration of the fitted relationship between caudate volume and age in normal ageing (blue) and patients with Huntington disease according to disease duration (gray) for male subjects with a total intracranial volume of 1500 mL. The black line shows the predicted trajectory (with the 90% confidence interval [CI] in thick gray) for a patient with HD with motor onset at 45 years of age. B, Fitted difference (with 90% CI) in caudate volume between patients with HD and controls according to disease duration. The difference is statistically significant ($P < .05$, 1-sided) ≤ 14 years before motor onset.⁴⁸

images due to iron deposition, and this finding is thought to constitute an early biomarker for the disease.⁴⁹ Other advanced MR imaging methods such as MR spectroscopy at a high-field strength may aid in showing changes associated with HD with decreased NAA and creatine within the caudate nucleus and putamen.⁵⁰

Neuroimaging may prognosticate the onset of disease progression in HD before the development of symptoms. A recent volumetric MR imaging study of patients before the clinical onset of HD symptoms noted that patients who would develop symptoms in 1–4 years following their scans demonstrated significantly smaller striatal volumes when they were still asymptomatic, particularly within the putamen.⁵¹ Other authors suggested that MR imaging can detect striatal atrophy even up to 20 years before motor deficits.⁵² This reduction in striatal volume was previously hypothesized to serve as a biomarker for likely clinical progression of HD.⁵³ Others have defined more global atrophy in cortical structures, perhaps later in the disease process, and these findings are more inconsistent than those involving the striatum.⁵² From the wealth of clinical studies performed to date, MR imaging has a powerful role in the diagnosis and prognostication of HD.

CONCLUSIONS

This first installment of a 2-part review of MR imaging findings in the diverse clinical manifestation of rapidly progressive dementia discussed the use of neuroimaging in diagnosing neurodegenerative conditions, ranging from the common aging-associated dementias to uncommon presentations of less prevalent conditions such as multiple-system atrophy. Newer technologies, such as amyloid imaging, may aid in distinguishing more unusual neurodegenerative causes of rapid cognitive decline and variants of the more common Alzheimer dementia. MR imaging with selective use of DWI, DTI, and MR spectroscopy is essential to narrow the differential diagnosis on the basis of the subtle differences between neurodegenerative dementias, and it plays a key role in establishing the diagnosis. The second part of this review will detail the imaging findings seen in a wide range of other causes of rapidly progressive dementia, including prion, infectious, inflammatory, autoimmune, neoplastic, metabolic, and nutritional conditions.

REFERENCES

- Kelley BJ, Boeve BF, Josephs KA. **Rapidly progressive young-onset dementia.** *Cogn Behav Neurol* 2009;22:22–27
- Heinemann U, Gawinecka J, Schmidt C, et al. **Differential diagnosis of rapid progressive dementia.** *Eur Neurol Rev* 2010;5:21–28
- Geschwind MD, Haman A, Miller BL. **Rapidly progressive dementia.** *Neurol Clin* 2007;25:783–807, vii
- Geschwind MD, Shu H, Haman A, et al. **Rapidly progressive dementia.** *Ann Neurol* 2008;64:97–108
- Frisoni GB, Pievani M, Testa C, et al. **The topography of grey matter involvement in early and late onset Alzheimer's disease.** *Brain* 2007;130:720–30
- Mueller S, Keiser D, Reiser M, et al. **Functional and structural MR imaging in neuropsychiatric disorders, part 1: imaging techniques and their application in mild cognitive impairment and Alzheimer disease.** *AJNR Am J Neuroradiol* 2011;33:1845–50
- Burton E, Barber R, Mukaetova-Ladinska E, et al. **Medial temporal lobe atrophy on MRI differentiates Alzheimer's disease from dementia with Lewy bodies and vascular cognitive impairment: a prospective study with pathological verification of diagnosis.** *Brain* 2009;132:195–203
- O'Riordan S, McMonagle P, Janssen JC, et al. **Presenilin-1 mutation (E280G), spastic paraparesis, and cranial MRI white-matter abnormalities.** *Neurology* 2002;59:1108–10
- Adair JC, Lee RR. **Abnormal fluid-attenuated inversion recovery signal foci in the splenium of a patient with presenilin-1 mutation.** *AJNR Am J Neuroradiol* 2004;25:1864–65
- Kantarci K. **1H magnetic resonance spectroscopy in dementia.** *Br J Radiol* 2007;80(spec No. 2):S146–52
- Kantarci K, Weigand SD, Petersen RC, et al. **Longitudinal 1H MRS changes in mild cognitive impairment and Alzheimer's disease.** *Neurobiol Aging* 2007;28:1330–39
- Yang Y, Jia HM, Liu BL. **(E)-5-styryl-1H-indole and (E)-6-styrylquinoline derivatives serve as probes for β -amyloid plaques.** *Molecules* 2012;17:4252–65
- Jack CR Jr. **Alzheimer disease: new concepts on its neurobiology and the clinical role imaging will play.** *Radiology* 2012;263:344–61
- Firbank MJ, Blamire AM, Teodorczuk A, et al. **Diffusion tensor imaging in Alzheimer's disease and dementia with Lewy bodies.** *Psychiatry Res* 2011;194:176–83
- Gaig C, Valldeoriola F, Gelpi E, et al. **Rapidly progressive diffuse Lewy body disease.** *Mov Disord* 2011;26:1316–23
- Burton EJ, Mukaetova-Ladinska EB, Perry RH, et al. **Neuropathological correlates of volumetric MRI in autopsy-confirmed Lewy body dementia.** *Neurobiol Aging* 2012;33:1228–36
- Taylor JP, O'Brien J. **Neuroimaging of dementia with Lewy bodies.** *Neuroimaging Clin N Am* 2012;22:67–81, vii
- Watson R, Blamire AM, O'Brien JT. **Magnetic resonance imaging in Lewy body dementias.** *Dement Geriatr Cogn Disord* 2009;28:493–506
- Bozzali M, Falini A, Cercignani M, et al. **Brain tissue damage in dementia with Lewy bodies: an in vivo diffusion tensor MRI study.** *Brain* 2005;128:1595–604
- Warr L, Walker Z. **Identification of biomarkers in Lewy-body disorders.** *Q J Nucl Med Mol Imaging* 2012;56:39–54
- Knopman DS, Boeve BF, Parisi JE, et al. **Antemortem diagnosis of frontotemporal lobar degeneration.** *Ann Neurol* 2005;57:480–88
- van der Flier W, Scheltens P. **Use of laboratory and imaging investigations in dementia.** *J Neurol Neurosurg Psychiatry* 2005;76:v45
- Gordon E, Rohrer J, Kim L, et al. **Measuring disease progression in frontotemporal lobar degeneration: a clinical and MRI study.** *Neurology* 2010;74:666–73
- Tokumaru AM, Saito Y, Murayama S, et al. **Imaging-pathologic correlation in corticobasal degeneration: imaging techniques and their application in mild cognitive impairment and Alzheimer disease.** *AJNR Am J Neuroradiol* 2009;30:1884–92
- Boxer AL, Geschwind MD, Belfor N, et al. **Patterns of brain atrophy that differentiate corticobasal degeneration syndrome from progressive supranuclear palsy.** *Arch Neurol* 2006;63:81–86
- Mascalchi M, Vella A, Ceravolo R. **Movement disorders: role of imaging in diagnosis.** *J Magn Reson Imaging* 2012;35:239–56
- Morris HR, Wood NW, Lees AJ. **Progressive supranuclear palsy (Steele-Richardson-Olszewski disease).** *Postgrad Med J* 1999;75:579–84
- Stamelou M, Knake S, Oertel WH, et al. **Magnetic resonance imaging in progressive supranuclear palsy.** *J Neurol* 2011;258:549–58
- Paviour DC, Price SL, Jahanshahi M, et al. **Longitudinal MRI in progressive supranuclear palsy and multiple system atrophy: rates and regions of atrophy.** *Brain* 2006;129:1040–49
- Righini A, Antonini A, De Notaris R, et al. **MR imaging of the superior profile of the midbrain: differential diagnosis between progressive supranuclear palsy and Parkinson disease—imaging techniques and their application in mild cognitive impairment and Alzheimer disease.** *AJNR Am J Neuroradiol* 2004;25:927–32
- Taki M, Ishii K, Fukuda T, et al. **Evaluation of cortical atrophy between progressive supranuclear palsy and corticobasal degeneration by hemispheric surface display of MR images: imaging tech-**

- niques and their application in mild cognitive impairment and Alzheimer disease. *AJNR Am J Neuradiol* 2004;25:1709–14
32. Seppi K, Schocke MF, Wenning GK, et al. **How to diagnose MSA early: the role of magnetic resonance imaging.** *J Neural Transm* 2005;112:1625–34
 33. Horimoto Y, Aiba I, Yasuda T, et al. **Cerebral atrophy in multiple system atrophy by MRI.** *J Neurol Sci* 2000;173:109–12
 34. Brooks DJ, Seppi K, for the Neuroimaging Working Group on MSA. **Proposed neuroimaging criteria for the diagnosis of multiple system atrophy.** *Mov Disord* 2009;24:949–64
 35. Okamoto K, Tokiguchi S, Furusawa T, et al. **MR features of diseases involving bilateral middle cerebellar peduncles: imaging techniques and their application in mild cognitive impairment and Alzheimer disease.** *AJNR Am J Neuradiol* 2003;24:1946–54
 36. Seppi K, Poewe W. **Brain magnetic resonance imaging techniques in the diagnosis of parkinsonian syndromes.** *Neuroimaging Clin N Am* 2010;20:29–55
 37. Kwon KY, Choi CG, Kim JS, et al. **Comparison of brain MRI and 18F-FDG PET in the differential diagnosis of multiple system atrophy from Parkinson's disease.** *Mov Disord* 2007;22:2352–58
 38. Horimoto Y, Aiba I, Yasuda T, et al. **Longitudinal MRI study of multiple system atrophy: when do the findings appear, and what is the course?** *J Neurol* 2002;249:847–54
 39. von Lewinski F, Werner C, Jorn T, et al. **T2*-weighted MRI in diagnosis of multiple system atrophy: a practical approach for clinicians.** *J Neurol* 2007;254:1184–88
 40. Shiga K, Yamada K, Yoshikawa K, et al. **Local tissue anisotropy decreases in cerebellopetal fibers and pyramidal tract in multiple system atrophy.** *J Neurol* 2005;252:589–96
 41. Blain CR, Barker GJ, Jarosz JM, et al. **Measuring brain stem and cerebellar damage in parkinsonian syndromes using diffusion tensor MRI.** *Neurology* 2006;67:2199–205
 42. Pellecchia MT, Barone P, Mollica C, et al. **Diffusion-weighted imaging in multiple system atrophy: a comparison between clinical subtypes.** *Mov Disord* 2009;24:689–96
 43. Schocke MF, Seppi K, Esterhammer R, et al. **Diffusion-weighted MRI differentiates the Parkinson variant of multiple system atrophy from PD.** *Neurology* 2002;58:575–80
 44. Seppi K, Schocke MF, Mair KJ, et al. **Progression of putaminal degeneration in multiple system atrophy: a serial diffusion MR study.** *Neuroimage* 2006;31:240–45
 45. Seppi K, Schocke MF, Prennschuetz-Schuetzenau K, et al. **Topography of putaminal degeneration in multiple system atrophy: a diffusion magnetic resonance study.** *Mov Disord* 2006;21:847–52
 46. Nicoletti G, Lodi R, Condino F, et al. **Apparent diffusion coefficient measurements of the middle cerebellar peduncle differentiate the Parkinson variant of MSA from Parkinson's disease and progressive supranuclear palsy.** *Brain* 2006;129:2679–87
 47. Montoya A, Price BH, Menear M, et al. **Brain imaging and cognitive dysfunctions in Huntington's disease.** *J Psychiatry Neurosci* 2006;31:21–29
 48. Hobbs NZ, Barnes J, Frost C, et al. **Onset and progression of pathologic atrophy in Huntington disease: a longitudinal MR imaging study.** *AJNR Am J Neuroradiol* 2010;31:1036–41
 49. Jurgens CK, Jasinschi R, Ekin A, et al. **MRI T2 hypointensities in basal ganglia of premanifest Huntington's disease.** *PLoS Curr* 2010;2: pii
 50. Versluis MJ, van der Grond J, van Buchem MA, et al. **High-field imaging of neurodegenerative diseases.** *Neuroimaging Clin N Am* 2012;22:159–71, ix
 51. Aylward EH, Liu D, Nopoulos PC, et al. **Striatal volume contributes to the prediction of onset of Huntington disease in incident cases.** *Biol Psychiatry* 2012;71:822–28
 52. Klöppel S, Henley SM, Hobbs NZ, et al. **Magnetic resonance imaging of Huntington's disease: preparing for clinical trials.** *Neuroscience* 2009;164:205–19
 53. Aylward EH. **Change in MRI striatal volumes as a biomarker in preclinical Huntington's disease.** *Brain Res Bull* 2007;72: 152–58

Neuroimaging of Rapidly Progressive Dementias, Part 2: Prion, Inflammatory, Neoplastic, and Other Etiologies

A.J. Degnan and L.M. Levy



ABSTRACT

SUMMARY: Most dementias begin insidiously, developing slowly and generally occurring in the elderly age group. The so-called rapidly progressive dementias constitute a different, diverse collection of conditions, many of which are reversible or treatable. For this reason, accurate identification and assessment of acute and subacute forms of dementia are critical to effective treatment; neuroimaging aids greatly in narrowing the diagnosis of these conditions. This second installment of a 2-part review of rapidly progressive dementias examines the use of imaging in an assortment of other etiologies in the differential diagnosis, from prion disease and neoplastic-related conditions to rare metabolic and other conditions such as Wernicke encephalopathy. In these clinical conditions, MR imaging has the potential to narrow this broad differential diagnosis and, at times, can definitively aid in the diagnosis of certain conditions on the basis of typical imaging patterns.

ABBREVIATIONS: CJD = Creutzfeldt-Jakob disease; LG = lymphomatoid granulomatosis; SREAT = steroid-responsive encephalopathy with autoimmune thyroiditis; SSPE = subacute sclerosing panencephalitis

Dementia features prominently as a common disability among the elderly and is only expected to increase with the aging population of developed countries worldwide. Dementia constitutes diverse combinations of a loss of normal executive function in decision making, a decline in memory encoding and retrieval, and an impairment of the ability to perform cognitive tasks. In the first part of this 2-part review of rapidly progressive dementias, the neurodegenerative conditions that feature prominently in the differential diagnosis of a presenile or rapidly progressive dementia were discussed. These include the common, inexorable dementias typically associated with old age such as Alzheimer dementia and dementia with Lewy bodies. As with any clinical evaluation, imaging cannot replace accurate and thorough physical examination and history, but it contributes greatly to discerning entities within the differential diagnosis of a rapidly progressive dementia.

Rapidly progressive dementias can result from a variety of etiologies, and in this second review article, we discuss the remaining etiologies summarized in the differential diagnosis On-line Table cited in Part 1. One striking characteristic of the differential diag-

nosis for this clinical presentation of dementia is the tremendous diversity of entities encountered. This review discusses the role of neuroimaging, particularly MR imaging, in the diagnosis of a wide array of dementia-inducing conditions, including the following: prion disease such as Creutzfeldt-Jakob disease; infectious entities such as HIV-associated dementia; autoimmune and inflammatory conditions such as Hashimoto encephalopathy; malignancy-related conditions such as primary CNS lymphoma; and rare manifestations of other causes such as Wilson disease. In many of these clinical scenarios, MR imaging plays a deciding role in clarifying the clinical diagnosis. Other authors have recently reviewed, in greater detail, the clinical work-up of rapidly progressive dementias^{1,2}; this article will focus on the consideration of these diseases when examining neuroimaging studies of rapidly progressive dementias.

Prion Disease

There are several rare disorders in which the pathophysiologic entity is the prion, a misfolded form of a normally found protein within the brain, which propagates itself by promoting changes in the conformation of the normal prion protein. The most common set of conditions involving the prion is Creutzfeldt-Jakob disease, which is either inherited in a familial fashion, sporadically occurring, or acquired through exposure. CJD may fall under both the neurodegenerative and infectious classifications; the latter is thought to occur in variant CJD or new-variant CJD, related to ingestion of mad-cow-infected beef.³ Of these types, the spo-

From the University of Pittsburgh Medical Center (A.J.D.), Pittsburgh, Pennsylvania; and Department of Radiology (L.M.L.), George Washington University Hospital, Washington, DC.

Please address correspondence to Lucien M. Levy, MD, 901 23rd St NW, Washington, DC 20037; e-mail: llevy@mfa.gwu.edu

Indicates open access to non-subscribers at www.ajnr.org

<http://dx.doi.org/10.3174/ajnr.A3455>

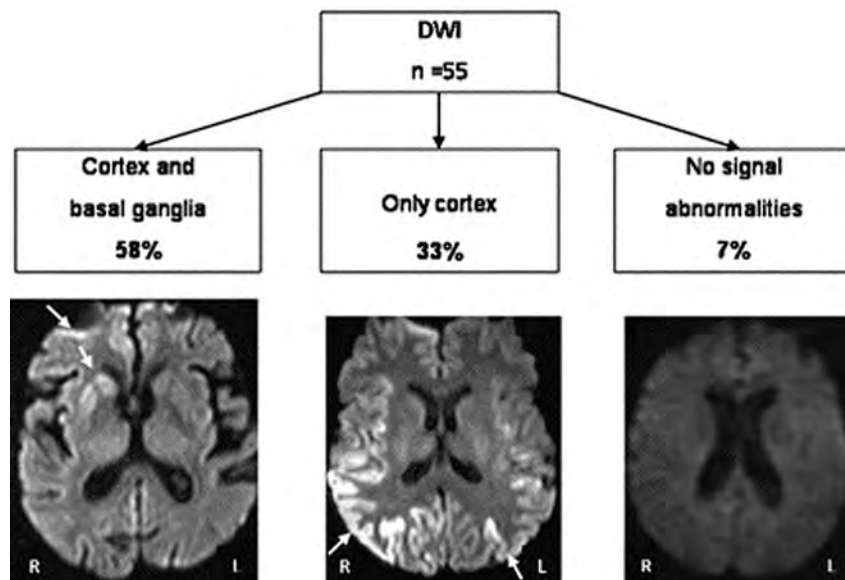


FIG 1. DWI in CJD. The most frequent MR imaging lesion patterns were defined by using DWI as the most sensitive technique. Cortex and basal ganglia hyperintensity was observed in approximately two-thirds (58%), and isolated cortical hyperintensity, in one-third (33%).⁷

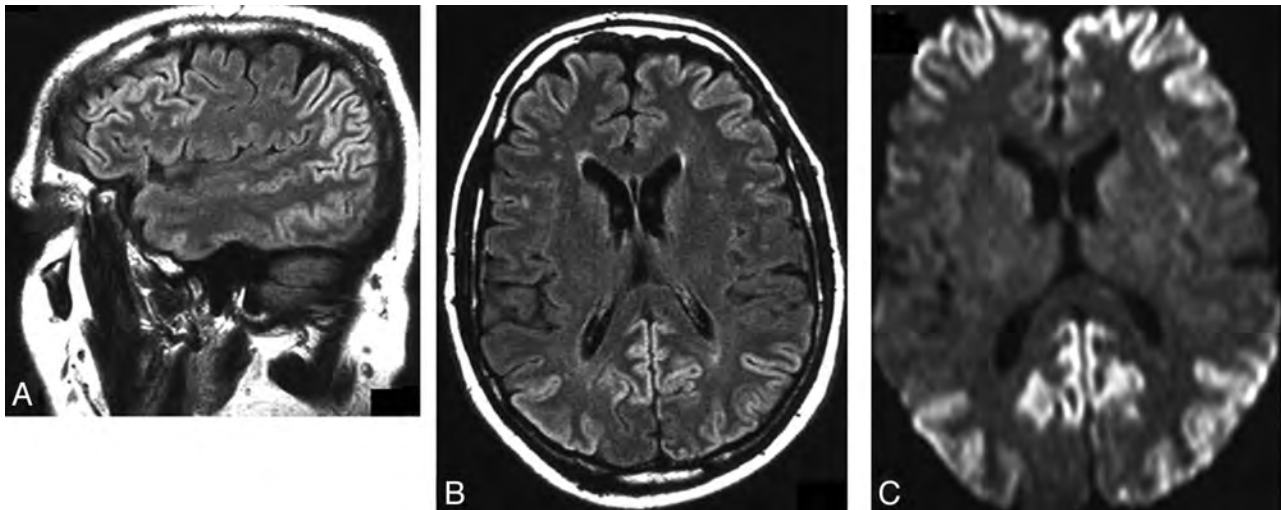


FIG 2. DWI in CJD. Involvement of the frontal and parietal lobes in patients with isolated cortical hyperintensities in the setting of Creutzfeldt-Jakob Disease. A, Sagittal FLAIR-weighted scan of a 58-year-old patient 3.5 months after the disease onset and 1 week before death shows signal-intensity increases in the frontal and parietal lobes. B, Axial FLAIR-weighted scan of the same patient shows frontal and parietal signal-intensity increases. C, DWI of the same patient shows frontal and parietal signal-intensity increases.⁷

radic form is the most common, followed by genetic and acquired forms.² This condition may differ clinically from many other conditions in the differential on the basis of its cerebellar dysfunction and common presence of myoclonus. Nevertheless, its clinical overlap with corticobasal degeneration and progressive supranuclear palsy necessitates the use of imaging to differentiate it from other rapidly progressive dementias.

The imaging findings typical of CJD, while observed on T2-weighted and FLAIR sequences, are best seen by using high-b-value DWI and are confirmed with reciprocal changes on ADC images.⁴⁻⁶ DWI typically demonstrates hyperintensities within the basal ganglia, the thalamus, and cortex (Figs 1 and 2).⁷ The “hockey stick” or “pulvinar” sign, which is formed by the confluent hyperintensity within the dorsomedial thalamus and the posterior thalamus (pulvinar), is thought to be indicative of vari-

ant (infectious acquired) CJD, though these signs may be seen in other forms of CJD.^{8,9} These imaging changes are much more sensitive and specific than previous noninvasive clinical methods for CJD diagnosis, including the presence of CSF protein 14–3–3 and periodic sharp waves on electroencephalography or neuron-specific enolase.^{3,9} For this reason, imaging findings are essential in making the diagnosis of CJD, despite their not being included in earlier clinical criteria.¹⁰

Infection-Related Etiologies

In younger patients with dementia symptoms, both infectious and inflammatory-related conditions are much more frequent than the neurodegenerative diseases. Encephalitis and other infections of the CNS are generally hyperacute in onset; when cognitive decline is present, these cognitive symptoms are likewise

hyperacute in onset. In addition, encephalopathic symptoms with marked confusion and neuropsychiatric manifestations also point clinically to this diagnosis, as do non-neurologic manifestations of infection such as cutaneous or respiratory presentations. Readers are referred to the work of Almeida and Lautenschlager¹¹ for a thorough clinical discussion of dementia associated with infections.

Encephalitis. The diagnosis of encephalitis in the acute setting may prove problematic: Clinical symptoms are generally nonspecific and may involve a variety of neurologic symptoms or none at all. While rarely presenting with dementia acutely, rapidly progressive dementia in younger individuals merits consideration of encephalitis. Even rapid polymerase chain reaction laboratory tests of herpes simplex may have negative findings in the very early stages of encephalitis, which make ancillary work-up imperative.

MR imaging can reveal pathologic changes manifest as FLAIR and T2 hyperintensity within the temporal (particularly, medial), insular, and inferior frontal cortices in patients with herpes encephalitis.^{12,13} In the much less common Japanese encephalitis, these abnormalities tend to be seen in subcortical gray matter regions.¹³ Patchy enhancement with gadolinium administration indicates nonspecific inflammatory changes generally seen in encephalitis. DWI augments the evaluation of encephalitis with earlier detection of changes than on conventional imaging, though it may not be as sensitive later in the clinical course.¹³⁻¹⁶ Restricted diffusion occurs in herpes encephalitis during the acute phase and appears less often in Japanese encephalitis, though other authors demonstrated diffusion changes in the thalamus in this condition.^{16,17} Moreover, magnetic-susceptibility-sensitive sequences (eg, gradient recalled-echo, susceptibility-weighted, and susceptibility angiography) may detect focal hemorrhage associated with sequelae of CNS infection.

HIV and AIDS-Related Dementias

The occurrence of dementia in HIV-infected individuals ranges from 1 in 10 to 1 in 3. HIV dementia may be considered a subcortical dementia with cognitive slowing, motor retardation, and impaired memory.¹¹ Fortunately, successful treatment with antiretroviral therapy has the potential to ameliorate cognitive symptoms and sometimes reverse cognitive deficits in HIV dementia.¹ For this reason, identification and establishment of an appropriate treatment regimen is of paramount importance. Imaging is also vital to ensure that no other AIDS-related CNS conditions are present, such as primary CNS lymphoma, progressive multifocal leukoencephalopathy (seen as demyelinating white matter lesions on MR imaging), or toxoplasmosis (with multiple deep gray matter lesions).¹⁸ With cognitive decline in the setting of HIV infection, volumetric studies observed atrophy by using MR imaging.¹⁹ These changes are not generally apparent on conventional MR imaging on an individual basis. DTI may, however, show reduced fractional anisotropy inversely correlated with viral loads.¹⁹⁻²¹ Magnetization transfer ratios also appear different when comparing HIV-infected patients to controls.¹⁹

MR spectroscopy can also detect changes that reflect dementia symptoms in HIV-infected patients, regardless of neuroanatomic changes; a recent study by Ernst et al²² demonstrated reductions in parietal gray matter glutamate in subjects with HIV with cog-

nitive deficits. Others have implicated decreased concentrations of NAA and combined glutamate and glutamine in HIV-infected patients with reductions in cortical, hippocampal, and subcortical volume, respectively.⁴

Neuroborreliosis. CNS manifestations related to Lyme disease caused by *Borrelia burgdorferi* are rare; contentious; and largely related to cranial nerve involvement, polyradiculopathy, or neuropsychiatric manifestations. Acute dementia in this setting has been previously reported, and though infrequent, may place this condition on the differential list of rapid-onset dementias.²³ An extensive review by Hildenbrand et al²⁴ discussed the neuroimaging findings and the clinical syndrome of neuroborreliosis in greater detail. Rarely, encephalomyelitis may develop from spirochete infiltration into the brain, as indicated by tumefactive white matter lesions.²⁵ Traditionally, more commonly seen in Lyme disease with CNS involvement are nonspecific FLAIR abnormalities predominantly within the frontal cortex; on the other hand, more recent, systematic investigation suggests that this is an uncommon occurrence with only 10% of patients with neuroborreliosis demonstrating T2 hyperintense foci.^{26,27} These lesions may mimic a demyelinating process; thus, in cases in which multiple sclerosis is considered a reasonable alternate explanation for T2 foci, DTI and magnetization transfer imaging are helpful in demonstrating the absence of occult white matter injury in Lyme disease in juxtaposition to multiple sclerosis.²⁸

Other Infectious Dementias. Of importance but rarely rapid in progression is tertiary syphilis, which should be clinically determined by using appropriate laboratory testing with rapid plasma reagin testing performed in all suspected patients with rapid or presenile dementia. Cognitive decline is the most common neurologic symptom in tertiary syphilis. Early MR imaging reports describe focal hyperintensities on T2-weighted images in an arterial distribution, in keeping with meningovascular pathophysiology.²⁹ Multiple areas of ischemia and infarction are thought to result from endarteritis in some cases of fulminant neurosyphilis.¹⁸ Cerebral gummatous disease may also occur in neurosyphilis, with lesions that are hypointense on T1- and hyperintense on T2-weighted images.²⁹

Other infectious etiologies such as fungal encephalitides may present with dementia, but as with most infections of the central nervous system, they also tend to present with neurologic dysfunction and other clinical features more often than simple dementia. There are reports of *Cryptococcus neoformans* as a causative agent of rapidly progressive cognitive dysfunction, with 1 case even misdiagnosed as Alzheimer disease.³⁰ Neurocysticercosis is rare in the developed world, but in places where it is endemic, it may present with dementia in a small fraction of cases.¹¹

Another infectious form of sudden dementia, typically seen in a much younger population of children and adolescents (in comparison with the remainder of conditions discussed in this article) is subacute sclerosing panencephalitis, which is a rare condition caused by the measles paramyxovirus, occurring months to years after infection. MR imaging findings are generally normal early in SSPE and may progress to involve high T2 signal within white matter or hyperintense lesions in the parietal and temporal lobes in the acute stage and then progress to involve atrophy and deep

and cortical gray matter changes.³¹⁻³³ MR spectroscopy in later stages of SSPE reveals decreased NAA, consistent with neuronal loss and elevated choline, lipid, and lactate concentrations consistent with inflammation.³⁴ More recent work indicates the use of DTI; notably, DTI detects reductions in fractional anisotropy even within normal-appearing white matter on conventional imaging, suggesting subtle disruption of white matter tracts in the early stages of SSPE.³⁵

Inflammatory and Autoimmune Conditions

Inflammatory and autoimmune conditions are often associated with diverse clinical symptoms and an amorphous presentation. They constitute the second largest group of rapidly progressive dementias in 2 large cohorts but are a much smaller portion of another group of presenile rapid dementias.^{3,36}

Multiple Sclerosis. Nearly 1 in 20 patients with MS manifest dementia, but the prevalence of other cognitive disturbances is much more common and subtle.³⁷ Most imaging reports of this phenomenon attribute the cognitive decline to the presence of nonspecific neuroanatomic atrophy, without particular observation of an affected structure.³⁸ The reason for this generalized atrophy has been discussed and examined at great length—even in normal-appearing white matter in MS, there are detectable correlates of neuronal loss with decreased NAA on MR spectroscopy within both normal white and gray matter in patients with MS.³⁹ Moreover, these measures of atrophy in patients with MS correlate with the progression of disability and were reviewed at great length by Anderson et al.³⁹ Nevertheless, dementia in the setting of patients with known MS should be evaluated as with any other rapidly progressive dementia, with MS-related dementia as a diagnosis of exclusion.

Hashimoto Encephalopathy. This condition related to Hashimoto thyroiditis is also referred to as steroid-responsive encephalopathy with autoimmune thyroiditis, which explains the nature of this syndrome that is believed to be related to a cross-reaction between autoimmune antithyroid antibodies and neurons, resulting in generalized CNS inflammation and neurologic impairment.^{3,40} Most interesting, patients may not demonstrate overt thyroid dysfunction at the time of neurologic presentation. MR imaging findings, as with many of these autoimmune conditions, are frequently normal (60% of cases) or nonspecific in nature, involving FLAIR and T2 abnormalities within subcortical white matter and contrast enhancement of the meninges.^{40,41} Making the diagnosis of SREAT is important because early initiation of corticosteroid pharmacotherapy yields symptom resolution and reversal of imaging findings.⁴¹

Neurosarcoidosis. As a systemic granulomatous disease, sarcoidosis may simulate many neurologic disorders, and likewise, imaging of neurosarcoidosis is complex.⁴² Neurologic involvement is also relatively common in neurosarcoidosis, with approximately 1 in 4 patients with sarcoidosis demonstrating CNS involvement at postmortem examination.⁴³ When present, the most frequent abnormalities observed on MR imaging are periventricular T2-weighted hyperintense lesions, enhancing granulomas, and leptomeningeal enhancement similar to that seen in meningitis.^{42,44} Dural masses may be seen, which are T2 hypointense; contrast

enhancement may be mistaken for meningioma, without a clinical history of sarcoidosis.⁴³

Vasculitides. Primary CNS vasculitis is a rare entity, but systemic vasculitides may also present with CNS manifestations with cognitive deficits in half of patients.^{45,46} Vasculitides can be differentiated from many other dementias in that there are frequently concomitant cerebrovascular events seen on MR imaging, with hemorrhage and infarct more likely present.³ FLAIR and T2-weighted hyperintensities are also prevalent in vasculitis, thickening of the vessels and extramural enhancement are more definitive findings, and findings of gadolinium enhancement within the meninges are not as commonplace as generally thought on the basis of the results of a large observational study.⁴⁵

Other Inflammatory and Autoimmune Conditions. Celiac disease, an intolerance of food products containing gluten, often with the presence of autoantibodies to the enzyme tissue transglutaminase, may present with neurologic symptoms, including dementia, though those reported are quite varied, ranging from chronic headaches to ataxia.^{47,48} Oddly, these symptoms can occur without gastrointestinal involvement and may improve with dietary changes.⁴⁹ MR imaging of the brain may reveal hyperintense T2-weighted posterior white matter foci with a reported prevalence of 1 in 5 in patients with celiac disease in 1 study, independent of the presence of neurologic symptoms.^{3,50} Most interesting, measured cerebral perfusion on SPECT imaging in 1 small study was significantly lower within several brain regions in patients with untreated celiac disease, while there was no significant difference between patients adhering to dietary restriction and controls.⁵¹ These findings suggest a process by which patients may sustain hypoperfusion with resultant brain injury, generating lesions visible on conventional MR imaging. Nevertheless, the evidence for and mechanism of neurologic involvement and the importance of MR imaging findings in celiac disease are controversial topics without conclusions.

Malignancy-Related Conditions

Paraneoplastic CNS Involvement. There are a number of paraneoplastic neurologic disorders with a diverse set of clinical presentations that may present with cognitive impairment or dementia. The most common symptoms that may suggest this condition in the differential diagnosis of rapidly progressive dementia involve retrograde and anterograde amnesia. The diagnosis of this condition is relatively straightforward in patients with established cancer (particularly, small cell lung cancer, germ cell tumors, thymoma) but must also be considered in the setting of occult malignancy as well. Paraneoplastic limbic encephalitis (Fig 3)⁵² is the most classic paraneoplastic disorder with anterograde memory impairment being most prominent; imaging reveals increased signal within the mesial temporal lobes.⁴¹ FLAIR hyperintensities within the caudate, anterior putamen, and sometimes the medial temporal lobe have been reported in the setting of paraneoplastic syndrome in small cell lung cancer with anti-CV2 antibodies.⁵³ Half of those patients with autoimmune dementia diagnosed with CSF autoantibodies will have a paraneoplastic syndrome. Other authors recommend the use of FDG-PET for any patient sus-

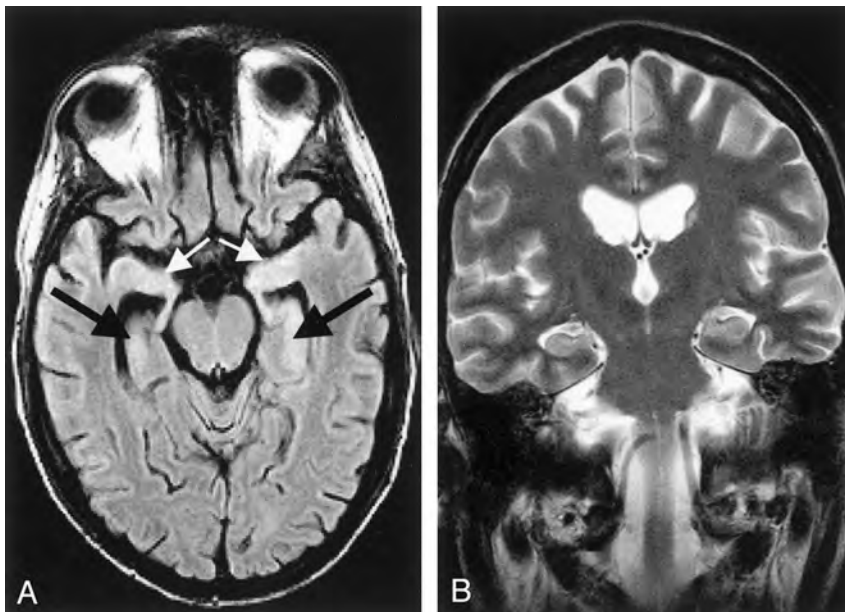


FIG 3. Acute limbic encephalitis. A 26-year-old man with underlying precursor T-cell acute lymphoblastic leukemia developed generalized seizures, had short-term memory loss, and was disoriented in time and place 1 month after undergoing unsuccessful allogeneic bone marrow transplantation. At autopsy, multifocal subacute polioencephalomyelitis in the brain regions that were shown as affected on MR images confirmed the diagnosis of paraneoplastic limbic encephalitis with neuronal loss. Initial MR images were obtained 1 day after the first generalized seizure occurred. A, Axial FLAIR image (TR/TE, 9000/110 ms; TI, 2261 ms) shows a slightly elevated signal intensity of both hippocampal formations (*black arrows*) and amygdala (*white arrows*). B, Coronal conventional T2-weighted turbo spin-echo image (TR/TE/NEX, 4462 ms/120 ms/3) shows no signal-intensity abnormality.⁵²

pected of having autoimmune dementia to potentially diagnose underlying malignancy.⁵⁴

Lymphoma. Primary CNS lymphoma is a malignancy of increased recognition and prevalence related to its presence in AIDS. Most of its neurologic manifestations are more related to mass-effect symptoms, but dementia has also been observed, thereby adding this neoplasm to the differential diagnosis of rapid-onset dementias.⁵⁵ Early diagnosis is important for averting the need for extensive resection with poorer outcomes.⁵⁶ MR imaging categorically reveals solitary or multiple supratentorial mass lesions with minimal edema, generally isointense-to-mildly hyperintense on T1-weighted imaging and hypointense on T2-weighted images, and almost always with enhancement.^{14,57} Solitary lesions are more common in immunocompetent individuals.¹⁴ Of importance, the lesion is capable of crossing the corpus callosum, forming a “butterfly” lesion.⁵⁷ There may also be diffuse extension of the white matter signal change classified as “lymphomatosis cerebri.” This form of diffusely infiltrating CNS lymphoma would be more likely to present as a progressive dementia.³

The clinical diagnosis of CNS lymphoma is frequently problematic, with nondiagnostic studies leading ultimately to the necessity of brain biopsy for definitive diagnosis; imaging may provide ancillary support to clinical evidence.³ MR spectroscopy may be particularly helpful in identifying a neoplastic pattern of metabolite concentrations evidenced by large choline concentrations with lipid and lactate present.¹⁴ MR perfusion may clarify diag-

nosis in contrast to other tumors in that primary lymphoma in the brain has lower relative cerebral blood volume.⁵⁶ Likewise, DWI with ADC maps demonstrate low ADC values compared with glioblastoma and metastatic lesions.⁵⁶ Brain thallium-201 SPECT may be combined with toxoplasma serology to improve diagnostic accuracy in excluding this potential infectious etiology with focal CNS mass lesions.⁵⁸

Intravascular lymphoma, a rare non-Hodgkin lymphoma, may likewise generate neurologic symptoms, including subacute dementia, concomitantly with cerebrovascular events.² As a result of its intravascular source, CNS involvement is characterized by diffuse T2-weighted hyperintensity with patchy enhancement and, on occasion, edema.^{2,59} There are some diffusion changes consistent with ischemia in the setting of intravascular lymphoma.⁶⁰ Angiography in these patients does not aid in the diagnosis because intravascular lymphoma appears consistent with vasculitis as a result of the intravascular malignancy.³ An antemortem diagnosis of intravascular lymphoma is particularly difficult.

Metastatic CNS Involvement. As with any intracranial process and as the most common cause of brain tumors, metastatic disease may present with rapidly progressive dementia, particularly in the setting of multifocal cortical involvement as has been reported in a few cases of rare miliary cerebral metastases presenting with subacute dementia.⁶¹⁻⁶³ Some patients have been reported to develop dementia during treatment as a result of metastatic disease, which could be mistaken for a side effect of therapy (particularly radiation therapy).⁶⁴ In each of these cases, diagnosis of the underlying cause of the dementia is often elusive until postmortem neuropathology. The imaging of most brain lesions consistent with metastatic cancer, aside from miliary spread, is more straightforward, and recognition is important so that patients may benefit from radiation therapy.⁶⁵ Imaging of brain metastases requires a dedicated review of its own.⁶⁶ Briefly, MR imaging generally reveals multiple lesions with a propensity for the gray-white matter junctions with T2 hyperintensity consistent with extensive edema.⁶⁷ Some of these lesions may hemorrhage, as may be evidenced by T1 hyperintensity. DWI and DTI aid in distinguishing metastases from other lesions such as abscesses in the setting of cystic metastasis with a relative lack of restricted diffusion (bright on ADC, dark on DWI); DTI demonstrates displacement of white matter fibers in metastasis.⁶⁸

Lymphomatoid Granulomatosis. Lymphomatoid granulomatosis, a B-cell lymphoma caused by the Epstein-Barr virus with prominent CNS involvement as a result of angi destructive pathophysiology, is one condition that has been reported to pres-

ent with dementia in a presenile population.⁶⁹ Generally, pulmonary manifestations exist in almost all patients with CNS manifestations of LG; this unusual constellation may provide the clinical clue necessary to make this diagnosis, whereas those cases with exclusively neurologic involvement are particularly difficult to diagnose.⁷⁰ Multifocal involvement on brain MR imaging is commonplace, with punctate or linear T2 hyperintensities within perivascular spaces with corresponding enhancement on T1 post-contrast images, particularly within frontal and parietal regions—a finding not exclusive to LG and seen in angitis and neurosarcoidosis but distinguishable from CNS lymphoma, which most often presents as a solitary lesion.⁷⁰⁻⁷³ These regions of enhancement correspond on histopathology to granulomatous infiltrates of lymphoid cells and precede hemorrhage.^{70,72} Ring-like enhancement may also appear in the lesions of LG.⁷⁴ Imaging may demonstrate temporal lobe atrophy, perhaps related to lymphocytic infiltration into cerebral blood vessels causing microvascular occlusion and resultant ischemia.^{69,75} Most interesting, research has borne out the importance of MR imaging in this malignancy with evidence that clinical imaging is more sensitive than CSF analysis.⁷³

Toxic, Nutritional, and Metabolic Etiologies

Most nutritional deficiencies that may manifest with neurologic symptoms are slowly progressive. The triad of dermatitis, diarrhea, and dementia, while rarely clinically observed now, characterizes pellagra or niacin deficiency. The role of imaging in this grouping of conditions is much more problematic than in the aforementioned diagnoses because imaging findings, if present, are generally nonspecific and may only offer a glimpse of the correct diagnosis, which may be more readily obtained with thorough history-taking and laboratory studies.

Toxic Causes of Dementia-Like Symptoms. Most cases of neurotoxic exposure are clinically marked by fulminant encephalopathic symptoms of acute onset with a clear source rather than by symptoms of a rapidly progressive dementia. Nevertheless, there are certain imaging features that may support these toxic (generally heavy metal) exposures as the source of neurologic symptoms. T1-weighted hyperintensity within the basal ganglia implies deposition of metals such as iron or manganese.⁷⁶ This finding on MR imaging has been reported in the globus pallidus of individuals exposed to manganese from their occupation as miners who developed cognitive impairment.⁷⁷ The imaging findings in many other exposures are not well-established, and clinical suspicion and appropriate laboratory investigations remain the cornerstone of evaluation of these forms of progressive dementia.

Wernicke Encephalopathy (Thiamine Deficiency). Clinically, the memory loss and cognitive symptoms seen in Wernicke encephalopathy are accompanied by ophthalmoplegias and ataxia; however, as already mentioned, several conditions within the spectrum of rapidly progressive dementia share these symptoms. Moreover, acute Wernicke encephalopathy is underappreciated, particularly in nonalcoholic patients.⁷⁸ Imaging clues may improve recognition of this underdiagnosed clinical entity, with excellent specificity of findings on MR imaging.⁷⁹ There may be T2-weighted and FLAIR hyperintensity within the area around

the third ventricle, periaqueductal regions, and bilateral thalami (particularly dorsomedial) in Wernicke encephalopathy—a finding that has been reported even in nonalcoholic cases.^{78,80,81} Moreover, serial imaging illustrates remission of these changes with successful treatment.⁸² DWI improves the neuroimaging evaluation and appears more sensitive to the presumed ischemic and cytotoxic pathophysiology of Wernicke encephalopathy in these regions, evidenced by restricted diffusion.⁸³ Therefore, clinical imaging demonstrating gadolinium enhancement or DWI abnormalities within the mammillary bodies and periaqueductal regions and thalami can be of clinical utility in clarifying the diagnosis.^{78,81} These imaging findings may conveniently correlate with the presence of hemorrhagic necrosis within these structures. Ancillary imaging with MR spectroscopy may show decreased or normal NAA with the notable presence of lactate.^{84,85}

Wilson Disease. Impaired copper transportation in this autosomal recessive disorder may precipitate either liver disease or neurologic dysfunction, which in the absence of liver disease, presents later in early adulthood. For this reason, progressive dementia with or without other neurologic findings may occur in an atypical age group with Wilson disease. Classically seen on MR imaging is the accumulation of copper within the putamen and thalami reflected by T2-weighted hyperintensity without evidence of restricted diffusion.⁸⁶ A few reports have described the presence of high signal intensity in T2-weighted images of the tegmentum and red nuclei to form the “face of the giant panda” and, inferiorly within the pons, to form the “face of the panda cub,” with relative hypointensity of the central portion with adjacent hyperintensity within the aqueduct.⁸⁶⁻⁸⁹ While these imaging findings may suggest impaired copper transportation as a cause, ultimately laboratory studies of copper and ceruloplasmin facilitate a definitive diagnosis.

Other Conditions. Metabolic diseases such as mitochondrial disease may also present with a characteristically subcortical dementia; there is impairment in attention and rousability early in the disease process that differentiates them from dementias. Prominent potential causes of subacute dementia are mitochondrial myopathy, encephalopathy, lactic acidosis, and strokelike episodes (MELAS). Imaging findings early in this disease may reveal cortical hyperintensities on FLAIR and T2-weighted images in a gyriform pattern.¹² DWI also depicts these lesions characteristic of MELAS as hyperintense regions of the cortex.⁹⁰

Osmotic myelinolysis is another potential cause of rapidly progressive dementia but will generally present more acutely and involve decreased levels of consciousness that exclude it from the rapidly progressive dementias. Central pontine myelinolysis is visible as a trident-shaped increased T2 signal intensity with sparing of the corticospinal tracts.⁷⁹ Extra-pontine myelinolysis, while rarer, may have T2 prolongation and DWI signal increases in the basal ganglia, thalamus, or cerebellum. The involvement of subcortical structures is an uncommon occurrence, but nevertheless I has been reported.^{79,91}

CONCLUSIONS

Presenile and rapidly progressive dementias are a diverse collection of conditions ranging from reversible to intransigent and

rapidly progressive. Distinctions within this heterogeneous group are best accomplished with a careful and thorough clinical and laboratory examination and may be greatly aided by the use of neuroimaging, particularly MR imaging. We discussed, in the first part of this review, the more frequently encountered neurodegenerative causes of dementia, and in this second installment, we conclude our discussion of rapidly progressive dementias with a review of prion, infectious, inflammatory, autoimmune, neoplastic, and other conditions. The need for further investigation in several areas of clinical investigation of all these conditions is particularly important, especially because a large number of these conditions have overlapping imaging and clinical findings that obfuscate accurate diagnosis. Both the clinician and radiologist alike should be open to the possibility of alternate diagnoses in the setting of rapidly progressive presenile dementias, particularly because several diseases within this group benefit from urgent and specific treatment.

REFERENCES

- Heinemann U, Gawinecka J, Schmidt C, et al. **Differential diagnosis of rapid progressive dementia.** *Eur Neurol Rev* 2010;5:21–28
- Geschwind MD, Haman A, Miller BL. **Rapidly progressive dementia.** *Neurol Clin* 2007;25:783–807, vii
- Geschwind MD, Shu H, Haman A, et al. **Rapidly progressive dementia.** *Ann Neurol* 2008;64:97–108
- Lee H, Hoffman C, Kingsley PB, et al. **Enhanced detection of diffusion reductions in Creutzfeldt-Jakob disease at a higher B factor.** *AJNR Am J Neuroradiol* 2010;31:49–54
- Hyare H, Thornton J, Stevens J, et al. **High-b-value diffusion MR imaging and basal nuclei apparent diffusion coefficient measurements in variant and sporadic Creutzfeldt-Jakob disease.** *AJNR Am J Neuroradiol* 2010;31:521–26
- Smart JM, Wood A. **Value of fluid-attenuated inversion recovery MR imaging in an unusual case of sporadic Creutzfeldt-Jakob disease.** *AJR Am J Roentgenol* 2001;177:948–49
- Meissner B, Kallenberg K, Sanchez-Juan P, et al. **Isolated cortical signal increase on MR imaging as a frequent lesion pattern in sporadic Creutzfeldt-Jakob disease.** *AJNR Am J Neuroradiol* 2008;29:1519–24
- Collie DA, Sellar RJ, Zeidler M, et al. **MRI of Creutzfeldt-Jakob disease: imaging features and recommended MRI protocol.** *Clin Radiol* 2001;56:726–39
- Vitali P, Maccagnano E, Caverzasi E, et al. **Diffusion-weighted MRI hyperintensity patterns differentiate CJD from other rapid dementias.** *Neurology* 2011;76:1711–19
- Zerr I, Kallenberg K, Summers DM, et al. **Updated clinical diagnostic criteria for sporadic Creutzfeldt-Jakob disease.** *Brain* 2009;132:2659–68
- Almeida OP, Lautenschlager NT. **Dementia associated with infectious diseases.** *Int Psychogeriatr* 2005;17(suppl 1):S65–77
- Ukisu R, Kushihashi T, Tanaka E, et al. **Diffusion-weighted MR imaging of early-stage Creutzfeldt-Jakob disease: typical and atypical manifestations.** *Radiographics* 2006;26(suppl 1):S191–204
- Misra U, Kalita J, Phadke R, et al. **Usefulness of various MRI sequences in the diagnosis of viral encephalitis.** *Acta Trop* 2010;116:206–11
- Küker W, Nagele T, Korfel A, et al. **Primary central nervous system lymphomas (PCNSL): MRI features at presentation in 100 patients.** *J Neurooncol* 2005;72:169–77
- McCabe K, Tyler K, Tanabe J. **Diffusion-weighted MRI abnormalities as a clue to the diagnosis of herpes simplex encephalitis.** *Neurology* 2003;61:1015–16
- Sawlani V. **Diffusion-weighted imaging and apparent diffusion coefficient evaluation of herpes simplex encephalitis and Japanese encephalitis.** *J Neurol Sci* 2009;287:221–26
- Prakash M, Kumar S, Gupta RK. **Diffusion-weighted MR imaging in Japanese encephalitis.** *J Comput Assist Tomogr* 2004;28:756–61
- Satishchandra P, Sinha S. **Relevance of neuroimaging in the diagnosis and management of tropical neurologic disorders.** *Neuroimaging Clin N Am* 2011;21:737–56, vii
- Tucker KA, Robertson KR, Lin W, et al. **Neuroimaging in human immunodeficiency virus infection.** *J Neuroimmunol* 2004;157:153–62
- Ragin AB, Storey P, Cohen BA, et al. **Disease burden in HIV-associated cognitive impairment: a study of whole-brain imaging measures.** *Neurology* 2004;63:2293–97
- Ragin AB, Storey P, Cohen BA, et al. **Whole brain diffusion tensor imaging in HIV-associated cognitive impairment.** *AJNR Am J Neuroradiol* 2004;25:195–200
- Ernst T, Jiang CS, Nakama H, et al. **Lower brain glutamate is associated with cognitive deficits in HIV patients: a new mechanism for HIV-associated neurocognitive disorder.** *J Magn Reson Imaging* 2010;32:1045–53
- Waniek C, Prohovnik I, Kaufman AA, et al. **Rapidly progressive frontal-type dementia associated with Lyme disease.** *J Neuropsychiatry Clin Neurosci* 1995;7:345–47
- Hildenbrand P, Craven D, Jones R, et al. **Lyme neuroborreliosis: manifestations of a rapidly emerging zoonosis.** *AJNR Am J Neuroradiol* 2009;30:1079–87
- Massengo SA, Bonnet F, Braun C, et al. **Severe neuroborreliosis: the benefit of prolonged high-dose combination of antimicrobial agents with steroids—an illustrative case.** *Diagn Microbiol Infect Dis* 2005;51:127–30
- Fernandez RE, Rothberg M, Ferencz G, et al. **Lyme disease of the CNS: MR imaging findings in 14 cases.** *AJNR Am J Neuroradiol* 1990;11:479–81
- Agarwal R, Sze G. **Neuro-lyme disease: MR imaging findings.** *Radiology* 2009;253:167–73
- Agosta F, Rocca MA, Benedetti B, et al. **MR imaging assessment of brain and cervical cord damage in patients with neuroborreliosis.** *AJNR Am J Neuroradiol* 2006;27:892–94
- Falcone S, Quencer RM, Post MJ. **Magnetic resonance imaging of unusual intracranial infections.** *Top Magn Reson Imaging* 1994;6:41–52
- Hoffmann M, Muniz J, Carroll E, et al. **Cryptococcal meningitis misdiagnosed as Alzheimer's disease: complete neurological and cognitive recovery with treatment.** *J Alzheimers Dis* 2009;16:517–20
- Oztürk A, Gurses C, Baykan B, et al. **Subacute sclerosing panencephalitis: clinical and magnetic resonance imaging evaluation of 36 patients.** *J Child Neurol* 2002;17:25–29
- Sener RN. **Subacute sclerosing panencephalitis findings at MR imaging, diffusion MR imaging, and proton MR spectroscopy.** *AJNR Am J Neuroradiol* 2004;25:892–94
- Tuncay R, Akman-Demir G, Gokyigit A, et al. **MRI in subacute sclerosing panencephalitis.** *Neuroradiology* 1996;38:636–40
- Alkan A, Sarac K, Kutlu R, et al. **Early- and late-state subacute sclerosing panencephalitis: chemical shift imaging and single-voxel MR spectroscopy.** *AJNR Am J Neuroradiol* 2003;24:501–06
- Trivedi R, Gupta RK, Agarwal A, et al. **Assessment of white matter damage in subacute sclerosing panencephalitis using quantitative diffusion tensor MR imaging.** *AJNR Am J Neuroradiol* 2006;27:1712–16
- Kelley BJ, Boeve BF, Josephs KA. **Rapidly progressive young-onset dementia.** *Cogn Behav Neurol* 2009;22:22–27
- Longley WA. **Multiple sclerosis-related dementia: relatively rare and often misunderstood.** *Brain Impairment* 2007;8:154–67
- Pelletier D, Garrison K, Henry R. **Measurement of whole-brain atrophy in multiple sclerosis.** *J Neuroimaging* 2004;14:11S–19S
- Anderson VM, Fox NC, Miller DH. **Magnetic resonance imaging measures of brain atrophy in multiple sclerosis.** *J Magn Reson Imaging* 2006;23:605–18
- Castillo P, Woodruff B, Caselli R, et al. **Steroid-responsive encephalopathy associated with autoimmune thyroiditis.** *Arch Neurol* 2006;63:197–202

41. Vernino S, Geschwind M, Boeve B. **Autoimmune encephalopathies.** *Neurologist* 2007;13:140–47
42. Pickuth D, Spielmann R, Heywang-Kobrunner S. **Role of radiology in the diagnosis of neurosarcoidosis.** *Eur Radiol* 2000;10:941–44
43. Christoforidis GA, Spickler EM, Recio MV, et al. **MR of CNS sarcoidosis: correlation of imaging features to clinical symptoms and response to treatment.** *AJNR Am J Neuroradiol* 1999;20:655–69
44. Lury KM, Smith JK, Matheus MG, et al. **Neurosarcoidosis: review of imaging findings.** *Semin Roentgenol* 2004;39:495–504
45. Giannini C, Salvarani C, Hunder G, et al. **Primary central nervous system vasculitis: pathology and mechanisms.** *Acta Neuropathol* 2012;123:759–72
46. Salvarani C, Brown RD Jr, Calamia KT, et al. **Primary central nervous system vasculitis: analysis of 101 patients.** *Ann Neurol* 2007;62:442–51
47. Zelnik N, Pacht A, Obeid R, et al. **Range of neurologic disorders in patients with celiac disease.** *Pediatrics* 2004;113:1672–76
48. Pengiran Tengah DS, Wills AJ, Holmes GK. **Neurological complications of coeliac disease.** *Postgrad Med J* 2002;78:393–98
49. Cicarelli G, Della Rocca G, Amboni M, et al. **Clinical and neurological abnormalities in adult celiac disease.** *Neurol Sci* 2003;24:311–17
50. Kieslich M, Errazuriz G, Posselt HG, et al. **Brain white-matter lesions in celiac disease: a prospective study of 75 diet-treated patients.** *Pediatrics* 2001;108:e21
51. Addolorato G, Di Giuda D, De Rossi G, et al. **Regional cerebral hypoperfusion in patients with celiac disease.** *Am J Med* 2004;116:312–17
52. Thuerl C, Muller K, Laubenberger J, et al. **MR imaging of autopsy-proved paraneoplastic limbic encephalitis in non-Hodgkin lymphoma.** *AJNR Am J Neuroradiol* 2003;24:507–11
53. Vernino S, Tuite P, Adler CH, et al. **Paraneoplastic chorea associated with CRMP-5 neuronal antibody and lung carcinoma.** *Ann Neurol* 2002;51:625–30
54. Murray AD. **Imaging approaches for dementia.** *AJNR Am J Neuroradiol* 2011;33:1836–44
55. Bataille B, Delwail V, Menet E, et al. **Primary intracerebral malignant lymphoma: report of 248 cases.** *J Neurosurg* 2000;92:261–66
56. Hussien AR, Mangla R, Liu X, et al. **An approach to improve the diagnosis of primary CNS lymphoma using conventional and advanced imaging techniques.** *Contemporary Diagn Radiol* 2012;35:1–8
57. Slone HW, Blake JJ, Shah R, et al. **CT and MRI findings of intracranial lymphoma.** *AJR Am J Roentgenol* 2005;184:1679–85
58. Skiest DJ, Erdman W, Chang WE, et al. **SPECT thallium-201 combined with toxoplasma serology for the presumptive diagnosis of focal central nervous system mass lesions in patients with AIDS.** *J Infect* 2000;40:274–81
59. Vieren M, Sciort R, Robberecht W. **Intravascular lymphomatosis of the brain: a diagnostic problem.** *Clin Neurol Neurosurg* 1999;101:33–36
60. Baehring JM, Henchcliffe C, Ledezma CJ, et al. **Intravascular lymphoma: magnetic resonance imaging correlates of disease dynamics within the central nervous system.** *J Neurol Neurosurg Psychiatry* 2005;76:540–44
61. Bouza G, Roel JE, Galich M, et al. **Rapidly progressive dementia caused by tumor microembolism in the central nervous system [in Spanish].** *Medicina (B Aires)* 1997;57:447–50
62. Fontan A, Zarranz J, Camarero C, et al. **Dementia caused by miliary cerebral metastasis of a hepatocarcinoma [in Spanish].** *Med Clin (Barc)* 1989;93:421–23
63. Rivas E, Sanchez-Herrero J, Alonso M, et al. **Miliary brain metastases presenting as rapidly progressive dementia.** *Neuropathology* 2005;25:153–58
64. Yamao Mochizuki S, Nishimura N, Inoue A, et al. **Miliary brain metastases in 2 cases with advanced non-small cell lung cancer harboring EGFR mutation during gefitinib treatment.** *Respir Investig* 2012;50:117–21
65. Tosoni A, Ermani M, Brandes AA. **The pathogenesis and treatment of brain metastases: a comprehensive review.** *Crit Rev Oncol Hematol* 2004;52:199–215
66. Barajas RF Jr, Cha S. **Imaging diagnosis of brain metastasis.** *Prog Neurol Surg* 2012;25:55–73
67. Grainger RG, Allison DJ, Adam A, et al. *Diagnostic Radiology: A Textbook of Medical Imaging.* London: Churchill Livingstone; 2001
68. Tsuchiya K, Fujikawa A, Nakajima M, et al. **Differentiation between solitary brain metastasis and high-grade glioma by diffusion tensor imaging.** *Br J Radiol* 2005;78:533–37
69. Carone DA, Benedict RHB, Zivadinov R, et al. **Progressive cerebral disease in lymphomatoid granulomatosis causes anterograde amnesia and neuropsychiatric disorder.** *J Neuroimaging* 2006;16:163–66
70. Tateishi U, Terae S, Ogata A, et al. **MR imaging of the brain in lymphomatoid granulomatosis.** *AJNR Am J Neuroradiol* 2001;22:1283–90
71. Kawai N, Miyake K, Nishiyama Y, et al. **FDG-PET findings of the brain in lymphomatoid granulomatosis.** *Ann Nucl Med* 2006;20:683–87
72. Miura H, Shimamura H, Tsuchiya K, et al. **Magnetic resonance imaging of lymphomatoid granulomatosis: punctate and linear enhancement preceding hemorrhage.** *Eur Radiol* 2003;13:2192–95
73. Patsalides AD, Atac G, Hedge U, et al. **Lymphomatoid granulomatosis: abnormalities of the brain at MR imaging.** *Radiology* 2005;237:265–73
74. Kiryu S, Okubo T, Takeuchi K, et al. **Magnetic resonance imaging and diffusion tensor analysis of lymphomatoid granulomatosis of the brain.** *Acta Radiol* 2006;47:509–13
75. Mizuno T, Takanashi Y, Onodera H, et al. **A case of lymphomatoid granulomatosis/angiocentric immunoproliferative lesion with long clinical course and diffuse brain involvement.** *J Neurol Sci* 2003;213:67–76
76. Yoshikawa K, Matsumoto M, Hamanaka M, et al. **A case of manganese induced parkinsonism in hereditary haemorrhagic telangiectasia.** *J Neurol Neurosurg Psychiatry* 2003;74:1312–14
77. Josephs K, Ahlskog J, Klos K, et al. **Neurologic manifestations in welders with pallidal MRI T1 hyperintensity.** *Neurology* 2005;64:2033–39
78. Unlu E, Cakir B, Asil T. **MRI findings of Wernicke encephalopathy revisited due to hunger strike.** *Eur J Radiol* 2006;57:43–53
79. Lim CC. **Neuroimaging in postinfectious demyelination and nutritional disorders of the central nervous system.** *Neuroimaging Clin N Am* 2011;21:843–58, viii
80. White ML, Zhang Y, Andrew LG, et al. **MR imaging with diffusion-weighted imaging in acute and chronic Wernicke encephalopathy.** *AJNR Am J Neuroradiol* 2005;26:2306–10
81. Fei GQ, Zhong C, Jin L, et al. **Clinical characteristics and MR imaging features of nonalcoholic Wernicke encephalopathy.** *AJNR Am J Neuroradiol* 2008;29:164–69
82. Zhong C, Jin L, Fei G. **MR imaging of nonalcoholic Wernicke encephalopathy: a follow-up study.** *AJNR Am J Neuroradiol* 2005;26:2301–05
83. Halavaara J, Brander A, Lyytinen J, et al. **Wernicke's encephalopathy: is diffusion-weighted MRI useful?** *Neuroradiology* 2003;45:519–23
84. Rugilo CA, Uribe Roca MC, Zurru MC, et al. **Proton MR spectroscopy in Wernicke encephalopathy.** *AJNR Am J Neuroradiol* 2003;24:952–55
85. Murata T, Fujito T, Kimura H, et al. **Serial MRI and (1)H-MRS of Wernicke's encephalopathy: report of a case with remarkable cerebellar lesions on MRI.** *Psychiatry Res* 2001;108:49–55
86. Singh P, Ahluwalia A, Sagar K, et al. **Wilson's disease: MRI features.** *J Pediatr Neurosci* 2011;6:27–28
87. Mascalchi M, Vella A, Ceravolo R. **Movement disorders: role of imaging in diagnosis.** *J Magn Reson Imaging* 2012;35:239–56
88. Shivakumar R, Thomas SV. **Teaching NeuroImages: face of the giant panda and her cub—MRI correlates of Wilson disease.** *Neurology* 2009;72:E50
89. Jacobs DA, Markowitz CE, Liebeskind DS, et al. **The “double panda sign” in Wilson's disease.** *Neurology* 2003;61:969–69
90. Wang XY, Noguchi K, Takashima S, et al. **Serial diffusion-weighted imaging in a patient with MELAS and presumed cytotoxic oedema.** *Neuroradiology* 2003;45:640–43
91. Tatewaki Y, Kato K, Tanabe Y, et al. **MRI findings of corticosubcortical lesions in osmotic myelinolysis: report of two cases.** *Br J Radiol* 2012;85:e87–90

WEB-DL Endovascular Treatment of Wide-Neck Bifurcation Aneurysms: Short- and Midterm Results in a European Study

B. Lubicz, J. Klisch, J.-Y. Gauvrit, I. Szikora, M. Leonardi, T. Liebig, N.P. Nuzzi, E. Boccardi, F.D. Paola, M. Holtmannspötter, W. Weber, E. Calgliari, V. Sychra, B. Mine, and L. Pierot



ABSTRACT

BACKGROUND AND PURPOSE: Flow disruption with the WEB-DL device has been used safely for the treatment of wide-neck bifurcation aneurysms, but the stability of aneurysm occlusion after this treatment is unknown. This retrospective multicenter European study analyzed short- and midterm data in patients treated with WEB-DL.

MATERIALS AND METHODS: Twelve European neurointerventional centers participated in the study. Clinical data and pre- and postoperative short- and midterm images were collected. An experienced interventional neuroradiologist independently analyzed the images. Aneurysm occlusion was classified into 4 grades: complete occlusion, opacification of the proximal recess of the device, neck remnant, and aneurysm remnant.

RESULTS: Forty-five patients (34 women and 11 men) 35–74 years of age (mean, 56.3 ± 9.6 years) with 45 aneurysms treated with the WEB device were included. Aneurysm locations were the middle cerebral artery in 26 patients, the posterior circulation in 13 patients, the anterior communicating artery in 5 patients, and the internal carotid artery terminus in 1 patient. Forty-two aneurysms were unruptured. Good clinical outcome (mRS < 2) was observed in 93.3% of patients at the last follow-up. Adequate occlusion (complete occlusion, opacification of the proximal recess, or neck remnant) was observed in 30/37 patients (81.1%) in short-term follow-up (median, 6 months) and in 26/29 patients (89.7%) in midterm follow-up (median, 13 months). Worsening of the aneurysm occlusion was observed in 2/28 patients (7.1%) at midterm follow-up.

CONCLUSIONS: The results suggest that the WEB endovascular treatment of wide-neck bifurcation aneurysms offers stable occlusion in a class of aneurysms that are historically unstable. Additionally, our data show that opacification of the WEB recess can be delineated from true neck or aneurysm remnants.

ABBREVIATIONS: WEB-DL = WEB Dual Layer; WEB-SL = WEB Single Layer; WEB-SLS = WEB Single Layer Sphere; CLARITY = Clinical and Anatomical Results in the Treatment of Ruptured Intracranial Aneurysms.

Endovascular treatment is now the first-line approach for both ruptured and unruptured aneurysms.^{1–4} However, the limitations of standard coiling have contributed to the development of

new endovascular approaches, including balloon-assisted coiling, stent-assisted coiling, flow diversion, and flow disruption.⁵

The WEB (Sequent Medical, Aliso Viejo, California) is an intrasaccular device designed to disrupt the intra-aneurysmal flow at the level of the neck.^{6–9} Several devices are now available in the WEB family: WEB-DL and the more recently introduced WEB-SL and WEB-SLS. Initial experience with the WEB-DL has shown the clinical utility of this device in wide-neck bifurcation aneurysms with high technical success and low acute morbidity and mortality.^{7–9} Also, the initial WEB-DL literature suggests good efficacy, with a high percentage of adequate occlusion (complete occlusion or neck remnant) in the postoperative period and in short-term follow-up. In the largest series, a significant number of neck remnants were observed at follow-up (56.7%).⁹ This was due, in part,

Received October 17, 2013; accepted after revision December 5.

From the Department of Neuroradiology (B.L., B.M.), Erasme University Hospital, Brussels, Belgium; Department of Diagnostic and Interventional Radiology and Neuroradiology (J.K., V.S.), Helios General Hospital, Erfurt, Germany; Department of Neuroradiology (J.-Y.G.), Centre Hospitalier Universitaire Rennes, Rennes, France; Department of Neuroradiology (I.S.), National Institute of Neurosciences, Budapest, Hungary; Department of Neuroradiology (M.L.), Ospedale Bellaria, Bologna University, Bologna, Italy; Department of Neuroradiology (T.L.), Universitaetsklinikum Koeln, Cologne, Germany; Department of Neuroradiology (N.P.N.), Ospedale Galliera, Genova, Italy; Department of Neuroradiology (E.B.), Ospedale Niguarda, Milano, Italy; Department of Neuroradiology (F.D.P.), Ospedale Santa Maria, Treviso, Italy; Department of Neuroradiology (M.H.), Rigshospitalet, Copenhagen, Denmark; Department of Neuroradiology (W.W.), Knappschafts Krankenhaus, Recklinghausen, Germany; Department of Neuroradiology (E.C.), Ospedale dell'Angelo, Mestre, Italy; and Department of Neuroradiology (L.P.), Hôpital Maison-Blanche, Université Reims-Champagne-Ardenne, Reims, France.

Please address correspondence to Laurent Pierot, MD, Service de Radiologie-Hôpital Maison-Blanche, 45, rue Cognac-Jay, 51092 Reims cedex, France; e-mail: lpi-erot@gmail.com

Indicates open access to non-subscribers at www.ajnr.org

Evidence-Based Medicine Level 2.

<http://dx.doi.org/10.3174/ajnr.A3869>

to the shape of the WEB-DL. The proximal surface of the WEB-DL is not flat but has a recess, which is concave from the direction of the parent artery. The WEB-DL and its recess conform to the aneurysm on the basis of the physician's WEB-DL size choice. For example, the physician may choose to minimize the WEB-DL parent vessel protrusion by allowing the recess to form within the aneurysm sac; however, this contributes to the appearance of a neck remnant, though this remnant is located centrally and proximally relative to the WEB-DL. Alternatively, with a different WEB-DL size choice, the recess can be removed and the proximal portion of the WEB-DL resides in the neck/parent vessel interface as a flow divider.

Aneurysm coil recanalization is an important issue in endovascular therapy, with approximately 20% of coiled aneurysms recanalized and 10% retreated.¹⁰ As previously shown, wide-neck aneurysms are highly prone to recanalization.¹¹

The goal of this retrospective, multicenter, European study was to analyze the midterm clinical outcome, short- (3–8 months) and midterm (≥ 9 months) anatomic results after WEB-DL aneurysm treatment, and the stability of the treatment as well as the rate of retreatment. A point of particular interest was to determine whether the opacification of the proximal recess was stable with time or was a feature promoting aneurysm recanalization.

MATERIALS AND METHODS

Population

The study received institutional review board approval, and according to the design of the trial, informed consent was waived. European neurointerventional centers were selected if the center treated at least 1 patient with the WEB-DL and the treatment occurred 1 year before the data collection cutoff date (May 2013). Twelve European centers participated in the study. In these centers, a total of 67 patients were treated at least 1 year before the cutoff date.

WEB-DL Device

The self-expanding WEB-DL is a globular, braided nitinol mesh. The device is composed of inner and outer braids held together by proximal, middle, and distal radiopaque markers. The WEB-DL implant is deployed—or retrieved before detachment—in a manner similar to that of conventional endovascular coil systems by using microcatheters with an internal diameter of ≥ 0.027 inches (WEB-DL width between 5 and 8 mm) or ≥ 0.032 inches (WEB-DL width between 9 and 11 mm). Once the device is deployed, it is fully retrievable. If a satisfactory position is achieved, electrothermal detachment is instantaneous. New WEB single-layer devices, in 2 shapes, were recently developed and introduced in the European market (WEB-SL and WEB-SLS), but they were not used in this series.

Procedural Modalities

In each institution, the indication for treatment and its technique (surgery or endovascular treatment) was decided on a case-by-case basis by a local multidisciplinary team, including neurosurgeons, neuroanesthesiologists, neurologists, and neuroradiologists. The selection of aneurysms treated with the WEB-DL device

was performed autonomously in each center by the interventional neuroradiologists according to aneurysm characteristics (aneurysm status, aneurysm location and size, neck size).

Aneurysms were treated with the WEB-DL by using techniques similar to those used in the treatment of aneurysms with coils (eg, general anesthesia, intraoperative treatment with intravenous heparin, single or double femoral approach). Pre-, intra-, and postoperative antiplatelet therapy was managed in each center as indicated for typical endovascular treatment with coils (or stent and coils if this approach was a potential alternative treatment).

After accurate evaluation of aneurysm anatomy (aneurysm morphology, aneurysm transverse diameter and height, and neck size) by the treating physician using MR angiography and digital subtraction angiography, whether the treatment with WEB-DL was indicated and the appropriate device sizing were determined.

After positioning a guiding catheter into the internal carotid artery or vertebral artery, we catheterized the aneurysm by using a microcatheter and chose the WEB-DL size according to aneurysm measurements and positioned it in the aneurysmal sac per methods described in Pierot et al (2013).⁹ A control angiogram was obtained to check the position of the device in the aneurysm and to evaluate flow stagnation inside it. XperCT (Philips Healthcare, Best, the Netherlands) and DynaCT (Siemens, Erlangen, Germany) are complementary acquisitions produced by a flat panel detector, which facilitate the visualization of the device after deployment because it is not completely visible on fluoroscopy. However, these were only used in a limited number of patients in the present series. If the position was not satisfactory, the device was resheathed and repositioned. If the size was not appropriate, the device was resheathed and another device was deployed into the aneurysm. When the right-sized device was correctly positioned, a final DSA run was performed. Treatment with ancillary devices (balloon, coils, and stent) was performed if deemed necessary by the treating physician.

Data Collection

Each center completed a patient file with the following data: patient age and sex, aneurysm status (ruptured/unruptured), aneurysm characteristics including location classified into 4 groups (internal carotid artery, middle cerebral artery, posterior circulation, anterior communicating artery), size and neck size, date of the procedure, occurrence of a complication during or after the procedure, use of an additional device during the procedure (coils, remodeling balloons, stents, or flow diverters), and modified Rankin Scale score at discharge and at last follow-up.

Pre- and postoperative short-term (3–8 months) and midterm images (at least 9 months) were collected. For DSA, frontal, lateral, and working views were collected as well as 3D angiography when available. For MRA and CT angiography, frontal, lateral, and working-view reconstructions were collected. MRA or CTA examinations were used exclusively when DSA was not performed.

Data Analysis

The collected patients included those from the earliest WEB-DL clinical experience (first patient treated in October

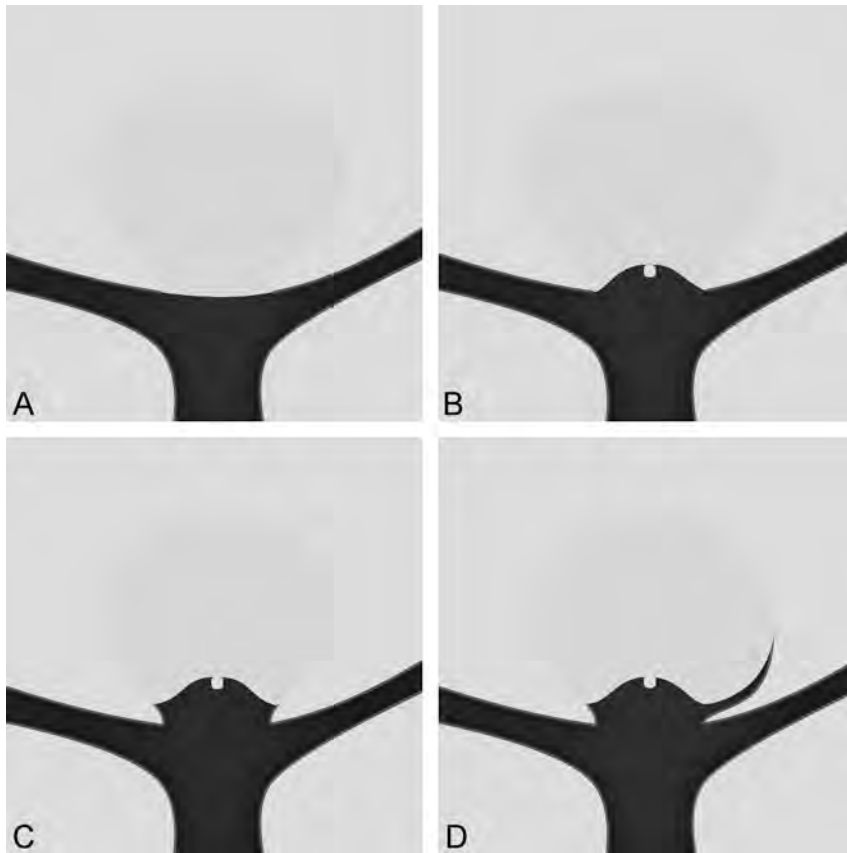


FIG 1. The drawings show the scale used for the anatomic results. *A*, Complete occlusion (grade A). There is no contrast inside the aneurysm. *B*, Complete occlusion with opacification of the proximal recess (grade AB). There is no contrast inside the aneurysm but contrast fills in the central area below the WEB-DL. *C*, Neck remnant (grade B). There is contrast at the aneurysmal wall but no contrast in the aneurysm or WEB-DL. *D*, Aneurysm remnant (grade C). There is contrast in the neck and in the aneurysm or WEB-DL.

2010), which did not have the benefit of the procedural and device learning curve. Therefore, to evaluate the anatomic results in a homogeneous population with typical indications for WEB-DL, the patients were included if their aneurysm met the following criteria:

- Located at a bifurcation: ICA, MCA, anterior communicating artery, basilar artery, posteroinferior cerebellar artery
- Nonthrombosed
- With a wide neck (≥ 4 mm)
- With a maximum diameter of ≤ 12 mm.

An independent reader who has experience with the WEB-DL but with no patient in the present series (J.-Y.G.) analyzed the images (pre- and postoperative and short-term and midterm follow-up) by using a 4-grade scale: complete occlusion, complete occlusion with opacification of the proximal recess of the device, neck remnant, and aneurysm remnant. He also analyzed the evolution of aneurysm occlusion between short- and midterm follow-up and classified it as improved, stable, or worsened.

Clinical data were reviewed by the 2 principal investigators of the study (B.L. and L.P.), who requested further clinical data if necessary.

RESULTS

Patient and Aneurysm Populations

Between October 2010 and May 2012, sixty-seven patients with 67 aneurysms were treated with the WEB-DL device in the 12 participating centers. According to the criteria defined in “Materials and Methods,” 22 patients with 22 aneurysms were excluded for the following reasons: neck of < 4 mm in 11 patients, aneurysm not located at a bifurcation in 4 patients, aneurysm size of > 12 mm in 3 patients, and partially thrombosed aneurysms in 2 patients. Two other patients were excluded due to the lack of clinical information.

Finally, the population of the study was 45 patients (34 women and 11 men), 35–74 years of age (mean, 56.3 ± 9.6 years), with 45 aneurysms treated with the WEB-DL device.

Aneurysm locations were the MCA in 26 patients, posterior circulation in 13 patients (including 11 patients with basilar artery aneurysms and 2 with posterior inferior cerebellar artery aneurysms), anterior communicating artery in 5 patients, and ICA terminus in 1 patient. Three aneurysms were ruptured, and 42 were unruptured. Aneurysm size was < 5 mm in 5 patients, 5–10 mm in 38 patients, and > 10 mm (and < 12 mm) in 2 patients.

Treatment Modalities

The treatment was conducted in a standard way in 38 patients with 1 device deployed in the aneurysm. In 1 patient, 2 WEB-DL devices were deployed in the aneurysm due to the aneurysm shape. In 4 patients, stent placement was used as an additional treatment due to WEB-DL protrusion (3 patients) and to thromboembolic complication treated with abciximab and stent (1 patient). One patient had an additional treatment with coils, and one, with coils and glue (see below).

Technical Issues, Complications, and Clinical Outcome

In 1 patient with a basilar artery aneurysm, a premature detachment of the device was observed when attempting to retrieve it because it was not an appropriate size. The device was easily removed by using standard maneuvers.

Four thromboembolic complications were observed during the treatment with the WEB-DL and were treated with intra-arterial administration of rtPA in 1 patient, IV administration of eptifibatid in 1 patient, IV abciximab and stent in 1 patient, and IV abciximab in 1 patient. In these 4 patients, the mRS score at discharge was 0 in 2 patients, 1 in 1 patient, and 2 in 1 patient. At last follow-up, the mRS score was 0 in 3 patients and 1 in 1 patient.

One patient with an MCA aneurysm had an intraoperative

rupture. The WEB-DL was deployed in a daughter sac, which was ruptured. The rupture was treated with coils and glue, and 1 branch of the MCA bifurcation was occluded, inducing an MCA infarct. The patient had an mRS score of 3 at discharge and last follow-up. This case was already published in Lubicz et al.⁸

One patient with multiple aneurysms was treated successfully with the WEB-DL for a large symptomatic posterior inferior cerebellar artery aneurysm, but 4 months after the WEB-DL procedure, the patient underwent surgical clipping of an MCA aneu-

rysm and developed aphasia and hemiparesis due to partial postsurgical occlusion of the MCA bifurcation (mRS 3). One patient with a ruptured aneurysm died 2 weeks after the treatment due to the severity of the subarachnoid hemorrhage (World Federation of Neurosurgical Societies grade 4 before treatment).

Overall clinical outcome results at last follow-up were as follows: 39 patients with mRS 0, three patients with mRS 1, two patients with mRS 3 (unrelated to the WEB-DL treatment in 1 patient), and 1 patient with mRS 6. The 2 patients with mRS 3 at

follow-up were mRS 0 before treatment. The patient with mRS 6 (ruptured aneurysm) was World Federation of Neurosurgical Societies grade 4 before treatment. Overall, good clinical outcome (mRS \leq 2) was observed in 42/45 patients (93.3%).

Retreatment

Four of 45 patients (8.9%) were retreated within months following the initial WEB-DL treatment. Two of these retreatments were planned according to aneurysm morphology and were part of the treatment strategy. In a 52-year-old woman with a right MCA aneurysm of >10 mm with a wide neck, the WEB-DL device was placed in the fundus and the neck was intentionally not completely occluded. Four months after the initial treatment, an additional treatment was performed with a stent and coils to close the neck. A similar approach was performed in a 47-year-old woman with an MCA aneurysm. The fundus was occluded with a WEB-DL, and the neck, with coils 7 months later.

Two retreatments were unplanned. In a 57-year-old man with a 10-mm basilar artery aneurysm, the WEB-DL was undersized. A thromboembolic

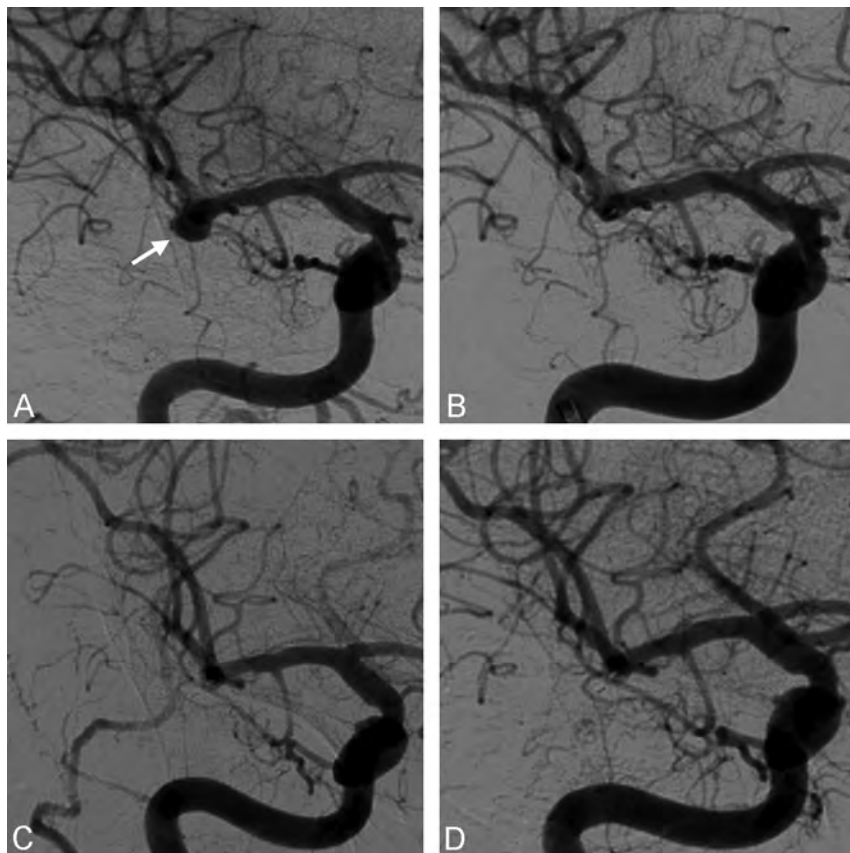


FIG 2. A 71-year-old woman with an unruptured right MCA. *A*, Preoperative DSA shows the wide-neck MCA aneurysm. *B*, Postoperative DSA shows no more intra-aneurysmal flow. *C*, Six-month follow-up DSA shows the complete occlusion of the aneurysm. *D*, Twelve-month follow-up DSA shows the stability of the complete occlusion.



FIG 3. A 57-year-old man with an unruptured anterior communicating artery aneurysm. *A*, Preoperative DSA shows the wide-neck anterior communicating artery aneurysm. *B*, Six-month DSA shows an opacification of the proximal recess of the device. *C*, Twelve-month DSA shows the stability of this opacification.

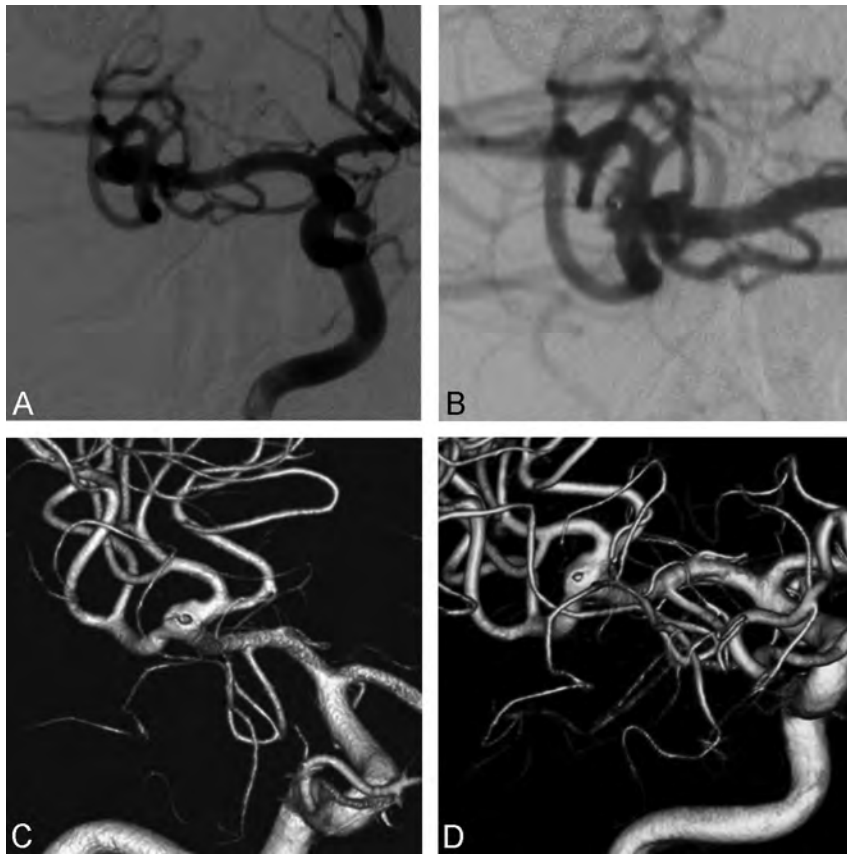


FIG 4. A 71-year-old woman with an unruptured right MCA aneurysm. *A*, Preoperative DSA shows the MCA aneurysm with a wide neck. *B*, Postoperative DSA shows a small residual opacification of the aneurysm neck with complete disappearance of flow in the dome. *C*, Seven-month 3D-DSA shows an opacification of the proximal recess of the device. *D*, Twelve-month 3D-DSA shows that this opacification is quite stable.

complication occurred intraoperatively in the left P1 segment and was treated with abciximab and stent placement. At 3 months, the aneurysm remnant was depicted, and it was retreated at 5 months with stent and coils. In a 39-year-old man, a wide-neck 7-mm MCA aneurysm recanalized 2 months after the treatment with an undersized (in height) WEB-DL. The aneurysm remnant was treated with coils 2 months after the initial treatment.

Short-Term Anatomic Outcome

Because the goal of the study was to evaluate the quality and stability of aneurysm occlusion after WEB-DL treatment, the 6 patients with additional coiling and/or stent placement were not included in the evaluation. One patient had no short-term follow-up imaging, and 1 patient died (see above). Finally, 37/45 patients (82.2%) were evaluated in the short-term. Short-term follow-up was obtained from 2 to 8 months after the initial treatment (mean, 5.0 ± 2.3 months; median, 6 months). Modalities of short-term follow-up were DSA in 33 patients, MRA in 3 patients, and CTA in 1 patient.

Complete aneurysm occlusion was obtained in 9/37 patients (24.3%) (Fig 1); opacification of the proximal recess with complete occlusion of the aneurysm, in 12/37 patients (32.4%) (Figs 2 and 3); neck remnant, in 9/37 patients (24.3%) (Figs 4 and 5); and aneurysm remnant, in 7/37 patients (18.9%). Adequate occlusion

(complete occlusion, opacification of the proximal recess, or neck remnant) was observed in 30/37 patients (81.1%).

Midterm Anatomic Outcome

Because the goal of the study was to evaluate the quality and stability of aneurysm occlusion after WEB-DL treatment, 9 patients with additional coiling and/or stent placement or retreatment were not included in the evaluation (1 patient had both additional treatment and retreatment). One patient died (see above), and 6 patients refused midterm follow-up examinations. Finally, 29/45 patients (64.4%) were evaluated in the midterm. Midterm follow-up was obtained from 9 to 28 months after the initial treatment (mean, 14.3 ± 7.0 months; median, 13 months). Modalities of midterm follow-up were DSA in 22 patients and MRA in 7 patients.

Complete aneurysm occlusion was obtained in 8/29 patients (27.6%); opacification of the proximal recess with complete occlusion of the aneurysm, in 12/29 patients (41.4%); neck remnant, in 6/29 patients (20.7%); and aneurysm remnant, in 3/29 patients (10.3%). Adequate occlusion (complete occlusion, opacification of the proximal recess, or neck remnant) was observed in 26/29 patients (89.7%).

Evolution between Short- and Midterm Follow-Up

Among the 29 patients with midterm follow-up, 1 had no short-term follow-up. Thus, the evolution of aneurysm occlusion was evaluable in 28 patients. In 26/28 patients (92.9%), aneurysm occlusion was stable (Fig 1). In 2/28 patients (7.1%) with neck remnants at 3 months, a worsening of the aneurysm occlusion was observed in midterm follow-up, with an aneurysm remnant in both cases (Fig 5).

All patients with opacification of the proximal recess at 3–6 months had a stable aneurysm occlusion at midterm follow-up (Figs 2 and 3).

DISCUSSION

Our retrospective study analyzed the midterm clinical outcome, and the short- and midterm results of the first WEB-DL-treated patients with wide-neck, bifurcation intracranial aneurysms in 12 European centers. This study included patients treated during the individual and global procedure/device learning curve; however, the data suggest several interesting aspects of WEB-DL intrasaccular flow disruption.

Overall the midterm clinical follow-up showed a very high rate of patients with good clinical outcome (93.3%), given that 1 patient had an mRS score of 3 due to surgical treatment of another aneurysm. This good midterm clinical outcome confirms what

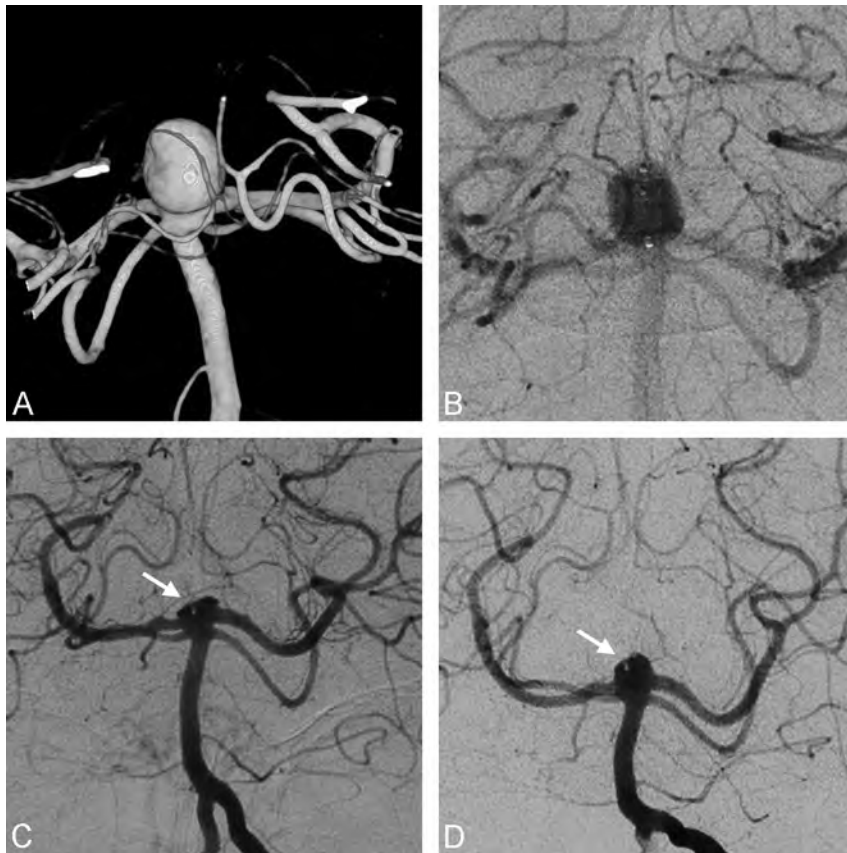


FIG 5. A 60-year-old woman with an unruptured basilar artery aneurysm. *A*, Preoperative 3D-DSA shows the aneurysm, which is wide-neck. *B*, Postoperative DSA shows contrast stagnation in the WEB and aneurysm; *C*, 3-month DSA shows a neck remnant. *D*, 9-month DSA shows the reopening of the aneurysm with a remnant.

was observed in previous WEB-DL series and compares favorably with outcomes of other sophisticated techniques like stent placement and flow diversion.^{7-9,12-14}

At the beginning of the global experience with WEB-DL, indications for treatment with the WEB-DL device were not precisely known and some aneurysms were initially treated that are now not typically treated with the WEB-DL device. Anatomic results were analyzed in patients with aneurysms that are now typical indications for WEB-DL (wide-neck, bifurcation aneurysms with an average width of >4 mm but <12 mm).

Because this series reflects the initial experience with the device, it is clear that the physicians had no technical experience and may have made some technical errors, for example in the sizing of the device, which is an important issue, likely explaining the rate of additional treatments performed during the initial procedures as well as the rate of retreatment observed in the months following the initial treatment. To accurately analyze the efficacy of the WEB-DL device alone, patients with aneurysms treated with WEB-DL and additional treatment were not included in the analysis of the anatomic results. For the same reason, patients with aneurysms retreated during the follow-up period were not included in the anatomic analysis.

The present series shows that in this group of complex wide-neck bifurcation aneurysms, appropriate occlusion was obtained in a high percentage of cases in the short- (81.1%) and midterm (89.7%) results. The treatment was quite stable with time, with

worsening of the occlusion status in only 7.1% between short- and midterm follow-up. Most important, all aneurysms with opacification of the proximal recess at short-term follow-up had stable occlusion at midterm follow-up.

As was previously shown, neck size is a critical factor for aneurysm recanalization and midterm anatomic results in aneurysms treated with coils. In the Clinical and Anatomical Results in the Treatment of Ruptured Intracranial Aneurysms (CLARITY) study—dealing with ruptured aneurysms—aneurysm neck size was identified as the single most important factor in the quality of aneurysm occlusion at midterm follow-up after standard endovascular treatment.¹¹ In this series, adequate occlusion was obtained in the whole population (narrow and wide-neck aneurysms) in 80.4% at midterm follow-up after bare platinum coil treatment. In wide-neck aneurysms, the rate of adequate occlusion was 68.2%, which is much lower than the 89.7% observed in the present series. Also in the review of Ferns et al¹⁰ dealing with narrow and wide-neck aneurysms, the rate of adequate occlusion at follow-up was only 83.4%, lower than the percentage in the

present series.

With WEB-DL treatment, aneurysm occlusion was stable (between short- and midterm follow-ups) in most aneurysms (92.9%), and worsening of aneurysm occlusion was observed in only 7.1% of cases. Worsening was exclusively observed in aneurysms with a neck remnant at short-term follow-up. In the CLARITY study,¹¹ worsening of aneurysm occlusion was observed in 51.1% of aneurysms in the whole group and in 62.1% in wide-neck aneurysms. Most interesting, the specific pattern “complete occlusion with opacification of the proximal recess” was not modified between short- and midterm follow-up, and it can be considered complete aneurysm occlusion.

The rate of retreatment in the present series (8.9%) is slightly higher than that reported in CLARITY (6.2%),¹¹ but it was slightly lower than that calculated in the Ferns et al review (10.3%).¹⁰ As previously mentioned, the present series dealt with the first cases treated in the 12 participating centers and clearly during the learning curve. In 2 retreatments, the WEB-DL device was undersized in the initial treatment; this result clearly reflected the lack of experience. In 2 other complex aneurysms, retreatment with coils was initially planned, with the WEB-DL device being used to modify the shape of the neck. Because these 2 cases are not true retreatments, the retreatment rate is, in fact, 2/45 aneurysms (4.4%), which is quite acceptable in the specific population of the series.

Our study has several limitations. First, the series is retrospec-

tive and has a limited number of patients ($n = 45$), and midterm follow-up was not available for all (29/45). However, because it is a new endovascular treatment, it was important to have a rapid and accurate preliminary evaluation of the quality and stability of aneurysm occlusion in the midterm. A second limitation is that short- and midterm anatomic evaluations were conducted by using different modalities (mostly DSA and MRA). However, recent publications confirm the value of MRA in the follow-up of intracranial aneurysms.^{15,16} A third limitation is that only the WEB-DL (and not WEB-SL and WEB-SLS) was evaluated.

CONCLUSIONS

In this series dedicated to clinical and anatomic follow-up of complex, wide-neck bifurcation aneurysms, treatment with the WEB-DL was associated with a high rate of good clinical outcome (93.3%) and appropriate occlusion in short- and midterm follow-ups (respectively, 81.1% and 89.7%) and limited worsening of the aneurysm occlusion between short- and midterm follow-ups (7.1%). Opacification of the proximal recess was not associated, in short- or midterm follow-up, with aneurysm recanalization and can be grouped with “complete occlusion.” Moreover, the presence of the WEB-DL recess can be delineated from true neck remnant and/or true aneurysm remnant by its central and proximal location relative to the WEB-DL.

Disclosures: Boris Lubicz—RELATED: Consulting Fee or Honorarium: Sequent Medical, Payment for Writing or Reviewing the Manuscript: Sequent Medical, UNRELATED: Consultancy: Codman, MicroVention, Covidien, Payment for Manuscript Preparation: Sequent Medical, Payment for Development of Educational Presentations: Codman.* Joachim Klisch—RELATED: Consulting Fee or Honorarium: Sequent.* Istvan Szikora—RELATED: Provision of writing assistance, medicines, equipment, or administrative support: Sequent Medical.* Comments: no money paid, some products provided free of charge. UNRELATED: Consultancy: Stryker Neurovascular, Codman, Covidien, Payment for Lectures (including service on Speakers Bureaus): Stryker Neurovascular, Codman. Thomas Liebig—UNRELATED: Consultancy: Stryker, Covidien, Sequent Medical, Comments: consulting fee regarding preclinical work and proctoring the product, Payment for Lectures (including service on Speakers Bureaus): Stryker, Sequent Medical, Comments: payment for lecturing in satellite symposia. Nunzio Paolo Nuzzi—RELATED: Consulting Fee or Honorarium: Sequent Medical, Comments: proctor for WEB clinical use, UNRELATED: Consultancy: Covidien, Comments: proctor for clinical use of Pipeline Embolization Device. Markus Holtmannspötter—UNRELATED: Consultancy: Covidien, MicroVention, Sequent Medical, Comments: proctoring and consulting fees; Payment for Lectures (including service on Speakers Bureaus): Covidien, MicroVention, Sequent Medical. Werner Weber—UNRELATED: Other: Sequent Medical, Comments: I am a proctor for the WEB device, and our institution is participating on the WEB Clinical Assessment of IntraSaccular Aneurysm Therapy study.* Laurent Pierot—RELATED: Consulting Fee or Honorarium: Sequent, UNRELATED: Consultancy: Codman, Covidien, MicroVention, Penumbra. *Money paid to the institution.

REFERENCES

1. Molyneux A, Kerr R, Stratton I, et al, for the International Subarachnoid Aneurysm Trial (ISAT) Collaborative Group. **International Subarachnoid Aneurysm Trial (ISAT) of neurosurgical clipping versus endovascular coiling in 2143 patients with ruptured intracranial aneurysms: a randomised trial.** *Lancet* 2002;360:1262–63
2. Mc Dougall CG, Spetzler RF, Zabramski JM, et al. **The Barrow Ruptured Aneurysm Trial.** *J Neurosurg* 2012;116:135–44
3. Cognard C, Pierot L, Anxionnat R, et al. **Results of embolization used as the first treatment choice in a consecutive non selected population of ruptured aneurysms: clinical results of the CLARITY GDC study.** *Neurosurgery* 2011;69:837–41
4. Pierot L, Spelle L, Vitry F, for the ATENA investigators. **Clinical outcome of patients harbouring unruptured intracranial aneurysms treated by endovascular approach: results of the ATENA trial.** *Stroke* 2008;39: 2497–504
5. Pierot L, Wakhloo A. **Endovascular treatment of intracranial aneurysms: current status.** *Stroke* 2013;44:2046–54
6. Ding YH, Lewis DA, Kardivel R, et al. **The Woven EndoBridge: a new aneurysm occlusion device.** *AJNR Am J Neuroradiol* 2011;32:607–11
7. Pierot L, Liebig T, Sychra V, et al. **Intrasaccular flow-disruption treatment of intracranial aneurysms: preliminary results of a multicenter clinical study.** *AJNR Am J Neuroradiol* 2012;33:1232–38
8. Lubicz B, Mine B, Collignon L, et al. **WEB device for endovascular treatment of wide-neck bifurcation aneurysms.** *AJNR Am J Neuroradiol* 2013;34:1209–14
9. Pierot L, Klisch J, Cognard C, et al. **Middle cerebral artery aneurysms: feasibility, clinical and anatomical results of the endovascular treatment by WEB flow disruption: preliminary evaluation in a multicenter study.** *Neurosurgery* 2013;73:27–34
10. Ferns SP, Sprengers ME, van Rooij WJ, et al. **Coiling of intracranial aneurysms: a systematic review on initial occlusion and reopening and retreatment rates.** *Stroke* 2009;40:e523–e529
11. Pierot L, Cognard C, Anxionnat R, et al. **Endovascular treatment of ruptured intracranial aneurysms: factors affecting mid-term quality anatomic results—analysis in a prospective multicenter series of patients (CLARITY).** *AJNR Am J Neuroradiol* 2012;33:1475–80
12. Shapiro M, Becske T, Sahlein, et al. **Stent-supported aneurysm coiling: a literature survey of treatment and follow-up.** *AJNR Am J Neuroradiol* 2012;33: 159–63
13. Pierot L. **Flow diverter stents in the treatment of intracranial aneurysms: where are we?** *J Neuroradiol* 2011;38:40–46
14. Becske T, Kallmes DF, Saatci I, et al. **Pipeline for uncoilable or failed aneurysms: results from a multicenter clinical trial.** *Radiology* 2013;267:858–68
15. Pierot L, Portefaix C, Gaurvit JY, et al. **Follow-up of coiled intracranial aneurysms: comparison of 3D time-of-flight at 3T and 1.5T in a large, prospective series.** *AJNR Am J Neuroradiol* 2012;33:2162–66
16. Pierot L, Portefaix C, Boulin A, et al. **Follow-up of coiled intracranial aneurysms: comparison of 3D-time-of-flight and contrast-enhanced magnetic resonance angiography at 3T in a large, prospective series.** *Eur Radiol* 2012;22:2255–63

Utility of Diffusion Tensor Imaging in Evaluation of the Peritumoral Region in Patients with Primary and Metastatic Brain Tumors

EJ. Sternberg, M.L. Lipton, and J. Burns

ABSTRACT

SUMMARY: In the brain, diffusion tensor imaging is a useful tool for defining white matter anatomy, planning a surgical approach to space-occupying lesions, and characterizing tumors, including distinguishing primary tumors from metastases. Recent studies have attempted, with varying success, to use DTI to define the extent of tumor microinfiltration beyond the apparent borders on T2-weighted imaging. In the present review, we discuss the current state of research on the utility of DTI for evaluating the peritumoral region of brain tumors.

ABBREVIATIONS: FA = fractional anisotropy; MD = mean diffusivity; TII = tumor infiltration index

Malignant brain tumors such as glioblastoma multiforme have an infiltrative pattern of growth, often invading the surrounding tissue.^{1,2} Actual tumor margins can extend microscopically for several centimeters past the radiographically detected margin of disease.³ Furthermore, infiltrative brain tumors are surrounded by extensive areas of edema, as detected on T2-weighted imaging. The transition between the tumor edge and peritumoral edema is ambiguous. In metastatic tumors, this peritumoral edema is thought to consist of pure water, which can obscure tumor borders. However, the peritumoral edema of infiltrative tumors such as glioblastoma multiforme has often been shown to contain tumor cells that have spread into the edematous tissue.⁴ Conventional imaging techniques such as MR imaging and CT are not able to detect this minute cellular infiltration, and studies show that tumor cells have been demonstrated beyond tumor borders as defined by these modalities.⁵⁻⁸ This limitation of conventional CT and MR imaging presents a serious challenge for treatment planning. In successful surgical resection or biopsy with adjuvant therapy, the tumor must be excised to the greatest extent possible while minimizing injury to nearby healthy tissue.

Standard imaging techniques tend to underestimate the extent of tumor involvement, a problem that can lead to suboptimal treatment and a worse prognosis.⁹

Studies of animal models provide insight into the mechanisms of change in DTI metrics and imply that DTI may have a role in more precisely defining the extent of tumor cell infiltration. Among other applications, DTI has been successfully used in animals for mapping white matter tracts,¹⁰ for characterizing the directionality of diffusion within tumors,¹¹ and as a marker of pathologic states such as demyelination.¹² Several animal studies have also used DTI to detect tumor microinfiltration into surrounding tissue, by using histologic analysis as the criterion standard.^{13,14} For example, Lope-Piedrafita et al (2008)¹⁵ implanted glioma cells (C6) into the brains of 6 adult rats and, by using DTI metrics, showed that fractional anisotropy (FA) values in the tissue contralateral to the tumor were relatively high and did not change significantly with time, while the FA values adjacent to the tumor, though they were initially similar to those of the contralateral side, tended to decrease as the tumor grew. This reduction in fractional anisotropy became significant by day 6 of growth, suggesting that as the tumor grew, cancer cells infiltrated the tissue surrounding the tumor. The introduction of these more randomly distributed cells among white matter axons caused a reduction in the uniformity of water diffusion within tissue, leading to lower FA values of the peritumoral white matter on DTI.

In a similar study, Kim et al (2008)¹⁶ used DTI to monitor the growth of rapid-growing F98 and the slower growing 9L tumor models in rats. In evaluating the peritumoral regions, they found that due to tissue compression from rapid growth, the coefficient of planar anisotropy was higher surrounding

Received May 9, 2013; accepted after revision June 12.

From Tufts University School of Medicine (E.J.S.), Boston, Massachusetts; the Gruss Magnetic Resonance Research Center and Departments of Radiology, Psychiatry, and Behavioral Sciences and the Dominick P. Purpura Department of Neuroscience (E.J.S., M.L.L.), Albert Einstein College of Medicine, Bronx, New York; Department of Radiology (M.L.L., J.B.), Montefiore Medical Center, Bronx, New York.

The authors declare that there are no conflicts of interest and no competing financial interests.

Please address correspondence to Judah Burns, MD, Division of Neuroradiology, Department of Radiology, Montefiore Medical Center, Albert Einstein College of Medicine III E 210th St, New York, NY 10467; e-mail: jburns@montefiore.org

<http://dx.doi.org/10.3174/ajnr.A3702>

Summary table of DTI studies of the peritumoral region

Article	No.	Design	Measures	Tumor types	Criterion Standard	Conclusion ^a
Deng et al, 2010 ²⁷	20	Prospective cohort study	FA, ADC	<input checked="" type="checkbox"/> Primary <input type="checkbox"/> Metastasis <input type="checkbox"/> Extra-axial	Tissue	Yes
Wang et al, 2009 ²⁸	49	Retrospective analysis	FA, p, q, L	<input checked="" type="checkbox"/> Primary <input type="checkbox"/> Metastasis <input type="checkbox"/> Extra-axial	None	Yes
Price et al, 2006 ²⁹	20	Prospective cohort study	FA, p, q	<input checked="" type="checkbox"/> Primary <input checked="" type="checkbox"/> Metastasis <input type="checkbox"/> Extra-axial	Tissue	Yes
Sinha et al, 2002 ¹³	9	Prospective cohort study	FA, MD	<input checked="" type="checkbox"/> Primary <input type="checkbox"/> Metastasis <input type="checkbox"/> Extra-axial	None	No
Provenzale et al, 2004 ²⁶	17	Retrospective analysis	FA, ADC	<input checked="" type="checkbox"/> Primary <input type="checkbox"/> Metastasis <input checked="" type="checkbox"/> Extra-axial	None	Yes
Lu et al, 2003 ²⁰	24	Prospective cohort study	FA, MD	<input checked="" type="checkbox"/> Primary <input checked="" type="checkbox"/> Metastasis <input type="checkbox"/> Extra-axial	None	Yes
Lu et al, 2004 ²⁴	40	Retrospective analysis	FA, MD, TII	<input checked="" type="checkbox"/> Primary <input checked="" type="checkbox"/> Metastasis <input checked="" type="checkbox"/> Extra-axial	None	Yes
Price et al, 2003 ²³	20	Prospective cohort study	RAI	<input checked="" type="checkbox"/> Primary <input checked="" type="checkbox"/> Metastasis <input type="checkbox"/> Extra-axial	None	Yes
Sundgren et al, 2006 ²¹	28	Prospective cohort study	FA, ADC	<input checked="" type="checkbox"/> Primary <input checked="" type="checkbox"/> Metastasis <input type="checkbox"/> Extra-axial	Follow-up	Yes
van Westen et al, 2006 ¹⁴	30	Prospective cohort study	FA, ADC	<input checked="" type="checkbox"/> Primary <input checked="" type="checkbox"/> Metastasis <input checked="" type="checkbox"/> Extra-axial	Tissue, cytology	No
Kinoshita et al, 2010 ³⁰	14	Retrospective analysis	FA, ADC, TII	<input checked="" type="checkbox"/> Primary <input checked="" type="checkbox"/> Metastasis <input checked="" type="checkbox"/> Extra-axial	None	No
Tropine et al, 2004 ²⁵	12	Prospective cohort study	FA, MD	<input checked="" type="checkbox"/> Primary <input type="checkbox"/> Metastasis <input checked="" type="checkbox"/> Extra-axial	None	Inconclusive

Note:—p indicates pure isotropic vector component; q, pure anisotropic vector component; L, total magnitude of the diffusion tensor; RAI, relative anisotropy index.
^a Whether the study data suggest that DTI has utility in determining the extent of brain tumor infiltration.

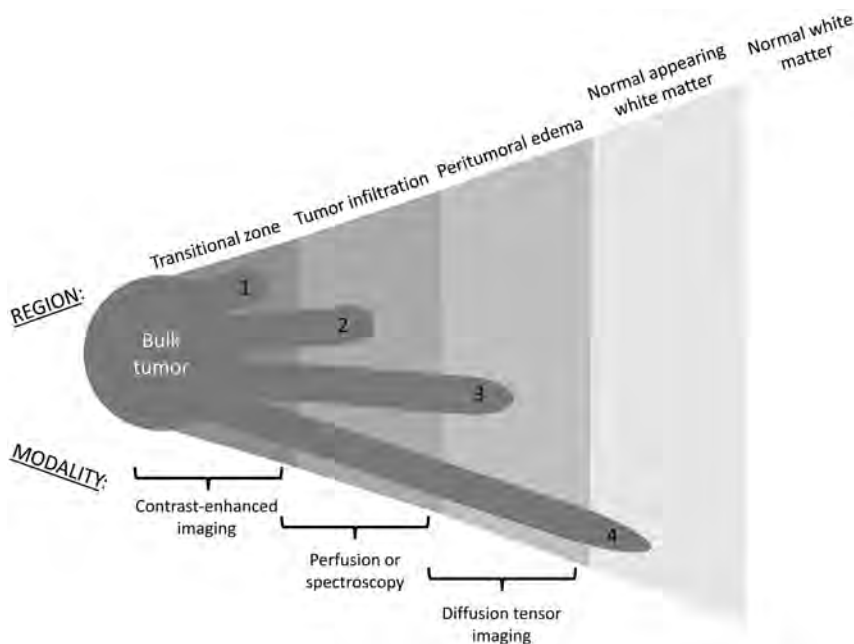


FIG 1. The peritumoral region and corresponding imaging modalities. Tumor cells can extend beyond the bulk tumor into vaguely concentric subdivisions of the peritumoral region, including the transitional zone (1), the region of tumor infiltration (2), the peritumoral edema (3), and even the normal-appearing white matter (4).

both tumors than in the tumor itself. Similarly, also due to mass effect, the tertiary eigenvalue was lower in the 9L peritumoral region compared with the tumor body. In contrast, despite the faster growth of F98 tumors, the tertiary eigenvalue in their peritumoral region was higher than that of the tumor body. It was suggested that this was due to infiltration of tumor cells into the peritumoral tissue, and this hypothesis was supported by histologic analysis of tumor invasiveness.¹⁶

Findings in animal models suggest that DTI may have a role in human tumor characterization. A number of studies have attempted to use DTI to more precisely delineate the margins of brain tumors in humans and detect changes in the normal-appearing tissue surrounding malignant gliomas that are not detectable on conventional MR imaging. There is good early investigational evidence to support the use of DTI in evaluating the peritumoral region; therefore, focused research in this regard will

be needed. The purpose of this review is to highlight the available literature as a basis for further research.

Literature Search Approach and Results

Using variations of the search term “diffusion tensor imaging brain tumor,” we acquired our raw list of articles from the PubMed data base. For completeness, we also looked for relevant articles cited by these publications. Our search yielded 252 articles that discussed DTI. Of those, there were 5 animal studies, 35 case reports, 2 letters, 1 meta-analysis, 137 randomized controlled trials, 21 retrospective studies, and 51 reviews. In terms of content, 33 articles concerned the peritumoral region; 108, white matter tractography and/or surgical approach; 46, bulk tumor characterization; and the rest covered miscellaneous topics. Of the peritumoral articles, 12 directly addressed the question of whether DTI has utility in evaluating tumor infiltration in the peritumoral region (Table). These studies typically used

ROIs and an expert rater to evaluate DTI results. A notable limitation in discussing these studies is that they are not consistent in precisely which subdivision of the peritumoral region (Fig 1) they address. FA values vary depending on location, such as whether they are measured in compact or noncompact regions of tissue. This must be taken into account in any DTI analysis so as not to compromise the specificity of study results.

Finally, the tractography results reviewed here are based on deterministic algorithms. Other approaches, such as probabilistic tractography and multishell dMRI, may overcome obstacles to tractography such as crossing-fiber zones and abnormal tissue. While these techniques may improve the delineation of tract-based ROIs in the peritumoral region, this review specifically focuses on assessments of scalar metrics of anisotropy because these comprise the methods that have been reported to date.

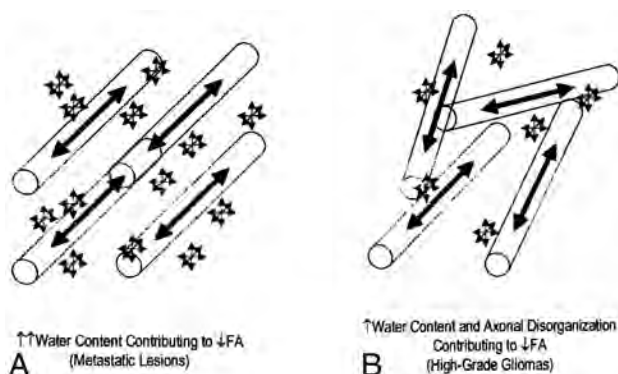


FIG 2. Schematic illustrating the factors behind the comparable change in peritumoral FA. *A*, Water content contributing to decreased FA in metastatic lesions. *B*, Water content and axonal disorganization contributing to decreased FA in high-grade gliomas. Reprinted from Lu et al.²⁰

Distinguishing Primary Brain Tumors from Metastases

Brain tumors, regardless of whether primary or metastatic, are surrounded by some degree of vasogenic edema, detectable as hyperintensity on T2-weighted images. Diffusion metrics have been shown to be altered within this surrounding edema, compared with internal controls, in both high-grade gliomas and metastatic tumors, reflecting the presence of, at minimum, increased extracellular water. It has been shown further, by using DWI, that the diffusivity of the peritumoral edema varies depending on the characteristics of the tumor it encompasses. High-grade gliomas are associated with edema of high trace value (mean diffusivity [MD], computed by averaging the diagonal elements of the matrix¹⁷), whereas the low-grade gliomas or nonglial tumors are associated with edema of low trace value. Morita et al (2005)¹⁸ found a similar range of anisotropy in both types of edema, yet the diffusivity was much greater in the edema surrounding high-grade gliomas. They concluded that the “higher diffusivity of water molecules within the area of edema associated with high-grade gliomas is likely to reflect destruction of the extracellular matrix ultrastructure by malignant cell infiltration.”¹⁸ This conclusion was supported by a subsequent study by Kimura et al¹⁹ by using changes in glutamate levels (as a marker of the integrity of the extracellular matrix) as the central measure. Figure 2 illustrates the factors behind comparable changes in peritumoral FA.

Current research demonstrates that surrounding both primary brain tumors and metastatic tumors, there is an increase in mean diffusivity and a decrease in FA compared with normal-appearing white matter, measurements best explained by increased extracellular water. The greater the amount of free water in tissue, the greater the magnitude of diffusion will be (increased MD) and the more disorganized the diffusion becomes (decreased FA).¹⁹ Lu et al (2003)²⁰ found that the peritumoral MD of metastatic lesions was greater than that of gliomas, while the peritumoral FA between the 2 tumor types demonstrated no significant difference. This finding implies that the reduced FA surrounding gliomas can be attributed not only to increased extracellular water but also to axonal disorganization caused by infiltration of the tumor beyond its detectable margin.

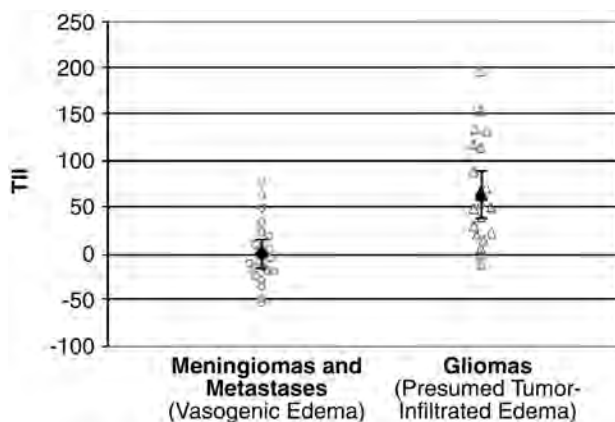


FIG 3. Graph of TII values in meningiomas and metastases compared with TII in gliomas. The mean TII of meningiomas and metastases is zero, with a 95% CI between -15 and 15. The mean TII of gliomas is 64, with a 95% CI between 38 and 90. Reprinted with permission from Lu S, Ahn D, Johnson G, et al. Diffusion-tensor MR imaging of intracranial neoplasia and associated peritumoral edema: introduction of the tumor infiltration index. *Radiology* 2004;232:221–28.²⁴

Distinguishing Tumor Extension from Edema of the Peritumoral Region

External support for this notion that reduced FA in peritumoral edema is a marker of tumor infiltration comes from the Sundgren et al (2006)²¹ study of recurrent and nonrecurrent brain tumors. Tumors that have great infiltrative potential are more likely to recur than tumors lacking such potential.²² Sundgren et al measured the FA values in the normal-appearing white matter bordering the peritumoral edema of recurrent and nonrecurrent tumors. These investigators reported significantly lower FA values in the normal tissue surrounding recurrent tumors compared with nonrecurrent tumors,²¹ suggesting the presence of microinfiltration by the recurrent tumors into the peritumoral white matter. This hypothesis could be neatly reconciled with the known correlation between tumors of high infiltrative capacity and the associated recurrence risk. Earlier work has similarly shown that changes in DTI metrics can identify subtle white matter disruption due to occult infiltration by aggressive cancers.²³

In a second study in 2004, Lu et al²⁴ looked retrospectively at DTI data from 40 patients and attempted to determine whether the MD and FA could be used to distinguish intra-axial from extra-axial lesions, metastatic lesions from gliomas, and high-grade (World Health Organization grades III–IV) from low-grade (World Health Organization grade II) gliomas. However, to better define the extent of tissue infiltration, these investigators used a third metric that they termed the “tumor infiltration index (TII),” which was calculated from DTI data by the following formula:

$$TII = (FA_{exp} - FA_{obs})10^3,$$

where FA_{exp} is the expected FA for the corresponding MD, assuming no tumor infiltration (as determined by a linear regression analysis of such data) and FA_{obs} is the currently measured FA. Thus, in order for the results to be consistent with those of the above study, the TII of noninfiltrative tumors should be approximately zero, while the TII of infiltrative tumors should be considerably higher. That is indeed the outcome achieved. Gliomas had a mean TII of 64, while metastases and meningiomas had a mean TII of 0 (Fig 3).

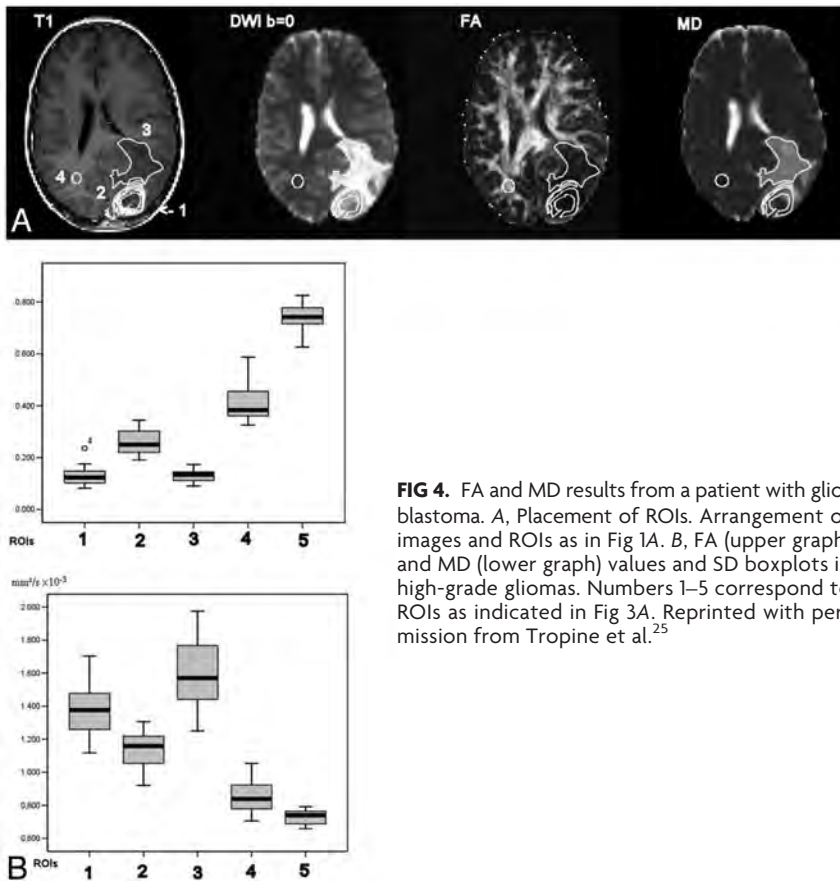


FIG 4. FA and MD results from a patient with glioblastoma. A, Placement of ROIs. Arrangement of images and ROIs as in Fig 1A. B, FA (upper graph) and MD (lower graph) values and SD boxplots in high-grade gliomas. Numbers 1–5 correspond to ROIs as indicated in Fig 3A. Reprinted with permission from Tropine et al.²⁵

A number of other studies have emerged that lend support to the notion that DTI metrics might be a useful marker of tumor infiltration into the surrounding tissue. For example, Tropine et al (2004)²⁵ found a reduction of FA in the peritumoral, T2 signal-enhancing region of glioblastomas compared with meningiomas and concluded that this may be an indicator of tumor cell infiltration, though they questioned the reliability of such a test given the evidence available. DTI results from a patient with glioblastoma are shown in Fig 4.

A similar study by Provenzale et al (2004)²⁶ further demonstrated the efficacy of DTI in differentiating normal and tumor-infiltrated peritumoral tissue. The investigators found that mean FA values in peritumoral hyperintense regions were 43% of the normal white matter value for gliomas and 65% of the normal white matter value for meningiomas ($P = .05$), while the mean FA values for normal-appearing white matter neighboring the tumors were 83% of the normal value for patients with gliomas and 100% of the normal value for those with meningiomas ($P = .01$).²⁶ In other words, there was a noticeable but statistically insignificant difference in FA in the hyperintense regions of gliomas and meningiomas. However, the magnitude of the decrease in FA in the normal-appearing, neighboring white matter was significant: The decrement was greater in patients with glioma ($P = .01$). The fact that DTI analysis reveals a disparity in the FA of peritumoral normal-appearing tissue and that this disparity is greater in the tissue neighboring the gliomas than in neighboring meningiomas perhaps implies that DTI has the potential to detect tumoral

infiltration that cannot be discerned by standard MR imaging techniques.

Recent evidence further supports the notion that DTI, specifically the FA value, is a useful tool in precisely delineating tumor margins. Deng et al (2010)²⁷ correlated fractional anisotropy with the distance from visible tumor margins in gliomas and found that the value increases as the distance from the tumor increases. In addition, by obtaining tissue samples from the regions of interest as determined on MR imaging, these investigators observed a negative association between FA values from the peritumoral edema of gliomas and the degree of tumor infiltration (categorized as mild, moderate, severe, or no infiltration).²⁷ These results are consistent with past findings that a reduction in FA in the peritumoral region could be used as a quantitative index of tumor cell infiltration.

In addition to FA and MD, several eigenvalues derived from DTI have been successfully used for studying the extent of brain tumor infiltration. These include the pure isotropic component (p), the pure anisotropic component (q), and the total magnitude of the diffusion tensor (L), where $L = \sqrt{p^2 + q^2}$.²⁸ It has

been found, for example, that by using the pure diffusion components, one can distinguish gross tumor (reduction of $q > 12\%$ from contralateral region) from tumor infiltration (increase $p > 10\%$ from contralateral region).²⁹ These metrics may perhaps strengthen the role of DTI in the analysis of the peritumoral region.

Limitations of DTI in Delineating Tumor Margins

In contrast to those studies discussed previously, several studies did not find conclusive evidence of the utility of DTI for detecting tumor infiltration. In a study of 9 patients by Sinha et al (2002),¹³ the FA values were significantly different in only 7 of the 9 patients studied and DTI was not found to have any advantage over the more conventional diffusion-weighted MR imaging (the FA differences paralleled the diffusivity differences and did not add any additional insight). With such a small study population, however, this result may not be representative.

A larger study conducted by van Westen et al (2006)¹⁴ measured the tumor-to-brain ratios of FA and ADC in T2 hyperintense regions surrounding gliomas, meningiomas, and metastases and the adjacent normal-appearing white matter of 30 patients. They found no difference among the 3 tumor types in terms of ADC magnitude, the lesion-to-brain ratios of ADC, the FA magnitude, the lesion-to-brain ratio, or FA within the peritumoral areas with T2 signal changes. Furthermore, they found no difference in the ADC or tumor-to-brain ratios of FA in the adjacent normal-appearing white matter. van Westen et al, therefore, con-

cluded that the FA was not helpful in identifying tumor-infiltrated edema. In addition, Kinoshita et al (2010)³⁰ re-evaluated the utility of the previously discussed tumor infiltration index in 14 patients, comparing DTI with ¹¹C-methionine PET, which has been shown to have utility in identifying tumor infiltration.³¹ In glioma cases ($n = 8$), the mean TII ranged from -127 to 96 , with an overall mean of 5.4 ± 65 . On the other hand, the TII for meningiomas ($n = 5$) and metastatic brain tumors ($n = 1$) ranged from -24 to 44 , with an overall mean of 6.8 ± 29 . However, these differences were not statistically significant—a finding that questions TII (a measure derived from the FA) as a tool for distinguishing tumor-infiltrated edema from vasogenic edema. However, voxel-by-voxel comparison of TII and ¹¹C-methionine PET in the areas of gliomas demonstrating T2-signal hyperintensity showed a positive correlation between the two modalities. This suggests that though TII may perhaps be unable to delineate tumor infiltration within vasogenic edema, it is still useful for identifying tumor cell infiltration into nonedematous regions.³² It has been further suggested that ¹¹C-methionine PET could be used as an adjunctive study with DTI to help distinguish tumor-infiltrated edema from typical vasogenic edema.³³

The concern may arise that the integration of results from multiple diffusion MRI studies creates the potential for systematic bias due to differences in data acquisition and analysis methods among studies. This concern is germane when quantitative measures are compared across studies. However, when study parameters (such as hardware, software, data acquisition, and analysis methods) are standardized across all subjects within a study, as in the articles reviewed herein, this concern is minimized, provided that the temporal stability of the diffusion MRI measurement is maintained during the period of data acquisition for the study sample. Because this review was based on the assessment of the findings of other studies but does not compare their quantitative measurements, this concern should be minimal in the context of this review.

CONCLUSIONS

From the evidence discussed above (Table), we contend that DTI is a sophisticated and useful tool to aid in the delineation of tumor margins and the detection of brain tumor infiltration. The evidence suggests that decreased fractional anisotropy in peritumoral tissue, compared with the corresponding contralateral brain region, is an indicator of tumor invasion past the tumor borders as detected on T2-weighted images. Although the architecture of the tissue can be highly variable and therefore create inconsistent or nonspecific results, the use of adjunctive DTI metrics can improve the quality of findings and facilitate accurate and specific conclusions.

We believe that the technique is promising but that the literature is currently insufficient to establish a definitive clinical role for DTI in the characterization of the peritumoral region. The primary reason for this is that though there have been many studies of the utility of DTI for this novel purpose (Table), few have used a criterion standard such as tissue histopathology to confirm their results. Future studies by using a criterion standard could lay the groundwork for an eventual meta-analysis that could conclusively quantify the overall effectiveness of the technique. In addition,

automated translation of DTI metrics to visual anatomic maps may make the process of evaluating the peritumoral region by using DTI more uniform and therefore more clinically relevant. We expect that continued research in this area will further advance the quality and utility of DTI for delineating tumor extent.

REFERENCES

1. Scherer HJ. **The forms of growth in gliomas and their practical significance.** *Brain* 1940;63:1–35
2. Johnson P, Hunt S, Drayer B. **Human cerebral gliomas: correlation of postmortem MR imaging and neuropathologic findings.** *Radiology* 1989;170:211–17
3. DeAngelis LM. **Brain tumors.** *N Engl J Med* 2001;344:114–23
4. Kelly P, Dumas-Duport C, Kispert D, et al. **Imaging-based stereotaxic serial biopsies in untreated intracranial glial neoplasms.** *J Neurosurg* 1987;66:865–74
5. Lilja A, Bergstrom K, Spannare B. **Reliability of computed tomography in assessing histopathological features of malignant supratentorial gliomas.** *J Comput Assist Tomogr* 1981;5:625–36
6. Selker RG, Mendelow H, Walker M, et al. **Pathological correlation of CT ring in recurrent, previously treated gliomas.** *Surg Neurol* 1982;17:251–54
7. Watanabe M, Tanaka R, Takeda N. **Magnetic resonance imaging and histopathology of cerebral gliomas.** *Neuroradiology* 1992;34:463–69
8. Burger P, Dubois P, Schold S, et al. **Computerized tomographic and pathologic studies of the untreated, quiescent, and recurrent glioblastoma multiforme.** *J Neurosurg* 1983;58:159–69
9. Tovi M. **MR imaging in cerebral gliomas analysis of tumour tissue components.** *Acta Radiol Suppl* 1993;384:1–24
10. Asanuma T, Doblas S, Tesiram YA, et al. **Diffusion tensor imaging and fiber tractography of C6 rat glioma.** *J Magn Reson Imaging* 2008;28:566–73
11. Zhang J, van Zijl PC, Laterra J, et al. **Unique patterns of diffusion directionality in rat brain tumors revealed by high-resolution diffusion tensor MRI.** *Magn Reson Med* 2007;58:454–62
12. Beaulieu C, Allen PS. **Determinants of anisotropic water diffusion in nerves.** *Magn Reson Med* 1994;31:394–400
13. Sinha S, Bastin ME, Whittle IR, et al. **Diffusion tensor MR imaging of high-grade cerebral gliomas.** *AJNR Am J Neuroradiol* 2002;23:520–27
14. van Westen D, Lätt J, Englund E, et al. **Tumor extension in high-grade gliomas assessed with diffusion magnetic resonance imaging: values and lesion-to-brain ratios of apparent diffusion coefficient and fractional anisotropy.** *Acta Radiol* 2006;47:311–19
15. Lope-Piedrafita S, Garcia-Martin ML, Galons JP, et al. **Longitudinal diffusion tensor imaging in a rat brain glioma model.** *NMR in Biomedicine*. 2008;21:799–808
16. Kim S, Pickup S, Hsu O, et al. **Diffusion tensor MRI in rat models of invasive and well-demarcated brain tumors.** *NMR in Biomedicine* 2008;21:208–16
17. Le Bihan D, Mangin JF, Poupon C, et al. **Diffusion tensor imaging: concepts and applications.** *J Magn Reson Imaging* 2001;13:534–46
18. Morita K, Matsuzawa H, Fujii Y, et al. **Diffusion tensor analysis of peritumoral edema using lambda chart analysis indicative of the heterogeneity of the microstructure within edema.** *J Neurosurg* 2005;102:336–41
19. Kimura T, Ohkubo M, Igarashi H, et al. **Increase in glutamate as a sensitive indicator of extracellular matrix integrity in peritumoral edema: a 3.0-Tesla proton magnetic resonance spectroscopy study.** *J Neurosurg* 2007;106:609–13
20. Lu S, Ahn D, Johnson G, Cha S. **Peritumoral diffusion tensor imaging of high grade gliomas and metastatic brain tumors.** *AJNR Am J Neuroradiol* 2003;24:937–41
21. Sundgren PC, Fan X, Weybright P, et al. **Differentiation of recurrent brain tumor versus radiation injury using diffusion tensor imaging in patients with new contrast-enhancing lesions.** *Magn Reson Imaging* 2006;24:1131–42

22. Kleihues P, Cavenee WB. *World Health Organization Classification of Tumors: Pathology and Genetics: Tumors of the Nervous System*. Lyon, France: IARC Press; 2000
23. Price SJ, Burnet NG, Donovan T, et al. **Diffusion tensor imaging of brain tumours at 3T: a potential tool for assessing white matter tract invasion?** *Clin Radiol* 2003;58:455–62
24. Lu S, Ahn D, Johnson G, et al. **Diffusion tensor MR imaging of intracranial neoplasia and associated peritumoral edema: introduction of the tumor infiltration index.** *Radiology* 2004;232:221–28
25. Tropine A, Vucurevic G, Delani P, et al. **Contribution of diffusion tensor imaging to delineation of gliomas and glioblastomas.** *J Magn Reson Imaging* 2004;20:905–12
26. Provenzale JM, McGraw P, Mhatre P, et al. **Peritumoral brain regions in gliomas and meningiomas: investigation with isotropic diffusion-weighted MR imaging and diffusion-tensor MR imaging.** *Radiology* 2004;232:451–60
27. Deng Z, Yan Y, Zhong D, et al. **Quantitative analysis of glioma cell invasion by diffusion tensor imaging.** *J Clin Neurosci* 2010;17:1530–06
28. Wang W, Steward CE, Desmond PM. **Diffusion tensor imaging in glioblastoma multiforme and brain metastases: the role of p, q, L, and fractional anisotropy.** *AJNR Am J Neuroradiol* 2009;30:203–08
29. Price SJ, Jena R, Burnet NG, et al. **Improved delineation of glioma margins and regions of infiltration with the use of diffusion tensor imaging: an image-guided biopsy study.** *AJNR Am J Neuroradiol* 2006;27:1969–74
30. Kinoshita M, Goto T, Okita Y, et al. **Diffusion tensor based tumor infiltration index cannot discriminate vasogenic edema from tumor infiltrated edema.** *J Neurooncol* 2010;96:409–15
31. Chen W. **Clinical applications of PET in brain tumors.** *J Nucl Med* 2007;48:1468–81
32. Kato T, Shinoda J, Nakayama N, et al. **Metabolic assessment of gliomas using 11C-methionine, [18F] fluorodeoxyglucose, and 11C-choline positron-emission tomography.** *AJNR Am J Neuroradiol* 2008;29:1176–82
33. Kinoshita M, Hashimoto N, Goto T, et al. **Use of fractional anisotropy for determination of the cut-off value in (11)C-methionine positron emission tomography for glioma.** *Neuroimage* 2009;45:312–18

Acute Intracranial Hemorrhage in CT: Benefits of Sinogram-Affirmed Iterative Reconstruction Techniques

B. Bodelle, E. Klein, N.N.N. Naguib, R.W. Bauer, J.M. Kerl, F. Al-Butmeh, J.L. Wichmann, H. Ackermann, T. Lehnert, T.J. Vogl, and B. Schulz



ABSTRACT

BACKGROUND AND PURPOSE: Acute intracranial hemorrhage represents a severe and time critical pathology that requires precise and quick diagnosis, mainly by performing a CT scan. The purpose of this study was to compare image quality and intracranial hemorrhage conspicuity in brain CT with sinogram-affirmed iterative reconstruction and filtered back-projection reconstruction techniques at standard (340 mAs) and low-dose tube current levels (260 mAs).

MATERIALS AND METHODS: A total of 94 consecutive patients with intracranial hemorrhage received CT scans either with standard or low-dose protocol by random assignment. Group 1 ($n=54$; mean age, 64 ± 20 years) received CT at 340 mAs, and group 2 ($n=40$; mean age, 57 ± 23 years) received CT at 260 mAs. Images of both groups were reconstructed with filtered back-projection reconstruction and 5 iterative strengths (S1–S5) and ranked blind by 2 radiologists for image quality and intracranial hemorrhage on a 5-point scale. Image noise, SNR, dose-length product (mGycm), and mean effective dose (mSv) were calculated.

RESULTS: In both groups, image quality and intracranial hemorrhage conspicuity were rated subjectively with an excellent/good image quality. A higher strength of sinogram-affirmed iterative reconstruction showed an increase in image quality with a difference to filtered back-projection reconstruction ($P < .05$). Subjective rating showed the best score of image quality and intracranial hemorrhage conspicuity achieved through S3/S4–5. Objective analysis of image quality showed an increase of SNR with a higher strength of sinogram-affirmed iterative reconstruction. Patients in group 2 (mean: 744 mGycm/1.71 mSv) were exposed to a significantly lower dose than those in group 1 (mean: 1045 mGycm/2.40 mSv, $P < .01$).

CONCLUSIONS: S3 provides better image quality and visualization of intracranial hemorrhage in brain CT at 260 mAs. Dose reduction by almost one-third is possible without significant loss in diagnostic quality.

ABBREVIATIONS: DLP = dose-length product; FBP = filtered back-projection reconstruction; HU = Hounsfield units; ICH = intracranial hemorrhage; SAFIRE = sinogram-affirmed iterative reconstruction

At present, CT of the brain is the imaging technique of choice for evaluation of an intracranial hemorrhage (ICH). CT imaging adds valuable information regarding the extent and severity of an ICH. Every effort should be made to accurately detect ICH because of the higher mortality rate without treatment.

CT examinations account for only a minority of radiologic procedures but represent a significant portion of the radiation

dose received from all medical procedures.^{1–6} Because of the potential radiation risk through ionizing radiation and because CT is frequently in use for patients with head trauma, every effort should be made to keep the dose as low as reasonably achievable.

Many approaches to reduce patient dose have been investigated including routine use of automated exposure control software, and reduction of tube current and tube potential. Reducing the tube current is eventually limited by increased noise leading to a decrease in image quality. Recently, iterative reconstruction techniques for CT have been introduced to decrease image noise as an alternative to the standard filtered back-projection (FBP) method.^{7–11} Earlier versions of iterative reconstruction algorithms required a high amount of computational calculating time and could not be used in this form for emergency radiologic procedures.¹² The second generation of iterative reconstruction processes, sinogram-affirmed iterative reconstruction (SAFIRE), is now commercially available. SAFIRE estimates the noise content

Received March 18, 2013; accepted after revision July 8.

From the Departments of Diagnostic and Interventional Radiology (B.B., E.K., N.N.N.N., R.W.B., J.M.K., F.A.-B., J.L.W., T.L., T.J.V., B.S.) and Biostatistics and Mathematical Modeling (H.A.), Goethe University, Frankfurt, Germany.

Paper previously presented in part at: European Congress of Radiology, March 7–11, 2013; Vienna, Austria.

Please address correspondence to Boris Bodelle, MD, Department of Diagnostic and Interventional Radiology, Goethe University, Theodor-Stern-Kai 7, 60590 Frankfurt, Germany; e-mail: bbodelle@googlemail.com



Evidence-Based Medicine Level 1.

<http://dx.doi.org/10.3174/ajnr.A3801>

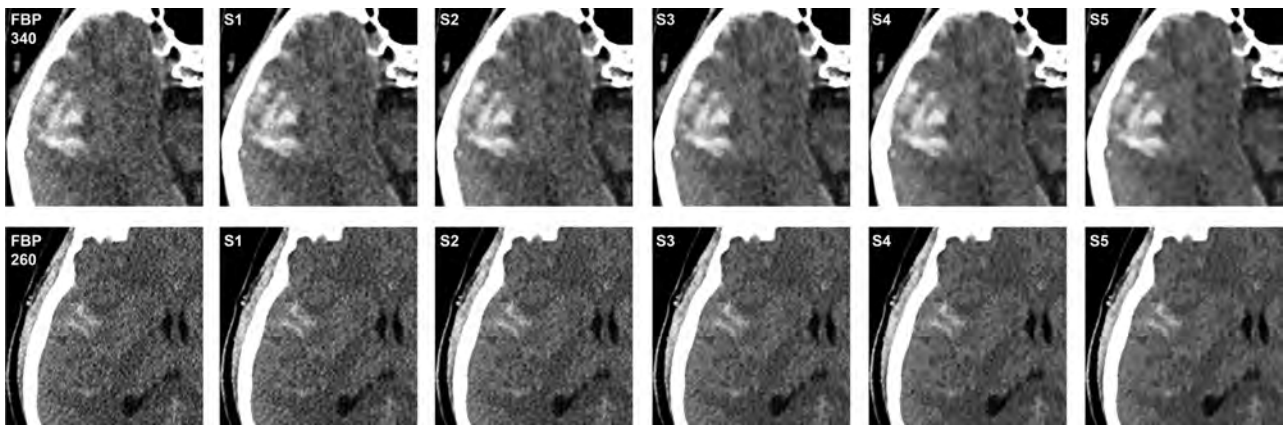


FIG 1. CT images of a 67-year-old man with intracerebral bleeding acquired with tube current–time product of 340 mAs (*upper row*) and a 48-year-old man with subarachnoid hemorrhage acquired with tube current–time product of 260 mAs (*lower row*), each with FBP and 5-strength of the SAFIRE technique.

in raw data caused by fluctuations in neighboring voxels and subtracts the noise stepwise in several validation loops. The result of the first correction loop is compared with the “master data,” and an updated image is generated for the next iteration, leading to further noise reduction. Offered by various vendors, this technique should be able to reduce the necessary radiation dose by 35%–76% while maintaining equivalent image quality.^{13–15} For this purpose, we conducted this study to compare the SAFIRE algorithm and FBP regarding image quality and detectability of ICH and reduction of radiation dose in brain CT scanning.

MATERIALS AND METHODS

Patient Selection

This study was approved by our institutional review board. The data analyzed in this study were acquired in a timeframe of 8 months. In this timeframe, all patients referred for CT of the brain were examined either with the standard CT protocol (group 1) or with the new protocol with reduced mAs (group 2) by random assignment. All consecutive patients with ICH were included: 54 patients from group 1 and 40 patients from group 2.

Examination Techniques

All patients underwent the examination on multidetector row CT scanners (Somatom Definition Flash/AS; Siemens, Erlangen, Germany). CT protocol settings followed the manufacturer’s recommendations. The parameters were kept constant, except the tube current–time products; 340 mAs was the standard scan parameter and 260 mAs was the new parameter for this study, as recommended by the manufacturer. The CT was acquired in axial image orientation, 48-mm detector coverage ($4 \times 20 \times 0.6$ mm), a small field of view, and 120 kVp. Images from the top to the base of the anterior cranial fossa were evaluated.

Image Reconstruction

Images of both tube current levels (340 mAs and 260 mAs) were reconstructed with a medium smooth kernel (H30s, J30s) into 4-mm sections by use of FBP and 5 different blending strengths of SAFIRE (S1–S5), which led to a total of 6 image datasets as shown in Fig 1. All image sets were sent for processing to a PACS workstation (Centricity 4.1; GE Healthcare, Dornstadt, Germany).

Dose Estimates

For the estimation of radiation doses, we recorded the dose-length product (DLP in mGycm) and the effective tube current–time product (effective mAs) from the patient protocol, which is automatically generated after the end of an examination and stored in the PACS of our department. The effective dose was calculated as the product of DLP and the normalized value of effective dose per DLP for the head (0.0023 mSv mGy⁻¹ cm⁻¹; European guideline on quality criteria for CT, European Commission, EUR 16262).

Subjective Image Quality

All CT image datasets were displayed in random order on a diagnostic monitor for the assessment of subjective image quality and with all images displayed on constant window settings (window width, 80 Hounsfield units [HU]; window level, 40 HU). These datasets were reviewed by 2 radiologists with experience in neuroradiology in a blinded manner. The overall image quality of brain structures and the image quality and identifiable properties of cerebral hemorrhage were ranked by use of a 5-point scale (1 = worst image quality, 2 = fair image quality, 3 = moderate image quality, 4 = good image quality, 5 = best image quality). The subjective image quality ratings from FBP and SAFIRE S1–S5 at each level of tube current–time product were compared with standard FBP at 340 mAs and FBP at 260 mAs.

Objective Analysis of Image Quality

As measures of image quality, 4 ROI measurements were performed on a PACS workstation by use of a circle tool with a diameter of 3–6 mm for the ROIs. The measurements were performed by a radiologist with 1 year of experience in CT of the brain. Image noise (*IN*) was determined as the standard deviation of air in the level of the frontal lobe. Mean attenuation values (*A*) and standard deviation were measured in the GM and WM in the superior frontal gyrus and in the center of the ICH: cerebral, epidural, subdural, and subarachnoid hemorrhage. The measurements for 6 image datasets of each patient were recorded and displayed in HU. On the basis of these measurements, SNR was determined according to the following equation:

$$SNR = A/IN$$

Table 1: Subjective image quality rating (1 = worst, 5 = best) for brain structures and intracranial hemorrhage for filtered back-projection and 5 strengths (S1–S5) of sinogram-affirmed iterative reconstruction technique

Image Reconstruction Technique	Rating Brain Structures				Rating Intracranial Hemorrhage			
	340 mAs		260 mAs		340 mAs		260 mAs	
		κ		κ		κ		κ
FBP	2.8 ± 0.4	0.71	2.0 ± 0.8	0.59	2.5 ± 0.7	0.9	2.1 ± 0.8	0.67
S1	3.5 ± 0.6 ^a	0.71	2.9 ± 0.6 ^a	0.48	3.15 ± 0.8 ^c	0.85	2.8 ± 0.8 ^{a,c}	0.9
S2	4.4 ± 0.6	0.77	3.7 ± 0.7 ^a	0.51	3.8 ± 0.7 ^c	0.82	3.4 ± 0.7 ^c	0.75
S3	4.5 ± 0.5 ^c	0.47	4.7 ± 0.5 ^c	0.62	4.39 ± 0.7 ^c	0.80	4.0 ± 0.7 ^c	0.72
S4	3.2 ± 0.7 ^{a,c}	0.86	3.4 ± 1.0 ^{a,c}	0.55	4.65 ± 0.6 ^c	0.81	4.65 ± 0.5 ^c	0.61
S5	2.0 ± 0.7 ^{b,c}	0.64	2.5 ± 0.9 ^{b,c}	0.37	4.44 ± 0.7 ^c	0.81	4.68 ± 0.6 ^c	0.55

Note: ^a $P > .05$ when compared with standard FBP at 340 mAs; ^b $P > .05$ when compared with FBP at 260 mAs; ^c $P > 0.1$ when compared with the same image reconstruction technique at different tube current–time product.

Interobserver agreement (slight [$\kappa < 0.3$], moderate [$\kappa = 0.3–0.7$], good agreement [$\kappa > 0.7$]).

Table 2: Objective image quality measurements with SNR and image noise for filtered back-projection and 5 strength (S1–S5) of sinogram-affirmed iterative reconstruction technique

Image Reconstruction Technique	SNR White Matter		SNR Gray Matter		SNR Intracranial Hemorrhage		Image Noise	
	340 mAs	260 mAs	340 mAs	260 mAs	340 mAs	260 mAs	340 mAs	260 mAs
FBP	15.9 ± 4.8 ^{b,c}	15.0 ± 2.9 ^{a,c}	25.1 ± 6.5 ^b	21.0 ± 3.8 ^a	38.2 ± 11.6 ^{b,c}	34.4 ± 7.4 ^{a,c}	1.76	1.97
S1	19.4 ± 5.6 ^{a,c}	17.0 ± 3.1 ^{a,b,c}	29.9 ± 6.9	23.7 ± 3.8 ^{a,b}	45.6 ± 12.8	39.0 ± 7.6 ^{a,b}	1.42	1.72
S2	21.9 ± 5.7 ^c	18.9 ± 3.6 ^{a,c}	34.0 ± 6.6	26.6 ± 4.8 ^a	52.1 ± 13.9 ^c	43.6 ± 9.6 ^{a,c}	1.21	1.55
S3	23.9 ± 6.9	20.8 ± 4.1	37.7 ± 9.1	29.1 ± 5.3	57.1 ± 16.5	47.9 ± 10.1	1.16	1.41
S4	26.0 ± 6.8	22.7 ± 4.6	41.1 ± 9.6	31.7 ± 6.1	63.2 ± 19.3	52.3 ± 11.2	1.03	1.30
S5	29.9 ± 7.3	25.4 ± 5.8	46.5 ± 9.4	35.5 ± 7.5	71.2 ± 20.2	58.4 ± 13.4	0.89	1.17

Note: ^a $P > .05$ for SNR when compared with standard FBP at 340 mAs; ^b $P > .05$ for SNR when compared with FBP at 260 mAs; ^c $P > .05$ when compared with the same image reconstruction technique at different tube current–time product (mAs = tube current × seconds).

The objective image quality ratings from FBP and SAFIRE S1–S5 at each level of tube current–time product were compared with standard FBP at 340 mAs and FBP at 260 mAs.

Statistical Analysis

Computer-based statistical analyses were performed with dedicated software (BiAS 9.17; Epsilon, Frankfurt, Germany). Patient age, image noise, SNR, subjective image quality, and DLP were expressed as mean values and standard deviations. Age and DLP were tested by use of the Wilcoxon–Mann–Whitney U test. For SNR and subjective image quality rating, the Fisher exact test with a Bonferroni-corrected P value was used. A P value of $< 5\%$ was considered to be statistically significant. Interobserver agreement of subjective image quality rating was assessed with the Cohen weighted κ analysis. Definitions of levels of agreement on the basis of κ values were as follows: $\kappa < 0.3$ indicated slight agreement; $\kappa = 0.3–0.7$, moderate agreement; and $\kappa > 0.7$ meant good agreement.

RESULTS

Patient Characteristics

In group 1 with the standard protocol, 54 patients with a mean age of 64 ± 20 years (age range, 17–90 years) were included. In group 2, with a reduced tube current–time product of 260 mAs, 40 patients with a mean age of 57 ± 23 years (age range, 16–95 years) were included. No significant differences regarding age were found concerning patient characteristics.

Subjective Image Quality Measurements

Subjective image quality was rated for FBP and SAFIRE S1–S5 at each level of tube current–time product. Data are summarized in Table 1. Subjective overall image quality of brain structures was rated with excellent interobserver agreement for both readers for

group 1 at 340 mAs ($\kappa = 0.91$) and group 2 with 260 mAs ($\kappa = 0.80$). In a likewise fashion, the image quality with visibility of ICH in group 1 and group 2 was rated subjectively with a good interobserver agreement ($\kappa = 0.92$ and $\kappa = 0.9$, respectively). The score for image quality of brain structures increased with a higher strength of SAFIRE at each level of tube current–time product up to S3 and for image quality of ICH up to S4–S5. The best score for the image quality of brain structures was achieved with SAFIRE S3 with significant difference to the FBP reconstruction in each group ($P < .05$). The best score for the visualization of ICH was achieved with SAFIRE S4 and S5 with significant difference to the FBP reconstruction in each group ($P < .05$). The difference between standard FBP at 340 mAs and SAFIRE 1 blending at 260 mAs had no predominant statistical significance for image quality of the brain structures and ICH ($P > .05$). When compared with 1 reconstruction technique on its own (FBP or SAFIRE S1–S5) between both tube current–time products, there was no statistically significant difference ($P > .1$) for S3–S5 depicting brain structures and for S1–S5 depicting ICH conspicuity.

Objective Image Quality Measurements

Statistical results of the objective image quality measurements are summarized in Table 2. Image noise was higher ($P > .05$) in group 2 (260 mAs) than in group 1 (340 mAs) for all reconstruction techniques. Image noise decreased with higher strength of SAFIRE; therefore, SNR increased with a higher strength of SAFIRE at each level of tube current–time product (mAs). The difference between FBP and SAFIRE 1 was statistically significant ($P < .05$) for SNR GM and ICH at 340 mAs, whereas no significant difference was reached for examination at 260 mAs. No statistically significant difference was shown for SNR WM at SAFIRE 1 for both groups. SNR of SAFIRE 3 up to 5 at 260 mAs and 340 mAs

was higher than FBP at each level of tube current–time product ($P < .05$). The highest SNR was reached with SAFIRE 5 in each group. When compared with 1 reconstruction technique on its own (FBP or SAFIRE S1–S5) between both tube current–time products, there was no statistically significant difference ($P > .05$) for FBP, S1 and S2 depicting WM, and FBP and S2 depicting ICH.

Radiation Dose

Patients examined with a tube current of 260 mAs were exposed to significantly less radiation dose than the group examined with 340 mAs (260 mAs: mean DLP, 744 ± 80 mGycm; 340 mAs: mean DLP, 1045 ± 108 mGycm; $P < .01$). Even the calculated mean effective dose was lower at 1.71 mSv (260 mAs) compared with 2.40 mSv (340 mAs).

DISCUSSION

Previous studies have applied the standard deviation to assess the objective image quality.^{8,16} To assess the objective image quality in the brain and to compare the level of the signal with the level of background noise, we applied the SNR of selected ROIs to WM and GM and the region with ICH as a measurement of objective image quality. Ren et al¹⁷ showed a possible reduction of the tube current–time product down to 200 mAs on CT of the brain with the adaptive statistical iterative reconstruction technique without focus on ICH. Because of ethical reasons, we followed the manufacturer's recommendations. With reduction of the tube current–time product from the standard 340 mAs down to 260 mAs, the mean effective dose decreased from 2.40–1.71 mSv, which results in a relevant reduction of 29%, higher than the 20.4% calculated by Korn et al,¹⁸ and similar to Ren et al¹⁷ and Kilic et al¹⁹ with 30% and 31% dose reductions, respectively.

Compared with the FBP reconstruction technique, all iterative reconstruction techniques increased SNR heterogeneously by 13%–88%, depending on the algorithm strength and tube current–time product. These results are similar to those of Schulz et al¹² for CT of the paranasal sinus and Leipsic et al⁹ for coronary CT angiography. There was no significant difference for SNR between FBP and SAFIRE S1 for group 2 at 260 mAs. Therefore, we concluded that SAFIRE 1 could not provide a better noise reduction than FBP in lower-dose examination at 260 mAs. We came to the conclusion that SAFIRE 3–5 is able to reduce noise and increase objective image quality in standard brain CT even with a lower tube current–time product.

SAFIRE 3 was rated best for overall image quality of the brain at both mAs levels, with the best κ value of 0.62 for examination at 260 mAs. SAFIRE 4–5 was rated best for the visualization of ICH, and we conclude that the higher noise reduction leads to a better demarcation of lesions with rich contrast. The use of the SAFIRE 1 reconstruction technique with a reduced tube current–time product of 260 mAs could achieve the same image quality as a standard examination at 340 mAs. SNR at 340 mAs is still higher than in low-dose examination at 260 mAs, but it does not affect radiologic diagnosis significantly. For standard use, we recommend a protocol at 260 mAs with an iterative algorithm. The benefit of higher SNR at 340 mAs can be assumed for postoperative or therapeutic cerebral status. An appropriate examination

protocol should be reserved for patients with a relevant medical history.

Although the SNR increases with a higher strength of SAFIRE, the subjective image quality with SAFIRE S4 and S5 is worse than with SAFIRE S3. We deduce that a high SAFIRE strength does not necessarily imply a good image quality. This phenomenon is similar to what has been reported in previous studies. Increased image blurring has been discussed in several publications that investigated iterative reconstruction techniques.^{9,12,14,20,21} Silva et al²⁰ suggested that the diminished noise manifests as an oversmoothing of the images. Singh et al⁸ thought that higher blending proportions of iterative reconstruction to FBP could substantially change the texture and characteristics of the images. As discussed before, SAFIRE offers a better reconstruction technique for the detection of ICH than FBP, and it can be assumed that a better reconstruction technique with SAFIRE reconstruction leads to a lower false-negative value of the detection of ICH, better treatment, and a possible reduction of radiation risk. Although the κ value varied for the subjective image qualities, the variation tendency of the 2 radiologists was consistent, probably because of different diagnostic experience and different understanding about the scales. These differences cannot be avoided, but in a randomized and blinded manner, they can be minimized.

For the future, iterative algorithms should be used for the detection of ICH. This should be accompanied by a lowering of the false-negative rate for the detection of ICH. SAFIRE 3 is the choice for evaluation of brain structures and SAFIRE 5, the choice for evaluation of ICH at both mAs levels. Inexperienced readers are recommended to use SAFIRE 3 for evaluation of the brain structures and SAFIRE 5 for evaluation and detection of ICH in combination. To optimize the processing time, experienced readers should rely on the SAFIRE 3 algorithm at 260 mAs for evaluation of the brain structures and detection of ICH with 1 reconstruction algorithm. The benefit of SAFIRE 5 compared with SAFIRE 3 concerning the conspicuity of ICH would not affect radiologic diagnosis significantly for experienced readers.

There were limitations to our study. First, we could not perform an inpatient comparison, but we had 2 groups with no significant difference regarding age, and all patients were referred for assessment of ICH. Second, the measurement by ROI did not provide information for the whole brain. However, with essential ROIs we received valid results as evidence for the subjective image quality in the whole brain. For future studies, SAFIRE can be used in combination with other dose-reduction techniques, for instance, automatic tube-current modulation, as proposed by Smith et al²² as an effective dose-reduction method or automatic tube-voltage modulation.

CONCLUSIONS

SAFIRE improves image quality and visualization of ICH on head CT with a normal-dose and a low-dose protocol. For standard use, we recommend a protocol at 260 mAs with a SAFIRE algorithm with the benefit of a reduction in radiation dose by approximately 29%. For evaluation in patients with postoperative or therapeutic cerebral status, a benefit at 340 mAs can be assumed. SAFIRE 3 showed an increased image quality for evaluation of brain structures and SAFIRE 5 for ICH conspicuity compared

with the FBP reconstruction technique at both mAs levels. The use of SAFIRE 3 at 260 mAs is recommended for evaluation of brain structures and detection of ICH, optimizing processing time for experienced readers. For unexperienced readers, SAFIRE 5 at 260 mAs should be used for evaluation of ICH in combination with SAFIRE 3 for evaluation of brain structures. SAFIRE should be used to diminish the false-negative rate. Therefore, a better detection with an iterative algorithm can result in better treatment.

Disclosures: Ralf Bauer—UNRELATED: Payment for Lectures (including service on speaker bureaus); Siemens AG. J. Matthias Kerl—UNRELATED: Payment for Lectures (including service on speaker bureaus); Siemens AG. J. Matthias Kerl and Ralf Bauer are consultants for Siemens Medical Care.

REFERENCES

- Linton OW, Mettler FA Jr. **National conference on dose reduction in CT, with an emphasis on pediatric patients.** *AJR Am J Roentgenol* 2003;181:321–29
- Yates SJ, Pike LC, Goldstone KE. **Effect of multislice scanners on patient dose from routine CT examinations in East Anglia.** *Br J Radiol* 2004;77:472–78
- Brix G, Nagel HD, Stamm G, et al. **Radiation exposure in multi-slice versus single-slice spiral CT: results of a nationwide survey.** *Eur Radiol* 2003;13:1979–91
- Brenner DJ, Hall EJ. **Computed tomography—an increasing source of radiation exposure.** *N Engl J Med* 2007;357:2277–84
- Wiest PW, Locken JA, Heintz PH, et al. **CT scanning: a major source of radiation exposure.** *Semin Ultrasound CT MR* 2002;23:402–10
- Schenzle JC, Sommer WH, Neumaier K, et al. **Dual energy CT of the chest: how about the dose?** *Invest Radiol* 2010;45:347–53
- Vandenberghe S, D'Asseler Y, Van de Walle R, et al. **Iterative reconstruction algorithms in nuclear medicine.** *Comput Med Imaging Graph* 2001;25:105–11
- Singh S, Kalra MK, Gilman MD, et al. **Adaptive statistical iterative reconstruction technique for radiation dose reduction in chest CT: a pilot study.** *Radiology* 2011;259:565–73
- Leipsic J, Labounty TM, Heilbron B, et al. **Adaptive statistical iterative reconstruction: assessment of image noise and image quality in coronary CT angiography.** *AJR Am J Roentgenol* 2010;195:649–54
- Hara AK, Paden RG, Silva AC, et al. **Iterative reconstruction technique for reducing body radiation dose at CT: feasibility study.** *AJR Am J Roentgenol* 2009;193:764–71
- Flicek KT, Hara AK, Silva AC, et al. **Reducing the radiation dose for CT colonography using adaptive statistical iterative reconstruction: A pilot study.** *AJR Am J Roentgenol* 2010;195:126–31
- Schulz B, Beeres M, Bodelle B, et al. **Performance of iterative image reconstruction in CT of the paranasal sinuses: a phantom study.** *AJNR Am J Neuroradiol* 2013;34:1072–76
- Funama Y, Taguchi K, Utsunomiya D, et al. **Combination of a low-tube-voltage technique with hybrid iterative reconstruction (iDose) algorithm at coronary computed tomographic angiography.** *J Comput Assist Tomogr* 2011;35:480–85
- Bulla S, Blanke P, Hassepass F, et al. **Reducing the radiation dose for low-dose CT of the paranasal sinuses using iterative reconstruction: feasibility and image quality.** *Eur J Radiol* 2012;81:2246–50
- Pontana F, Duhamel A, Pagniez J, et al. **Chest computed tomography using iterative reconstruction vs filtered back projection (Part 2): image quality of low-dose CT examinations in 80 patients.** *Eur Radiol* 2011;21:636–43
- Birnbaum BA, Hindman N, Lee J, et al. **Multi-detector row CT attenuation measurements: assessment of intra- and interscanner variability with an anthropomorphic body CT phantom.** *Radiology* 2007;242:109–19
- Ren Q, Dewan SK, Li M, et al. **Comparison of adaptive statistical iterative and filtered back projection reconstruction techniques in brain CT.** *Eur J Radiol* 2012;81:2597–601
- Korn A, Fenchel M, Bender B, et al. **Iterative reconstruction in head CT: image quality of routine and low-dose protocols in comparison with standard filtered back-projection.** *AJNR Am J Neuroradiol* 2012;33:218–24
- Kilic K, Erbas G, Guryildirim M, et al. **Lowering the dose in head CT using adaptive statistical iterative reconstruction.** *AJNR Am J Neuroradiol* 2011;32:1578–82
- Silva AC, Lawder HJ, Hara A, et al. **Innovations in CT dose reduction strategy: application of the adaptive statistical iterative reconstruction algorithm.** *AJR Am J Roentgenol* 2010;194:191–99
- Mitsumori LM, Shuman WP, Busey JM, et al. **Adaptive statistical iterative reconstruction versus filtered back projection in the same patient: 64 channel liver CT image quality and patient radiation dose.** *Eur Radiol* 2012;22:138–43
- Smith AB, Dillon WP, Gould R, et al. **Radiation dose-reduction strategies for neuroradiology CT protocols.** *AJNR Am J Neuroradiol* 2007;28:1628–32

Improved Quality and Diagnostic Confidence Achieved by Use of Dose-Reduced Gadolinium Blood-Pool Agents for Time-Resolved Intracranial MR Angiography

S. Dehkharghani, J. Kang, and A.M. Saindane



ABSTRACT

BACKGROUND AND PURPOSE: Time-resolved MRA with the use of bolus injection of paramagnetic agents has proved valuable in neurovascular imaging. Standard contrast agents have limited blood-pool residence times, motivating the development of highly protein-bound blood-pool agents with greater relaxivity and longer intravascular residence, affording improved image quality at lesser doses. This study represents the first comparison of blood-pool agents to standard agents in time-resolved cerebral MRA.

MATERIALS AND METHODS: One hundred datasets were acquired at 1.5T by use of a standardized, time-resolved MRA protocol. Patients received either unit dosing of a standard extracellular agent at 0.1 mmol/kg or a blood-pool agent at 0.03 mmol/kg. Peak arterial and venous enhancement phases were identified and subsequently scored qualitatively by use of a 4-point Likert scale, with attention to 6 vascular segments: 1) intracranial ICA; 2) MCA M1; 3) MCA M2; 4) MCA M3; 5) deep cerebral veins; and 6) dural venous sinuses.

RESULTS: Fifty MR angiographies were acquired with each agent. No significant differences were found between agents in generation of uncontaminated arteriograms. Blood-pool agents, at 67% dose reduction, were of significantly greater quality across most vascular segments, including ICA ($P = .019$), M2 ($P = .003$), and M3 ($P < .01$). Superiority in the M1 segment approached significance ($P = .059$). Significantly better venographic quality was noted for deep venous structures ($P = .016$) with the use of blood-pool agents.

CONCLUSIONS: Blood-pool agents provide superior demonstration of most intracranial vessels in time-resolved MRA compared with standard agents, at reduced doses. The greater relaxation enhancement and more favorable dosing profile make blood-pool agents superior to standard agents for use in cerebral time-resolved MRA.

ABBREVIATIONS: TR-MRA = time-resolved MRA; BPA = blood-pool agents; SCA = standard contrast agents; DAVF = dural arteriovenous malformation

Time-resolved MRA (TR-MRA) techniques have shown great potential as noninvasive approaches to probing vascular flow in a temporally sensitive manner.¹⁻³ Efforts to rapidly image contrast kinetics have benefited from acquisition schemes aimed at accelerated data collection, primarily through the use of parallel receive algorithms and novel k -space trajectories.^{1,3,4} Inherent to most time-resolved techniques is the intravenous bolus injection of paramagnetic agents, providing relaxation enhancement of

blood T1.¹⁻⁵ Growing concerns regarding the safety profile of such agents, particularly in the setting of renal insufficiency, can limit their widespread use.⁶ The small molecular size of many gadolinium-based vascular contrast agents results in limited blood-pool residence times; thus, the motivation for development of blood-pool agents (BPA) exhibiting higher protein binding and prolonged vascular dwelling.^{4,7-9} Some BPA formulations have been observed to augment T1 relaxation enhancement at 1.5T in water, plasma, and, blood, owing to the multiple paramagnetic ions attached to each macromolecule.⁹ Their pharmacokinetic profiles may therefore afford flexibility in allowing for smaller administered doses at theoretically comparable diagnostic quality.

The first BPA, gadofosveset trisodium (Vasovist; Bayer Schering Pharma, Berlin, Germany—European, Asian rights; Lantheus Medical Imaging, Billerica, Massachusetts—North American, Australian rights) was approved for use in the United States in 2008, and previously in Europe in 2005.⁴ By comparison to the 100-second distribution phase half-life of standard extracellular

Received April 5, 2013; accepted after revision June 7.

From Neuroradiology Division, Department of Radiology and Imaging Sciences (S.D., A.M.S.), Emory University Hospital, Atlanta, Georgia; and Department of Biostatistics and Bioinformatics (J.K.), Rollins School of Public Health, Emory University, Atlanta, Georgia.

Abstract previously presented at: Annual Meeting of the American Society of Neuroradiology, May 20–23, 2013; San Diego, California.

Please address correspondence to Seena Dehkharghani, MD, Neuroradiology Division, Department of Radiology and Imaging Sciences, Emory University Hospital, 1364 Clifton Rd, NE, Atlanta, GA 30322; e-mail: seena.dehkharghani@gmail.com

Indicates open access to non-subscribers at www.ajnr.org

<http://dx.doi.org/10.3174/ajnr.A3693>

Table 1: Analysis of enhancement kinetics: BPA versus SCA

Category	BPA	SCA	P Value
Presence of uncontaminated arterial phase, ^a %	68 ± 47	68 ± 47	1
Peak arterial phase ^b (sub)	6.96 ± 1.63	6.15 ± 1.84	.023
Peak arterial phase ^b (unsub)	6.96 ± 1.63	6.15 ± 1.84	.023
Peak venous phase ^b (sub)	8.52 ± 1.64	8.0 ± 1.68	.123
Peak venous phase ^b (unsub)	8.52 ± 1.64	8.0 ± 1.68	.123
Peak venous–peak arterial phase ^b (sub)	1.56 ± 1.07	1.88 ± 1.19	.161
Peak venous–peak arterial phase ^b (unsub)	1.56 ± 1.07	1.86 ± 1.18	.186

Note:—All values are reported as mean ± standard deviation; sub, unsub reflect background subtracted and non-subtracted volumes.

^aPercentage of cases with uncontaminated arteriographic phase (see text).

^bExpressed in terms of average, time-resolved phase number.

gadolinium chelates, gadofosveset achieves a mean initial plasma half-life of 29 minutes in the distribution phase through reversible albumin binding.^{10–12}

Past studies have investigated the use of BPA for steady-state MRA, with attention to the theoretic advantages of prolonged vascular residence for high-resolution angiography; however, more recent investigations have demonstrated the advantages of BPA for TR-MRA, exploiting their profile for peripheral and thoracic first-pass MRA and focused imaging during the equilibrium phase.^{4,13–17} We propose to compare the qualitative efficacy of BPA with a low protein-bound, standard contrast agent (SCA) in time-resolved cerebral MR angiography.

MATERIALS AND METHODS

Imaging Protocol

One hundred TR-MRA datasets divided equally between BPA and SCA were acquired on clinical 1.5T systems (Signa HDxH; GE Healthcare, Milwaukee, Wisconsin) by use of body transmit and signal reception with a dedicated 8-channel head coil. Patients were selected continuously from an electronic query of the radiology informatics system for the primary field of time-resolved brain MRA between November 2010 and September 2012. Institutional review board approval was obtained for this investigation. The administered agent was selected arbitrarily at the time of examination and without a predefined or set pattern of prescription. Most patients underwent TR-MRA for either known or suspected aneurysm, known or suspected dural arteriovenous malformation (DAVF), aneurysm after treatment (after either endovascular coil or Pipeline Embolization Device [Covidien, Irvine, California]), or DAVF after embolization. Imaging evaluation included a product iteration of 3D time-resolved imaging of contrast kinetics (TR = 4.5 ms; TE = min; flip angle = 35°; frequency field of view = 17 cm; matrix = 256 × 160 zero-filled and interpolated to 512 × 512; averages, 0.75; bandwidth, 62.5 KHz; array spatial sensitivity encoding technique acceleration factor = 2) yielding 10 or 12 dynamic, temporally discrete postcontrast phases at approximately 4.0-second temporal update.

TR-MRA in all patients was performed after the injection of either a low protein-bound SCA gadobenate dimeglumine (MultiHance; Bracco Diagnostics, Princeton, New Jersey), prescribed at 0.1 mmol/kg and 2 mL/s injection rate, or the BPA gadofosveset trisodium at 0.03 mmol/kg and 1.5 mL/s injection rate. Slower injection rates for BPA were used to ameliorate seldom-reported midsection burning and discomfort at higher rates as well as to optimize the biophysical profile of gadofosveset relaxation

enhancement at 1.5T (see Discussion section). Bolus infusion in both protocols was followed immediately by 25–30 mL normal saline flush at 2 mL/s. Postinjection delay and sequence triggering were prescribed in an automated fashion, without user input, by the scanner/sequence manufacturer. The dynamic data generated by the time-resolved imaging of contrast kinetics sequence are presented in numbered temporal datasets. The scan baseline reflects the simultaneous initiation of the

sequence and initiation of contrast injection, both occurring under fully automated parameters prescribed by the scanner/sequence manufacturer, and without user input. Before contrast/sequence triggering, a noncontrast mask is acquired for subtraction. Background subtraction of the precontrast imaging volume was performed in-line during acquisition, allowing for production of both background-subtracted and unsubtracted TR-MRA volumes.

Image Analysis

All data were analyzed by the consensus evaluation of 2 neuroradiologists, both with subspecialty certification in neuroradiology. Both readers were blinded to the administered agent at the time of review. Evaluation was performed as follows: for each examination, background-subtracted and unsubtracted maximum intensity projection volumes (temporal frames) were simultaneously evaluated for identification of the temporal phase displaying peak arterial and venous enhancement. Any temporal discordance between the 2 volumes was recorded, and the presence or absence of an uncontaminated (ie, free of venous enhancement) angiographic phase was specifically noted for each case. Peak enhancement phases were determined from the proximal branches of the circle of Willis and transverse sinuses for arterial and venous phases, respectively, and numeric temporal phase was recorded for analysis. Peak enhancement phases and qualitative analysis of TR-MRA (see below) was generally assessed by inspection of the bilateral anatomy; however, for cases in which large vascular abnormalities, shunt physiology, or artifacts related to stent placement confounded this methodology, characterization was limited to the disease-free or untreated side.

After determination of peak arterial and venous phases, the corresponding axial source volumes were selected for further qualitative analysis. For both phases, subtracted and unsubtracted source data were synchronized to allow for the simultaneous analysis of TR-MRA quality, with attention to 6 vascular segments: 1) cavernous and supraclinoid ICAs; 2) MCA M1 segment; 3) MCA M2; 4) MCA M3; 5) deep venous system (vein of Galen, internal cerebral veins, thalamostriate veins); and 6) superficial venous system (transverse, sigmoid, and superior sagittal sinuses). The above vascular segments were inspected and scored by the following Likert-type scale proposed by Frydrychowicz et al¹³: 0 = severely limited, nondiagnostic examination; 1 = fair, diagnosis possible but limited; 2 = good, diagnosis readily possible; and 3 = excellent diagnostic quality.

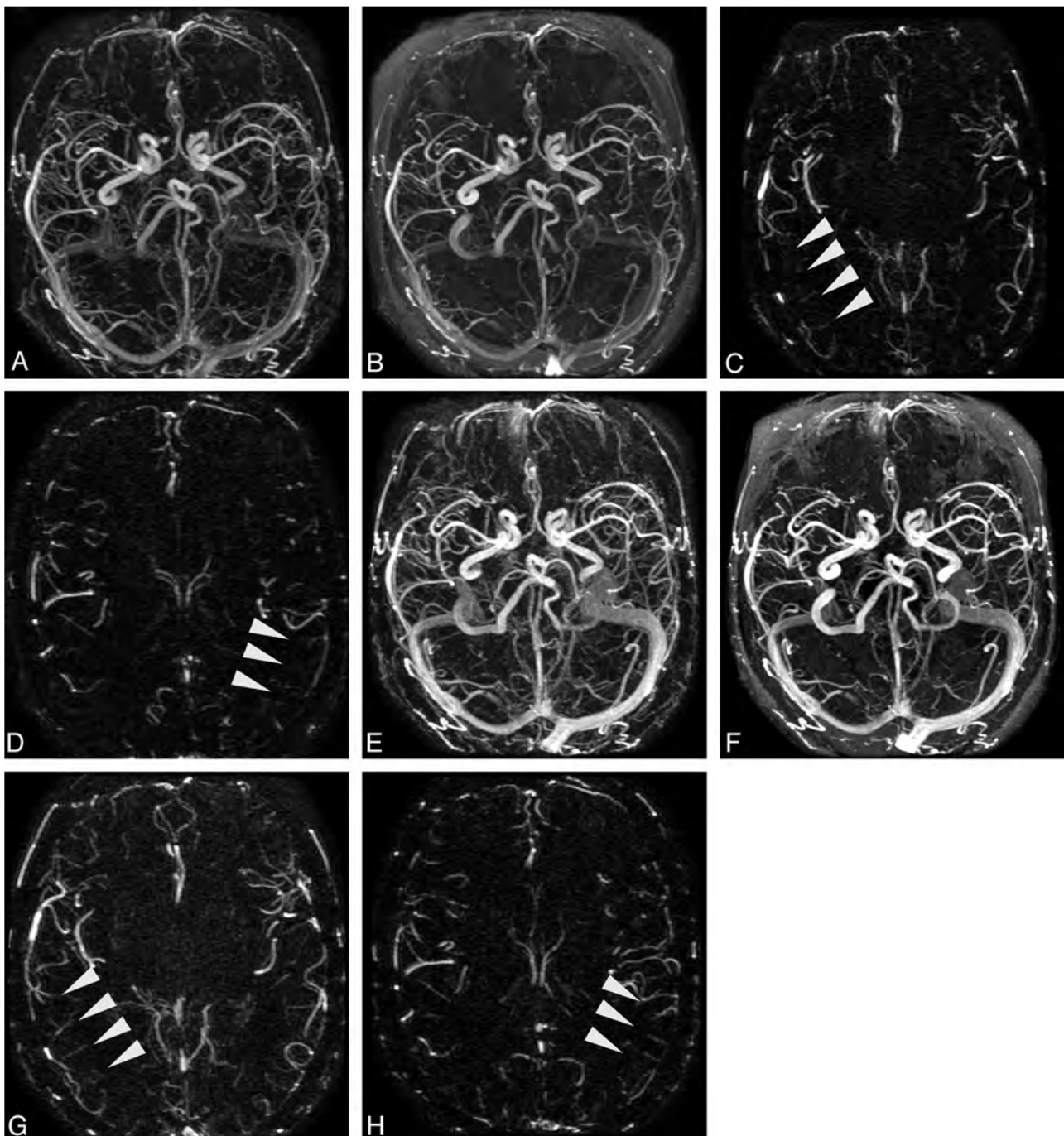


FIG 1. Patient (71-year-old man) undergoing successive TR-MRA, spaced approximately 1 year apart, for evaluation of previously coiled left ophthalmic artery aneurysm. Images obtained after injection of SCA (A–D) and obtained with BPA (E–H). Background-subtracted (A and E) and unsubtracted (B and F) axial MIP volumes from SCA and BPA TR-MRA, respectively; C, G, D, and H are background-subtracted axial source MRA images from peak arterial phases derived from SCA (phase 7) and BPA (phase 9) examinations. Note the improved demonstration of mid and distal MCA branches in both hemispheres with administration of the blood-pool agent.

Images were further characterized for artifact-related degradation, including motion, ghosting, and residual aliasing or other artifacts related to parallel acceleration or the view sharing process. Scoring for artifactual degradation was performed as follows: 0 = severe degradation precluding diagnosis; 1 = moderate artifacts, diagnosis possible but limited; 2 = minor artifacts not affecting diagnosis; and 3 = no artifacts. Binary assessment of background subtraction quality for each case was rendered as satisfactory or unsatisfactory.

Statistical Analysis

Categorical data, including the binary determination of the presence versus absence of an uncontaminated arteriographic phase—specifically if the peak arteriographic phase was uncontaminated—as well as the presence or absence of satisfactory background suppression were assessed by Fisher exact test. Phase of peak arterial and peak venous enhancement, as well as the qualitative analysis of vessel segments and artifactual degradation, were treated as continuous variables, and analyzed by Student *t* test.

Table 2: Qualitative analysis of image quality: BPA versus SCA

	BPA ^a	SCA ^a	P Value
Arterial segment			
ICA (sub)	2.74 ± 0.56	2.42 ± 0.76	.019
ICA (unsub)	2.88 ± 0.33	2.56 ± 0.61	.002
M1 (sub)	2.60 ± 0.67	2.50 ± 0.58	.427
M1 (unsub)	2.80 ± 0.45	2.62 ± 0.49	.059
M2 (sub)	2.38 ± 0.75	2.00 ± 0.78	.015
M2 (unsub)	2.62 ± 0.57	2.24 ± 0.69	.003
M3 (sub)	2.18 ± 0.77	1.56 ± 0.93	<.001
M3 (unsub)	2.44 ± 0.58	1.76 ± 0.92	<.001
Venous segment			
Superficial (sub)	2.94 ± 0.24	2.96 ± 0.20	.650
Superficial (unsub)	2.98 ± 0.14	2.96 ± 0.2	.562
Artifactual degradation			
Deep (sub)	2.80 ± 0.4	2.60 ± 0.53	.037
Deep (unsub)	2.92 ± 0.27	2.74 ± 0.44	.016
Subtracted	2.78 ± 0.55	2.74 ± 0.53	.781
Unsubtracted	2.82 ± 0.44	2.74 ± 0.53	.473
Subtraction ^b			
Subtraction	0.98 ± 0.14	0.92 ± 0.27	.172

Note:—All values are reported as mean ± standard deviation; 0 indicates nondiagnostic; 1, diagnosis possible but limited; 2, good; 3, excellent; sub, unsub, subtracted and nonsubtracted.

^a Qualitative designation of diagnostic quality derived from 4-point scale (see text).

^b Indicates percentage of cases for which background subtraction was satisfactory.

RESULTS

Ninety-two patients (69 women, 23 men; age, 16–97 years; median = 61.5 years) constituted the study population. Eight patients underwent multiple scans; specifically, 1 patient underwent 4 TR-MR angiographies (3 with SCA, 1 with BPA), 5 patients underwent 2 TR-MRA (1 each with SCA and BPA), and 2 patients underwent scanning twice with SCA. No subjects received BPA on more than a single scanning session. All available scans for all patients within the accrual period were analyzed, irrespective of administered agent.

All datasets were complete and deemed to be satisfactory for assessment. Patients undergoing scanning with SCA were examined for the following reasons: known or suspected aneurysm ($n = 8$); aneurysm imaging status after coil embolization ($n = 22$); vessel imaging status after Pipeline stent placement ($n = 3$); known or suspected DAVF ($n = 7$); DAVF imaging status after endovascular therapy ($n = 5$); and miscellaneous (including dizziness, dementia, and tumor imaging) ($n = 5$). Among patients undergoing scanning with BPA, indications included known or suspected aneurysm ($n = 18$); aneurysm imaging status after coil embolization ($n = 10$); aneurysm imaging status after surgical clipping ($n = 1$); vessel imaging status after Pipeline stent placement ($n = 6$); known or suspected DAVF ($n = 7$); DAVF imaging status after endovascular therapy ($n = 6$); and miscellaneous (including hypertension and tumor) ($n = 2$).

Significant differences were not found between agents in their likelihood of generating uncontaminated arterial phase volumes (Table 1), observed for both agents in approximately 68% of examinations. Despite this similarity, significantly delayed peak arterial phase enhancement (Fig 1) was observed for both the subtracted and unsubtracted BPA angiograms (expressed in terms of numeric phase) as compared with SCA (6.96 ± 1.63 versus 6.15 ± 1.84 , respectively; $P = .023$). Minor differences in peak venous enhancement between the agents did not reach statistical significance.

BPA angiograms were of generally greater quality across all interrogated vascular segments (Table 2), with average rating compared with SCA on unsubtracted volumes as follows: ICA = 2.88 ± 0.33 versus 2.56 ± 0.61 , $P = .002$; M2 = 2.62 ± 0.57 versus 2.24 ± 0.69 , $P = .003$; M3 = 2.44 ± 0.58 versus 1.76 ± 0.92 , $P < .001$ (Fig 2). A trend toward superiority of BPA, not reaching statistical significance, was observed for the M1 segment of the MCA: 2.8 ± 0.45 versus 2.62 ± 0.49 , $P = .059$; subtracted volumes similarly showed significantly improved quality on BPA angiograms for most segments.

Whereas significant differences in quality were not identified between the agents for characterization of the superficial venous segments, venography of the deep system demonstrated significant superiority of BPA over SCA on subtracted and unsubtracted volumes

(unsubtracted 2.92 ± 0.27 versus 2.74 ± 0.44 , $P = .016$; subtracted 2.8 ± 0.4 versus 2.6 ± 0.53 , $P = .037$, respectively).

Artifactual degradation and the quality of subtraction did not differ significantly between the 2 populations (Table 2).

DISCUSSION

The present study confirms the feasibility and qualitative superiority of the BPA gadofosveset disodium over the SCA gadobenate dimeglumine for use in time-resolved cerebral MRA. The findings suggest that several theoretic advantages to the use of BPA for such CNS applications may be fully realized when dosing strategies and delivery are optimized. Specifically, the higher protein-binding capacity of BPA (80–96% reversible albumin binding), together with augmented T1 relaxation enhancement at clinical field strengths ($r1 = 19$ versus $r1 = 6.3$ at 1.5 T) increases the duration of the available acquisition window and provides improved vascular-to-background contrast, respectively.⁹ Furthermore, the benefits of greater T1 relaxivity afford flexibility in dosing strategies, as demonstrated by the 70% dose reduction (0.03 mmol versus 0.1 mmol) in our implementation, notably at uniformly improved angiographic quality. Given the superiority of gadobenate over many other extracellular SCA, including its greater relaxivity and its transient protein interaction, we believe that our findings may be readily generalizable to many other SCA as well.^{9,18,19}

Although the benefits of BPA for use in high-resolution, steady-state MRA were the subject of earlier studies, more recent reports have highlighted their potential advantages for use in non-CNS TR-MRA.^{4,13–17} A number of vendor-based approaches to accelerated time-resolved imaging have been introduced, generally coupling some combination of parallel acceleration and variable k -space sampling attenuation with temporal interpolation and view sharing.^{1,3,20} While facilitating the timing of contrast-enhanced MRA and approximating catheter angiographic

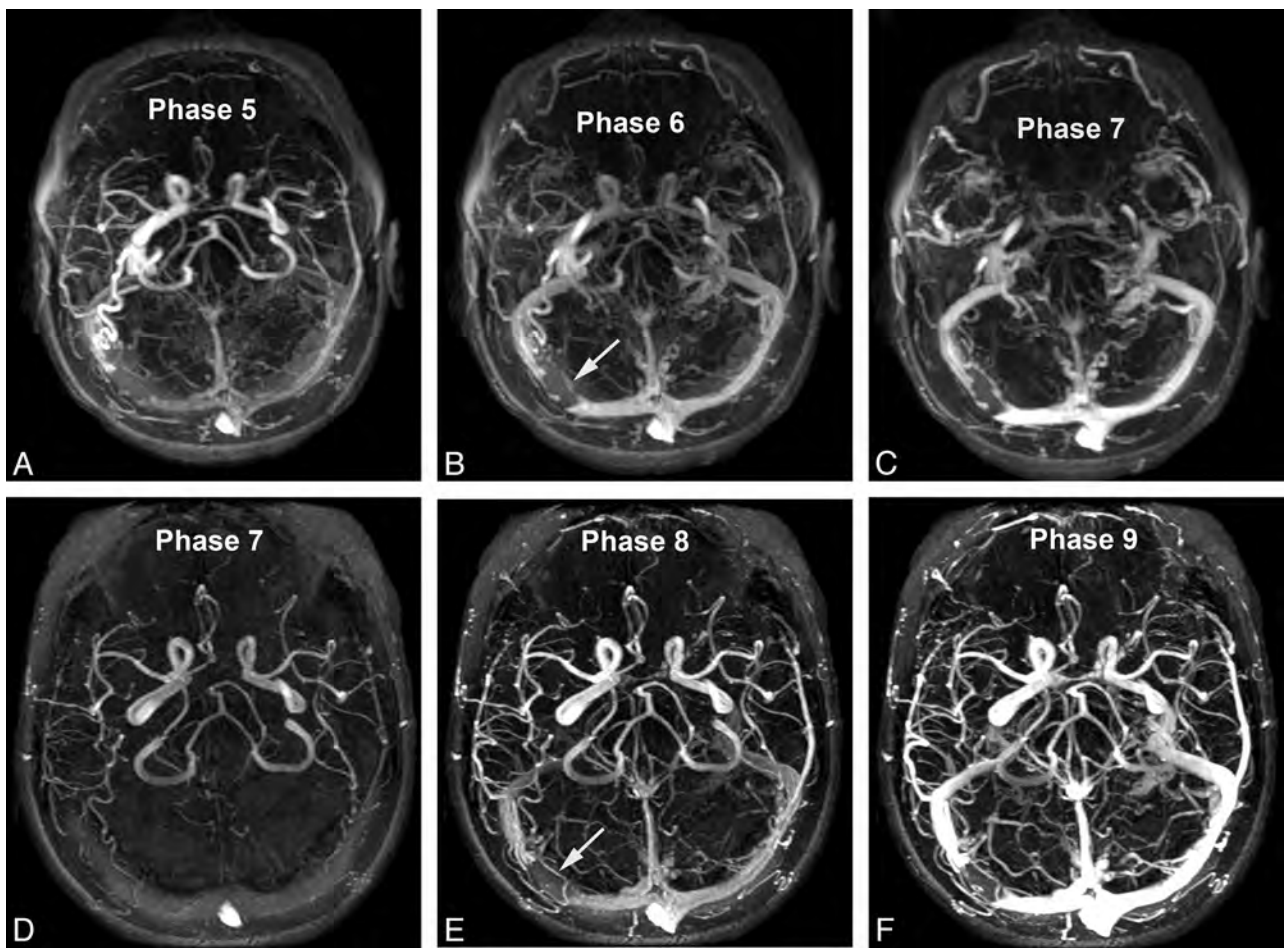


FIG 2. Patient (68-year-old woman) undergoing successive TR-MRA spaced approximately 1 year apart, for evaluation of angiographically documented indirect dural arteriovenous fistula (*arrow*). Images in A–C were obtained with injection of SCA; images in D–F were obtained with BPA. Early arterial (A, D), late arterial (B, E), and venous (C, F) axial MIP phases are presented as indicated. Qualitatively superior time-resolved angiography was scored for all temporal phases and arterial segments, with consideration to diagnostic confidence and vessel-background contrast. Note the generally delayed arrival/temporal phases with the slower administration rate of BPA.

physiologic information, such approaches may be prone to various degrees of temporal smearing, more common with traditional keyhole undersampling algorithms, which may confound interpretation of dynamic information when severe. We have not observed these effects to be particularly problematic in most cases; however, practitioners should remain aware of their potential to mimic shunt physiology and premature venous enhancement.

We have adopted a slower injection rate for BPA than that used in a similar, recent study by Frydrychowicz et al¹³ comparing BPA with SCA in thoracic TR-MRA (1.5 mL/s versus 3 mL/s, respectively). In combination with other factors, this difference may be nontrivial, given the nearly uniform superiority of BPA over SCA in our study, in contrast to the qualitative comparability between the 2 agents as described by the authors therein. Whereas differences in thoracic versus cerebral anatomy, particularly differences in vessel size, make conclusive judgments in this respect difficult, the significance of injection rate is strongly considered, given the preferential effects of BPA on transverse (r_2) over longitudinal (r_1) relaxation enhancement, approaching 6:1 at 3T.⁹ This may be especially problematic at high field, or in large vessels such as the subclavian arteries, in which unanticipated signal loss may occur at peak bolus as the result of T2* effects. Dose and

injection rate reductions, as well as lower field scanning, may therefore ameliorate such factors when relevant. The use of 1.5T clinical systems may have further benefited this investigation, as the r_1 and the rate of longitudinal relaxation enhancement (R1) have shown to be optimized for the macromolecular structure of BPA at 1.5T, whereas the differences compared with SCA are less pronounced at 3T.⁹ In our experience, inner-thigh and midsection burning and discomfort, sometimes described on more rapid injection of BPA, are mitigated by the slower injection rate prescribed in our studies.²¹

Frydrychowicz et al¹³ estimated both SNR and contrast-to-noise ratio (CNR) between SCA and BPA; however as they point out, and as thoroughly expounded previously by Reeder et al,²² SNR and CNR measurements of multichannel receive datasets are not straightforward, given the spatial nonuniformity of noise amplification inherent to parallel acceleration. For this reason, we believe qualitative estimates of image quality and quantitative descriptions of contrast kinetics to be more relevant to clinical practice. It is worth noting, however, that their study described the inferiority of arterial SNR and CNR with BPA, again possibly relating to degradation in imaging quality related to T2* effects. Interestingly, their findings described a reversal of this effect dur-

ing the venous phase, in which relative dilution of the BPA is believed to restore the benefits of greater longitudinal relaxation enhancement. Among the quantitative details considered in this study, we found no significant difference in the likelihood of the 2 agents to produce uncontaminated (ie, free of venous enhancement) arteriograms; however, as might be anticipated from the slower injection rate of BPA, the peak arterial phase was encountered significantly later than with SCA.

Although use of early formulations of blood-pool prototypes was complicated by their tendency for tissue retention, gadofosveset trisodium was the first BPA, which progressed to human trials because of its efficient excretion.¹¹ Its high protein binding occurs almost immediately on injection, ensuring prolonged plasma half-life without extravasation—and therefore excellent blood-to-tissue contrast—while the maintenance of a predictable equilibrium between free and bound fractions ensures ready glomerular filtration of the free fraction, thus preventing retention within viscera.¹¹ Together with the excellent relaxation enhancement properties of its macromolecular structure, the profile of gadofosveset is therefore well-suited to such applications.

Limitations of this study include its retrospective design; however, both readers were fully blinded to the administered agent before review of both the raw volumes and MIP datasets. We chose to perform consensus reads of the study data to ensure uniformity in qualitative analyses, because our primary aim was to establish the qualitative superiority of an administered agent for TR-MRA rather than specifically to investigate the comparative diagnostic accuracy of one agent against the other. Given the extremely large datasets, which were examined across broad vascular anatomic boundaries precluding reliable uniformity in data presentation, we found a consensus evaluation of angiographic quality among the proposed metrics to be most generalizable to future clinical use. This approach, unfortunately, did not permit determination of interreader variability. All data were, however, reviewed with a uniform and reproducible methodology to approximate clinical practice as closely as achievable.

Our large study population of 100 TR-MR angiographies, comprising 50 studies, each performed with either BPA or SCA, constitutes a considerably larger study sample than comparable prior investigations, ranging between 10–30 TR-MRA examinations.^{4,13,15–17,23–26} Not all patients were disease-free in our study population; attention was focused on the anatomically normal side for analysis, and we thus believe the findings to be readily generalizable to clinical practice and advocate strongly for the use of BPA for cerebral TR-MRA when feasible. We propose that the superior quality, comparable enhancement kinetics, and flexibility toward a 70% dose reduction compared with SCA underscore the advantages of BPA for TR-MRA, particularly at 1.5T scanning; however, at approximately 4 times the cost per dose, supplanting standard agents for all applications may be impractical at present.

CONCLUSIONS

The present study confirms the superiority of BPA for use in cerebral TR-MRA over conventional SCA. Superior quality was noted for BPA across all interrogated arterial segments, as well as

the deep venous anatomy. No significant loss in the generation of uncorrupted arteriographic phases was noted, despite the considerably smaller dose of injected gadolinium chelate with BPA. Our findings confirm not only technical feasibility but also augmented diagnostic confidence with BPA over SCA for TR-MRA, together with an advantageous dose profile in patients undergoing steady-state or dynamic MRA.

REFERENCES

1. Korosec FR, Frayne R, Grist TM, et al. **Time-resolved contrast-enhanced 3D MR angiography.** *Magn Reson Med* 1996;36:345–51
2. Lim RP, Shapiro M, Wang EY, et al. **3D time-resolved MR angiography (MRA) of the carotid arteries with time-resolved imaging with stochastic trajectories: comparison with 3D contrast-enhanced bolus-chase MRA and 3D time-of-flight MRA.** *AJNR Am J Neuroradiol* 2008;29:1847–54
3. Willinek WA, Hadizadeh DR, von Falkenhausen M, et al. **4D time-resolved MR angiography with keyhole (4D-TRAK): more than 60 times accelerated MRA using a combination of CENTRA, keyhole, and SENSE at 3.0T.** *J Magn Reson Imaging* 2008;27:1455–60
4. Maki JH, Wang M, Wilson GJ, et al. **Highly accelerated first-pass contrast-enhanced magnetic resonance angiography of the peripheral vasculature: comparison of gadofosveset trisodium with gadopentetate dimeglumine contrast agents.** *J Magn Reson Imaging* 2009;30:1085–92
5. Lin W, Haacke EM, Smith AS, et al. **Gadolinium-enhanced high-resolution MR angiography with adaptive vessel tracking: preliminary results in the intracranial circulation.** *J Magn Reson Imaging* 1992;2:277–84
6. Collidge TA, Thomson PC, Mark PB, et al. **Gadolinium-enhanced MR imaging and nephrogenic systemic fibrosis: retrospective study of a renal replacement therapy cohort.** *Radiology* 2007;245:168–75
7. Caravan P, Cloutier NJ, Greenfield MT, et al. **The interaction of MS-325 with human serum albumin and its effect on proton relaxation rates.** *J Am Chem Soc* 2002;124:3152–62
8. Muller RN, Gillis P, Moiny F, et al. **Transverse relaxivity of particulate MRI contrast media: from theories to experiments.** *Magn Reson Med* 1991;22:178–82
9. Rohrer M, Bauer H, Mintorovitch J, et al. **Comparison of magnetic properties of MRI contrast media solutions at different magnetic field strengths.** *Invest Radiol* 2005;40:715–24
10. Hartmann M, Wiethoff AJ, Hentrich HR, et al. **Initial imaging recommendations for Vasovist angiography.** *Eur Radiol* 2006;16(Suppl 2):B15–23
11. Lauffer RB, Parmelee DJ, Dunham SU, et al. **MS-325: albumin-targeted contrast agent for MR angiography.** *Radiology* 1998;207:529–38
12. Niendorf HP, Felix R, Laniado M, et al. **Gadolinium-DTPA: a new contrast agent for magnetic resonance imaging.** *Radiat Med* 1985;3:7–12
13. Frydrychowicz A, Russe MF, Bock J, et al. **Comparison of gadofosveset trisodium and gadobenate dimeglumine during time-resolved thoracic MR angiography at 3T.** *Acad Radiol* 2010;17:1394–400
14. Klessen C, Hein PA, Huppertz A, et al. **First-pass whole-body magnetic resonance angiography (MRA) using the blood-pool contrast medium gadofosveset trisodium: comparison to gadopentetate dimeglumine.** *Invest Radiol* 2007;42:659–64
15. Naehle CP, Muller A, Willinek WA, et al. **First-pass and steady-state magnetic resonance angiography of the thoracic vasculature using gadofosveset trisodium.** *J Magn Reson Imaging* 2009;30:809–16
16. Nielsen YW, Eiberg JP, Logager VB, et al. **Whole-body MR angiography with body coil acquisition at 3 T in patients with peripheral arterial disease using the contrast agent gadofosveset trisodium.** *Acad Radiol* 2009;16:654–61
17. Nissen JC, Attenberger UI, Fink C, et al. **Thoracic and abdominal**

- MRA with gadofosveset: influence of injection rate on vessel signal and image quality.** *Eur Radiol* 2009;19:1932–38
18. Bleicher AG, Kanal E. **A serial dilution study of gadolinium-based MR imaging contrast agents.** *AJNR Am J Neuroradiol* 2008;29:668–73
 19. Pintaske J, Martirosian P, Graf H, et al. **Relaxivity of gadopentetate dimeglumine (Magnevist), gadobutrol (Gadovist), and gadobenate dimeglumine (MultiHance) in human blood plasma at 0.2, 1.5, and 3 Tesla.** *Invest Radiol* 2006;41:213–21
 20. Kiefer C, El-Koussy M, Schroth G, et al. **Theoretical and clinical aspects of TWIST based 4D time-resolved MR angiography.** In: Dössel O, Schlegel W, eds. *World Congress on Medical Physics and Biomedical Engineering, September 7–12, 2009, Munich, Germany.* Berlin/Heidelberg: Springer-Verlag; 2009:466–69
 21. Rapp JH, Wolff SD, Quinn SF, et al. **Aortoiliac occlusive disease in patients with known or suspected peripheral vascular disease: safety and efficacy of gadofosveset-enhanced MR angiography: multicenter comparative phase III study.** *Radiology* 2005;236:71–78
 22. Reeder SB, Wintersperger BJ, Dietrich O, et al. **Practical approaches to the evaluation of signal-to-noise ratio performance with parallel imaging: application with cardiac imaging and a 32-channel cardiac coil.** *Magn Reson Med* 2005;54:748–54
 23. Bluemke DA, Stillman AE, Bis KG, et al. **Carotid MR angiography: phase II study of safety and efficacy for MS-325.** *Radiology* 2001;219:114–22
 24. Hadizadeh DR, Gieseke J, Lohmaier SH, et al. **Peripheral MR angiography with blood pool contrast agent: prospective intraindividual comparative study of high-spatial-resolution steady-state MR angiography versus standard-resolution first-pass MR angiography and DSA.** *Radiology* 2008;249:701–11
 25. Michaely HJ, Attenberger UI, Dietrich O, et al. **Feasibility of gadofosveset-enhanced steady-state magnetic resonance angiography of the peripheral vessels at 3 Tesla with Dixon fat saturation.** *Invest Radiol* 2008;43:635–41
 26. Michaely HJ, Kramer H, Dietrich O, et al. **Intraindividual comparison of high-spatial-resolution abdominal MR angiography at 1.5 T and 3.0 T: initial experience.** *Radiology* 2007;244:907–13

Genetics of Alzheimer Disease

A.T. Rao, A.J. Degnan, and L.M. Levy

ABSTRACT

SUMMARY: Alzheimer disease prevails as a major cause of disability in the elderly population and ranks as the most common form of dementia that affects 1 of 8 individuals older than 65 years of age. Most AD cases are late in onset and are probably influenced by both genetic and environmental factors. Apart from age, the risk factors include family history; brain injury, both traumatic and vascular; and metabolic diseases, such as diabetes, hypercholesterolemia, and obesity. Based on twin studies, inheritance plays a role in approximately 80% of cases (familial and sporadic).

ABBREVIATIONS: AD = Alzheimer disease; APP = amyloid protein precursor; PSEN1 = presenilin 1; PSEN2 = presenilin 2; A β = amyloid- β ; APOE = apolipoprotein E

While current therapies remain largely limited, advances have been made in clarifying genetic factors related to the development of Alzheimer disease. Autosomal dominant inheritance of 3 genes, *PSEN1*, *PSEN2*, and *APP*, is associated with an early-onset form. Late-onset disease is the most common form and has a risk association with the *APOE* ϵ 4 allele. Genetic testing is available for these mutations, and research continues to improve prognostication and may inspire novel treatments.

WHAT IS ALZHEIMER DISEASE AND HOW IS IT DIAGNOSED?

AD is an irreversible and progressive brain disease that slowly destroys memory and other cognitive functions such as thinking and reasoning and involves behavior abnormalities, which gradually interfere with a person's everyday life and activities. It is now believed that the AD pathophysiologic process starts years before detectable cognitive changes and perhaps decades prior the onset of clinical dementia.¹ The concept of the "AD pathophysiologic process" is thus separated from "AD dementia."

There are 3 distinct clinical stages:

- 1) In preclinical AD, there are no clinical signs. Measurable changes in the molecular and imaging biomarkers for presymptomatic evaluation are being investigated.

- 2) In mild cognitive impairment AD, there are mild serial changes in memory and cognitive status that can be detected by careful examination and do not interfere with day-to-day activities. Other causes of dementia should be excluded. Genetic testing for specific mutations can be performed in cases of early-onset familial Alzheimer disease.
- 3) In Alzheimer dementia, AD is characterized by progressive cognitive decline that interferes with day-to-day activities. The new guidelines propose 4 possible classifications of dementia caused by AD: probable AD dementia; probable AD dementia with an increased level of certainty; possible AD dementia; and probable or possible AD dementia with evidence of an AD pathophysiologic process. Abnormal biomarkers such as elevated CSF levels of τ protein and decreased levels of A β , decreased glucose uptake on PET imaging, and temporal lobe atrophy on MR imaging may add to the certainty of diagnosis.

WHAT ARE THE CLINICAL PRESENTATIONS OF ALZHEIMER DISEASE?

Alzheimer disease is the most common form of neurodegenerative dementia that increases in prevalence with age with a lifetime risk of 1 in 10.¹ Like most dementias, the clinical course begins insidiously with a gradual decline in memory classified as mild cognitive impairment and then progresses to involve other symptoms. Executive dysfunction such as poor judgment, behavior disturbances, and changes in mood all may occur in AD.² Symptoms span the course of several years to a decade, and mortality is frequently related to deconditioning. Management is mostly supportive with modest functional improvement in some individuals by using an acetylcholinesterase inhibitor or *N*-Methyl-D-aspartate antagonist.

Received January 28, 2012; accepted January 29.

From the George Washington University Medical Center (A.T.R., L.M.L.), Washington, DC; and University of Pittsburgh Medical Center (A.J.D.), Pittsburgh, Pennsylvania.

Please address correspondence to Lucien M. Levy, MD, PhD, Professor of Radiology and Director of Neuroradiology, George Washington University Medical Center, 901 23rd St NW, Washington, DC 20037; e-mail: llevy@mfa.gwu.edu

<http://dx.doi.org/10.3174/ajnr.A3545>

Major genetic forms of Alzheimer disease

Gene Name	Locus	AD Type
<i>PSEN1</i>	14q24.3	Early-onset
<i>PSEN2</i>	1q31-q42	Early-onset
<i>APP</i>	21q21	Early-onset
<i>APOE</i> ε4 allele	19q13.2	Late-onset

WHAT IS THE PATHOPHYSIOLOGY OF AD?

Accumulation of amyloid- β protein and τ protein within neurofibrillary tangles (abnormally phosphorylated τ protein) is the fundamental neuropathologic finding in AD. The amyloid cascade hypothesis proposes that the intracellular deposition of $A\beta$ is the initiating lesion that may ultimately lead to AD, though the presence of tangles appears essential to dementia. A definite diagnosis is often not evident in the early stages of the disease, especially in the presence of confounding clinical and imaging changes. Abnormalities such as amyloidopathy and tauopathy are not specific individually for AD. Definitive diagnosis is based on the presence of the plaques and tangles and positive staining with $A\beta$. When the clinical diagnosis appears reliable, such as in the late stages, autopsy and neuropathologic examination are frequently omitted.¹ Imaging methods involve targeting amyloid protein first with Pittsburgh compound B and most recently with florbetapir, a clinically approved PET imaging $A\beta$ ligand.³ However, there is controversy over whether amyloid pathology alone explains AD.⁴

HOW DO GENES INFLUENCE THE AGE OF ONSET OF AD?

There is a clear genetic influence in the manifestation of AD. Having a first-order relative with AD more than doubles the risk of developing AD in one's lifetime. AD can be thought of as 2 separate entities: a rare early-onset form (early-onset familial Alzheimer disease) before 65 years of age and a common late-onset form (late-onset Alzheimer disease), which manifests at divergent ages. Each involves a different set of genes. There is also a dichotomy between the inheritance patterns, with early-onset familial Alzheimer disease following a more Mendelian pattern, whereas late-onset Alzheimer disease appears to occur in a more sporadic pattern with partial susceptibility conferred by familial history. Three autosomal dominant causal genes have been reliably associated with early-onset familial Alzheimer disease: *presenilin 1*, *presenilin 2*, and *amyloid precursor protein*.⁵ Mutations of these 3 genes make up approximately 7 of 10 cases of early-onset familial Alzheimer disease; *PSEN1* is the most common and *PSEN2* is the rarest (Table).^{2,5} In patients with late-onset Alzheimer disease, there is a greater risk of AD with the presence of the $\epsilon 4$ allele of the *apolipoprotein E* gene, whereas other alleles such as $\epsilon 2$ have a lower risk. Other causes such as trisomy 21 may lead to AD due to an identifiable genetic etiology.

IS THERE GENETIC TESTING AVAILABLE FOR AD?

Individuals with first-degree relatives with early-onset AD may seek genetic counseling to determine the risk for developing early-onset familial Alzheimer disease. Presently, presymptomatic testing is available for mutations of *APP*, *PSEN1*, and *PSEN2*. There is

also genetic testing to assess the presence of the *APOE* $\epsilon 4$ allele, but those with relatives with late-onset AD are not advised to pursue testing before symptom development.⁵

ARE THERE ANY OTHER HYPOTHESIZED GENETIC ASSOCIATIONS WITH AD?

Because AD is one of the most extensively researched conditions, a plethora of putative gene associations have been put forth. There are several databases, such as AlzGene (<http://www.alzgene.org>), that include several hundred genes, linkage studies, and other genomic evidence. A few promising genes are *GAB2*, which is associated with increased τ phosphorylation, and *SORL1*, which has an unclear role in AD and has not been well-replicated.⁵ Numerous studies are presently examining the possible causative and susceptibility effects of these and many other genes as well as a variety of epigenetic mechanisms to better predict the development of AD.⁴ Future work may aid in the earlier diagnosis of AD and may even direct gene-based therapies.

AD BIOMARKERS

The AD biomarkers are based on the 2 major pathophysiologic pathways of $A\beta$ and τ protein. There are 5 major biomarkers that have been widely studied.⁶ The biomarkers of $A\beta$ accumulation are a low CSF $A\beta$ 42 level and abnormal tracer uptake on PET amyloid plaque imaging. On imaging, ¹¹C Pittsburgh compound (PiB) has been the most validated tracer for amyloid pathology. A new tracer, florbetapir ¹⁸F, offers the advantage of the longer half-life of ¹⁸F of 110 minutes versus 20 minutes for PiB, potentially offering more extensive use for clinical and research purposes.

The biomarkers for neurodegeneration include elevated levels of total and phosphorylated τ protein in the CSF and neuroimaging correlates of hippocampal atrophy on structural MR imaging and symmetric decreased metabolism in the temporoparietal regions on FDG-PET.

WHAT IS THE ROLE OF STRUCTURAL NEUROIMAGING IN AD?

The traditional role of structural neuroimaging in dementia has been to exclude a treatable cause for cognitive decline such as a subdural hematoma or a tumor. However, with the development of newer technologies, including PET/MR imaging, the role of neuroimaging is being redefined as an aid in the clinical diagnosis of dementias, including AD.

REFERENCES

1. Bird TD. Genetic aspects of Alzheimer's disease. *Genet Med* 2008;10:231–39
2. Bekris LM, Yu CE, Bird TD, et al. Genetics of Alzheimer's disease. *J Geriatr Psychiatry Neurol* 2010;23:213–27
3. Clark CM, Schneider JA, Bedell BJ, et al. Use of florbetapir-PET for imaging B-amyloid pathology. *JAMA* 2011;305:275–83
4. Alagiakrishnan K, Gill SS, Fagarasanu A. Genetics and epigenetics of Alzheimer's disease. *Postgrad Med J* 2012;88:522–29
5. Williamson J, Goldman J, Marder KS. Genetic aspects of Alzheimer's disease. *Neurologist* 2009;15:80–86
6. Jack CR Jr. Alzheimer's disease: new concepts on its neurobiology and the clinical role imaging will play. *Radiology* 2012;263:344–61

Appropriate Use of CT Perfusion following Aneurysmal Subarachnoid Hemorrhage: A Bayesian Analysis Approach

R.P. Killeen, A. Gupta, H. Delaney, C.E. Johnson, A.J. Tsiouris, J. Comunale, M.E. Fink, H.S. Mangat, A.Z. Segal, A.I. Mushlin, and P.C. Sanelli



ABSTRACT

BACKGROUND AND PURPOSE: In recent years CTP has been used as a complementary diagnostic tool in the evaluation of delayed cerebral ischemia and vasospasm. Our aim was to determine the test characteristics of CTP for detecting delayed cerebral ischemia and vasospasm in SAH, and then to apply Bayesian analysis to identify subgroups for its appropriate use.

MATERIALS AND METHODS: Our retrospective cohort comprised consecutive patients with SAH and CTP performed between days 6 and 8 following aneurysm rupture. Delayed cerebral ischemia was determined according to primary outcome measures of infarction and/or permanent neurologic deficits. Vasospasm was determined by using DSA. The test characteristics of CTP and its 95% CIs were calculated. Graphs of conditional probabilities were constructed by using Bayesian techniques. Local treatment thresholds (posttest probability of delayed cerebral ischemia needed to initiate induced hypertension, hypervolemia, and hemodilution or intra-arterial therapy) were determined via a survey of 6 independent neurologists.

RESULTS: Ninety-seven patients with SAH were included in the study; 39% (38/97) developed delayed cerebral ischemia. Qualitative CTP deficits were seen in 49% (48/97), occurring in 84% (32/38) with delayed cerebral ischemia and 27% (16/59) without. The sensitivity, specificity, and positive and negative predictive values (95% CI) for CTP were 0.84 (0.73–0.96), 0.73 (0.62–0.84), 0.67 (0.51–0.79), and 0.88 (0.74–0.94), respectively. A subgroup of 57 patients underwent DSA; 63% (36/57) developed vasospasm. Qualitative CTP deficits were seen in 70% (40/57), occurring in 97% (35/36) with vasospasm and 23% (5/21) without. The sensitivity, specificity, and positive and negative predictive values (95% CI) for CTP were 0.97 (0.92–1.0), 0.76 (0.58–0.94), 0.88 (0.72–0.95), and 0.94 (0.69–0.99), respectively. Treatment thresholds were determined as 30% for induced hypertension, hypervolemia, and hemodilution and 70% for intra-arterial therapy.

CONCLUSIONS: Positive CTP findings identify patients who should be carefully considered for induced hypertension, hypervolemia, and hemodilution and/or intra-arterial therapy while negative CTP findings are useful in guiding a no-treatment decision.

ABBREVIATIONS: aSAH = aneurysmal subarachnoid hemorrhage; DCI = delayed cerebral ischemia; GCP = graph of conditional probabilities; HHH = induced hypertension, hypervolemia, and hemodilution

Aneurysmal subarachnoid hemorrhage (aSAH) is a devastating condition, with complications of vasospasm and delayed cerebral ischemia (DCI) resulting in significant morbidity and

mortality. The pathophysiology of vasospasm and DCI is complex and poorly understood, leading to delayed diagnosis and treatment.¹ Currently, both clinical and imaging findings are used to detect vasospasm and DCI. The clinical findings of new symptoms not attributed to other known causes coupled with imaging evidence of vasospasm may prompt treatment to prevent DCI and subsequent infarction. The diagnosis remains challenging because many patients are critically ill, precluding thorough clinical assessment,² and discrepant findings between clinical and imaging examinations lead to indeterminate diagnoses. Prior studies have reported that almost half of patients with severe vasospasm

Received February 15, 2013; accepted after revision July 1.

From the Departments of Radiology (R.P.K., A.G., H.D., C.E.J., A.J.T., J.C., P.C.S.), Neurology (M.E.F., H.S.M., A.Z.S.), and Public Health (A.I.M., P.C.S.), Weill Cornell Medical College, New York-Presbyterian Hospital, New York, New York.

This work was supported by grant 5K23NS058387–04 from the National Institute of Neurological Disorders and Stroke, a component of the National Institutes of Health.

Paper previously presented in part at: Annual Meeting of the American Society of Neuroradiology and the Foundation of the ASNR Symposium, New York; April 21–26, 2012.

The views herein are solely those of the authors and do not necessarily represent the official view of the National Institute of Neurological Disorders and Stroke or the National Institutes of Health.

Please address correspondence to Pina C. Sanelli, MD, MPH, Department of Radiology, Weill Cornell Medical College, New York-Presbyterian Hospital, 525 East 68th St, Starr 8A, Box 141, New York, NY 10065; e-mail: pcs9001@med.cornell.edu

Indicates open access to non-subscribers at www.ajnr.org

<http://dx.doi.org/10.3174/ajnr.A3767>

do not have DCI.³ Additionally, DCI is not always attributed to vasospasm and may occur in the absence of arterial narrowing, indicating that the relationship between vasospasm and DCI is not completely understood. Thus, it is important to consider vasospasm and DCI as 2 related but somewhat different clinical entities. DCI has been recently defined by expert consensus by using the primary outcome measures of functional disability and/or cerebral infarction not attributed to other causes,¹ and “vasospasm” has been defined as arterial narrowing seen on imaging studies.

In recent years, CTP has been added as a complementary diagnostic tool for determining vasospasm and DCI. Several reports describe its high sensitivity and specificity to detect perfusion abnormalities thought to occur in both vasospasm and DCI.³⁻⁸ CTP has several other advantages in this critically ill population, including its widespread access, acquisition speed, and few patient contraindications. However, CTP also has disadvantages, with the main concern being increased radiation exposure relative to non-contrast CT of the head, due to its cine scanning technique.⁹ Biologic effects from radiation exposure, including temporary epilation and erythema, have been described in patients with aSAH and acute stroke who have undergone CTP.^{10,11} As a result, the FDA issued a notification to health care providers to promote radiation safety and appropriate use of CT imaging.¹¹ Currently, there are no guidelines for the appropriate use of CTP in aSAH, which may potentially result in overuse of CTP with unnecessary radiation exposure, contrast reactions, and increased cost. There is also potential for underuse, in which the diagnosis of vasospasm and DCI may remain elusive and patients will not receive optimal and timely treatment. Thus, it is important to identify patients who will benefit most from CTP to outweigh its associated risks.

Our hypothesis is that application of Bayesian analysis¹²⁻¹⁵ can guide appropriate use of CTP in aSAH by identifying subgroups in which CTP results affect treatment decisions. Bayesian analysis uses probability theory to calculate the posttest probability of vasospasm or DCI following a positive or negative CTP finding. The purpose of this study was to determine the test characteristics of qualitative CTP for identifying 2 separate but related entities in aSAH, angiographic vasospasm and DCI, and then to apply Bayesian analysis to identify subgroups for its appropriate use.

MATERIALS AND METHODS

Study Design

We performed a retrospective study of consecutive patients with aSAH enrolled in an institutional review board–approved clinical accuracy trial from December 2004 to December 2008. Inclusion criteria were adult patients (18 years and older) with documented aSAH at admission determined by initial noncontrast head CT, CSF analysis, CTA, and/or DSA. Exclusion criteria were CTP examinations with severe motion degradation and CTP examinations performed after infarction or treatment of vasospasm had occurred. All patients underwent surgical clipping and/or endovascular coiling for aneurysm repair and were monitored in the neurointensive care unit, as per the usual standard-of-care procedures.

Chart review was performed for the clinical and demographic characteristics of the study population. During hospitalization,

patients were assessed for symptoms of vasospasm and DCI, defined as delayed onset of neurologic deterioration, which was not explained by other causes, such as aneurysm rebleeding, intracranial hemorrhage, hydrocephalus, infection, metabolic disturbance, seizure, and so forth. Neurologic deterioration may manifest as alterations in consciousness, worsening on the Glasgow Coma Scale, or new neurologic deficits (aphasia, paresis, and so forth). In patients with suspected vasospasm or DCI, based on neurologic deterioration and transcranial Doppler sonography, DSA with the potential for endovascular treatment was performed. Management decisions were based on all clinical and imaging data, except CTP.

CTP Protocol and Data Processing

CTP was performed during the typical time of vasospasm and DCI, between days 6 and 8 in asymptomatic patients (patients without neurologic deterioration) and on the same day that neurologic deterioration occurred in symptomatic patients. Of note, CTP examinations were performed at the diagnostic stage, before treatment for vasospasm or DCI and before patients developed infarction. There is a standard scanning protocol for CTP at our institution by using LightSpeed or Pro 16 scanners (GE Healthcare, Milwaukee, Wisconsin) with a cine 4i scanning mode and a 45-second acquisition at 1 rotation per second by using 80 kV (peak) and 190 mA. To minimize radiation exposure to the lenses, we used a scanning volume of 2.0 cm with its inferior extent selected above the orbits and at the level of the basal ganglia. Approximately 45 mL of nonionic iodinated contrast was administered intravenously at 5 mL/s by using a power injector with a 5-second delay.

Postprocessing of the acquired images into MTT, CBF, and CBV maps was performed on an Advantage Workstation (GE Healthcare) by using CT Perfusion software, Version 3.0 (GE Healthcare). The postprocessing technique was standardized for all patients according to recommended guidelines, with the arterial input function as the A2 segment of the anterior cerebral artery and the venous function as the superior sagittal sinus.¹⁶

The perfusion maps were qualitatively evaluated by 2 neuro-radiologists (with 10 and 7 years' experience, respectively) to determine the presence of perfusion deficits, defined as areas of decreased CBF and/or prolonged MTT. Focal perfusion abnormalities due to the primary hemorrhagic event and/or surgical intervention were not considered as perfusion deficits from vasospasm or DCI. After reviewing the images independently, consensus judgment was determined. CTP examinations were analyzed blinded to all clinical and imaging data to limit test-review bias.

Reference Standard for Vasospasm and DCI

Vasospasm and DCI were assessed by 2 separate reference standards. The diagnosis of vasospasm was based on angiographic criteria by using DSA to determine arterial luminal narrowing compared with the healthy parent vessel and with DSA performed on the initial presentation. Arterial narrowing of >50% compared with the parent vessel was classified as vasospasm. DSA interpretations were performed by 2 observers, an interventional neuroradiologist who performed the examination (with either 10 or 25 years' experience) and a neuroradiologist blinded to all clin-

Table 1: Clinical and demographic characteristics of the study population and subgroups

	Study Population			Subgroup		
	(n = 97)			(DSA as Reference Standard) (n = 57)		
	All (n = 97)	DCI (n = 38)	No DCI (n = 59)	All (n = 57)	Vasospasm (n = 36)	No vasospasm (n = 21)
Age (yr) (median)	49	54	48	51	48	55
(Range)	28–80	34–78	28–80	28–80	30–78	28–80
Sex (%) (No.)						
Male	27 (26/97)	32 (12/38)	24 (14/59)	25 (14/57)	25 (9/36)	24 (5/21)
Female	73 (71/97)	68 (26/38)	76 (45/59)	75 (43/57)	75 (27/36)	76 (16/21)
Aneurysm location (%) (No.)						
Anterior	92 (89/97)	92 (35/38)	93 (55/59)	95 (54/57)	92 (33/36)	100 (21/21)
Posterior	8 (8/97)	8 (3/38)	7 (4/59)	5 (3/57)	8 (3/36)	0 (0/21)
Treatment type (%) (No.)						
Surgical clipping	55 (53/97)	63 (24/38)	49 (29/59)	65 (37/57)	56 (20/36)	81 (17/21)
Coil embolization	45 (44/97)	37 (14/38)	51 (30/59)	35 (20/57)	44 (16/36)	19 (4/21)
Hunt and Hess grade (%) (No.)						
Low (grades 1 and 2)	53 (51/97)	37 (14/38)	61 (36/59)	46 (26/57)	36 (13/36)	62 (13/21)
High (grades 3, 4 and 5)	47 (46/97)	63 (24/38)	39 (23/59)	54 (31/57)	64 (23/36)	38 (8/21)

ical and imaging data (with 22 years' experience). For disagreements, a third neuroradiologist (with 10 years' experience) independently reviewed the DSA in a blinded fashion to determine consensus.

The reference standard for DCI was based on the expert consensus opinion¹ by using the following outcome measures: 1) cerebral infarction demonstrated on CT or MR imaging within 6 weeks after aSAH, which was not present on imaging up to 48 hours after aneurysm occlusion and was not attributable to other causes such as surgical clipping, endovascular treatment, ventricular catheter placement, or intraparenchymal hematoma (this criterion for cerebral infarction has been used to effectively exclude primary brain damage from aSAH and/or surgical interventions^{17,18}); and/or 2) permanent neurologic deficit on clinical examination, distinct from the deficit at baseline produced by the aneurysm rupture or surgical intervention and not attributable to other causes. Thorough chart review was performed and consensus was determined by expert neurologists (with 14 and 4 years' experience) and a neuroradiologist (with 10 years' experience) to classify patients according to these criteria.

Statistical Analysis

The sensitivity, specificity, and likelihood ratios were calculated for qualitative CTP deficits in determining vasospasm and DCI, separately.¹⁹ The 95% confidence interval was calculated as the measure of variance.

The entire spectrum of posttest probabilities was calculated for positive and negative CTP findings by multiplying the pretest odds and the positive and negative likelihood ratios, respectively, which are represented as a graph of conditional probability (GCP). Construction of the GCPs was performed by using an available data analysis Web-based spreadsheet (www.ebr.ie).^{12,20} The posttest probabilities are represented on the y-axis, and pretest probabilities, on the x-axis. To illustrate the usefulness of CTP in the Bayesian analysis, we based selection of the pretest probabilities for vasospasm and DCI on commonly used clinical classification schemes in the literature, such as the Hunt and Hess scale, Fisher grade, modified Fisher scale, and Glasgow Coma Scale.²¹ Given the variability in pretest probabilities of DCI for each of these classification schemes, Bayesian analysis was applied to each

classification scheme separately to determine posttest probabilities after CTP testing to demonstrate whether differences in CTP use existed among these prediction tools.

Locally observed treatment thresholds for initiating medical management with induced hypertension, hypervolemia, and hemodilution (HHH) and intra-arterial therapy with vasodilatory agents and/or angioplasty were evaluated by an independent survey of 6 neurologists (range, 1–29 years' experience) at our institution, to demonstrate the role of CTP in decision-making. Each neurologist described the minimum posttest probability for DCI needed to initiate HHH or intra-arterial therapy by considering the benefits and risks of treatment. Review of survey results and median treatment thresholds were determined by an independent group of 2 other authors not involved in the survey.

RESULTS

Study Population Characteristics

Ninety-seven patients were included in the statistical analysis from the 104 patients enrolled in the prospective study. Seven patients were excluded for the following reasons: CTP examinations were not performed before treatment for vasospasm ($n = 4$), CTP acquired data were not retrievable from the archives for postprocessing ($n = 2$), and postprocessing could not be performed due to severe motion degradation ($n = 1$). The median age (range) was 49 years (28–80 years), and 73% (71/97) were women. Ninety-two percent (89/97) of the aneurysms were located in the anterior circulation. The treatment for aneurysm repair in this study population was 55% (53/97) by surgical clipping and 45% (44/97) via endovascular coiling procedures. The clinical Hunt and Hess scale grades on presentation were 47% (46/97) high grades 3, 4, and 5 and 53% (51/97) low grades 1 and 2. Table 1) presents the demographic and clinical characteristics of the study population according to DCI and vasospasm groups.

According to the reference standard, DCI was diagnosed in 39% (38/97) of patients. Thirty-two percent (12/38) of patients who developed DCI were initially asymptomatic. For the vasospasm analysis, 57 patients were available who also had DSA performed to determine the reference standard. In this subgroup, vasospasm was diagnosed in 63% (36/57) of these patients.

Qualitative CTP Analysis

Day 7 was the median time when CTP was performed (range, 2–17 days). Qualitative CTP deficits were seen in 49% (48/97) of the study population, occurring in 84% (32/38) of patients with DCI and 27% (16/59) without DCI. The sensitivity, specificity, and positive and negative predictive values (95% CI) of CTP for determining DCI were 0.84 (0.73–0.96), 0.73 (0.62–0.84), 0.67 (0.51–0.79), and 0.88 (0.74–0.94), respectively. The positive and negative likelihood ratios (95% CI) were 3.1 (2.0–4.8) and 0.2 (0.10–0.46), respectively.

In the subgroup of patients who had DSA performed, qualitative CTP deficits were seen in 70% (40/57), occurring in 97% (35/36) of patients with vasospasm and 23% (5/21) of patients without vasospasm. The sensitivity, specificity, and positive and negative predictive values (95% CI) of CTP for detecting vasospasm were 0.97 (0.92–1.0), 0.76 (0.58–0.94), 0.88 (0.72–0.95), and 0.94 (0.69–0.99), respectively. The positive and negative likelihood (95% CI) ratios were 4.1 (1.9–8.8) and 0.04 (0.005–0.25), respectively. The median time between CTP and DSA was 1 day (range, 1–3 days).

Bayesian Analysis

The GCPs of CTP for determining DCI and vasospasm are shown in Fig 1A, -B, respectively. The GCP represents the spectrum of

posttest probabilities for a positive or negative CTP test result over a range of pretest probabilities. Table 2 displays the pretest probabilities of DCI based on the classification schemes commonly used in clinical practice. To illustrate the effect of CTP, we calculated the posttest probabilities of DCI for each classification scheme when CTP yielded a positive or negative result.

The median treatment thresholds at our institution for HHH and intra-arterial therapy were 30% and 70%, respectively, indicating that a patient with a posttest probability of >30% following CTP should be considered for treatment with HHH and of >70%, for intra-arterial therapy. These treatment thresholds, which could vary by local practice pattern, are strictly used for illustrative purposes in this study to demonstrate the utility of CTP by using Bayesian analysis and have been incorporated in the GCPs (Fig 1). Overall, a positive CTP finding will increase the posttest probability of DCI above the HHH treatment threshold in any patient with a pretest probability of $\geq 12\%$. On the other hand, a negative CTP finding will decrease the posttest probability below the HHH treatment threshold in any patient with a pretest probability of <67%. A positive CTP finding will increase the posttest probability of vasospasm above the HHH treatment threshold in any patient with a pretest probability of $\geq 10\%$, and a negative CTP finding will decrease the posttest probability below the treatment threshold in any patient with a pretest probability of <92%.

Table 2: Pretest and posttest probabilities of DCI based on clinical classification schemes^a

Clinical Classification Schemes	Pretest Probability (95% CI)	Posttest Probability	
		CTP-Positive (95% CI)	CTP-Negative (95% CI)
Hunt and Hess grades 1–2 ²¹	0.35 (0.25–0.45)	0.62 (0.52–0.72)	0.10 (0.04–0.16)
Hunt and Hess grades 3–5 ²¹	0.61 (0.53–0.70)	0.82 (0.74–0.90)	0.25 (0.16–0.34)
Glasgow Coma Scale ≥ 9 ²¹	0.45 (0.38–0.53)	0.72 (0.63–0.81)	0.15 (0.08–0.22)
Glasgow Coma Scale <9 ²¹	0.71 (0.57–0.86)	0.88 (0.82–0.95)	0.35 (0.26–0.45)
Modified Fisher grade 1 ²⁶	0.13 (0.0–0.29)	0.31 (0.22–0.40)	0.03 (0.0–0.06)
Modified Fisher grade 2, 3 ²⁶	0.20 (0.11–0.28)	0.44 (0.34–0.54)	0.05 (0.01–0.09)
Modified Fisher grade 4 ²⁶	0.36 (0.24–0.47)	0.66 (0.57–0.75)	0.11 (0.05–0.17)

^a The pretest probabilities are based on literature review and the posttest probabilities are calculated from the CTP test characteristics derived from this study.

DISCUSSION

The application of CTP for detecting vasospasm and DCI has been increasing in patients with aSAH partly due to its high sensitivity and specificity reported in the literature.^{6,8,22–24} Our sensitivity (95% CI) of 0.84 (0.73–0.96) and specificity (95% CI) of 0.73 (0.62–0.84) for CTP detecting DCI are similar to those reported in the literature.^{3,4} Additionally, we report a sensitivity (95% CI) of 0.97 (0.92–1.0) and a specificity (95% CI) of 0.76

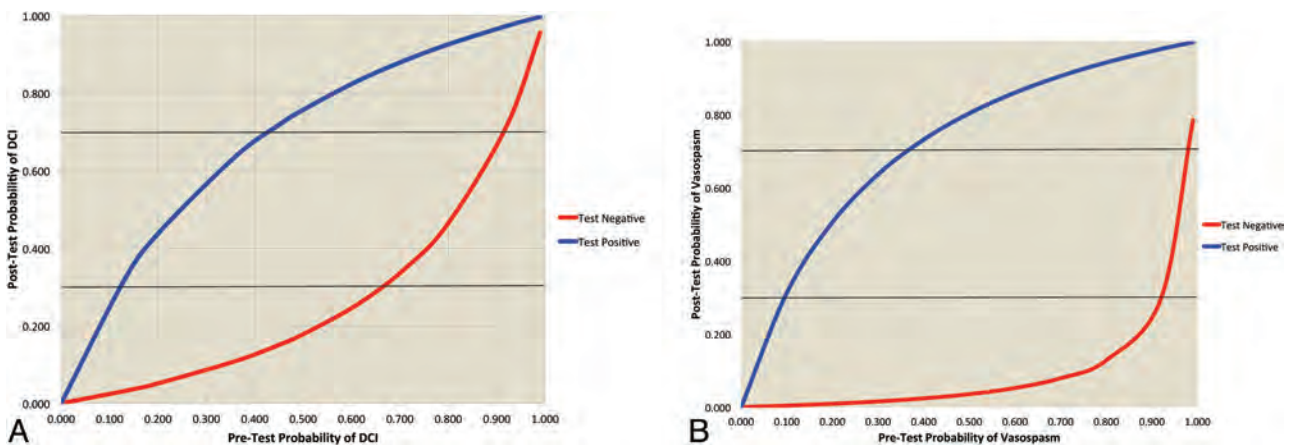


FIG 1. A, Graph of conditional probabilities for CTP determining DCI in aSAH. The blue curve represents the spectrum of posttest probabilities for a positive CTP finding. The red curve represents the spectrum of posttest probabilities for a negative CTP finding. The horizontal black lines represent the treatment threshold posttest probabilities of 30% and 70% for HHH and intra-arterial therapy, respectively. B, Graph of conditional probabilities for CTP determining vasospasm in aSAH. The blue curve represents the spectrum of posttest probabilities for a positive CTP finding. The red curve represents the spectrum of posttest probabilities for a negative CTP finding. The horizontal black lines represent the posttest probability treatment thresholds of 30% and 70%, for HHH and intra-arterial therapy, respectively.

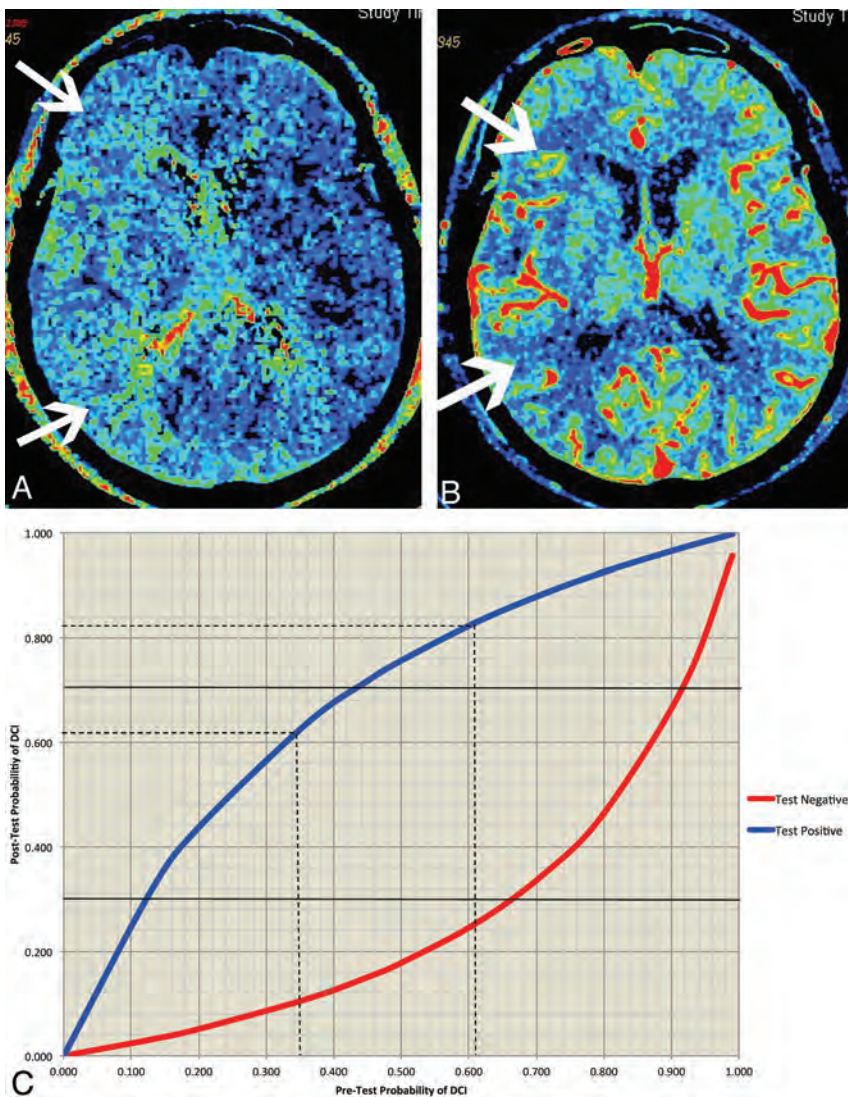


FIG 2. A 65-year-old woman with a CTP examination 6 days following aSAH. *A*, The MTT map demonstrates diffuse prolongation of MTT in the vascular territory of the right middle cerebral artery (arrows). *B*, The CBF map from the same level demonstrates a reduction in CBF in a similar distribution. *C*, The GCP for DCI is customized for this patient on the basis of the Hunt and Hess scale scores, as a sample clinical predictor. The vertical dashed lines represent the pretest probabilities of 35% and 61% for Hunt and Hess scale grades 1–2 and 3–5, respectively. The horizontal dashed lines indicate the posttest probabilities for these 2 Hunt and Hess scale grade classifications. The posttest probabilities for a positive CTP finding remain above the HHH treatment threshold and do not contribute to treatment decisions. However, the posttest probabilities of a negative CTP finding are below the HHH treatment threshold and do alter treatment decisions. Thereby, performing CTP to assist in HHH treatment decisions is considered appropriate in both low and high Hunt and Hess scale grades.

(0.58–0.94) for CTP detecting vasospasm, similar to that in the literature.^{7,25} Construction of the GCPs for Bayesian analysis was based on these test characteristics, suggesting that our results may be applicable to other patient populations with aSAH as well.

Bayesian analysis can assist in treatment decision-making by determining the posttest probability of vasospasm or DCI by using the sensitivity and specificity of CTP along with the pretest probability. The pretest probability is based on all of the patient’s clinical and imaging data before CTP. Even though the treatment threshold is variable in different clinical/disease settings, the principles of its application are the same. At our institution, following a survey of 6 neurologists with expertise

in neurointensive care, the median treatment threshold is a posttest probability of 30% for HHH and 70% for intra-arterial therapy. Intra-arterial therapy may be considered as an adjunct to HHH in patients with posttest probabilities of $\geq 70\%$. These treatment thresholds have not been empirically validated and are used strictly for illustrative purposes in this study to demonstrate the application and value of Bayesian analysis by using locally derived treatment thresholds. The aim of this study was to indicate the most appropriate range of pretest probabilities for the use of CTP, with the understanding that the range of pretest probabilities in which CTP should be used will vary depending on the individual physician’s treatment thresholds.

In this study, a positive CTP finding will increase the posttest probability above the HHH treatment threshold for patients suspected of DCI with a pretest probability of $\geq 12\%$ (Fig 1A). On the other hand, a negative CTP finding will decrease the posttest probability below the treatment threshold in patients with a pretest probability of $< 67\%$. These pretest probabilities indicate the lower and upper boundaries when CTP is most appropriately used in aSAH for detecting DCI. For example, when the pretest probability of DCI is $\geq 67\%$, a positive or negative CTP finding does not reduce the posttest probability below the HHH treatment threshold and the CTP results will, therefore, not contribute to decision-making. Similarly, when the pretest probability of DCI is $< 12\%$, a positive or negative CTP finding does not elevate the posttest probability above the HHH treatment threshold and thereby does not contribute to decision-making. Similar concepts are also applied to patients suspected of vasospasm (Fig 1B). The results

of CTP affect treatment decisions in patients with pretest probabilities of vasospasm between 10% and 92%, when using the treatment thresholds applied in our study.

In clinical practice, pretest probabilities are informally derived from multiple clinical and imaging predictors before imaging. To date, there are no validated models available for assessing the combined pretest probability by using multiple factors. Therefore, the examples used in this study are focused on pretest probabilities derived from single clinical predictors. Table 2 demonstrates the pretest probabilities for different classification schemes commonly used in clinical practice. The posttest probabilities are calculated for a positive and negative CTP finding. These data can

be applied to a specific patient for individualization of care. For example, the modified Fisher scale is used in clinical practice to more accurately predict DCI by stratifying patients.^{26,27} In all modified Fisher scale grades, performing CTP contributes to treatment decisions because a positive or negative CTP finding alters the posttest probability above or below the treatment threshold compared with the pretest probability. Similarly, when one uses Hunt and Hess scale grades to determine pretest probability, CTP is also helpful in determining treatment (Fig 2). In this clinical scenario, a negative CTP finding has a greater effect on treatment decisions than a positive CTP finding. However, this is not the case for the Glasgow Coma Scale. Patients with a Glasgow Coma Scale score of <9 have a pretest probability that is above the treatment threshold. A positive or negative CTP finding does not alter the posttest probability for treatment decisions. Several clinical classification schemes are presented as the pretest probabilities, given their variable use in clinical practice. Selecting the most appropriate classification scheme for a particular patient population is beyond the scope of this study.

Comparison of the GCPs for DCI (Fig 1A) and vasospasm (Fig 1B) indicates that CTP is appropriate for a wider range of pretest probabilities in patients suspected of having vasospasm rather than DCI. These data are reflected by the higher positive and negative predictive values of CTP for determining vasospasm. A possible explanation for the differences observed in the test characteristics of CTP may be that the reference standards used to determine DCI and vasospasm were assessed by using primary outcome measures of cerebral infarction and permanent neurologic deficits determined at the end of hospitalization. A CTP, performed typically between days 6 and 8 following aSAH, may have shown a perfusion deficit that subsequently resolved without an infarction or a permanent deficit. On the other hand, a CTP finding may have been negative at days 6–8, but the patient could have developed ischemia later. Thus, the DCI outcome measures may have worse temporal resolution in relation to the presence or absence of perfusion deficits on CTP. In contrast, for assessment of patients with vasospasm, the CTP and DSA examinations were performed within a short time only in patients with symptoms of vasospasm; that difference may partly explain the superior test characteristics of CTP in determining vasospasm. Another difference noted in the characteristics of the patient group with DSA performed, compared with patients without DSA, is that the DSA group had more patients with neurologic deterioration not explained by other causes because these symptomatic patients were more likely to undergo further testing with DSA and possible intra-arterial treatment.

There are several limitations in this study. The pretest probabilities in the examples were based on single clinical predictors. However, in clinical practice, the pretest probability of a patient represents an estimated likelihood based on the overall evaluation of the patient before CTP, including all available clinical and imaging data. Deriving this overall estimated pretest probability is a complex clinical task because it is affected by a weighted value assigned to each of the clinical and imaging data according to the physician's judgment. Therefore, single clinical predictors were used in this study to illustrate the concepts of applying GCP and to demonstrate the role of CTP in patients with aSAH. Another po-

tential limitation is that the results are dependent on the treatment threshold, which may vary among physicians and institutions. However, GCP can be applied in different patient populations by using the specified treatment thresholds established for a specific practice. Furthermore, the sensitivity and specificity of CTP may also vary in different settings, depending on the quality of the imaging and its interpretation. The GCP may also be customized for a local practice setting by using the www.ebr.ie Web site.²⁰

CONCLUSIONS

Given the potential risks associated with over- and underuse of CTP in aSAH for determining vasospasm and DCI, Bayesian analysis can help guide its most appropriate use in this patient population. Our study indicates that over a wide range of pretest probabilities, a positive CTP finding identifies patients who should be carefully considered for HHH and/or intra-arterial therapy. On the other hand, a negative CTP finding is particularly useful for avoiding treatment-related complications.^{28,29} Treatment thresholds vary in practice and, in lieu of empiric evidence, must be determined by the treating physicians. Future research should be performed to further evaluate these findings in a prospective clinical trial assessing the impact of CTP on patient outcomes.

Disclosures: Holly Delaney—RELATED: Grant: National Institutes of Health.* Comments: National Institutes of Health grant-funded research. Carl E. Johnson—RELATED: Grant: National Institute of Neurological Diseases and Stroke.* Matthew E. Fink—RELATED: Consultancy: Navigant Consultants, Proctor & Gamble, Maquet; Employment: Editor, *Neurology Alert*, AHC Media, *Expert Testimony*: medicolegal, Payment for Development of Educational Presentations: AHC Media-WEbinar. Pina C. Sanelli—RELATED: Grant: National Institute of Neurological Diseases and Stroke.* *Money paid to the institution.

REFERENCES

1. Vergouwen MD, Vermeulen M, van Gijn J, et al. **Definition of delayed cerebral ischemia after aneurysmal subarachnoid hemorrhage as an outcome event in clinical trials and observational studies: proposal of a multidisciplinary research group.** *Stroke* 2010;41:2391–95
2. Schmidt JM, Wartenberg KE, Fernandez A, et al. **Frequency and clinical impact of asymptomatic cerebral infarction due to vasospasm after subarachnoid hemorrhage.** *J Neurosurg* 2008;109:1052–59
3. Dankbaar JW, de Rooij NK, Velthuis BK, et al. **Diagnosing delayed cerebral ischemia with different CT modalities in patients with subarachnoid hemorrhage with clinical deterioration.** *Stroke* 2009;40:3493–98
4. Killeen RP, Mushlin AI, Johnson CE, et al. **Comparison of CT perfusion and digital subtraction angiography in the evaluation of delayed cerebral ischemia.** *Acad Radiol* 2011;18:1094–100
5. Dankbaar JW, de Rooij NK, Rijdsdijk M, et al. **Diagnostic threshold values of cerebral perfusion measured with computed tomography for delayed cerebral ischemia after aneurysmal subarachnoid hemorrhage.** *Stroke* 2010;41:1927–32
6. Sanelli PC, Ugorec I, Johnson CE, et al. **Using quantitative CT perfusion for evaluation of delayed cerebral ischemia following aneurysmal subarachnoid hemorrhage.** *AJNR Am J Neuroradiol* 2011;32:2047–53
7. Wintermark M, Ko NU, Smith WS, et al. **Vasospasm after subarachnoid hemorrhage: utility of perfusion CT and CT angiography on diagnosis and management.** *AJNR Am J Neuroradiol* 2006;27:26–34
8. Aralasmak A, Akyuz M, Ozkaynak C, et al. **CT angiography and perfusion imaging in patients with subarachnoid hemorrhage: correlation of vasospasm to perfusion abnormality.** *Neuroradiology* 2009;51:85–93

9. Cohnen M, Wittsack HJ, Assadi S, et al. **Radiation exposure of patients in comprehensive computed tomography of the head in acute stroke.** *AJNR Am J Neuroradiol* 2006;27:1741–45
10. Imanishi Y, Fukui A, Niimi H, et al. **Radiation-induced temporary hair loss as a radiation damage only occurring in patients who had the combination of MDCT and DSA.** *Eur Radiol* 2005;15:41–46
11. US Food and Drug Administration. **Safety Investigation of CT Brain Perfusion Scans: Update 11/9/2010.** www.fda.gov/medicaldevices/safety/alertsandnotices/ucm185898.htm. Accessed June 1, 2012
12. Maceneaney PM, Malone DE. **The meaning of diagnostic test results: a spreadsheet for swift data analysis.** *Clin Radiol* 2000;55:227–35
13. Joseph L, Reinhold C. **Fundamentals of clinical research for radiologists. Introduction to probability theory and sampling distributions.** *AJR Am J Roentgenol* 2003;180:917–23
14. Heffernan EJ, Dodd JD, Malone DE. **Cardiac multidetector CT: technical and diagnostic evaluation with evidence-based practice techniques.** *Radiology* 2008;248:366–77
15. Dodd JD. **Evidence-based practice in radiology: steps 3 and 4—appraise and apply diagnostic radiology literature.** *Radiology* 2007;242:342–54
16. Sanelli PC, Lev MH, Eastwood JD, et al. **The effect of varying user-selected input parameters on quantitative values in CT perfusion maps.** *Acad Radiol* 2004;11:1085–92
17. Frontera JA, Fernandez A, Schmidt JM, et al. **Defining vasospasm after subarachnoid hemorrhage: what is the most clinically relevant definition?** *Stroke* 2009;40:1963–68
18. Powsner RA, O'Tuama LA, Jabre A, et al. **SPECT imaging in cerebral vasospasm following subarachnoid hemorrhage.** *J Nucl Med* 1998;39:765–69
19. Lowry R. **Clinical calculator 1: from an observed sample—estimates of population prevalence, sensitivity, specificity, predictive values, and likelihood ratios.** <http://faculty.vassar.edu/lowry/clin1.html>. Accessed December 1, 2011
20. **Practice Based Learning: Research in to Practice** (St. Vincent's University Hospital, Dublin, Ireland). <http://www.ebr.ie>. Accessed December 1, 2011
21. Yousef K, Crago E, Kuo CW, et al. **Predictors of delayed cerebral ischemia after aneurysmal subarachnoid hemorrhage: a cardiac focus.** *Neurocrit Care* 2010;13:366–72
22. Wintermark M, Dillon WP, Smith WS, et al. **Visual grading system for vasospasm based on perfusion CT imaging: comparisons with conventional angiography and quantitative perfusion CT.** *Cerebrovasc Dis* 2008;26:163–70
23. Dankbaar JW, Rijdsdijk M, van der Schaaf IC, et al. **Relationship between vasospasm, cerebral perfusion, and delayed cerebral ischemia after aneurysmal subarachnoid hemorrhage.** *Neuroradiology* 2009;51:813–19
24. Binaghi S, Colleoni ML, Maeder P, et al. **CT angiography and perfusion CT in cerebral vasospasm after subarachnoid hemorrhage.** *AJNR Am J Neuroradiol* 2007;28:750–58
25. Wintermark M, Sincic R, Sridhar D, et al. **Cerebral perfusion CT: technique and clinical applications.** *J Neuroradiol* 2008;35:253–60
26. Ko SB, Choi HA, Carpenter AM, et al. **Quantitative analysis of hemorrhage volume for predicting delayed cerebral ischemia after subarachnoid hemorrhage.** *Stroke* 2011;42:669–74
27. Frontera JA, Claassen J, Schmidt JM, et al. **Prediction of symptomatic vasospasm after subarachnoid hemorrhage: the modified Fisher scale.** *Neurosurgery* 2006;59:21–27
28. Warnock NG, Gandhi MR, Bergvall U, et al. **Complications of intraarterial digital subtraction angiography in patients investigated for cerebral vascular disease.** *Br J Radiol* 1993;66:855–58
29. Ferguson S, Macdonald RL. **Predictors of cerebral infarction in patients with aneurysmal subarachnoid hemorrhage.** *Neurosurgery* 2007;60:658–67

Long Insular Artery Infarction: Characteristics of a Previously Unrecognized Entity

A. Tamura, T. Kasai, K. Akazawa, Y. Nagakane, T. Yoshida, Y. Fujiwara, N. Kuriyama, K. Yamada, T. Mizuno, and M. Nakagawa

ABSTRACT

BACKGROUND AND PURPOSE: The infarctions arising in the long insular arteries of the M2 segment have been poorly described in the past. The purpose of this study was to investigate the incidence, clinical characteristics, and pathogenesis of long insular artery infarcts.

MATERIALS AND METHODS: Patients with acute isolated infarcts in territories of the long insular arteries and lenticulostriate arteries were retrospectively reviewed. The long insular artery territory was defined as the area above the lenticulostriate artery territory at the level of centrum semiovale. On the coronal section, it lies between the tip of the anterior horn and the top of the superior limb of the insular cleft. Clinical features and prevalence of embolic sources were compared between the 2 groups.

RESULTS: Of 356 consecutive patients with acute ischemic stroke, 8 (2.2%) had a long insular artery infarct (long insular artery group) and 50 (14.0%) had a lenticulostriate artery infarct (lenticulostriate artery group). There were no differences in age, sex, prevalence of risk factors, neurologic deficit, or incidence of lacunar syndromes between these groups. Abrupt onset was more common in the long insular artery than in the lenticulostriate artery group ($P = .004$). The prevalence of embolic high-risk sources (eg, atrial fibrillation) was not significantly different between these groups, but the combined prevalence of all embolic sources, including moderate-risk sources, was significantly higher in the long insular artery group ($P = .048$).

CONCLUSIONS: Isolated infarction caused by long insular artery occlusion is not rare. Abrupt onset is more common for long insular artery infarction, and this finding could be attributed to the higher incidence of an embolic etiology as the pathogenesis of infarction.

ABBREVIATIONS: LIA = long insular artery; LSA = lenticulostriate artery; TEE = transesophageal echocardiography; WMMA = white matter medullary artery

Periventricular white matter has 2 major vascular territories supplied by the deep and superficial penetrating arteries.¹⁻⁸ Among the deep penetrating arteries, the lenticulostriate arteries (LSAs) arise from the M1 segment of the MCA and supply the lower part of the corona radiata.⁷⁻¹⁰ The superficial penetrating arteries, namely the white matter medullary arteries (WMMAs), arise from the cortical branches of the MCA and feed the periventricular deep white matter.¹⁻⁶ Several reports suggest that WMMA infarction should be distinguished from LSA infarction and

treated differently because of their different clinical and etiologic backgrounds.⁴⁻⁶

The long insular artery (LIA) is a unique supplier of the periventricular white matter. It is one of the medullary arteries in close vicinity to the territory of deep perforators. The LIA infarction has been recognized mainly by neurosurgeons because interruption of this artery during the resection of opercular glioma often results in postoperative hemiparesis and characteristic corona radiata infarction.⁹⁻¹² This entity has, however, attracted much less attention from physicians in other fields.

The LIA arises from the insular segment of MCA and has, therefore, been anatomically recognized as a subtype of the WMMA. The LIA has characteristics that are anatomically intermediate between the LSA and the WMMA, in that it supplies the insular cortex, extreme capsule, claustrum, and external capsule and quite often extends to the corona radiata (Fig. 1A).

Clinically, isolated LIA infarction is due to a single or a few occluded LIAs with no involvement of the main trunk of the in-

Received January 23, 2013; accepted after revision June 10.

From the Departments of Neurology (A.T., T.K., Y.N., T.Y., Y.F., N.K., T.M., M.N.) and Radiology (K.A., K.Y.), Kyoto Prefectural University of Medicine, Kyoto, Japan.

This work was supported by a grant from The Japan Heart Foundation/Bayer Yakuhin Research Grant Abroad (T.K.).

Please address correspondence to Takashi Kasai, MD, Department of Neurology, Kyoto Prefectural University of Medicine, 465 Kajii-cho, Kamigyo-ku, Kyoto 602-8566, Japan; e-mail: kasaita@koto.kpu-m.ac.jp

<http://dx.doi.org/10.3174/ajnr.A3704>

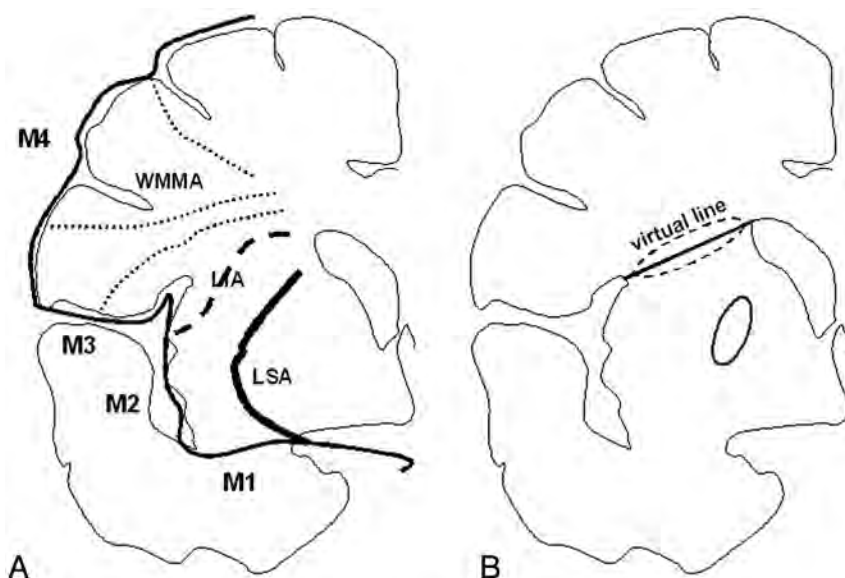


FIG 1. Vascular territories of subcortical white matter and the basal ganglia on coronal images are schematically shown (figure based on a microangiogram of a postmortem brain section of Kumabe et al¹¹). These areas are supplied with 3 individual arteries branching from the MCA, the LSA (bold line) from the M1 segment, the LIA (dashed line) from the M2 segment, and the WMMA (dotted lines) from the M3 or M4 segment (A). To standardize radiologic interpretation, interpreters drew the virtual line from the tip of the anterior horn to the top of the superior limb of the insular cleft (the A-I line), which almost corresponds to the vascular territory of the LIA. Then, subcortical infarctions involving the A-I line (dashed line circle) were categorized into the LIA group, and those situated under the A-I line (solid line circle) were classified as the LSA group (B).

sular artery. Hereafter, isolated LIA infarction is referred to as LIA infarction. The clinical features of LIA infarction have only rarely been reported¹¹ because the sizes and shapes of LIA and LSA infarct lesions are similar and thus difficult to discriminate by using only transaxial MR imaging (Fig 2). These findings suggest that LIA infarcts are most likely frequently categorized as LSA infarcts. However, the LIA is a subtype of the WMMA; therefore, characteristics of LIA infarcts remain poorly investigated. To address these issues, we conducted a retrospective chart review to compare the occurrence, clinical features, and pathogenesis of LIA infarctions with the more commonly encountered LSA infarctions.

MATERIALS AND METHODS

Definition of Vascular Territories

According to the figure of the coronal microangiogram of a postmortem brain obtained by Kumabe et al,¹¹ the subcortical white matter and basal ganglia on coronal images was divided into the 3 individual vascular territories: the WMMA territory, the LIA territory, and the LSA territory, as shown in Fig 1A. The fact that stroke associated with sacrificed insular perforators during resection of an opercular glioma was located from the top of the insular cortex to the periventricular corona radiata is in accordance with this anatomic vascular distribution.¹¹ In this study, to standardize radiologic interpretation, we drew a virtual line from the tip of the anterior horn to the top of the superior limb of the insular cleft in reference to the microangiogram of the LIA¹¹ (referred to as the A-I line), because this corresponds closely to the previously reported vascular territory of the LIA (Fig 1B).^{9,10} Radiologic classifications were independently made by 1 neurologist with 10

years of experience under the supervision of a neuroradiologist with >20 years of experience, and by 1 neuroradiologist with 13 years of experience. When these investigators reached different decisions, the judgment from the neurologist supervised by the neuroradiologist was adopted. They were instructed to classify those infarctions involving the A-I line into the LIA group and to classify those situated under the A-I line and extending vertically (craniocaudal) as the LSA group. (Infarctions presenting over the A-I line were not included in this report.)

Patient Selection

With institutional ethics committee approval, clinical records of all patients with ischemic stroke who presented at our hospital between April 2003 and August 2010 and underwent MR imaging, including DWI and MRA, within 7 days of symptom onset were retrospectively reviewed. Patients with an isolated infarct in the LIA or LSA territories were included in this study. On the basis of the geographic distribution of a hyperintense area on coronal reconstructed images from DWI, patients were classified into the LIA group or LSA group, as described above (Figs 1 and 2). Patients with multiple infarcts or a large subcortical infarct (>15 mm) were excluded.

Patients with multiple infarcts or a large subcortical infarct (>15 mm) were excluded.

Clinical and Demographic Data

The following clinical data were obtained on each patient: 1) age; 2) sex; 3) vascular risk factors including hypertension, diabetes mellitus, hyperlipidemia, and smoking; 4) blood pressure value on admission; 5) NIHSS score on admission; 6) classic lacunar syndrome, which consisted of pure motor stroke, pure sensory stroke, sensorimotor stroke, ataxic hemiparesis, and dysarthria-clumsy hand syndrome; 7) mode of neurologic symptom onset, being either abrupt, gradual, or on awakening; 8) frequency of poor outcome, defined as a modified Rankin Scale ≥ 3 at 3 months after onset; and 9) embolic sources.

We also identified the following vascular risk factors: hypertension, defined as prior diagnosis or blood pressure >140/90 mm Hg persisting for >2 weeks after admission; diabetes mellitus, defined as prior diagnosis or fasting serum blood glucose >126 mg/dL or hemoglobin A1c >6.5%; hyperlipidemia, defined as prior diagnosis or fasting, serum low-attenuation lipoprotein cholesterol >140 mg/dL or fasting serum total cholesterol >220 mg/dL; and smoking, defined as regular daily cigarette use within the past 2 years.

Mode of neurologic symptom onset was defined in the following manner: abrupt, an abruptly started single episode reaching maximum severity within 30 minutes after onset; gradual, an episode reaching maximum severity >30 minutes

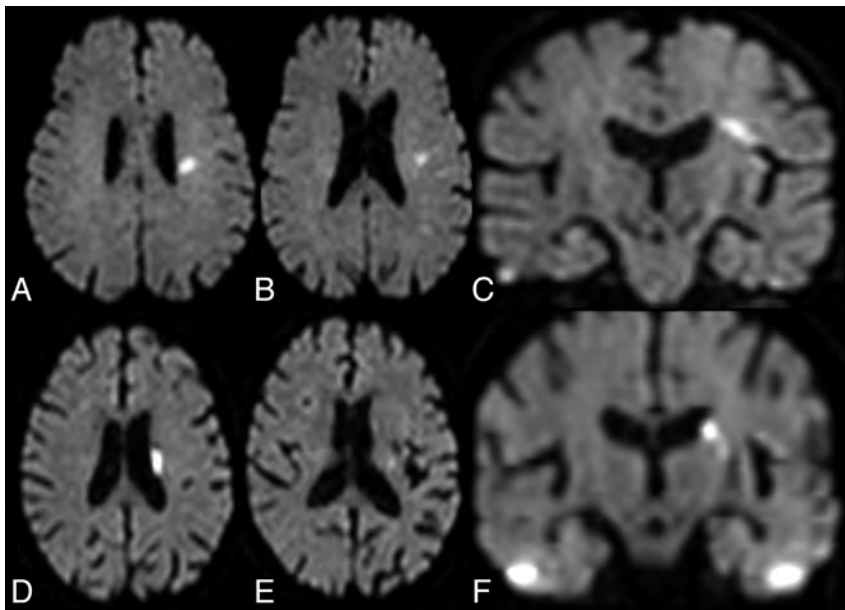


FIG 2. Axial and coronal reconstructed images from diffusion-weighted MR imaging in patients with an LIA infarct (A–C) and an LSA infarct (D–F) are shown. In each axial image, a small infarct of similar size can be observed. No apparent difference could be found between them. A, B and D, E: However, the coronal reconstructed images demonstrate that the former (C) is horizontally located from periventricular white matter to the top of the insular cortex or extreme capsule, while the latter (F) extends vertically (longitudinally) from the periventricular white matter to the putamen.

after onset with gradually progressing or fluctuating symptoms; and on awakening, an episode with stroke symptoms noticed on awakening.

In this study, embolic sources included both cardiac and aortic sources. On the basis of a previously described definition, cardiac sources of embolism were further divided into groups associated with embolic high-risk sources and embolic moderate-risk sources.¹³ Atrial fibrillation, left ventricular aneurysm or thrombus, left atrial thrombus, recent transmural anterior myocardial infarction, rheumatic valvular disease, mechanical prosthetic valve, endocarditis, and primary intracardiac tumors were regarded as embolic high-risk sources. Embolic moderate-risk sources consisted of mitral annular calcification, mitral valve prolapse, cardiomyopathy, segmental wall-motion abnormality, patent foramen ovale, atrial flutter, sick sinus syndrome, valve strands, and left atrial spontaneous echo contrast. Aortic sources of embolism included ipsilateral occlusive arterial disease and aortic atheroma. Criteria for occlusive arterial disease were the presence of stenosis $\geq 50\%$ by the NASCET criteria¹⁴ or occlusion in the ipsilateral extracranial carotid artery and stenosis $\geq 50\%$ or occlusion in the ipsilateral intracranial carotid artery by measurement with MRA. Aortic atheroma was defined as an aortic plaque with thickness of ≥ 4 mm, mobile elements, or ulceration on transesophageal echocardiography (TEE). All patients underwent 12-lead electrocardiography, 24-hour electrocardiography monitoring, color-flow duplex carotid sonography, and transthoracic echocardiography to detect an embolic source. TEE was suggested to patients showing abrupt onset with no embolic source and was performed after informed consent was obtained.

MR Imaging

MR imaging was performed on a 1.5T MR imaging unit (Intera Achieva Pulsar scanner; Philips Healthcare, Best, the Netherlands) with echo-planar capabilities. An acquisition time of approximately 4 minutes was used for DWI. Images were acquired by using a single-shot echo-planar imaging technique with the following parameters: 6000/88 ms (TR/TE), with a motion-probing gradient in 15 orientations; b-value = 1000 s/mm²; and averaging 2 times. A parallel imaging technique was used to record data with a 128 × 128 spatial resolution for a 230 × 230 mm FOV. A total of 41 sections were obtained, with a section thickness of 3 mm and no intersection gap. Coronal DWI was reconstructed from DWI data by using the multiplanar reconstruction of the PACS.

Analyses

Statistical analysis was undertaken by using a commercially available software package (Statistical Package for the Social Sciences for Windows, Version 11; IBM,

Armonk, New York). The degree of interrater agreement was determined by calculation of the κ statistic. Baseline characteristics were compared with a χ^2 test (for proportions), a *t* test (for means), or a Mann-Whitney test (for medians), between the 2 groups. Differences with a *P* value < .05 were considered statistically significant.

RESULTS

Among 356 consecutive patients with acute ischemic stroke, there were 8 (2.2%) patients with an LIA infarct (LIA group) and 50 (14.0%) with an LSA infarct (LSA group). The strength of interrater agreement for the classification was very good ($\kappa = 0.923$; 95% CI, 0.847–1.000). Axial and coronal reconstructed DWI from all cases of the LIA group are shown in Fig 3. Clinical and demographic features of the LIA and LSA groups are shown in the Table. Four patients in the LIA group and 4 patients in LSA group underwent TEE. No significant differences were seen between the 2 groups in sex, age, vascular risk factors, and blood pressure on admission.

All patients with an LIA infarct and most patients with an LSA infarct (86%, 43/50) had classic lacunar syndromes. Seven patients exhibiting nonlacunar symptoms in the LSA group included 3 patients with major hemispheric symptoms, 3 with pure dysarthria, and 1 with monoparesis.

The LIA group included 3 pure motor strokes (37.5%) and 1 pure sensory stroke (12.5%). The remaining 4 patients (50%) exhibited ataxic hemiparesis or its variant, dysarthria–clumsy hand syndrome. The median NIHSS score in the LIA group on admission was 1.5, showing no significant difference from that in the LSA group. Modified Rankin Scale scores at 3 months

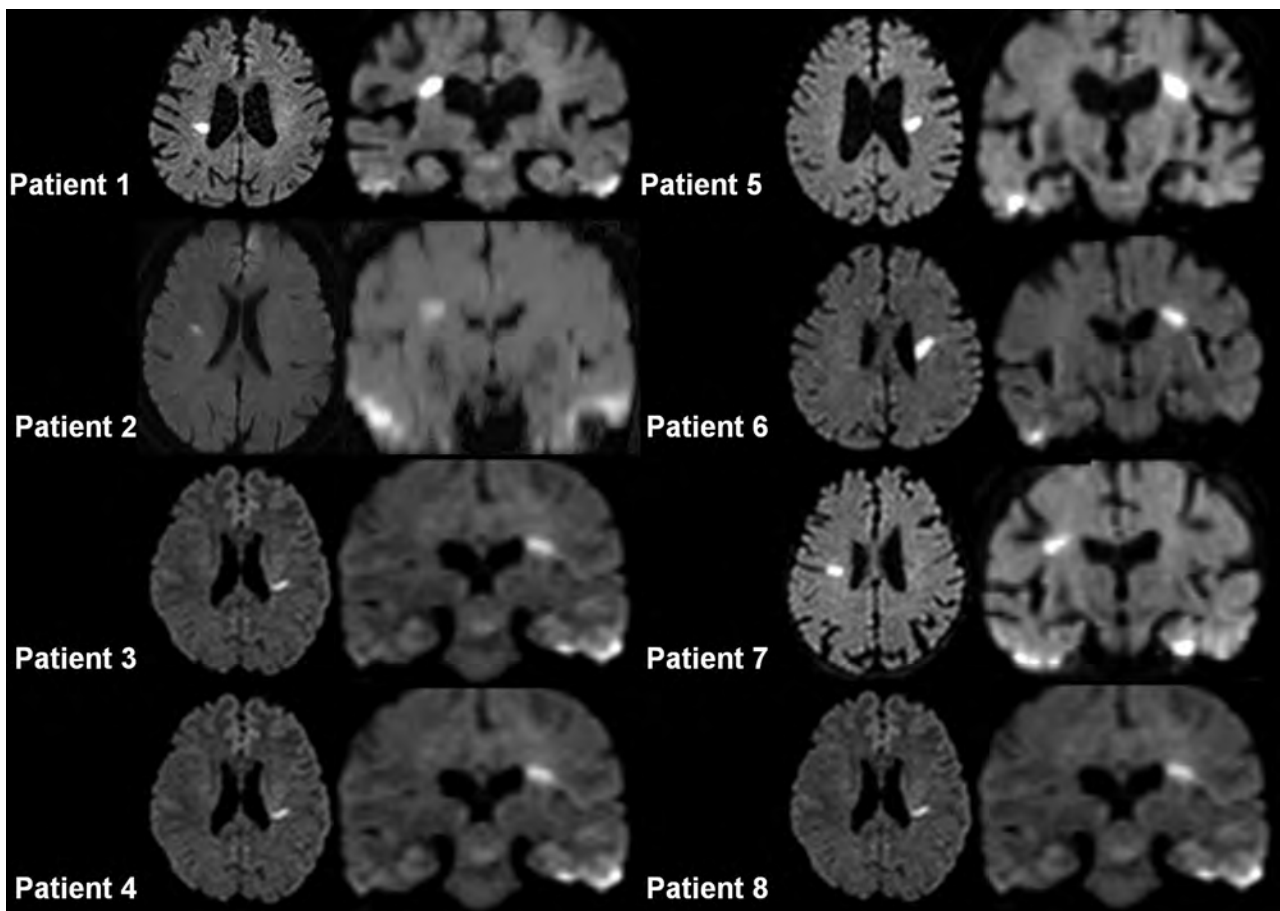


FIG 3. Axial and coronal reconstructed images from DWI of each patient with a long insular artery infarct. Coronal reconstructed images show that infarcts are horizontally located from the anterior horn to the top of the insular cortex and involve the A-I line.

after onset ranged from 0 to 2. No significant difference in the frequency of poor outcome (%) was observed between groups.

Regarding the onset of neurologic symptoms, abrupt onset was significantly more frequent in the LIA than in the LSA group (63% versus 12%, respectively; $P = .004$), while gradual onset was more frequent in the LSA than in the LIA group (25% versus 78%, respectively; $P = .006$).

The prevalence of embolic high-risk sources was not different between the 2 groups (1 patient with atrial fibrillation in the LIA group [13%] compared with 4 patients with atrial fibrillation in the LSA group [8%]). On the other hand, embolic moderate-risk sources were significantly higher in the LIA than in the LSA group (2 patients with patent foramen ovale in the LIA group [25%] compared with 0% in the LSA group; $P = .01$); thus, the combined prevalence of embolic high-risk sources and moderate-risk sources was significantly higher in the LIA than in the LSA group (37.5% versus 8.0%, respectively; $P = .048$). Neither ipsilateral occlusive arterial disease nor aortic atheroma was observed in either group.

DISCUSSION

This study, which is the first to clarify the clinical characteristics of LIA infarction, resulted in 3 major findings.

First, it clarified the incidence of LIA infarction at an unexpectedly high rate of 2.2% of all strokes. One of the reasons that

LIA infarction has been less recognized as a type of subcortical stroke in previous studies is probably due to the difficulty of its detection. Türe et al¹⁰ reported that the diameters of the LIA and LSA were so similar that size-based discrimination between these vessels was difficult. However, they also reported that there was no communication observed between them. These observations suggest that these 2 entities can be distinguished on the basis of their geographic distribution (especially on coronal images, in which both the LIA and the LSA run parallel to the imaging section). In fact, the present discrimination criteria based on coronal DWI had quite a high level of interrater agreement, suggesting that coronal DWI can be the key to identifying LIA infarcts.

Second, this study showed that all patients with an LIA infarct demonstrated classic lacunar syndromes, similar to those with LSA infarcts. In a previous study investigating the clinical differences between WMMA and LSA infarction, the incidence of non-lacunar syndromes was significantly higher in WMMA infarcts (observed in approximately half) than in LSA infarcts.⁶ Most interesting, clinical symptoms of LIA infarction resemble those of the LSA infarction rather than WMMA infarction, though the LIAs are anatomically recognized as a subtype of the WMMA. This feature also suggests that LIA infarcts cannot be distinguished from LSA infarcts by clinical symptoms alone. The clinical difference between WMMA and LIA/LSA infarcts was

Demographic and clinical features of patients with long insular artery infarction (LIA group) and lenticulostriate artery infarction (LSA group)

	LIA Group (n = 8)	LSA Group (n = 50)	P Value
Sex (male/female)	5:3	35:15	.11
Age (yr) (mean)	67.1 ± 14.4	68.40 ± 12.9	.80
Vascular risk factors			
Hypertension (%)	6 (75.0)	38 (76.0)	.00
Hyperlipidemia (%)	1 (12.5)	19 (38.0)	.24
Diabetes mellitus (%)	3 (37.5)	12 (24.0)	.44
Smoking (%)	2 (25.0)	23 (46.0)	.45
Systolic BP (mean)	168.9 ± 29.6	164.4 ± 28.8	.69
Diastolic BP (mean)	93.1 ± 17.5	91.9 ± 16.1	.84
NIHSS score			
Median	1.5	2	.13
Minimum	0	0	
Maximum	4	15	
Lacunar syndrome (%)	8 (100)	43 (86.0)	.58
Pure motor	3	28	
Pure sensory	1	0	
Sensorimotor	0	8	
Ataxic hemiparesis	1	5	
Dysarthria–clumsy hand syndrome	3	2	
Non-lacunar syndrome (%) onset			
Abrupt (%)	5 (62.5)	6 (12.0)	.58
Gradual (%)	2 (25.0)	39 (78.0)	.006
On awakening (%)	1 (12.5)	5 (10.0)	1.00
Poor outcome (%)	0	13 (26.0)	.18
Combined embolic source (%)			
Embolic high-risk source (%)	3 (37.5)	4 (8.0)	.048
Embolic moderate-risk source (%)	1 (12.5)	4 (8.0)	.54
Embolic low-risk source (%)	2 (25.0)	0 (0)	.01

Note:—BP indicates blood pressure.

probably caused by different attenuations of the subcortical pyramidal tract fibers, which are denser in the middle and lower part supplied by the LIA or LSA rather than in the upper part supplied by the WMMA.

Finally, the present study showed that 5 of 8 patients with LIA infarcts (63%) experienced an abrupt onset of symptoms, which was less commonly observed in the LSA group. This finding implies that an embolic etiology is more common in the pathogenesis of LIA infarcts than in LSA infarcts. Although the prevalence of high-risk embolic sources was not significantly different between the 2 groups, the fact that the combined prevalence of embolic high-risk sources and moderate-risk sources was higher in the LIA (38%) than in the LSA group (8%) might provide supportive evidence for this speculation. Most important, an embolic mechanism has also been suggested for WMMA infarction.³⁻⁶ Because LIAs are a subtype of WMMA, the pathogenesis of the LIA infarction could be similar to that of the WMMA infarction. The size or shape of LIA and LSA infarcts corresponds with so-called lacunar infarction, for which stroke physicians often place a low priority for the evaluation of embolic sources and frequently recommend antiplatelet agents, because this pathology has been regarded as a small-vessel disease. Our results imply that LIA infarction represents a subgroup requiring attention in terms of embolism and might warrant proper secondary preventive measures, including administration of anticoagulants like warfarin.

This study was limited in the identification of embolic sources because TEE was not performed in all patients. Because it is not common to recommend that patients with lacunar syndrome

undergo TEE, selection bias might be present. More than half of the LIA group and <10% of the LSA group underwent TEE. This discrepancy is partially due to the lower frequency of abrupt onset in LSA infarctions and implies that the incidence of embolic sources in LSA infarction might be underestimated. On the other hand, no embolic sources were detected in 4 TEE results from the LSA group, even though all showed abrupt onset. Such an ambiguity should be clarified in a further prospective study with a detailed protocol of echocardiographic evaluation.

CONCLUSIONS

LIA infarction was found to be more common than previously thought and possess clinical characteristics similar to those of LSA infarction. Furthermore, embolic phenomena might be a more common etiologic factor in LIA than in LSA infarctions. Data collection with a section thickness of 3 mm and no intersection gap¹⁵ enabling coronal reconstruction can be the key to identifying LIA infarcts, to draw the attention of clinicians to the possibility

of embolism. Prospective large-scale studies are needed to make clear the etiologic characteristics of LIA infarcts.

Disclosures: Takashi Kasai—RELATED: Grant: The Japan Heart Foundation/Bayer Yakuhin Research Grant Abroad. Kei Yamada—UNRELATED: Consultancy: Lundbeck Japan, Grants/Grants Pending: JSPS Kakenhi.* Payment for Lectures (including service on Speakers Bureaus): Daiichi-Sankyo, Bayer, Eisai, Kyorin, Mitsubishi-Tanabe Pharma, Nippon Medi-physics, Philips Healthcare, Siemens, Sanofi, Aventis, Terumo, Travel/Accommodations/Meeting Expenses Unrelated to Activities Listed: Daiichi-Sankyo, Bayer, Eisai, Kyorin, Mitsubishi Tanabe Pharma, Nippon Medi-physics, Philips Healthcare, Siemens, Sanofi-Aventis, Terumo. *Money paid to the institution.

REFERENCES

1. Read SJ, Pettigrew L, Schimmel L, et al. **White matter medullary infarcts: acute subcortical infarction in the centrum ovale.** *Cerebrovasc Dis* 1998;8:289–95
2. Bogousslavsky J, Regli F. **Centrum ovale infarcts: subcortical infarction in the superficial territory of the middle cerebral artery.** *Neurology* 1992;42:1992–98
3. Lammie GA, Wardlaw JM. **Small centrum ovale infarcts: a pathological study.** *Cerebrovasc Dis* 1999;9:82–90
4. Lee PH, Bang OY, Oh SH, et al. **Subcortical white matter infarcts: comparison of superficial perforating artery and internal border-zone infarcts using diffusion-weighted magnetic resonance imaging.** *Stroke* 2003;34:2630–35
5. Lee PH, Oh SH, Bang OY, et al. **Pathogenesis of deep white matter medullary infarcts: a diffusion weighted magnetic resonance imaging study.** *J Neurol Neurosurg Psychiatry* 2005;76:1659–63
6. Yonemura K, Kimura K, Minematsu K, et al. **Small centrum ovale infarcts on diffusion-weighted magnetic resonance imaging.** *Stroke* 2002;33:1541–44
7. Marinkovic S, Gibo H, Milisavljevic M, et al. **Anatomic and clinical correlations of the lenticulostriate arteries.** *Clin Anat* 2001;14: 190–95

8. Marinkovic SV, Milisavljevic MM, Kovacevic MS, et al. **Perforating branches of the middle cerebral artery: microanatomy and clinical significance of their intracerebral segments.** *Stroke* 1985;16:1022–29
9. Lang FF, Olansen NE, DeMonte F, et al. **Surgical resection of intrinsic insular tumors: complication avoidance.** *J Neurosurg* 2001;95:638–50
10. Türe U, Yasargil MG, Al-Mefty O, et al. **Arteries of the insula.** *J Neurosurg* 2000;92:676–87
11. Kumabe T, Higano S, Takahashi S, et al. **Ischemic complications associated with resection of opercular glioma.** *J Neurosurg* 2007;106:263–69
12. Tanriover N, Rhoton AL Jr, Kawashima M, et al. **Microsurgical anatomy of the insula and the sylvian fissure.** *J Neurosurg* 2004;100:891–922
13. Furie K. **Cardioembolism.** In: Gilman S, ed. *Neurobiology of Disease.* Amsterdam, the Netherlands: Elsevier 2006:235–40
14. **Beneficial effect of carotid endarterectomy in symptomatic patients with high-grade carotid stenosis: North American Symptomatic Carotid Endarterectomy Trial Collaborators.** *N Engl J Med* 1991;325:445–53
15. Nakamura H, Yamada K, Kizu O, et al. **Effect of thin-section diffusion-weighted MR imaging on stroke diagnosis.** *AJNR Am J Neuroradiol* 2005;26:560–65

Toward Patient-Tailored Perfusion Thresholds for Prediction of Stroke Outcome

A. Eilaghi, C.D. d'Este, T.Y. Lee, R. Jakubovic, J. Brooks, R.T.-K. Liu, L. Zhang, R.H. Swartz, and R.I. Aviv



ABSTRACT

BACKGROUND AND PURPOSE: Multiple patient-specific clinical and radiologic parameters impact traditional perfusion thresholds used to classify/determine tissue outcome. We sought to determine whether modified baseline perfusion thresholds calculated by integrating baseline perfusion and clinical factors better predict tissue fate and clinical outcome.

MATERIALS AND METHODS: CTP within 4.5 hours of acute anterior circulation stroke onset and 5- to 7-day MR imaging were performed for 203 patients with stroke, divided into derivation ($n = 114$) and validation ($n = 89$) data bases. Affected regions were operationally classified as infarct and noninfarct according to baseline CTP and follow-up FLAIR imaging. Perfusion thresholds were derived for each of the infarct and noninfarct regions, without and with transformation by baseline clinical and radiologic variables by using a general linear mixed model. Performance of transformed and nontransformed perfusion thresholds for tissue fate and 90-day clinical outcome prediction was then tested in the derivation data base. Reproducibility of models was verified by using bootstrapping and validated in an independent cohort.

RESULTS: Perfusion threshold transformation by clinical and radiologic baseline parameters significantly improved tissue fate prediction for both gray matter and white matter ($P < .001$). Transformed thresholds improved the 90-day outcome prediction for CBF and time-to-maximum ($P < .001$). Transformed relative CBF and absolute time-to-maximum values demonstrated maximal GM and WM accuracies in the derivation and validation cohorts (relative CBF GM: 91%, 86%; WM: 86%, 83%; absolute time-to-maximum 88%, 79%, and 80%, 76% respectively).

CONCLUSIONS: Transformation of baseline perfusion parameters by patient-specific clinical and radiologic parameters significantly improves the accuracy of tissue fate and clinical outcome prediction.

ABBREVIATION: T_{max} = time-to-maximum

Thrombolytic therapy remains the mainstay of acute stroke therapy.¹ CTP may distinguish hypoperfused but potentially salvageable tissue from irreversibly infarcted tissue² by using single or combinations of perfusion variables.³ However, in addition to these perfusion parameters, multiple baseline clinical and radiologic parameters are also significantly associated with tissue outcome, including age,⁴ sex,⁵ time-to-scan,⁶ NIHSS score,⁴ hypoattenuation extent or ASPECTS,⁷ rtPA administration,⁴ hyperglycemia,⁸ collateral score, and clot burden score.⁹ Many studies

intuitively show that consideration of baseline clinical parameters together with imaging features in multivariable models better predicts final infarct and outcome status.^{10,11} These predictive models do not provide a practical way to integrate the multiple baseline findings with the perfusion parameter thresholds used for classifying tissue fate, leaving the clinician to balance a combination of factors before deciding on treatment. Integration of this information is crucial to assist clinicians in determining the best treatment strategies for individual patients. For example, a patient with euglycemia and good collaterals may tolerate a lower CBF reduction without infarction better than a patient with hyperglycemia without collaterals. Therefore, using a single CBF threshold will overestimate final infarction. We exploited a derivation CTP data base ($n = 114$), including 90-day clinical outcome, to calculate, on a per-patient basis, the relative impact of multiple important baseline clinical and radiologic factors on baseline perfusion parameters to define tissue outcome. We used a general linear model for each perfusion variable with region fate (infarct versus noninfarct) as the outcome. The model then cal-

Received February 14, 2013; accepted after revision May 31.

From the Robarts Research Institute (A.E., C.D.d., T.Y.L.), University of Western Ontario, London, Ontario, Canada; and Department of Medical Imaging (A.E., R.J., J.B., R.T.-K.L., R.I.A.), Odette Cancer Centre (L.Z.), and Department of Neurology (R.H.S.), Sunnybrook Health Sciences Centre, University of Toronto, Toronto, Ontario, Canada.

Please address correspondence to Richard I. Aviv, MD, Sunnybrook Health Sciences Centre, 2075 Bayview Ave, Room AG 31, Toronto, ON, M4N 3M5, Canada; e-mail: richard.aviv@sunnybrook.ca

Indicates article with supplemental on-line tables.

<http://dx.doi.org/10.3174/ajnr.A3740>

culated a transformed perfusion parameter on the basis of the relative impact of each clinical variable on the baseline perfusion parameter for the defined outcome in the derivation ($n = 114$) and validation ($n = 89$) datasets. The result was a patient-specific perfusion variable transformation that integrates the important clinical and radiologic data for each region. The purpose of this study was to determine whether these transformed patient-specific models better predict tissue fate and clinical outcome than a nontransformed model.

MATERIALS AND METHODS

Study Design and Patient Cohort

The study was approved by the local research ethics board. Patients included were consecutive tertiary stroke center emergency department admissions, assessed by a stroke neurologist, presenting within 4.5 hours of stroke symptoms, undergoing a CT stroke protocol, and demonstrating an anterior circulation vessel occlusion. Follow-up MR imaging was performed at 5–7 days. Baseline clinical data (ie, age, sex, NIHSS score, rtPA treatment, and cardiovascular risk factors) were collected by a stroke neurologist (with 4 years' experience). Informed consent was obtained from all patients or legal decision-makers. Patients were randomly divided into derivation and validation cohorts. In total, 252 eligible patients were screened. Patients from whom consent could not be obtained ($n = 13$) and those with a posterior circulation stroke ($n = 24$) and MR imaging contraindications ($n = 12$ cases) were not included. The final patient derivation and validation cohorts consisted of 114 and 89 patients, respectively.

Scan Protocol

CT stroke imaging was performed on a 64-section CT scanner (VCT; GE Healthcare, Milwaukee, Wisconsin), including the following: pre- (NCCT) and postcontrast CT head scans (120 kVp, 300 mA, 1-second rotation, 5-mm-thick sections, 5-mm space); and baseline and 24-hour CT angiography (0.7-mL/kg iodinated contrast agent up to a maximum 90 mL [iohexol, Omnipaque, 300-mg Iodine/mL; GE Healthcare, Piscataway, New Jersey], 5- to 10-second delay, 120 kVp, 270 mA, 1-second/rotation, 1.25-mm-thick sections, table speed of 20.62 mm/rotation). CTP was performed from the basal ganglia to the lateral ventricles (80 kVp, 150 mA, 8×5 mm, 1 second per rotation). Iodinated contrast agent at 0.5 mL/kg (maximum, 50 mL) was injected at 5 mL per second⁻¹ at 3–5 seconds before sequence start. Cerebral blood flow and volume, mean transit time, and time-to-maximum (Tmax) maps were calculated as previously described by using delay-corrected CTP 4 (GE Healthcare). Follow-up MR imaging was performed at 5–7 days on all patients and minimally included DWI (8125 ms/min [TR/TE]; FOV, 26 cm; image matrix, 128×128 pixels; section thickness, 5 mm with no gap) and FLAIR (8000/120/200 [TR/TE/TI]; FOV, 22 cm; matrix, 320×224 ; section thickness, 5; 1-mm gap).

Image Analysis

Baseline imaging was scored blinded to outcome and included ASPECTS,¹² clot burden score for thrombus extent, and collateral score for collateral flow.⁹ Recanalization was classified as present or absent, comparing the baseline and 24-hour CTA as previously

described.⁹ Infarct was delineated on FLAIR imaging by using Medical Image Processing, Analysis and Visualization, Version 4.4.1 (Center for Information Technology, National Institutes of Health, Bethesda, Maryland). All baseline and follow-up imaging assessments were performed by the same neuroradiologist (R.I.A.; with 7 years' experience). FLAIR imaging and baseline CTP were coregistered with NCCT, and the appropriate transformation matrices were applied to each region of interest by using SPM8 (Wellcome Department of Imaging Neuroscience, London, UK). A brain tissue probability map template (Montreal Neurological Institute) was registered to the baseline NCCT by using SPM8. GM and white matter tissue binary masks were generated by creating tissue probability maps within SPM8. Final ROIs were created by intersecting the traced regions with GM and WM masks. A mirror region was created and segmented to provide normal GM and WM regions for relative calculations. Final infarct was defined as the intersection between the MTT perfusion abnormalities and the follow-up MR imaging. Noninfarct regions comprised MTT perfusion abnormality outside the final infarct. To minimize the contribution of blood vessels, we excluded pixels with $\text{CBF} > 100 \text{ mL} \times 100 \text{ g}^{-1} \times \text{min}^{-1}$ or $\text{CBV} > 8 \text{ mL} \times 100 \text{ g}^{-1}$.¹³

Statistics

Mean and SD were calculated for age and time-to-scan; median and interquartile ranges for ASPECTS, clot burden score, collateral score, and NIHSS score; and proportions for sex, recanalization, and hyperglycemia. For each patient, mean CBF, CBV, MTT, and Tmax values were calculated from infarct and noninfarct ROIs representing nontransformed baseline parameters. To account for within-subject variability and for unbalanced repeated measures, we used a general linear mixed model,¹⁴ previously used in the context of tissue outcome prediction in human¹⁵ and animal¹⁶ stroke models. Individual patients were considered as random effects; the region, as a fixed effect; and compound symmetry, as a covariance structure. Multiple baseline clinical and radiologic covariates were examined by univariate analysis including age, sex, time-to-scan, rtPA treatment status (1 = yes; 0 = no), hyperglycemia (1 = yes; 0 = no), NIHSS score, ASPECTS, clot burden score, and collateral score. Significant (ie, $P < .05$) or important (ie, $P < .2$) baseline covariates were then used to transform mean regional (infarct and noninfarct) absolute and relative baseline perfusion parameters as follows:

Transformed regional mean perfusion parameter = *Original Mean Perfusion Parameter* + βX_{β} , where β and X_{β} are vectors of covariates and associated coefficients. ROC analysis was then performed for each of the nontransformed and transformed perfusion parameters to determine the optimal thresholds best predicting final infarct-versus-noninfarct status, similar to prior threshold-based studies. For each nontransformed (model A) and transformed (model B) threshold, the accuracy for tissue fate prediction was then derived. The accuracy was defined as $(TP + TN)/(P + N)$, where TP , TN , P , and N are true-positive, true-negative, all positive (ie, infarct) and all negative (ie, noninfarct). Performance of the nontransformed and transformed thresholds was evaluated with Akaike Information Criterion ($\text{AIC} = L_{RES} + 2K$). A lower Akaike Information Criterion indicates a better model fit,

where L_{RES} represents the restricted maximized $-2 \times \log$ likelihood ($-2L$) of the model, and k , the number of parameters in the model. The G^2 likelihood ratio statistic is the difference between $-2L$ of the fitted model (transformed threshold) and the reference model (nontransformed threshold). A 2-sided P value was obtained from the G^2 likelihood ratio χ^2 test. Effect size was calculated for the mean difference divided by the pooled SD between 2 groups of patients by using nontransformed model (model A) and transformed model (model B). To test the reproducibility of the models, we used bootstrapping with unrestricted random sampling.¹⁷ We drew 1000 bootstrap samples from the derivation dataset. For each bootstrap sample, the general linear mixed model was conducted with clinical covariates (model B). For each clinical covariate, 1000 estimates of coefficient were calculated. The mean and standard error of coefficient estimates were calculated for each clinical covariate.

Cochran-Mantel-Haenszel statistics and 1-way analysis of variance for unbalanced sample sizes were used for group comparisons. Logistic regression was used to determine whether the transformed model (model B) better predicted the clinical outcome than the nontransformed model (model A) by using a dichotomized 90-day modified Rankin score, where mRS ≤ 2

was defined as a good outcome. The entropy R^2 was used to compare model A and model B. R^2 equals $(L_O - L_M)/L_O$, where L_O and L_M represent the maximized $-2L$ of the null model and the fitted model A or model B, respectively. All calculations were performed by using SAS, Version 9.2 (SAS Institute, Cary, North Carolina).

RESULTS

No significant differences for baseline variables were seen between the derivation and validation cohorts (On-line Table 1). In derivation ($n = 114$)/validation ($n = 89$) cohorts, 74 (65%)/61 patients (69%) had >1 vessel segment occlusion with a total n of 42/25 ICA, 108/58 MCA-M1, 81/67 M2, 12/9 M3, and 9/9 M4 occlusions. All measured perfusion parameters were expectedly different between the infarct and noninfarct ($P < .001$) regions. Similarly, significantly different regional CBF and CBV thresholds existed for GM and WM ($P < .001$) but not for Tmax and MTT ($P > .326$). Therefore subsequent analysis considered GM and WM separately.

GM and WM relative CBF and absolute Tmax best discriminated infarct from noninfarct tissue designations, both in models without and with baseline covariates (Table 1). Effect size for relative CBF in GM and WM was 2.18 and 1.62, and for Tmax in GM and WM, it was 1.46 and 1.26. The remaining transformed and nontransformed cutoff thresholds for infarct and noninfarct tissue classification are presented in On-line Table 2. The Akaike Information Criterion and G^2 likelihood statistic improved significantly for both GM and WM for transformed thresholds compared with nontransformed thresholds, indicating significantly better goodness-of-fit for all perfusion parameters except for absolute CBV in WM ($P = .12$). Transformed thresholds were superior to nontransformed thresholds for prediction of infarct region from the noninfarct region in the derivation and validation cohorts (Table 2). Maximal accuracies for GM were 91% and 86% and for WM were 86% and 83% in the derivation and validation cohorts, respectively. Figure 1 shows predictions with and without transformation and compares them with the follow-up MR images for the patient.

The transformed absolute Tmax threshold and relative CBF WM represented the most robust overall discriminators of good

clinical outcome (Table 3). Results for all perfusion parameters are provided in On-line Table 3. Transformed absolute and relative thresholds for CBV were not significantly improved relative to the nontransformed threshold model for GM or WM. Bootstrapping samples showed the reproducibility of the covariate models with an average (SD) decrease in the standard error of 46% (12%) (On-line Table 4).

DISCUSSION

Transformation of baseline perfusion thresholds with patient-specific baseline clinical and radiologic parameters significantly improves goodness-of-fit and ac-

Table 1: Model performance without and with baseline clinical covariates for distinguishing infarct from noninfarct regions for the best performing perfusion parameters^a

In All Patients	Cutoff			
	Value	Accuracy	AIC	P Value
CBF-GM-Rel				
A) Without any covariate	0.64	0.88	2465.9	
B) With covariates	0.78	0.91	2401.4	<.0001 ^b
CBF-WM-Rel				
A) Without any covariate	0.80	0.85	2693.6	
B) With covariates	0.87	0.86	2593.6	<.0001 ^b
Tmax-GM-Abs				
A) Without any covariate	6.0	0.84	1377.8	
B) With covariates	4.4	0.88	1358.5	.013 ^b
Tmax-WM-Abs				
A) Without any covariate	5.9	0.79	1251.5	
B) With covariates	3.7	0.80	1232.1	.0108 ^b

Note:—Rel indicates relative to the contralateral side; Abs, absolute value; AIC, Akaike Information Criterion.

^a Remaining parameters are presented in On-line Table 2.

^b Significant.

Table 2: Performance of selected nontransformed (model A) and covariate transformed (model B) perfusion thresholds for tissue fate prediction in derivation and validation data bases

Perfusion Parameter	Derivation Data Base			Validation Data Base		
	Sens.	Spec.	Acc.	Sens.	Spec.	Acc.
CBF-GM-Rel						
A) Without any covariate	0.88	0.89	0.88	0.72	1	0.82
B) With covariates	0.89	0.93	0.91	0.78	1	0.86
CBF-WM-Rel						
A) Without any covariate	0.86	0.84	0.85	0.76	0.95	0.82
B) With covariates	0.90	0.80	0.86	0.79	0.91	0.83
Tmax-GM-Abs						
A) Without any covariate	0.80	0.92	0.84	0.70	0.93	0.78
B) With covariates	0.84	0.96	0.88	0.69	0.97	0.79
Tmax-WM-Abs						
A) Without any covariate	0.76	0.85	0.79	0.70	0.88	0.76
B) With covariates	0.80	0.80	0.80	0.64	0.94	0.76

Note:—Rel indicates relative to the contralateral side; Abs, absolute value; Sens, sensitivity; Spec, specificity; Acc, accuracy.

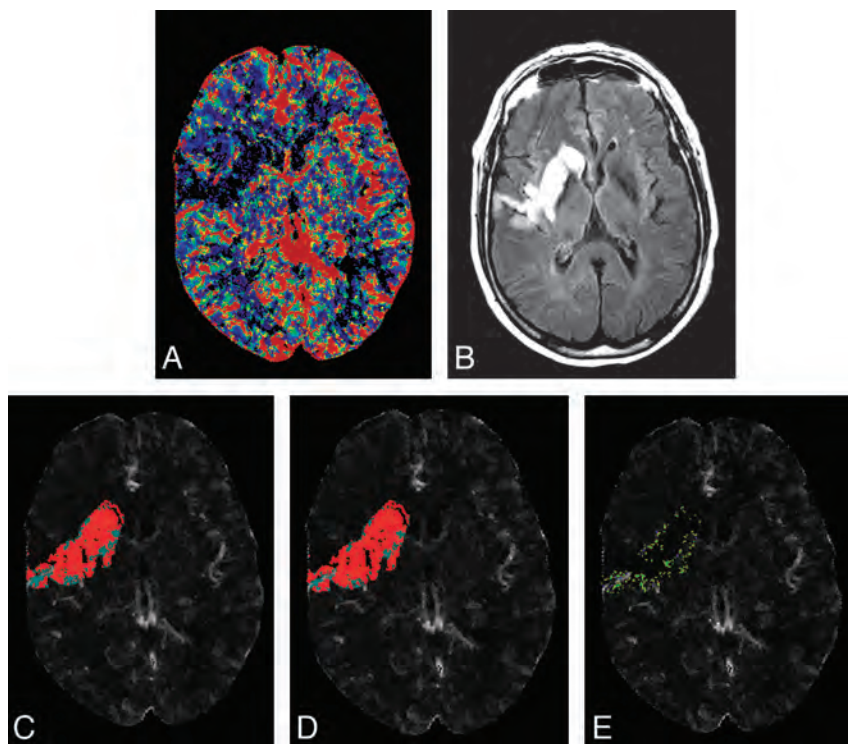


FIG 1. Admission CBF (A) and 7-day follow-up FLAIR (B) of a 74-year-old man with an ICA and M1 branch occlusion scanned 168 minutes after symptom onset and administered intravenous rtPA. The region of abnormality on follow-up FLAIR is coregistered to CBF and thresholded on the basis of without (C) and with covariate (D) thresholds from Table 1. Red voxels present predicted infarct, and cyan voxels present predicted noninfarct tissues on C and D. E, A subtraction of C and D representing voxels that were designated as infarcted tissue (green) and noninfarcted (pink, very few mainly located adjacent to blood vessels on E) only on the model with covariates.

Table 3: Selected model performance without and with clinical covariates for good clinical outcome prediction^a

In All Patients	AIC	G ²	P Value
CBF-GM-Rel			
Null model	291.5	—	
A) Without any covariate	291.7	1.796	.1803
B) With covariates	291.3	2.247	.1338
CBF-WM-Rel			
Null model	282.5	—	
A) Without any covariate	280.4	4.080	.0434
B) With covariates	268.9	15.613	<.0001 ^b
Tmax-GM-Abs			
Null model	291.5	—	
A) Without any covariate	291.3	2.255	.1332
B) With covariates	285.4	8.116	.0044 ^b
Tmax-WM-Abs			
Null model	282.5	—	
A) Without any covariate	280.9	3.643	.0563
B) With covariates	266.2	18.328	<.0001 ^b

Note:—Rel indicates relative to the contralateral side; Abs, absolute value; AIC, Akaike Information Criterion; G², the difference between $-2 \times \ln$ of the fitted model (transformed threshold) and the reference model (nontransformed threshold).

^a Remaining parameters are presented in On-line Table 3.

^b Significant.

accuracy for final infarct prediction in derivation and validation cohorts. Transformed CBF, Tmax, and MTT thresholds demonstrated improved prediction of good clinical outcome compared with a standard threshold approach. The best discriminator of infarction was transformed relative CBF followed by Tmax. A bootstrap analysis confirmed the reproducibility of covariates for

infarct and noninfarct tissue determination. Expected thresholds were demonstrated for GM compared with WM ($P < .001$) for all regions of interests.

The observations in the present study have clear and practical clinical implications. An emerging role of advanced stroke imaging is to use hemodynamic data to characterize tissue and estimate the relative proportion of “at-risk” tissue to tissue infarction. Prior studies emphasized the need for parameters that more accurately classify tissue fate. The present study used a novel approach to improving the accuracy for correct tissue characterization by integrating clinically relevant factors with baseline perfusion imaging. Our results show improved tissue characterization and clinical outcome prediction with this approach. Better tissue classification is essential to better facilitate targeted patient selection for thrombolytic therapy.

Use of a single perfusion parameter to characterize tissue is appealing, allowing quick tissue characterization. Automated patient identification as beneficial targets for reperfusion therapy based on a ratio of core-to-penumbra tissue by using Tmax is shown with the RAPID software (Stanford Stroke Centre, Palo Alto, California)

applied to MR imaging.¹⁸ However, the selection algorithm requires DWI for core identification, unavailable on CT. Single-parameter use also does not consider the multitude of other clinical factors that are present within a given patient that impact perfusion threshold techniques. Our findings show that Tmax and CBF thresholds modified by patient-specific parameters may be used to distinguish infarct from noninfarct tissue. These modified thresholds can similarly be used to generate ratios in a fashion similar to RAPID to identify patients most likely to benefit from therapy. The ideal single-perfusion parameter or parameter combination¹³ predicting tissue fate remains uncertain. Among studied parameters, CBF best predicted final infarct consistent with other studies.^{19,20} The reduced performance of CBV for infarct determination in the present study is consistent with prior studies.²⁰ This result is intuitive if we consider that CBV reduction may represent already infarcted tissue with minimal prospects for improvement irrespective of other clinical factors such as collaterals and rtPA treatment.²¹

Prognostic models incorporating both baseline clinical and radiologic parameters have previously been proposed.²² Imaging parameters, including clot burden score, the Boston Acute Stroke Imaging Scale and CBV ASPECTS;⁹ clot burden and collateral scores;⁹ baseline CT features with an admission NIHSS score;²³ and ASPECT scoring of CTP maps,²⁴ improve prediction of stroke outcome models. The current study is the first to use baseline clinical and radiologic parameters to transform baseline per-

fusion thresholds by a general linear mixed model and compare the performance solely of the transformed threshold against the conventional threshold for tissue fate and clinical outcome prediction. While clinical factors were used to transform the perfusion threshold, it was only the transformed threshold performance that was compared against the nontransformed threshold for outcome prediction. While the threshold transformations appear relatively modest, they improved not only the accuracy of tissue fate prediction but also prediction of good clinical outcome. The entropy (R^2 parameter in On-line Table 3) for transformed models, though small in value,²⁵ provided significant improvement in clinical outcome predictions in most studied perfusion parameters. These results underscore the contribution of such parameters and confirm a modest but significant modulation of traditional perfusion thresholds. Inclusion of such information is intuitive and considers patient-specific physiology. For example, patients with good baseline collateral supply are more likely to sustain tissue-at-risk even under extreme perfusion conditions compared with patients with poor collateral supply and less severe hypoperfusion.²⁶ Therefore, lower thresholds than those in patients with poor collateral supply may be needed in patients with good supply to cause infarction. The transformed thresholds make allowances for such circumstances.

The current study has limitations. The reported perfusion thresholds in this study apply to those centers using similar acquisition and postprocessing techniques.²⁰ This limitation is true of every perfusion study and does not imply nongeneralizability. Although thresholds may vary by center, it is reasonable to assume that similar transformation of baseline perfusion thresholds will be achieved by inclusion of baseline clinical and radiologic parameters. DWI is the preferred technique for acute infarct detection but becomes less sensitive within the subacute period²⁷ compared with FLAIR sensitivity, which progressively increases. No significant DWI and FLAIR mean lesion volume differences were reported beyond 12 hours.²⁷ Strong correlation between final infarct and 5-day FLAIR volume was reported with a tendency toward slight overestimation.²⁸ Use of a 5- to 7-day FLAIR for final infarct determination is a pragmatic measure for clinical stroke research and is also consistent with the methodology of several prior publications¹³; most recently Diffusion and Perfusion Imaging Evaluation for Understanding Stroke Evolution II (DEFUSE II).²⁹

Recanalization³⁰ and reperfusion³¹ statuses, though among the strongest surrogates for clinical outcome, are not available at stroke presentation and are not included in the covariate model. This approach is similar to that in the DEFUSE selection model, whereby the intent is to create a baseline model for optimal patient selection through accurate tissue classification. Recanalization and reperfusion are, however, strongly associated with several important baseline parameters included in the model. For example, IV rtPA treatment, highly correlated with recanalization, is included, thereby considering the intent of the neurologist to administer thrombolytic therapy at baseline. Similarly clot burden score, age, and collateral score are available at baseline and strongly correlate with recanalization.⁹ Further variations of a model including recanalization, reperfusion index,³¹ and NIHSS score change could be developed that may be applied at later time

points. While these models may also improve tissue fate and clinical outcome prediction, they will not have the clinical utility of a baseline tool as presented. The improved prediction for tissue fate and clinical outcome was achieved by transformed thresholds solely on the basis of baseline parameters, in the absence of recanalization status, and adds validity to the proposed model as a tool to guide baseline decision-making at a time when the recanalization status is not yet known.

CONCLUSIONS

In summary, transformation of baseline perfusion thresholds with clinical and radiologic parameters improves the accuracy of tissue fate and clinical outcome prediction over existing threshold methods. Modified thresholds may facilitate more accurate and patient-specific outcome prediction. Greater accuracy could potentially improve patient selection and individualize stroke therapy based on modified perfusion maps.

Disclosures: Ting-Yim Lee—RELATED: Grant: Heart and Stroke Foundation of Canada*; UNRELATED: Royalties: GE Healthcare.* Richard H. Swartz—UNRELATED: Grants/Grants Pending: Heart and Stroke Foundation of Canada*; Payment for Lectures (including service on Speakers Bureaus): Sanofi-Aventis, Bristol Myers Squibb, Comments: Advisory Board (Bristol Myers Squibb). Richard I. Aviv—RELATED: Grant: MITACS.* *Money paid to the institution.

REFERENCES

1. Konstas AA, Wintermark M, Lev MH. CT perfusion imaging in acute stroke. *Neuroimaging Clin N Am* 2011;21:215–38, ix
2. Kamalian S, Konstas AA, Maas MB, et al. CT perfusion mean transit time maps optimally distinguish benign oligemia from true “at-risk” ischemic penumbra, but thresholds vary by postprocessing technique. *AJNR Am J Neuroradiol* 2012;33:545–49
3. Dani KA, Thomas RG, Chappell FM, et al. Computed tomography and magnetic resonance perfusion imaging in ischemic stroke: definitions and thresholds. *Ann Neurol* 2011;70:384–401
4. Kwiatkowski TG, Libman RB, Frankel M, et al. Effects of tissue plasminogen activator for acute ischemic stroke at one year. *N Engl J Med* 1999;340:1781–87
5. De Silva DA, Ebinger M, Davis SM. Gender issues in acute stroke thrombolysis. *J Clin Neurosci* 2009;16:501–04
6. Adams HP Jr, Adams RJ, Brott T, et al. Guidelines for the early management of patients with ischemic stroke: a scientific statement from the Stroke Council of the American Stroke Association. *Stroke* 2003;34:1056–83
7. Sillanpaa N, Saarinen JT, Rusanen H, et al. The clot burden score, the Boston Acute Stroke Imaging Scale, the cerebral blood volume ASPECTS, and two novel imaging parameters in the prediction of clinical outcome of ischemic stroke patients receiving intravenous thrombolytic therapy. *Neuroradiology* 2012;54:663–72
8. Bruno A, Biller J, Adams HP Jr, et al. Acute blood glucose level and outcome from ischemic stroke. *Neurology* 1999;52:280–84
9. Tan IY, Demchuk AM, Hopyan J, et al. CT angiography clot burden score and collateral score: correlation with clinical and radiologic outcomes in acute middle cerebral artery infarct. *AJNR Am J Neuroradiol* 2009;30:525–31
10. Saposnik G, Fang J, Kapral MK, et al. The iScore predicts effectiveness of thrombolytic therapy for acute ischemic stroke. *Stroke* 2012;43:1315–22
11. Fargen KM, Chaudry I, Turner RD, et al. A novel clinical and imaging based score for predicting outcome prior to endovascular treatment of acute ischemic stroke. *J Neurointerv Surg* 2013;5(suppl 1):i38–i43
12. Barber PA, Demchuk AM, Zhang J, et al. Validity and reliability of a quantitative computed tomography score in predicting outcome of hyperacute stroke before thrombolytic therapy: ASPECTS Study

- Group—Alberta Stroke Programme Early CT Score. *Lancet* 2000;355:1670–74
13. Murphy BD, Fox AJ, Lee DH, et al. **Identification of penumbra and infarct in acute ischemic stroke using computed tomography perfusion-derived blood flow and blood volume measurements.** *Stroke* 2006;37:1771–77
 14. Cnaan A, Laird NM, Slasor P. **Using the general linear mixed model to analyse unbalanced repeated measures and longitudinal data.** *Stat Med* 1997;16:2349–80
 15. Wu O, Koroshetz WJ, Ostergaard L, et al. **Predicting tissue outcome in acute human cerebral ischemia using combined diffusion- and perfusion-weighted MR imaging.** *Stroke* 2001;32:933–42
 16. Wu O, Sumii T, Asahi M, et al. **Infarct prediction and treatment assessment with MRI-based algorithms in experimental stroke models.** *J Cereb Blood Flow Metab* 2007;27:196–204
 17. Efron B. **Bootstrap methods: another look at the jackknife.** *Ann Stat* 1979;7:1–26
 18. Lansberg MG, Lee J, Christensen S, et al. **RAPID automated patient selection for reperfusion therapy: a pooled analysis of the Echoplanar Imaging Thrombolytic Evaluation Trial (EPITHET) and the Diffusion and Perfusion Imaging Evaluation for Understanding Stroke Evolution (DEFUSE) Study.** *Stroke* 2011;42:1608–14
 19. Campbell BC, Christensen S, Levi CR, et al. **Cerebral blood flow is the optimal CT perfusion parameter for assessing infarct core.** *Stroke* 2011;42:3435–40
 20. Kamalian S, Maas MB, Goldmacher GV, et al. **CT cerebral blood flow maps optimally correlate with admission diffusion-weighted imaging in acute stroke but thresholds vary by postprocessing platform.** *Stroke* 2011;42:1923–28
 21. Wintermark M, Flanders AE, Velthuis B, et al. **Perfusion-CT assessment of infarct core and penumbra: receiver operating characteristic curve analysis in 130 patients suspected of acute hemispheric stroke.** *Stroke* 2006;37:979–85
 22. Reid JM, Gubitz GJ, Dai D, et al. **Predicting functional outcome after stroke by modelling baseline clinical and CT variables.** *Age Ageing* 2010;39:360–66
 23. Lam WW, Leung TW, Chu WC, et al. **Hyperacute extensive middle cerebral artery territory infarcts: role of computed tomography in predicting outcome.** *J Comput Assist Tomogr* 2004;28:650–53
 24. Kloska SP, Dittrich R, Fischer T, et al. **Perfusion CT in acute stroke: prediction of vessel recanalization and clinical outcome in intravenous thrombolytic therapy.** *Eur Radiol* 2007;17:2491–98
 25. Cohen J. *Statistical Power Analysis for the Behavioral Sciences.* Hillsdale, New Jersey: Lawrence Erlbaum Associates; 1987
 26. Liebeskind DS. **Collateral circulation.** *Stroke* 2003;34:2279–84
 27. van Everdingen KJ, van der Grond J, Kappelle LJ, et al. **Diffusion-weighted magnetic resonance imaging in acute stroke.** *Stroke* 1998;29:1783–90
 28. Gaudinski MR, Henning EC, Miracle A, et al. **Establishing final infarct volume: stroke lesion evolution past 30 days is insignificant.** *Stroke* 2008;39:2765–68
 29. Diffusion Weighted Imaging Evaluation for Understanding Stroke Evolution Study-2 (DEFUSE-2). ClinicalTrials.gov. <http://clinicaltrials.gov/show/NCT01349946>. Accessed May 11, 2012
 30. Rha JH, Saver JL. **The impact of recanalization on ischemic stroke outcome: a meta-analysis.** *Stroke* 2007;38:967–73
 31. Soares BP, Tong E, Hom J, et al. **Reperfusion is a more accurate predictor of follow-up infarct volume than recanalization: a proof of concept using CT in acute ischemic stroke patients.** *Stroke* 2010;41:e34–40

Pretreatment Advanced Imaging in Patients with Stroke Treated with IV Thrombolysis: Evaluation of a Multihospital Data Base

J.S. McDonald, J. Fan, D.F. Kallmes, and H.J. Cloft



ABSTRACT

BACKGROUND AND PURPOSE: CT angiography, CT perfusion, and MR imaging have all been advocated as potentially useful in treatment planning for patients with acute ischemic stroke. We evaluated a large multihospital data base to determine how the use of advanced imaging is evolving in patients treated with intravenous thrombolysis.

MATERIALS AND METHODS: Patients with acute ischemic stroke receiving IV thrombolytic therapy from 2008 to 2011 were identified by using the Premier Perspective data base. Mortality and discharge to long-term care rates were compared following multivariate logistic regression between patients who received head CT only versus those who received CTA without CT perfusion, CT perfusion, or MR imaging.

RESULTS: Of 12,429 included patients, 7305 (59%) were in the CT group, 2359 (19%) were in the CTA group, 848 (7%) were in the CTP group, and 1917 (15%) were in the MR group. From 2008 to 2011, the percentage of patients receiving head CT only decreased from 64% to 55%, while the percentage who received cerebral CT perfusion increased from 3% to 8%. The use of CT angiography and MR imaging marginally increased (1%–2%). Outcomes were similar between CT only and advanced imaging patients, except discharge to long-term care was slightly more frequent in the CTP group (OR = 1.17 [95% CI, 0.96–1.43]; $P = .0412$) and MR group (OR = 1.14 [95% CI, 1.01–1.28]; $P = .0177$) and mortality was lower in the MR group (OR = 0.64 [95% CI, 0.52–0.79]; $P < .0001$).

CONCLUSIONS: Use of advanced imaging is increasing in patients treated with IV thrombolysis. While there were differences in outcomes among imaging groups, the clinical effect of advanced imaging remains unclear.

The potential benefit of intravenous thrombolytic therapy for acute ischemic stroke decreases rapidly with time. Because of wide variability in collateral circulation, time elapsed since onset is a crude indicator of the potential benefit of treatment in each patient. Advanced imaging might provide a means to refine selection of patients who could potentially benefit from revascularization therapy. The advanced imaging techniques that might add clinically useful information in the setting of acute ischemic stroke include CT angiography, CT perfusion, and MR imaging. CT angiography can be used to identify patients with large-artery occlusions potentially amenable to intra-arterial therapy,^{1–3} and CT angiography source images have been proposed as a means of

evaluating collateral circulation.^{4–6} CT perfusion may potentially allow discrimination between salvageable brain (“penumbra”) and brain already doomed to infarction (“ischemic core”)^{2,7–10} and thus may be useful in helping to refine selection of patients for IV thrombolysis^{11,12} or intra-arterial thrombectomy.^{13–15} MR perfusion and diffusion imaging have also been reported to be useful in screening patients for intravenous therapy.^{16–22}

While advanced imaging techniques hold promise for the evaluation of patients with acute ischemic stroke, there is variation in techniques and definitions of parameters that limit wide application and acceptance of these techniques.^{4,23–25} There is currently no consensus on a standard imaging approach for acute ischemic stroke. We studied a large data base of hospitals in the United States to assess the recent use of advanced imaging in patients with acute ischemic stroke treated with intravenous thrombolysis, including an evaluation of the use of advanced imaging, with respect to patient outcome.

MATERIALS AND METHODS

Data Source and Study Population

The Perspective data base is a voluntary, fee-supported collection of data developed by Premier Inc (Charlotte, North Carolina) to

Received June 11, 2013; accepted after revision July 3.

From the Departments of Radiology (J.S.M., D.F.K., H.J.C.), Health Sciences Research (J.F.), and Neurosurgery (D.F.K., H.J.C.), Mayo Clinic, Rochester, Minnesota.

Please address correspondence to Jennifer S. McDonald, PhD, Department of Radiology, Mayo Clinic, 200 1st St SW, Rochester, MN 55905; e-mail: mcdonald.jennifer@mayo.edu

 Indicates article with supplemental on-line table.

<http://dx.doi.org/10.3174/ajnr.A3797>

assess quality and resource use. As of 2011, the Perspective data base consisted of approximately 15% of hospitalizations nationwide and represented >600 US hospitals. Detailed information of a patient's hospitalization, including patient demographics, hospital information, diagnoses, procedures, discharge status, payer, and all billed items are recorded.

Patients who presented with acute ischemic stroke (ICD-9-CM diagnostic codes 433.x1 and 434.x1) from 2008 through 2011 were identified from the Perspective data base. Patients were included only if the stroke code was listed as the primary hospitalization diagnosis to avoid including patients with a history of stroke. Patients in this cohort who received IV thrombolysis during their hospitalization were identified by using the ICD-9 procedural code 99.10.

Relevant imaging performed during hospitalization was retrieved by using billing information. Imaging was included if it was performed before or on the day of thrombolysis. Patients were included if they underwent a noncontrast head CT during hospitalization. Advanced imaging modalities of head CT angiography, cerebral CT perfusion, head MR imaging, and head MR angiography were also retrieved.

Outcome Analysis

The outcomes examined in this study were in-hospital mortality and discharge to long-term care (discharge to a rehabilitation facility, long-term care hospital, or nursing facility). Patients were divided into the following subgroups on the basis of imaging received: noncontrast head CT only (CT group), CT with cerebral CT angiography but no CT perfusion (CTA group), CT with cerebral CT perfusion (CTP group), and CT with head MR imaging or MR angiography (MR group). Statistical analyses were performed by using JMP, Version 9, and SAS, Version 9.3 (SAS Institute, Cary, North Carolina). Differences among imaging groups and admit years were compared by using the Pearson χ^2 test and linear regression, respectively. The likelihood of mortality or discharge to long-term care was compared among imaging subgroups following multivariate logistic regression to minimize differences in clinical characteristics among groups. The generalized estimating equation was used to adjust for the possible clustering effect of hospitals in the patient population.²⁶ Models were estimated by using the SAS GENMOD procedure (<http://www.math.wpi.edu/saspdf/stat/chap29.pdf>). Two models were created, a full model that encompassed all patient and hospital characteristics as shown in On-line Table 1 and a reduced model that encompassed only significant characteristics as determined by the stepwise selection option in the SAS LOGISTIC procedure (http://support.sas.com/documentation/cdl/en/statug/63347/HTML/default/viewer.htm#logistic_toc.htm).

RESULTS

Of the 176,991 patients identified who were hospitalized from 2008 to 2011 with acute ischemic stroke listed as a primary diagnostic code, 15,470 patients (8.7%) received IV thrombolytic therapy during hospitalization. Of that group, 12,429 patients (80%) underwent a head CT during hospitalization. Within that group, 2359 patients (19%) also underwent a head CT angiography; 848 patients (6.8%), cerebral CT perfusion; and 1917 pa-

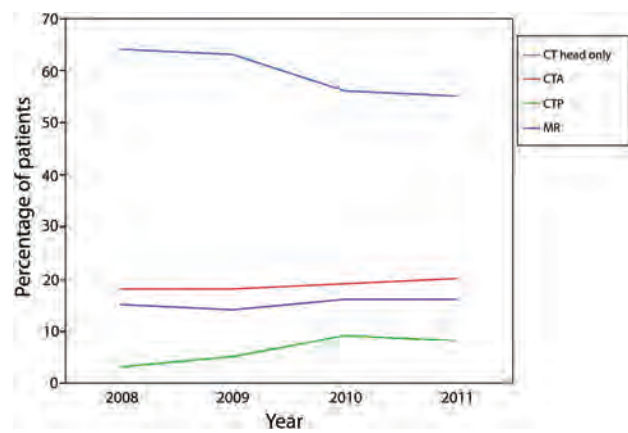


FIG 1. Trends in the use of head CT and advanced imaging in patients treated with IV thrombolysis from 2008 to 2011. Patients who received only head CT (blue line), head CT with CT angiography (red line), head CT with CT perfusion (green line), or head CT with MR imaging (purple line) are shown.

tients (15%), MR imaging. Patient and hospital characteristics of the 4 imaging subgroups are shown in On-line Table 1.

Trends in the use of head CT and advanced imaging are shown in Fig 1. From 2008 to 2011, the percentage of patients treated with thrombolysis who only underwent a noncontrast head CT decreased slightly from 64% to 55% ($P = .0570$), while the percentage of patients who underwent cerebral CT perfusion increased from 3% to 8% ($P = .11$). Use of CT angiography and MR imaging each increased slightly from 18% to 20% ($P = .0561$) and from 15% to 16% ($P = .33$), respectively, during this time.

The incidence of in-hospital mortality was lower in the MR group (6.2%) than in the CT, CTA, and CTP groups (10.2%, 12.4%, and 12.4%, respectively; $P < .0001$) (Table 1). The incidence of discharge to long-term care was slightly higher in the CTP group (47%) compared with the CT, CTA, and MR groups (43%, 41%, and 43%, respectively; $P = .0352$). Following multivariate logistic regression by using the full model, the likelihood of mortality was significantly lower in the MR group compared with the CT group (OR = 0.64 [95% CI, 0.52–0.79]; $P < .0001$) but was similar between the CTA and CT groups ($P = .99$) and between the CTP and CT groups ($P = .20$) (Table 2). The likelihood of discharge to long-term care was significantly higher in the MR group compared with the CT group (OR = 1.14 [95% CI, 1.01–1.28]; $P = .0177$), was slightly higher in the CTP group compared with the CT group (OR = 1.17 [95% CI, 0.96–1.43]; $P = .0412$), and was similar between the CT and CTA groups ($P = .31$). Similar findings were observed by using the reduced regression models.

DISCUSSION

Our analysis of a large, multihospital data base found wide variation in the use of imaging in patients with acute ischemic stroke. From 2008 to 2011, the percentage of patients treated with thrombolysis who received only a head CT decreased slightly from 64% to 55%. If this trend continues, more than half of the patients treated with thrombolysis will receive some form of advanced imaging during their hospitalization. This growth in the use of

Table 1: Outcome incidences by imaging subgroup

	CT Group	CTA Group	CTP Group	MR Group
In-hospital mortality	748/7305 (10.2%)	241/2359 (12.4%)	105/848 (12.4%)	119/1917 (6.2%)
Discharge to long-term care	3170/7305 (43%)	975/2359 (41%)	399/848 (47%)	828/1917 (43%)

Table 2: Patient outcomes following logistic regression analysis

	Odds Ratio (95% CI)	P Value
In-hospital mortality		
Full model		
CT	1.00 (reference)	—
CTA	1.00 (0.83–1.21)	.99
CTP	1.17 (0.93–1.47)	.20
MRI	0.64 (0.52–0.79)	<.0001
Reduced model		
CT	1.00 (reference)	—
CTA	1.03 (0.86–1.24)	.75
CTP	1.14 (0.92–1.40)	.22
MRI	0.65 (0.53–0.79)	<.0001
Discharge to long-term care		
Full model		
CT	1.00 (reference)	—
CTA	0.95 (0.83–1.09)	.31
CTP	1.17 (0.96–1.43)	.0412
MRI	1.14 (1.01–1.28)	.0177
Reduced model		
CT	1.00 (reference)	—
CTA	0.89 (0.66–1.18)	.59
CTP	1.33 (1.00–1.77)	.12
MRI	1.15 (0.73–1.83)	.0471

Note: — indicates no P value was calculated for the CT reference group.

advanced imaging is primarily attributable to increased use of CT perfusion but also to increased use of CT angiography and MR imaging.

Imaging has been an essential part of stroke treatment planning since the introduction of CT.²⁷ Unenhanced CT has been useful for demonstrating acute hemorrhage or other mimicking lesions, as well as showing cytotoxic edema from evolving infarction. CT is standard for trauma patients in emergency departments and has been the historical standard for patients with acute neurologic conditions, so CT is already fully integrated into emergency department culture and is readily available to patients with acute ischemic stroke. In fact, readily available head CT is a defining characteristic of a primary stroke center in the United States.²⁸ If the patient is already going to the CT scanner for the standard unenhanced imaging, it is generally not very time-consuming to add additional CT angiography and/or CT perfusion studies.² However, advanced CT, including high-quality CT perfusion and CT angiography, requires hardware and software that are not available at every hospital treating patients with stroke; this circumstance might limit adoption of these imaging techniques. As CT scanners are replaced and upgraded with time, advanced CT techniques are becoming uniformly available; this availability might account for some of the increased use demonstrated in our study. The clinical utility of such advanced CT imaging, however, is not universally accepted.

Our study showed that from 2008 to 2011, screening with MR imaging had a negligible increase from 15% to 16% of patients undergoing IV thrombolysis. These results suggest that MR imaging has not been widely adopted. MR imaging has been proposed as an effective means of identifying candidates for intrave-

nous thrombolysis in the 3- to 4.5-hour time window.¹⁶⁻²² The exact time of onset relative to the time of imaging or the time of thrombolytic administration is not available in the Perspective data base, so we cannot determine how often MR imaging was used for screening patients in the 3- to 4.5-hour time window. In addition, MR imaging is not typically as readily available as CT in an emergency setting. Safety screening for implants can slow down the process of acquiring MR imaging, especially if it is not possible to immediately obtain an accurate and complete history, which occurs reasonably often in the setting of acute ischemic stroke. Another impediment is that rapid, emergent acquisition of MR imaging is not part of the culture at many hospital emergency departments.

We found that patients who underwent MR imaging had lower in-hospital mortality rates compared with patients who underwent a head CT only or other types of advanced imaging. However, patients who received MR imaging or CT perfusion had a higher rate of being discharged to long-term care compared with the head CT group. These findings suggest that the use of advanced imaging may affect these patient outcomes; however, a causal link cannot be confirmed from our observational study. It is likely that patients treated with IV thrombolysis who underwent imaging with only unenhanced CT were clinically different from those who underwent additional imaging. Patients who underwent only CT were more likely to be admitted from the emergency department compared with patients who also underwent advanced imaging. While we performed multivariate logistic regression to minimize these differences in clinical characteristics between imaging groups, differences in unmeasured clinical variables may affect our results. For example, patients treated with IV thrombolysis who underwent additional imaging were probably more likely to have severe stroke compared with patients who only underwent CT imaging, with the additional imaging used to help determine whether mechanical embolectomy was warranted. We cannot quantify such a trend because we cannot assess stroke severity at presentation.

Our study of a national cohort of inpatients who received IV thrombolysis did not show that the use of CT angiography or CT perfusion significantly improved patient outcomes. However, these findings do not suggest that these imaging examinations are not useful in specific clinical settings, such as studies comparing IV thrombolysis with combined IV and intra-arterial treatments. In such studies, CT angiography may be useful in both identifying and characterizing pretreatment arterial occlusive lesions and in identifying post treatment recanalization effects.

This study has several additional limitations. We acknowledge that coding inaccuracies occur, which can affect a retrospective study of any administrative data base; however, it is unlikely that such inaccuracies would be more prevalent in one imaging group over another. As noted above, we cannot assess stroke severity at the time of presentation. We are unable to identify patients with similar stroke severity who did not receive intravenous thrombol-

ysis, so we do not have a control group to allow assessment of the benefit from different treatments. We cannot determine whether screening imaging was used uniformly at each center and thus was not subject to selection bias. We also are unable to assess the time of presentation, but the patients undergoing intravenous thrombolysis would typically be expected to have presented early enough for initiation of intravenous therapy within 3 hours of symptom onset. However, some patients may have been evaluated with imaging specifically for broadening of the time window to 4.5 hours, especially with MR imaging.^{16–22} Our study focused on the use of advanced imaging before or on the day of thrombolysis; the use of advanced imaging after treatment was not examined. Additional studies are needed to examine the use of advanced imaging in patients treated with IV thrombolysis and to examine the effect of this imaging on patient outcomes.

CONCLUSIONS

Significant variation occurs in imaging of patients with acute ischemic stroke treated with intravenous thrombolysis in the United States. The use of advanced imaging is increasing in these patients. While there were differences in outcome among the imaging groups, the clinical effect of advanced imaging remains unclear.

Disclosures: Jennifer S. McDonald—UNRELATED: Grants/Grants Pending: GE Healthcare,* Comments: unrelated investigator-initiated research grant. David F. Kallmes—UNRELATED: Consultancy: Codman,* ev3,* Medtronic,* Comments: planning and implementation of clinical trials, Grants/Grants Pending: Microvention,* Codman,* ev3,* Sequent,* Surmodics,* Comments: preclinical and clinical studies, Royalties: University of Virginia Patent Foundation, Comments: spine fusion. Harry J. Cloft—UNRELATED: Grants/Grants Pending: Cordis Endovascular,* Comments: site principal investigator at enrolling site for Stenting and Angioplasty with Protection in Patients and High Risk for Endarterectomy registry sponsored by Cordis Endovascular. *Money paid to the institution.

REFERENCES

- Sylaja PN, Puetz V, Dzialowski I, et al. Prognostic value of CT angiography in patients with suspected vertebrobasilar ischemia. *J Neuroimaging* 2008;18:46–49
- de Lucas EM, Sanchez E, Gutierrez A, et al. CT protocol for acute stroke: tips and tricks for general radiologists. *Radiographics* 2008;28:1673–87
- Frölich AM, Psychogios MN, Klotz E, et al. Angiographic reconstructions from whole-brain perfusion CT for the detection of large vessel occlusion in acute stroke. *Stroke* 2012;43:97–102
- Pulli B, Schaefer PW, Hakimelahi R, et al. Acute ischemic stroke: infarct core estimation on CT angiography source images depends on CT angiography protocol. *Radiology* 2012;262:593–604
- Pulli B, Yoo AJ. CT angiography source images with modern multi-section CT scanners: delay time from contrast injection to imaging determines correlation with infarct core. *AJNR Am J Neuroradiol* 2012;33:E61, author reply E62
- Brunner F, Tomandl B, Hanken K, et al. Impact of collateral circulation on early outcome and risk of hemorrhagic complications after systemic thrombolysis. *Int J Stroke* 2012 Oct 23. [Epub ahead of print]
- Campbell BC, Christensen S, Levi CR, et al. Cerebral blood flow is the optimal CT perfusion parameter for assessing infarct core. *Stroke* 2011;42:3435–40
- Kamalian S, Konstas AA, Maas MB, et al. CT perfusion mean transit time maps optimally distinguish benign oligemia from true “at-risk” ischemic penumbra, but thresholds vary by postprocessing technique. *AJNR Am J Neuroradiol* 2012;33:545–49
- Konstas AA, Goldmakher GV, Lee TY, et al. Theoretic basis and technical implementations of CT perfusion in acute ischemic stroke, Part 2. Technical implementations. *AJNR Am J Neuroradiol* 2009;30:885–92
- Konstas AA, Goldmakher GV, Lee TY, et al. Theoretic basis and technical implementations of CT perfusion in acute ischemic stroke, Part 1. Theoretic basis. *AJNR Am J Neuroradiol* 2009;30:662–68
- Sztrihai LK, Manawadu D, Jarosz J, et al. Safety and clinical outcome of thrombolysis in ischaemic stroke using a perfusion CT mismatch between 3 and 6 hours. *PLoS One* 2011;6:e25796
- Obach V, Oleaga L, Urra X, et al. Multimodal CT-assisted thrombolysis in patients with acute stroke: a cohort study. *Stroke* 2011;42:1129–31
- Hesselmann V, Niederstadt T, Dziewas R, et al. Reperfusion by combined thrombolysis and mechanical thrombectomy in acute stroke: effect of collateralization, mismatch, and time to and grade of recanalization on clinical and tissue outcome. *AJNR Am J Neuroradiol* 2012;33:336–42
- Turk A, Magarik JA, Chaudry I, et al. CT perfusion-guided patient selection for endovascular treatment of acute ischemic stroke is safe and effective. *J Neurointerv Surg* 2012;4:261–65
- Amenta PS, Ali MS, Dumont AS, et al. Computed tomography perfusion-based selection of patients for endovascular recanalization. *Neurosurg Focus* 2011;30:E6
- Albers GW, Thijs VN, Wechsler L, et al. Magnetic resonance imaging profiles predict clinical response to early reperfusion: the Diffusion and Perfusion Imaging Evaluation for Understanding Stroke Evolution (DEFUSE) study. *Ann Neurol* 2006;60:508–17
- Davis SM, Donnan GA, Parsons MW, et al. Effects of alteplase beyond 3 h after stroke in the Echoplanar Imaging Thrombolytic Evaluation Trial (EPITHET): a placebo-controlled randomised trial. *Lancet Neurol* 2008;7:299–309
- Butcher K, Parsons M, Allport L, et al. Rapid assessment of perfusion-diffusion mismatch. *Stroke* 2008;39:75–81
- Furlan AJ, Eyding D, Albers GW, et al. Dose escalation of Desmoteplase for Acute Ischemic Stroke (DEDAS): evidence of safety and efficacy 3 to 9 hours after stroke onset. *Stroke* 2006;37:1227–31
- Hacke W, Albers G, Al-Rawi Y, et al. The Desmoteplase in Acute Ischemic Stroke Trial (DIAS): a phase II MRI-based 9-hour window acute stroke thrombolysis trial with intravenous desmoteplase. *Stroke* 2005;36:66–73
- Mishra NK, Albers GW, Davis SM, et al. Mismatch-based delayed thrombolysis: a meta-analysis. *Stroke* 2010;41:e25–33
- Förster A, Gass A, Kern R, et al. MR imaging-guided intravenous thrombolysis in posterior cerebral artery stroke. *AJNR Am J Neuroradiol* 2011;32:419–21
- Dani KA, Thomas RG, Chappell FM, et al. Computed tomography and magnetic resonance perfusion imaging in ischemic stroke: definitions and thresholds. *Ann Neurol* 2011;70:384–401
- Zussman BM, Boghosian G, Gorniak RJ, et al. The relative effect of vendor variability in CT perfusion results: a method comparison study. *AJNR Am J Neuroradiol* 2011;197:468–73
- Zussman B, Jabbour P, Talekar K, et al. Sources of variability in computed tomography perfusion: implications for acute stroke management. *Neurosurg Focus* 2011;30:E8
- Zeger SL, Liang KY. Longitudinal data analysis using generalized linear models. *Biometrics* 1986;42:121–30
- Katzman R, Clasen R, Klatzo I, et al. Report of joint committee for stroke resources. IV. Brain edema in stroke. *Stroke* 1977;8:512–40
- http://www.jointcommission.org/certification/primary_stroke_centers.aspx Accessed October 31, 2013

Arterial Spin-Labeling Assessment of Normalized Vascular Intratumoral Signal Intensity as a Predictor of Histologic Grade of Astrocytic Neoplasms

J. Furtner, V. Schöpf, K. Schewzow, G. Kasprian, M. Weber, R. Woitek, U. Asenbaum, M. Preusser, C. Marosi, J.A. Hainfellner, G. Widhalm, S. Wolfsberger, and D. Prayer



ABSTRACT

BACKGROUND AND PURPOSE: Pulsed arterial spin-labeling is a noninvasive MR imaging perfusion method performed with the use of water in the arterial blood as an endogenous contrast agent. The purpose of this study was to determine the inversion time with the largest difference in normalized intratumoral signal intensity between high-grade and low-grade astrocytomas.

MATERIALS AND METHODS: Thirty-three patients with gliomas, histologically classified as low-grade ($n = 7$) or high-grade astrocytomas ($n = 26$) according to the World Health Organization brain tumor classification, were included. A 3T MR scanner was used to perform pulsed arterial spin-labeling measurements at 8 different inversion times (370 ms, 614 ms, 864 ms, 1114 ms, 1364 ms, 1614 ms, 1864 ms, and 2114 ms). Normalized intratumoral signal intensity was calculated, which was defined by the signal intensity ratio of the tumor and the contralateral normal brain tissue for all fixed inversion times. A 3-way mixed ANOVA was used to reveal potential differences in the normalized vascular intratumoral signal intensity between high-grade and low-grade astrocytomas.

RESULTS: The difference in normalized vascular intratumoral signal intensity between high-grade and low-grade astrocytomas obtained the most statistically significant results at 370 ms ($P = .003$, other P values ranged from .012–.955).

CONCLUSIONS: The inversion time by which to differentiate high-grade and low-grade astrocytomas by use of normalized vascular intratumoral signal intensity was 370 ms in our study. The normalized vascular intratumoral signal intensity values at this inversion time mainly reflect the labeled intra-arterial blood bolus and therefore could be referred to as normalized vascular intratumoral signal intensity. Our data indicate that the use of normalized vascular intratumoral signal intensity values allows differentiation between low-grade and high-grade astrocytomas and thus may serve as a new, noninvasive marker for astrocytoma grading.

ABBREVIATIONS: ASL = arterial spin-labeling; nITS = normalized intratumoral signal intensity; nVITS = normalized vascular intratumoral signal intensity; PASL = pulsed arterial spin-labeling; PICORE = proximal inversion with a control for off-resonance effects; ROC = receiver operating characteristic; WHO = World Health Organization

Gliomas are the most frequently occurring primary brain tumors in adults. More than three-quarters of all glial tumors show astrocytic features.^{1,2} Grading of astrocytic tumors is important to establish optimal therapy planning and to determine the prognosis.³ According to the World Health Organization (WHO) classification, diffuse astrocytic gliomas are divided into 3

categories, on the basis of the grade of malignancy: diffuse astrocytomas (WHO grade II); anaplastic astrocytomas (WHO grade III); and glioblastomas (WHO grade IV). This histopathologic categorization relies on histologic features, including cell attenuation, nuclear atypia, mitotic activity, necrosis, and neovascularization.⁴ Diffuse astrocytomas are considered low-grade gliomas, whereas anaplastic astrocytomas and glioblastomas are considered high-grade gliomas.

The differentiation of high-grade versus low-grade astrocytic neoplasms by use of conventional MR imaging with gadolinium-based contrast medium is still the reference standard in the routine clinical setting. However, this technique alone can sometimes be difficult because contrast media enhancement reflects the disruption of the blood-brain barrier rather than an assessment of tumor vascularity. Therefore, advanced MR techniques, such as MR perfusion, have also come to play an increasingly important role in glial brain tumor diagnosis. The reference standard for the

Received January 31, 2013; accepted after revision May 12.

From the Department of Biomedical Imaging and Image-Guided Therapy (J.F., V.S., G.K., M.W., R.W., U.A., D.P.), Department of Medicine I (M.P., C.M.), Institute of Neurology (J.A.H.), Department of Neurosurgery (G.W., S.W.), Comprehensive Cancer Center—Central Nervous System Tumors Unit (J.F., M.P., C.M., J.A.H., G.W., S.W., D.P.), Centre of Medical Physics and Biomedical Engineering (K.S.), and MR Centre of Excellence (K.S.), Medical University of Vienna, Vienna, Austria.

Please address correspondence to Julia Furtner, MD, Department of Biomedical Imaging and Image-Guided Therapy, Medical University of Vienna, Waehringer Guertel 18-20, A-1090 Vienna, Austria; e-mail: julia.furtner@meduniwien.ac.at

Indicates article with supplemental on-line table.

<http://dx.doi.org/10.3174/ajnr.A3705>

evaluation of tumor perfusion is dynamic susceptibility contrast perfusion imaging.^{5,6} This technique is able to assess, among other values, CBV and CBF simultaneously. Previous studies have shown that optimization of this technique, by use of preload dosing or baseline subtraction techniques, could maximize CBV accuracy.⁷

One of the disadvantages of the dynamic susceptibility contrast imaging technique is that it relies on the intravenous application of contrast media. This is primarily a challenge for people with allergic reactions to contrast media.

Arterial spin-labeling (ASL) is an MR imaging technique that allows for a quantitative determination of tissue blood flow values without the need for the administration of contrast agents, thus offering a noninvasive MR imaging perfusion sequence for the generation of cerebral perfusion maps. This method takes advantage of the fact that water protons of the arterial blood in the feeding vasculature of the brain are magnetically labeled and used as an endogenous tracer. After a certain inversion time, the labeled blood arrives at the image plane in which the image is acquired. Conventional ASL techniques are characterized by a moderate spatial and temporal resolution; however, the increased clinical availability of high-field MR scanners has helped to increase the SNR. ASL benefits from higher field strengths because of the increased perfusion-weighted signal caused by higher SNR and the prolonged T1-relaxation times at higher field strengths, allowing for longer inflow and imaging times.⁸ Thus, this technique can be easily included in routine diagnostic MR imaging. ASL perfusion measurements have been shown to have a high test-retest reliability.⁹ In addition, ASL data were characterized as a reliable alternative to invasive measurement techniques, such as dynamic susceptibility MR imaging perfusion¹⁰⁻¹⁴ and positron-emission tomography.¹⁵ There are also some weaknesses of this perfusion technique. First, pulsed arterial spin-labeling (PASL) sequences usually involve long acquisition times. For extended multimodal tumor MR imaging protocols, the acquisition time of each sequence should be as short as possible, in terms of patient care. Another important shortcoming for ASL perfusion is the dependency of the perfusion signal on the inversion time. Previous studies reported that tumor-brain blood flow ratios determined by arterial spin-labeling were markedly greater than those obtained with dynamic susceptibility-weighted contrast-enhanced MR imaging.¹¹ This is probably caused by the underestimation of perfusion in brain regions with long arterial transit times, for example, white matter. The use of higher inversion times would overcome these limitations; however, this would conversely lead to a decrease in the SNR caused by the rapid decay of the ASL perfusion signal over time.

Typically, an ASL measurement is conducted at a single inversion time, on the basis of the T1 decay of blood, which is approximately 1200 ms at 1.5T and 1600 ms at 3T.^{16,17} With the use of this single inversion time, recent studies have indicated that the increase in tumor perfusion correlates with the tumor grade in gliomas.^{11,18} However, the selected inversion times of those studies were related to normal rather than tumorous brain tissue.

In the present study, a multiple-inversion time PASL approach was used to track the labeled bolus dynamically over time. The purpose of this study was to determine the inversion time

with the largest differences in normalized intratumoral signal intensity between high-grade and low-grade astrocytomas, offering a totally noninvasive and fast tool for glioma grading.

MATERIALS AND METHODS

Patient Population

Thirty-three patients (14 women, 19 men; mean age = 54 years; standard deviation = 16.5 years; range = 20–84 years) with new-onset astrocytomas were consecutively included into this prospective study, from September 2009 to January 2012. The local institutional ethics review board approved the study. Written informed consent was obtained from all patients after the nature, scope, and possible consequences of the examination had been explained to them. The study was performed in accordance with the guidelines of the Declaration of Helsinki, including current revisions. All patients had a prior conventional MR imaging examination in which a glial tumor was suspected. Because of the known different perfusion pattern of oligodendrogliomas,¹⁹ all astrocytic neoplasms with histologic oligodendroglial features were excluded.

Data Acquisition

All MR imaging examinations were performed on a whole-body 3T Trio system (Siemens, Erlangen, Germany), with actively shielded imaging gradients, in conjunction with an 8-channel head coil.

Patients were scanned in the supine position, without the administration of any kind of sedative. Patients were asked to avoid any movements, especially head movements, during the whole scan time, and padding was arranged around the subject's head to minimize movements.

All patients underwent a standard conventional MR examination for tumor detection, localization, and expansion, including an axial T2-weighted turbo-inversion recovery-magnitude sequence (TE = 100 ms; TR = 9220 ms; number of sections = 36; section thickness = 4 mm; field of view = 230 × 176 mm; flip angle = 150°), a coronal T2-weighted turbo spin-echo sequence (TE = 94 ms; TR = 2750 ms; number of sections = 56; section thickness = 2 mm; field of view = 180 × 180 mm; flip angle = 120°), and an axial T1-weighted sequence (TE = 379 ms; TR = 1800 ms; number of sections = 192; section thickness = 1 mm; field of view = 220 × 200 mm; flip angle = 12°) before and after intravenous contrast media application (0.1 mmol/kg body weight of a gadolinium-based contrast agent).

In addition to the routine preoperative examination, all patients underwent scanning with pulsed quantitative imaging of perfusion with a single subtraction with thin-section TI₁ periodic saturation or Q2TIPS ASL sequences. The ASL tagging scheme was a proximal inversion with a control for off-resonance effects (PICORE) technique, a modification of the echo-planar imaging and signal targeting with alternating radiofrequency technique. With the use of PICORE, the acquisition of the tag image is identical to that in echo-planar imaging and signal targeting with alternating radio-frequency technique, but, during the acquisition of the control image, a nonselective off-resonance inversion pulse is applied, which has the same frequency offset relative to the

imaging section as in the tag image. For a detailed description of the PICORE technique, see Wong et al.²⁰

The imaging parameters used to perform the multisection PICORE technique were as follows: TE = 11 ms; TR = 2750 ms; field of view = 192 × 100 mm; number of sections = 14; section thickness = 6 mm; section gap = 1.5 mm; flip angle = 90°; number of measurement repetitions = 25. PASL images were acquired at 8 different inversion times (370 ms, 614 ms, 864 ms, 1114 ms, 1364 ms, 1614 ms, 1864 ms, and 2114 ms). For all 8 measurements, the imaging parameters were identical. No vessel suppression techniques were used to receive vascular intratumoral signals at low inversion times. One PASL sequence had an acquisition time of 1 minute, 19 seconds, which resulted in an imaging time of 10 minutes, 32 seconds, for all 8 ASL inversion times listed. The overall acquisition time for the anatomic and the ASL sequences used in this study was approximately 30 minutes. For all patients, the acquisition of ASL data was performed before the application of contrast media because of the known T1 shortening effect of gadolinium-based contrast agents, which results in a reduction of the SNR.¹⁶

The perfusion imaging section covered from the base of the skull (first section) to the vertex (last section) and was aligned parallel to the corpus callosum in the sagittal plane and to the midline structures in the axial and coronal planes.

Data Analysis

Postprocessing was performed on an off-line workstation (Leonardo Workplace, Siemens) by use of a z-transformation. Tumor ROIs (mean, 670 mm²; range, 150–2489 mm²) were manually drawn by an experienced neuroradiologist, blinded to the tumor histopathology. To approximate the whole tumor volume, multiple ROIs were drawn for each subject. Turbo inversion recovery magnitude or T1 postcontrast images were selected, which reflected the maximum spatial tumor extension, including nonenhancing and contrast-enhancing tumor components, on the basis of Response Assessment in Neuro-Oncology criteria.²¹ ROIs were drawn in such a way so as to spare areas with extended necrosis. The mean signal intensity value of each ROI on every tumor section was used to calculate the average mean signal intensity for the whole tumor (tumor ROI). These images were then assigned to co-registered PASL images for all 8 inversion times. In addition, an ROI of equal size was positioned exactly in the contralateral healthy hemisphere (in most cases containing white matter, gray matter, and vascular structures) to calculate the average mean signal intensity of the size-matched contralateral normal brain tissue (normal ROI). This normalization was applied to exclude signal from “normal” vascular and parenchymal structures. Normalized intratumoral signal intensity (nITS) was defined by the mean signal intensity value ratio of tumor ROI and normal ROI (nITS = signal intensity [tumor ROI]/signal intensity [normal ROI]) for each inversion time. The nITS value does not allow evaluation of absolute CBF values but assesses the ratio of intratumoral signal intensity to the signal intensity in the contralateral hemisphere. No multicentric or multifocal tumors were included in this study.

Visualization of selected characteristic sections of patients and corresponding times was performed in Matlab (version 7.8.347, R2009a; MathWorks, Natick, Massachusetts).

Statistical Analysis

Statistical analyses were performed by use of SPSS, version 17.0.2 software package (IBM, Armonk, New York). Testing for time-related differences (different inversion times: 370 ms, 614 ms, 864 ms, 1114 ms, 1364 ms, 1614 ms, 1864 ms, 2114 ms) for nITS for all 3 glioma categories was performed by use of a 3-way, mixed-model ANOVA, treating time and side as within-subject factors and glioma categories as between-subject factors. The within-subject factor side indicates size-matched healthy brain tissue (normal ROI) and tumor ROI. In addition, 1-way ANOVAs and post hoc tests according to Games-Howell were used to compare the intratumoral signal intensity differences and nITS values between glioma types for each inversion time separately. The sensitivity and specificity of nITS values for the discrimination of high-grade and low-grade gliomas were calculated for all inversion times by use of an optimal cutoff value determined by receiver operator characteristic (ROC) analysis. The area-under-the-ROC curve values for nITS values were calculated for all inversion times. To avoid the complications of age-related normal white matter signal differences, an intraindividual normalization by use of the contralateral normal brain tissue was performed by use of a *t* test. A value of *P* < .05 was considered to indicate significant results.

Histopathologic Assessment

Histopathologic diagnosis was evaluated by a panel of experienced neuropathologists (J.A.H. and colleagues), by use of a multiheaded microscope, on routinely processed formalin-fixed and paraffin-embedded tumor tissue with conventional H&E staining and Ki67 immunostaining. Tumor typing and grading were performed according to the criteria of the 4th edition of the *World Health Organization Classification of Tumors of the Central Nervous System*.⁴

Tissue for histopathologic assessment had been obtained at stereotactic biopsy (*n* = 11) or surgical resection (*n* = 22). Stereotactic biopsies were intraoperatively guided (Neuronavigation Stealth Station; Medtronic, Minneapolis, Minnesota) and targeted toward the most malignant portion of the tumor, on the basis of imaging findings. The histologic assessment according to the current WHO criteria revealed 7 diffuse astrocytomas (WHO grade II), 7 anaplastic astrocytomas (WHO grade III), and 19 glioblastomas (WHO grade IV).

RESULTS

Table 1 provides an overview of patient characteristics and distribution of tumor types. Detailed information about the number of patients, sex, age, tumor type, and the extent of resection are shown in the On-line Table. Table 2 provides descriptive values of nITS for all tumor types at the inversion time of 370 ms.

Examples of ASL maps at 3 different inversion times, the corresponding T2-weighted turbo inversion recovery magnitude images, and T1-weighted postcontrast images for a glioblastoma, a diffuse astrocytoma, and an anaplastic astrocytoma are shown in Figs 1, 2, and 3, respectively.

Statistical analysis revealed significant differences in the measured signal intensities between the ipsilateral and contralateral sides for all inversion times and all 3 tumor types (*P* < .001). An

Table 1: Patient characteristics

	Histopathologic Diagnosis		
	Diffuse Astrocytoma (WHO Grade II)	Anaplastic Astrocytoma (WHO Grade III)	Glioblastoma (WHO Grade IV)
No. of patients (% of all)	7 (21)	7 (21)	19 (58)
Sex ratio, women:men	3:4	3:4	8:11
Age, median, y (range)	48 (32–69)	41 (28–55)	60 (20–84)
Surgery:biopsy	6:1	3:4	13:6

Table 2: Descriptive values, including the mean of nITS values, standard deviation, standard error, and confidence interval for all tumor types at 370 ms

	No. of Patients	Mean	SD	SE	95% CI for Mean	
					Lower Bound	Upper Bound
LGA	7	1.08	0.39	0.15	0.73	1.44
AA	7	2.62	1.17	0.44	1.54	3.70
GB	19	3.26	2.90	0.66	1.87	4.66

Note:—Mean indicates mean of nITS values; SD, standard deviation; SE, standard error; LGA, diffuse astrocytoma; AA, anaplastic astrocytoma; GB, glioblastoma.

additional test for analyzing 3-way interaction of tumor type, inversion time, and side revealed a similar trend for all 3 tumor types toward higher signal intensities with higher inversion time ($P = .09$). Additional testing for the largest difference in nITS values between tumor types by use of a Welch test revealed the most statistically significant results for 370 ms ($P = .003$) (Fig 4). To avoid the complications of age-related normal-appearing white matter signal differences, an intraindividual normalization by use of the contralateral normal brain tissue was performed. Furthermore, no significant age differences, and therefore, no differences in normal-appearing white matter signal intensities, were found between low-grade and high-grade gliomas at any of the inversion times by use of a t test.

Fig 5 provides a time-series of PASL maps at all measured inversion times (columns) for 5 patients (rows A–E). The CE-T1-weighted images provide information about the tumor localization. The PASL maps at an inversion time of 370 ms show the highest contrast between high-grade gliomas and contralateral normal brain tissue signal compared with all other measured inversion times.

To provide information about the sensitivity and specificity of the nITS values in the differentiation of low-grade and high-grade gliomas, an ROC analysis for all inversion times was calculated. Fig 6 shows the ROC curves for nITS values at different inversion times. The area-under-the-ROC curve values for the nITS values at different inversion times were 0.912 (370 ms), 0.805 (614 ms), 0.632 (864 ms), 0.580 (1114 ms), 0.437 (1364 ms), 0.500 (1614 ms), 0.464 (1864 ms), and 0.555 (2114 ms). The optimal cutoff for nITS values at an inversion time of 370 ms was 1.48, with 85% sensitivity and 100% specificity. A nITS value of ≥ 1.48 suggested high-grade, whereas a nITS of < 1.48 suggested low-grade glioma.

DISCUSSION

In this study, 370 ms was determined to be the inversion time that showed the largest difference in normalized intratumoral signal intensity between high-grade and low-grade astrocytomas in a routine clinical setting. The use of multiple inversion times allows

tracking of the labeled bolus dynamically over time, providing additional information about tumor physiology. Previous PASL studies, by use of multiple inversion times, focused primarily on healthy subjects or on patients with arterial occlusive disease and have shown that the choice of inversion time is essential.^{22,23} MacIntosh et al²³ recently (2010) showed that the

mean arterial transit time in healthy volunteers is approximately 641–935 ms, depending on the brain region. If the delay between labeling and imaging is very short, the labeled spins are located primarily within the vessel. At a very late inversion time, the magnetization of the labeled bolus disappears as the result of longitudinal relaxation. We used PASL imaging at 8 different inversion times in the range of 370–2114 ms, with a gap of approximately 250 ms, along the lines of already published data,^{22,23} to determine which inversion time showed the largest difference in normalized intratumoral signal intensity between high-grade and low-grade gliomas.

Previous ASL studies, focused on tumor perfusion, have already demonstrated that PASL perfusion measurements can improve the diagnostic accuracy of glioma by use of a single inversion time of 1200 ms,^{18,24} which resulted in a sensitivity of 82.9% and a specificity of 96.2%.¹⁹ We did not focus on absolute tumor perfusion but rather investigated the largest signal difference between tumorous brain tissue and contralateral normal brain tissue by evaluating the nITS values at different inversion times. However, the sensitivity and specificity in this study were 85% and 100%, respectively, by use of nITS values at an inversion time of 370 ms. Our method, therefore, is comparable to previously published PASL techniques for the differentiation of high-grade and low-grade gliomas.

The results of this study point out that the inversion time before expected cerebral perfusion shows the most significant difference, as well as the highest sensitivity and specificity of nITS values, between high-grade and low-grade gliomas. The nITS value does not allow evaluation of the absolute value of CBF but reflects the signal ratio between tumor and normal tissue. Our results demonstrate that high-grade gliomas show significantly higher nITS values than low-grade gliomas at low inversion times (Fig 4).

Previous studies have reported that at very low inversion times, the labeled blood is assumed to be intravascular. Recently, Liu et al²⁵ assessed the labeled spin localization at multiple post-labeling delay times by use of T2 of the arterial spin-labeling signal as a marker. Because of the T2 of arterial blood (approximately 152 ms) and the tissue T2 (approximately 90 ms), they proposed that especially at very low inversion times (below the average range of arterial transit time), the labeled spins are primarily located in arterial vessels. They inferred that a postlabeling delay time of 2 seconds is sufficient to allow the spins to completely enter the tissue space for gray matter, and even longer inversion times are needed for white matter.²⁵ Therefore, we suggest that the most significant intratumoral signal intensity in our study depicts tumor circulation but not tumor perfusion and should be more precisely called “normalized vascular intratumoral signal

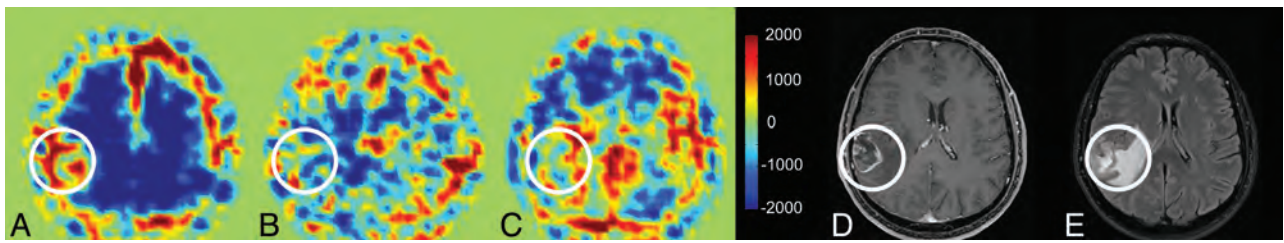


FIG 1. A 55-year-old man with histologically proven glioblastoma (WHO grade IV), right parieto-temporal (highlighted with a white circle). Axial PASL map at an inversion time of 370 ms (A), at 1114 ms (B), at 2114 ms (C), the contrast-enhanced T1-weighted image (D), and the T2-weighted turbo inversion recovery magnitude image (E). The increased signal intensity on the PASL maps of the glioblastoma is apparent at 370 ms. Images A–C were visualized and preprocessed in Matlab (version 7.8.347, R2009a).

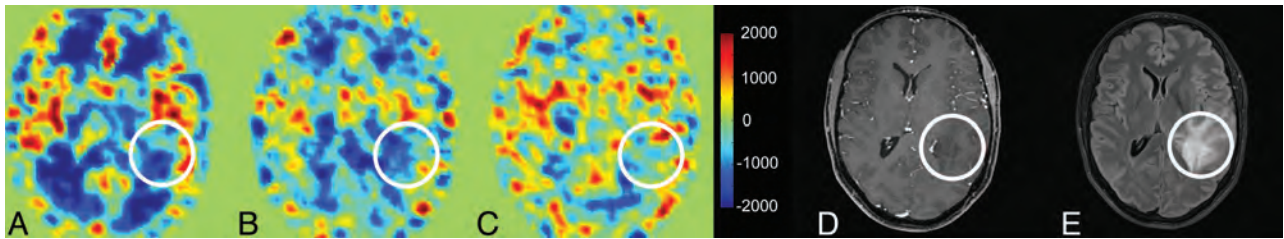


FIG 2. A 37-year-old man with histologically proven diffuse astrocytoma (WHO grade II), left parieto-temporal (highlighted with a white circle). Axial PASL CBF parameter map at an inversion time of 370 ms (A), at 1114 ms (B), at 2114 ms (C), the contrast-enhanced T1-weighted image (D), and the T2-weighted turbo inversion recovery magnitude image (E). On the PASL maps, no difference in signal intensity in the region of the tumor can be detected at each different inversion time. Images A–C were visualized and preprocessed in Matlab (version 7.8.347, R2009a).

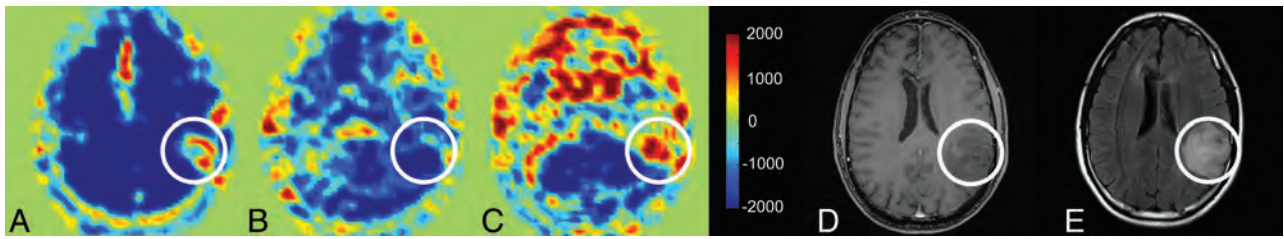


FIG 3. A 42-year-old man with histologically proven anaplastic astrocytoma (WHO III), left parietal (highlighted with a white circle). Axial PASL map at an inversion time of 370 ms (A), at 1114 ms (B), at 2114 ms (C), the contrast-enhanced T1-weighted image (D), and the T2-weighted turbo inversion recovery magnitude image (E). Although on contrast-enhanced T1-weighted images no tumoral contrast enhancement can be detected, the PASL maps show increased signal intensity that could be most accurately detected at 370 ms, indicating a high-grade astrocytic neoplasm. Images A–C were visualized and preprocessed in Matlab (version 7.8.347, R2009a).

intensity” (nVITS). On the basis of the significance of neovascularization as the driving force of brain tumor growth, high-grade astrocytomas are supposed to show higher vessel densities than low-grade astrocytomas. Thus, glioblastomas ($P = .023$) and anaplastic astrocytomas ($P = .004$) showed significantly higher nVITS compared with low-grade astrocytomas, as revealed by post hoc comparisons. Although tumoral neoangiogenesis increases the vascular intratumoral signal as the result of higher tumoral vessel attenuation, it cannot be excluded that some of the vascular intratumoral signal refers to an early arrival of the spins, because of variability in the size of tumor vessels. However, rather than by use of relative tumor blood flow, this study indicates that it is feasible to use nVITS values for astrocytoma subtyping.

The main advantage of the use of the nVITS for noninvasive astrocytoma subtyping is that the acquisition time of the PASL sequence at the inversion time of 370 ms is 1 minute, 20 seconds. Compared with other ASL acquisition times in recently published data, which ranged from 3 minutes, 26 seconds, to 5 minutes, 52 seconds, this results in an acceleration factor of approximately 3.5.^{13,18} This acceleration was achieved as the result of the reduc-

tion of measurement repetitions to 25 rather than the formerly suggested 50 repetitions.^{11,12} This was accomplished by the signal intensification of intravascular blood flow compared with perfusion blood flow. The reduction of the measurement repetitions results in a reduced SNR, which is assumed to be the reason for the missing nITS differences between the different grades of astrocytoma at 1200 ms reported in the literature.^{11,18,26} However, because of the extended multimodal tumor MR imaging protocol, the acquisition time of each sequence should be as short as possible, in terms of patient care, to obtain as much usable information about the tumor characteristics as possible. Another advantage is that the calculation of nVITS values requires no further manual postprocessing of the data and is immediately available after the examination, in contrast to other MR imaging and CT perfusion techniques. Therefore, nVITS provides a truly noninvasive method by which to depict tumor vascularization and also offers a beneficial, fast, and easily applicable tool for integration into routine MR imaging diagnostics.

The differentiation of high-grade and low-grade astrocytomas by use of conventional MR imaging with gadolinium-based con-

trast medium alone can sometimes be misleading; published data demonstrated that 32% of histologically proven high-grade gliomas do not show a pathologic contrast enhancement.²⁷ However, one of the most important clinical questions in astrocytoma diagnosis is the detection of malignant transformation of low-grade gliomas into anaplastic astrocytomas as soon as possible to adapt treatment strategies. More recently, published data have shown that the additional use of MR spectroscopy and MR perfusion significantly improve the predictive values and sensitivity of glioma grading.²⁸

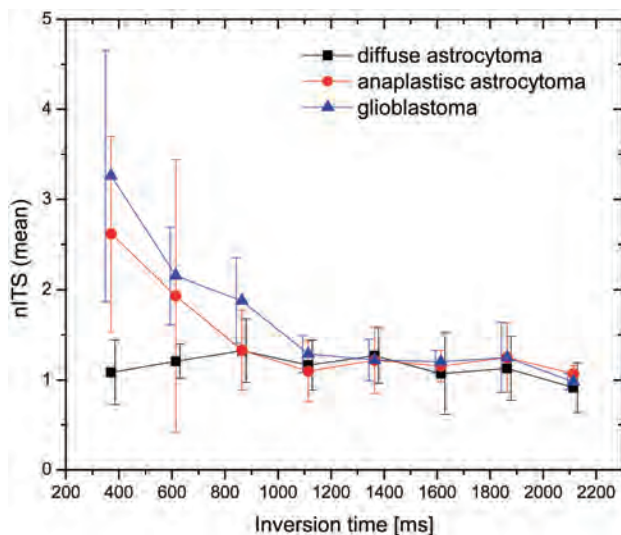


FIG 4. Comparison of nITS values for different astrocytoma types at 8 different inversion times (370 ms, $P = .003$; 614 ms, $P = .012$; 864 ms, $P = .129$; 1114 ms, $P = .519$; 1364 ms, $P = .955$; 1614 ms, $P = .746$; 1864 ms, $P = .848$; 2114 ms, $P = .162$) with corresponding error bars.

Because the growth and state of malignancy of an astrocytoma depends, among other factors, on angiogenesis, nVITS values are thought to be an especially fast and noninvasive measure that supports the detection of malignant transformation, particularly because contrast enhancement reflects the disruption of the blood-brain barrier rather than the assessment of tumor vascularity.

Furthermore, the nVITS values of tumors may facilitate the assessment of tumoral response to antiangiogenic therapy. Previous investigations demonstrated an expeditious decrease in tumorous tissue contrast enhancement after the initiation of treatment with antiangiogenic agents, especially in cases of vascular endothelial growth factor-targeted therapy, such as bevacizumab.^{29,30} This effect is thought to result partly from the normalization of abnormally permeable tumor vessels rather than from real antitumor effects and is also referred to as pseudoreponse. The advantage of obtaining the nVITS values of tumors could consist in depicting tumor circulation, which is thought to display the effects of antiangiogenic therapy more accurately than the contrast enhancement of tumors.

A potential limitation of ASL is that arterial occlusion could lead to a delay of the labeled arterial blood.²² This prolonged arterial transit time would result in an underestimation of tumorous vascular blood flow values, which would consequently lead to an underestimation of tumor malignancy. To minimize this potential bias, profound arterial occlusion should be excluded before the MR examination by use of non-contrast-dependent techniques, such as time-of-flight angiography. However, detection of a marginal reduction of vascular blood flow, which could also interfere with ASL data at such low inversion times, remains challenging.

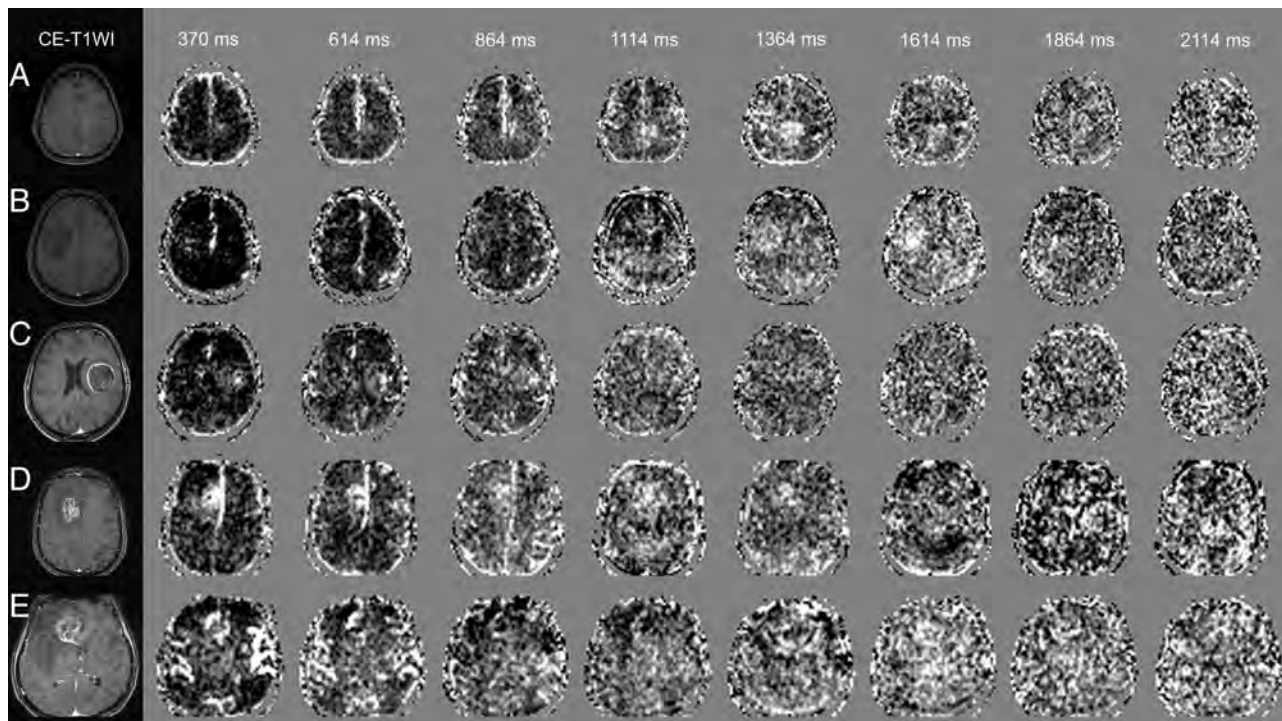


FIG 5. Contrast-enhanced T1-weighted images and time-series of PASL perfusion maps at all measured inversion times (370 ms, 614 ms, 864 ms, 1114 ms, 1364 ms, 1614 ms, 1864 ms, 2114 ms) of 5 patients (A–E) with high-grade gliomas.

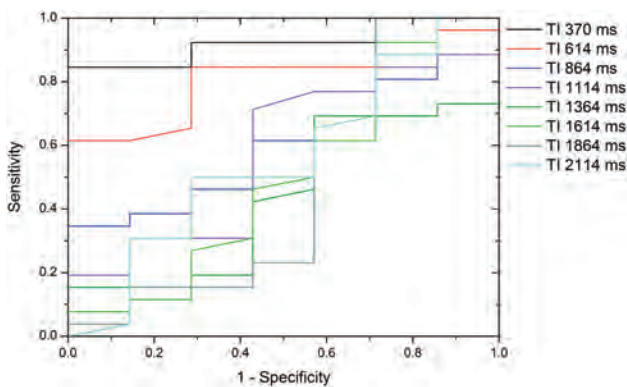


FIG 6. ROC curves of nITS values for the differentiation of low-grade and high-grade gliomas for all inversion times.

Another limitation of this study is the limited number of patients with low-grade astrocytoma. This was a result of the lower local and overall incidence of low-grade astrocytoma compared with high-grade astrocytoma.^{1,2}

Future investigation is needed to characterize the distribution function of the vascular bolus more precisely. Therefore, inversion times <370 ms must be investigated.

Because of the multiple PASL measurements (8 different inversion times), an acceleration of PASL acquisition time was essential, in terms of patient care, which resulted in a reduced SNR and an increased susceptibility to artifacts, which is another limitation of this study. Nevertheless, the PASL sequence used in this study proved to be able to differentiate between different glioma grades. Further investigation about SNR improvement is necessary but was beyond the scope of this investigation.

CONCLUSIONS

The data from our study confirm that nVITS, obtained at an inversion time of 370 ms, is a feasible value in the clinical setting for the differentiation of low-grade and high-grade astrocytic neoplasms. The use of normalized vascular intratumoral signal intensity facilitates a noninvasive, rapid radiologic characterization of astrocytomas. This value should be considered as a first step for the use of lower inversion times in PASL imaging to obtain further information about tumor vascularization. Future investigation will be needed to focus on sequence optimization and more detailed correlation of MR findings and histopathologic data (eg, vascular patterns and densities).

ACKNOWLEDGMENTS

The authors wish to thank Siemens Health Care (Erlangen, Germany) for providing the pulsed arterial spin-labeling sequence.

Disclosures: Matthias Preusser—UNRELATED: Grants/Grants Pending: Roche,* GSK* (*money paid to institution).

REFERENCES

1. Wöhrer A, Waldhör T, Heinzl H, et al. **The Austrian Brain Tumour Registry: a cooperative way to establish a population-based brain tumour registry.** *J NeuroOncol* 2009;95:401–11
2. Surawicz TS, McCarthy BJ, Kupelian V, et al. **Descriptive epidemiology of primary brain and CNS tumors: results from the Central Brain Tumor Registry of the United States, 1990–1994.** *NeuroOncol* 1999;1:14–25

3. Pope WB, Sayre J, Perlina A, et al. **MR imaging correlates of survival in patients with high-grade gliomas.** *AJNR Am J Neuroradiol* 2005;26:2466–74
4. Dumas-Duport C, Scheithauer B, O'Fallon J, et al. **Grading of astrocytomas: a simple and reproducible method.** *Cancer* 1988; 62:2152–65
5. Knopp E, Cha S, Johnson G, et al. **Glial neoplasms: dynamic contrast-enhanced T2*-weighted MR imaging.** *Radiology* 1999;211: 791–98
6. Law M, Yang S, Babb JS, et al. **Comparison of cerebral blood volume and vascular permeability from dynamic susceptibility contrast-enhanced perfusion MR imaging with glioma grade.** *AJNR Am J Neuroradiol* 2004;25:746–55
7. Hu LS, Baxter LC, Pinnaduwa DS, et al. **Optimized preload leakage-correction methods to improve the diagnostic accuracy of dynamic susceptibility-weighted contrast-enhanced perfusion MR imaging in posttreatment gliomas.** *AJNR Am J Neuroradiol* 2010;31:40–48
8. Golay X, Petersen E. **Arterial spin labeling: benefits and pitfalls of high magnetic field.** *Neuroimaging Clin North Am* 2006;16:259–68
9. Chen Y, Wang DJJ, Detre JA. **Test-retest reliability of arterial spin labeling with common labeling strategies.** *J Magn Reson Imaging* 2011;33:940–49
10. Järnum H, Steffensen EG, Knutsson L, et al. **Perfusion MRI of brain tumours: a comparative study of pseudo-continuous arterial spin labelling and dynamic susceptibility contrast imaging.** *Neuroradiology* 2010;52:307–17
11. Warmuth C, Gunther M, Zimmer C. **Quantification of blood flow in brain tumors: comparison of arterial spin labeling and dynamic susceptibility-weighted contrast-enhanced MR imaging.** *Radiology* 2003;228:523–32
12. Weber M-A, Günther M, Lichy MP, et al. **Comparison of arterial spin-labeling techniques and dynamic susceptibility-weighted contrast-enhanced MRI in perfusion imaging of normal brain tissue.** *Invest Radiol* 2003;38:712–18
13. Hirai T, Kitajima M, Nakamura H, et al. **Quantitative blood flow measurements in gliomas using arterial spin-labeling at 3T: intermodality agreement and inter- and intraobserver reproducibility study.** *AJNR Am J Neuroradiol* 2011;32:2073–79
14. Koziak AM, Winter J, Lee T-Y, et al. **Validation study of a pulsed arterial spin labeling technique by comparison to perfusion computed tomography.** *Magn Reson Imaging* 2008;26:543–53
15. Weber M-A, Henze M, Tüttenberg J, et al. **Biopsy targeting gliomas: do functional imaging techniques identify similar target areas?** *Invest Radiol* 2010;45:755–68
16. Deibler AR, Pollock JM, Kraft RA, et al. **Arterial spin-labeling in routine clinical practice, part 1: technique and artifacts.** *AJNR Am J Neuroradiol* 2008;29:1228–34
17. Lu H, Clingman C, Golay X, et al. **Determining the longitudinal relaxation time (T1) of blood at 3.0 Tesla.** *Magn Reson Med* 2004;52:679–82
18. Kim MJ, Kim HS, Kim J-H, et al. **Diagnostic accuracy and interobserver variability of pulsed arterial spin labeling for glioma grading.** *Acta Radiol* 2008;49:450–57
19. Lev MH, Ozsunar Y, Henson JW, et al. **Glial tumor grading and outcome prediction using dynamic spin-echo MR susceptibility mapping compared with conventional contrast-enhanced MR: confounding effect of elevated rCBV of oligodendrogliomas.** *AJNR Am J Neuroradiol* 2004;25:214–21
20. Wong EC, Buxton RB, Frank LR. **Implementation of quantitative perfusion imaging techniques for functional brain mapping using pulsed arterial spin labeling.** *NMR Biomed* 1997;10:237–49
21. Wen PY, Macdonald DR, Reardon DA, et al. **Updated response assessment criteria for high-grade gliomas: response assessment in neuro-oncology working group.** *J Clin Oncol* 2010;28:1963–72
22. Hendrikse J, Van Osch M, Rutgers D, et al. **Internal carotid artery occlusion assessed at pulsed arterial spin-labeling perfusion MR imaging at multiple delay times.** *Radiology* 2004;233:899–904

23. MacIntosh BJ, Filippini N, Chappell MA, et al. **Assessment of arterial arrival times derived from multiple inversion time pulsed arterial spin labeling MRI.** *Magn Reson Med* 2010;63:641–47
24. Chawla S, Wang S, Wolf RL, et al. **Arterial spin-labeling and MR spectroscopy in the differentiation of gliomas.** *AJNR Am J Neuroradiol* 2007;28:1683–89
25. Liu P, Uh J, Lu H. **Determination of spin compartment in arterial spin labeling MRI.** *Magn Reson Med* 2011;65:120–27
26. Wolf RL, Wang J, Wang S, et al. **Grading of CNS neoplasms using continuous arterial spin labeled perfusion MR imaging at 3 Tesla.** *J Magn Reson Imaging* 2005;22:475–82
27. Barker FG, Chang SM, Huhn SL, et al. **Age and the risk of anaplasia in magnetic resonance–nonenhancing supratentorial cerebral tumors.** *Cancer* 1997;80:936–41
28. Law M, Yang S, Wang H, et al. **Glioma grading: sensitivity, specificity, and predictive values of perfusion MR imaging and proton MR spectroscopic imaging compared with conventional MR imaging.** *AJNR Am J Neuroradiol* 2003;24:1989–98
29. Friedman HS, Prados MD, Wen PY, et al. **Bevacizumab alone and in combination with irinotecan in recurrent glioblastoma.** *J Clin Oncol* 2009;27:4733–40
30. Vredenburgh JJ, Desjardins A, Herndon JE, et al. **Bevacizumab plus irinotecan in recurrent glioblastoma multiforme.** *J Clin Oncol* 2007;25:4722–29

Histogram Analysis of Intravoxel Incoherent Motion for Differentiating Recurrent Tumor from Treatment Effect in Patients with Glioblastoma: Initial Clinical Experience

H.S. Kim, C.H. Suh, N. Kim, C.-G. Choi, and S.J. Kim



ABSTRACT

BACKGROUND AND PURPOSE: Intravoxel incoherent motion can simultaneously measure diffusion and perfusion characteristics. Our aim was to determine whether the perfusion and diffusion parameters derived from intravoxel incoherent motion could act as imaging biomarkers for distinguishing recurrent tumor from treatment effect in patients with glioblastoma.

MATERIALS AND METHODS: Fifty-one patients with pathologically confirmed recurrent tumor ($n = 31$) or treatment effect ($n = 20$) were assessed by means of intravoxel incoherent motion MR imaging. The histogram cutoffs of the 90th percentiles for perfusion and normalized CBV and the 10th percentiles for diffusion and ADC were calculated and correlated with the final pathology results. A leave-one-out cross-validation was used to evaluate the diagnostic performance of our classifiers.

RESULTS: The mean 90th percentile for perfusion was significantly higher in the recurrent tumor group (0.084 ± 0.020) than in the treatment effect group (0.040 ± 0.010) ($P < .001$). The 90th percentile for perfusion provided a smaller number of patients within an overlap zone in which misclassifications can occur, compared with the 90th percentile for normalized CBV. The mean 10th percentile for diffusion was significantly lower in the recurrent tumor group than in the treatment effect group ($P = .006$). Receiver operating characteristic curve analyses showed the 90th percentile for perfusion to be a significant predictor for differentiation, with a sensitivity of 87.1% and a specificity of 95.0%. There was a significant positive correlation between the 90th percentiles for perfusion and normalized CBV ($r = 0.674$; $P < .001$).

CONCLUSIONS: A histogram analysis of intravoxel incoherent motion parameters can be used as a noninvasive imaging biomarker for differentiating recurrent tumor from treatment effect in patients with glioblastoma.

ABBREVIATIONS: IVIM = intravoxel incoherent motion; ROC = receiver operating characteristic; AUC = area under the ROC curve; nCBV = normalized CBV

In clinical practice, it is often difficult to determine whether a progressively enhancing lesion occurring after concurrent chemoradiotherapy is caused by a recurrent tumor or by treatment effect.¹ Several studies have used physiologic imaging techniques, such as T2*-weighted dynamic susceptibility-weighted contrast-enhanced perfusion MR imaging, to differ-

entiate recurrent tumor from treatment effect.^{1,2} Intravoxel incoherent motion (IVIM) was introduced by Le Bihan et al^{3,4} as a method for simultaneously measuring perfusion and diffusion. Le Bihan et al⁴ defined IVIM as the microscopic translational motions that occur in each image voxel in MR imaging. In biologic tissues, these incoherent motions include molecular diffusion of water and microcirculation of blood in the capillary network, called “perfusion.” These 2 phenomena account for the bi-exponential decay of the signal intensity on DWI when different diffusion b-values are applied. With the use of IVIM theory, both true molecular diffusion and water molecule motion in the capillary network can be estimated by means of a single diffusion imaging acquisition technique. The major advantages of IVIM MR imaging are as follows: it allows the simultaneous acquisition of diffusion and perfusion parameters, which can provide perfusion measures within corresponding solid lesions on ADC or the D-map without the requirement for a co-registration processing step; intravenous

Received May 10, 2013; accepted after revision July 1.

From the Department of Radiology, Research Institute of Radiology, Asan Medical Center, University of Ulsan College of Medicine, Seoul, Korea.

This study was supported by the Basic Science Research Program through the National Research Foundation of Korea, funded by the Ministry of Education, Science, and Technology (grant 2009–0076988).

Please address correspondence to Ho Sung Kim, MD, Department of Radiology, Research Institute of Radiology, Asan Medical Center, University of Ulsan, College of Medicine, 86, Asanbyeongwon-gil, Songpa-gu, Seoul, 138–736, Korea; e-mail: radhskim@gmail.com

Indicates open access to non-subscribers at www.ajnr.org

<http://dx.doi.org/10.3174/ajnr.A3719>

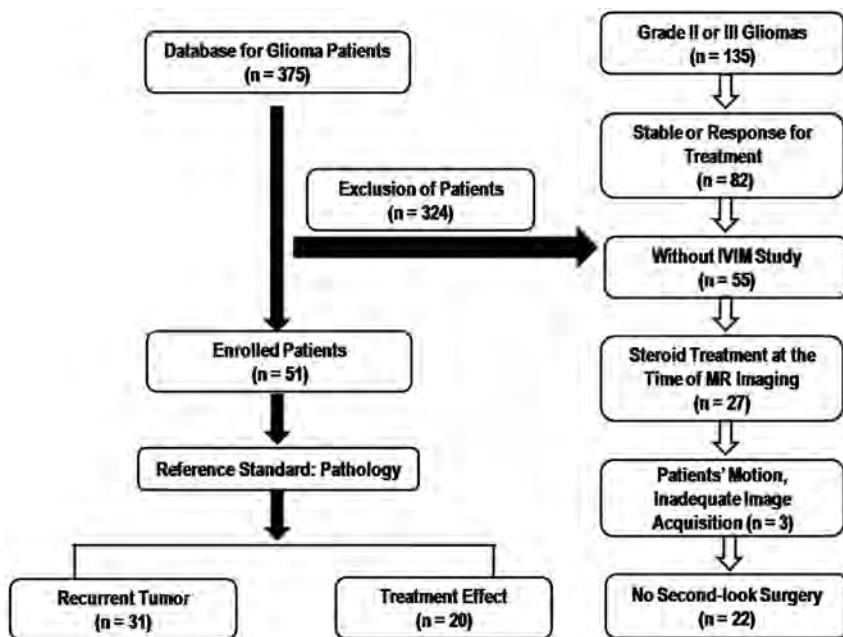


FIG 1. Flow chart of our study population.

contrast injection is not required; and it allows processing and image analysis to be performed within a reasonable timeframe.

In the present study, we attempted to validate IVIM-derived perfusion and diffusion parameters through the use of both the pathologic correlation and normalized CBV (nCBV) derived from DSC MR perfusion imaging, which has been commonly used as a perfusion parameter for assessing the glioblastoma treatment response. For pathologic correlation, we used IVIM MR imaging in patients with pathologically confirmed recurrent tumor or treatment effect.

Our first hypothesis was that the difference in vascularity between recurrent tumor and treatment effect can be assessed by means of an IVIM-derived perfusion fraction (f), and it would correlate with the value of nCBV derived from DSC MR perfusion imaging. Our second hypothesis was that the true diffusion parameter (D), derived from a biexponential model that separates perfusion effects, may be more significantly different between the recurrent tumor and the treatment effect groups than ADC. The purpose of this study was to determine whether the perfusion (f) and diffusion (D) parameters derived from IVIM can act as imaging biomarkers for distinguishing recurrent tumor from treatment effect in patients with glioblastoma.

MATERIALS AND METHODS

Our institutional review board approved this retrospective study and waived the informed consent requirement.

Patients

A retrospective review of our institution's data base identified 375 patients who had undergone MR imaging studies for pretreatment and posttreatment glioma evaluation between May 2011 and April 2013. Among these patients, 51 were included on the basis of the following criteria: 1) had pathologically confirmed glioblastomas before standard glioblastoma treatment; 2) under-

went concurrent chemoradiotherapy after surgical resection; 3) demonstrated new or enlarged contrast-enhancing lesions seen on serial follow-up MR images including IVIM MR imaging; 4) did not have corticosteroid administration between the prior follow-up MR imaging and the time of IVIM MR imaging; 5) had adequate image acquisition and quality without patient motion or a significant susceptibility artifact; and 6) were pathologically confirmed with recurrent tumor or treatment effect after their second surgical resection. The study patient accrual process is summarized in Fig 1. Of the 51 study patients, 31 had recurrent tumor (mean age, 52.2 years; range, 35–72 years) and 20 had treatment effect (mean age, 50.5 years; range, 25–67 years).

Histopathologic Diagnosis

Well-recognized pathologic features of a recurrent tumor included cellular sheets and/or nests of atypical cells, often with

mitotic figures. The finding of fewer atypical cells, in a linear infiltrative configuration in parenchyma without prominent reactive changes, was also classified as recurrence. Pathologic features of treatment effects were geographic coagulative necrosis without pseudopalisading, vascular necrosis, vascular hyalinization, reactive vascular changes, dystrophic calcification, perivascular chronic inflammation, and gliosis with atypia.⁵

IVIM Model

In biologic tissue, IVIM includes microcirculation of blood in the capillary network, also referred to as perfusion.⁵ The relationship between signal variation and b factors with an IVIM-type sequence can be expressed by use of the Equation⁶:

$$\frac{S(b)}{S_0} = (1-f)^{-bD} + fe^{-bD^*},$$

where S is the mean signal intensity, S_0 is the signal intensity without diffusion, f is the fraction of the diffusion linked to microcirculation, D is the diffusion parameter representing pure molecular diffusion (the slow component of diffusion), and D^* is the diffusion parameter representing incoherent microcirculation within the voxel, that is, perfusion-related diffusion or the fast component of diffusion (Fig 2).

MR Imaging Protocols

MR imaging was performed with the use of a 3T system (Achieva; Philips Medical Systems, Best, the Netherlands) with an 8-channel sensitivity-encoding head coil. We acquired 16 different b -values (0, 10, 20, 40, 60, 80, 100, 120, 140, 160, 180, 200, 300, 500, 700, and 900 s/mm²) in 3 orthogonal directions. The distribution of b -values was chosen to cover both the initial pseudodiffusion decay ($b < 200$ s/mm²) and the molecular diffusion decay ($b \geq 200$ s/mm²).⁷ We used a large number of lower b -values in our study to improve the accuracy of the pseudodiffusion (D^*). The depen-

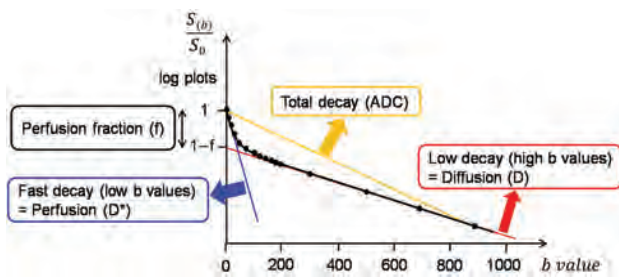


FIG 2. Example of biexponential signal decay as a function of the 16 different diffusion b-values in a given voxel of a recurrent tumor. Bold, solid line is the IVIM nonlinear regression fit providing D, D*, and f. Blue line is the biexponential fit providing fast decay associated with perfusion; red line is slow decay of the biexponential fit, indicating true diffusion; yellow line is the monoexponential fit providing ADC.

dence of the diffusion-weighted signal (in log plots) on the b-value is no longer straight, as would have been expected for free diffusion, but curved, thus reflecting the multiplicity of the underlying process.⁸ Perfusion is expected to contribute to this curvature in a biexponential mode⁴ for b-values in the very low range (0–200 s/mm² or higher for very slow flow). The total acquisition time was 4 minutes, 21 seconds. The DWI with multiple b-values was performed before contrast-enhanced MR imaging.

DSC MR perfusion imaging was performed with the use of a gradient-echo, echo-planar sequence during administration of contrast material (Dotarem; Guerbet, Paris, France) at a rate of 4 mL/s by use of an MR imaging-compatible power injector (Spectris; Medrad, Pittsburgh, Pennsylvania). The bolus of contrast material was followed by a 20-mL bolus of saline administered at the same injection rate. The detailed imaging parameters for the DSC study were as follows: repetition time/echo time, 1407/40; flip angle, 35°; field of view, 24 cm; matrix, 128 × 128; and number of sections, 20. The total DSC MR image acquisition time was 1 minute, 30 seconds.

Image Processing

All imaging data were transferred from the MR scanner to an independent, personal computer for quantitative IVIM and DSC MR perfusion analyses. An in-house program with Matlab2010b TM (MathWorks, Natick, Massachusetts) was developed to evaluate the diffusion process, not only of the monoexponential model but also of the biexponential model. Simplified biexponential models, including the Le Bihan simplified method, the Luciani method, and the Sigmund method, were implemented. A full biexponential model was also implemented to evaluate the exact IVIM diffusion parameters. IVIM parameters, including f and D, were calculated by means of the Le Bihan simplified method.

The DSC perfusion parametric map was obtained through the use of a commercial software package (nordicICE; Nordic-NeuroLab, Bergen, Norway). For DSC MR perfusion imaging, after eliminating recirculation of the contrast agent by use of γ -variate curve fitting and contrast agent leakage correction, the relative CBV was computed by numeric integration of the curve. On a pixel-by-pixel basis, the nCBV maps were calculated by dividing each relative CBV value by an unaffected, white matter–relative CBV value defined by an experienced neuroradiologist

(H.S.K., with 9 years of clinical experience in neuro-oncologic imaging).

For quantitative analysis, contrast-enhancing lesion volumes were segmented on 3D, postcontrast, T1-weighted images by use of a semi-automated adaptive thresholding technique so that all of the pixels above the threshold value were selected. Therefore, significant regions of macroscopic necrosis that were not enhancing, as well as cystic areas, were excluded. The resulting entire enhancing tumor volumes were verified by the experienced neuroradiologist (H.S.K.), who was blinded to the clinical outcome, and they were co-registered and mapped to the f, D, nCBV, and ADC maps. Each parametric value was calculated on a pixel-by-pixel basis for the segmented contrast-enhancing volume and used for the histogram analysis (Fig 3). For the cumulative histogram parameters, the 90th percentile for f (f90) and nCBV (nCBV90) and the 10th percentile for D (D10) and ADC (ADC10) were derived (the *n*th percentile is the point at which *n*% of the voxel values that form the histogram are found to the left).

Statistical Analysis

Kaplan-Meier curves and log-rank tests were used to evaluate the association of the pathologic results (recurrent tumor/treatment effect) with overall survival. All data are expressed as mean \pm standard deviation. The Student *t* test was used to assess significant differences in f90, nCBV90, D10, and ADC10 between the recurrent tumor and the treatment effect groups.

In the receiver operating characteristic (ROC) curve analysis, the cutoff points, determined by maximizing the sum of the sensitivity and specificity, were calculated to differentiate the 2 entities. A leave-one-out cross-validation was used to evaluate the performance of our classifiers. In each round of the leave-one-out validation, one participant was selected as a testing sample. The remaining participants were used as training samples to construct the classifier. The testing sample was then classified with the trained classifier. This procedure was repeated until each participant was tested once. The performance of the histogram parameters was evaluated with sensitivity and specificity. Sensitivity was determined as TP/(TP + FN), and specificity was determined as TN/(TN + FP), where TP is a true-positive finding (test results showed recurrent tumor, and the final pathologic diagnosis was also recurrent tumor); TN, a true-negative finding (test results showed treatment effect, and the final pathologic diagnosis was also treatment effect); FP, a false-positive finding (test results showed recurrent tumor, but the final pathologic diagnosis was treatment effect); and FN, a false-negative finding (test results showed treatment effect, but the final pathologic diagnosis was recurrent tumor).

The association of f90 and nCBV90 was assessed by means of Pearson and partial correlation analyses. SPSS 19.0 for Windows (IBM, Armonk, New York) was used to perform all statistical analyses. Probability values $<.05$ were considered to indicate statistically significant differences.

RESULTS

The mean interval between IVIM MR imaging and second-look surgery was 12.5 days. The mean time for postprocessing of the IVIM histogram was 3 minutes, 37 seconds. Descriptive statistics

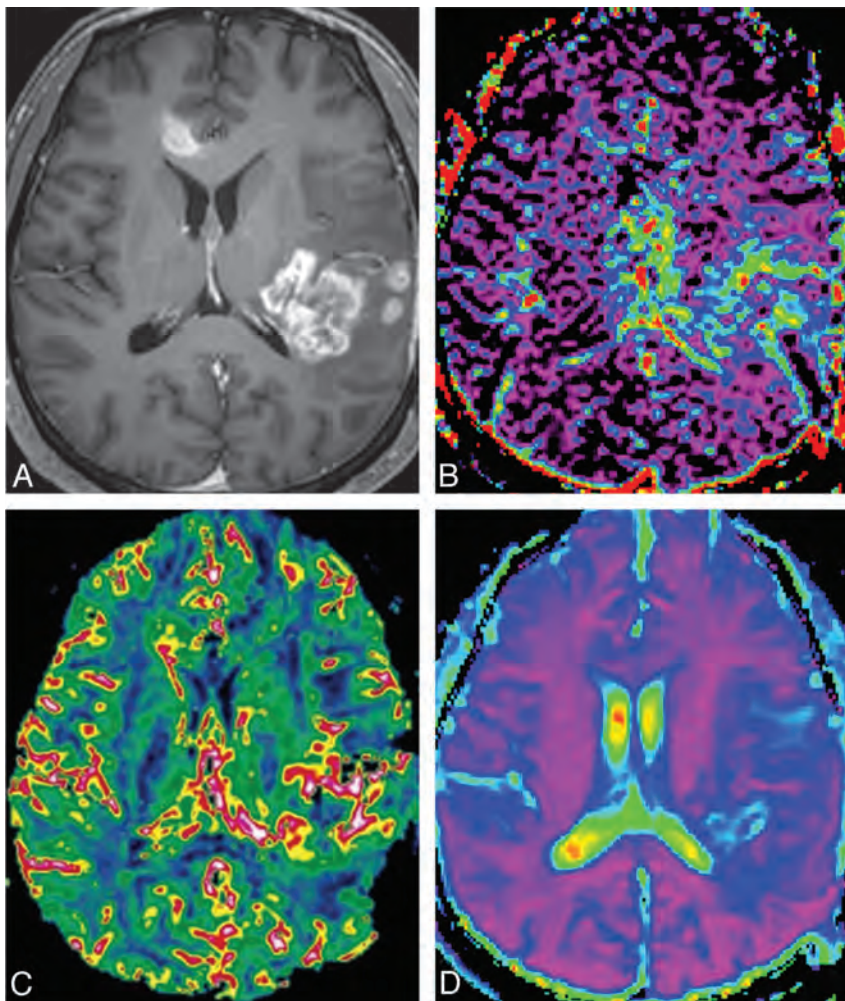


FIG 3. A 51-year-old man with recurrent tumor. A, Axial contrast-enhanced T1-weighted image shows a necrotic contrast-enhancing lesion in the left temporoparietal lobe. The f-map (B) and nCBV map (C) show visual increases of the f and nCBV values in the corresponding areas of the contrast-enhancing lesion. The visual D-value (D) is similar to that of white matter.

Table 1: Comparison of study patient demographic data

Variables	Recurrent Tumor	Treatment Effect	P Value
No. of male patients	14 (46.9%)	11 (60.0%)	.147
No. of female patients	17 (53.1%)	9 (40.0%)	
Age, y ^a	52.2 ± 8.9	550.5 ± 8.6	.376
Mean radiation dose at CCRT, Gy ^a	59.5 ± 0.7	59.7 ± 0.5	.856
Mean KPS ^a	94.5 ± 5.0	92.2 ± 8.1	.722
Tumor volume, cm ^{3a}	51.2 ± 11.7	50.7 ± 17.5	.701
Surgical extent before CCRT			.554
Biopsy	2	2	
Subtotal resection	14	9	
Gross total resection	15	9	
Surgical extent at second-look surgery			.391
Biopsy	6	3	
Subtotal resection	11	6	
Gross total resection	14	11	
Time interval between CCRT and new or enlarged contrast-enhancing lesion, wk ^a	42.1 ± 19.1	45.3 ± 16.3	.505
Median survival, wk	73.5	80.5	.079

Note:—CCRT indicates concurrent chemoradiotherapy; Gy, gray; KPS, Karnofsky Performance Score.

^aData are mean ± standard deviation.

regarding the demographic data obtained in both the patients with recurrent tumor and treatment effect are summarized in Table 1. When the Kaplan-Meier curves and log-rank tests were used to evaluate the association of the pathologic results (recurrent tumor/treatment effect) with overall survival, we found that the differences were not statistically significant, though the patient group with treatment effect tended to have longer overall survival than those with recurrent tumor (Table 1).

Visual Analysis of the IVIM MR Parameters and Histogram Distribution

Among the 51 study patients, all patients with recurrent tumor and 5 patients with treatment effect showed that the signal decay curve, plotted as a function of the diffusion b-values, was biexponential and ranged from 0–900 s/mm². Recurrent tumors show more rapid signal decay than do treatment effects in the range of lower b-values (b < 200 s/mm²). In the remaining 15 of the 20 patients with treatment effect, the signal decay curve was similar to the monoexponential pattern. The f histogram in recurrent tumors showed a higher relative frequency at a high f value compared with treatment effects, thus resulting in substantial divergence between recurrent tumors and treatment effects at the high end of the cumulative histograms. The D-histogram in recurrent tumors showed a higher relative frequency at a low D value compared with treatment effects, thus resulting in a substantial divergence between recurrent tumors and treatment effects at the low end of the cumulative histograms. The f- and D-maps and their histograms of representative cases of recurrent tumor and treatment effect are shown in Figs 3 and 4.

Diagnostic Performance of the IVIM Histogram Parameters

The mean ± standard deviation of f90, D10, nCBV90, and ADC10 in both the recurrent tumor and treatment effect groups are shown in Table 2, and representative cases of each group are shown in Figs 3 and 4. f90 showed statistically significant differences between recurrent tumor and treatment effect, with the recurrent tumor group showing higher f90

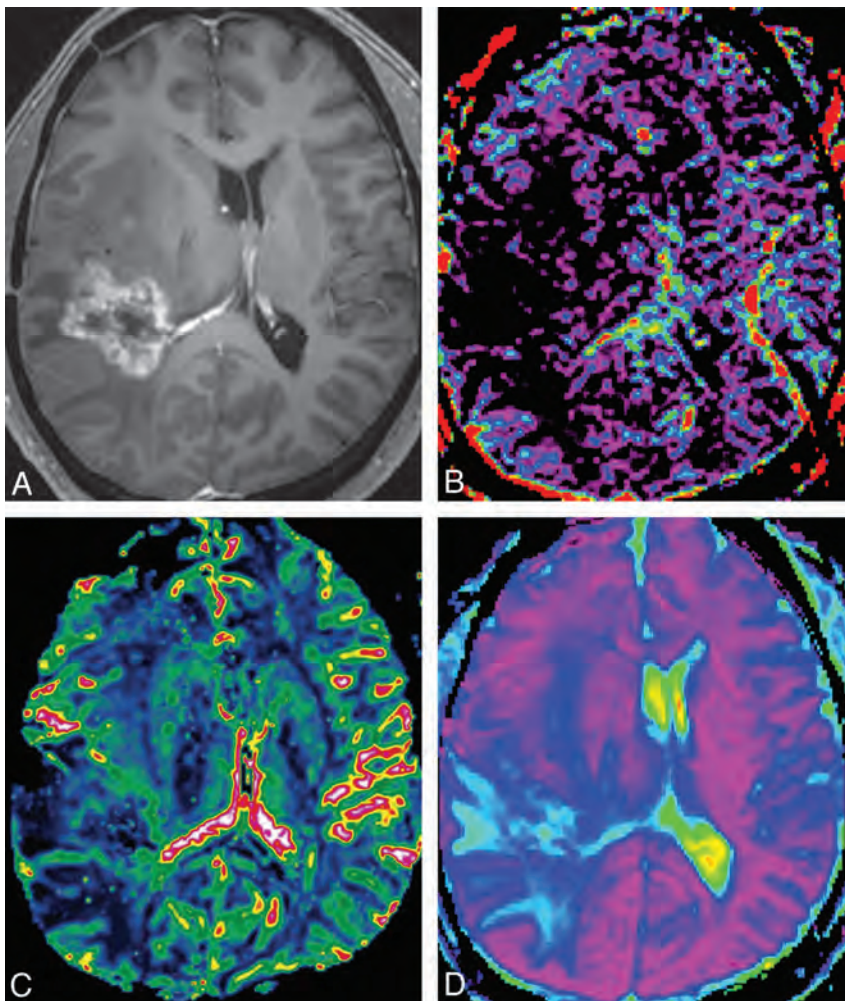


FIG 4. A 45-year-old man with treatment effect. A, Axial contrast-enhanced T1-weighted image shows a necrotic contrast-enhancing lesion in the right temporoparietal lobe. The f-map (B) and nCBV map (C) show no visual increase of the f and nCBV values in the corresponding areas of the contrast-enhancing lesion. D-map (D) shows visual increase of the D value.

Table 2: Difference of the mean cumulative histogram cutoff values of IVIM MR imaging parameters, nCBV, and ADC in patients with recurrent tumor and treatment effect

Parameters	Recurrent Tumor	Treatment Effect	P Value
f90	0.084 ± 0.020	0.040 ± 0.010	<.001
D10, 10 ⁻³ ·mm ² ·s ⁻¹	0.940 ± 0.097	1.008 ± 0.045	.006
nCBV90	4.374 ± 1.133	2.505 ± 0.426	<.001
ADC10, 10 ⁻³ ·mm ² ·s ⁻¹	0.961 ± 0.090	1.011 ± 0.054	.032

Note:—f90 indicates 90th percentile histogram cutoff of f; D10, 10th percentile histogram cutoff of D; nCBV90, 90th percentile histogram cutoff of nCBV; ADC10, 10th percentile histogram cutoff of ADC.

Data are mean ± standard deviation.

(mean ± standard deviation, 0.084 ± 0.020 versus 0.040 ± 0.010; $P < .001$). On the ROC curve and box-and-whisker plots, f90 showed a clear difference between the 2 groups and provided a smaller number of patients within an overlap zone in which misclassifications can occur compared with nCBV90 (14 patients versus 19 patients; Figs 5 and 6). The mean D10 was significantly lower in the recurrent tumor group (mean ± standard deviation; 0.940 ± 0.097 [10⁻³·mm²·s⁻¹]) than in the treatment effect group (1.008 ± 0.045 [10⁻³·mm²·s⁻¹]) ($P = .006$).

The results of the ROC analyses of the quantitative IVIM his-

togram parameters used to distinguish recurrent tumor from treatment effect are summarized in Table 3. ROC curve analyses showed f90 to be the best predictor for differentiating recurrent tumor from treatment effect (area under the ROC curve [AUC], 0.957; 95% CI, 0.860–0.994). Although f90 showed the largest AUC, the difference of AUC between f90 and nCBV90 was not significant. ROC curve analysis indicated that the diagnostic models that were based on all of the IVIM histogram parameters had a statistically significant P value.

According to ROC curve analyses for distinguishing recurrent tumor from treatment effect, the cutoff values were 0.056 for f90 and 0.970 for D10 when all 51 patients were regarded as a training set. With f90 as a discriminative index, sensitivity and specificity for differentiation were 87.1% (27 of 31 patients with recurrent tumor) and 95.0% (19 of 20 patients with treatment effect), respectively. With D10 as a discriminative index, sensitivity and specificity were 71.0% (22 of 31 patients with recurrent tumor) and 75.0% (15 of 20 patients with treatment effect), respectively (Table 3).

Partial correlation analysis showed a significantly positive correlation between f90 and nCBV90 ($r = 0.674$; $P < .001$) for all cases with histopathology as the controlling variable.

DISCUSSION

To the best of our knowledge, the treatment response evaluation for brain tumor

by use of the IVIM method has not yet been reported. In the present study, we attempted to validate the IVIM-derived perfusion and diffusion parameters to determine whether an enlarging, contrast-enhancing lesion was caused by recurrent tumor or by treatment effect as the perfusion and diffusion characteristics of posttreatment tumors can differ from those suggested by the Le Bihan biexponential model. Our study clarified the different perfusion characteristics of recurrent tumor and treatment effect on the basis of the IVIM biexponential model. We found that the mean f90 had a significantly higher value in the recurrent tumor group than in the treatment effect group. According to ROC curve analysis, f90 and D10 showed excellent diagnostic accuracy as predictors for differentiating recurrent tumor from treatment effect.

Previous reports have proposed that DSC perfusion MR imaging has the potential to distinguish tumor recurrence from treatment effect through the use of relative CBV maps.^{9,10} In the present study, we found that the diagnostic performance of IVIM-derived perfusion and diffusion parameters were more successful for differentiating recurrent tumor from treatment effect than

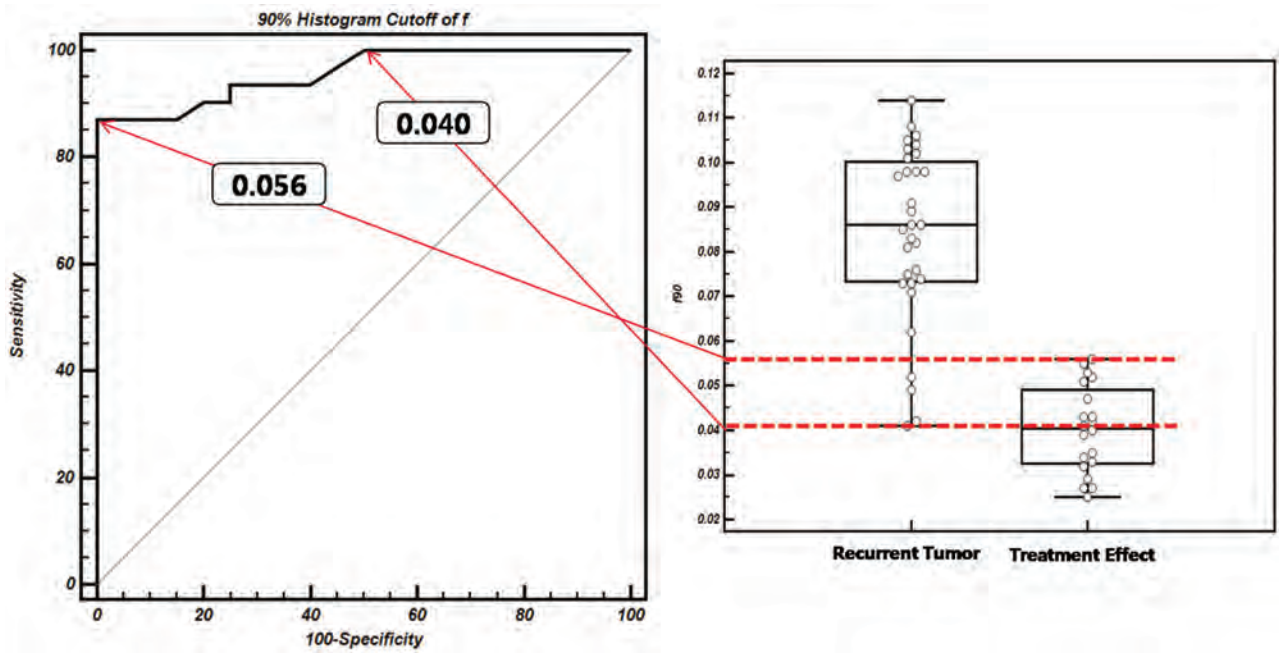


FIG 5. ROC curve indicates the sensitivities and specificities of f_{90} -based differentiation between recurrent tumor and treatment effect. The overlap zone (14 patients) between dotted lines on the box-and-whisker plot shows the same interval in which misclassifications can occur on the ROC curve.

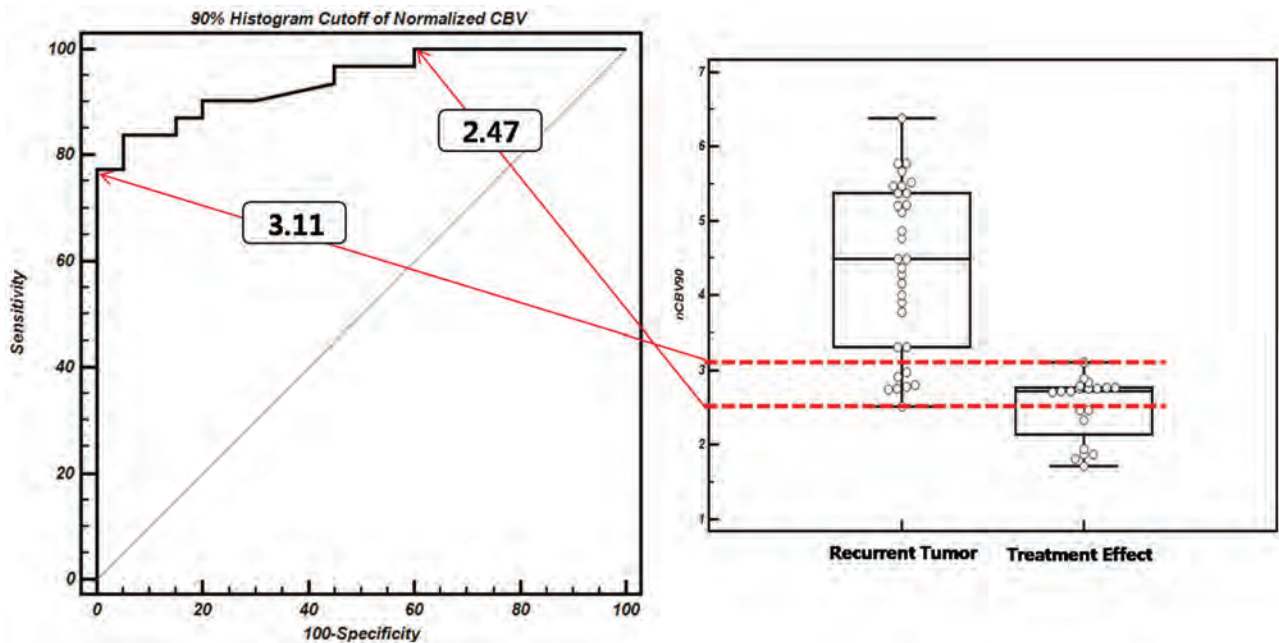


FIG 6. ROC curve indicates the sensitivities and specificities of $nCBV_{90}$ -based differentiation between recurrent tumor and treatment effect. Overlap zone (19 patients) between dotted lines on the box-and-whisker plot shows the same interval in which misclassifications can occur on the ROC curve.

prior work that was based on perfusion and diffusion imaging alone; however, the difference was not statistically significant. The possible explanation for this result might be attributed to the contrast agent leakage effects, which depend on the attenuation and spatial distribution of tumor cells within the extracellular extravascular space and can lead to an additional susceptibility calibration factor. Moreover, IVIM MR imaging by use of spin-echo-based DWI can be less sensitive to $T2^*$ susceptibility artifact than is DSC MR imaging.

Le Bihan et al⁶ suggested that the f value measures the fractional volume of capillary blood flowing in each voxel. Regarding tumor angiogenesis and its correlation with perfusion parameters, tumor angiogenesis is a complex multistep process and is characterized morphologically by an increase in the number of blood vessels and endothelial cell proliferation.^{11,12} Recurrent tumors are usually higher-grade tumors with increased neoangiogenesis, which leads to increased CBV as well as increased permeability surface area product. In the present study, we did not find

Table 3: Diagnostic performance of the cumulative histogram cutoff values of the IVIM MR imaging parameters, nCBV, and ADC values for differentiating recurrent tumor from treatment effect

Parameters	AUC ^a	Cutoff	Sensitivity	Specificity
f90	0.957 (0.860, 0.994)	0.056	87.1%	95.0%
D10, 10 ⁻³ ·mm ² ·s ⁻¹	0.756 (0.615, 0.865)	0.970	71.0%	75.0%
nCBV90	0.940 (0.835, 0.987)	2.892	83.9%	95.0%
ADC10, 10 ⁻³ ·mm ² ·s ⁻¹	0.697 (0.552, 0.818)	0.995	67.7%	75.0%

Note:—f90 indicates 90th percentile histogram cutoff of f; D10, 10th percentile histogram cutoff of D; nCBV90, 90th percentile histogram cutoff of nCBV; ADC10, 10th percentile histogram cutoff of ADC; AUC, the largest area under the ROC curve.

There was no statistically significant difference between the AUC for f90 and that for nCBV90.

^a Numbers in parentheses are 95% confidence intervals.

any visual discordance between the nCBV and IVIM-derived perfusion parameters for differentiating recurrent tumor and treatment effect. However, the correlation coefficient between f90 and nCBV90 was not as high as we had expected. There can be a number of reasons that account for this correlation result. The most important reason could be that these 2 perfusion parameters represent different aspects of tumor vessels. CBV measures mainly microvascular attenuation, and f measures microscopic translational motions associated with microcirculation of blood. Similarly, Jain et al¹³ reported that CBV showed a significant positive correlation with microvascular attenuation, whereas permeability parameter showed a significant positive correlation with microvascular cellular proliferation, which suggests that these perfusion parameters represent different aspects of tumor vessels. Moreover, spin-echo-based IVIM imaging has a substantially different vessel size sensitivity profile from that of gradient-echo-based DSC MR imaging. Further studies that correlate the IVIM-derived perfusion fraction with various MR perfusion parameters, including CBF and permeability parameters, are needed for understanding the exact meaning of the IVIM-derived perfusion parameter.

On quantitative analysis, 4 of 31 patients with recurrent tumors showed false-negative findings on both IVIM and DSC perfusion MR images. The detailed mechanism of these concordance false-negative findings of the 2 imaging methods remains unclear. However, the possible mechanism is that tumor vessels can be compromised as the result of the rapid growth of the tumor cells, necrosis, and increased permeability of the vessels causing interstitial edema, which can result in compression of the smaller vessels, also leading to areas of hypoperfusion. Another mechanism may be a technical limitation that the diffusion parameters estimated from the biexponential model could be sensitive to noise and to the initial values used for data fitting.

DWI with the use of quantitative summary measures such as the ADC has shown the potential to distinguish tumor regrowth from radiation injury. Several previous studies have shown that the ADC value with a monoexponential model can help to differentiate tumor recurrence from treatment-related change.^{14,15} Our study showed that D10 differed more significantly between the recurrent tumor and the treatment effect groups than did ADC10. Although the exact pathophysiologic mechanism for determining the difference between the ADC10 and D10 results is unclear, the significant perfusion difference between the recurrent tumor and the treatment effect groups may contribute to the ADC-D difference. Similarly, Yamada et al¹⁶ reported lower

IVIM-derived D values compared with ADC in enhancing lesions of the liver, confirming that ADC is contaminated by perfusion.

To date, no objective study of IVIM MR imaging has been used to assess the treatment response of brain tumor. IVIM MR imaging has several major advantages. First, it is clinically relevant to simultaneously obtain diffusion and perfusion information¹⁷ and can provide ADC or D-map-guided perfusion measures

without a co-registration processing step. Second, although we used a contrast-enhanced protocol for direct comparison between DSC perfusion MR and IVIM parameters, IVIM MR imaging can provide perfusion information without the need for intravenous contrast media. This is particularly relevant in patients with compromised renal function or severe allergies and those who cannot be given intravenous, gadolinium-based contrast media.¹⁸ Last, the IVIM method can provide standardized values if the same modeling was used; therefore this method has potential to be used in multicenter clinical trials.

Our study has several limitations. First, the number of study patients was relatively small. Further prospective analyses with a larger number of patients will be needed to validate our results. Second, 9 of 51 study patients underwent stereotactic biopsy, which is subject to sampling errors, at the time of second-look surgery, and our pathology estimates of regions of recurrent tumor versus treatment effect were not determined by direct correlation between tissue-specimen histopathology and corresponding region of parametric map, as shown by Hu et al.² However, in clinical practice, such quantitative correlation is very difficult to achieve and may be less clinically important than determining a robust method for distinguishing areas of abnormality that are unlikely to progress rapidly from areas that are likely to progress. Last, the set of b-values used in our study was not optimized. To achieve a shorter examination time without sacrificing the precision of the techniques, the b-values might be further optimized in a separate study as a function of the available IVIM parameter values in the brain.

CONCLUSIONS

IVIM-derived perfusion and diffusion parameters can act as non-invasive imaging biomarkers for assessing the treatment response in patients with posttreatment glioblastoma.

REFERENCES

- Barajas RF, Chang JS, Segal MR, et al. **Differentiation of recurrent glioblastoma multiforme from radiation necrosis after external beam radiation therapy with dynamic susceptibility-weighted contrast-enhanced perfusion MR imaging.** *Radiology* 2009;253:486–96
- Hu LS, Baxter LC, Smith KA, et al. **Relative cerebral blood volume values to differentiate high-grade glioma recurrence from post-treatment radiation effect: direct correlation between image-guided tissue histopathology and localized dynamic susceptibility-weighted contrast-enhanced perfusion MR imaging measurements.** *AJNR Am J Neuroradiol* 2009;30:552–58
- Le Bihan D, Breton E, Lallemand D, et al. **MR imaging of intravoxel**

- incoherent motions: application to diffusion and perfusion in neurologic disorders.** *Radiology* 1986;161:401–07
4. Le Bihan D, Breton E, Lallemand D, et al. **Separation of diffusion and perfusion in intravoxel incoherent motion MR imaging.** *Radiology* 1988;168:497–505
 5. Tihan T, Barletta J, Parney I, et al. **Prognostic value of detecting recurrent glioblastoma multiforme in surgical specimens from patients after radiotherapy: should pathology evaluation alter treatment decisions?** *Hum Pathol* 2006;37:272–82
 6. Le Bihan D, Turner R, MacFall JR. **Effects of intravoxel incoherent motions (IVIM) in steady-state free precession (SSFP) imaging: application to molecular diffusion imaging.** *Magn Reson Med* 1989;10:324–37
 7. Dyvorne HA, Galea N, Nevers T, et al. **Diffusion-weighted imaging of the liver with multiple b values: effect of diffusion gradient polarity and breathing acquisition on image quality and intravoxel incoherent motion parameters: a pilot study.** *Radiology* 2012;266:920–29
 8. Le Bihan D. **Intravoxel incoherent motion perfusion MR imaging: a wake-up call.** *Radiology* 2008;249:748–52
 9. Fatterpekar GM, Galheigo D, Narayana A, et al. **Treatment-related change versus tumor recurrence in high-grade gliomas: a diagnostic conundrum: use of dynamic susceptibility contrast-enhanced (DSC) perfusion MRI.** *AJR Am J Roentgenol* 2012;198:19–26
 10. Sugahara T, Korogi Y, Tomiguchi S, et al. **Posttherapeutic intraaxial brain tumor: the value of perfusion-sensitive contrast-enhanced MR imaging for differentiating tumor recurrence from nonneoplastic contrast-enhancing tissue.** *AJNR Am J Neuroradiol* 2000;21:901–09
 11. Folkman J. **The role of angiogenesis in tumor growth.** *Semin Cancer Biol* 1992;3:65–71
 12. Jain R, Gutierrez J, Narang J, et al. **In vivo correlation of tumor blood volume and permeability with histologic and molecular angiogenic markers in gliomas.** *AJNR Am J Neuroradiol* 2011;32:388–94
 13. Jain R, Narang J, Schultz L, et al. **Permeability estimates in histopathology-proved treatment-induced necrosis using perfusion CT: can these add to other perfusion parameters in differentiating from recurrent/progressive tumors?** *AJNR Am J Neuroradiol* 2011;32:658–63
 14. Provenzale JM, Mukundan S, Barboriak DP. **Diffusion-weighted and perfusion MR imaging for brain tumor characterization and assessment of treatment response.** *Radiology* 2006;239:632–49
 15. Al Sayyari A, Buckley R, McHenry C, et al. **Distinguishing recurrent primary brain tumor from radiation injury: a preliminary study using a susceptibility-weighted MR imaging-guided apparent diffusion coefficient analysis strategy.** *AJNR Am J Neuroradiol* 2010;31:1049–54
 16. Yamada I, Aung W, Himeno Y, et al. **Diffusion coefficients in abdominal organs and hepatic lesions: evaluation with intravoxel incoherent motion echo-planar MR imaging.** *Radiology* 1999;210:617–23
 17. Federau C, Maeder P, O'Brien K, et al. **Quantitative measurement of brain perfusion with intravoxel incoherent motion MR imaging.** *Radiology* 2012;265:874–81
 18. Prince MR, Zhang HL, Roditi GH, et al. **Risk factors for NSF: a literature review.** *J Magn Reson Imaging* 2009;30:1298–308

Semiautomated Volumetric Measurement on Postcontrast MR Imaging for Analysis of Recurrent and Residual Disease in Glioblastoma Multiforme

D.S. Chow, J. Qi, X. Guo, V.Z. Miloushev, F.M. Iwamoto, J.N. Bruce, A.B. Lassman, L.H. Schwartz, A. Lignelli, B. Zhao, and C.G. Filippi

ABSTRACT

BACKGROUND AND PURPOSE: A limitation in postoperative monitoring of patients with glioblastoma is the lack of objective measures to quantify residual and recurrent disease. Automated computer-assisted volumetric analysis of contrast-enhancing tissue represents a potential tool to aid the radiologist in following these patients. In this study, we hypothesize that computer-assisted volumetry will show increased precision and speed over conventional 1D and 2D techniques in assessing residual and/or recurrent tumor.

MATERIALS AND METHODS: This retrospective study included patients with native glioblastomas with MR imaging performed at 24–48 hours following resection and 2–4 months postoperatively. 1D and 2D measurements were performed by 2 neuroradiologists with Certificates of Added Qualification. Volumetry was performed by using manual segmentation and computer-assisted volumetry, which combines region-based active contours and a level set approach. Tumor response was assessed by using established 1D, 2D, and volumetric standards. Manual and computer-assisted volumetry segmentation times were compared. Interobserver correlation was determined among 1D, 2D, and volumetric techniques.

RESULTS: Twenty-nine patients were analyzed. Discrepancy in disease status between 1D and 2D compared with computer-assisted volumetry was 10.3% (3/29) and 17.2% (5/29), respectively. The mean time for segmentation between manual and computer-assisted volumetry techniques was 9.7 minutes and <1 minute, respectively ($P < .01$). Interobserver correlation was highest for volumetric measurements (0.995; 95% CI, 0.990–0.997) compared with 1D (0.826; 95% CI, 0.695–0.904) and 2D (0.905; 95% CI, 0.828–0.948) measurements.

CONCLUSIONS: Computer-assisted volumetry provides a reproducible and faster volumetric assessment of enhancing tumor burden, which has implications for monitoring disease progression and quantification of tumor burden in treatment trials.

ABBREVIATIONS: CAV = computer-assisted volumetry; GBM = glioblastoma multiforme; RANO = Response Assessment in Neuro-Oncology

Glioblastoma multiforme (GBM) is an invasive and highly aggressive tumor with a median patient survival of 14.6 months with combined radiation therapy and temozolomide.¹ New therapies are being developed to treat GBM, which may decrease morbidity and lengthen the period of progression-free survival. However, to fully use new therapies in the treatment of GBM, quantitative MR imaging metrics are needed to guide therapy, risk stratify patients undergoing therapy, and prognosticate outcome.^{2,3} A major limitation is this lack of prognostic imaging parameters.⁴ Simple radio-

graphic monitoring with freehand measurements of the amount of contrast-enhancing tumor in 2 or 3 planes is commonly used for assessing response to different therapies, which is used to guide treatment strategies.^{5,6} Commonly used techniques include the Response Evaluation Criteria in Solid Tumors and the MacDonald criteria, which use unidimensional and bidimensional measurements, respectively.^{7–9} However, the postsurgical cavity tends to be highly irregular in shape, which may increase the difficulty in obtaining accurate and reproducible measurements. In particular, single-dimensional techniques may be inaccurate, given the propensity of high-grade gliomas to grow in an eccentric and nodular fashion, and may not be reflective of change in actual tumor burden.¹⁰

Received April 14, 2013; accepted after revision June 22.

From the Departments of Radiology (D.S.C., J.Q., X.G., V.Z.M., L.H.S., A.L., B.Z., C.G.F.), Neurology (F.M.I., A.B.L.), and Neurosurgery (J.N.B.), College of Physicians and Surgeons, Columbia University, New York, New York.

Author contributions: guarantors of integrity of entire study: D.S.C., C.G.F.; study concepts/study design: D.S.C., B.Z., A.L., C.G.F.; study data acquisition or data analysis/interpretation: D.S.C., J.Q., X.G., V.Z.M., A.L., B.Z., C.G.F.; manuscript drafting or manuscript revision for important intellectual content: D.S.C., J.Q., X.G., V.Z.M., F.M.I., J.N.B., A.B.L., L.H.S., A.L., B.Z., C.G.F.; manuscript editing: D.S.C., L.H.S., B.Z., C.G.F.; literature research: D.S.C., L.H.S., B.Z., C.G.F.; approval of the final version of the submitted manuscript: D.S.C., J.Q., X.G., V.Z.M., F.M.I., J.N.B., A.B.L., L.H.S., A.L., B.Z., C.G.F.

Paper previously presented in part at: 51st Annual Meeting of the American Society of Neuroradiology, May 18–23, 2013; San Diego, California, under the title “Semi-Automated Measurement of Recurrent and Residual Disease in Glioblastoma Multiforme: A Potential New Objective Metric.”

Please address correspondence to Daniel S. Chow, MD, College of Physicians and Surgeons, Columbia University Medical Center, 180 Fort Washington Ave, HP-3-311, New York, NY; e-mail: dsc9004@nyp.org

<http://dx.doi.org/10.3174/ajnr.A3724>

Recently, the Response Assessment in Neuro-Oncology (RANO) Working Group proposed new recommendations for assessing response criteria for high-grade gliomas, which included a modification to the MacDonald criteria.¹¹ While the RANO criterion used 2D measurements, the Working Group suggested that volumetric analysis could provide more accurate measurements with respect to bidimensional techniques.¹¹ Outside the central nervous system, volumetric assessment has been proved superior to unidimensional measurements when used to assess treatment response in hepatic, pulmonary, and pancreatic malignancies.^{12,13}

Despite the potential advantages of volumetric assessment, this technique requires manual outlining of the contrast-enhancing border, which can be both time-consuming and technically challenging.^{5,10} This technique may be further limited in cases with irregular enhancement and subependymal extension.¹⁰ For these reasons, computer-aided volumetry techniques applied to the contrast-enhancing tissue represent a potential tool to aid the radiologist in following these patients. Such techniques may increase both the accuracy and reproducibility in assessing GBM recurrence. Thus far, such automation has been explored in the assessment of advanced lung cancer with promising results.¹⁴ Application of computer-assisted volumetry (CAV) has been explored for the evaluation of gliomas; however, these studies have dealt with native nontreated disease and have not been validated against other measurement techniques.¹⁵⁻¹⁷

In this study, we describe a novel CAV technique for assessment of tumor burden in the patient with GBM. Specifically, we describe the reliability and feasibility of this technique compared with traditional linear-based measurements in the patient with postresection GBM.

MATERIALS AND METHODS

Subjects

After institutional review board approval of this Health Insurance Portability and Accountability Act–complaint study, a query of the neuropathology department data base at our institution from January 2011 to November 2012 was conducted. Specifically, patients who had undergone primary resection of glioblastomas were evaluated. Given that many of our patients are referred from other facilities for resections, we specifically examined patients who had undergone MR imaging evaluation at our institution where standardization of MR imaging protocols allows a better comparison of scans. A retrospective review of these medical records was conducted to determine demographic information including sex, age at time of resection, extent of resection, and duration between follow-up imaging examinations. All patients received combination radiation therapy with concurrent chemotherapy following maximal resection.

Imaging Techniques

All imaging was performed on a 3T MR imaging system (Signa; GE Healthcare, Milwaukee, Wisconsin) by using an 8-channel head-array coil (Signa HDxt; GE Healthcare). We obtained the following sequences: axial T1-weighted pre- and postcontrast, T2, and FLAIR. Volumetric acquisitions were also acquired for all postcontrast images with a T1-weighted 3D inversion recovery fast spoiled gradient-recalled sequence with the following parameters: TI, 450 ms; TR, 10.2 ms; TE, 4.2 ms; α , 13°; bandwidth, 25

KHz; FOV, 25 cm; matrix, 256 × 256; section thickness, 1.2 mm. Total scanning time was approximately 4 minutes 15 seconds. Postcontrast images were acquired by using intravenous gadobenate dimeglumine (MultiHance; Bracco, Milan, Italy) with a weight-based dose of 0.2 mL/kg. The time between intravenous injection and postcontrast imaging was 5 minutes. All immediate postoperative imaging was performed within 2 days of resection by using the same MR imaging parameters. Follow-up imaging was performed between 2 and 4 months after surgery.

Imaging Interpretation

Two radiologists (C.G.F. and A.B.L.), who were blinded to the final calculated volume, each measured the major and minor axes for each tumor on postcontrast sequences. The major axis was defined as the longest diameter, and the minor axis was defined as the longest diameter perpendicular to the major axis. Gross total resection was defined as the absence of enhancing tissue at postoperative examination. Nonmeasurable lesions were defined as enhancing masses with lesions with maximal thickness of <4 mm (2 times the imaging section thickness) to reduce variability from volume averaging.¹¹ Additionally, the surgical cavity, cysts, and necrosis were not included in measurements per the RANO criteria.¹¹ In cases of multiple enhancing foci, individual diameters were measured and summed for response evaluation.^{10,11}

Manual volumetric segmentations were performed by 1 radiologist (D.S.C.), who was blinded to the final CAV calculation, by performing manual tracing around the enhancing lesion on volumetric sequences (section thickness, 0.2 mm). All manual segmentations were performed at a dedicated workstation (Advantage Workstation, Version 4.3; GE Healthcare Europe, Buc, France). All measurements were performed by comparison with precontrast T1 images to avoid T1 shortening effects from postsurgical changes (ie, blood products). The time required to perform manual segmentation was also recorded.

CAV measurements were performed by a separate radiologist (J.Q.) who was blinded to final manual volumetric measurements. Tumor contours were delineated on immediate and 2- to 4-month postsurgery T1-weighted MR images by using an in-house, proprietary segmentation algorithm developed to assist the computer-aided volume calculation of this project. Our CAV algorithm was originally developed for hepatic lesions and has since been adapted for different applications including brain and renal malignancies, lymphoma, and peritoneal mesothelioma.¹⁸⁻²² The semiautomated algorithm combines the region-based active contours and a level set approach and has the advantages of easy initialization, quick segmentation, and efficient modification. An operator manually selects a region of interest that roughly encloses the tumor on a single image. Boundary localization of the tumor and exclusion of the nonviable tissue inside the tumor are then performed automatically by the developed algorithm. Once the segmentation is completed on an image, the tumor contour is propagated to its neighboring images, serving as an initial region of interest for subsequent segmentations on the neighboring images. This process continues iteratively until all the tumor images are segmented. To ensure correct results, computer-generated tumor contours are superimposed on the original images for inspection and modification as needed by a radiologist. Once the segmentation is finalized, tumor volume is automatically calculated (Fig 1). This seg-

mentation algorithm and a number of manual interaction functions, such as selection of a region of interest and modification of suboptimal contour results, have been integrated into a user-friendly image-viewing system developed with the Matlab (MathWorks, Natick, Massachusetts) computer language by the research group.

Definition of Response

Tumor response was assessed for each study by using established 1D, 2D and volumetric standards extrapolated from bi-dimensional standards.⁷⁻⁹ Cases of discrepancy between readers were re-reviewed to reach a consensus. Volumetric standards were established by using an extrapolation from the MacDonald criteria by converting orthogonal measurements to a volume assuming a spheric lesion (Table 1).¹⁰ "Complete response" was defined as complete absence of contrast-enhancing tumor for all techniques. "Partial response" was defined as >30% decrease in the sum of maximal diameters for 1D, >50% decrease in the product of orthogonal diameters for 2D, and >65% in volume for volumetric techniques. "Progression of disease" was defined as a 20% increase in the sum of maximal diameters for 1D, >25% increase in the product of orthogonal diameters for 2D, and >40% increase in volume for volumetric techniques. "Stable disease" was defined as all other changes for 1D, 2D, and volumetric techniques. Tumor response counts and discrepancy between agreements were calculated among the different measuring methods.

Statistical Tests

Manual and semiautomated volumetric measurements and segmentation times were compared by using a paired *t* test. Pearson correlation coefficients with corresponding confidence intervals were used to assess interobserver correlations of 1D, 2D, and volumetric measurements. The inter-rater agreement statistic with

corresponding confidence intervals was calculated for tumor response by using weighted κ values. κ values were interpreted as follows: 0.40–0.60, moderate; 0.61–0.80, good; and 0.81–1.00, very good. Statistical analysis was conducted with MedCalc for Windows, Version 12.2.1 (MedCalc Software, Mariakerke, Belgium). A *P* value < .05 was considered statistically significant.

RESULTS

Subjects

In total, we identified 90 patients who had a GBM resection at our institution between January 2011 and November 2012, of whom 32.2% (29/90) had undergone all standardized postoperative MR imaging at our institution. The mean age of patients was 62.2 ± 8.5 years (range, 38–81 years); of whom 55% (16/29) were men and 45% (13/29) were women. With respect to the extent of resection, 5/29 and 24/29 underwent gross total resection and subtotal resection, respectively. Demographic information is summarized in Table 2. The mean time to follow-up from baseline postoperative imaging was 12.3 ± 3 weeks (range, 6–16 weeks).

Disease Response

Discrepancies in disease response for 1D, 2D, and volumetric techniques were encountered in 17.2% (5/29), 10.3% (3/29), and 3.4% (1/29) of patients. Following review of discrepancies, the complete response rate was 3.4% (1/29) for all measuring techniques. The partial response rate was 10.3% (3/29), 10.3% (3/29), and 6.9% (2/29) for 1D, 2D, and CAV techniques, respectively. The stable disease rate was 10.3% (3/29), 10.3% (3/29), and 17.2% (5/29) for 1D, 2D, and CAV techniques, respectively. The progressive disease rate was 75.9% (22/29), 75.9% (22/29), and 72.4% (21/29) for 1D, 2D, and CAV techniques, respectively. These results are summarized in Table 3.

Discrepancies in disease classification between 1D and 2D compared with CAV were observed in 10.3% (3/29) and 17.2% (5/29) of cases (Figs 2 and 3). The discrepancy between 1D and 2D was 6.8% (2/29).

Analysis of Measurement Techniques

The mean volume for manual and CAV analyses was 10.0 and 9.5 mL, respectively ($P = .11$). The mean time for segmentation between manual and CAV techniques was 9.7 minutes and <1 minute, respectively ($P < .01$). The Pearson correlation between manual and CAV analysis was 0.995 (95% CI, 0.990–0.997). This correlation was significantly higher than interobserver correlations for 1D (Pearson correlation, 0.826; 95% CI, 0.695–0.904; $P < .0001$) and 2D

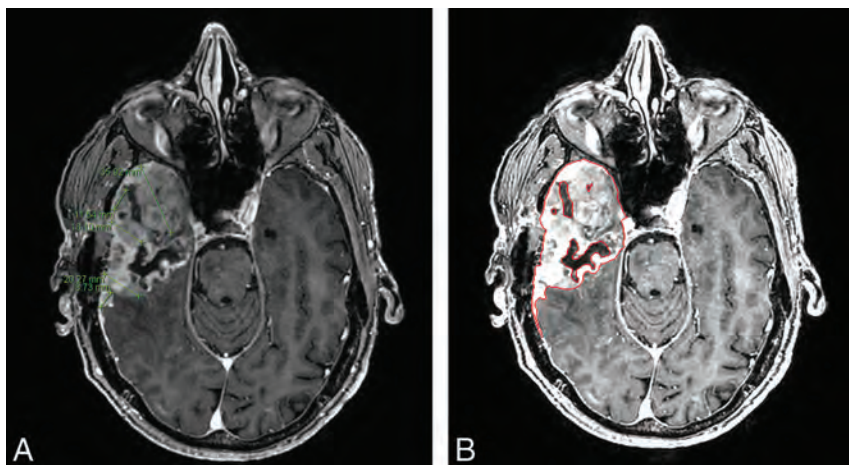


FIG 1. Comparison of linear 1D measurements (A) and CAV analysis (B) in a 64-year-old man with glioblastoma multiforme 11 weeks following resection. Our readers found volumetric analysis preferable, given the irregularity of recurrence.

Table 1: Definition of response criteria for unidimensional (RECIST), bidimensional (Macdonald), and volumetric techniques

Criteria	CR	PR	SD	PD
RECIST	Resolution of all enhancement	$\geq 30\%$ Decrease in sum of max dimensions	All others	$\geq 20\%$ Increase in sum of max dimensions
Macdonald	Resolution of all enhancement	$\geq 50\%$ Decrease in product of 2 orthogonal dimensions	All others	$\geq 25\%$ Increase in product of 2 orthogonal dimensions
Volumetric	Resolution of all enhancement	$\geq 65\%$ Decrease in volume	All others	$\geq 40\%$ Increase in volume

Note:—CR indicates complete response; PR, partial response; SD, stable disease; PD, progression of disease; RECIST, Response Evaluation Criteria in Solid Tumors; max, maximal.

(Pearson correlation, 0.905; 95% CI, 0.828–0.948; $P < .0001$) measurements (Table 4). No significant difference was observed between 1D and 2D correlations ($P = .12$). With regard to classifying disease response, inter-reader agreement was significantly higher for volumetric techniques ($\kappa = 0.948$; 95% CI, 0.845–1.000) compared with 1D ($P = .0002$; $\kappa = 0.760$; 95% CI, 0.682–1.000) and 2D ($P = .01$;

$\kappa = 0.851$; 95% CI, 0.555–0.966) measurements (Table 5). No significant difference was observed between 1D and 2D agreements ($P = .25$).

DISCUSSION

Surveillance and management of patients with GBM are reliant on imaging; however, measurement of residual disease can be challenging. In the present study, we examined a CAV approach to quantify residual disease and noted no significant difference compared with manual volumetric measurements, which are time-consuming and impractical in a busy clinical or academic practice. Additionally, CAV assessment was least variable compared with unidimensional and bidimensional techniques. These results are in line with other studies comparing manual volumetric tracing with diameter-based approaches, which have also noted less inter-reader and intrareader variability for volumetric techniques.²³ While volumetric analysis is technically challenging and time-consuming, the CAV process that we have developed was both significantly faster and reliable, making application for routine clinical use and investigative purposes feasible. Other studies have described similar computer-aided techniques in the evaluation of gliomas; however, validation against other measurement techniques is lacking.¹⁵

Bidimensional techniques used in the MacDonald and RANO criteria are currently the most commonly used techniques for GBM assessment; however, studies have reported high interobserver and intraobserver variability, even among individuals with specialty training in neuroradiology.^{24,25} The increased variability in diameter-based approaches likely stems from the inherent irregularities in GBM. Specifically, GBMs are not solid ellipsoid lesions but instead typically display complex morphology with infiltrative margins and eccentric growth and demonstrate heterogeneity with areas of cystic degeneration and necrosis. Additionally, linear measurements may be affected by differences in head positioning at the time of examination and scan section techniques. These limitations are further compounded in the postoperative patient in whom blood products may be mistaken for enhancing tumor and the surgical cavity itself may have collapsed.²⁶

Assessing residual volume in patients with GBM has been shown to be a significant and independent predictor.^{4,27,28} Intuitively, 3D volumetric analysis is a more accurate method for assessing tumor size compared with alternative linear-based techniques.^{23,26,29} Dempsey et al⁵ found volumetric analysis to be predictive of survival compared with diameter-based analysis, which failed to adequately assess tumor size in recurrent gliomas. Such volumetric

Table 2: Demographic information of included patients

Variable	Value
Male/female (No.)	16:13
Mean age at resection (yr, SD)	62.2 (8.5)
Mean follow-up (wk, SD)	12.3 (3.0)
Extent of resection (No., %)	
GTR	5 (17.2)
STR	24 (82.8)

Note:—GTR indicates gross total resection; STR, subtotal resection.

Table 3: Response counts of 1D, 2D, and CAV ($n = 29$)

	CR	PR	SD	PD
1D	1	3	3	22
2D	1	4	2	22
CAV	1	2	5	21

Note:—CR indicates complete response; PR, partial response; SD, stable disease; PD, progression of disease.

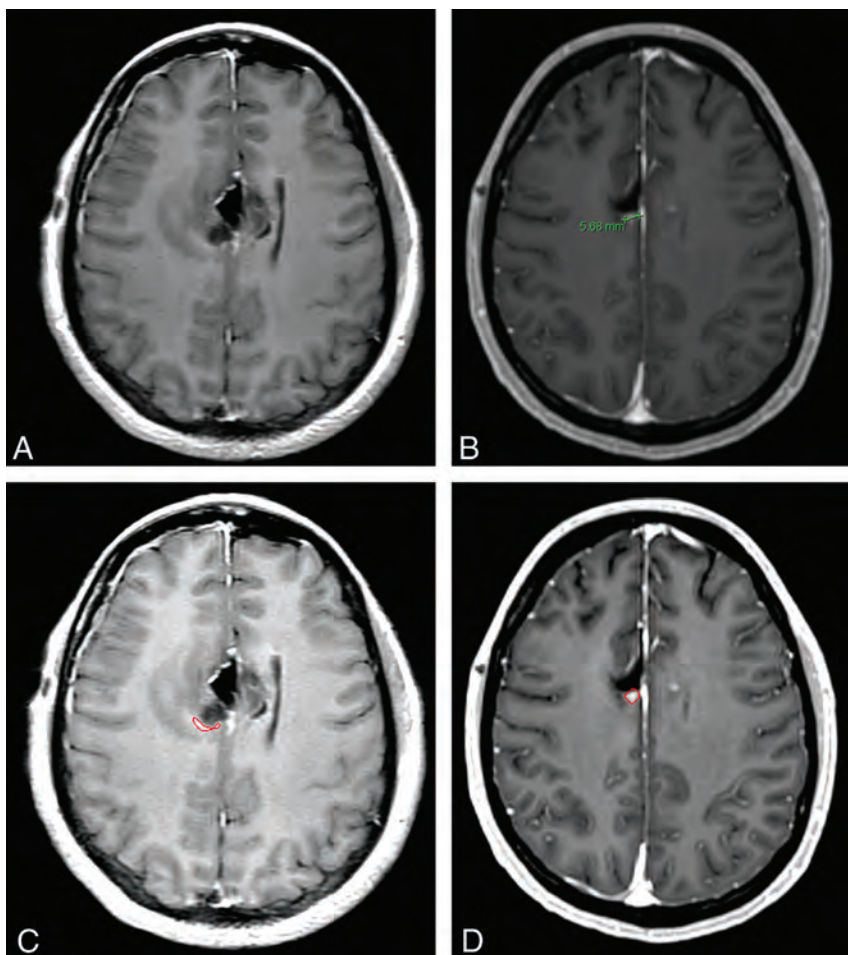


FIG 2. Disease status categorization in a 38-year-old woman with glioblastoma following resection, at 24 hours and at 12 weeks. 1D measurement found the contrast enhancement on initial postoperative imaging nonmeasurable (A) and subsequently labeled this case disease progression on follow-up imaging (B). CAV measurement labeled this case stable disease between baseline (C) and follow-up imaging (D).

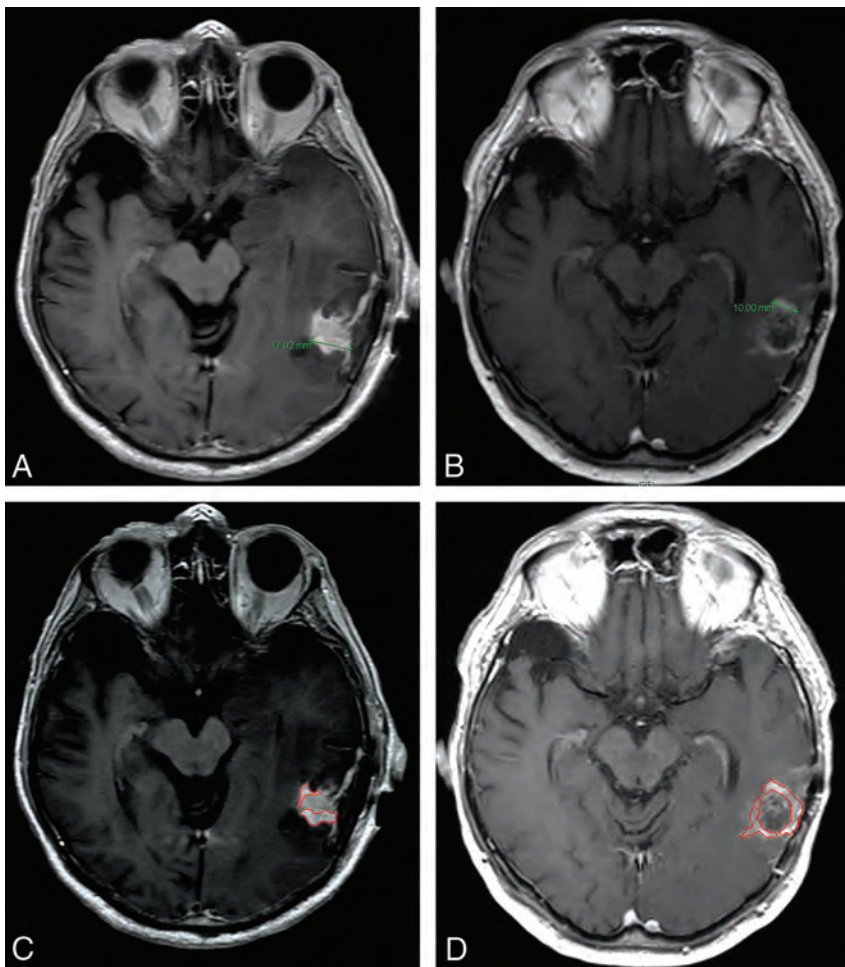


FIG 3. Disease status categorization in an 81-year-old man with glioblastoma following resection at 24 hours and at 12 weeks. 1D measurement labeled this case partial response between baseline (A) and follow-up imaging (B). CAV measurement labeled this case stable disease between baseline (C) and follow-up imaging (D).

Table 4: Interobserver correlation^a of 1D, 2D, and volumetric^b measurements

	Interobserver Pearson Correlation	95% CI	
		Lower Limit	Upper Limit
1D	0.814	0.686	0.897
2D	0.904	0.825	0.948
Volumetric	0.995	0.990	0.997

^a Assessed with the Pearson correlation coefficient.

^b Manual and CAV analysis.

Table 5: Interobserver agreement^a of 1D, 2D, and volumetric^b measurements

	Interobserver κ Correlation	95% CI	
		Lower Limit	Upper Limit
1D	0.760	0.555	0.966
2D	0.851	0.682	1.000
Volumetric	0.948	0.845	1.000

^a Assessed with the κ coefficient.

^b Manual and CAV analysis.

assessment has several unique advantages over linear-based techniques, including its ability to objectively accommodate the irregular and eccentric growth of GBMs, exclude cystic and necrotic components, and account for changes in the shape of the postoperative resection cavity.^{10,29}

Accurate assessment of tumor volume is important for clinical management and particularly in the development of new therapies and trials. This is of particular importance in the evaluation of GBM, given its exceedingly aggressive behavior.³⁰ When assessing clinical response determined by different models, we observed a 17.2% difference in outcome classification when comparing volumetric with bidimensional techniques; however, similar studies have observed up to a 40% discrepancy.²⁴ Additionally, disease status categorizations are defined on thresholds based on presumed ellipsoid geometry, which may, in turn, lead to increased variability in assessing GBM, given the inherent morphologic features. Such variability has been observed within 2D measurements by the same reader with a reported 14% false-positive rate for diagnosis of disease progression in otherwise stable disease.²⁵

In this study, we subjectively observed a greater discordance between extrapolated volumes of linear-based techniques and volumetric assessment for tumors with increased eccentricity and necrotic changes. Specifically, linear measurements obtained for eccentric tumors would often be overestimated. Additionally, linear measurements obtained for cystic and necrotic tumors would often be overestimated. We also observed that extrapolated volumes for linear-based measurements of rounded nodular lesions were closer to the volumetric assessment.

For reasons described previously, linear-based measurements are problematic for GBM assessment, given that these tumors are not typically solid ellipsoid lesions but display complex morphology. Such inconsistencies and potential inaccuracies may result in classifying effective treatments as ineffective or ineffective treatments as effective, which underscores the need for a reliable, reproducible, standard process of accurately determining tumor volume.⁶ With respect to use of computer-aided tools, researchers in body imaging have previously demonstrated improved accuracy over linear-based measurements by using a similar automated technique in the evaluation of lung, liver, and lymph node tumors.⁶

When one interprets the results of our study, several limitations should be kept in mind. First, this study is retrospective in design and subject to its limitations. Second, we have limited our analysis to enhancing contrast-enhancing tissue, which only represents increased blood-brain barrier permeability. While this may represent enhancing tumor, other possibilities may include inflammation, subacute ischemia, and so forth. However, there is no clear consensus on how to best assess the extent of residual and/or recurrent disease, which tends to default to the standard 1D or 2D measurement techniques, which are suboptimal. Additionally, there is no clear objective consensus on how to assess nonenhancing disease. Last, several

patients were imaged within 12 weeks following resection, which is within the timeframe of pseudoprogression. It would have been optimal to repeat those studies to ensure that enhancement detected by CAV was indeed disease progression.¹¹ However, histopathologic confirmation of recurrent disease was available for all except 1 patient imaged within the timeframe of pseudoprogression. Furthermore, the primary goal of this study was to assess the volumetric technique in comparison with other methods.

CONCLUSIONS

We have demonstrated the feasibility of a semiautomated segmentation technique to determine recurrent and/or residual tumor volume in patients with GBM, and this more reliable, reproducible, and significantly faster volumetric assessment of enhancing tumor burden has implications for the monitoring of disease progression and a potential role in therapy and novel treatment trials. Future studies should address patient outcomes with volumetric disease categorization, assess reliability among a larger number of readers, and compare reliability among different CAV algorithms.

Disclosures: Andrew B. Lassman—UNRELATED: Consultancy: Genentech, Merck Sharp & Dohme, GlaxoSmithKline, Abbott, Ludwig Institute for Cancer Research, Kyowa Hakko Kirin Pharma, Novartis, RadMD, Roche, CampusBio, Qatar National Research Fund, Italian Association for Cancer Research, Grants/Grants Pending: Abbott,* Aeterna Zentaris,* Agenus,* Amgen,* Bayer and Onyx,* Boehringer Ingelheim,* Bristol-Myers Squibb,* Cell-dex,* Genentech,* Keryx Biopharmaceuticals,* Medimmune,* Merck Sharp & Dohme,* Millenium,* Northwest Biotherapeutics,* Novartis,* Pfizer,* Plexxicon,* Roche,* Sigma Tau,* Theorum Clinical Research,* Payment for Lectures (including service on Speakers Bureaus): Merck Sharp & Dohme, Omniprex, American College of Radiation Oncology, Travel/Accommodations/Meeting Expenses Unrelated to Activities Listed: American Academy of Neurology, United Council for Neurologic Subspecialties. Binsheng Zhao—UNRELATED: Patents (planned, pending, or issued): A patent for our in-house segmentation algorithm is pending (no payment received). Christopher G. Filippi—UNRELATED: Consultancy: MRI Advisory Board for Guerbet LLC. Comments: I spent 1 day listening to lectures on an ionic macrocyclic contrast agent developed by this company and used primarily in Europe with no cases of nephrogenic systemic fibrosis to date. I offered advice to the company on whether such an agent would be beneficial in the United States. I received a \$2000 honorarium for the day, Grants/Grants Pending: 10% effort on R01CA161404 of Dr Jeffrey N. Bruce, neurosurgeon, Comments: Phase II trial on pigs with new chemotherapy for GBM (I am responsible for the MR imaging component). *Money paid to the institution.

REFERENCES

- Stupp R, Hegi ME, Mason WP, et al. **Effects of radiotherapy with concomitant and adjuvant temozolomide versus radiotherapy alone on survival in glioblastoma in a randomised phase III study: 5-year analysis of the EORTC-NCIC trial.** *Lancet Oncol* 2009;10:459–66
- Reardon DA, Galanis E, DeGroot JF, et al. **Clinical trial end points for high-grade glioma: the evolving landscape.** *Neuro Oncol* 2011;13:353–61
- van den Bent MJ, Vogelbaum MA, Wen PY, et al. **End point assessment in gliomas: novel treatments limit usefulness of classical Macdonald's criteria.** *J Clin Oncol* 2009;27:2905–08
- Iliadis G, Kotoula V, Chatzizotiriou A, et al. **Volumetric and MGMT parameters in glioblastoma patients: survival analysis.** *BMC Cancer* 2012;12:3
- Dempsey MF, Condon BR, Hadley DM. **Measurement of tumor "size" in recurrent malignant glioma: 1D, 2D, or 3D?** *AJNR Am J Neuroradiol* 2005;26:770–76
- Schwartz LH, Ginsberg MS, DeCorato D, et al. **Evaluation of tumor measurements in oncology: use of film-based and electronic techniques.** *J Clin Oncol* 2000;18:2179–84
- Therasse P, Arbuck SG, Eisenhauer EA, et al. **New guidelines to evaluate the response to treatment in solid tumors: European Organization for Research and Treatment of Cancer, National Cancer Institute of the United States, National Cancer Institute of Canada.** *J Natl Cancer Inst* 2000;92:205–16

- Macdonald DR, Cascino TL, Schold SC Jr, et al. **Response criteria for phase II studies of supratentorial malignant glioma.** *J Clin Oncol* 1990;8:1277–80
- Eisenhauer EA, Therasse P, Bogaerts J, et al. **New response evaluation criteria in solid tumours: revised RECIST guideline (version 1.1).** *Eur J Cancer* 2009;45:228–47
- Henson JW, Ulmer S, Harris GJ. **Brain tumor imaging in clinical trials.** *AJNR Am J Neuroradiol* 2008;29:419–24
- Wen PY, Macdonald DR, Reardon DA, et al. **Updated response assessment criteria for high-grade gliomas: response assessment in neuro-oncology working group.** *J Clin Oncol* 2010;28:1963–72
- Welsh JL, Bodeker K, Fallon E, et al. **Comparison of response evaluation criteria in solid tumors with volumetric measurements for estimation of tumor burden in pancreatic adenocarcinoma and hepatocellular carcinoma.** *Am J Surg* 2012;204:580–85
- Zhao B, Oxnard GR, Moskowitz CS, et al. **A pilot study of volume measurement as a method of tumor response evaluation to aid biomarker development.** *Clin Cancer Res* 2010;16:4647–53
- Mozley PD, Bendtsen C, Zhao B, et al. **Measurement of tumor volumes improves RECIST-based response assessments in advanced lung cancer.** *Transl Oncol* 2012;5:19–25
- Kanly CW, Ding D, Mehta AI, et al. **A novel method for volumetric MRI response assessment of enhancing brain tumors.** *PLoS One* 2011;6:e16031
- Egger J, Kapur T, Fedorov A, et al. **GBM volumetry using the 3D Slicer medical image computing platform.** *Sci Rep* 2013;3:1364
- Zhu Y, Young GS, Xue Z, et al. **Semi-automatic segmentation software for quantitative clinical brain glioblastoma evaluation.** *Acad Radiol* 2012;19:977–85
- Computer-aided tumor segmentation using local region-based active contours.** Columbia University Invention Report IR #2906
- Methods and Systems for Segmentation of Organs and Tumors and Objects. Patent (pending) PCT/US13/36166. April, 2013
- Zaretsky J, Guo X, Fu J, et al. **Novel radiologic features to predict hepatocellular carcinoma recurrence after liver transplantation: a pilot study.** In: *62nd Annual Meeting of the American Association for the Study of Liver Diseases (AASLD)*, San Francisco, California. Nov 3–8, 2011
- Abou-Alfa GK, Zhao B, Capanu M, et al. **Effects of Radiologic Tumor Response of Anti-Glypican 3 GC33 and Multi Tyrosine Kinases Inhibitor Sorafenib in Hepatocellular Carcinoma.** In: *24th EORTC-NCI-AACR Symposium on Molecular Targets and Cancer Therapeutics*. Dublin, Ireland. November 6–9, 2012
- Leinwand J, Zhao B, Guo X, et al. **Quantitative CT peritoneography in malignant peritoneal mesothelioma patients receiving intraperitoneal chemotherapy.** *Ann Surg Oncol* 2013 May 24. [Epub ahead of print]
- Sorensen AG, Patel S, Harmath C, et al. **Comparison of diameter and perimeter methods for tumor volume calculation.** *J Clin Oncol* 2001;19:551–57
- Provenzale JM, Mancini MC. **Assessment of intra-observer variability in measurement of high-grade brain tumors.** *J Neurooncol* 2012;108:477–83
- Provenzale JM, Ison C, Delong D. **Bidimensional measurements in brain tumors: assessment of interobserver variability.** *AJR Am J Roentgenol* 2009;193:W515–22
- Sorensen AG, Batchelor TT, Wen PY, et al. **Response criteria for glioma.** *Nat Clin Pract Oncol* 2008;5:634–44
- Keles GE, Lamborn KR, Chang SM, et al. **Volume of residual disease as a predictor of outcome in adult patients with recurrent supratentorial glioblastomas multiforme who are undergoing chemotherapy.** *J Neurosurg* 2004;100:41–46
- Lacroix M, Abi-Said D, Fournay DR, et al. **A multivariate analysis of 416 patients with glioblastoma multiforme: prognosis, extent of resection, and survival.** *J Neurosurg* 2001;95:190–98
- Warren KE, Patronas N, Aikin AA, et al. **Comparison of one-, two-, and three-dimensional measurements of childhood brain tumors.** *J Natl Cancer Inst* 2001;93:1401–05
- Gladwish A, Koh ES, Hoisak J, et al. **Evaluation of early imaging response criteria in glioblastoma multiforme.** *Radiat Oncol* 2011;6:121

Evaluation of Common Structural Brain Changes in Aging and Alzheimer Disease with the Use of an MRI-Based Brain Atrophy and Lesion Index: A Comparison Between T1WI and T2WI at 1.5T and 3T

H. Guo, X. Song, R. Vandorpe, Y. Zhang, W. Chen, N. Zhang, M.H. Schmidt, and K. Rockwood,
for the Alzheimer's Disease Neuroimaging Initiative



ABSTRACT

BACKGROUND AND PURPOSE: The Brain Atrophy and Lesion Index combines several common, aging-related structural brain changes and has been validated for high-field MR imaging. In this study, we evaluated measurement properties of the Brain Atrophy and Lesion Index by use of T1WI and T2WI at 1.5T and 3T MR imaging to comprehensively assess the usefulness of the lower field-strength testing.

MATERIALS AND METHODS: Data were obtained from the Alzheimer's Disease Neuroimaging Initiative. Images of subjects ($n = 127$) who had T1WI and T2WI at both 3T and 1.5T on the same day were evaluated, applying the Brain Atrophy and Lesion Index rating. Criterion and construct validity and interrater agreement were tested for each field strength and image type.

RESULTS: Regarding reliability, the intraclass correlation coefficients for the Brain Atrophy and Lesion Index score were consistently high (>0.8) across image type and field strength. Regarding construct validity, the Brain Atrophy and Lesion Index score differed among diagnostic groups, being lowest in people without cognitive impairment and highest in those with Alzheimer disease ($F > 5.14$; $P < .007$). Brain Atrophy and Lesion Index scores correlated with age ($r > 0.37$, $P < .001$) and cognitive performance ($r > 0.38$, $P < .001$) and were associated with positive amyloid- β test ($F > 3.96$, $P < .050$). The T1WI and T2WI Brain Atrophy and Lesion Index scores were correlated ($r > 0.93$, $P < .001$), with the T2WI scores slightly greater than the T1WI scores ($F > 4.25$, $P < .041$). Regarding criterion validation of the 1.5T images, the 1.5T scores were highly correlated with the 3T Brain Atrophy and Lesion Index scores ($r > 0.93$, $P < .001$).

CONCLUSIONS: The higher field and T2WI more sensitively detect subtle changes in the deep white matter and perivascular spaces in particular. Even so, 1.5T Brain Atrophy and Lesion Index scores are similar to those obtained by use of 3T images. The Brain Atrophy and Lesion Index may have use in quantifying the impact of dementia on brain structures.

ABBREVIATIONS: AD = Alzheimer disease; ADNI = Alzheimer's Disease Neuroimaging Initiative; BALI = Brain Atrophy and Lesion Index; DWM = deep white matter lesions; GM-SV = gray matter lesions and subcortical dilated perivascular spaces; HC = healthy control subjects; MCI = mild cognitive impairment

Aging involves multiple structural changes in the brain that can have an additive effect on cognition.¹⁻³ Such common brain changes include global atrophy, white matter injury, small-

vessel ischemia, and microhemorrhages.⁴⁻⁸ These changes are more frequent and more severe in neurodegenerative and neurovascular conditions such as Alzheimer disease (AD), than in healthy aging.⁹⁻¹¹ To collectively evaluate multiple common brain changes and their additive effects on brain function, a semi-quantitative rating scale, the Brain Atrophy and Lesion Index (BALI), has been validated.^{12,13} The BALI assesses global atrophy and lesions in the supratentorial and the infratentorial compartments, including lesions in the gray matter (eg, cortical infarcts) and

Received May 8, 2013; accepted after revision June 20.

From the Neuroimaging Research Laboratory, Biomedical Translational Imaging Center (H.G., X.S., W.C., N.Z.), QEII & IWK Health Centre (former National Research Council Canada Institute for Biodiagnostics-Atlantic), Halifax, Nova Scotia, Canada; Department of Radiology (G.H., Y.Z., W.C., N.Z.), General Hospital of Tianjin Medical University, Tianjin, China; Departments of Medicine (X.S., K.R.), Radiology (R.V., M.H.S.), and Neurology (K.R.), Dalhousie University, Halifax, Nova Scotia, Canada; and Centre for Health Care of the Elderly (X.S., K.R.) and Department of Diagnostic Imaging (R.V., M.H.S.), QEII Health Sciences Centre, Halifax, Nova Scotia, Canada.

This research was supported by a Catalyst Grant on Secondary Neuroimaging Analysis from the Canadian Institutes of Health Research (CIHR CSE125739) and a China-Canada Joint Health Research Project from the National Science Foundation of China and the Canadian Institutes of Health Research (NSF-CIHR81010072). G.H. was supported by a collaborative project between the National Research Council Canada's Institute for Biodiagnostics-Atlantic and the General Hospital of Tianjin Medical University as a visiting postdoctoral research fellow to work in Halifax. K.R.

was supported by Dalhousie Medical Research Foundation as the Kathryn Weldon Chair of Alzheimer's Research.

Please address correspondence to Xiaowei Song, PhD, MScS, Neuroimaging Research Laboratory, Dalhousie University, Suite 3900, 1796 Summer St, Halifax, Nova Scotia B3H 3A7, Canada; e-mail: xiaowei.song@dal.ca

Indicates open access to non-subscribers at www.ajnr.org

Indicates article with supplemental on-line tables

Indicates article with supplemental on-line figures

<http://dx.doi.org/10.3174/ajnr.A3709>

dilated perivascular spaces in the subcortical white matter as well as lesions in the periventricular regions, deep white matter, basal ganglia, and the surrounding regions.^{12,13} Through the use of different datasets, for example, the Alzheimer's Disease Neuroimaging Initiative (ADNI),¹⁴ the BALI has been used to distinguish AD from healthy aging¹⁵ and to evaluate the dynamics of brain structural changes with aging.¹⁶ To date, BALI has been applied only to MR imaging acquired at 3T and 4T to exploit the higher SNR.¹⁷ Although high-field systems represent the mainstream in future research and clinical settings, large amounts of data have been collected at 1.5T. To generalize the BALI to 1.5T MR imaging has potential value in understanding brain aging.

Our goal was to test the measurement properties of the BALI at both 1.5T and 3T MR imaging, for both T1WI and T2WI. In consequence, we compared BALI scores derived from T1WI and T2WI at both 3T and 1.5T and tested the relationship of the score with age, cognitive test scores, AD and mild cognitive impairment (MCI) diagnosis, and AD biomarkers. Our specific objectives were to validate BALI in 1.5T MR imaging by investigating 1) its criterion validity, for example, how well brain images acquired at 1.5T can be used to capture various structural changes in aging, and 2) whether T1WI and T2WI can both be used in the evaluation of global brain changes at 1.5T.

MATERIALS AND METHODS

Data

Data used in the preparation of this article were obtained from the ADNI data base (adni.loni.ucla.edu). The ADNI was launched in 2003 with a primary goal to test whether serial MR imaging, PET, other biologic markers and clinical and neuropsychological assessments can be combined to measure the progression of MCI and early AD. The initial goal of the ADNI was to recruit 800 subjects, but the ADNI has been followed by ADNI-GO and ADNI-2. To date, these 3 protocols have recruited more than 1500 research participants, ages 55–90 years, consisting of cognitively normal older individuals, people with early or late MCI, and people with early AD.¹⁴

For this secondary analysis, data from ADNI participants who had T1WI and T2WI at both 1.5T and 3T on the same day ($n = 135$) were retrieved. Subjects who had at least 1 image with severe artifacts were excluded ($n = 8$). A set of the 4 images from each of the remaining subjects (AD = 37; MCI = 45; healthy control subjects [HC] = 45) was analyzed (ie, the first-time, same-day scans, so that each set represents unique individuals). At both 3T and 1.5T, the T1WI scans used 3D MPRAGE (TR/TE = 2300–3000/3–4 ms; flip angle = 8–9°; section thickness = 1.2 mm; 256 reconstructed axial sections), whereas the T2WI scans used a 2D FSE/TSE (TR/TE = 3000–4000/96–103 ms; flip angle = 90° or 150°; section thickness = 3 mm; 48 axial sections).¹⁸ Clinical assessment data were also obtained, including the Mini-Mental State Examination, Clinical Dementia Rating Scale, and the Alzheimer's Disease Assessment Scale–cognitive subscale.¹⁹ The clinical assessments had been completed within 14 days of the MR imaging scans. Diagnostic categorization (AD, MCI, and HC) had been made by ADNI site physicians in accordance with the National Institute of Neurologic and Communicative Disorders and Stroke/Alzheimer Disease and Related Disorders Association

(NINCDS/ADRDA) criteria and reviewed by ADNI clinical monitors. In addition, for subjects in whom CSF biomarkers were tested, the baseline amyloid- β 1–42 peptide ($A\beta_{1-42}$), phospho- τ , and total τ protein data were obtained (AD = 21, MCI = 28, HC = 23) and their values were dichotomized (positive/negative tests).²⁰

Evaluation of the BALI

The BALI is a semi-quantitative measure, adapted from several existing scales that assess localized structural changes.^{12,13} Index variables integrate information from several sources (in the present report, types and locations of structural lesions) and are well-suited to evaluating change at a system level.²¹ Changes in 7 categories were evaluated by use of BALI (Fig 1; On-line Table 1). These included gray matter lesions and subcortical dilated perivascular spaces (GM-SV), deep white matter lesions (DWM), periventricular white matter lesions, lesions in the basal ganglia and surrounding areas (including the caudate, putamen, globus pallidus, thalamus, and internal capsule), lesions in the infratentorial compartments (including the cerebellum and the brain stem), and global atrophy. In addition, an “other findings” category was included to record other possible changes such as neoplasm, trauma, idiopathic normal-pressure hydrocephalus, focal asymmetry, and deformity, each of which, in our experience, is sometimes seen in older adults, even though no subjects in this sample showed a change in the “other findings” category. A value between 0–3 was assigned to each category on the basis of the severity of change, with a higher score meaning greater severity (Fig 1; On-line Table 1; On-line Figs 1–4). Values of 4 and 5 were also used to capture more severe changes in the DWM and global atrophy categories, without a ceiling effect (On-line Figs 1–4). The BALI total score was calculated as the sum of the subscores of all the 7 categories, with a possible maximum of 25.

Five certified neuroradiologists, each with many years of experience in brain MR imaging evaluation, performed the image evaluation. The raters were trained with the BALI rating method chiefly through studying the rating schema and examples and discussing selected cases. Images were displayed using MRICron (<http://www.nitrc.org/projects/mricron/>). Each rater performed ratings independently, blinded to the information concerning the subject demographics, diagnosis, cognitive test results, and imaging field strength. T1WI and T2WI were assessed separately on different days to minimize possible recall bias. For both T1WI and T2WI, the images were rated in random order. Only axial images were used.

Analysis

We tested interrater agreement to evaluate reliability. To test construct validity, we correlated each of the 4 sets of measures (both field strengths and both image types) with age, cognitive test scores, and biomarkers. Criterion validity refers to comparison with a reference standard²²; in the present study, we used the 3T images as the reference standard and correlated 1.5T images against them. Given that all lesions are less common and less severe in healthy aging people, compared with people with dementia, analyses are presented in relation to cognitive diagnosis. To evaluate the reliability of BALI, interrater agreement was as-

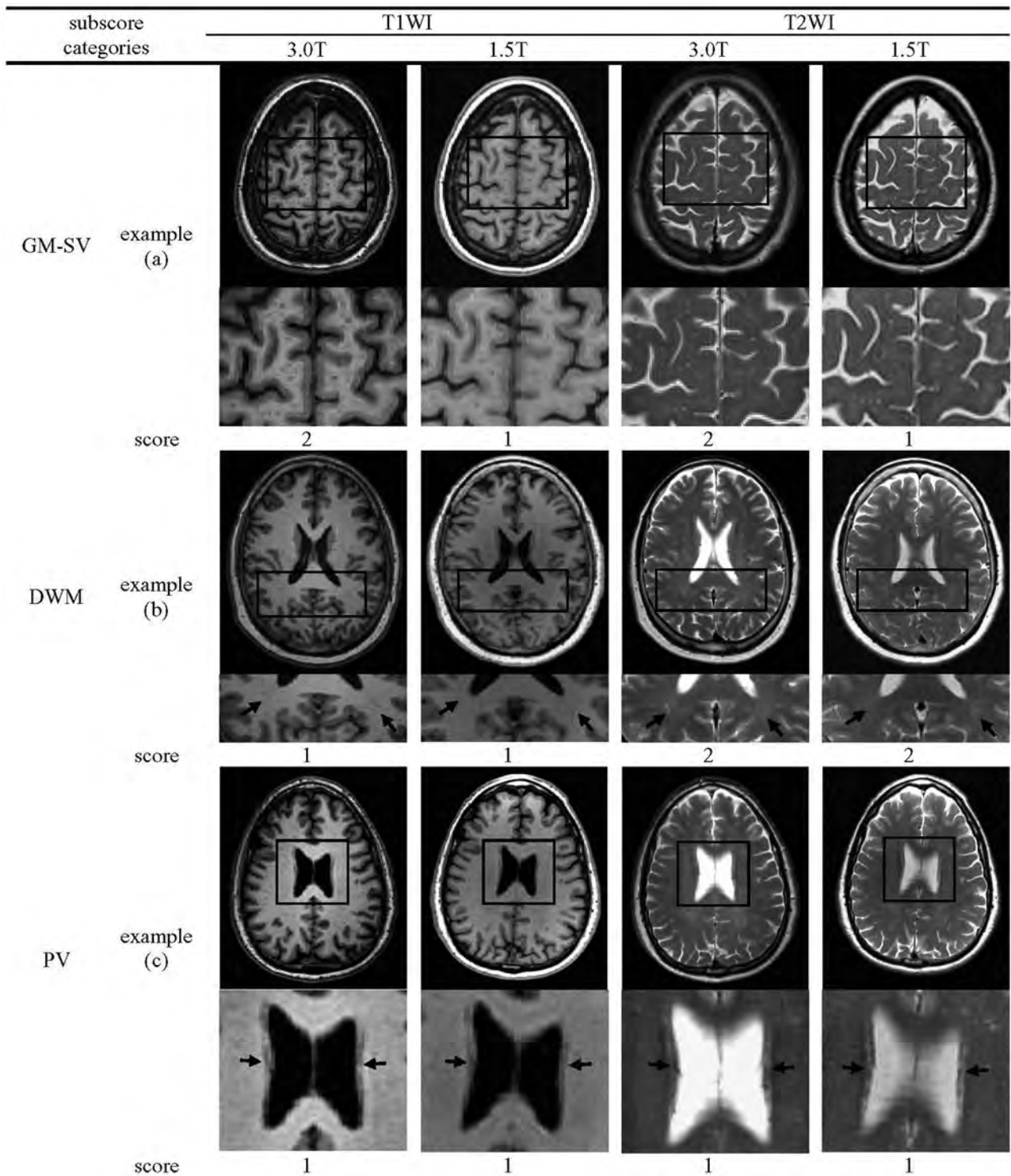


FIG 1. Example images showing BALI rating. Regions highlighted by black squares are magnified in rows underneath. Black arrows indicate targeted lesions. GM-SV indicates gray matter lesions and subcortical dilated perivascular spaces; DWM, deep white matter lesions; PV, periventricular white matter lesions; BG, lesions in the basal ganglia and surrounding areas; IT, lesions in the infratentorial regions; GA, global atrophy. (a), multiple dilated perivascular spaces could be seen at 1.5T but were more readily observed at 3T. (b), T2WI at both 3T and 1.5T showed the beginning of confluence hyperintensity foci in the bilateral parietal lobes, whereas on T1WI, only punctuate hypointensity foci were observed. (c), each image showed the pencil-thin lining lesion, scored as 1. (d), each image showed large confluent lesions, scored as 3. (e), lesions were seen more easily by T2WI than by T1WI at both 3T and 1.5T. (f), images showed severe atrophy with obviously dilated ventricles and widened sulci.

essed by use of the intraclass correlation coefficient for the BALI total scores (interval variable), with intraclass correlation coefficient values compared by use of Fisher Z tests and the Cohen κ

coefficient for the categoric subscores. A 2-way random model was used, with both subject-sample and rater as random factors. The agreement rate was assessed independently for image type

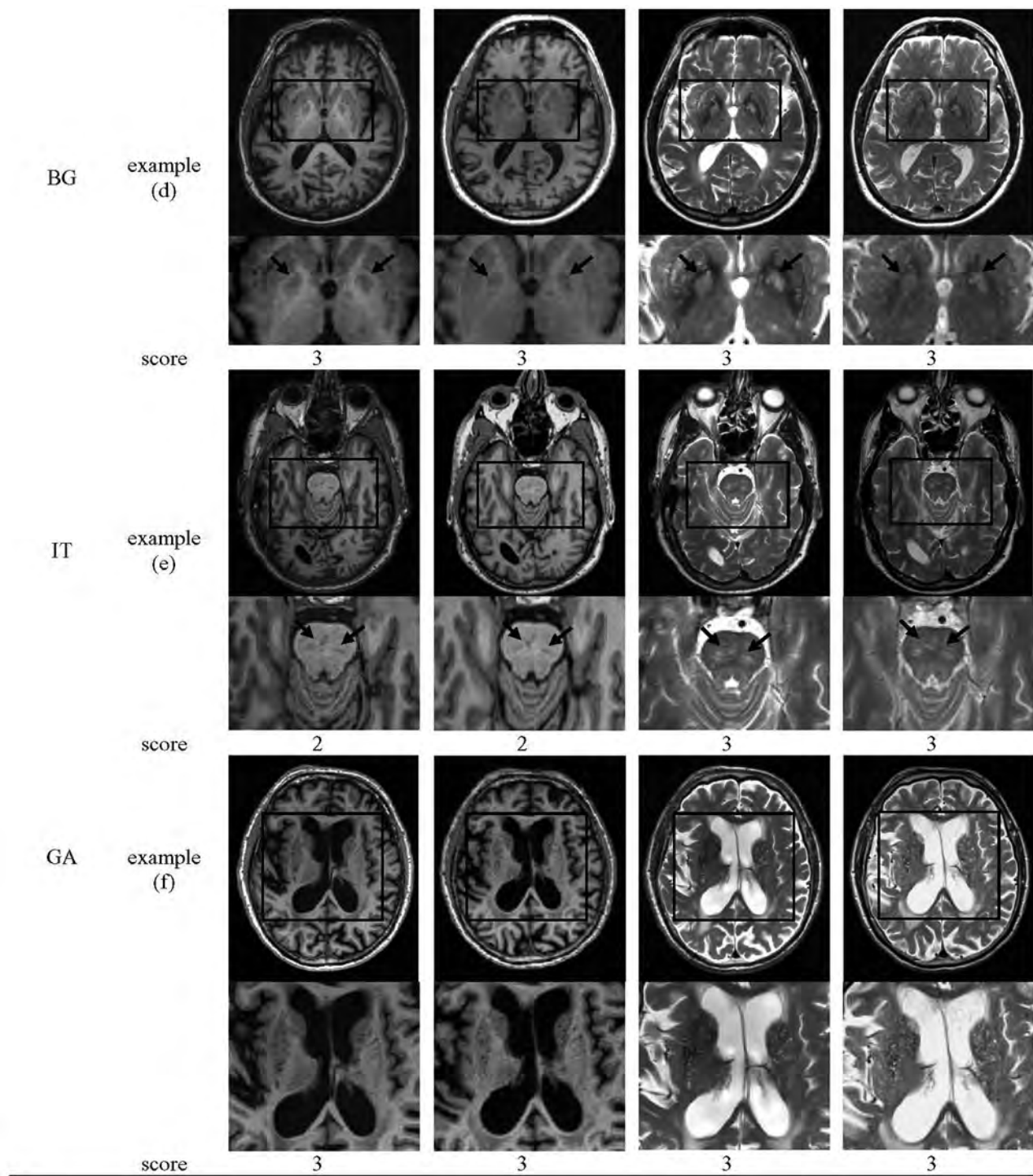


FIG 1. Continued

and field strength, for example, 1.5T T1WI, 1.5T T2WI, 3T T1WI, and 3T T2WI. As commonly done, the agreement was examined by use of a random subsampling of 20% of subjects among 3 raters and generalized with 5 raters by use of 9% random subsampling.²³ Demographic characteristics across diagnostic groups were examined by use of the Kruskal-Wallis nonparametric test for interval data (eg, age) and χ^2 for categoric data (eg, sex). Comparisons of the mean BALI total scores and the subscores between and within different groups, by diagnosis or biomarker, were conducted by

use of ANOVA and the Kruskal-Wallis nonparametric tests, respectively. The interrelations of BALI total score between 3T and 1.5T and between T1WI and T2WI were examined by use of correlation analyses. Relationships between BALI total score and age/cognitive tests were examined by use of regression analyses. Performance of the BALI scores in identifying individuals with different diagnoses was evaluated by use of the area under the curve of receiver operating characteristic analysis. All analyses were performed with the use of PASW 17 (IBM, Armonk, New

Table 1: Demographics and characteristics of the sample by diagnosis

	AD	MCI	HC	K-W/ χ^2	P
Sample size, <i>n</i>	37	45	45		
Women, %	59.5	31.1	62.2	10.43	.005
Age, y	74.0 ± 7.9	75.7 ± 7.2	76.8 ± 4.9	1.73	.420
Education, y	14.1 ± 3.3	16.3 ± 2.9	16.2 ± 2.2	12.40	.002
CDR (/3) [#]	0.8 ± 0.3 (1.0)	0.5 ± 0.1 (0.5)	0 ± 0.1 (0)	141.50	<.001
MMSE (/30)	22.1 ± 4.4	26.4 ± 2.7	28.9 ± 1.2	67.78	<.001
ADAS-cog (/70)	19.6 ± 8.9	12.3 ± 6.0	5.6 ± 3.2	66.54	<.001
A β_{1-42} , pg/mL	149.4 ± 36.1	169.7 ± 44.7	212.9 ± 57.2	16.27	<.001
τ , pg/mL	121.2 ± 47.3	94.7 ± 62.6	68.3 ± 29.1	16.94	<.001
p- τ , pg/mL	45.9 ± 19.5	31.2 ± 15.1	24.6 ± 13.9	17.35	<.001

Note:—Data are presented as mean ± standard deviation, otherwise as indicated. CSF biomarker data were available from a portion of the ADNI sample at baseline (AD = 21, MCI = 28, HC = 23).

CDR indicates Clinical Dementia Rating Scale; MMSE, Mini-Mental State Examination; ADAS-cog, Alzheimer's Disease Assessment Scale—cognitive subscale; A β_{1-42} , amyloid- β -peptides 1–42; τ , total τ protein; p- τ , phospho- τ proteins; K-W/ χ^2 , statistics for the Kruskal-Wallis test.

York); codes were developed by use of Matlab 2008 (MathWorks, Natick, Massachusetts). The level of significance was set at $P < .05$.

RESULTS

There was no diagnostic group difference in age (Table 1). Subjects with MCI were more likely to be men. As expected, people with AD had significantly lower cognitive testing scores compared with those with cognitively healthy aging, with MCI showing an intermediate level on average. Subjects with AD also had levels of education lower than those in the HC or MCI groups. Significant differences were also present in the AD biomarkers (Table 1).

Considering reliability, the intraclass correlation coefficient indicated at least strong agreement, with a value of 0.81 (CI = 0.67–0.94) for 1.5T T1WI, 0.86 (0.70–0.95) for 1.5T T2WI, 0.89 (CI = 0.71–0.96) for 3T T1WI, and 0.88 (0.73–0.96) for 3T T2WI (Fisher $Z = 0.05$ – 0.29 , $P > .770$), indicating indifference in the agreement rates between BALI scores on the basis of different image types and field strengths. The κ coefficients for the BALI category were moderate to substantial, between 0.45 with DWM by use of T1WI at 1.5T and 0.76 with lesions in the infratentorial regions by use of T1WI at 3T (Fig 2).

Multiple structural changes were present commonly in each diagnostic group. Regardless of field strength and imaging type, on average, subjects with AD showed the highest values of the BALI total scores, followed by those with MCI (Online Table 2). Significant differences in BALI total score were found among diagnostic groups in T1WI and T2WI at both 1.5T and 3T ($F > 5.14$; $P < .007$). Similar differences by diagnosis existed in the global atrophy subscores ($\chi^2 > 14.38$, $P < .001$), whereas other subscores also showed the trend. Within each diagnostic group, the 3T T2WI-based BALI total score was the highest, followed by 1.5T T2WI, 3T T1WI, and 1.5T T1WI. A significant difference in the total score was found between T2WI and T1WI ($F > 4.25$, $P < .041$) and marginally between 3T and 1.5T ($F < 3.23$, $P < .074$), without interaction ($F < 0.02$, $P > .898$). Similar differences between field strengths and the image types were observed for GM-SV (ie, 3T $>$ 1.5T; T2WI $>$ T1WI), though the lesions in the infratentorial regions, DWM, periventricular white matter lesions, and lesions in the basal ganglia and surrounding areas subscores also showed such a tendency without a significant differences (Online Table 2).

The 3T-based and 1.5T-based BALI total scores were correlated for both T1WI ($r = 0.94$, $P < .001$) and T2WI ($r = 0.93$, $P <$

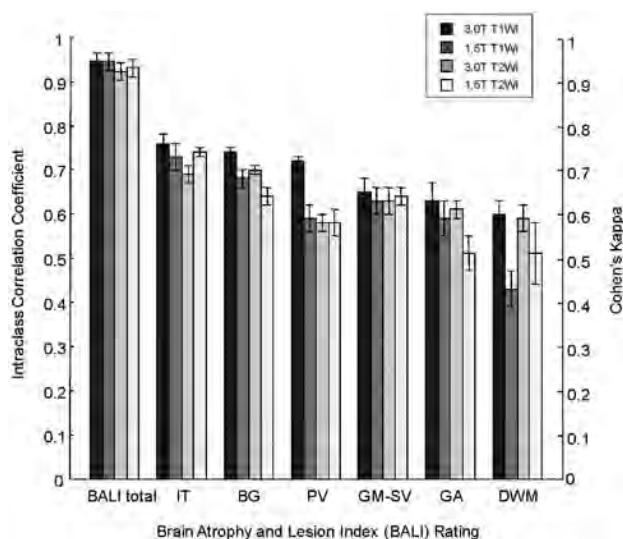


FIG 2. Interrater agreement for the BALI rating. Images were rated by 3 raters independently by use of 20% of randomly selected subsample. The interrater agreement was calculated for the total scores (interval data) by use of intraclass correlation coefficient, whereas that for the category subscores (categorical data) used Cohen κ . IT indicates lesions in the infratentorial regions; BG, lesions in the basal ganglia and surrounding areas; PV, periventricular white matter lesions; GM-SV, gray matter lesions and subcortical dilated perivascular spaces; GA, global atrophy; DWM, deep white matter lesions. Bars from dark to light-gray: 3T T1WI, 1.5T T1WI, 3T T2WI, and 1.5T T2WI. Error bars indicate standard deviation of the mean value in a 2-way random model, with subject-sample and rater as random factors.

.001; Fig 3A, -B), as were the T1WI- and T2WI-based scores ($r = 0.93$, $P < .001$ at 3T; $r = 0.94$, $P < .001$ at 1.5T; Fig 3C, -D). The BALI total score increased significantly with age, regardless of image type and field strength (the regression coefficients $r = 0.37$ – 0.40 ; Table 2). A higher BALI total score also consistently correlated with cognitive testing scores ($r \geq 0.42$ for Mini-Mental State Examination, $r \geq 0.38$ for Alzheimer's Disease Assessment Scale—cognitive subscale; Table 2) and identified individuals with AD versus HC with the accuracy reached at 0.71 ± 0.06 ($P < .007$; 70% sensitivity, 68% specificity). The BALI scores also differed significantly between amyloid- β -negative ($n = 25$) versus amyloid- β -positive ($n = 47$) groups, especially at the higher field (accuracy = 0.64 ± 0.07 – 0.66 ± 0.07 ; $F > 3.96$, $P < .050$).

DISCUSSION

In the present study, we compared BALI scores on the basis of the ADNI MR imaging data that were concurrently acquired at 1.5T and 3T. Evaluations were made with the use of T1WI and T2WI at each field strength. The results demonstrated that several common brain changes can be captured and summarized by the use of BALI, thereby providing a way to quantify the impact of global structural changes on brain function. BALI scores on the basis of T1WI and T2WI at 1.5T are comparable with those at 3T. Notably, the higher field images give better definition of white matter

changes and perivascular spaces, as is well known.^{12,17} To the best of our knowledge, this is the first report on integrating multiple structural brain changes through the use of lower-field 1.5T MR imaging. Given the wealth of 1.5T MR imaging data in clinical and research settings, extending the global assessment beyond high fields can allow more effective use of existing (and not inexpensive) neuroimaging data in the study of aging and AD dementia.

This study has several strengths. It has been suggested that multiple structural brain changes often coexist in the process of aging, reflecting heterogeneous profiles. Each of these changes can

individually be related to an increased, albeit small, dementia risk; however, when combined, they produce additive effects on function.^{11,24,25} It has also been suggested that many changes are interrelated, for example, more severe white matter damage and vascular lesions are associated with more severe gray matter and hippocampal atrophy,²⁶⁻²⁸ producing a combined effect on cognition, though the relationships typically are nonlinear.^{29,30} By combining these changes, their overall effect can be understood more comprehensively. This argument appears to be supported by our data: the BALI total score differed significantly among diagnostic groups (ie, AD > MCI > HC), correlated closely with age and cognition, and was associated with amyloid- β status.

This study has taken advantage of the well-established open-access ADNI protocol,¹⁴ in which a relatively large number of subjects had concurrent standard anatomic MR imaging scans at both high and lower fields on the same day. Because the standard 1.5T and 3T T1WI and T2WI were acquired in the same individuals on the same day, the analyses were performed with maximum control of potential differences caused by time-related variations such as disease and cognition worsening and treatment influence. In consequence, evaluations of morphologic features on MR imaging can be optimally performed, comparing the field strengths and image types.

The study made use of multiple raters; each is experienced in clinical neu-

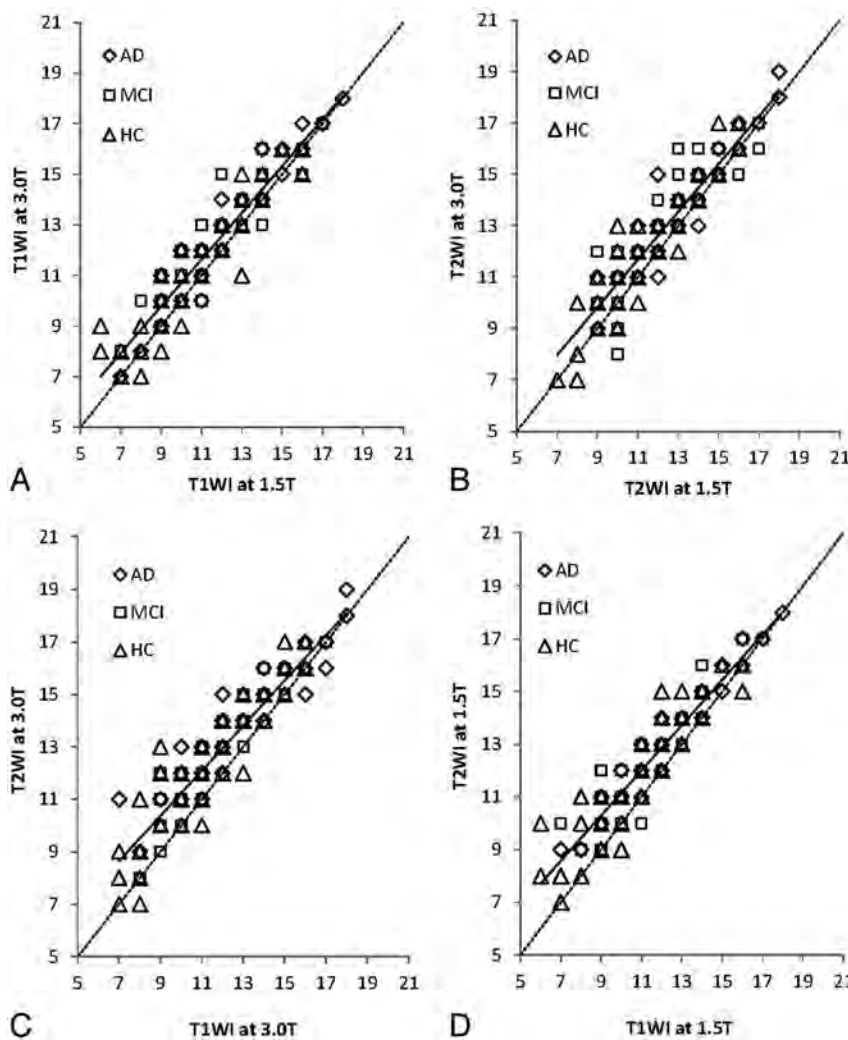


FIG 3. Relationships between BALI total scores. Symbols: diamonds indicate Alzheimer disease (AD, $n = 37$); squares, mild cognitive impairment (MCI, $n = 45$); triangles, healthy control subjects (HC, $n = 45$). Dotted diagonal line indicates x -values = y -values. Solid line indicates the linear fit $y = a + bx$. A, T1WI, 3T versus 1.5T (y -axis versus x -axis; $a = 1.47$, $b = 0.92$, $r = 0.94$; $P < .001$). B, T2WI, 3T versus 1.5T ($a = 1.46$, $b = 0.93$, $r = 0.93$; $P < .001$). C, 3T T2WI versus T1WI ($a = 2.64$, $b = 0.86$, $r = 0.93$, $P < .001$). D, 1.5T T2WI versus T1WI ($a = 2.57$, $b = 0.86$, $r = 0.94$; $P < .001$).

Table 2: Brain Atrophy and Lesion Index total score in relation to age and cognitive testing scores

BALI Total Score		Age				MMSE Total				ADAS-cog Total			
Image Type	Field Strength	r	r^2	T	P	r	r^2	T	P	r	r^2	T	P
T1WI	3T	0.39	0.15	4.75	<.001	0.44	0.19	-5.50	<.001	0.43	0.18	5.31	<.001
	1.5T	0.40	0.16	4.80	<.001	0.42	0.18	-5.23	<.001	0.38	0.14	4.58	<.001
T2WI	3T	0.37	0.14	4.50	<.001	0.42	0.18	-5.10	<.001	0.40	0.16	4.86	<.001
	1.5T	0.38	0.14	4.53	<.001	0.42	0.18	-5.23	<.001	0.38	0.14	4.60	<.001

Note.—MMSE indicates Mini-Mental State Examination; ADAS-cog, Alzheimer's Disease Assessment Scale—cognitive subscale.

roimaging evaluation. Trained in the method, mainly through the use of the rating schema descriptions, examples, and case discussions, each rater mastered the BALI rating quickly and rated an image independently, typically within a few minutes. Such a quick and easy application can be particularly beneficial and is welcome in clinical settings when evaluation time is a concern.³¹ The interrater agreement rate of BALI scores was quite strong across the raters, consistently with the image types and the field strengths, suggesting the robustness of the BALI rating. Further research will be needed to validate whether BALI rating by non-neuroradiologists is possible.

As a semi-quantitative rating scale, the BALI can be coarse, relative to other measures with more precise morphometric or volumetric quantifications.^{32,33} Even so, quantitative methods are usually highly image quality–dependent, and this can be difficult to satisfy in multicenter studies; what is more, the high precision may not always be necessary.³¹ Against this background, a quick and easy visual rating is sufficient and may even be favorable.³⁴ The BALI grading system has been established by adapting several validated rating scales, and the BALI itself has been validated in previous research by use of several independent datasets. Our data now suggest that it is reasonable to expand its use.

On the basis of the widely available T1WI and T2WI, BALI focuses on morphologic changes and not on their pathologic causes (which would require additional imaging sequences such as FLAIR and gradient recalled-echo/T2*). The high-field strength and the T2WI showed a greater sensitivity, particularly for evaluating subtle changes of the imaging-contrast–reliant categories (eg, GM-SV and DMW), leading to slightly higher BALI total scores in these conditions. This is not surprising because subtle lesions are more conspicuous on T2WI, and higher field strength allows higher SNR and thus greater image contrast.¹⁷ The argument appears to be supported by our data demonstrating the relationships between T2WI versus T1WI and between 3T versus 1.5T; in each case, the difference was more obvious at the relatively low level of changes (Fig 3A–D). The T2WI was more sensitive for the small lesions than was T1WI, even though the T1WI section thickness was less and hence had greater spatial resolution. Against this background, a field-strength–related difference may or may not be reflected in interrater agreement rate. For example, a subtle change in GM-SV at 1.5T was not as easy to see by the raters, leading to lower subscores at 1.5T than that at 3T, whereas the interrater agreement was not necessarily lower (Fig 1). Meanwhile, small changes in DMW were more variably seen by different rates at 1.5T than at 3T (eg, by use of T1WI), resulting in a relatively lower value of both the DMW subscore and the agreement rate at 1.5T (Fig 1). Even with these detailed differences, the BALI total scores obtained under different conditions were reliable, correlated with each other, and were related to age and cognition in the same manner, suggesting each may be used to evaluate the global structure changes in the aging brain.

Our data must be integrated with caution. In the present study, the mean values of the BALI rating appeared to be slightly higher than previously reported with the use of other samples, including a different sample of the ADNI dataset at baseline.

Given the demonstrated reliability of the approach, this probably reflects that the concurrent MR imaging at both field strengths studied was performed at a follow-up of up to 36 months, instead of at baseline. In consequence, structural brain changes, which represent worsening on average, would be reflected in higher BALI scores.

A few further caveats are needed in relation to how to best evaluate each category. First, dilated perivascular spaces are seen in several regions.⁷ Perivascular spaces along the ventral aspect of the lentiform nuclei at the level of the anterior commissure are extremely common even in healthy people³⁵ and thus were not counted. Second, the “large confluent lesions” notion appeared to be broad, because “large” can vary, depending on brain structure. For example, a “large” change regarding the relatively smaller lesions in the infratentorial regions and lesions in the basal ganglia and surrounding areas may not necessarily be judged as “large” regarding the DWM, even though our data suggested only a 1-point difference between raters typically, if any. Further research will be needed to better understand whether a more detailed definition, for example, categorizing DWM, lesions in the basal ganglia and surrounding areas, and lesions in the infratentorial regions in terms of their size in millimeters can help to further improve the robustness of the rating. Third, the BALI does not distinguish between lacunar infarcts and microangiopathic white matter changes, disregarding underlying pathophysiological mechanisms. Whether assigning a category rating to lacunar infarcts specifically can improve the applicability of the BALI rating deserves a separate investigation. To maintain the quickness and ease of BALI, caution must be taken to avoid unnecessary complexity.

Finally, how to best aggregate the subscores that may contribute to cognition differently is challenging. For example, the effect of white matter lesions can differ by location.^{5,8} Accordingly, integrating several white matter subscores may be sensible. In this regard, introducing a weighting factor may be beneficial, as shown in a previous study that combined BALI and the medial temporal lobe atrophy to improve AD discrimination and prediction.¹⁵ This raises the possibility of its potential application in differentiating dementia subtypes, though that proposition remains to be tested. Even so, values of weights often rely on specific outcomes and methods used, so that weighting may limit the general application of a measure.³⁶ Whereas this challenge has motivated the current research of our group, the merit of combining multiple brain changes can already be seen simply by summing them up.

CONCLUSIONS

Our study suggests that multiple structural changes in the aging brain have an additive effect on cognition and can be collectively evaluated by use of the BALI total score. Although high field strength and T2WI have a better sensitivity in detecting subtle changes in the deep white matter and perivascular spaces in particular, both T1WI and T2WI at 1.5T as in the ADNI protocol have good reliability in robustly capturing global brain changes.

ACKNOWLEDGMENTS

We acknowledge Drs S. Black, J. Fisk, S. Darvesh, A. Mitnitski, J. Zhang, R. D'Arcy, S. Beyea, and C. Bowen for critical discussions with the development of BALI and Mrs E. Vandermolen for proofreading the manuscript.

Data collection and sharing for this project was funded by the ADNI (National Institutes of Health Grant U01 AG024904). ADNI is funded by the National Institute on Aging (NIA), the National Institute of Biomedical Imaging and Bioengineering, and through generous contributions from many public and private sections, as a multi-million dollar, multi-year public-private partnership.²⁰ ADNI is the result of efforts of many co-investigators from a broad range of academic institutions and private corporations, and subjects have been recruited from over 50 sites across the United States and Canada. The Principal Investigator of this initiative is Michael W. Weiner, MD, VA Medical Center and University of California, San Francisco. The Canadian Institutes of Health Research is providing funds to support ADNI clinical sites in Canada. Private sector contributions are facilitated by the Foundation for the National Institutes of Health (www.fnih.org). The grantee organization is the Northern California Institute for Research and Education, and the study is coordinated by the Alzheimer Disease Cooperative Study at the University of California, San Diego. ADNI data are disseminated by the Laboratory for Neuro Imaging at the University of California, Los Angeles. The ADNI was also supported by NIH grants P30 AG010129 and K01 AG030514.

Data used in preparation of this article were obtained from the ADNI data base (adni.loni.ucla.edu). As such, the investigators within the ADNI contributed to the design and implementation of ADNI and/or provided data but did not participate in analysis or writing of this report. For a complete list of the investigators, visit http://adni.loni.ucla.edu/wp-content/uploads/how_to_apply/ADNI_Acknowledgement_List.pdf.

Disclosures: Hui Guo—RELATED: Grant: CIHR CSE125739, Comments: Worked as a postdoctoral research fellow (see Acknowledgments). Kenneth Rockwood—UNRELATED: Consultancy: Merck Canada, Comments: 2012 Merck Canada, The Cognigram Cognitive Screening Test consultant; Grants/Grants Pending: Canadian Institutes of Health Research,* Comments: Dynamics of cognitive change in older adults (Canadian Institutes of Health Research MOP-209888 2010–2015); The Research to Action Program in Dementia: the Canadian Dementia Knowledge Translation Network (Canadian Institutes of Health Research 200711DIP 2008–2013); Travel/Accommodations/Meeting Expenses Unrelated to Activities Listed: University of Alberta, McMaster University, Comments: "The Joy of Geriatrics," 13th Annual Dr Gerald Zetter Memorial Guest Lecturer, University of Alberta, Edmonton, AB, Canada, September 11, 2012; "How Does Wealth Affect Health in Ageing?," Alberta Association on Gerontology invited speaker, Edmonton, AB, Canada, September 11, 2012; "Complex Care of Frail Older Adults Who are Acutely Ill, Anything to Know?," Geriatric Academic Rounds, Division of Geriatric Medicine, Department of Medicine, McMaster University, Hamilton, ON, Canada, February 11, 2013; Other: DGI Clinical/Videx Canada, Comments: With colleagues, I have applied to various Canadian government schemes to commercialize a version of the frailty index, based on a comprehensive assessment, and an expanded version of the clinical frailty scale. To this end, they have asserted copyright on the new instruments and formed a company called Videx Canada (*money paid to institution).

REFERENCES

1. Appel J, Potter E, Bhatia N, et al. **Association of white matter hyperintensity measurements on brain MR imaging with cognitive status, medial temporal atrophy, and cardiovascular risk factors.** *AJNR Am J Neuroradiol* 2009;30:1870–76
2. Sinka L, Kovari E, Gold G, et al. **Small vascular and Alzheimer disease-related pathologic determinants of dementia in the oldest-old.** *J Neuropathol Exp Neurol* 2010;69:1247–55
3. Barnes J, Carmichael OT, Leung KK, et al. **Vascular and Alzheimer's disease markers independently predict brain atrophy rate in Alzheimer's Disease Neuroimaging Initiative controls.** *Neurobiol Aging* 2013;34:1996–2002
4. Jagust WJ, Zheng L, Harvey DJ, et al. **Neuropathological basis of magnetic resonance images in aging and dementia.** *Ann Neurol* 2008;63:72–80
5. Kim KW, MacFall JR, Payne ME. **Classification of white matter lesions on magnetic resonance imaging in elderly persons.** *Biol Psychiatry* 2008;64:273–80
6. Black S, Gao F, Bilbao J. **Understanding white matter disease: imaging: pathological correlations in vascular cognitive impairment.** *Stroke* 2009;40:S48–52
7. Chen W, Song X, Zhang Y. **Assessment of the Virchow-Robin spaces in Alzheimer disease, mild cognitive impairment, and normal aging, using high-field MRI.** *AJNR Am J Neuroradiol* 2011;32:1490–95
8. Kim HJ, Kang SJ, Kim C, et al. **The effects of small vessel disease and amyloid burden on neuropsychiatric symptoms: a study among patients with subcortical vascular cognitive impairments.** *Neurobiol Aging* 2013;34:1913–20
9. Duara R, Loewenstein DA, Potter E, et al. **Medial temporal lobe atrophy on MRI scans and the diagnosis of Alzheimer disease.** *Neurology* 2008;71:1986–92
10. Moon WJ, Kim HJ, Roh HG, et al. **Atrophy measurement of the anterior commissure and substantia innominata with 3T high-resolution MR imaging: does the measurement differ for patients with frontotemporal lobar degeneration and Alzheimer disease and for healthy subjects?** *AJNR Am J Neuroradiol* 2008;29:1308–13
11. Savva GM, Wharton SB, Ince PG, et al. **Age, neuropathology, and dementia.** *N Engl J Med* 2009;360:2302–09
12. Chen W, Song X, Zhang Y, et al. **An MRI-based semiquantitative index for the evaluation of brain atrophy and lesions in Alzheimer's disease, mild cognitive impairment and normal aging.** *Dement Geriatr Cogn Disord* 2010;30:121–30
13. Zhang N, Song X, Zhang Y, et al. **An MRI brain atrophy and lesion index to assess the progression of structural changes in Alzheimer's disease, mild cognitive impairment, and normal aging: a follow-up study.** *J Alzheimers Dis* 2011;26:359–67
14. Weiner MW, Aisen PS, Jack CR Jr, et al. **The Alzheimer's Disease Neuroimaging Initiative: progress report and future plans.** *Alzheimers Dement* 2010;6:201–11
15. Zhang N, Song X, Zhang Y. **Combining structural brain changes improves the prediction of Alzheimer's disease and mild cognitive impairment.** *Dement Geriatr Cogn Disord* 2012;33:318–26
16. Song X, Mitnitski A, Zhang, et al. **Dynamics of brain structure and cognitive function in the Alzheimer's disease neuroimaging initiative.** *J Neurol Neurosurg Psychiatry* 2013;84:71–78
17. Alvarez-Linera J. **3T MRI: advances in brain imaging.** *Eur J Radiol* 2008;67:415–26
18. Jack CR Jr, Bernstein MA, Fox NC, et al. **The Alzheimer's Disease Neuroimaging Initiative (ADNI): MRI methods.** *J Magn Reson Imaging* 2008;27:685–91
19. Aisen PS, Petersen RC, Donohue MC, et al. **Clinical core of the Alzheimer's Disease Neuroimaging Initiative: progress and plans.** *Alzheimers Dement* 2010;6:239–46
20. Shaw LM, Vanderstichele H, Knapik-Czajka M, et al. **Cerebrospinal fluid biomarker signature in Alzheimer's disease neuroimaging initiative subjects.** *Ann Neurol* 2009;65:403–13
21. Song X, Mitnitski A, Rockwood K. **Index variables for studying outcomes in vascular cognitive impairment.** *Neuroepidemiology* 2005;25:196–204
22. Streiner D, Norman G. *Health Measurement Scales: A Practical Guide to Their Development and Use.* 4th ed. New York: Oxford University Press; 2008
23. Walter SD, Eliasziw M, Donner A. **Sample size and optimal designs for reliability studies.** *Stat Med* 1998;17:101–10

24. Karas G, Sluimer J, Goekoop R, et al. **Amnesic mild cognitive impairment: structural MR imaging findings predictive of conversion to Alzheimer disease.** *AJNR Am J Neuroradiol* 2008;29:944–49
25. Frisoni GB, Fox NC, Jack CR Jr, et al. **The clinical use of structural MRI in Alzheimer disease.** *Nat Rev Neurol* 2010;6:67–77
26. Agosta F, Pievani M, Sala S, et al. **White matter damage in Alzheimer disease and its relationship to gray matter atrophy.** *Radiology* 2011;258:853–63
27. Eckerstrom C, Olsson E, Klasson N, et al. **High white matter lesion load is associated with hippocampal atrophy in mild cognitive impairment.** *Dement Geriatr Cogn Disord* 2011;31:132–38
28. Raji CA, Lopez OL, Kuller LH, et al. **White matter lesions and brain gray matter volume in cognitively normal elders.** *Neurobiol Aging* 2012;33:e7–16
29. Neuropathology Group. **Medical Research Council Cognitive Function and Aging Study: pathological correlates of late-onset dementia in a multicentre, community-based population in England and Wales: Neuropathology Group of the Medical Research Council Cognitive Function and Aging Study (MRC CFAS).** *Lancet* 2001;357:169–75
30. Launer LJ, Hughes TM, White LR. **Microinfarcts, brain atrophy, and cognitive function: the Honolulu Asia Aging Study Autopsy Study.** *Ann Neurol* 2011;70:774–80
31. Gouw AA, van der Flier WM, Pantoni L, et al. **On the etiology of incident brain lacunes: longitudinal observations from the LADIS study.** *Stroke* 2008;39:3083–85
32. Jack CR Jr, Shiung MM, Gunter JL, et al. **Comparison of different MRI brain atrophy rate measures with clinical disease progression in AD.** *Neurology* 2004;62:591–600
33. Fox NC, Freeborough PA, Rossor MN. **Visualisation and quantification of rates of atrophy in Alzheimer's disease.** *Lancet* 1996;348:94–97
34. Shen Q, Loewenstein DA, Potter E, et al. **Volumetric and visual rating of magnetic resonance imaging scans in the diagnosis of amnesic mild cognitive impairment and Alzheimer's disease.** *Alzheimers Dement* 2011;7:e101–08
35. Bryan RN, Cai J, Burke G, et al. **Prevalence and anatomic characteristics of infarct-like lesions on MR images of middle-aged adults: the atherosclerosis risk in communities study.** *AJNR Am J Neuroradiol* 1999;20:1273–80
36. Song X, Mitnitski A, MacKnight C, et al. **Assessment of individual risk of death using self-report data: an artificial neural network compared with a frailty index.** *J Am Geriatr Soc* 2004;52:1180–84

Volumetric Assessment of Optic Nerve Sheath and Hypophysis in Idiopathic Intracranial Hypertension

J. Hoffmann, C. Schmidt, H. Kunte, R. Klingebiel, L. Harms, H.-J. Huppertz, L. Lüdemann, and E. Wiener



ABSTRACT

BACKGROUND AND PURPOSE: Idiopathic intracranial hypertension is a headache syndrome characterized by increased CSF pressure. Compression of the hypophysis and distension of the optic nerve sheath are reliable imaging signs. The purpose of the study was to validate, in patients with idiopathic intracranial hypertension, MR imaging–based volumetric measurements of the optic nerve sheath and hypophysis as an objective observation method for more accurate diagnosis and posttreatment follow-up.

MATERIALS AND METHODS: Twenty-three patients with idiopathic intracranial hypertension as well as age-, sex-, and body mass index–matched controls underwent volumetric measurements of the optic nerve, optic nerve sheath, and hypophysis on high-resolution T2-weighted MR images by using a 7-cm surface coil, followed by correlation with CSF opening pressures and clinical symptom scores of visual disturbances and headache.

RESULTS: Mean values of optic nerve sheath ($341.86 \pm 163.69 \text{ mm}^3$ versus $127.56 \pm 53.17 \text{ mm}^3$, $P < .001$) and hypophysis volumes ($554.59 \pm 142.82 \text{ mm}^3$ versus $686.60 \pm 137.84 \text{ mm}^3$, $P < .05$) differed significantly between healthy and diseased subjects. No significant differences between mean optic nerve volumes were observed. Receiver operating characteristic analysis showed optic nerve sheath volumes of $>201.30 \text{ mm}^3$ (sensitivity, 86.96%; specificity, 91.30%) and hypophysis volumes of $<611.21 \text{ mm}^3$ (sensitivity, 78.26%; specificity, 69.57%) to be indicative of idiopathic intracranial hypertension diagnosis. In patients with idiopathic intracranial hypertension, no correlations were found between optic nerve sheath and hypophysis volumes and CSF opening pressures or clinical scores of visual disturbances and headache.

CONCLUSIONS: Semiautomated volumetric measurement of optic nerve sheath and hypophysis has the potential to more accurately diagnose and follow patients with idiopathic intracranial hypertension.

ABBREVIATIONS: cc = correlation coefficient; IIH = idiopathic intracranial hypertension; ON = optic nerve; ONS = optic nerve sheath

Idiopathic intracranial hypertension (IIH) is an uncommon headache syndrome associated with elevated intracranial pressure in the absence of a space-occupying lesion. Initially used terms such as “meningitis serosa” coined by Quincke in 1893 or “pseudotumor cerebri” by Nonne in 1904 are now obsolete and

have been replaced in recent classifications by the descriptive denomination “idiopathic intracranial hypertension.”^{1,2} Because IIH predominantly affects obese women of childbearing age and the incidence of obesity in industrialized countries is growing, IIH has been the focus of recent research. The underlying pathophysiologic mechanism of the disease is not fully understood. Diagnosis of IIH is based on clinical symptoms such as headache and visual disturbances; characteristic neuroimaging findings,³ including a compression of the hypophysis (ie, empty sella); flattening of the posterior globe; and a dilated optic nerve sheath (ONS) in combination with an opening pressure during lumbar puncture of $>25 \text{ cm H}_2\text{O}$, with normal CSF parameters (modified Dandy criteria).^{4–6} The diagnostic criteria have undergone several modifications, and the disease is now defined in the Headache Classification of the International Headache Society.⁷ The interpretation of subtle changes on MR images obtained for the initial diagnosis or for follow-up after treatment can be challenging.

Received April 9, 2013; accepted after revision June 4.

From the Departments of Neurology (J.H., H.K., L.H.) and Neuroradiology (C.S., R.K., E.W.), Charité-Universitätsmedizin Berlin, Berlin, Germany; Klinik im Park (R.K.), Institute of Neuroradiology and Radiology, Zürich, Switzerland; Medical Imaging (H.-J.H.), Swiss Epilepsy Centre, Zürich, Switzerland; and Department of Radiotherapy (L.L.), University Clinic Essen, Essen, Germany.

J. Hoffmann and C. Schmidt contributed equally to this work.

Please address correspondence to Edzard Wiener, MD, Department of Neuroradiology, Charité-Universitätsmedizin Berlin, Charitéplatz 1, 10117 Berlin, Germany; e-mail: Edzard.Wiener@charite.de



Indicates article with supplemental on-line table



Indicates article with supplemental on-line figure

<http://dx.doi.org/10.3174/ajnr.A3694>

We compared hypophysis and optic nerve sheath and optic nerve (ON) volumes measured on high-resolution MR images in patients with IIH and age-, sex-, and body mass index–matched controls to evaluate the potential of MR imaging–based volumetric measurements as an objective method to diagnose IIH and follow-up effects of treatment.

MATERIALS AND METHODS

The study was approved by the local ethics committee of the Charité-Universitätsmedizin Berlin. A statement of written informed consent was obtained from all patients and healthy volunteers participating in the study.

Patient Subjects

Clinical records of 190 patients with IIH referred to our clinic between November 2005 and May 2010 were retrospectively screened. We therefore searched the electronic medical records system of the university hospital via retrieval algorithms for the International Classification of Diseases-10 classification code G93.2.⁸ We enrolled only patients with a minimum age of 18 years at presentation and a definite diagnosis of IIH according to the revised Dandy criteria: 1) signs and symptoms of increased intracranial pressure (headache, nausea, vomiting, transient visual obscurations, or papilledema); 2) no focal signs except abducens nerve palsy; 3) CSF opening pressure of >25 cm H₂O with normal CSF composition; and 4) evidence of neither hydrocephalus, mass, structural, or vascular lesion on MR imaging nor any other cause of intracranial hypertension identified.⁹ All patients were of white descent. Exclusion criteria comprised systemic conditions or medication that might have an effect on intracranial pressure, inadequate follow-up, pregnancy or postpartum status, body weight >160 kg, and clinical history of surgical procedures affecting CSF circulation (eg, shunting procedures or fenestration of the ONS). Medical histories of 190 patients were analyzed to identify those who fully met the inclusion criteria. Because IIH is often regarded as a diagnosis of exclusion, many of the retrospectively identified patients had a probable IIH but did not fulfill all the required criteria for the diagnosis and could, therefore, not be included in the study. Other patients had additional diseases and were therefore excluded from study participation. We found only 71 patients who definitely met the modified Dandy criteria. Fifteen patients were excluded by the exclusion criteria: shunt surgery ($n = 6$), body weight >160 kg ($n = 3$), pregnancy ($n = 1$), and claustrophobia ($n = 4$). One patient ($n = 1$) fulfilled the criteria for major depression (diagnosed by the Becks Depression Inventory and Hamilton Rating Scale for Depression) and was ruled out. Eighteen patients could not be reached; 15 refused participation in the study.

The mean age of the remaining 23 patients (20 women, 3 men) was 37.04 ± 13.72 years (range, 20–63 years). The mean body mass index was 33.51 ± 7.67 kg/m² (range, 24.9–54.57 kg/m²). All patients were carefully questioned about disease symptoms by using a standardized clinical questionnaire (based on the modified Dandy criteria and the diagnostic criteria established by the International Headache Society). During hospitalization, all patients with IIH underwent lumbar puncture, and CSF opening pressures were obtained before MR imaging.

Measurements of visual acuity and perimetry of the visual field were performed.

Control Subjects

Twenty-three healthy controls of white descent were included by using a match-to-pair technique regarding sex ($n = 20$ women, $n = 3$ men, $P = 1.0$), age (mean, 37.91 ± 11.84 years [range, 22–61 years], $P = .819$), and body mass index (mean, 33.56 ± 7.01 kg/m² [range, 25.53–48.89 kg/m²], $P = .982$). Control subjects were recruited from the obesity center of the University Hospital and from the hospital staff. Exclusion criteria included a known history of central nervous system disease or primary headache syndromes (migraine, tension-type headache, trigeminal neuralgia, cluster headache, hemicrania continua).

MR Imaging

MR imaging was performed on a 1.5T scanner (Avanto Magnetom; Siemens, Erlangen, Germany). A surface loop coil (medium size, 70 mm diameter; Siemens) was used in addition to the circularly polarized head coil. The surface coil was placed over the eye with maximum visual disturbances within the head coil and fixed with tape. A coronal non-fat-saturated TSE sequence with a TR of 6960 ms, a TE of 99 ms, an FOV of 85×85 mm², a matrix size of 256×256 mm² (in-plane resolution, 0.332×0.332 mm²), and contiguous sections with a section thickness of 2 mm was used to evaluate the ON and ONS. The acquisition time was 7 minutes 20 seconds. A sagittal non-fat-saturated T2-weighted TSE sequence with a TR of 5170 ms, a TE of 99 ms, an FOV of 170×170 mm², a matrix size of 256×320 mm² (in-plane resolution, 0.664×0.531 mm²), and contiguous sections with a section thickness of 2 mm was used to evaluate the hypophysis. The acquisition time was 5 minutes 27 seconds. Additionally, MR imaging of the whole brain, including a time-of-flight venography (TR, 23 ms; TE, 6.5 ms; FOV, 250×250 mm²; section thickness, 2 mm; acquisition time, 7 minutes 40 seconds) was performed to exclude intracranial pathology and venous sinus thrombosis as a secondary cause of IIH and to identify venous sinus stenoses.

Volume Segmentation

MR images were converted from DICOM into Neuroimaging Informatics Technology Initiative format by using the DICOM to Neuroimaging Informatics Technology Initiative format converter dcm2nii (<http://www.mccauslandcenter.sc.edu/mricro/mricron/dcm2nii.html>). Volume measurements were performed by using Amira 5.3.2 (Visage Imaging, San Diego, California) on a Debian Linux distribution. On each T2-weighted coronal image, the ON and ONS were marked by a region of interest, starting from the papilla and ending at the point of convergence of the extraocular muscles at the tendinous ring of the orbital apex. The mean number of sections was 12 with a section thickness of 2 mm (Fig 3 and On-line Fig 1). On each T2-weighted sagittal image, the hypophysis was marked with a region of interest. The mean number of sections was 4, with a section thickness of 2 mm (Fig 3 and On-line Fig 1). Neuroradiologists were blinded with respect to the subject group (patients with IIH versus healthy volunteers), and the interobserver variability was calculated.

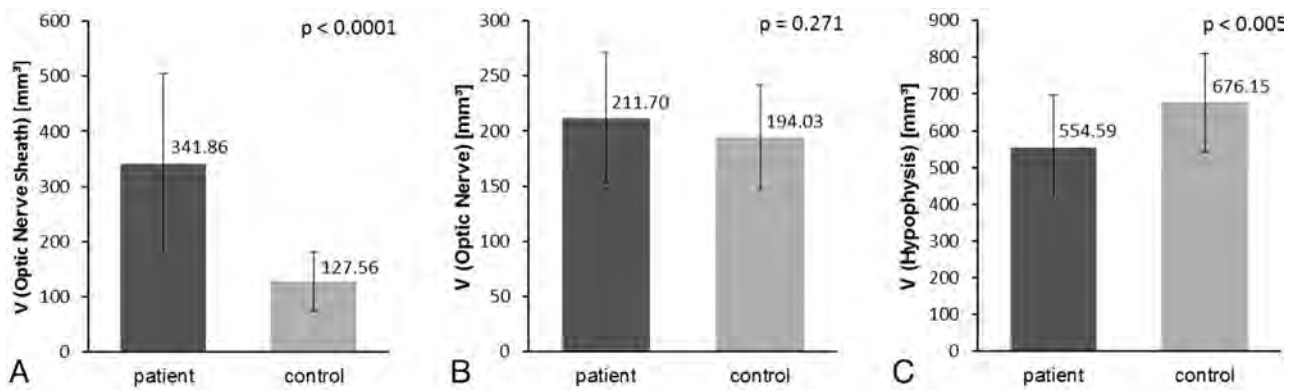


FIG 1. Significance of measurements. *A*, Significance of ONS volume. Bar graph shows significant differences of mean ONS volumes and corresponding ranges of patient and control groups. *B*, Significance of OS volume. Note a tendency toward an increased mean OS volume in patients with IIH compared with controls, which, however, does not reach statistical significance. *C*, Significance of hypophysis volume. This bar graph clearly shows significantly lower mean volumes of hypophysis in patients compared with controls.

Morphologic Analysis

The configuration of the hypophysis was classified into 4 categories according to a modification of the hypophysis/sella turcica ratio of Yuh et al¹⁰: convex, mild concave (more than one-half the height of the sella), severe concave (less than one-half the height of the sella), and empty sella (≤ 2 mm). The appearance of the superior boarder of the hypophysis was classified into anterior and posterior or equal (without predominance of either anterior or posterior deviation of the hypophysary stalk) formation relative to the direction of displacement of the hypophysary stalk.

The classification of stenoses was defined by the highest percentage of stenosis on axial images and maximum-intensity-projection images. Stenoses were categorized into either stenosis of $<50\%$ or $>50\%$ of the lumen. Absence of any discontinuity was classified as nonoccurrence of stenosis. Venous sinus stenoses were classified into a left and/or right position as well as assigned to the transverse or sigmoid sinus. The incidence of bilateral stenoses (stenoses in left and right transverse or sigmoid sinus) was statistically listed as 2 stenoses.

Statistical Analysis

The volumetric data were analyzed by using XLSTAT, Version 2011.3.01 (Addinsoft S.A.R.L., New York, New York). The Student *t* test was used to compare the group means. Statistical significance was assumed at $P < .05$. The Pearson correlation coefficient and correlation matrices were calculated to identify the strength of the correlation of the different parameters. Receiver operating characteristic analysis was used to select an optimal cut-point for prediction and to assess the predictive value in terms of sensitivity, specificity, and accuracy.¹¹ Selection of the optimal cut-point was based on the Youden index (ie, the maximum sum of sensitivity and specificity). The 95% confidence interval for the area under curve was calculated by bootstrapping.

Interobserver variability was determined by calculating intraclass correlation coefficients, including 95% confidence intervals, for volumetric measurements of ON, ONS, and hypophysis volumes by using PASW Statistics 18, release Version 18.0.0 (IBM, Armonk, New York).

RESULTS

Clinical Profile of Patients with IIH

Sixteen (69.6%) patients presented with headache. The mean pain intensity was 2.22 ± 2.53 (range, 0.0–7.5) according to the visual analog scale before examination, and a mean pain intensity maximum was 7.09 ± 2.62 (range, 0.95–9.86) (visual analog scale). Impaired vision was reported by 91.30% of patients with IIH. The visual impairment was categorized according to the On-line Table: worsening of visual acuity, 47.83%; flashes, 39.13%; transient visual obscurations, 43.48%; scotoma, 73.91%; papilledema, 56.52%; blurred vision, 52.17%; and diplopia, 43.48%. No case of optic nerve atrophy was observed. Of the 39.13% of patients reporting tinnitus, 44.44% characterized their tinnitus as pulsatile. Light sensitivity (60.87%), noise sensitivity (52.17%), and vertigo (60.87%) were common symptoms. Medical history revealed a mean value of maximum CSF opening pressure of 37.61 ± 6.93 cm H₂O (range, 29.0–50.0 cm H₂O) (On-line Table).

Comparison of Volume Parameters among Patients with IIH and Controls

Patient mean ONS volume (On-line Fig 1A) was 341.86 ± 163.69 mm³ (range, 105.61–796.57 mm³), whereas control mean ONS volume was 127.56 ± 53.17 mm³ (range, 29.24–239.00 mm³) ($P < .0001$). Mean ON volume for patients (On-line Fig 1B) was 211.70 ± 59.22 mm³ (range, 125.67–319.00 mm³), and for controls, 194.03 ± 47.77 mm³ (range, 126.56–342.61 mm³), with no significant difference ($P = .271$). Mean hypophysis volume (On-line Fig 1C) of patients with IIH was 554.59 ± 142.82 mm³ (range, 334.43–855.15 mm³); that of controls was 676.15 ± 133.32 mm³ (range, 392.86–1045.65 mm³) ($P < .005$). The intraclass correlation coefficient for ON volume was 0.940 (95% CI, 0.864–0.974); for ONS volume, it was 0.947 (95% CI, 0.939–0.989); and for hypophysis volume, 0.981 (95% CI, 0.957–0.992).

Cutoff Values

The receiver operating characteristic analysis (Fig 3 and Table) revealed an optimal cutoff value of 201.30 mm³ for mean ONS volume, with a sensitivity of 86.96%, a specificity of 91.30%, and an accuracy of 89.13% to distinguish those with IIH and healthy controls. For mean hypophysis volumes, the optimal cutoff value

was 611.21 mm³, with a sensitivity of 78.26%, a specificity of 69.57%, and an accuracy of 73.91%. With area under the curve values of 0.934 and 0.724, respectively, receiver operating characteristic analysis showed significant group differences for mean ONS volume ($P < .0001$) and for hypophysis volume ($P < .005$). For mean ON volume, the receiver operating characteristic analysis showed no significant difference between the groups; the area under curve was 0.580 ($P = .338$).

Morphology of the Hypophysis

Morphology of the hypophysis in patients with IIH showed 0 convex, 4 mild concave, 11 severe concave, and 8 empty sella configurations, whereas controls had 13 convex ($P < .05$), 4 mild

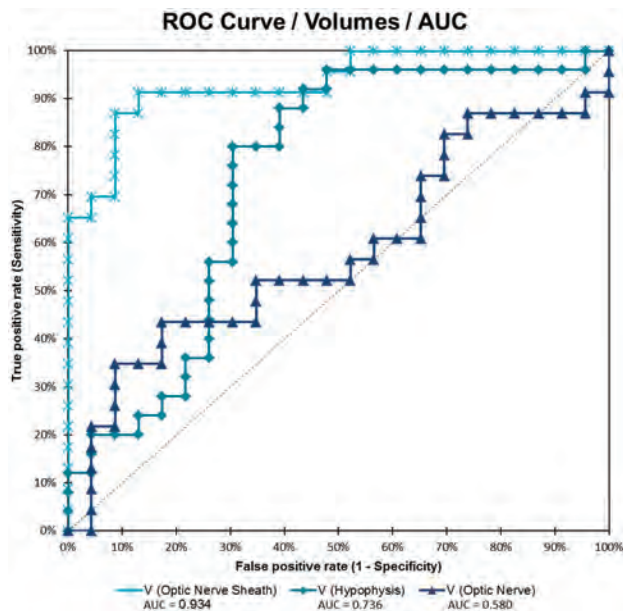


FIG 2. Receiver operating characteristic analysis curve for volumes of ONS, ON, and hypophysis.

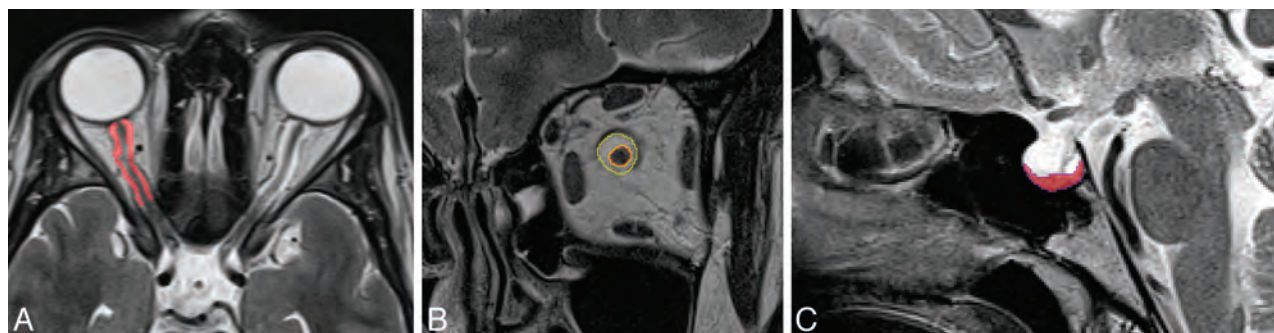


FIG 3. Voxel-based analysis of control MR images of healthy controls and normal configuration of the ONS and hypophysis. A, Axial scan with segmentation of ONS volume (red). B, Coronal scan with selection of ONS (yellow) and ON (red) volume segmentation. C, Midsagittal scan shows normal configuration of the hypophysis.

Area under the receiver operating characteristic curve and cut-off values

Parameter (Volume)	AUC	SE	P	95% CI		Cut-Off Value ^a (mm)
				Lower Bound	Upper Bound	
ONS	0.934	0.027	<.0001	0.881	0.987	201.30
ON	0.580	0.084	.338	0.416	0.745	228.64
Hypophysis	0.724	0.076	.003	0.574	0.874	611.21

Note:—AUC indicates area under the curve.

^a Calculated with the Youden Index ($Y = \text{Sensitivity} + \text{Specificity} - 1$).

concave ($P = .311$), 3 severe concave ($P < .05$), and 0 empty sella cases ($P < .05$). In relation to the displacement of the hypophyseal stalk, 14 patients (60.87%) and 18 controls (78.26%) had equal appearance of the superior border of the hypophysis ($P = .209$). Eight patients (34.78%) and 4 controls (17.39%) were found to have anterior deviation of the stalk ($P = .187$), whereas 1 patient (4.35%) and 1 control (4.35%) showed posterior deviation ($P = 1.0$).

Venous Sinus Stenoses

Nine venous sinus stenoses were detected in 6 patients with IIH, compared with 1 stenosis in the control group ($P < .05$). In both groups, no stenosis of $<50\%$ of the lumen was detected. Among patients with IIH with detected venous sinus stenoses, 3 showed bilateral transverse sinus stenosis, while 3 had unilateral stenoses (1 stenosis in the left transverse sinus and 2 stenoses in left sinus sigmoideus). The control subject with the identified venous sinus stenosis had 1 stenosis in left transverse sinus. In both groups, no stenoses in only the right venous sinuses were detected.

Correlation of Volume Measurement with Clinical Findings

Within the IIH group or the control group, ONS and hypophysis volume correlated with neither CSF maximum opening pressures (IIH: correlation coefficient [cc] = 0.0307, $P = .892$; control: $cc = 0.2055$, $P = .359$) nor with the severity of visual disturbances (IIH: $cc = 0.0777$, $P = .725$; control: $cc = 0.2237$, $P = .305$). In patients with IIH, maximum headache intensities did not correlate with CSF maximum opening pressures ($cc = 0.0964$, $P = .669$), ONS ($cc = -0.1347$, $P = .540$) or hypophysis volume ($cc = -0.3490$, $P = .103$).

DISCUSSION

Imaging findings in IIH are often subtle, and the radiologic signs have a strong component of subjective interpretation. Therefore,

the radiologic diagnosis is critically affected by the experience of the radiologist.

Several recent studies have reported significant correlations of imaging findings, such as hypophysis compression and empty sella, ONS distension, and ON tortuosity, with the diagnosis of IIH.^{3,6,12} Measurements of ONS diameters demonstrated wider ONS in individuals with IIH.^{6,13} On the other hand, a few studies have questioned these findings as not being statistically significant.^{6,14,15} Morphologic studies of the hypophysis in IIH were more consistent and showed a significant reduction of the ratio of the hypophysis to the sella turcica in patients with IIH.^{10,14} Relevance of slit-like ventricular morphology¹⁶ was postulated in early reports, but subsequent studies dissented from this hypothesis by verifying normal ventricle configuration in patients with IIH.¹⁷

We have shown that volumetric measurements of ONS and hypophysis volumes can be used to accurately diagnose patients with IIH. ONS volumes of $>201.30 \text{ mm}^3$ (sensitivity, 86.96%; specificity, 91.30%; accuracy, 89.13%) and hypophysis volumes of $< 611.21 \text{ mm}^3$ (sensitivity, 78.26%; specificity, 69.57%; accuracy, 73.91%) were significantly associated with the diagnosis of IIH. In comparison with previous studies by using metric analysis of ONS (sensitivity, 66.7%; specificity, 82.1%; accuracy, 76.73%) and hypophysis (sensitivity, 53.3%; specificity, 75%; accuracy, 67.44%), volumetric measurements increase the diagnostic reliability,³ including low interobserver variability. Brodsky⁶ observed an increased ONS diameter in 9 of 20 patients (45%), whereas our findings showed a dilated perioptic subarachnoid space in 20 of 23 patients (86.96%). Among patients with IIH, we did not observe a significant correlation between imaging findings and CSF opening pressure (ONS: $cc = 0.0307$, $P = .892$; hypophysis: $cc = 0.2055$, $P = .359$). Therefore, the results suggest that abnormal imaging findings may not be exclusively a direct result of elevated CSF pressure. Consequently, definite diagnosis (ie, according to the revised Dandy criteria) still requires liquor puncture (intracranial pressure $> 25 \text{ cm H}_2\text{O}$).⁹

The underlying cause of IIH still remains largely unknown, but the hypotheses of increased CSF production, reduced CSF absorption, and venous outflow obstruction as well as metabolic alterations are discussed.^{18,19} Venous sinus stenoses may lead to increased resistance in venous drainage and, as a consequence, to increased intracranial pressure. It is controversially debated whether obstructed venous drainage is the primary mechanism or is secondary to another pathologic process. In this context, compressed venous sinuses may also be the result of external compression²⁰⁻²⁴ by increased intracranial pressure. Galgano and Deshaies²⁵ stated that flow-related artifacts in noncontrast MR venography may be challenging to distinguish from pathologic venous sinus stenosis. Therefore, venous sinus abnormalities in IIH have to be assessed carefully.^{25,26} We did observe venous sinus stenoses in 6 patients with IIH and in 1 healthy control. In the present study, TOF-MR venography was performed to identify venous sinus abnormalities. However, detection of stenosis definitely depends on the imaging technique used. Compared with contrast-enhanced MRA or DSA and even though analyzed by a highly experienced neuroradiologist, results are slightly more prone to misinterpretation, owing to the underlying technical limitations of TOF-MR venography.^{27,28}

In our study, the mean ON volume of patients was slightly increased compared with that in controls (211.7 mm^3 versus 194.03 mm^3 , On-line Fig 1B), but this effect was not statistically significant ($P = .271$; sensitivity, 43.48%; specificity, 82.61%). It has been assumed that increased intracranial pressure leads to increased transmission of CSF into the intraorbital ONS, which impedes axoplasmic transport of synaptic vesicles, organelles, and molecules followed by optic nerve fiber swelling and flattening of the posterior globe.²⁹ Yet, we have not found a correlation of intracranial pressure and volume parameters supporting this hypothesis. Neither the degree of hypophysis compression nor the distention of ONS was augmented with increasing intracranial pressure. These results are in agreement with the observation that reduction of intracranial pressure by lumbar puncture has only a temporary effect.³⁰ Furthermore, these findings indicate that macroscopic deformations are indirect or comorbid changes rather than direct results of increased intracranial pressure. Therefore, it remains unclear in which way and to what extent the CSF space is affected in response to increasing intracranial pressure. We have considered the body mass index, which is especially important due to the strong association between IIH and obesity.^{18,31-35}

Morphologic signs become clearly visible only in advanced disease stages on conventional MR imaging analysis, whereas volumetric measurements allow an improved diagnostic reliability and possibly earlier detection, with potential impact on monitoring treatment efficacy. In a routine radiologic setting, image post-processing with quantitative analysis as previously specified can be achieved rapidly (≤ 10 minutes) by experienced radiologists. Software-assisted volumetric measurement has the potential to facilitate decision-making due to objective statistical parameters.

Possible automatization of measurement procedures could provide even faster and more reliable ways of assessment.^{36,37} Our relatively small study sample represents a potential limitation and requires confirmation by subsequent investigations.

CONCLUSIONS

As opposed to MR imaging-based metric measurements of hypophysis and ONS in patients with IIH, which have a confined diagnostic value due to their limited reproducibility and strong observer dependency, semiautomated volumetric analysis has the potential to objectify diagnosis and follow-up procedures by reducing interobserver bias.

Disclosures: Jan Hoffmann—UNRELATED: Grants/Grants Pending: German Research Foundation (Deutsche Forschungsgemeinschaft), Travel/Accommodations/Meeting Expenses Unrelated to Activities Listed: Allergan (travel expenses to meeting), Hagen Kunte—UNRELATED: Payment for Lectures (including service on Speakers Bureaus): Biogen-Idec (for speaking), Travel/Accommodations/Meeting Expenses Unrelated to Activities Listed: Biogen-Idec, Merck-Serono, Almirall, Lutz Harms—UNRELATED: Board Membership: Biogen Idec, Sanofi, Novartis, Consultancy: Biomarin, Payment for Lectures (including service on Speakers Bureaus): Biogen Idec, Bayer, Merck Serono, Novartis; Travel/Accommodations/Meeting Expenses Unrelated to Activities Listed: Bayer, Biogen Idec. Lutz Lüdemann—UNRELATED: Consultancy: local state ethics committee of the city of Berlin, Grants/Grants Pending: Deutsche Forschungsgemeinschaft, German research community,* Comments: Project: biological radiation treatment planning. Payment for Lectures (including service on Speakers Bureaus): Haus der Technik Essen. *Money paid to the institution.

REFERENCES

1. Pearce JM. From pseudotumour cerebri to idiopathic intracranial hypertension. *Pract Neurol* 2009;9:353–56
2. Spennato P, Ruggiero C, Parlato RS, et al. Pseudotumor cerebri. *Childs Nerv Syst* 2011;27:215–35
3. Agid R, Farb RI, Willinsky RA, et al. Idiopathic intracranial hypertension: the validity of cross-sectional neuroimaging signs. *Neuroradiology* 2006;48:521–27
4. Friedman DI, Jacobson DM. Diagnostic criteria for idiopathic intracranial hypertension. *Neurology* 2002;59:1492–95
5. Skau M, Brennum J, Gjerris F, et al. What is new about idiopathic intracranial hypertension? An updated review of mechanism and treatment. *Cephalalgia* 2006;26:384–99
6. Brodsky M. Magnetic resonance imaging in pseudotumor cerebri. *Ophthalmology* 1998;105:1686–93
7. Headache Classification Subcommittee of the International Headache Society. The International Classification of Headache Disorders. 2nd edition. *Cephalalgia* 2004;24(suppl 1):9–160
8. World Health Organization. *International Statistical Classification of Diseases and Related Health Problems*. Geneva, Switzerland: World Health Organization; 2004
9. Friedman DI. Idiopathic intracranial hypertension with Dan and beyond: the 2010 Jacobson Lecture. *J Neuroophthalmol* 2010;30:380–85
10. Yuh WT, Zhu M, Taoka T, et al. MR imaging of pituitary morphology in idiopathic intracranial hypertension. *J Magn Reson Imaging* 2000;12:808–13
11. Bewick V, Cheek L, Ball J. Statistics review 13: receiver operating characteristic curves. *Crit Care* 2004;8:508–12
12. Manfré L, Lagalla R, Mangiameli A, et al. Idiopathic intracranial hypertension: orbital MRI. *Neuroradiology* 1995;37:459–61
13. Degnan AJ, Levy LM. Narrowing of Meckel's cave and cavernous sinus and enlargement of the optic nerve sheath in pseudotumor cerebri. *J Comput Assist Tomogr* 2011;35:308–12
14. Gibby WA, Cohen MS, Goldberg HI, et al. Pseudotumor cerebri: CT findings and correlation with vision loss. *AJR Am J Roentgenol* 1993;160:143–46
15. Gass A, Barker GJ, Riordan-Eva P, et al. MRI of the optic nerve in benign intracranial hypertension. *Neuroradiology* 1996;38:769–73
16. Weisberg LA. Computed tomography in benign intracranial hypertension. *Neurology* 1985;35:1075–78
17. Jacobson DM, Karanjia PN, Olson KA, et al. Computed tomography ventricular size has no predictive value in diagnosing pseudotumor cerebri. *Neurology* 1990;40:1454–55
18. Kesler A, Kliper E, Shenkerman G, et al. Idiopathic intracranial hypertension is associated with lower body adiposity. *Ophthalmology* 2010;117:169–74
19. Degnan AJ, Levy LM. Pseudotumor cerebri: brief review of clinical syndrome and imaging findings. *AJNR Am J Neuroradiol* 2011;32:1986–93
20. Ahmed R, Friedman DI, Halmagyi GM. Stenting of the transverse sinuses in idiopathic intracranial hypertension. *J Neuroophthalmol* 2011;31:374–80
21. Stienen A, Weinzierl M, Ludolph A, et al. Obstruction of cerebral venous sinus secondary to idiopathic intracranial hypertension. *Eur J Neurol* 2008;15:1416–18
22. Higgins JN, Pickard JD. Lateral sinus stenoses in idiopathic intracranial hypertension resolving after CSF diversion. *Neurology* 2004;62:1907–08
23. Lee SW, Gates P, Morris P, et al. Idiopathic intracranial hypertension; immediate resolution of venous sinus “obstruction” after reducing cerebrospinal fluid pressure to <10cmH(2)O. *J Clin Neurosci* 2009;16:1690–92
24. Scoffings DJ, Pickard JD, Higgins JN. Resolution of transverse sinus stenoses immediately after CSF withdrawal in idiopathic intracranial hypertension. *J Neurol Neurosurg Psychiatry* 2007;78:911–12
25. Galgano MA, Deshaies EM. An update on the management of pseudotumor cerebri. *Clin Neurol Neurosurg* 2013;115:252–59
26. Peng KP, Fuh JL, Wang SJ. High-pressure headaches: idiopathic intracranial hypertension and its mimics. *Nat Rev Neurol* 2012;8:700–10
27. Nedelmann M, Kaps M, Mueller-Forell W. Venous obstruction and jugular valve insufficiency in idiopathic intracranial hypertension. *J Neurol* 2009;256:964–69
28. Fera F, Bono F, Messina D, et al. Comparison of different MR venography techniques for detecting transverse sinus stenosis in idiopathic intracranial hypertension. *J Neurol* 2005;252:1021–25
29. Acheson JF. Idiopathic intracranial hypertension and visual function. *Br Med Bull* 2006;79–80:233–44
30. Johnston I, Paterson A. Benign intracranial hypertension. II. CSF pressure and circulation. *Brain* 1974;97:301–12
31. Kupersmith MJ, Gamell L, Turbin R, et al. Effects of weight loss on the course of idiopathic intracranial hypertension in women. *Neurology* 1998;50:1094–98
32. Wall M. Idiopathic intracranial hypertension. *Neurol Clin* 2010;28:593–617
33. Ko MW, Chang SC, Ridha MA, et al. Weight gain and recurrence in idiopathic intracranial hypertension: a case-control study. *Neurology* 2011;76:1564–67
34. Ball AK, Clarke CE. Idiopathic intracranial hypertension. *Lancet Neurol* 2006;5:433–42
35. Sugerma HJ, Felton WL 3rd, Salvant JB Jr, et al. Effects of surgically induced weight loss on idiopathic intracranial hypertension in morbid obesity. *Neurology* 1995;45:1655–59
36. Kassubek J, Pinkhardt EH, Dietmaier A, et al. Fully automated atlas-based MR imaging volumetry in Huntington disease, compared with manual volumetry. *AJNR Am J Neuroradiol* 2011;32:1328–32
37. Huppertz HJ, Kroll-Seeger J, Danek A, et al. Automatic striatal volumetry allows for identification of patients with chorea-acanthocytosis at single subject level. *J Neural Transm* 2008;115:1393–400

Accuracy of Postcontrast 3D Turbo Spin-Echo MR Sequence for the Detection of Enhanced Inflammatory Lesions in Patients with Multiple Sclerosis

J. Hodel, O. Outteryck, E. Ryo, A.-L. Bocher, O. Lambert, D. Chéchin, H. Zéphir, A. Lacour, J.-P. Pruvo, P. Vermersch, and X. Leclerc

ABSTRACT

BACKGROUND AND PURPOSE: Therapeutic strategies for patients with MS partly rely on contrast-enhanced MR imaging. Our aim was to assess the diagnostic performance of 3D turbo spin-echo MR imaging with variable refocusing flip angles at 3T for the detection of enhanced inflammatory lesions in patients with multiple sclerosis.

MATERIALS AND METHODS: Fifty-six patients with MS were prospectively investigated by using postcontrast T1-weighted axial 2D spin-echo and 3D TSE MR images. The order in which both sequences were performed was randomized. Axial reformats from 3D T1 TSE were generated to match the 2D spin-echo images. The reference standard was defined by using clinical data and all MR images available. Three separate sets of MR images (2D spin-echo images, axial reformats, and multiplanar images from 3D TSE sequences) were examined in a blinded fashion by 2 neuroradiologists separately for the detection of enhanced MS lesions. Image artifacts and contrast were evaluated.

RESULTS: No artifacts related to vascular pulsation were observed on 3D TSE images, whereas image artifacts were demonstrated on 2D spin-echo images in 41 patients. One hundred twelve enhanced MS lesions were identified in 19 patients. Sixty-four lesions were correctly diagnosed by using 2D spin-echo images; 90, by using 3D TSE axial reformatted views; and 106, by using multiplanar analysis of the 3D TSE sequence. Multiplanar analysis was 94.7% sensitive and 100% specific for the diagnosis of patients with at least 1 enhanced lesion. Contrast of enhanced MS lesions was significantly improved by using the 3D TSE sequence ($P < .01$).

CONCLUSIONS: The 3D TSE sequence with multiplanar analysis is a useful tool for the detection of enhanced MS lesions.

ABBREVIATIONS: CR = contrast rate; DIR = double inversion recovery; GRE = gradient recalled-echo; SE = spin-echo

The diagnosis of multiple sclerosis needs to demonstrate dissemination of brain lesions in space and time and to exclude alternative diagnoses. In some circumstances, dissemination of brain lesions in space and time can be established by a single MR imaging.¹ In such patients, dissemination of brain lesions in time is demonstrated by the simultaneous presence of asymptomatic gadolinium-enhancing and nonenhancing lesions at any time.¹ Indeed, therapeutic strategies for patients with MS partly rely on contrast-enhanced MR imaging. Updated recommendations on the use of MR imaging in MS suggest that axial 2D T1-weighted spin-echo (SE) MR imaging should be performed for the detection of enhanced MS lesions,^{2,3} whereas T1-weighted 3D gradient

recalled-echo (GRE) MR images are reported to be useful for the assessment of brain atrophy.²⁻⁴ As previously reported,⁵ the sensitivity of the 2D T1-weighted SE sequence for the detection of enhanced MS lesions is progressively increased from 5 to 10 minutes after intravenous injection of gadolinium.

Recently, a new technique has been introduced to generate 3D T1-weighted images of the brain (BrainView, Philips Healthcare, Best, the Netherlands; Cube, GE Healthcare, Milwaukee, Wisconsin; SPACE, Siemens, Erlangen, Germany). The BrainView sequence is based on a turbo spin-echo acquisition with variable refocusing flip angles and short echo spacing, allowing longer echo-train readouts and reduced signal losses.⁶ Such an approach provides high spatial resolution and signal-to-noise ratio without the blurring commonly associated with long echo-trains. Thinner section images can be acquired, minimizing the partial volume effect between small lesions and surrounding brain parenchyma. The added value of the postcontrast 3D TSE sequence with variable flip angles was recently reported in patients with brain metastasis.^{7,8}

No data are available on the diagnostic performance of the

Received May 7, 2013; accepted after revision July 2.

From the Departments of Neuroradiology (J.H., E.R., A.-L.B., J.-P.P., X.L.) and Neurology (O.O., H.Z., A.L., P.V.), Hôpital Roger Salengro, Lille, France; Department of Neuroradiology (O.L.), Fondation Ophtalmologique Rothschild, Paris, France; and Philips Medical Systems (D.C.), Suresnes, France.

Please address correspondence to Jérôme Hodel, MD, Department of Neuroradiology, Hôpital Roger Salengro, Rue Emile Laine 59037 Lille, France; e-mail: jerome.hodel@gmail.com

<http://dx.doi.org/10.3174/ajnr.A3795>

Parameters for all sequences

Parameter	3D DIR	2D FLAIR	2D T1 SE	3D T1 TSE
TR (ms)	5500	11,000	600–700	400
TE (ms)	251	125	10	26
T1 (ms)	625–2600	2800	N/A	N/A
Echo-train length	173	31	N/A	30
No. of sections/slab	300	31	36	267
Section thickness (mm)	1.3	5	4	1.2 (reformat 4)
Matrix size	208 × 208	276 × 126	232 × 165	256 × 215
Voxel size (mm)	1.2 × 1.2 × 1.3	0.85 × 1.42 × 5	1 × 1.10 × 4	1 × 1.10 × 1.2 (reformat 1 × 1.10 × 4)
FOV (mm)	250 × 250	230 × 176	230 × 182	250 × 237
Acquisition plane	Sagittal	Axial	Axial	Sagittal
Acquisition time	6 min 30 sec	2 min 56 sec	3 min 30 sec	5 min 30 sec

Note:—N/A indicates not applicable; No. of sections, number of sections acquired; reformat, 4-mm-thick axial reformatted views of the 3D T1 TSE sequence; 2D, T1 SE images and 4-mm-thick axial reformatted views of the 3D T1 TSE sequence with the same voxel size.

postcontrast 3D T1-weighted TSE sequence for the detection of enhanced inflammatory lesions in patients with MS. Our purpose was to assess the detectable enhanced MS lesions by using the 3D BrainView sequence compared with the conventional axial 2D SE sequence.

MATERIALS AND METHODS

Patients

This study was approved by our institutional review board. Informed consent was obtained from all patients. From July to December 2012, fifty-nine consecutive patients with MS according to the 2010 McDonald criteria were examined by using 3T MR imaging for follow-up. Three of these 59 patients were excluded because of motion artifacts. Finally, 56 consecutive patients (20 men, 36 women; mean age, 41.2 ± 13.9 years) were included in the study.

Image Acquisition

All patients were examined on a 3T MR imaging scanner (Achieva; Philips Healthcare) by using a 32-channel array head coil. The routine MR imaging protocol included 2D axial MR images (pre- and postcontrast T1 SE, diffusion-weighted T2 TSE, and FLAIR) and 3D double inversion recovery (DIR) MR images. In addition, the postcontrast 3D TSE T1-weighted sequence (3D BrainView) was performed in all patients. The 3D TSE sequence is characterized by a long TSE impulsion train and a combination of advanced features, among which are variable refocusing angles. A specific refocalization scheme is also applied to preserve T1 contrast and minimize the blurring effect. Intravenous gadobutrol (Gadovist 1.0; Bayer-Schering Pharma, Berlin, Germany) was administered at a concentration of 0.1 mmol/kg. The 2D axial SE and 3D TSE T1-weighted postcontrast MR images were obtained 10 minutes after the gadolinium administration for all patients. The order in which these 2 postcontrast sequences were performed was randomized. 3D TSE source images were reformatted into 4-mm-thick axial sections to match the section thickness and the acquisition plane of the 2D SE T1-weighted images.

The parameters for each MR image are summarized in the Table.

Image Analysis

The reference standard for the diagnosis of enhanced MS lesions was defined by 2 neuroradiologists (X.L. and J.-P.P.) with >25

years' experience. They reviewed together all the MR imaging datasets by using clinical data and all the MR images available. An enhanced MS lesion was defined as a focal enhancement on post-contrast images, with a size superior to 2 mm, involving gray or white matter and associated with a parenchymal hyperintensity on FLAIR or DIR images. Focal enhancement without DIR- or FLAIR-associated hyperintensities was not considered a real MS lesion. First, the readers were asked to assess enhanced MS lesions for each patient. Second, the readers were asked to notice high-signal-intensity artifacts related to vascular pulsation within the postcontrast 2D SE and 3D TSE images according to the following scale: 0, no artifacts; 1, artifacts that did not impair image analysis; 2, artifacts that impaired image analysis.

For the evaluation of the 3D TSE sequence, 2 neuroradiologists (E.R. and A.-L.B.) with 7 and 6 years' experience, respectively, analyzed, independently and separately, all postcontrast T1-weighted images on a PACS workstation. First, the readers assessed 3 sets of images in a randomized order: 1) 2D axial SE images, 2) 4-mm-thick axial reformations from 3D TSE sequences, and 3) multiplanar analysis from 3D TSE sequences with thin sections and MIP reformations in arbitrary planes. They were blinded to clinical data and to other MR images and were asked to notice the number and location of the enhanced inflammatory lesions for each patient. An enhanced lesion was retained when a focal enhancement involving the gray or white matter was detected. Second, a consensus reading was performed between the 2 blinded readers to resolve their disagreements.

One radiologist (X.L.) measured the contrast rate (CR) of the largest enhanced MS lesions (ie, measuring at least 1 cm) by using both the axial 2D T1 SE images (4-mm-thick) and the 4-mm-thick axial reformatted views from the 3D TSE sequence. For each patient, regions of interest were drawn within the enhanced MS lesions and their background (ie, adjacent white matter), allowing the measurement of signal intensities (SI). Using the PACS workstation, we drew the same ROIs on the 2D images and axial reformatted views. As previously reported,^{8,9} the contrast rate was calculated between the MS lesion and its background according to the following formula: $CR = [(SI \text{ Lesion} - SI \text{ Background})/SI \text{ Background}] \times 100$.

Statistical Analysis

All statistical analyses were performed by using R Statistical Software (Version 3.0.0; <http://www.r-project.org/>).

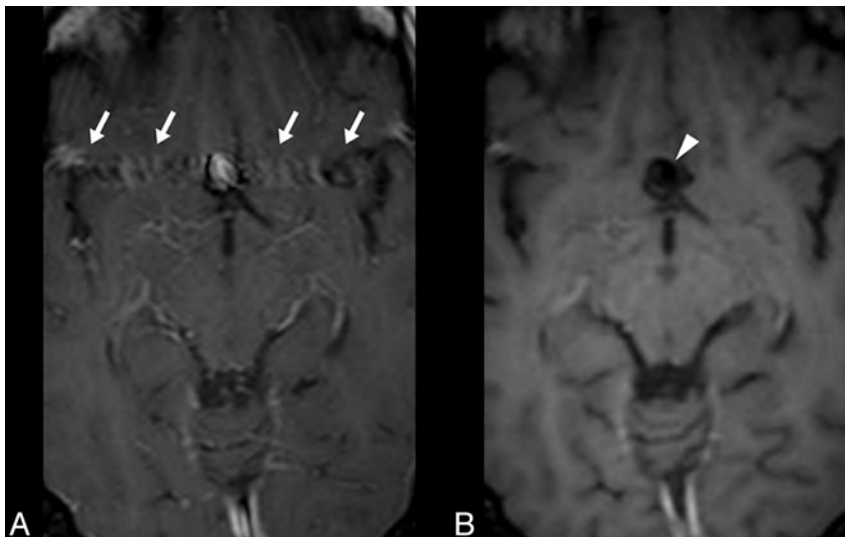


FIG 1. Postcontrast T1-weighted 2D SE (A) and a 4-mm-thick axial reformatted view of the 3D TSE (B) images of patient 5 with MS and an aneurysm of the anterior communicating artery. High-signal-intensity artifacts related to vascular pulsation are observed beside the aneurysm (A, arrows) by using axial 2D SE images, while these artifacts are not visible on 3D TSE images (B, arrowhead). Similar differences can be noted between the 2 postcontrast sequences within the brain sinuses. Indeed, while the 2D SE sequence is still influenced by blood flow effects, a black-blood effect is induced by the long echo-trains used with the 3D TSE sequence (B, arrowhead). This technical aspect may also partly explain the improved diagnostic performance observed with the 3D TSE sequence.

Interobserver agreement was calculated by using the Cohen κ test. κ values were interpreted as follows: $\kappa = 0$ indicates poor agreement; $\kappa = 0.01$ – 0.20 , minor agreement; $\kappa = 0.21$ – 0.40 , fair agreement; $\kappa = 0.41$ – 0.60 , moderate agreement; $\kappa = 0.61$ – 0.80 , good agreement; and $\kappa = 0.81$ – 1 , excellent agreement.

To compare 2D SE and 3D TSE sequences, we evaluated both the overall number of enhanced MS lesions detected and the number of patients diagnosed with at least 1 enhanced MS lesion. The overall number of enhanced MS lesions detected by using 2D axial SE images, 4-mm-thick axial reformations from 3D TSE sequences, and multiplanar analysis of the 3D TSE sequences was compared with the reference standard by using the Cohen κ test. For the diagnosis of patients with at least 1 enhanced MS lesion, standard diagnostic accuracy parameters (sensitivity and specificity) of 2D axial SE images, 4-mm-thick axial reformations from the 3D TSE sequences, and multiplanar analysis of the 3D TSE sequences were calculated according to the reference standard.

Comparisons of κ values were performed to determine whether the agreements were significantly different for each parameter evaluated.

We also compared the MS lesion contrast rate and the artifacts grading between 2D SE and 3D TSE sequences by using a non-parametric statistical test (Wilcoxon test). P values $< .05$ were considered statistically significant.

RESULTS

Overall Image Quality

High-signal-intensity artifacts related to vascular pulsation were observed in 41 of the 56 included patients by using the 2D T1 sequence involving the posterior fossa ($n = 38$) or the frontal lobes ($n = 8$) (median score = 1). In comparison with the 2D SE sequence, there were no artifacts related to vascular pulsation by

using the 3D TSE sequence ($P < .001$). A slight blurring was reported for 15 patients on 3D TSE images, which did not impair the data analysis.

Figure 1 illustrates the reduction of artifacts by using the 3D TSE sequence.

Reference Standard for the Diagnosis of Enhanced MS Lesions

Using clinical data and all the MR images available, we diagnosed 112 MS lesions in 19 patients; 9 lesions involved the gray matter while 103 lesions involved the periventricular or deep white matter. Six of the 112 enhanced lesions were only confirmed with the DIR images and were not visible on conventional 2D FLAIR images.

Interobserver Agreement

For the detection of enhanced MS lesions, interobserver agreement was substantial for 2D axial SE images ($\kappa = 0.62$) and good for 3D TSE images ($\kappa = 0.75$). Comparison of the κ values showed that the interobserver agreement was not significantly

different between 2D axial SE and 3D TSE images ($P = .2140$).

Comparison of 2D T1 SE and 3D TSE MR Images

Compared with the reference standard, reader 1 correctly identified 57.1% of the enhanced MS lesions by using the 2D T1 SE sequence, 77.68% by using 4-mm-thick axial reformatted views, and 93.8% by using the multiplanar analysis. Reader 2 identified 56.3%, 79.5%, and 93.8% of the enhanced MS lesions, respectively. No enhanced MS lesion was visible only on 2D T1-weighted SE images.

Using the 2D SE and 3D TSE MR images, the 2 blinded readers misdiagnosed a total of 22 focal venous enhancements as enhanced MS lesions (ie, 22 false-positive lesions because these lesions were not previously considered real MS lesions according to the reference standard). Twelve false-positive lesions were observed by using the 2D T1-weighted SE sequence, 7 by using 4-mm-thick axial reformatted views, and 3 by using the multiplanar analysis of the 3D TSE sequence.

The agreement with the reference standard was fair by using the 2D T1 SE images ($\kappa = 0.284$), moderate by using 4-mm-thick axial reformatted views ($\kappa = 0.507$), and good by using the multiplanar analysis ($\kappa = 0.735$). Agreement with the reference standard was significantly improved by using the multiplanar analysis of the 3D TSE sequence compared with 2D T1 SE images ($P = .0007$) or 4-mm-thick axial reformatted views ($P = .0465$).

On the basis of consensus statements between the blinded readers, 64 enhanced MS lesions were correctly identified by using the 2D T1-weighted SE sequence. Forty-two additional lesions were visible by using the 3D TSE sequence; 26 lesions, on 4-mm-thick axial reformatted views (90 lesions detected); and 16 other

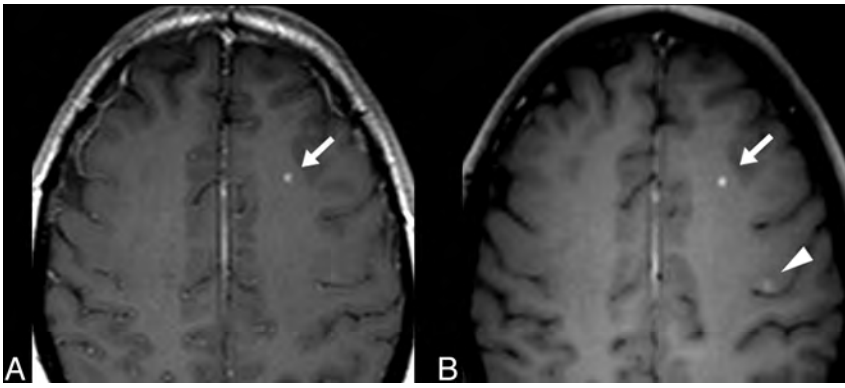


FIG 2. Postcontrast T1-weighted 2D SE (A) and 4-mm-thick axial reformatted views of the 3D TSE (B) images of patient 24 with MS. An active enhanced MS lesion is detected within the left frontal white matter by using both axial 2D SE images (A, arrow) and a 4-mm-thick axial reformatted view of the 3D TSE sequence (B, arrow). Due to improved image contrast, an additional lesion involving the precentral sulcus is visible by using the 3D TSE sequence (B, arrowhead).

lesions, by using the multiplanar analysis (106 lesions detected). The 26 additional lesions revealed by the axial reformatted views involved the periventricular white matter ($n = 12$), the optic nerves ($n = 2$), the pons ($n = 5$), the cerebellum ($n = 4$), and the temporal ($n = 2$) and the frontal ($n = 1$) white matter. The 16 additional lesions detected by multiplanar analysis involved the periventricular white matter ($n = 6$), the corpus callosum ($n = 3$), the cingulum ($n = 1$), the brain stem ($n = 4$), the parietal white matter ($n = 1$), and the optic nerve ($n = 1$).

Sixteen of the 56 patients presented with at least 1 enhanced MS lesion with 2D SE images; 17, with axial reformatted views; and 19, with multiplanar analysis of the 3D TSE sequences. Indeed 3 patients were correctly diagnosed with at least 1 MS enhanced lesion only with the 3D TSE sequence. Such findings had an impact on clinical management by switching on second-line immunosuppressive therapy. For the diagnosis of the patients with at least 1 MS enhanced lesion, 2D axial SE images were 84.2% sensitive and 78.4% specific, 4-mm-thick axial reformations of the 3D TSE sequences were 84.2% sensitive and 89.2% specific, and multiplanar analysis of the 3D TSE sequences was 94.7% sensitive and 100% specific.

Contrast Rate

ROIs were drawn within MS active lesions that measured at least 1 cm (11 patients). With 2D SE images, the median CR was 39.5 (11.9; 100.3), while, with 3D TSE images, the median CR was 46.9 (10.3; 128). The CR of the enhanced MS lesions was significantly higher by using the 3D TSE sequence ($P < .011$).

An example of the improved detectability of enhanced MS lesions by using the 3D TSE sequence is given in Fig 2.

DISCUSSION

In this study, we demonstrated that the 3D TSE sequence improved the detection of enhanced MS lesions due to a better image contrast and the suppression of artifacts related to vascular pulsation. The use of thinner sections and MIP reformations further improved the diagnosis of small MS lesions. These findings are clinically relevant, considering the importance of enhanced asymptomatic lesions for the diagnosis and management of patients with MS.

To improve the comparison between 2D SE and 3D TSE postcontrast MR images, we first used 4-mm-thick axial reformations from the 3D TSE sequence leading to the same voxel size. This approach confirmed that the diagnostic performance of the 3D TSE sequence was significantly superior to that of the 2D T1 SE. This difference could be partly explained by the suppression of artifacts related to vascular pulsation. As previously suggested,¹⁰ the black-blood effect of the 3D TSE sequence is due to the dephasing of spins induced by the long echo-trains used. In our study, we systematically observed this effect within brain arteries, while a discontinuous enhancement was still observed within large cortical veins.

The non-spatially selective pulse, which affects the entire imaging slab by using the 3D TSE sequence, may also contribute to the absence of artifacts related to vascular pulsation.⁶ In our study, such technical aspects were particularly useful for the detection of MS lesions involving the brain stem or the cerebellum.

The diagnostic performance of the 3D TSE sequence was further improved when using thinner sections and multiplanar analysis. There are several advantages of using 3D thinner sections for the detection of enhanced MS lesions. First, it has been previously reported that the decrease in section thickness (ie, of the partial volume effect) is strongly associated with increased lesion detection.¹¹⁻¹³ Second, 3D images can be registered more accurately, allowing a more precise assessment of spatiotemporal disease activity that is crucial in patients with MS. In our study, registration of MR images was also useful to define the reference standard. Indeed, the 3D DIR images were registered with the 3D T1 TSE images, optimizing the detectability of small enhanced MS lesions.¹⁴⁻¹⁶ Third, 3D sequences, with their higher SNR and isotropic voxel size, allow image postprocessing with MIP reformations in arbitrary planes. MIP views can be routinely obtained with the 3D TSE sequence because the contrast between gray and white matter appears significantly reduced. This is not the case when using 3D T1-weighted GRE MR images. We may hypothesize that MIP reformatted views could improve the time efficiency for the detection of enhanced MS lesions. Further studies including a larger cohort of patients with enhanced MS lesions may confirm this hypothesis.

Our study has several limitations. We used the DIR sequence, which is not a standard pulse sequence for clinical use. The DIR sequence may have further improved the detection of cortical and brain stem MS lesions as previously reported.¹⁴⁻¹⁶ However, the relatively small number of enhanced MS lesions confirmed only with DIR images should not limit the generalizability of our findings to clinical practice. The parameter setting of the 3D TSE sequence in the present study was optimized before scanning patients to decrease image artifacts and to improve the image contrast. An acquisition time of more than 20 minutes would be required to achieve a full brain coverage with the same section thickness for both axial SE and 3D TSE sequences (ie, 1.2 mm).

Then, the use of axial 4-mm-thick reformatting views of the BrainView sequence, which perfectly matched the axial T1 SE images, appeared acceptable to achieve an equivalent comparison between the 2 postcontrast MR images.

Using the 3D TSE sequence, there was a slightly increased scanning time compared with the 2D SE sequence. The duration of the 3D TSE sequence could be reduced by applying a higher parallel imaging acceleration factor. Moreover, in most centers, the MR imaging protocol usually includes 2 postcontrast T1-weighted 2D SE sequences in the coronal and axial planes for routine evaluation. Image blurring may be observed on 3D TSE images due to the longer echo-trains. However, this did not prevent image interpretation, and a specific refocalization scheme was developed to minimize these artifacts. Finally, discontinuous enhancement within large cortical veins may be misinterpreted as an enhanced MS lesion on 3D TSE images. In our study, due to the high spatial resolution of this sequence, multiplanar reformations were particularly useful to distinguish these veins from brain MS lesions.

CONCLUSIONS

This study suggests that the 3D T1-weighted TSE MR imaging with variable refocusing flip angles is superior to the conventional 2D SE axial sequence for the detection of enhanced MS lesions. In addition, multiplanar analysis with thinner sections and MIP reformatted views further improves the diagnostic performance of the 3D TSE sequence.

ACKNOWLEDGMENTS

Level of contributions: Jérôme Hodel: data acquisition and analysis, manuscript editing; Olivier Outteryck and Xavier Leclerc: data analysis, manuscript editing; Edouard Ryo, Anne-Laure Bocher, and Jean-Pierre Pruvo: data acquisition and analysis; David Chéchin: data analysis; Patrick Vermersch, Héléne Zéphir, Arnaud Lacour: data acquisition; and O. Lambert: statistical analysis.

Disclosures: Oliver Outteryck—UNRELATED: Travel/Accommodations/Meeting Expenses Unrelated to Activities Listed: Bayer-Schering,* Biogen Idec,* Teva Pharmaceuticals,* Merck-Serono,* Novartis. David Chéchin—OTHER RELATIONSHIPS: employment at Philips Healthcare. Comments: I am employed by Philips Healthcare, and this work was done on a Philips 3T MRI system. I supported this work by installing, evaluating, and optimizing the sequences. Héléne Zéphir—UNRELATED: Consultancy: Biogen Idec, Genzyme, Sanofi, Merck, Teva, Novartis, Bayer, Grants/Grants Pending: Teva.* Patrick Vermersch—UNRELATED: Consultancy: Biogen Idec, Novartis, Bayer, Merck-Serono, Teva, Sanofi-Genzyme, Grants/Grants Pending: Biogen Idec,* Bayer,* Merck-Serono,* Sanofi-Genzyme,* Travel/Accommodations/Meeting Expenses Unrelated to Activities Listed: Biogen Idec, Novartis, Bayer, Merck-Serono, Teva, Sanofi-Genzyme. *Money paid to the institution.

REFERENCES

1. Polman CH, Reingold SC, Banwell B, et al. **Diagnostic criteria for multiple sclerosis: 2010 revisions to the McDonald criteria.** *Ann Neurol* 2011;69:292–302
2. Lövblad KO, Anzalone N, Dorfler A, et al. **MR imaging in multiple sclerosis: review and recommendations for current practice.** *AJNR Am J Neuroradiol* 2010;31:983–89
3. Filippi M, Rocca MA. **MR imaging of multiple sclerosis.** *Radiology* 2011;259:659–81
4. Bergsland N, Horakova D, Dwyer MG, et al. **Subcortical and cortical gray matter atrophy in a large sample of patients with clinically isolated syndrome and early relapsing-remitting multiple sclerosis.** *AJNR Am J Neuroradiol* 2012;33:1573–78
5. Uysal E, Erturk SM, Yildirim H, et al. **Sensitivity of immediate and delayed gadolinium-enhanced MRI after injection of 0.5 M and 1.0 M gadolinium chelates for detecting multiple sclerosis lesions.** *AJR Am J Roentgenol* 2007;188:697–702
6. Mugler JP 3rd, Bao S, Mulkern RV, et al. **Optimized single-slab three-dimensional spin-echo MR imaging of the brain.** *Radiology* 2000;216:891–99
7. Reichert M, Morelli JN, Runge VM, et al. **Contrast-enhanced 3-dimensional SPACE versus MP-RAGE for the detection of brain metastases: considerations with a 32-channel head coil.** *Invest Radiol* 2013;48:55–60
8. Kato Y, Higano S, Tamura H, et al. **Usefulness of contrast-enhanced T1-weighted sampling perfection with application-optimized contrasts by using different flip angle evolutions in detection of small brain metastasis at 3T MR imaging: comparison with magnetization-prepared rapid acquisition of gradient echo imaging.** *AJNR Am J Neuroradiol* 2009;30:923–29
9. Rand S, Maravilla KR, Schmiedl U. **Lesion enhancement in radio-frequency spoiled gradient-echo imaging: theory, experimental evaluation, and clinical implications.** *AJNR Am J Neuroradiol* 1994;15:27–35
10. Busse RF, Brau AC, Vu A, et al. **Effects of refocusing flip angle modulation and view ordering in 3D fast spin echo.** *Magn Reson Med* 2008;60:640–49
11. Dolezal O, Dwyer MG, Horakova D, et al. **Detection of cortical lesions is dependent on choice of slice thickness in patients with multiple sclerosis.** *Int Rev Neurobiol* 2007;79:475–89
12. Molyneux PD, Tubridy N, Parker GJ, et al. **The effect of section thickness on MR lesion detection and quantification in multiple sclerosis.** *AJNR Am J Neuroradiol* 1998;19:1715–20
13. Bink A, Schmitt M, Gaa J, et al. **Detection of lesions in multiple sclerosis by 2D FLAIR and single-slab 3D FLAIR sequences at 3.0 T: initial results.** *Eur Radiol* 2006;16:1104–10
14. Moraal B, Roosendaal SD, Pouwels PJ, et al. **Multi-contrast, isotropic, single-slab 3D MR imaging in multiple sclerosis.** *Eur Radiol* 2008;18:2311–20
15. Simon B, Schmidt S, Lukas C, et al. **Improved in vivo detection of cortical lesions in multiple sclerosis using double inversion recovery MR imaging at 3 Tesla.** *Eur Radiol* 2010;20:1675–83
16. Geurts JJ, Pouwels PJ, Uitdehaag BM, et al. **Intracortical lesions in multiple sclerosis: improved detection with 3D double inversion-recovery MR imaging.** *Radiology* 2005;236:254–60

Complications of Endovascular Treatment for Acute Stroke in the SWIFT Trial with Solitaire and Merci Devices

P.T. Akins, A.P. Amar, R.S. Pakbaz, and J.D. Fields, on behalf of the SWIFT Investigators



ABSTRACT

BACKGROUND AND PURPOSE: Treatment of patients with ischemic stroke after endovascular treatment requires in-depth knowledge of complications. The goal of this study was to make endovascular treatment for acute ischemic stroke safer through an in-depth review of the major periprocedural complications observed in the Solitaire FR With Intention for Thrombectomy (SWIFT) trial.

MATERIALS AND METHODS: The SWIFT data base was searched for major peri-procedural complications defined as symptomatic intracranial hemorrhage within 36 hours, SAH, air emboli, vessel dissection, major groin complications, and emboli to new vascular territories.

RESULTS: Major peri-procedural complications occurred in 18 of 144 patients (12.5%) as follows: symptomatic intracranial hemorrhage, 4.9%; air emboli, 1.4%; vessel dissection, 4.2%; major groin complications, 2.8%; and emboli to new vascular territories, 0.7%. Rates of symptomatic intracranial bleeding by subtype were PH1, 0.7%; PH2, 0.7% (PH1 indicates hematoma within ischemic field with some mild space-occupying effect but involving $\leq 30\%$ of the infarcted area; PH2, hematoma within ischemic field with space-occupying effect involving $> 30\%$ of the infarcted area); intracranial hemorrhage remote from ischemic zone, 0%; intraventricular hemorrhage, 0.7%; and SAH, 3.5%. We did not observe any statistically significant associations of peri-procedural complications with age; type of treatment center; duration of stroke symptoms; NIHSS score, IV thrombolytics, atrial fibrillation, site of vessel occlusion; rescue therapy administered after endovascular treatment; or device. Comparing the Merci with the Solitaire FR retrieval device, we observed symptomatic cerebral hemorrhage (10.9% versus 1.1%; $P = .013$); symptomatic SAH (7.3% versus 1.1%; $P = .07$), air emboli (1.8% versus 1.1%; $P = 1.0$), emboli to new vascular territories (1.8% versus 0%; $P = .38$), vessel dissection (1.8% versus 4.5%; $P = .65$), and major groin complications (3.6% versus 7.9%; $P = .48$). Angiographic vasospasm was common but without clinical sequelae.

CONCLUSIONS: Understanding of procedural complications is important for treatment of patients with stroke after endovascular treatment. We observed fewer endovascular complications with the Solitaire FR device treatment compared with Merci device treatment, particularly symptomatic cerebral hemorrhage.

ABBREVIATION: SICH = symptomatic intracranial hemorrhage; TIMI = Thrombolysis in Myocardial Infarction; CEC = Clinical Events Committee

Intravenous tissue plasminogen activator has been proven to be efficacious in recanalization of occluded intracranial vessels and improvement of clinical outcome for acute ischemic stroke.¹ A meta-analysis of 53 studies including 2066 patients with acute

stroke demonstrated a 46.2% overall recanalization rate with IV fibrinolysis.^{1,2} However, IV tPA has limited ability to open occlusions of medium and large arteries such as the internal carotid artery, proximal middle cerebral artery, or basilar artery, with recanalization rates reported as low as 10%.^{2,3} Because of these limitations, catheter-based approaches for acute ischemic stroke have been developed to directly infuse thrombolytics at the site of the thrombus or mechanically extract and disrupt the clot.³⁻¹³ As with systemic thrombolytics, endovascular treatments for acute ischemic stroke carry the risk of intracranial bleeding. These treatments also carry additional risks related to vascular access, catheter placement, direct vessel injury, and the type of device deployed.

The Solitaire FR With Intention for Thrombectomy (SWIFT) trial provides additional information about endovascular ap-

Received March 26, 2013; accepted after revision May 16.

From the Department of Neurosurgery (P.T.A.), Kaiser Permanente, Sacramento, California; Department of Neurosurgery (A.P.A.), University of Southern California, Los Angeles, California; Department of Neurosurgery (R.S.P.), University of California, San Diego, San Diego, California; and Department of Neurology and Interventional Neuro-radiology (J.D.F.), Oregon Health and Sciences University, Portland, Oregon.

Please address correspondence to Paul T. Akins, MD, PhD, Department of Neurosurgery, Kaiser Permanente, 2025 Morse Ave, Sacramento, CA 95825; e-mail: paul.t.akins@kp.org

Evidence-Based Medicine Level 2.

<http://dx.doi.org/10.3174/ajnr.A3707>

proaches for acute stroke and directly compares the Solitaire FR device (Covidien, Irvine, California) with the Merci retrieval device (Stryker Neurovascular, Fremont, California) in a prospective, randomized trial. Results of the primary end point for this study have been reported separately.¹³ Acute stroke trials have consistently highlighted the importance of achieving early reperfusion while keeping procedural complication risks as low as possible. The therapeutic time windows are tight, and gains achieved by flow restoration are easily erased by symptomatic intracranial bleeding caused by procedural complications. The SWIFT trial reports a significant technical advance for mechanical thrombectomy by use of the Solitaire device compared with current technology (Merci retriever); the focus of this report is an in-depth analysis of the major procedural complications of this trial.

MATERIALS AND METHODS

The SWIFT trial was a multicenter, prospective, randomized, parallel-group, noninferiority study enrolling patients diagnosed with acute ischemic stroke for which endovascular intervention was indicated.¹³ After a roll-in phase in which the investigational Solitaire FR device was used for 2 patients at each participating center, subsequent patients were randomly assigned on a 1:1 basis for thrombectomy with either the investigational Solitaire FR device or the US Food and Drug Administration–cleared Merci retriever. The Solitaire device consists of a self-expanding stent integrated onto a delivery wire. The stent is deployed across the thrombus, allowing its tines to intercalate with the thrombus, and is then retracted into a guide catheter by traction on the wire. The Merci retriever system has received Food and Drug Administration clearance for removal of thrombus and consists of a helical terminus that is deployed distally to the thrombus and then pulled back into the guide catheter. The aim of the SWIFT study was to demonstrate substantial equivalence by obtaining prospective clinical data on the safety and efficacy of the Solitaire FR device compared with the Merci device for patients diagnosed with acute ischemic stroke. On the basis of the SWIFT study results, the Solitaire FR received Food and Drug Administration clearance in March 2012.

The primary efficacy end point of the study was arterial recanalization of the occluded target vessel measured by Thrombolysis in Myocardial Infarction (TIMI) score¹⁴ of 2 or 3 after the use of the study device. All patients received clinical evaluations at 24 hours, 30 days, and 90 days after the procedure.

Clinical and technical complications were prospectively collected for patients enrolled into the SWIFT trial. These events were independently reviewed and adjudicated by a central Clinical Events Committee (CEC). The type, timing, severity, outcome, relationship to study device or procedure, and other attributes of each complication were assessed. The CEC followed conventions and definitions established by the Common Terminology Criteria for Adverse Events of the National Cancer Institute.¹⁵ Neuroimaging was independently reviewed by a core lab. Because of early termination of the study, data were available on 31 roll-in patients treated with Solitaire FR device and 113 patients randomly assigned to either the Merci device or the Solitaire FR device.

Definitions

A clinical or technical event was judged to be procedure- or treatment-related when there was a strong temporal relationship to the procedure or device implantation, such as bleeding from femoral puncture site or adverse reaction to contrast administration.

The major intracranial procedural complications in this study are defined as symptomatic intracranial hemorrhage (SICH), SAH, air emboli, vessel dissection, serious groin complication, and emboli to new vascular territory. Cerebral hemorrhages were classified according to the European Cooperative Acute Stroke Study (ECASS) criteria¹⁶ as follows:

SICH is defined as any PH1, PH2, RIH, SAH, or intraventricular hemorrhage associated with a decline in NIHSS score ≥ 4 within 24 hours (PH1 indicates hematoma within ischemic field with some mild space-occupying effect but involving $\leq 30\%$ of the infarcted area; PH2, hematoma within ischemic field with space-occupying effect involving $>30\%$ of the infarcted area; RIH, any intraparenchymal hemorrhage remote from the ischemic field).

Asymptomatic intracranial hemorrhage is defined as any intracranial hemorrhage within 24 hours not meeting the above criteria for symptomatic intracranial hemorrhage.

The major extracranial procedural complications in this study are defined as extracranial vessel dissection and serious groin complication.

Device-Related: Study Devices and Ancillary Devices

A study device–related adverse event is defined as an event with a strong temporal relationship to the use of the device and no plausible alternative etiology. An example is an arterial wall dissection caused by the study device. In some patients, the CEC was unable to distinguish whether the study device or ancillary devices (such as guidewires) contributed to the complication. In these circumstances, the CEC took a conservative view, and these events were adjudicated to the study device.

An ancillary device–related adverse event is directly related to the delivery catheter (system), and another cause is unlikely. An example is a vessel perforated by a guidewire.

Adverse events classified as major access site adverse events are defined as access site pseudoaneurysm, femoral hematoma, retroperitoneal hematoma, access site bleeding, access site bruising/ecchymosis, and access site occlusion.

Statistical analysis was completed by use of SAS version 9.2 (SAS Institute, Cary, North Carolina). Descriptive statistics were tabulated, and probability values were computed by use of the Fisher exact test, comparing patients as assigned with their respective roll-in or randomly assigned treatment groups.

RESULTS

The SWIFT trial enrolled 144 patients. The study population consisted of 31 patients treated during the roll-in phase with the Solitaire FR device and 113 randomly assigned patients (58 Solitaire FR; 55 Merci). A prespecified efficacy stopping rule triggered early trial termination. The CEC adjudicated 644 adverse events, and the core imaging lab reviewed neuroimaging. The overall rate for major peri-procedural events was 12.5% (Table 1). Mortality rates without and with major peri-procedural events were 23.8%

Table 1: Major procedural complications

	Present	Absent	Percentage
Symptomatic cerebral hemorrhage	7	137	4.9%
Air emboli	2	142	1.4%
Emboli to new vascular territory	1	143	0.7%
Serious groin complication	4	140	2.8%
Vessel dissection	5	139	3.5%
Total number of patients	18	126	12.5%

Table 2: Intracranial bleeding complications

Type of Intracranial Bleeding	Asymptomatic (%)	Symptomatic (%)	Total (%)
PHI	6 (4.2)	1 (0.7)	7 (4.9)
PH2	5 (3.5)	1 (0.7)	6 (4.2)
RIH	1 (0.7)	0 (0)	1 (0.7)
IVH	5 (3.5)	1 (0.7)	6 (4.2)
SAH	6 (4.2)	5 (3.5)	11 (7.6)

Note:—Total number of subjects with symptomatic cerebral hemorrhage is less than the sum of individual subtype rows because some subjects had more than 1 radiologic subtype of intracranial hemorrhage. RIH indicates any intraparenchymal hemorrhage remote from the ischemic field; IVH, intraventricular hemorrhage.

and 33.3%, respectively ($P = .39$). The major peri-procedural events can be categorized as intracranial or extracranial.

The major intracranial complications were classified as symptomatic cerebral hemorrhage, air emboli, and emboli to new vascular territory (Table 1). The pattern of SICH ($n = 7/144$, 4.9%) was categorized by the core imaging lab as follows (Table 2): isolated intracerebral hemorrhage ($n = 2$), isolated SAH ($n = 4$), isolated intraventricular hemorrhage ($n = 1$), and combined intracerebral and subarachnoid hemorrhage ($n = 0$). Asymptomatic intracerebral hemorrhage was present in 44 of 144 (30.5%) and included hemorrhagic infarctions. On radiographic review of CT brain imaging after the endovascular treatment, air emboli (Fig 1D) were present in 2 of 144 patients (1.4%), and 1 was determined to be a serious adverse event. Six patients with major intracranial complications underwent hemicraniectomy (Solitaire FR roll-in, 0/31, 0%; Solitaire FR randomized, 1/58, 1.7%; Merci randomized, 5/55, 9.1%, $P = .11$ for randomly assigned groups).

The major extracranial, peri-procedural complications were classified as vessel dissection and serious groin complication (Table 1). Complications were present in 7% of patients, but no long-term disability or death was attributed to these events. One patient underwent fasciotomy related to leg ischemia attributed to femoral artery access. Angiographic vasospasm was commonly observed (29/144, 20%), but no clinical sequelae were observed. Vessel dissection occurred in 5 patients (3.5%; Table 5) and was adjudicated as a serious adverse event in 1. The sites of vessel dissection were in the cervical carotid artery except for 1 patient with dissections involving both the cervical and petrous portions of the ICA. Three dissections were managed conservatively, 1 dissection was treated with balloon angioplasty, and 1 dissection was treated with stent placement.

We compared rates of peri-procedural complications against clinical (Table 3) and technical factors (Table 4). Although statistically significant differences were not observed for any clinical or technical factors, we wish to highlight the numerically higher rates observed for duration of symptoms ≥ 6 hours, NIHSS score ≥ 20 , tPA failure, and presence of atrial fibrillation.

Table 3: Association of major procedural complications and clinical factors

Major Procedural Complications	Yes, n (%)	No, n (%)	P
Age, 22–64 y	8 (13.8%)	50 (86.2%)	.80
Age, 65+ y	10 (11.6%)	76 (88.4%)	
Duration of symptoms <4 hours	3 (11.5%)	23 (88.5%)	.68
Duration of symptoms 4–6 hours	7 (10.9%)	57 (89.1%)	
Duration of symptoms 6+ hours	5 (14.7%)	29 (85.3%)	
NIHSS score 0–10	1 (12.5%)	7 (87.5%)	.81
NIHSS score 11–20	12 (12.0%)	88 (88.0%)	
NIHSS score >20	5 (13.9%)	31 (86.1%)	
IV tPA contraindicated	8 (10.5%)	68 (89.5%)	.46
IV tPA failed	10 (15.2%)	56 (84.8%)	
Atrial fibrillation	11 (14.7%)	64 (85.3%)	.46
No atrial fibrillation	7 (10.1%)	62 (89.9%)	

Table 4: Analysis of major procedural complications and technical factors

Major Procedural Complications	Present n (%)	P
Academic centers	14 (13.9%)	.59
Community centers	4 (9.3%)	
Roll-in patients	3 (9.7%)	.76
Randomly assigned patients	15 (13.3%)	
Solitaire FR	10 (11.2%)	.61
Merci	8 (14.5%)	
No rescue therapy administered	12 (11.9%)	.79
Rescue therapy administered	6 (14.0%)	
Carotid T occlusion	5 (19.2%)	.53
ICA occlusion	0 (0.0%)	
MCA occlusion	12 (11.5%)	
M1 occlusion	8 (9.5%)	
M2 occlusion	4 (20.0%)	
VB occlusion	0 (0.0%)	
Successful revascularization (TIMI 2–3)	7 (43.8%)	.6
Unsuccessful revascularization	63 (53.4%)	

Note:—VB indicates vertebrobasilar.

The head-to-head comparison of peri-procedural complications observed with the Merci and Solitaire FR devices is shown in Table 5. Higher rates of SICH were observed after treatment with the Merci device compared with the Solitaire FR device (Solitaire FR 1/89, 1.1%; Merci 6/55, 10.9%; $P = .013$). Restoration of TIMI grade 2–3 flow was higher after treatment with the Solitaire FR device compared with the Merci device (TIMI grade 2–3 flow: Solitaire roll-in, 17/27, 63%; Solitaire randomized, 37/54, 68.5%; Merci randomized, 16/53, 30.2%; $P = .0001$). SICH followed successful revascularization (TIMI grade 2 or 3 flow) in 3 of 70 patients (Solitaire FR roll-in, 0/17, 0%; Solitaire FR randomized, 1/37, 2.7%; Merci, 2/16, 12.5%; $P = .21$). Rates of SAH trended lower with the Solitaire FR device compared with the Merci device (Table 5).

DISCUSSION

We observed important differences between complications of systemic (IV) thrombolysis and endovascular (intra-arterial) treatment (Table 6). The major risk of systemic thrombolysis is symptomatic intracranial bleeding and is generally intraparenchymal. This complication carries a 50% mortality rate.¹ In comparison, the pattern of intracranial bleeding after endovascular therapy is more variable and carries a greater risk of SAH. Rates of symptomatic intracranial bleeding in the SWIFT trial in the Solitaire FR treatment arm¹³ (1.1%) were significantly lower compared with

Table 5: Association of major procedural complications and embolectomy device

Type of Complication	MERCI	Solitaire	P
	% (n/N) [events]	% (n/N) [events]	
SAH symptomatic	7.3% (4/55) [4]	1.1% (1/89) [1]	.070
SAH asymptomatic	5.5% (3/55) [3]	3.4% (3/89) [3]	.67
ICH PH1 symptomatic	1.8% (1/55) [1]	0.0% (0/89) [0]	.38
ICH PH2 symptomatic	1.8% (1/55) [1]	0.0% (0/89) [0]	.38
IVH symptomatic	1.8% (1/55) [1]	0.0% (0/89) [0]	.38
ICH asymptomatic	27.3% (15/55) [15]	27.0% (24/89) [25]	1.00
Ischemic stroke symptomatic	12.7% (7/55) [7]	3.4% (3/89) [3]	.044
All symptomatic ICH	10.9% (6/55) [6]	1.1% (1/89) [1]	.013
Air emboli	1.8% (1/55) [1]	1.1% (1/89) [1]	1.00
Emboli to same vascular territory	5.5% (3/55) [3]	4.5% (4/89) [4]	1.00
Emboli to new vascular territory	1.8% (1/55) [1]	0.0% (0/89) [0]	.38
Device detachment	0.0% (0/55) [0]	0.0% (0/89) [0]	1.00
Vessel dissection	1.8% (1/55) [1]	4.5% (4/89) [4]	.65
Vessel vasospasm on angiography	16.4% (9/55) [10]	22.5% (20/89) [20]	.40
Vessel vasospasm symptomatic	0.0% (0/55) [0]	0.0% (0/89) [0]	1.00
Major access site issues	3.6% (2/55) [2]	7.9% (7/89) [8]	.48
Study device-related AE	16.4% (9/55) [13]	10.1% (9/89) [14]	.31
Ancillary device-related AE	3.6% (2/55) [2]	7.9% (7/89) [8]	.48
Technical difficulty with device	7.3% (4/55) [4]	10.1% (9/89) [12]	.77

Note:—IVH indicates intraventricular hemorrhage; ICH, intracerebral hemorrhage; AE, adverse event.

Table 6: Complications of systemic (IV) thrombolysis and endovascular (intra-arterial) treatment

Trial	Symptomatic ICH	SAH
NINDS	6.4%	0%
PROACT I	15.4%	na
PROACT II	10.2%	na
IMS I	6.3%	0%
IMS II	9.9%	na
Merci	7.8%	3.5%
Multi-Merci	9.8%	9.9%
Penumbra	10%	5%
SWIFT-all	4.9%	7.6%
SWIFT-Merci arm	10.9%	12.7%
SWIFT-Solitaire arm	1.1%	4.5%

the NINDS trial¹ (6.4%) and the SWIFT Merci treatment arm (10.9%) and were lower than published trials that used intra-arterial thrombolysis^{4,5,6,8} or the Penumbra device (Penumbra, Alameda, California).⁹ The SICH rate observed with the Merci device in the SWIFT trial (10.9%) was similar to that in prior studies^{7,10} (Table 6).

SAH was not reported in the NINDS IV tPA trial¹ but has been reported in other device trials (Table 6) and case series.¹⁷ The rate of SAH was higher in this trial compared with earlier interventional stroke trials but similar to rates in a recent study by UCLA¹⁷ and the Multi-MERCI trial (Table 6). A key difference between earlier interventional stroke trials such as the PROACT trials and more recent trials is the use of thrombectomy devices in addition to intracranial placement of microcatheters and infusion of intra-arterial thrombolytics. In the MERCI trial,⁷ 5 patients were adjudicated with symptomatic SAH (5/141; 3.5%), and the authors attributed the symptomatic SAH to vessel perforations. Asymptomatic SAH was not reported separately in this trial; therefore the total SAH encountered probably exceeds this rate. In the Multi-MERCI trial, 3 (2.7%) patients had symptomatic SAH and 8 (7.2%) had asymptomatic SAH, for a total SAH rate of 9.9% (11/111).

Our hypothesis that thrombectomy devices pose a greater risk of SAH compared with microcatheter delivery of intra-arterial

thrombolytics is supported by a recent analysis by the UCLA Endovascular Stroke Therapy Investigators.¹⁷ They reported that SAH was detected after primary intra-arterial thrombolysis (6.5%) but was numerically more likely after Merci retriever thrombectomy (14.1%). They had an overall 15.6% rate of SAH after endovascular treatment of acute ischemic stroke (20/128 procedures), and independent predictors of SAH in their study were procedure-related vessel perforation, rescue angioplasty after thrombectomy, distal MCA occlusion, and hypertension. The IMS I and II Investigators¹⁸ also suggested that microcatheter contrast injections may contribute to intracranial bleeding caused by pressure-related effects or toxicity of contrast agents. Four instances of vessel perforation were observed in SWIFT: 1

patient treated with Solitaire (1/58; 1.7%) and 3 treated with Merci (3/55, 5.5%; $P = .35^{13}$). The trend toward lower rates of symptomatic SAH with the Solitaire FR device (1.1%) compared with the Merci device is encouraging (7.3%, Table 6).

Reperfusion is a double-edged sword. Early reperfusion will limit ischemic damage to both the brain and the cerebrovasculature. Late reperfusion can cause cerebral hemorrhage by restoration of cerebral blood flow to infarcted brain and associated vasculature and may contribute to brain edema.¹⁹ Theoretically, reperfusion by use of mechanical thrombectomy should have a lower rate of hemorrhagic transformation when direct vessel injury is minimized and flow restoration occurs quickly. The results of the Solitaire FR treatment arm of the SWIFT trial are consistent with this concept. One advantage of the Solitaire device over the Merci device is the rapid flow restoration with stent deployment that occurs before clot removal. Whether this expediency in flow restoration contributed to the lower SICH rates observed with Solitaire FR versus Merci will require additional analysis.

The lower rates of SICH observed with Solitaire FR compared with Merci devices may be related to other technical factors besides the higher and more rapid rate of reperfusion. After advancement of the embolectomy devices into the intracranial thrombus, the withdrawal of the devices into the guide catheter exerts traction on the arterial tree. These mechanical forces may contribute to SICH by direct endoluminal trauma or through shear forces on the perforating vessels as the parent vessel undergoes traction. In a preclinical model, less endovascular injury was observed with Solitaire as compared with Merci use.²⁰

The IMS III trial results²¹ highlight the importance of rapid restoration of flow. A favorable functional outcome at 3 months (a modified Rankin Scale score of 0–2) occurred in 12.7% of patients with TICI score of 0, 27.6% with TICI score of 1, 34.3–47.9% with TICI score of 2a or 2b, and 71.4% with TICI score of 3. In this trial, treating physicians used different devices and intra-arterial tPA doses at their discretion. Only 4 patients enrolled in this trial were treated with the Solitaire FR device.

This study has strengths and weaknesses. The strengths include the multicenter, randomized, prospective study design, independent adjudication of adverse events by a CEC, and review of neuroimaging by a core lab. This is the first endovascular stroke trial to directly compare 2 thrombectomy devices. The weakness of this study is the limited sample size ($n = 144$) and the variability in operator experience and skill with mechanical thromboembolism that is inherent to multicenter studies.

CONCLUSIONS

“Experience is what you get when you don’t get what you want.”²² Detailed knowledge of peri-procedural complications is important for the treatment of patients with stroke after endovascular treatment. The results of the IMS III trial highlight the importance of maximizing the time to restore flow while keeping procedural complication risks low for acute ischemic stroke. Fewer endovascular complications were observed with Solitaire FR device treatment compared with Merci device treatment, particularly symptomatic cerebral hemorrhage. Device registries will be helpful to gain deeper understanding of rare events. This trial illustrates a significant technical advance for mechanical thrombectomy by use of the Solitaire device compared with current technology (Merci retriever); this report has focused on the major procedural complications.

ACKNOWLEDGMENTS

Funding for the SWIFT trial was provided by ev3/Covidien. No funding was provided to the authors for data analysis and manuscript preparation and submission.

Drs Akins, Pakbaz, and Amar served on the Clinical Events Committee and received modest time-based compensation as consultants. Dr Fields served as a clinical site co-investigator in the SWIFT trial, and his institution received modest enrollment-based compensation to offset study costs.

Disclosures: Paul T. Akins—RELATED: Consulting Fee or Honorarium: ev3*; Fees for Participation in Review Activities, Such as Data Monitoring Boards, Statistical Analysis, Endpoint Committees, and the Like: ev3.* Comments: I served on the Clinical Events Committee for the SWIFT trial. I did not receive compensation directly and fees were paid to The Permanente Medical Group. Arun P. Amar—RELATED: Fees for Participation in Review Activities, Such as Data Monitoring Boards, Statistical Analysis, Endpoint Committees, and the Like: Covidien, Comments: Received market value time-based compensation to serve as chairman of Clinical Events Committee for the SWIFT trial; UNRELATED: Consultancy: Reverse Medical, Comments: Received market value time-based compensation to serve as chairman of Clinical Events Committee for PUFFS trial (Covidien), to be paid market value time-based compensation. Ramin Pakbaz—RELATED: Grant: Covidien,* Comments: Fellowship grant; Fees for Participation in Review Activities, Such as Data Monitoring Boards, Statistical Analysis, Endpoint Committees, and the Like: Covidien, Comments: Complication adjudication committee member. Jeremy Fields—RELATED: Consulting Fee or Honorarium: Covidien, Stryker, Comments: I have lectured on interventional treatment of stroke for Covidien (manufacturer of Solitaire). I have acted as a trainer for various devices marketed by Stryker (manufacturer of the Merci retriever) (*money paid to institution).

REFERENCES

- National Institute of Neurological Disorders and Stroke rt-PA Stroke Study Group. **Tissue plasminogen activator for acute ischemic stroke.** *N Engl J Med* 1995;333:1581–87
- Rha J, Saver JL. **The impact of recanalization on ischemic stroke outcome: a meta-analysis.** *Stroke* 2007;38:967–73
- Tenser MS, Amar AP, Mack WJ. **Mechanical thrombectomy for acute ischemic stroke using the Merci retriever and Penumbra aspiration systems.** *World Neurosurg* 2011;76(6 Suppl):S16–23
- Del Zoppo GJ, Higashida RT, Furlan AJ, et al, and the PROACT Investigators. **PROACT: a phase II randomized trial of recombinant pro-urokinase by direct arterial delivery in acute middle cerebral artery stroke.** *Stroke* 1998;29:4–11
- Furlan A, Higashida R, Wechsler L, et al, for the PROACT Investigators. **Intra-arterial prourokinase for acute ischemic stroke: the PROACT II Study: a randomized controlled trial** *JAMA* 1999;282:2003–11
- IMS Study Investigators. **Combined intravenous and intra-arterial recanalization for acute ischemic stroke: the Interventional Management of Stroke Study.** *Stroke* 2004;35:904–11
- Smith WS, Sung G, Starkman S, et al, for the MERCY Trial Investigators. **Safety and efficacy of mechanical embolectomy in acute ischemic stroke: results of the MERCY Trial.** *Stroke* 2005;36:1432–40
- IMS II Trial Investigators. **The Interventional Management of Stroke (IMS) II Study.** *Stroke* 2007;38:2127–35
- Bose A, Henkes H, Alfke K, et al, for the Penumbra Phase 1 Stroke Trial Investigators. **The Penumbra system: a mechanical device for the treatment of acute stroke due to thromboembolism.** *AJNR Am J Neuroradiol* 2008;29:1409–13
- Smith WS, Sung G, Saver J, et al, Multi MERCY Investigators. **Mechanical thrombectomy for acute ischemic stroke: final results of the Multi MERCY trial.** *Stroke* 2008;39:1205–12
- Miteff F, Faulder KC, Goh AC, et al. **Mechanical thrombectomy with a self-expanding retrievable intracranial stent (Solitaire AB): experience in 26 patients with acute cerebral occlusion.** *AJNR Am J Neuroradiol* 2011;32:1078–81
- Machi P, Costalat V, Lobotesis K, et al. **Solitaire FR thrombectomy system: immediate results in 56 consecutive acute ischemic stroke patients.** *J Neurointerv Surg* 2012;4:62–66
- Saver JL, Jahan R, Levy EI, et al, for the SWIFT trialists. **Solitaire flow restoration device versus the Merci retriever in patients with acute ischaemic stroke (SWIFT): a randomized, parallel-group, non-inferiority trial.** *Lancet* 2012;380:1241–49
- TIMI Study Group. **The Thrombolysis in Myocardial Infarction (TIMI) trial: phase I findings.** *N Engl J Med* 1984;33:523–30
- Cancer Therapy Evaluation Program, Common Terminology Criteria for Adverse Events, Version 3.0, DCTD, NCI, NIH, DHHS March 31, 2003 (<http://ctep.cancer.gov>), Publish Date: August 9, 2006
- Hacke W, Kaste M, Fieschi C, et al, for the ECASS Study Group. **Intravenous thrombolysis with recombinant tissue plasminogen activator for acute hemispheric stroke: the European Cooperative Acute Stroke Study (ECASS).** *JAMA* 1995;274:1017–25
- Shi Z-S, Liebeskind DS, Loh Y, et al, and UCLA Endovascular Stroke Therapy Investigators. **Predictors of subarachnoid hemorrhage in acute ischemic stroke with endovascular therapy.** *Stroke* 2010;41:2775–81
- Khatri P, Broderick JP, Khoury JC, et al, IMS I and II Investigators. **Microcatheter contrast injections during intra-arterial thrombolysis may increase intracranial hemorrhage risk.** *Stroke* 2008;39:3283–87
- Teal PA, Pessin MS. **Hemorrhagic transformation: the spectrum of ischemia-related brain hemorrhage.** *Neurosurg Clin North Am* 1992;3:601–10
- Mehra M, Hendricks GH, O’Callaghan JM, et al. **Preclinical in-vivo safety evaluation of thrombectomy devices in the canine cerebrovasculature (abstract).** *Stroke* 2012;43:A139
- Broderick JP, Palesch YY, Demchuk AM, et al, for the IMS III Investigators. **Endovascular therapy after intravenous t-PA versus t-PA alone for stroke.** *N Engl J Med* 2013;368:893–903
- Pausch R. *The Last Lecture.* New York: Hyperion Books; 2008

Endovascular Treatment of Middle Cerebral Artery Aneurysms with Flow Modification with the Use of the Pipeline Embolization Device

K. Yavuz, S. Geyik, I. Saatci, and H.S. Cekirge



ABSTRACT

BACKGROUND AND PURPOSE: The Pipeline Embolization Device was reported to be safe and effective in the treatment of sidewall aneurysms, preserving the patency of the vessels covered by the construct. However, to date, the safety and efficacy of this device in treating bifurcation aneurysms remains unknown. We report our preliminary experience with the use of the Pipeline Embolization Device in the management of MCA aneurysms located at the bifurcations, including mid- and long-term follow-up data.

MATERIALS AND METHODS: Wide-neck MCA aneurysms, which give rise to a bifurcating or distal branch in which other endovascular techniques are thought to be unfeasible or more risky, were included. Data including demographics, aneurysm features, antiplatelet therapy, complications, and angiographic follow-up results for up to 30 months were recorded.

RESULTS: Twenty-five aneurysms located at the MCA bifurcation ($n = 21$) or distal ($n = 4$) were treated. Of these, 22 were small and 3 were large. A single device was used in all but 2. No deaths occurred in the series. All patients had at least 1 control angiographic study, 21 of which were DSA (3–30 months), which showed that 12 of the rising branches were patent whereas 6 were filling in reduced caliber and 3 were occluded asymptotically. According to the last angiographic follow-up, complete occlusion was revealed in 21 of 25 aneurysms (84%).

CONCLUSIONS: The Pipeline Embolization Device provides a safe and effective treatment alternative for wide-neck MCA aneurysms that give rise to a bifurcating or distal branch when other endovascular techniques are thought to be unfeasible or more risky.

ABBREVIATION: PED = Pipeline Embolization Device

Providing diseased parent artery reconstruction in addition to exclusion of the aneurysm from the circulation by means of flow disruption, spontaneous aneurysm thrombosis, and endotelialization mechanisms, flow diversion is a new but widely accepted endovascular treatment technique for intracranial aneurysms. The use of self-expandable neurovascular stents (designed to be used in conjunction with coil embolization) as a monotherapy was previously reported with the implantation of 1 or more stents.^{1–5} A few case series with the use of the sole stent placement technique in the treatment of complex fusiform MCA aneurysms also exist in the literature.^{6,7} Additionally, Y-stent flow diversion by use of self-expandable stents with a closed-cell design

without endosaccular coiling has also been reported to be effective in a small, selected case series, including 5 MCA bifurcation aneurysms with complete occlusion in the follow-up.⁸

The introduction of the Pipeline Embolization Device (PED) (Covidien/ev3, Irvine, California) as a dedicated flow diverter added a new dimension to this treatment strategy, with its being porous enough to preserve the patency of the branch vessels covered by the construct.⁹ The previous experience with the PED in the treatment of saccular aneurysms revealed that when a branch was originating directly from the aneurysm sac, this branch was kept patent when there was a flow demand through it.¹⁰ Although, to date, the safety and efficacy of this device in treating bifurcation aneurysms remains unknown. This inspired us to use the PED for treatment of MCA bifurcation or M2 aneurysms in which one of the bifurcating branches or a distal branch originate directly from the aneurysm sac, when other endovascular techniques were deemed unfeasible or more risky. There have been limited numbers of MCA aneurysms reported to be treated with the PED within different case series^{11–15}; however, none included bifurcation aneurysms. We report, to our

Received March 4, 2013; accepted after revision May 23.

From the Department of Radiology, Hacettepe University Hospitals, Ankara, Turkey.

Please address correspondence to Kivilcim Yavuz, MD, Hacettepe University Hospitals, Department of Radiology, 06100 Sıhhiye, Ankara, Turkey; e-mail: kivilcimyvz@yahoo.com

Indicates article with supplemental on-line table.

<http://dx.doi.org/10.3174/ajnr.A3692>

knowledge, the first case series focused on the use of the PED in the management of MCA aneurysms, in which a bifurcating or a distal branch emanates directly from the aneurysm sac.

MATERIALS AND METHODS

Patient Population and Aneurysm Characteristics

Twenty-five MCA aneurysms in 21 patients (12 female and 9 male) with an average age of 56 years (range, 34–74 years) were treated with the use of the PED (On-line Table). All procedures were performed with the provision of written informed consent. This series included MCA aneurysms located at or distal to the bifurcation in which a bifurcating or distal branch emanated directly from the aneurysm sac and was treated with PED, 4 of which were included in a previous report.¹⁰ Aneurysms located at the M1 segment of the MCA were out of the scope of this report.

All patients presented with headache. All aneurysms except for 1 were unruptured. One patient with bilateral MCA aneurysms had a previous treatment of her ruptured right MCA aneurysm with balloon-assisted coiling at the acute stage of SAH. This aneurysm showed recanalization at follow-up and was treated at the same session as the unruptured left MCA aneurysm treatment with the PED. There were 3 other patients who had previous treatments, as indicated in the On-line Table.

Aneurysm sizes were classified as small (<1 cm), large (≥ 1 cm and ≤ 2.5 cm), and giant (> 2.5 cm). The aneurysms were referred to as wide-neck when the dome/neck ratio was ≤ 1.5 and/or neck length was ≥ 4 mm.

Treatment and Medication

All patients were premedicated with double antiplatelet therapy and diligently investigated for sufficient level of thrombocyte inhibition before the treatment, as described previously.¹⁰ All patients received heparin to maintain an activated clotting time level elevated to 2–3 times the baseline value during the procedure. Patients who had large aneurysms received dexamethasone, with an initial dose of 8 mg given during the procedure and continued 4 \times 4 mg daily for 1 week; the dose was then tapered within 1 week and discontinued.

All patients were prescribed clopidogrel/ticlopidine until the 6-month follow-up angiography and discontinued after the patency of the PED was shown angiographically. Aspirin use (300 mg daily) was prescribed life-long.

All procedures were performed under general anesthesia. Parent artery measurements were obtained by using both 3D and 2D images at the working projections.

In all patients, through a 6F introducer sheath placed in the common carotid artery, a 6F guiding catheter was advanced into the internal carotid artery as distal as possible. A Marksman (Covidien/ev3) microcatheter was then navigated, over different microguidewires as necessary, to the selected MCA branch. The technique of PED deployment was performed as described previously.¹⁰

The PED was used as a monotherapy in all but 3 patients without any adjunctive endosaccular coils. In 3 patients who had PED placement as retreatment, 3 aneurysms had coils from the previous treatments. Among these, in 1 patient, a self-expandable stent

(Enterprise, Codman & Shurtleff, Raynham, Massachusetts) was also present from the previous stent-assisted coiling treatment.

Follow-Up

All patients were designated to have a clinical and angiographic follow-up at 6 months. However, when a patient had ongoing headache or any new symptoms, 1- to 3-month angiographic control was obtained either with CTA or DSA. If the 6-month control angiography revealed incomplete aneurysmal occlusion, an additional angiographic control was performed during the 12th month and another at 18 months when necessary. A longer-term follow-up was planned for 1–2 years after demonstration of complete occlusion.

RESULTS

This series included 25 wide-neck MCA aneurysms located at the bifurcation in 21 cases and the M2 segment in 4 cases. Of these, 22 were small and 3 were large.

All devices except for 2 were placed properly, without technical difficulties. In 2 patients with bifurcation aneurysms, the distal end of the first PED moved backward during the microcatheter loading maneuver and did not cover the aneurysm neck adequately; therefore, another PED was placed distally, overlapping its proximal part with the distal portion of the first PED. Other than these cases, only 1 PED was used in all aneurysms, and a single device was used to treat 2 aneurysms located at the bifurcation with separate necks in 2 patients.

In this series, there were no deaths. The only procedural complication was SAH of unknown origin revealed by DynaCT (Siemens, Erlangen, Germany) during the procedure. The patient, in whom 2 overlapping PEDs were used as described above, awakened from the anesthesia without any neurologic deficit; however, she had ischemic symptoms for several days after the procedure (rather attributed to vasospasm) and was discharged with mild right upper-extremity paresis and dysphasia. She was independent at 6 months after the treatment (mRS 1), and DSA confirmed the patency of all bifurcating branches. Other than this patient, all were discharged without any neurologic deficits. Two patients had slight left hemiparesis 4 weeks after surgery, after the treatment of their right MCA bifurcation aneurysms. MR imaging was obtained for both patients. In the first (patient 3), with a small aneurysm treated by use of 2 overlapping devices, MR imaging, including DWI/ADC sequences, did not show any abnormalities and CTA revealed patency of the devices as well as near-complete occlusion of the aneurysm with minimal residual filling. Additional low-molecular-weight heparin for 3 days was prescribed. In the other (patient 15), with a large aneurysm, MR imaging showed perianeurysmal edema after cessation of dexamethasone. Steroid therapy was given for an additional 2 weeks and tapered afterward. Both of these patients became asymptomatic after the additional treatments.

One patient, who discontinued clopidogrel, presented with transient right hemiparesis 3 months after her left MCA bifurcation aneurysm had been treated. MR imaging showed a few acute ischemic lesions in the left frontal lobe. Immediate DSA was performed, in which significant decelerated flow of the left anterior cerebral artery A1 segment, which had been jailed with the PED

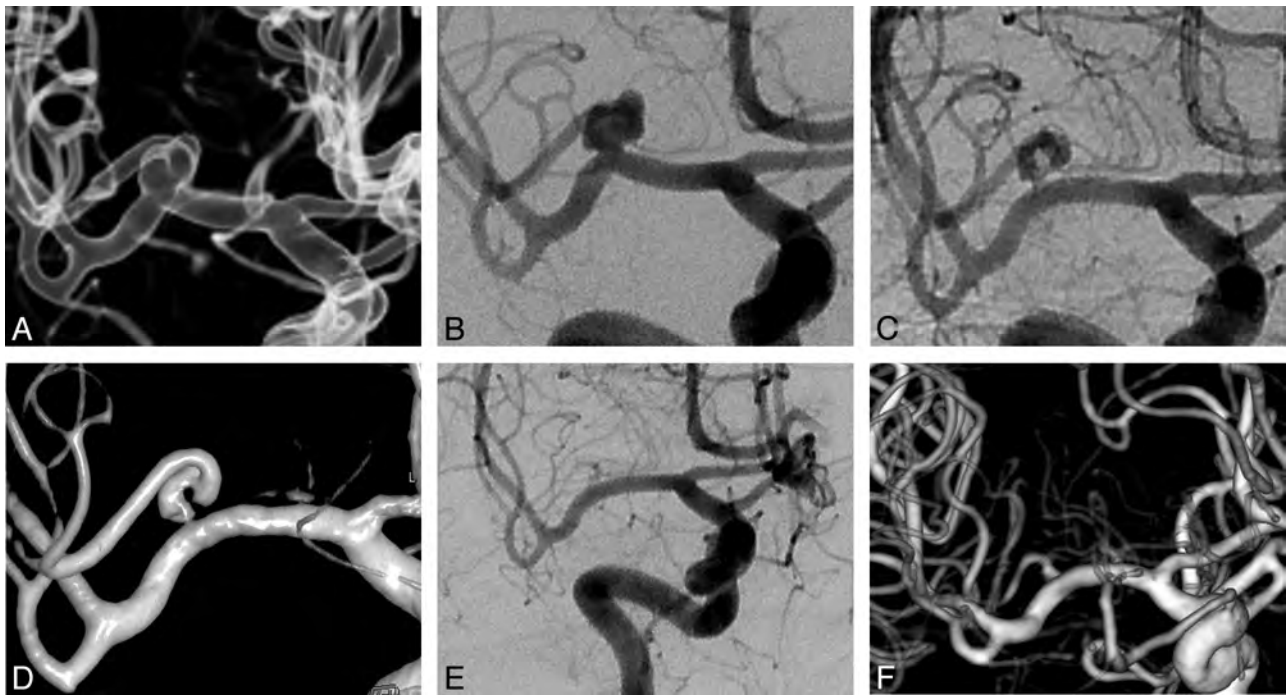


FIG 1. Occlusion process of right MCA bifurcation aneurysm. *A* and *B*, Preoperative 3D reconstruction and DSA images show the early bifurcating branch originating from the aneurysm sac. *C* and *D*, Six-month control angiogram and 3D image demonstrate the “remodeled artery.” *E* and *F*, Eighteen-month control angiogram and 3D image show the complete occlusion of the aneurysm with the bifurcating branch filling in reduced caliber.

during the treatment, was noted. This was the only patient in whom the proximal end of the PED construct extended back in to the ICA. The level of P2Y₁₂ receptor blockade test was found to decrease to a value of 10%. Low-molecular-weight heparin (enoxaparin; 2 × 40 mg, 1 day) and a loading dose of clopidogrel were administered immediately. This patient did not have a neurologic deficit when she arrived at the hospital and left the hospital with the same neurologic status.

The angiographic data of the follow-up examinations are given in the On-line Table. All patients had at least 1 control angiographic study. Six patients underwent an angiographic control at 1–3 months (with DSA in 2 patients and CTA in 4 patients) because of ongoing headache ($n = 4$) or ischemic symptoms ($n = 2$). Two of these aneurysms showed complete occlusion at 3 months. Others showed decreased filling.

Six-month follow-up angiograms were obtained in 21 aneurysms, showing complete occlusion in 16 and significantly decreased residual filling in 3. In the remaining 2 patients, we observed the so-called “remodeled artery,” which we previously defined as the “infundibulum-like” appearance resulting from the branch coming off the parent artery with a bulking origin caused by the significant shrinkage of the aneurysm due to flow change¹⁰ (Figs 1–3). The appearance of an “interruption” between the remodeled artery and the bifurcation, which we referred to as the “healing zone,” was noted in 1 of these patients (Fig 3). The 1-year angiogram that was obtained for 1 of these remodeled aneurysms showed no significant change in its appearance. However, this aneurysm showed complete occlusion at the 18-month angiogram. Two aneurysms with residual filling at 6 months showed complete occlusion in the 18-month DSA. Eight patients with 9 aneurysms underwent a long-term follow-up of more than 1 year;

all showed complete occlusion. According to the last angiographic follow-up, complete occlusion was revealed in 21 aneurysms (84%; 21/25); among the remaining 4 aneurysms, the latest control angiography was performed at 1–3 months in 2 and at 6 months in 2.

Overall 21 aneurysms underwent at least 1 DSA control (3–30 months). Patency of PEDs as well as the branches originating from the aneurysm sacs was evaluated in all these angiograms. All PEDs were patent, with no significant intimal changes. According to the last follow-up, of the branches emanating from the aneurysm sacs, 12 were patent, whereas 6 were filling in reduced caliber and 3 were occluded asymptotically. In 1 patient with 6-month, 1-year, and 18-month follow-up angiograms, the bifurcating branch was filling in reduced caliber at 6-month and 1-year controls. Clopidogrel was not discontinued in this patient, and the branch showed filling in normal caliber at 18 months (patient 5) (Fig 2). In 2 more patients with reduced-sized branches, clopidogrel was continued; further follow-ups are pending.

DISCUSSION

The PED represents the flow-diverting device designed to exclude the aneurysm from the circulation by disrupting intra-aneurysmal flow, yet allow enough flow through the side branches as well as small perforators arising along the parent vessel covered by the construct. In an experimental study in rabbits, Kallmes et al¹⁶ demonstrated that the vessels covered by the devices remained patent at long-term follow-up. On the other hand, in a recent clinical study,¹⁷ evaluating patency of the ophthalmic artery after treatment of paraclinoid aneurysms, it was demonstrated that nearly one-quarter of ophthalmic arteries covered by PEDs underwent occlusion; however, none of these patients had visual

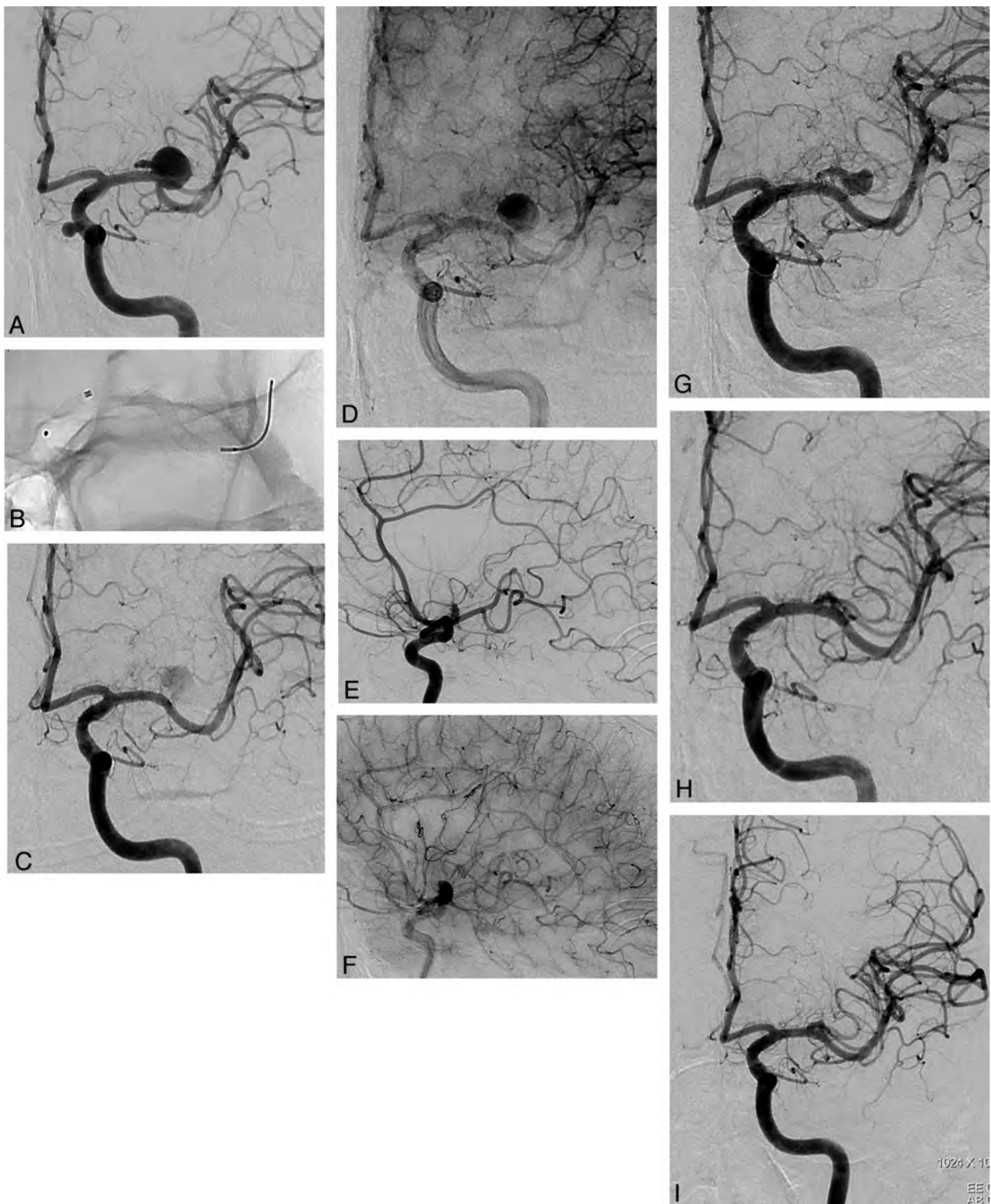


FIG 2. Occlusion stages of left MCA bifurcation aneurysm. *A*, DSA image shows the aneurysm giving rise to superior trunk. *B*, Fluoroscopic image shows the deployment of the PED in the inferior trunk. *C* and *D*, Early and late phases of 6-month control angiogram demonstrate the reduced and delayed filling of the aneurysm sac with the significant stagnation. Bifurcating branch is also filling belated in reduced caliber. *E* and *F*, Early and late phases of 6-month control angiogram (lateral view) show reduced filling of the superior trunk with retrograde filling of the distal branches through pial collaterals. *G*, One-year control angiogram demonstrates the remodeled superior trunk. The superior trunk and its branches are still filling in reduced caliber. *H*, Eighteen-month control angiogram shows complete occlusion of the aneurysm, with the superior trunk coming to its original size. *I*, Thirty-month control angiogram shows the stable occlusion of the aneurysm with the patency of the bifurcating branch (note the carotid cave aneurysm in *A*, treated with PED as well).

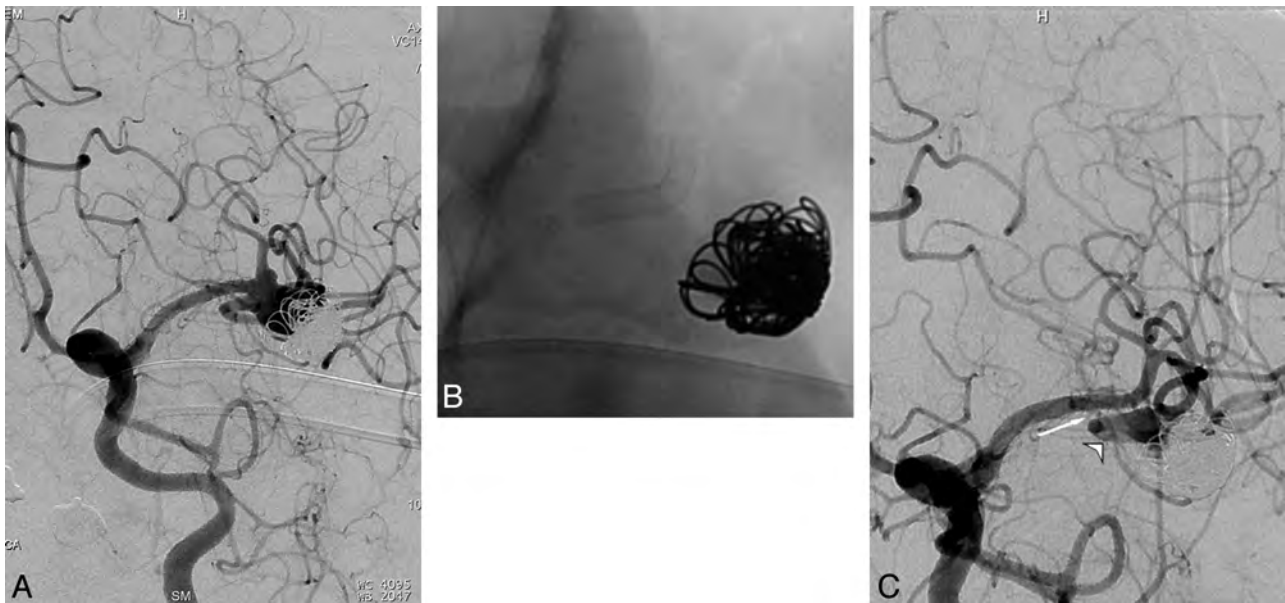


FIG 3. Recanalized left MCA bifurcation aneurysm. *A*, Preoperative angiogram shows recanalization of the aneurysm previously treated by use of balloon-assisted coiling. Inferior trunk is emanating from the neck. *B*, Nonsubtracted image shows the PED placed within the superior trunk. *C*, Six-month control angiogram shows the remodeled inferior trunk (*arrowhead*). The “healing zone” appears as the “interruption” between the remodeled artery and bifurcation (*arrow*).

loss. This can be explained with the abundant distal collateral supply of the ophthalmic artery from the external carotid branches. Correspondingly, in another study including 46 aneurysms in which a branch originated from the sac (excluding the ophthalmic aneurysms), only in 5 aneurysms was the originating branch (exclusively posterior communicating artery in all 5) occluded, with the ipsilateral posterior cerebral artery filling from the posterior circulation.¹⁰ Other branches such as the anterior choroidal artery stayed open, which led us to postulate that the branches through which there is a flow demand because of insufficient distal collateral supply or toward which there is enough pressure gradient between the high-pressure parent arteries, are kept patent when covered by a flow diverter. Nevertheless, our findings in this previous study emerged with the use of a single device in the treatment of each aneurysm. Limited cases in the literature reported the use of more than 1 device in the treatment of aneurysms with the coverage of perforating arteries demonstrating occlusion of the lenticulostriate branches and infarction in the related territory.^{11,18} In the present study, all aneurysms except for 2 were treated by use of a single PED. One of the 2 patients treated with 2 overlapping devices was admitted to the hospital in the fourth postoperative week. The MR imaging did not show any ischemic lesions, and CTA showed patency of the MCA branches, which was confirmed with 6-month control DSA. Furthermore, we prescribed low-molecular-weight heparin in addition to the antiplatelet therapy for 1 week, and the patient did not have a recurrent event. The remaining patient was the one with procedural SAH who had ischemic symptoms with unclear etiology as described above.

In this series, there was 1 PED placed within a pre-existing intraluminal construct (Enterprise stent), which had been placed during the previous endosaccular coiling. Lylyk et al¹⁹ postulated in their previous study that endoluminal constructs might represent potential impediments to the efficacy of the PED. In our

patient, we did not experience any technical difficulty in deploying the PED. This was the patient in whom we discovered perianeurysmal edema 4 weeks after the procedure, which we think was unrelated to the pre-existing stent and PED combination. Six-month DSA control revealed complete occlusion of the aneurysm with patent bifurcating branches.

The main periprocedural and postprocedural complications of the use of flow diverters in the endovascular treatment of intracranial aneurysms are hemorrhagic and thromboembolic events. Early and delayed aneurysm ruptures²⁰⁻²³ and distal ipsilateral hemorrhage^{10,14,24,25} have emerged as the hemorrhagic complications that are probably related to flow diversion. In this series, 1 hemorrhagic event occurred as an SAH with unknown origin during the procedure. No extravasation was observed in DSA images during the treatment; however, DynaCT revealed SAH. This bleeding may have been caused by a small, invisible dissection/wire perforation during catheterization of the MCA branch.

The only thromboembolic event (presented with transient ischemic attack 3 months after the procedure) with radiologic findings in this series occurred in 1 patient as the result of cessation of the antiplatelet drugs. There was no recurrent ischemic attack after antiplatelet and anticoagulant medication as described above. This result corroborates the importance of rigorously evaluating the thrombocyte inhibition level in response to clopidogrel or ticlopidine and safety of the PED use with the coverage of perforators and bifurcating branches, at least when a single device is used. We used whole-blood impedance platelet aggregation and the rapid platelet function assay VerifyNow P2Y12 (Accumetrics, San Diego, California) in all patients and performed the procedure only if there was no resistance to the drug and the value of Verify Now test was >30%.

In this series, all patients had at least 1 control angiographic study. According to the last angiographic follow-up, complete

occlusion was revealed in 21 aneurysms (84%; 21/25). In our experience, we have observed that there are generally 3 phases, though not necessarily, in the occlusion process of aneurysms bearing a bifurcating branch by using the PED: 1) moderate to significant decrease in the aneurysm filling (1–3 months), 2) the infundibulum-like appearance resulting from the branch coming off the parent artery with a bulking origin caused by significant shrinkage of the aneurysm due to flow change, the so-called “remodeled artery” (3–12 months), and 3) complete occlusion (6–18 months) (Figs 1–3). We recommend performing the first angiographic control at 6 months to evaluate the degree of occlusion as well as the patency of the device and the branch(es) covered by the device. When the device is patent, with cessation of clopidogrel or ticlopidine, and continuation of aspirin monotherapy, 18-month follow-up can be scheduled. According to the last follow-up, 12 of the branches originating from the aneurysms were patent, whereas 6 were filling in reduced caliber and 3 were occluded asymptotically. In 1 patient, the bifurcating branch was filling in reduced caliber at 6-month and 1-year controls. Clopidogrel was not discontinued in this patient, and the branch was revealed to fill in normal caliber at 18 months (Fig 2). Our anticipation is that a branch is kept patent whenever there is a flow demand through it in the absence of rich distal collateral flow. Even so, the operator may extend the duration of dual antiplatelet treatment to 1 year or more.

Endovascular treatment of wide-neck bifurcation aneurysms, especially when the bifurcating branches emanate directly from the base of the aneurysm, is still challenging. With the introduction of the Y-stent placement technique with or without endosaccular coiling,^{8,26,27} many of these difficult aneurysms have become amenable to treatment while preserving the parent arteries. However, in cases in which the branch has an acute angle relative to the main trunk, intra-aneurysmal maneuvers as well as exchange procedures are necessitated to catheterize this branch, increasing the risk of procedural hemorrhagic complications caused by aneurysmal rupture and wire perforation.

To date, to our knowledge, this series including 21 aneurysms located at the MCA bifurcations is the first study reporting specifically the use of the PED in bifurcation aneurysms. The PED, being technically more simple and straightforward, provides a safer procedure in cases of existing acutely angled branches. The difficult branch and the aneurysm sac are not to be catheterized; therefore, hemorrhagic risks caused by catheterization as well as endosaccular embolization can be avoided.

We acknowledge the limitations of our study, with the lack of longer follow-up data as well as the limited number of cases. Therefore, we do not advocate this treatment alternative for aneurysms that can be treated with conventional techniques, including clipping. However, the results of our preliminary experience of PED use in the endovascular management of challenging MCA aneurysms are encouraging, enabling the treatment of more complex aneurysms with less procedural risk.

CONCLUSIONS

The PED provides a safe and effective solution for wide-neck MCA aneurysms located at the bifurcation or M2 segment in which 1 of the bifurcating or distal branches emanates directly

from the sac and when other endovascular techniques are thought to be unfeasible or more risky. Preliminary results are promising with low complication rates as well as high angiographic occlusion with the remodeling of the emanating branch. Yet, the safe use of more than 1 device at these locations remains ambiguous. Larger series with longer-term follow-up examinations are required to show the long-term safety and durability of this treatment alternative.

Disclosures: Isil Saatci—RELATED: Consulting Fee or Honorarium: Covidien/ev3, Saruhan Cekirge—RELATED: Consulting Fee or Honorarium: Covidien/ev3; UNRELATED: Consultancy: Covidien/ev3, MicroVention.

REFERENCES

1. Doerfler A, Wanke I, Egelhof T, et al. **Double-stent method: therapeutic alternative for small wide necked aneurysm: technical note.** *J Neurosurg* 2004;100:150–54
2. Canton G, Levy DI, Lasheras JC, et al. **Flow changes caused by the sequential placement of stents across the neck of sidewall cerebral aneurysms.** *J Neurosurg* 2005;103:891–902
3. Zenteno MA, Santos-Franco JA, Freitas-Modenesi JM, et al. **Use of the sole stenting technique for the management of aneurysms in the posterior circulation in a prospective series of 20 patients.** *J Neurosurg* 2008;108:1104–18
4. Fiorella D, Albuquerque FC, Deshmukh VR, et al. **Endovascular reconstruction with the Neuroform stent as monotherapy for the treatment of uncoilable intradural pseudoaneurysms.** *Neurosurgery* 2006;59:291–300
5. Park SI, Kim BM, Kim DI, et al. **Clinical and angiographic follow-up of stent-only therapy for acute intracranial vertebrobasilar dissecting aneurysms.** *AJNR Am J Neuroradiol* 2009;30:1351–56
6. Pumar JM, Lete I, Pardo MI, et al. **LEO stent monotherapy for the endovascular reconstruction of fusiform aneurysm of the middle cerebral artery.** *AJNR Am J Neuroradiol* 2008;29:1775–76
7. Kim YJ. **Sole stenting technique for treatment of complex aneurysms.** *J Korean Neurosurg* 2009;46:545–51
8. Cekirge HS, Yavuz K, Geyik S, et al. **A novel ‘Y’ stent flow diversion technique for the endovascular treatment of bifurcation aneurysms without endosaccular coiling.** *AJNR Am J Neuroradiol* 2011;32:1262–68
9. Fiorella D, Woo HH, Albuquerque FC, et al. **Definitive reconstruction of circumferential, fusiform intracranial aneurysms with the Pipeline embolization device.** *Neurosurgery* 2008;62:1115–21
10. Saatci I, Yavuz K, Ozer C, et al. **Treatment of intracranial aneurysms using the Pipeline flow-diverter embolization device: a single-center experience with long-term follow-up results.** *AJNR Am J Neuroradiol* 2012;33:1436–46
11. Nelson PK, Lylyk P, Szikora I, et al. **The Pipeline embolization device for the intracranial treatment of aneurysms trial.** *AJNR Am J Neuroradiol* 2011;32:34–40
12. Siddiqui AH, Kan P, Abla A, et al. **Complications after treatment with Pipeline embolization for giant intracranial aneurysms with or without coil embolization.** *Neurosurgery* 2012;71:509–13
13. Chitale R, Gonzalez LF, Randazzo C, et al. **Single center experience with Pipeline stent: feasibility, technique, and complications.** *Neurosurgery* 2012;71:679–91
14. O’Kelly CJ, Spears J, Chow M, et al. **Canadian experience with the Pipeline embolization device for repair of unruptured intracranial aneurysms.** *AJNR Am J Neuroradiol* 2013;34:381–87
15. Burrows AM, Zipfel G, Lanzino G. **Treatment of a pediatric recurrent fusiform middle cerebral artery (MCA) aneurysm with a flow diverter.** *BMJ Case Rep* 2012 Nov 15;2012
16. Kallmes DF, Ding YH, Dai D, et al. **A new endoluminal, flow-disrupting device for treatment of saccular aneurysms.** *Stroke* 2007;38:2346–52

17. Puffer RC, Kallmes DF, Cloft HJ, et al. **Patency of the ophthalmic artery after flow diversion treatment of paraclinoid aneurysms.** *J Neurosurg* 2012;116:892–96
18. van Rooij, Sluzewski M. **Perforator infarction after placement of a Pipeline flow-diverting stent for an unruptured A1 aneurysm.** *AJNR Am J Neuroradiol* 2010;31:E43–44
19. Lylyk P, Miranda C, Ceratto R, et al. **Curative endovascular reconstruction of cerebral aneurysms with the Pipeline embolization device: the Buenos Aires experience.** *Neurosurgery* 2009;64:632–43
20. Kulcsar Z, Houdart E, Bonafe A, et al. **Intra-aneurysmal thrombosis as a possible cause of delayed aneurysm rupture after flow-diversion treatment.** *AJNR Am J Neuroradiol* 2011;32:20–25
21. Turowski B, Macht S, Kulcsar Z, et al. **Early fatal hemorrhage after endovascular cerebral aneurysm treatment with a flow-diverter (Silk-stent): do we need to rethink our concepts?** *Neuroradiology* 2011;53:37–41
22. Cebal JR, Mut F, Raschi, et al. **Aneurysm rupture following treatment with flow-diverting stents: computational hemodynamics analysis of treatment.** *AJNR Am J Neuroradiol* 2011;32:27–33
23. Hampton T, Walsh D, Tolia C, et al. **Mural destabilization after aneurysm treatment with a flow-diverting device: a report of two cases.** *J Neurointerv Surg* 2011;3:167–71
24. Fischer S, Vajda Z, Perez MA, et al. **Pipeline embolization device (PED) for neurovascular reconstruction: initial experience in treatment of 101 intracranial aneurysms and dissections.** *Neuroradiology* 2012;54:369–82
25. Cruz JP, Chow M, O’Kelly C, et al. **Delayed ipsilateral parenchymal hemorrhage following flow diversion for the treatment of anterior circulation aneurysms.** *AJNR Am J Neuroradiol* 2012;33:603–08
26. Yavuz K, Geyik S, Cekirge S, et al. **Double stent-assisted coil embolization treatment for bifurcation aneurysms: immediate treatment results and long-term angiographic outcome.** *AJNR Am J Neuroradiol* 2013;34:1778–84
27. Thorell WE, Chow MM, Woo HH, et al. **Y-configured dual intracranial stent-assisted coil embolization for the treatment of wide-necked basilar tip aneurysms.** *Neurosurgery* 2005;56:1035–40

Mind the Gap: Impact of Computational Fluid Dynamics Solution Strategy on Prediction of Intracranial Aneurysm Hemodynamics and Rupture Status Indicators

K. Valen-Sendstad and D.A. Steinman



ABSTRACT

BACKGROUND AND PURPOSE: Computational fluid dynamics has become a popular tool for studying intracranial aneurysm hemodynamics, demonstrating success for retrospectively discriminating rupture status; however, recent highly refined simulations suggest potential deficiencies in solution strategies normally used in the aneurysm computational fluid dynamics literature. The purpose of the present study was to determine the impact of this gap.

MATERIALS AND METHODS: Pulsatile flow in 12 realistic MCA aneurysms was simulated by using both high-resolution and normal-resolution strategies. Velocity fields were compared at selected instants via domain-averaged error. We also compared wall shear stress fields and various reduced hemodynamic indices: cycle-averaged mean and maximum wall shear stress, oscillatory shear index, low shear area, viscous dissipation ratio, and kinetic energy ratio.

RESULTS: Instantaneous differences in flow and wall shear stress patterns were appreciable, especially for bifurcation aneurysms. Linear regressions revealed strong correlations ($R^2 > 0.9$) between high-resolution and normal-resolution solutions for all indices except kinetic energy ratio ($R^2 = 0.25$) and oscillatory shear index ($R^2 = 0.23$); however, for most indices, the slopes were significantly <1 , reflecting a pronounced underestimation by the normal-resolution simulations. Some high-resolution simulations were highly unstable, with fluctuating wall shear stresses reflected by the poor oscillatory shear index correlation.

CONCLUSIONS: Typical computational fluid dynamics solution strategies may ultimately be adequate for augmenting rupture risk assessment on the basis of certain highly reduced indices; however, they cannot be relied on for predicting the magnitude and character of the complex biomechanical stimuli to which the aneurysm wall may be exposed. This impact of the computational fluid dynamics solution strategy is likely greater than that for other modeling assumptions or uncertainties.

ABBREVIATIONS: CFD = computational fluid dynamics; HR = high-resolution; NR = normal-resolution; OSI = oscillatory shear index; WSS = wall shear stress

Hemodynamic forces, notably wall shear stresses (WSSs), are thought to contribute to wall adaptation and remodeling.¹ Computational fluid dynamics (CFD) can nominally describe the

hemodynamic environment to which the wall is exposed and, therefore, predict the presence of abnormal wall shear stress as a plausible surrogate marker of focal wall weakening. Using highly automated algorithms, recent CFD studies have been successful in retrospectively classifying hundreds of aneurysms according to their rupture status.²⁻⁴ Although it has been questioned whether these simulations are really patient specific owing to the various modeling assumptions and uncertainties,⁵ CFD is, arguably, a promising tool for future clinical use.^{6,7}

Key factors that determine the accuracy of a particular CFD simulation are the temporal and spatial discretizations specified by the operator. In principle, these are chosen in anticipation of the expected hemodynamics and then must be demonstrated to converge to within some desired error tolerance via methodical refinement studies.⁸ In practice however, discretizations are usu-

Received April 22, 2013; accepted after revision July 13.

From the Biomedical Simulation Lab (K.V.-S., D.A.S.), Department of Mechanical and Industrial Engineering, University of Toronto, Toronto, Canada; and Center for Biomedical Computing (K.V.-S.), Simula Research Laboratory, Lysaker, Norway.

This work was supported by Canadian Institutes of Health Research grant MOP-62934 to D.A.S.; and a Research Council of Norway Center of Excellence grant to the Center for Biomedical Computing at Simula. K.V.-S. was supported in part by a Government of Canada postdoctoral research fellowship. D.A.S. also acknowledges the support of a Career Investigator salary award from the Heart and Stroke Foundation of Canada.

Previously presented in part at: International Symposium on Biomechanics in Vascular Biology and Cardiovascular Disease, April 18–19, 2013; Rotterdam, the Netherlands.

Please address correspondence to D.A. Steinman, 5 King's College Rd, Toronto, Ontario, Canada M5S 3G8; e-mail: steinman@mie.utoronto.ca

Indicates open access to non-subscribers at www.ajnr.org

Indicates article with supplemental on-line video.

<http://dx.doi.org/10.3174/ajnr.A3793>

ally constrained by available computational resources and/or desired solution times, and rarely are proper convergence studies performed or reported. Moreover, commercial CFD solvers tend to use low-order stabilization terms as the default^{9,10} to ensure a result, even for otherwise-inadequate discretizations; this tendency amounts to adding artificial viscosity or dissipation to the solution. These are not minor technical issues because inexperienced individuals can now readily use commercial CFD solvers; solutions are being sought within clinical timeframes; and CFD can have an impact on clinical decision-making.¹¹⁻¹³

To illustrate the potential gap between what may be termed normal-resolution (NR) and high-resolution (HR) solution strategies, consider that the broadest CFD-based studies of aneurysm rupture status have reported using 100 time-steps per cardiac cycle with meshes of 1 to 5 million tetrahedra¹⁴ or 1000 time-steps per cycle with 300,000 to 1 million elements.² On the other hand, recent case studies using tens of thousands of time-steps per cardiac cycle and tens of millions of tetrahedral elements (or the equivalent) have reported the presence of highly unstable and possibly turbulent flows,¹⁵⁻¹⁸ consistent with clinical observations¹⁹ but seemingly at odds with most published aneurysm CFD studies. The impact of the solution strategy was also evident in a recent CFD Challenge,²⁰ which highlighted, for the same aneurysm case, a wide variety of aneurysm inflow patterns contributed by 25 groups, most using a range of NR strategies.

Nevertheless, discrimination of aneurysm rupture status tends to rely on hemodynamic indices that reduce complex velocity and WSS fields to a single number or category via integration over the cardiac cycle and/or aneurysm dome, with the potential for ameliorating differences in velocity and WSS fields predicted by HR-versus-NR strategies. The aim of the present study was, therefore, to investigate the impact of solution strategy on the prediction of aneurysm velocity and WSS fields, to determine whether NR solution strategies may be sufficient for hemodynamic indices commonly used for discrimination of rupture status. Not having access to the datasets of other groups, we achieved this by performing a controlled numeric experiment wherein a representative HR and NR solution strategy was applied to the same set of aneurysm cases.

MATERIALS AND METHODS

Patients and Imaging

The original cohort consisted of 20 consecutive patients with MCA aneurysms treated at the Department of Neurosurgery, University Hospital of North Norway. Of these patients, 12 were suitable for image-based CFD modeling and, by convention, are identified by their original case numbers, between 1 and 20. The register was approved by the local ethics committee and the data inspectorate; included patients gave consent for use of imaging and clinical data. 3D imaging of the intracranial arteries and aneurysms was obtained on a 16-multidetector row spiral CT scanner with 0.3- to 0.5-mm resolution. The resulting cases included both sidewall and bifurcation aneurysm types and stable and unstable flow types. Further details, including morphologic characterizations, are provided elsewhere.¹⁸

HR-versus-NR Solution Strategies

To ensure as controlled a numeric experiment as possible, we performed simulations by using solvers developed and validated within the same open-source finite-element method library, FEniCS (<http://fenicsproject.org/>)²¹; for HR, a minimally dissipative solver; for NR, a solver using a standard stabilization scheme. Most important, both HR and NR simulations were performed by using the same finite-element mesh for each case; the only difference was the use of quadratic-versus-linear elements for HR versus NR, or better than a 2× increase in spatial resolution or an 8× increase in linear elements.

For HR simulations, we used a conditionally stable incremental pressure-correction scheme,^{18,21} based on Stanford's well-known CDP solver widely used in high-performance CFD research.²² For our solver, we used second-order Taylor-Hood tetrahedral elements and a second-order semi-implicit time-stepping scheme. The number of time-steps per cardiac cycle was set to 20,000 to minimize artificial diffusion and capture possible flow instabilities.¹⁸

For the NR set of simulations, we used an unconditionally stable implicit PSIO (pressure implicit with splitting of operators') scheme, widely used in commercial CFD solvers. The number of time-steps per cardiac cycle was set to 1000, the finer of the time-step sizes from the 2 largest rupture-status CFD studies.^{2,3} At such temporal resolutions, the CFD solver needs to be stabilized because numeric stability criteria are not met. We used a first-order streamline-upwind/Petrov-Galerkin stabilization, which is the default approach in commercial solvers like Fluent (ANSYS, Canonsburg, Pennsylvania) and Star-CD (CD-adapco, Melville, New York).^{9,10} We used first-order accurate continuous Galerkin elements for both the velocity and pressure and advanced the solution in time by using a fully implicit first-order scheme. This solution strategy is representative of most aneurysm CFD studies published in the clinical literature, and most solutions contributed to a recent aneurysm CFD Challenge.²⁰

Common Solution Parameters

The CT-imaged aneurysms were digitally segmented and meshed by using the Vascular Modeling ToolKit (www.vmtk.org). We included as much as possible from the surrounding arteries, and vessels were extended by 10 diameters to reduce boundary effects. Mesh density was chosen to be highest in the vicinity of the aneurysm sac, where the tetrahedron side length was 0.12 mm on average (eg, compared to Cebal et al,¹⁴ who reported a minimum resolution between 0.2 and 0.1 mm). Two layers of boundary elements were used throughout the domain, with a total thickness set equal to one-quarter of the tetrahedron side length. The number of tetrahedral elements was 1.44 million on average, ranging from 1.1 to 2.0 million elements. As a result, the HR meshes, by using second-order elements, were at least equivalent to linear tetrahedral meshes with 8.8- to 16-million elements and a side length of 0.06 mm.

We assumed rigid walls, a blood viscosity of 0.0035 Pa · s, and blood density of 1025 kg/m³. A fully developed Womersley velocity profile was applied at the inlet on the basis of a representative older adult ICA flow waveform²³ damped by 30% to account for the reduced pulsatility at the MCA.²⁴ A cycle-averaged cross-

tional mean velocity of 0.37 m/s was applied to the inlet in all cases, under the assumption that flow rate scales approximately with cross-sectional area. The resulting peak systolic cross-sectional mean velocity was 0.55 m/s. To represent the downstream vasculature, we applied resistance boundary conditions²⁵ to ensure a physiologic outflow division. Simulations were run until the flow exhibited cycle-to-cycle convergence or 4 cycles, whichever came first. We assumed a period of 1 second, and the analysis was based on the output from 100 uniformly spaced time-steps from the third cycle.

All simulations were performed on dual 2.5GHz quad-core processors (Xeon L5420; Intel, Santa Clara, California). Simulations performed using our highly optimized HR solver required an average of 5 days per cardiac cycle (range, 3–9 days). The NR solver, implemented for the purpose of this study and so not optimized, typically required <1 day per cycle.

Hemodynamic Indices

Velocity fields were compared quantitatively at selected instants via the L_2 error of the velocity ($\|HR - NR\|_{L_2} / \|HR\|_{L_2}$), based on the entire CFD model. We computed the following normalized hemodynamic indices defined by Xiang et al,² which we refer to as “reduced” because they are vector quantities reduced to magnitudes that are further averaged over both time and space: cycle-averaged mean and maximum WSS, oscillatory shear index (OSI), and low shear area. We also computed the viscous dissipation ratio and kinetic energy ratio as defined by Cezbral et al.³ For the indices of Xiang et al, the normalizing WSS was based on integrating the cycle-averaged parent artery WSS starting from an automatically identified “clipping point” proximal to the sac²⁶ and ending 1 diameter upstream. The aneurysm dome over which WSS, OSI, and low shear area were determined was defined as the portion of the aneurysm sac above an automatically defined ostium plane.²⁶ For viscous dissipation ratio and kinetic energy ratio, the extent of the “near-vessel region” was defined as locations below and within 10 mm of the centroid of the aforementioned ostium plane. Agreement between HR- and NR-derived hemodynamic indices was quantified via linear regression.

RESULTS

As shown in Fig 1, domain-averaged velocity differences between HR and NR simulations were up to 44%. Point-wise errors, especially within the, sac were higher, often exceeding 100%. All NR simulations showed a smooth and laminar flow, with convergence between the second and third cycle. For the HR simulations, cycle-to-cycle convergence was reached for all except 2 bifurcation cases (numbers 12 and 16). Inspection of selected velocity traces revealed unstable flow, starting just after peak systole, for these 2 cases as well as 2 other bifurcation cases (numbers 3 and 11), broadly consistent with what was previously reported under steady inflow conditions.¹⁸ As demonstrated by Fig 1, the 4 unstable-flow bifurcation cases exhibited the largest differences between NR and HR solutions, followed by the stable-flow bifurcation cases, then the (stable-flow) sidewall cases.

The large errors in velocity and WSS patterns for NR simulations of the unstable-flow bifurcation cases are evident in Fig 2A. In particular, velocity isosurfaces for the HR simulations were

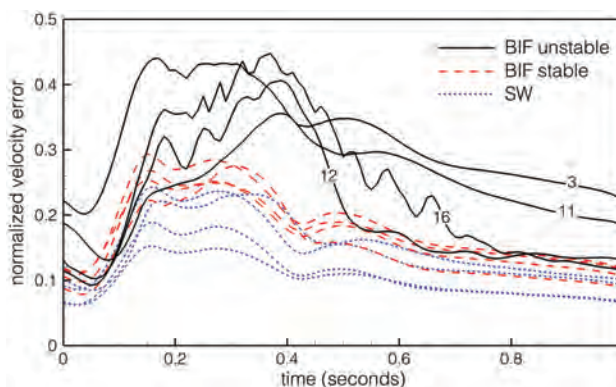


FIG 1. Instantaneous domain-averaged velocity errors in NR solutions, by using the HR solutions as a reference standard. The 12 cases are divided into sidewall (SW) and bifurcation (BIF) types, the latter subdivided into cases exhibiting stable and unstable flows. Note the identification numbers for the BIF unstable cases.

more complicated and showed deeper penetration into the aneurysm sac (cases 11, 12, and 16) or more dynamic flow at the ostium (case 3). Cycle-averaged WSS distributions were surprisingly similar in light of the large-velocity errors; however, OSI was substantially underpredicted by the NR simulations. (As discussed later, this is a consequence of large instantaneous and/or point-wise differences in WSS predicted by HR-versus-NR simulations.) For stable-flow bifurcation cases (Fig 2B), marked differences in NR-versus-HR velocity patterns were evident for all except case 20. Cycle-averaged WSS and OSI patterns were broadly consistent for NR versus HR; however, WSS levels for NR simulations were substantially lower for cases 9 and 18. Differences in velocity and WSS patterns were less evident for the NR-versus-HR sidewall cases (Fig 2C), with the exception of velocity patterns for case 1 and OSI levels for case 5.

Linear regressions of the reduced hemodynamic indices for NR-versus-HR simulations (Fig 3) showed varying levels of correlation. Whereas WSS, maximum WSS, low shear area, and viscous dissipation ratio were highly correlated and thus could be relied on to stratify cases similarly whether based on NR or HR simulations, OSI and kinetic energy ratio showed weak correlation. When one looks at the slopes of the regression lines, however, it is clear that, with the exception of low shear area, NR simulations substantially underpredicted the value of a given hemodynamic index. This outcome was confirmed by paired *t* tests, which showed that NR indices were significantly lower than corresponding HR indices ($P < .005$) for all except the low shear area.

DISCUSSION

We have demonstrated, in a numeric experiment intended to be as simple as possible, that the CFD solution strategy can have a substantial impact on intracranial aneurysm flow patterns and the magnitude of reduced hemodynamic indices. On the basis of Fig 2, we can conclude that NR simulations, representative of many of the strategies reported in the aneurysm CFD literature, can provide only a limited understanding of aneurysm flow, especially for bifurcation aneurysms. Moreover, NR simulations cannot be relied on for predicting the magnitude of hemodynamic forces to which the aneurysm wall is exposed. HR simulations are necessary for detecting flow instabilities, describing proper jet penetration,

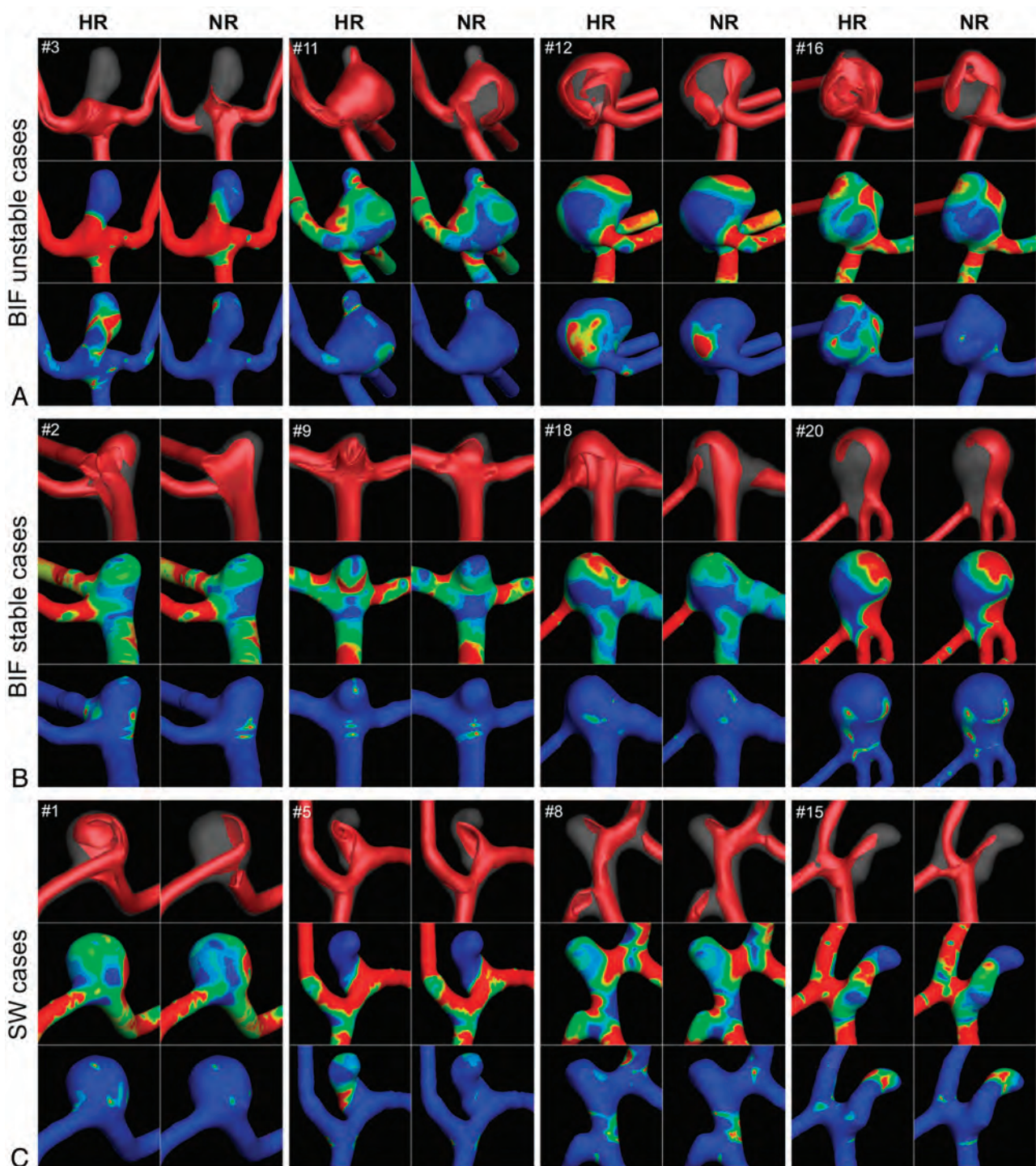


FIG 2. Qualitative differences in HR-versus-NR velocity and WSS fields for bifurcation cases with unstable flows (A), bifurcation cases with stable flows (B), and sidewall cases (C). For each case, the top row compares the isovelocity surfaces at the time of maximum domain-averaged error, the middle row compares the cycle-averaged WSS distributions, and the bottom row compares the OSI distributions.

and calculating absolute values of hemodynamic quantities. Although certain highly reduced indices seem to be relatively robust to the solution strategy, our results suggest that HR strategies may be essential for gaining insights into the mechanobiology of wall remodeling in aneurysms.

Arguably the most striking finding was the gap between predictions of OSI by NR-versus-HR simulations, whereas there was much better correspondence for WSS. For HR simulations, in-

spection of Fig 2 reveals that sites of low WSS tended to correlate with sites of high OSI. This finding reflects the fact that particularly for the unstable bifurcation cases, HR simulations revealed instantaneously high shear in these regions with strong oscillations, in both magnitude and direction, over the cardiac cycle, whereas NR simulations predicted persistently low shear and underestimated its temporal and directional variations (ie, OSI). An example of this is shown in Fig 4 and the On-line Video. Thus, in

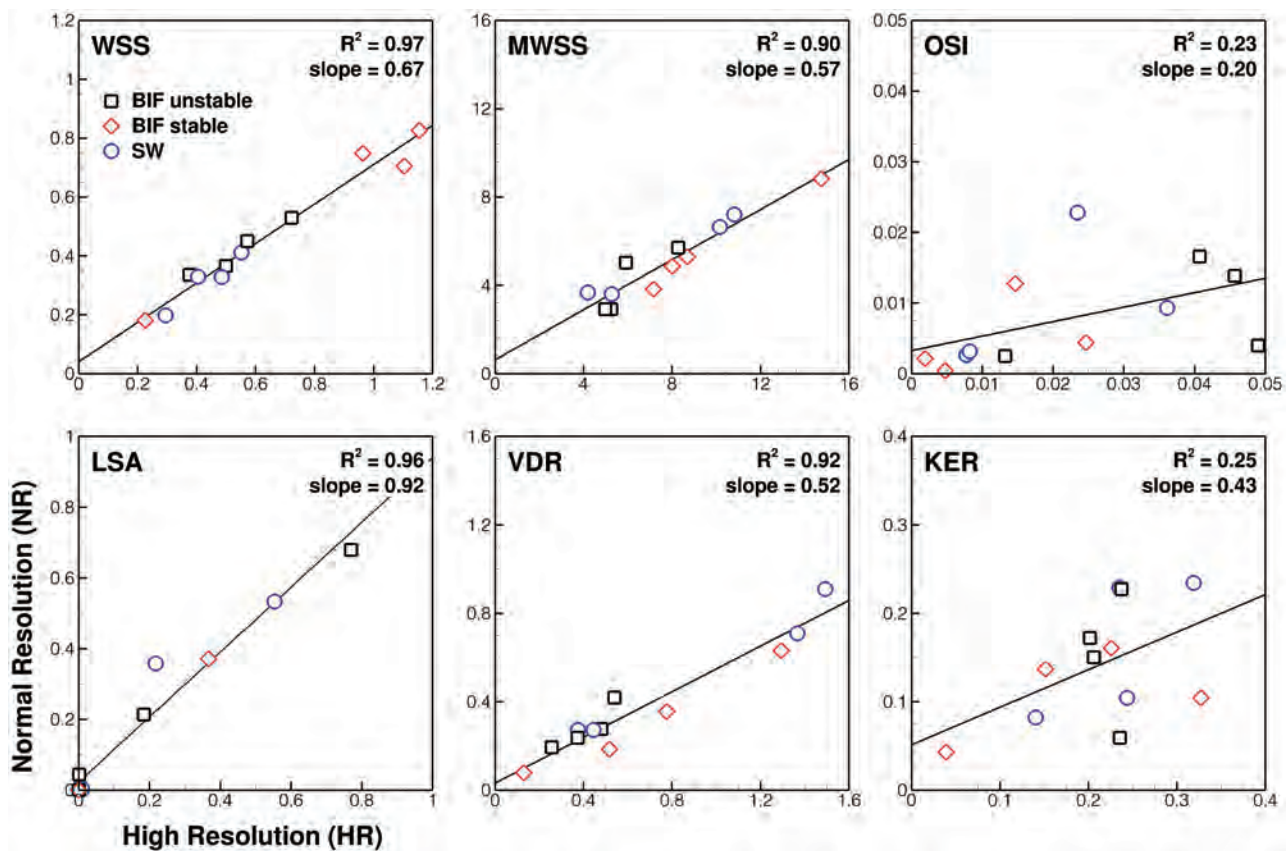


FIG 3. Comparison of various normalized hemodynamic indices determined from HR-versus-NR solutions. The top left of each plot identifies the index. The top right shows the coefficient of determination (R^2) and the slope of the linear regressions as measures of correlation and agreement, respectively. Note that different symbols are used to highlight the 3 different groups of cases, per the legend of the top left plot; KER indicates kinetic energy ratio; LSA, low shear area; VDR, viscous dissipation ratio; MWSS, maximum wall shear stress.

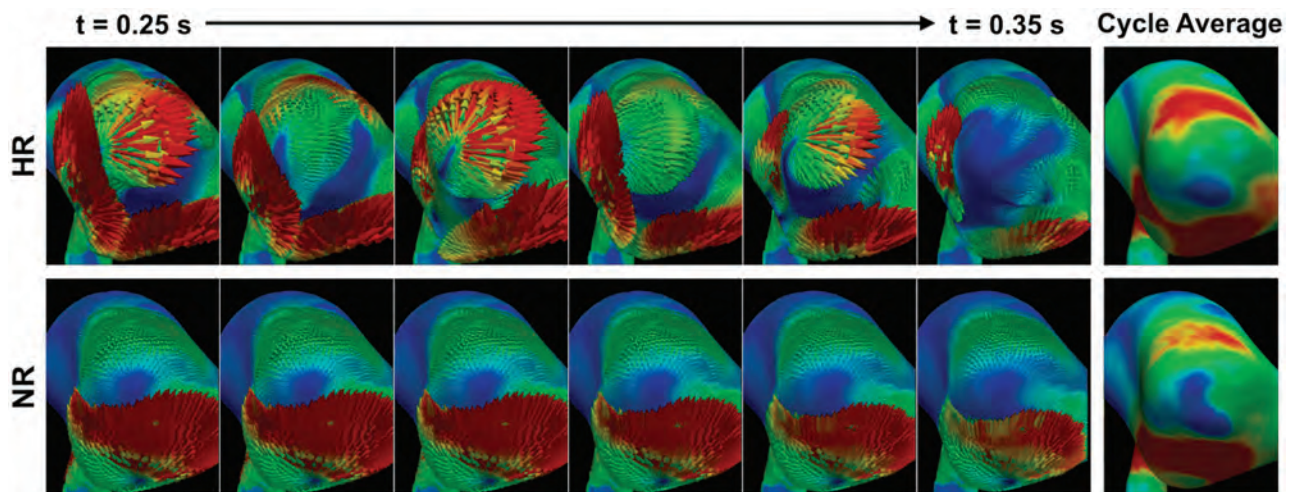


FIG 4. Top: HR simulations of bifurcation unstable case 16 demonstrate large variations in WSS vectors during a brief (0.1 second) period of postsystolic flow deceleration. Bottom: Corresponding NR simulations show negligible variations during this same period, despite having comparable cycle-averaged WSS distributions (right column). See the On-line Video for a comparison during the entire cardiac cycle.

cases in which such dynamic flows are present, NR simulations could lead to a conclusion that low WSS is a stimulus for pathologic wall remodeling leading to rupture, whereas the mechanistic link to rupture status might not necessarily be low WSS, but rather temporally high fluctuating WSS that is low on average. In this context, in the odds ratio equation proposed by Xiang et al,² the

OSI term actually contributes very little to the discrimination of rupture compared with the WSS term. In other words, mischaracterization of WSS dynamics might be at the root of ongoing debates about whether low or high WSS is correlated with aneurysm rupture status.⁵ This scenario is particularly true for bifurcation aneurysms, where we have clearly demonstrated a strong

impact of solution strategy on the predicted hemodynamics, as opposed to sidewall aneurysms, for which NR simulations were largely adequate. Baharoglu et al²⁷ recently reported a dichotomy between sidewall and bifurcation aneurysms (ie, morphologic discriminants were accurate for sidewall aneurysms, but not for bifurcation aneurysms). This finding suggests that there may be a different mechanistic link to rupture in bifurcation aneurysms.

Another potentially important gap is the detection of flow instabilities, which are thought to be the ultimate source of aneurysm bruits.^{19,28} Our pulsatile HR simulations detected highly unstable flow during and after systolic deceleration for certain of the bifurcation aneurysm cases, namely those for which flow instabilities were previously reported under stationary inflow conditions¹⁸; however, no such features were evident from the NR simulations. Indeed, there is now independent evidence for such flow instabilities based on high-resolution particle image velocimetry of realistic flow in a compliant model of a patient-specific aneurysm, which revealed transitional flow phenomena during the deceleration phase,²⁹ consistent with data presented in the current study. Hence, as has previously been argued on the basis of HR CFD findings^{17,18} and as the authors of the particle image velocimetry study also emphasized,²⁹ though there is a widely held conception that aneurysm flow is laminar (ie, stable, or with periodic instabilities and/or vortex shedding; as opposed to turbulent flows or laminar/transitional flows, with high-frequency, non-periodic instabilities having small spatial and temporal scales), evidence suggests that this a priori assumption, which is often used implicitly or explicitly to rationalize NR solution strategies, must be reconsidered.

Irrespective of the nature of aneurysm flow, Fig 3 highlights another gap between NR and HR simulations, namely a consistent underestimation of all of the reduced hemodynamic indices that were assessed, with the exception of low shear area. When one considers absolute values (ie, not normalized by the parent artery WSS) of cycle-averaged WSS and maximum WSS, for example, HR predictions were, on average, 30% higher for WSS (3.96 ± 2.00 Pa versus 3.03 ± 1.41 Pa) and 60% higher for maximum WSS (49.2 ± 14.6 Pa versus 30.7 ± 10.6 Pa). In other words, point-wise WSS magnitudes are more challenging to properly resolve than dome-integrated values; and high WSS may be disproportionately underestimated by NR strategies compared with low WSS values. To illustrate this further, in Fig 5 we plot mean and maximum WSS for sidewall case 15 from our HR and NR solutions; but also from additional NR simulations, which we performed using coarser meshes ranging from 810,000 down to 170,000 elements. It can be seen that convergence, particularly for maximum WSS, is difficult to justify for meshes even around 1 million elements.

The above example highlights the importance of performing proper convergence studies to prove that a numeric solution is independent of the chosen parameters, such as mesh size and time-step. When dealing with nonlinear equations such as those that govern fluid flow, convergence studies become even more important because a linear convergence cannot be expected (eg, it was previously demonstrated for stationary flow of a normal left anterior descending artery that a uniform mesh refinement strategy did not show a consistent decrease in WSS errors and that an extreme mesh convergence strategy was necessary to obtain con-

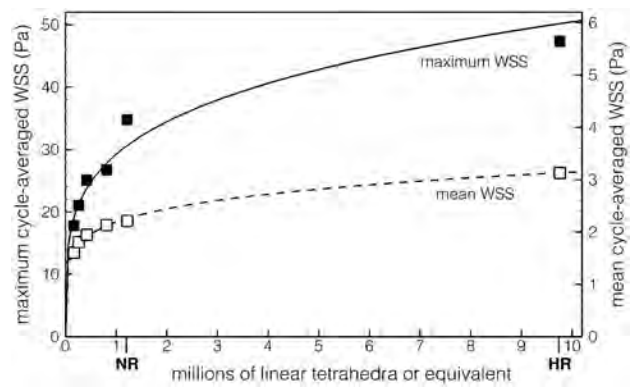


FIG 5. Impact of mesh resolution on the sac maximum and mean cycle-averaged WSS for case 15. Symbols identify data from individual simulations; the lines show power-law fits through the respective data. Note the identification of the NR and HR resolutions on the x-axis.

vergence³⁰). Although most published CFD studies of aneurysms claim spatial and temporal convergence, neither the criteria nor results are normally presented. Even in the CFD studies in which refinement studies are mentioned, the general approach is to increase the number of elements by 50% and evaluate the change in some reduced hemodynamic index, typically with a tolerance of a few percent. However, in 3D, a 50% increase in elements is roughly equivalent to only a 14% decrease in cell side length (ie, $1.50^{1/3} = 1.14$) along a given direction and should be considered just the first step of a refinement study.

These “routine” convergence studies appear to fall significantly short of what is needed, as may be deduced from the aneurysm CFD convergence study reported by Hodis et al,⁸ in which it was concluded that “the grid convergence errors showed oscillatory behavior; therefore, each patient-specific model required its own grid convergence study to establish the accuracy of the analysis.” The impact on hemodynamic indices was not addressed in that study, and for our HR simulations, the average element side length in the aneurysm sac was 0.06 mm, well below the 0.08 mm reported for the converged solutions of Hodis et al.⁸

The pronounced impact of the CFD solution strategy on the magnitude of derived hemodynamic indices implies that the solution strategy must be acknowledged as an additional source of variability, especially if and when the findings of different groups, potentially using a wide range of strategies, are compared or analyzed together. In striving for more patient-specific simulations, most studies have focused on the impact of other assumptions or uncertainties such as inflow/outflow conditions,³¹ non-Newtonian rheology,³² compliance,³³ and choice of imaging technique.^{34,35} Although it is difficult to draw a direct comparison between their findings and the results of the present study, inspection of figures from those studies suggests that the qualitative differences due to those assumptions are less than the differences due to choice of CFD solution strategy as demonstrated in our study. By evaluating point-wise differences, we found changes on the order of hundreds of percent (in both space and time) in some cases, suggesting that adequate CFD resolution is a central issue that cannot be ignored if patient-specific simulations are desired. It is also possible that those other sources of variability need to be revisited in light of the more complex and dynamic flows evident

from HR simulations versus the NR strategies used previously to infer their influence.

The present results are also interesting in the light of the previously expressed frustration of Kallmes⁵ over the many hemodynamic parameters and indices clinicians have to understand and relate to. We found it difficult to find a consistent definition for what constituted the aneurysm dome over which WSS quantities were integrated or the parent artery region used to determine the normalizing WSS. Moreover, we found that the reduced hemodynamic indices were often imprecisely or variously defined (eg, maximum WSS and low shear area,^{2,3}), suggesting a further source of variability that must be resolved by a standardization of definitions and parameters before meta-analyses or multicenter studies can be considered.

A limitation of our study is that the change in solution strategy involved 2 aspects: resolution and stabilization. The latter was unavoidable because coarsening the resolution causes the numerical stability criteria to no longer be met by a minimally dissipative solver such as the one we used for the HR simulations. For the NR simulations we did, however, choose a widely used stabilized solution strategy that is the default in several commercial CFD solvers used in the aneurysm CFD literature. To minimize the likelihood of overestimating the impact of solution strategy, we consciously chose the highest of the mesh and, separately, temporal resolutions reported by the 3 largest clinical studies to date²⁻⁴; a cursory inspection of other aneurysm CFD studies recently published in the clinical literature³⁴⁻³⁹ suggests that the resolutions of our NR simulations are, if anything, on the high side. Nevertheless, as noted by a recent aneurysm CFD Challenge,²⁰ it is difficult to compare node spacing, element types, and sizes from one study to another; there are simply not enough details provided about the solver parameters and cell distributions to exactly reproduce what other groups are using. Nevertheless, our NR simulations are likely finer than those of most of the above-mentioned studies, particularly because we concentrated our elements in the vicinity of the aneurysm rather than assuming a uniform mesh density throughout the domain. Our demonstrated impact of solution strategy can also be considered conservative because of our choice of flow rates. For example, a recently published CFD study of MCA aneurysms³⁷ reported using a mean inlet Reynolds number of 500 (versus our Reynolds number of 260) and a common carotid artery flow waveform (versus our deliberate choice of a damped waveform more representative of the reduced pulsatility at the MCA).

Like most image-based CFD studies of intracranial aneurysms, we cannot exclude the possibility that the ostium area might have been overestimated⁴⁰ because we did not have 2D DSA to compare against. As a result, assuming the same boundary conditions, the effect of the solution strategy may have been overestimated in sidewall aneurysms but underestimated in bifurcation aneurysms. We made the standard assumption of rigid walls and Newtonian fluid, and we did not have the patient-specific waveforms and flow rates. Our sample size was small and limited to 1 vascular territory (MCA). Furthermore, we do not claim that the HR simulations are fully resolved, but we are confident that they capture the correct flow states and eddies with the most energy. The smallest scales of the flow are therefore not resolved, but

on the other hand, the continuum hypothesis breaks down at some point, and how to deal with this is an open question.⁴¹

CONCLUSIONS

The CFD solution strategy has a pronounced effect on the prediction of intracranial aneurysm hemodynamics, likely more so than other modeling assumptions or uncertainties. Retrospective discrimination of rupture status based on certain highly reduced hemodynamic indices may therefore be considered relatively immune to solution strategy, but only if the same strategy is used for all cases. On the other hand, NR simulations might well mask clinically relevant correlations for indices that do require HR strategies, such as OSI. Moreover, regions of dynamic WSS are more likely to be mistaken for regions of persistently low WSS by NR strategies. In short, clinically expedient CFD solution strategies might prove useful when and if they are eventually incorporated into clinical rupture-risk assessment, but HR strategies are required to elucidate the underlying mechanisms of aneurysmal wall remodeling and rupture.

REFERENCES

1. Krings T, Mandell DM, Kiehl TR, et al. **Intracranial aneurysms: from vessel wall pathology to therapeutic approach.** *Nat Rev Neurol* 2011;7:547–59
2. Xiang J, Natarajan SK, Tremmel M, et al. **Hemodynamic-morphologic discriminants for intracranial aneurysm rupture.** *Stroke* 2011;42:144–52
3. Cebral JR, Mut F, Weir J, et al. **Quantitative characterization of the hemodynamic environment in ruptured and unruptured brain aneurysms.** *AJNR Am J Neuroradiol* 2011;32:145–51
4. Miura Y, Ishida F, Umeda Y, et al. **Low wall shear stress is independently associated with the rupture status of middle cerebral artery aneurysms.** *Stroke* 2013;44:519–21
5. Kallmes DF. **Point: CFD—computational fluid dynamics or confounding factor dissemination.** *AJNR Am J Neuroradiol* 2012;33:395–96
6. Cebral JR, Meng H. **Counterpoint: realizing the clinical utility of computational fluid dynamics—closing the gap.** *AJNR Am J Neuroradiol* 2012;33:396–98
7. Robertson AM, Watton PN. **Computational fluid dynamics in aneurysm research: critical reflections, future directions.** *AJNR Am J Neuroradiol* 2012;33:992–95
8. Hodis S, Uthamaraj S, Smith AL, et al. **Grid convergence errors in hemodynamic solution of patient-specific cerebral aneurysms.** *J Biomech* 2012;45:2907–13
9. *Ansys Fluent 14.0: User's Guide.* Canonsburg, Pennsylvania: Ansys Inc; 2011:p. 1317
10. *CCM Tutorials, Star-CD 4.02.* Melville, NY: CD-adapco; 2006: p. 10–18
11. Cebral JR, Mut F, Raschi M, et al. **Aneurysm rupture following treatment with flow-diverting stents: computational hemodynamics analysis of treatment.** *AJNR Am J Neuroradiol* 2011;32:27–33
12. Steinman DA. **Computational modeling and flow diverters: a teaching moment.** *AJNR Am J Neuroradiol* 2011;32:981–83
13. Fiorella D, Sadasivan C, Woo HH, et al. **Regarding “Aneurysm rupture following treatment with flow-diverting stents: computational hemodynamics analysis of treatment.”** *AJNR Am J Neuroradiol* 2011;32:E95–97, author reply E98–100
14. Cebral JR, Mut F, Weir J, et al. **Association of hemodynamic characteristics and cerebral aneurysm rupture.** *AJNR Am J Neuroradiol* 2011;32:264–70
15. Baek H, Jayaraman MV, Richardson PD, et al. **Flow instability and wall shear stress variation in intracranial aneurysms.** *J R Soc Interface* 2010;7:967–88

16. Ford MD, Piomelli U. Exploring high frequency temporal fluctuations in the terminal aneurysms of the basilar bifurcation. *J Biomech Eng* 2012;134:091003
17. Valen-Sendstad K, Mardal KA, Mortensen M, et al. Direct numerical simulation of transitional flow in a patient-specific intracranial aneurysm. *J Biomech* 2011;44:2826–32
18. Valen-Sendstad K, Mardal KA, Steinman DA. High-resolution CFD detects high-frequency velocity fluctuations in bifurcation, but not sidewall, aneurysms. *J Biomech* 2013;46:402–07
19. Ferguson GG. Turbulence in human intracranial saccular aneurysms. *J Neurosurg* 1970;33:485–97
20. Steinman DA, Hoi Y, Fahy P, et al. Variability of computational fluid dynamics solutions for pressure and flow in a giant aneurysm: the ASME 2012 Summer Bioengineering Conference CFD Challenge. *J Biomech Eng* 2013;135:021016
21. Logg A, Mardal KA, Wells G. *Automated Solution of Differential Equations by the Finite Element Method: The FEniCS Book*. Heidelberg, Germany: Springer-Verlag; 2012
22. Mahesh K, Constantinescu G, Moin P. A numerical method for large-eddy simulation in complex geometries. *J Comput Phys* 2004;197:215–40
23. Hoi Y, Wasserman BA, Xie YJ, et al. Characterization of volumetric flow rate waveforms at the carotid bifurcations of older adults. *Physiol Meas* 2010;31:291–302
24. Krejza J, Mariak Z, Walecki J, et al. Transcranial color Doppler sonography of basal cerebral arteries in 182 healthy subjects: age and sex variability and normal reference values for blood flow parameters. *AJR Am J Roentgenol* 1999;172:213–18
25. Alastruey J, Parker KH, Peiro J, et al. Modelling the circle of Willis to assess the effects of anatomical variations and occlusions on cerebral flows. *J Biomech* 2007;40:1794–805
26. Piccinelli M, Steinman DA, Hoi Y, et al. Automatic neck plane detection and 3D geometric characterization of aneurysmal sacs. *Ann Biomed Eng* 2012;40:2188–211
27. Baharoglu MI, Lauric A, Gao BL, et al. Identification of a dichotomy in morphological predictors of rupture status between sidewall- and bifurcation-type intracranial aneurysms. *J Neurosurg* 2012;116:871–81
28. Simkins TE, Stehbins WE. Vibrational behavior of arterial aneurysms. *Lett Appl Engr Sci* 1973;1:85–100
29. Yagi T, Sato A, Shinke M, et al. Experimental insights into flow impingement in cerebral aneurysm by stereoscopic particle image velocimetry: transition from a laminar regime. *J R Soc Interface* 2013;10:20121031
30. Prakash S, Ethier CR. Requirements for mesh resolution in 3D computational hemodynamics. *J Biomech Eng* 2001;123:134–44
31. Venugopal P, Valentino D, Schmitt H, et al. Sensitivity of patient-specific numerical simulation of cerebral aneurysm hemodynamics to inflow boundary conditions. *J Neurosurg* 2007;106:1051–60
32. Xiang J, Tremmel M, Kolega J, et al. Newtonian viscosity model could overestimate wall shear stress in intracranial aneurysm domes and underestimate rupture risk. *J Neurointerv Surg* 2012;4:351–57
33. Torii R, Oshima M, Kobayashi T, et al. Influencing factors in image-based fluid-structure interaction computation of cerebral aneurysms. *International Journal for Numerical Methods in Fluids* 2011;65:324–40
34. Geers AJ, Larrabide I, Radaelli AG, et al. Patient-specific computational hemodynamics of intracranial aneurysms from 3D rotational angiography and CT angiography: an in vivo reproducibility study. *AJNR Am J Neuroradiol* 2011;32:581–86
35. Schneiders JJ, Marquering HA, Antiga L, et al. Intracranial aneurysm neck size overestimation with 3D rotational angiography: the impact on intra-aneurysmal hemodynamics simulated with computational fluid dynamics. *AJNR Am J Neuroradiol* 2013;34:121–28
36. Kulcsár Z, Ugron A, Marosfoi M, et al. Hemodynamics of cerebral aneurysm initiation: the role of wall shear stress and spatial wall shear stress gradient. *AJNR Am J Neuroradiol* 2011;32:587–94
37. Takao H, Murayama Y, Otsuka S, et al. Hemodynamic differences between unruptured and ruptured intracranial aneurysms during observation. *Stroke* 2012;43:1436–39
38. Baharoglu MI, Schirmer CM, Hoit DA, et al. Aneurysm inflow-angle as a discriminant for rupture in sidewall cerebral aneurysms: morphometric and computational fluid dynamic analysis. *Stroke* 2010;41:1423–30
39. Chien A, Sayre J, Vinuela F. Quantitative comparison of the dynamic flow waveform changes in 12 ruptured and 29 unruptured ICA-ophthalmic artery aneurysms. *Neuroradiology* 2013;55:313–20
40. Brinjikji W, Cloft H, Lanzino G, et al. Comparison of 2D digital subtraction angiography and 3D rotational angiography in the evaluation of dome-to-neck ratio. *AJNR Am J Neuroradiol* 2009;30:831–34
41. Antiga L, Steinman DA. Rethinking turbulence in blood. *Biorheology* 2009;46:77–81

Resolving the Issue of Resolution

This Journal, as well as practically all publications that deal, directly or indirectly, with hemodynamics and vascular pathophysiology (from a clinical or biomechanical perspective, if there is a difference) have seen an explosion of articles using computational methodologies—often tagged with the CFD acronym, Computational Fluid Dynamics. This research addresses conditions like atherosclerosis, stenosis, and, of interest to this article, aneurysms. In light of this undeniable surge of interest, an article like the one published in this volume entitled, “Mind the Gap: Impact of Computational Fluid Dynamics Solution Strategy on Prediction of Intracranial Aneurysm Hemodynamics and Rupture Status Indicators,”¹ by Valen-Sendstad and Steinman, which documents in very robust, quantifiable, and indisputable terms “how to do it right” is most welcome and will certainly become indispensable guidance in the computational hemodynamics for aneurysms community.

If I were to summarize the article in 2 sentences, I would say that thorough literature inspection and reproduction of published cases shows that often under-resolved simulations (ie, simulations involving meshes that are coarser than necessary) are used to generate hemodynamic data for aneurysm cases. The consequence of this process is that quantitative deductions may be less accurate and specific than necessary. The authors demonstrated their case excellently, and there is little ground for argument. From a certain perspective, this article contributes to a very lively discussion involving CFD that started with the article of Kallmes² and attracted many subsequent commentaries and editorials. The discussion that emanated from Kallmes² focused more on the “why” of CFD, whereas the article of Valen-Sendstad and Steinman¹ emphasized the “how.”

Nevertheless, I think that the “Mind the Gap” part of the title of the article implies “Re-mind the Gap.” As the authors clearly show, often simulations are conducted and presented with computational effort that does not do justice to the complexity of the fluid dynamics involved in aneurysm flows. Actually, only recently, very-high-accuracy modeling showed that blood flow features that can be of great fundamental and diagnostic interest may be present in aneurysms and may be missed if not computed at the level of detail necessary.³ Nevertheless, the computational fluid

mechanics community knows how to confirm adequate mesh resolution and has established techniques and protocols that can be followed to ensure that the resolution used for every flow problem covers the fluid physics adequately. One can mention, for example, the National Aeronautics and Space Administration–led initiative: the National Project for Application-Oriented Research in CFD Alliance and its CFD Verification and the Validation Website (<http://www.grc.nasa.gov/WWW/wind/valid>), where a formal procedure to ensure grid independence in CFD has been established. Similarly, journals involving flow computations, published by the American Society of Mechanical Engineers, like the *Journal of Fluids Engineering – Transactions of the American Society of Mechanical Engineers* compel authors to abide by their “Statement on the Control of Numerical Accuracy,” a formal editorial policy for these journals (<http://journaltool.asme.org/templates/JFENumAccuracy.pdf>). Maybe, given the explosion of computational modeling in the field of neuroradiology, a similar set of guidelines can be inspired by the article of Valen-Sendstad and Steinman¹ for the *American Journal of Neuroradiology*.

There is another side to consider when one argues necessary resolution (and the price modelers and users are willing to pay, in terms of computational cost): what is the clinical question the simulation is aspiring to answer and, consequently, what is the required level of accuracy for responding to that particular question effectively? Although many different aspects of aneurysm health care management have been examined computationally, I can categorize the clinically relevant studies into 3 broad themes:

1) Computation of hemodynamics is used to extract indicators that are then directly correlated to inception, growth, or rupture.^{4,5} Usually, statistically meaningful numbers of cases are examined in such studies. In effect, such approaches strive to bypass the biologic complexity of vascular wall biomechanics and link hemodynamics with system-level responses and clinical outcomes directly.

2) At the next level, hemodynamics is combined with arterial wall biology modeling, attempting an almost first-principles coupling of mechanical stimuli (flow-induced wall shear stress, for example) with outcomes (inception, growth, or rupture) by ac-

counting explicitly for the vascular growth and remodeling processes at play.⁶

The first strand of studies mentioned above is more mature and is already used to extract interesting conclusions regarding the effect of hemodynamics in aneurysmal evolution. In contrast, the second thrust is still at a relatively early stage of development, with qualitative and, especially, quantitative know-how regarding the biologic signaling, mechanotransduction, and inflammatory processes often missing. I will come back to that.

The 2 themes above aspire to address the same clinical question—that is, the risk of rupture for a detected aneurysm. Contrary to that, a similarly important question involves the design, application, and performance assessment of interventional devices:

3) Computation of aneurysmal hemodynamics in the presence of interventional devices,^{7–10} in which the desired outcome is to evaluate whether a particular device will introduce adequate blood flow stagnation and thus lead to stable thrombus formation.

An interesting point can be made here if articles pertaining to these 3 themes are inspected: There is a stronger motivation for very high accuracy when the first and third classes of studies are involved than when the second theme is examined. I believe that the reason behind this correlation, which is indicated by the article of Valen-Sendstad and Steinman,¹ is that the reward for the higher computational cost involved in better resolved simulations is directly redeemable for device-evaluation modeling: A clear-cut answer that indicates which device performs better is acquired, and this effectively responds directly and in a predictive manner to a clinical question. On the other hand, the causality connected with the second theme above involves several unknowns from the biologic side, but also uncertainty regarding relatively fundamental quantities involved in growth and remodeling studies. Consider, for example, that imaging cannot give us, yet, a good estimate of aneurysm dome wall thickness—a parameter of undisputed importance if a reliable rupture-risk model is to be established. In such a framework, a 10% or 20% uncertainty in the estimation of, say, wall shear stress is less important because it is to be fed through a biologic pathway that presents us with at least similar uncertainties. A similar point can be made regarding the fibrous composition of the wall, endothelial coverage, proteomic activity, and so forth. It is extremely promising that improvements in imaging modalities, in image processing, and in molecular imaging are all making important steps in closing the gap: The information available is becoming more complete and more comprehensive; therefore, the need for accuracy and consistency

has become more pressing and more persistent, as Valen-Sendstad and Steinman¹ correctly assert.

The overall message is very positive and should be iterated here, as is expressed in the “Mind the Gap”¹ article: CFD can provide useful and valuable answers if the right questions are asked and if it is done properly. The neuroradiology-CFD community needs to be reminded that the ease and availability of computational simulations currently do not relax the requirements for rigor, adequate resolution and consistency; instead, they further emphasize these requirements. The general fluid mechanics community has introduced formal “re-minders” of these requirements, as mentioned above, and it is extremely important that medically geared modelers are similarly “re-minded”—the article by Valen-Sendstad and Steinman¹ does that in a most convincing manner.

REFERENCES

1. Valen-Sendstad K, Steinman DA. **Mind the gap: impact of Computational Fluid Dynamics solution strategy on prediction of intracranial aneurysm hemodynamics and rupture status indicators.** *AJNR Am J Neuroradiol* 2014;35:536–43
2. Kallmes DF. **Point: CFD-computational fluid dynamics or confounding factor dissemination.** *AJNR Am J Neuroradiol* 2012;33:395–96
3. Baek H, Jayaraman MV, Richardson PD, et al. **Flow instability and wall shear stress variation in intracranial aneurysms.** *J R Soc Interface* 2010;7:967–88
4. Cebral JR, Mut F, Weir J, et al. **Association of hemodynamic characteristics and cerebral aneurysm rupture.** *AJNR Am J Neuroradiol* 2011;32:264–70
5. Chen HY, Selimovic A, Thompson H, et al. **Investigating the influence of haemodynamic stimuli on intracranial aneurysm inception.** *Ann Biomed Eng* 2013;41:1492–504
6. Watton PN, Selimovic A, Raberger NB, et al. **Modelling evolution and the evolving mechanical environment of saccular cerebral aneurysms.** *Biomech Model Mechanobiol* 2011;10:109–32
7. Cebral JR, Mut F, Raschi M, et al. **Aneurysm rupture following treatment with flow-diverting stents: computational hemodynamics analysis of treatment.** *AJNR Am J Neuroradiol* 2011;32:27–33
8. Larrabide I, Aguilar ML, Morales HG, et al. **Intra-aneurysmal pressure and flow changes induced by flow diverters: relation to aneurysm size and shape.** *AJNR Am J Neuroradiol* 2013;34:816–22
9. Mitsos AP, Kakalis NMP, Ventikos YP, et al. **Haemodynamic simulation of aneurysm coiling in an anatomically accurate computational fluid dynamics model: technical note.** *Neuroradiology* 2008;50:341–47
10. Stuhne GR, Steinman DA. **Finite-element modeling of the hemodynamics of stented aneurysms.** *J Biomech Eng* 2004;126:382–87

Y. Ventikos

Department of Mechanical Engineering
University College London
London, United Kingdom

<http://dx.doi.org/10.3174/ajnr.A3894>

Coiling of Large and Giant Aneurysms: Complications and Long-Term Results of 334 Cases

N. Chalouhi, S. Tjoumakaris, L.F. Gonzalez, A.S. Dumont, R.M. Starke, D. Hasan, C. Wu, S. Singhal, L.A. Moukartzel, R. Rosenwasser, and P. Jabbour



ABSTRACT

BACKGROUND AND PURPOSE: Large and giant intracranial aneurysms are increasingly treated with endovascular techniques. The goal of this study was to retrospectively analyze the complications and long-term results of coiling in large and giant aneurysms (≥ 10 mm) and identify predictors of outcome.

MATERIALS AND METHODS: A total of 334 large or giant aneurysms (≥ 10 mm) were coiled in our institution between 2004 and 2011. Medical charts and imaging studies were reviewed to determine baseline characteristics, procedural complications, and clinical/angiographic outcomes. Aneurysm size was 15 mm on average. Two hundred twenty-five aneurysms were treated with conventional coiling; 88, with stent-assisted coiling; 14, with parent vessel occlusion; and 7, with balloon-assisted coiling.

RESULTS: Complications occurred in 10.5% of patients, with 1 death (0.3%). Aneurysm location and ruptured aneurysms predicted complications. Angiographic follow-up was available for 84% of patients at 25.4 months on average. Recanalization and retreatment rates were 39% and 33%, respectively. Larger aneurysm size, increasing follow-up time, conventional coiling, and aneurysm location predicted both recurrence and retreatment. The annual rebleeding rate was 1.9%. Larger aneurysm size, increasing follow-up time, and aneurysm location predicted new or recurrent hemorrhage. Favorable outcomes occurred in 92% of patients. Larger aneurysm size, poor Hunt and Hess grades, and new or recurrent hemorrhage predicted poor outcome.

CONCLUSIONS: Coiling of large and giant aneurysms has a reasonable safety profile with good clinical outcomes, but aneurysm reopening remains very common. Stent-assisted coiling has lower recurrence, retreatment, and new or recurrent hemorrhage rates with no additional morbidity compared with conventional coiling. Aneurysm size was a major determinant of recanalization, retreatment, new or recurrent hemorrhage, and poor outcome.

ABBREVIATIONS: GOS = Glasgow Outcome Score; PED = Pipeline Embolization Device

Large and giant intracranial aneurysms (≥ 10 mm) have a poor natural history and usually warrant intervention. A recently published study from Japan reported an annual rupture rate of 4.37% for 10- to 24-mm aneurysms and 33.4% for aneurysms larger than 24 mm.¹ Treatment options for large and giant aneurysms include open surgery or endovascular techniques. Surgical treatment is often challenging and can be associated with significant morbidity.^{2,3} Endovascular therapy has emerged as a minimally in-

vasive alternative to open surgery in most neurovascular centers.^{4,5} Available endovascular modalities include endosaccular coiling with or without stent/balloon assistance, endovascular parent vessel deconstruction, Onyx HD-500 (ev3, Irvine, California) embolization, and, recently, flow diversion.⁶ Endosaccular coiling is currently the most commonly used treatment technique for large and giant aneurysms, especially in the setting of subarachnoid hemorrhage. Parent vessel occlusion, when tolerated, is also a reliable and durable treatment typically considered in giant aneurysms.⁴

Despite increasing and widespread use of endovascular techniques, little is known about the morbidity rates, rehemorrhage rates, and long-term angiographic results of coiling in large and giant aneurysms. In addition, predictors of treatment outcome have not been identified. In this study, we analyzed the complications and long-term results of coiling in the largest series of large and giant aneurysms (≥ 10 mm) to date. In addition, a multivariate logistic regression analysis was conducted to identify predictors of complications,

Received April 29, 2013; accepted after revision May 28.

From the Department of Neurosurgery (N.C., S.T., L.F.G., A.S.D., R.M.S., C.W., S.S., L.A.M., R.R., P.J.), Thomas Jefferson University and Jefferson Hospital for Neuroscience, Philadelphia, Pennsylvania; and Department of Neurosurgery (D.H.), University of Iowa, Iowa City, Iowa.

Please address correspondence to Pascal M. Jabbour, MD, Department of Neurosurgery, Division of Neurovascular Surgery and Endovascular Neurosurgery, Thomas Jefferson University Hospital, 901 Walnut St, 3rd Floor, Philadelphia, PA 19107; e-mail: pascal.jabbour@jefferson.edu

<http://dx.doi.org/10.3174/ajnr.A3696>

recurrence, retreatment, new or recurrent hemorrhage, and clinical outcome.

MATERIALS AND METHODS

Study Design, Participants, and Setting

The university institutional review board approved the study protocol. We searched our prospectively maintained data base for all patients with large or giant aneurysms (>10 mm) who were treated with primary coil embolization in our institution between May 2004 and May 2011. A total of 324 consecutive patients with 334 aneurysms met the study criteria and constituted our study population. During the same time, 139 large or giant aneurysms were clipped at our institution; these patients were not included in the analysis. The decision to treat aneurysms with endovascular therapy was based on patient preferences, aneurysm morphology, aneurysm–parent vessel relationship, and comorbidities that rendered a patient a poor surgical candidate.

Medical charts and imaging studies were reviewed to determine patient age, sex, aneurysm size, aneurysm location, aneurysm morphology, Hunt and Hess grade, procedural specifics, procedural morbidity and mortality, immediate and follow-up angiographic results, need for retreatment, morbidity associated with recoiling, angiographic outcome of recoiling, new or recurrent hemorrhage, and clinical outcome. Treatment failure was defined as an inability to place coils into an aneurysm. Procedure-related complications (ischemia, hemorrhage, dissections, new cranial nerve deficits) were reported regardless of their clinical significance. Thromboembolic complications were diagnosed intraoperatively on digital subtraction angiography, clinically as new deficits or change in the level of consciousness, or on CT/MR imaging (new infarcts) performed in cases of sudden neurologic compromise. Ischemic/thromboembolic complications were also recorded through follow-up. Radiographic follow-up (DSA or MR) was scheduled at 6 months, 1 year, 2 years, and 5 years after endovascular procedures. Initial aneurysm occlusion was determined as a percentage occlusion rate. Initial and follow-up angiographic images were compared to determine the rate of aneurysm recanalization. Any aneurysm that displayed a recurrence of $\geq 5\%$ on follow-up angiography was considered recurrent. Clinical outcomes were retrospectively collected at discharge and at follow-up from follow-up notes of the attending physician and classified by using the Glasgow Outcome Score (GOS) as follows: I, deceased; II, vegetative state; III, severely disabled; IV, moderately disabled; and V, mildly or not disabled.

Aneurysm Coiling

The decision to treat aneurysms with endovascular therapy was based on patient preferences, aneurysm morphology, aneurysm–parent vessel relationship, and comorbidities that rendered a patient a poor surgical candidate. In aneurysms with a favorable geometry, the aim of treatment was selective and complete coiling of the aneurysm with preservation of the patency of the parent artery. Depending on operator preferences, wide-neck aneurysms were coiled either with stent assistance by using Neuroform (Stryker Neurovascular, Fremont, California) and Enterprise (Codman & Shurtleff, Raynham, Massachusetts) stents or with balloon assistance by using the HyperGlide or HyperForm balloon (ev3). For unruptured aneurysms, endosaccular coiling was performed with an initial 100 U/Kg of heparin bolus and mainte-

nance of activated clotting time of 2 times the patient's baseline intraoperatively. Coils (bare platinum) were placed until satisfactory aneurysm obliteration was achieved and/or placement of additional coils was not possible. Patients in whom the use of a stent was anticipated were pretreated with 81 mg of aspirin and 75 mg of clopidogrel 10 days before the procedure. For stent-assisted procedures performed in the setting of a subarachnoid hemorrhage, patients were loaded with 600 mg of clopidogrel intraprocedurally and a 50-U/kg heparin bolus after deployment of the first coil. Patients were then maintained on daily doses of 75 mg of clopidogrel and 81 mg of aspirin for 2 months, followed by aspirin, 81 mg daily, indefinitely. Because several operators performed the procedures, the protocols and techniques may have varied to some extent.

Parent Vessel Occlusion

Parent vessel occlusion was typically considered in giant and/or fusiform aneurysms of the internal carotid artery. Patient tolerance for permanent vessel occlusion was first assessed with a balloon test occlusion. Briefly, a balloon was advanced over a microguidewire and slowly inflated at the planned occlusion site. Complete balloon occlusion of the parent vessel was verified by proximal contrast injection. The awake patient was then monitored for 30 minutes with continuous clinical examination. The test was performed under normotensive parameters for the first 15 minutes followed by a hypotensive challenge for the remaining 15 minutes. The extent of intracranial collateral circulation was concurrently examined by angiography. The balloon test occlusion was "passed" by patients who remained neurologically intact during the test. The balloon was kept inflated, and flow arrest was confirmed angiographically. Vessel occlusion was then achieved with coils alone or with a combination of Onyx and coils. In the latter case, a few coils were initially deployed in the vessel through the inflated balloon or a separate microcatheter to create a framework for subsequent Onyx injection. Patients were closely monitored in the neurointensive care unit. All patients, including those who had experienced a subarachnoid hemorrhage, were prescribed maintenance antiplatelet therapy (usually daily aspirin).

Statistical Analysis

Data are presented as mean and range for continuous variables and as frequency for categorical variables. Analysis was carried out by using an unpaired *t* test, χ^2 test, Fisher exact test, and analysis of variance as appropriate. Univariate analysis was used to test covariates predictive of dependent variables: procedural complications, aneurysm recanalization, aneurysm retreatment, new or recurrent hemorrhage, and patient outcome (GOS IV-V versus I-II-III). Interaction and confounding were assessed through stratification and relevant expansion covariates. Factors predictive in univariate analysis ($P < .15$)⁷ were entered into a multivariate logistic regression analysis. *P* values $\leq .05$ were considered statistically significant. Statistical analysis was performed with STATA 10.0 (StataCorp, College Station, Texas).

RESULTS

A total of 324 patients with 334 large or giant aneurysms underwent coiling at our institution. Mean age was 57 years (range, 15–89 years). Seventy-seven percent of patients ($n = 250$) were

Table 1: Location of treated aneurysms and respective complication and recurrence rates

Location	No. of Aneurysms (%)	Complications (%)	Recurrence (%)	Retreatment (%)
Paraclinoid	63 (18.9)	9 (14.3)	26/53 (49)	22/53 (41.5)
Basilar artery	53 (15.9)	4 (7.5)	16/43 (37.2)	15/43 (34.9)
Posterior communicating artery	48 (14.4)	6 (12.5)	11/33 (33.3)	10/33 (30.3)
Carotid ophthalmic	47 (14.1)	3 (6.4)	12/39 (30.8)	10/39 (25.6)
Anterior communicating artery	34 (10.2)	5 (14.7)	6/25 (24)	5/25 (20)
Carotid cavernous	27 (8.0)	4 (14.8)	9/21 (42.9)	6/21 (28.6)
Middle cerebral artery	25 (7.5)	2 (8)	8/16 (50)	5/16 (31.3)
Carotid terminus	17 (5.1)	0	5/11 (45.5)	4/11 (36.4)
Vertebral artery	13 (3.9)	1 (7.7)	5/12 (41.7)	5/12 (41.7)
Anterior cerebral artery	6 (1.8)	0	4/6 (66.7)	4/6 (66.7)
Posterior cerebral artery	1 (0.3)	0	0/1	0/1
Total	334	34	102	85

female. Aneurysm size was 15 mm on average (range, 10–45 mm). Of 334 aneurysms, 216 (64%) were between 10 and 14 mm, 86 (26%) were between 15 and 24 mm, and 32 (10%) were ≥ 25 mm. Aneurysm locations are summarized in Table 1. Eighty percent of aneurysms ($n = 268$) were located in the anterior circulation (including posterior communicating artery aneurysms). Fourteen aneurysms (4.1%) had a fusiform morphology. Hunt and Hess grades were zero in 175 (54%) patients, I in 32 (10%) patients, II in 16 (4.9%) patients, III in 63 (19.4%) patients, IV in 34 (10.5%) patients, and V in 4 (1.2%) patients.

Initial Treatment

Of 334 aneurysms, 14 (2.4%) were initially treated with parent vessel occlusion, and 320 (97.6%), with endosaccular coiling. Parent vessel occlusion was performed with coils alone in 5 patients and with a combination of Onyx and coils in 9 patients. Among the other 320 aneurysms, 7 (2.2%) were treated with balloon-assisted coiling; 88 (27.5%), with stent-assisted coiling; and 225 (70.3%), with unassisted coiling. Three patients (0.9%) had an unsuccessful procedure and underwent surgical clipping. Seven patients were stent-coiled in the acute setting of subarachnoid hemorrhage.

Complications related to the initial procedure occurred in 34 (10.5%) patients, resulting in 1 death (0.3%). Seventeen patients died during initial hospitalization from causes unrelated to aneurysm embolization. Complications were as follows: 31 (9.6%) thromboembolic or ischemic events (including 3 clinically silent infarcts), 2 (0.6%) intraprocedural aneurysm ruptures, and 1 (0.3%) cranial nerve palsy. Specifically, procedural complications occurred in 22 (9.8%) patients treated with unassisted coiling, 10 (11.4%) patients treated with stent-assisted coiling, and 2 (14.3%) patients treated with parent vessel occlusion ($P = .7$). The complication rate was 7.4% ($n = 13$) for patients with unruptured aneurysms and 14% ($n = 21$) for those with ruptured aneurysms ($P = .05$). Complication rates were 10.2% ($n = 22$) for aneurysms between 10 and 14 mm, 10.4% ($n = 9$) for aneurysms between 15 and 24 mm, and 9.4% ($n = 3$) for aneurysms of ≥ 25 mm ($P = .8$).

Table 1 summarizes complication rates per aneurysm location. Patients who were stented in the acute setting of hemorrhage did not have any hemorrhagic complications. In multivariate analysis, carotid cavernous–paraclinoid–anterior communicating artery aneurysms (OR = 2.1; 95% CI, 1.1–3.9; $P = .02$) and

Table 2: Complications and angiographic outcomes per aneurysm size

	10–14 mm	15–24 mm	≥ 25 mm
Complications	22/216 (10.2%)	9/86 (10.4%)	3/32 (9.4%)
Recurrence	62/177 (35%)	29/62 (46.8%)	11/21 (52%)
Retreatment	52/177 (29.3%)	23/62 (37.1%)	10/21 (47.6%)

ruptured aneurysms (OR = 2.4; 95% CI, 1.1–4.3; $P = .04$) were predictive of complications. There was also a trend toward anterior circulation-versus-posterior circulation aneurysms (OR = 2; 95% CI, 0.9–5.0; $P = .09$) to predict complications. The type of treatment and aneurysm size were not predictive factors.

Immediate occlusion ($\geq 95\%$) was achieved in 290 (87.6%) aneurysms. Excluding the 3 patients with a failed procedure and the 18 patients who died during initial hospitalization, angiographic follow-up was available for 85% of patients (260/303) at a mean of 25.4 months. Of 260 aneurysms, 102 (39%) showed recanalization at follow-up and 85 (33%) required further treatment. Initial retreatment consisted of additional coiling in 51 aneurysms, balloon-assisted coiling in 2, stent-assisted coiling in 19, Onyx HD 500 embolization in 2, Pipeline Embolization Device (PED) therapy in 2, parent vessel occlusion in 3, and microsurgical clipping in 6. Recurrence and retreatment rates (Table 2) were, respectively, 35% (62/177) and 29.3% (52/177) for aneurysms between 10 and 14 mm, 46.8% (29/62) and 37.1% (23/62) for aneurysms between 15 and 24 mm, and 52% (11/21) and 47.6% (10/21) for aneurysms ≥ 25 mm ($P = .005$, $P = .003$). Recurrence and retreatment rates were, respectively, 44% (72/164) and 37.2% (61/164) for unassisted coiling, 32.5% (26/80) and 26% (21/80) for stent-assisted coiling, 40% (2/5) and 40% (2/5) for balloon-assisted coiling, and 18.2% (2/11) and 9.1% (1/11) for parent vessel occlusion ($P = .03$, $P = .02$). Table 1 summarizes recanalization and recurrence rates per aneurysm location. In multivariate analysis, larger aneurysm size, increasing follow-up time, unassisted coiling and balloon-assisted coiling versus stent-assisted coiling or parent vessel occlusion, and carotid cavernous–paraclinoid–anterior cerebral artery–vertebral artery–carotid terminus–middle cerebral artery aneurysms were independent predictors of both recurrence and retreatment (Table 3).

At discharge, 89% ($n = 286$) of patients attained a favorable outcome (GOS IV–V) (Table 4). Specifically, a favorable outcome was noted in 98% ($n = 172$) of patients with unruptured aneurysms and 77% ($n = 114$) of patients with ruptured aneurysms.

Table 3: Predictors of recurrence and retreatment

	Odds Ratio	95% CI	P Value
Procedural complications			
Ruptured aneurysms	2.4	1.1–4.3	.04 ^a
Aneurysm location	2.1	1.1–3.9	.02 ^a
Anterior circulation aneurysms	2.0	0.9–5.0	.09
Recurrence			
Aneurysm size	1.07	1.02–1.14	.006 ^a
Follow-up time	1.04	1.02–1.06	<.001 ^a
Unassisted coiling and balloon remodeling	2	1.1–3.3	.02 ^a
Aneurysm location	1.9	1.1–3.4	.02 ^a
Retreatment			
Aneurysm size	1.08	1.02–1.14	.003 ^a
Follow-up time	1.02	1.02–1.06	.002 ^a
Unassisted coiling and balloon remodeling	2.5	1.1–3.3	.005 ^a
Aneurysm location	2.02	1.1–3.4	.02 ^a
New or recurrent hemorrhage			
Aneurysm size	1.1	1.0–1.2	.04 ^a
Follow-up time	1.03	1.0–1.1	.05 ^a
Aneurysm location	2.5	1.5–7	.01 ^a
Clinical outcome			
Aneurysm size	0.89	0.82–0.97	.01 ^a
Hunt and Hess grades	0.36	0.24–0.55	<.001 ^a
New or recurrent hemorrhage	0.04	0.005–0.28	.002 ^a

^a Statistically significant values. Factors tested as predictors of complications: age, sex, embolization, initial aneurysm occlusion, and date of treatment. Factors tested as predictors of recurrence, retreatment, and new or recurrent hemorrhage: age, sex, aneurysm size, location, ruptured aneurysm status, Hunt and Hess grades, type of embolization, initial aneurysm occlusion, date of treatment, procedural complications, GOS at discharge, and follow-up time. Factors tested as predictors of clinical outcome: age, sex, aneurysm size, location, ruptured aneurysm status, Hunt and Hess grades, type of embolization, initial aneurysm occlusion, date of treatment, procedural complications, GOS at discharge, follow-up time, recurrence, retreatment, and new or recurrent hemorrhage.

Table 4: Clinical outcome of treated patients

GOS	Discharge (%)	Follow-Up (%)
I, Death	17 (5.3)	7 (2.7)
II, Vegetative state	1 (0.3)	1 (0.4)
III, Severe disability	18 (5.6)	12 (4.7)
IV, Moderate disability	21 (6.5)	17 (6.6)
V, Mild/no disability	265 (82.3)	219 (85.6)

Aneurysm Recoiling: Morbidity and Angiographic Outcome

Angiographic follow-up was available for 55 of the 75 aneurysms that were recoiled (including stent/balloon-assisted coiling and parent vessel occlusion). Among these 55 aneurysms, 30 (54.5%) showed another recurrence at follow-up. Specifically, a recurrence was noted in 37.5% (6/16) of aneurysms retreated with stent-assisted coiling versus 61.5% (24/39) of those recoiled without stent assistance ($P = .1$).

Of the 30 aneurysms that showed a second recurrence after coiling, 24 (43.6%) required retreatment, including recoiling in 19 aneurysms. Angiographic follow-up was available for 15 of these 19 aneurysms, and a third recurrence was noted in 8 of these 15 aneurysms (53.3%), requiring further treatment in 6 (40%).

Complications were noted in 5 of the 75 patients (6.6%) whose aneurysms required further coiling. The rate of complications per recoiling procedure was 5% (5/100).

New or Recurrent Hemorrhage and Long-Term Clinical Outcome

Eleven patients (4.2%, $n = 256$) had a new or recurrent subarachnoid hemorrhage at a median of 12 months (range, 1 week to 7 years) following successful aneurysm treatment. The annual rate

of new or recurrent hemorrhage was 1.9% (11 hemorrhages in 564 years of follow-up). Seven of these patients had aneurysm occlusion of $\geq 95\%$ after initial embolization. Four hemorrhages occurred within 2 months of treatment. Five of these patients died, and 3 remained severely disabled at follow-up. Mean aneurysm size was 17 mm in this group. Ten patients had been initially treated with conventional coiling, and only 1, with stent-assisted coiling. Thus, the rate of new or recurrent hemorrhage was 6.0% for conventional coiling versus 1.3% for stent-assisted coiling ($P = .1$). In multivariate analysis, larger aneurysm size (> 15 mm) (OR = 1.1; 95% CI, 1.0–1.2; $P = .04$), increasing follow-up time (OR = 1.03; 95% CI, 1.0–1.1; $P = .05$), and basilar tip–anterior communicating–posterior communicating aneurysm locations (OR = 2.5; 95% CI, 1.5–7; $P = .01$) were independent predictors of new or recurrent hemorrhage. The type of initial aneurysm treatment fell short of statistical significance.

Clinical follow-up was available for 85% of patients ($n = 256$) at a mean of 26.3 months, excluding patients with a failed procedure and those who died during the initial hospitalization. A favorable outcome (GOS IV–V) was attained by 92% ($n = 236$) of patients at follow-up. Specifically, 87% (93/107) of patients with ruptured aneurysms and 96% (143/149) of patients with unruptured aneurysms achieved a favorable outcome (GOS IV–V). In multivariate analysis, increasing aneurysm size (OR = 0.89; 95% CI, 0.82–0.97; $P = .01$), poor Hunt and Hess grades (OR = 0.36; 95% CI, 0.24–0.55; $P < .001$), and new or recurrent hemorrhage (OR = 0.04; 95% CI, 0.005–0.28; $P = .002$) were negative independent predictors of favorable outcome (GOS IV–V).

DISCUSSION

In this study, we have reviewed our experience with coil embolization of large and giant aneurysms (≥ 10 mm) and identified several independent predictors of treatment outcome. This report may serve as a reference for comparison with other treatment options for this category of aneurysm, namely flow diversion and surgical clipping. Our study has also afforded an opportunity to compare different endovascular techniques in terms of complications and angiographic outcome.

Coil embolization remains the most commonly used endovascular technique for securing large and giant aneurysms. Complications occurred in 10.5% of patients in our series, but many were clinically silent or minor events. The procedural mortality rate was minimal (0.3%), and the rate of favorable outcome at clinical follow-up (92%) was high. Unfortunately, to our knowledge, there are no reports in the literature pertaining specifically to large and giant aneurysms (> 10 mm) with which to compare

our findings. In a systematic review of giant aneurysms (≥ 25 mm) treated with conventional endovascular approaches, the rates of morbidity and mortality were 17% and 8%, respectively.⁸ Gruber et al⁹ treated 31 very large and giant aneurysms (> 20 mm) with endosaccular coiling with a 13.3% procedure-related morbidity rate and a 6.7% procedure-related mortality rate and reported favorable outcomes in 73.3% of patients. Likewise, Sluzewski et al¹⁰ achieved a good clinical outcome in nearly 80% of patients with very large and giant aneurysms (> 20 mm) treated with coiling. The higher rate of favorable outcomes in our study likely reflects the inclusion of smaller aneurysms (10–20 mm) in the analysis. In fact, increasing aneurysm size was independently predictive of poor outcome, recanalization, retreatment, and new or recurrent hemorrhage in multivariate analysis. Overall, coiling of large and giant aneurysms (≥ 10 mm) in our experience was associated with a reasonable safety profile and good clinical outcomes. Patients with larger aneurysms, however, are at higher risk of poor outcome.

The present study demonstrates high rates of recurrence (39%) and retreatment (33%) for large and giant aneurysms treated with coiling. Moreover, the risk of aneurysm recurrence was 54.5% after the first recoiling and 53.3% after the second recoiling. Aneurysm reopening remains, therefore, the major shortcoming of coiling (and repeat coiling) in large and giant aneurysms. This has been attributed to thrombus resolution, coil migration into the thrombus mass, and suboptimal packing of these aneurysms.¹⁰ Our results are remarkably similar to those of Murayama et al,¹¹ who reported, in 2003, their 11-year experience with aneurysm embolization. The recanalization rate was 35.3% for large aneurysms in their study and 59.1% for giant aneurysms. The lack of improvement relative to this prior series published 10 years ago suggests that further improvement in occlusion/recanalization rates for large aneurysms may well require adjunctive therapy. The fact that stent-assisted coiling was associated with lower recurrence rates in multivariate analysis compared with conventional coiling (with or without balloon assistance) is a crucial finding of our study. In addition, the risk of a second aneurysm recurrence was lower when recoiling was performed with-versus-without stent assistance (37.5% versus 61.5%). Moreover, there was a lower incidence of new or recurrent hemorrhage in patients treated with stent-assisted coiling versus conventional coiling (1.1% versus 4.7%).

Several reasons may account for the improved durability of treatment with self-expanding stents, including denser aneurysm packing with increased neck coverage, flow diversion, parent vessel straightening, and fibroelastic tissue formation along the neck of the aneurysm.^{12–16} Most important, the lower recurrence and rebleeding rates with stent-assisted techniques did not occur at the expense of an increased rate of complications. Previously, Piontin et al¹⁷ reported permanent neurologic deficit and mortality rates as high as 7.4% and 4.6%, respectively, with stent-assisted coiling compared with 3.8% and 1.2% with conventional coiling. Our study emphasizes the safety and efficacy of stent-assisted coiling and suggests that it may be the preferred treatment technique over conventional coiling for large and giant aneurysms.

The annual rebleeding rate was 1.9% in our study, exceeding the rate reported in the endovascular arm of the International

Subarachnoid Aneurysm Trial.¹⁸ This is expected given that 92% of coiled aneurysms in this trial were ≤ 10 mm. Rebleeding occurred both early and late after initial coiling and was independently predictive of poor clinical outcome. Larger aneurysms (> 15 mm) and basilar tip, anterior communicating, and posterior communicating aneurysms were strong predictors of rebleeding. Thus, patients with these risk factors should be very carefully followed and retreated, preferentially with stent-assisted techniques, in the event of aneurysm reopening to prevent rehemorrhage.

Recoiling in the present study was associated with a relatively low complication rate (5%) and no mortality. Previous studies have reported similarly low morbidity rates with recoiling. A multicenter study of 100 aneurysms requiring additional coiling because of an enlarging remnant and subtotal occlusion reported minor permanent neurologic deficits in only 3% of cases.¹⁹ Likewise, Kang et al²⁰ and Slob et al²¹ observed no complications during repeat embolization of recurrent aneurysms and suggested that procedural morbidity for retreatment may be lower than that for initial coiling.

The rate of complications for unruptured large and giant aneurysms in our study was low (7.4%), and excellent outcomes were achieved in this group. The best endovascular technique for these aneurysms (ie, coiling versus flow diversion), however, is not clear. In a small series of 42 patients, Lanzino et al²² reported similar rates of morbidity and a higher rate of complete angiographic obliteration with the PED (mean aneurysm size, 14.9 mm) compared with standard endovascular techniques (mean aneurysm size, 13.9 mm). The authors concluded that careful long-term follow-up was important to definitively validate flow diversion as a superior treatment for proximal internal carotid artery aneurysms. Elsewhere, flow diversion was associated with significant procedural risks. A recent systematic review on unruptured aneurysms treated with endovascular techniques found that flow diversion was associated with significantly higher risks compared with other endovascular techniques.²³ The risk of major stroke or neurologic death was 5.6% in the Pipeline for Uncoilable or Failed Aneurysms trial²⁴ (mean aneurysm size, 14.6 mm) and 8.5% (including 4 fatal postprocedural hemorrhages) in a recent multicenter study from 7 American neurosurgical centers (proportion of aneurysms larger than 7 mm, 83%).²⁵ In the Canadian experience (mean aneurysm size, 19 mm), the overall morbidity and mortality rate associated with PED treatment was 10.7% (6.3% mortality, 4.4% morbidity).²⁶

These data suggest that the risk associated with flow diversion is not insignificant and that further study is needed to elucidate the best treatment option for unruptured large and giant aneurysms. On the other hand, for patients with acutely ruptured aneurysms, flow diversion is barely an option and almost all aneurysms are either coiled or clipped. McAuliffe and Wenderoth²⁷ treated 11 patients with recently ruptured aneurysms by using the PED and reported 2 deaths during the acute illness due to aneurysm rebleeding (18%). The authors recommended that the device be used as a coil scaffold rather than a flow diverter. In the posterior circulation as well, flow diversion is generally used very cautiously because it is associated with significant morbidity and high rates of perforator infarcts.^{25,28,29} Conversely, in the present

study, there was a trend toward lower complication rates with coiling in the posterior circulation. Thus, coiling remains the preferred option for ruptured aneurysms and posterior circulation aneurysms.

Parent vessel occlusion is widely used in the management of giant intracranial aneurysms. The complication rate in the present series (14.3%) was within the range reported in the literature,^{16,30-33} and aneurysm reopening was somewhat uncommon. The advantage of the technique is that it excludes the aneurysm definitely from the circulation and may not require follow-up imaging.⁴ In contrast to flow diverters and endosaccular coiling, there is practically no risk of delayed aneurysm rupture after parent vessel occlusion. For some authors, parent vessel occlusion is the safest and most effective treatment for large and giant aneurysms and remains the first-line option in this setting.³⁴ The main disadvantage of parent vessel occlusion is the risk of development of postoperative stroke. Therefore, it is important to perform a balloon test occlusion to determine patient tolerance for permanent arterial occlusion because the incidence of postoperative stroke is substantially higher without previous tolerance testing.³⁵⁻³⁷ Also, in the setting of subarachnoid hemorrhage, parent vessel occlusion is generally avoided due to potential aggravation of ischemic complications of vasospasm.

This was a retrospective review of a single-center experience with coiling of large and giant aneurysms. There was no randomization of the different subgroups of the study. Comparison with other studies reporting on flow diversion or surgical clipping remains limited by inherent differences in methodology and design. In the future, it would be interesting to compare conventional endovascular techniques with flow diversion or surgical clipping to determine the best technique in this setting.

CONCLUSIONS

In this study, coiling of large and giant aneurysms was associated with a reasonable safety profile and good clinical outcome. Aneurysm reopening, however, was very common after endosaccular coiling. Larger aneurysm size was independently predictive of recanalization, retreatment, new or recurrent hemorrhage, and poor outcome. Stent-assisted coiling was associated with lower recurrence, retreatment, and new or recurrent hemorrhage rates with no additional morbidity compared with conventional coiling. Thus, stent-assisted coiling should probably be considered the preferred treatment option over conventional coiling for large and giant aneurysms. The annual rebleeding rate was 1.9%, and larger aneurysms (>15 mm) and basilar tip, anterior communicating artery, and posterior communicating artery aneurysms were strong predictive factors. The major determinants of clinical outcome were aneurysm size, Hunt and Hess grades, and new or recurrent hemorrhage.

Disclosures: Stavropoula Tjounmakaris—UNRELATED: Consultancy: Stryker. Aaron S. Dumont—UNRELATED: Consultancy: ev3. Pascal Jabbour—UNRELATED: Consultancy: ev3, CNV.

REFERENCES

1. Morita A, Kirino T, Hashi K, et al. **The natural course of unruptured cerebral aneurysms in a Japanese cohort.** *N Engl J Med* 2012;366:2474–82
2. Sundt TM Jr, Piegras DG. **Surgical approach to giant intracranial aneurysms: operative experience with 80 cases.** *J Neurosurg* 1979;51:731–42
3. Kalani MY, Zabramski JM, Hu YC, et al. **Extracranial-intracranial bypass and vessel occlusion for the treatment of unclippable giant middle cerebral artery aneurysms.** *Neurosurgery* 2013;72:428–35, discussion 435–36
4. van Rooij WJ, Sluzewski M. **Endovascular treatment of large and giant aneurysms.** *AJNR Am J Neuroradiol* 2009;30:12–18
5. Roy D, Milot G, Raymond J. **Endovascular treatment of unruptured aneurysms.** *Stroke* 2001;32:1998–2004
6. Chalouhi N, Jabbour P, Singhal S, et al. **Stent-assisted coiling of intracranial aneurysms: predictors of complications, recanalization, and outcome in 508 cases.** *Stroke* 2013;44:1348–53
7. Altman DG. *Practical Statistics for Medical Research.* Boca Raton, Florida: Chapman & Hall/CRC; 1999
8. Parkinson RJ, Eddleman CS, Batjer HH, et al. **Giant intracranial aneurysms: endovascular challenges.** *Neurosurgery* 2008;62(6 suppl 3):1336–45
9. Gruber A, Killer M, Bavinzski G, et al. **Clinical and angiographic results of endosaccular coiling treatment of giant and very large intracranial aneurysms: a 7-year, single-center experience.** *Neurosurgery* 1999;45:793–803, discussion 803–04
10. Sluzewski M, Menovsky T, van Rooij WJ, et al. **Coiling of very large or giant cerebral aneurysms: long-term clinical and serial angiographic results.** *AJNR Am J Neuroradiol* 2003;24:257–62
11. Murayama Y, Nien YL, Duckwiler G, et al. **Guglielmi detachable coil embolization of cerebral aneurysms: 11 years' experience.** *J Neurosurg* 2003;98:959–66
12. Chalouhi N, Dumont AS, Hasan D, et al. **Is packing density important in stent-assisted coiling?** *Neurosurgery* 2012;71:381–86, discussion 386–87
13. Chalouhi N, Drueding R, Starke RM, et al. **In-stent stenosis after stent-assisted coiling: incidence, predictors and clinical outcomes of 435 cases.** *Neurosurgery* 2013;72:390–96
14. Chalouhi N, Jabbour P, Gonzalez LF, et al. **Safety and efficacy of endovascular treatment of basilar tip aneurysms by coiling with and without stent assistance: a review of 235 cases.** *Neurosurgery* 2012;71:785–94
15. Jahshan S, Abla AA, Natarajan SK, et al. **Results of stent-assisted vs non-stent-assisted endovascular therapies in 489 cerebral aneurysms: single-center experience.** *Neurosurgery* 2013;72:232–39
16. Chalouhi N, Starke RM, Koltz MT, et al. **Stent-assisted coiling versus balloon remodeling of wide-neck aneurysms: comparison of angiographic outcomes.** *AJNR Am J Neuroradiol* 2013;34:1987–92
17. Piotin M, Blanc R, Spelle L, et al. **Stent-assisted coiling of intracranial aneurysms: clinical and angiographic results in 216 consecutive aneurysms.** *Stroke* 2010;41:110–15
18. Molyneux AJ, Kerr RS, Birks J, et al. **Risk of recurrent subarachnoid haemorrhage, death, or dependence and standardised mortality ratios after clipping or coiling of an intracranial aneurysm in the International Subarachnoid Aneurysm Trial (ISAT): long-term follow-up.** *Lancet Neurol* 2009;8:427–33
19. Renowden SA, Koumellis P, Benes V, et al. **Retreatment of previously embolized cerebral aneurysms: the risk of further coil embolization does not negate the advantage of the initial embolization.** *AJNR Am J Neuroradiol* 2008;29:1401–04
20. Kang HS, Han MH, Kwon BJ, et al. **Repeat endovascular treatment in post-embolization recurrent intracranial aneurysms.** *Neurosurgery* 2006;58:60–70, discussion 60–70
21. Slob MJ, Sluzewski M, van Rooij WJ, et al. **Additional coiling of previously coiled cerebral aneurysms: clinical and angiographic results.** *AJNR Am J Neuroradiol* 2004;25:1373–76
22. Lanzino G, Crobeddu E, Cloft HJ, et al. **Efficacy and safety of flow diversion for paraclinoid aneurysms: a matched-pair analysis compared with standard endovascular approaches.** *AJNR Am J Neuroradiol* 2012;33:2158–61
23. Naggara ON, Lecler A, Oppenheim C, et al. **Endovascular treatment**

- of intracranial unruptured aneurysms: a systematic review of the literature on safety with emphasis on subgroup analyses. *Radiology* 2012;263:828–35
24. Becske T, Kallmes DF, Saatci I, et al. Pipeline for uncoilable or failed aneurysms: results from a multicenter clinical trial. *Radiology* 2013;267:858–68
 25. Kan P, Siddiqui AH, Veznedaroglu E, et al. Early postmarket results after treatment of intracranial aneurysms with the Pipeline embolization device: a U.S. multicenter experience. *Neurosurgery* 2012;71:1080–88, discussion 1087–88
 26. O’Kelly CJ, Spears J, Chow M, et al. Canadian experience with the Pipeline embolization device for repair of unruptured intracranial aneurysms. *AJNR Am J Neuroradiol* 2013;34:381–87
 27. McAuliffe W, Wenderoth JD. Immediate and midterm results following treatment of recently ruptured intracranial aneurysms with the Pipeline embolization device. *AJNR Am J Neuroradiol* 2012;33:487–93
 28. Phillips TJ, Wenderoth JD, Phatouros CC, et al. Safety of the Pipeline embolization device in treatment of posterior circulation aneurysms. *AJNR Am J Neuroradiol* 2012;33:1225–31
 29. Chalouhi N, Tjoumakaris S, Dumont AS, et al. Treatment of posterior circulation aneurysms with the Pipeline embolization device. *Neurosurgery* 2013;72:883–89
 30. Barr JD, Lemley TJ. Endovascular arterial occlusion accomplished using microcoils deployed with and without proximal flow arrest: results in 19 patients. *AJNR Am J Neuroradiol* 1999;20:1452–56
 31. Graves VB, Perl J 2nd, Strother CM, et al. Endovascular occlusion of the carotid or vertebral artery with temporary proximal flow arrest and microcoils: clinical results. *AJNR Am J Neuroradiol* 1997;18:1201–06
 32. Larson JJ, Tew JM Jr, Tomsick TA, et al. Treatment of aneurysms of the internal carotid artery by intravascular balloon occlusion: long-term follow-up of 58 patients. *Neurosurgery* 1995;36:26–30, discussion 30
 33. Lewis AI, Tomsick TA, Tew JM Jr. Management of 100 consecutive direct carotid-cavernous fistulas: results of treatment with detachable balloons. *Neurosurgery* 1995;36:239–44, discussion 244–45
 34. van Rooij WJ, Sluzewski M, van der Laak C. Flow diverters for unruptured internal carotid artery aneurysms: dangerous and not yet an alternative for conventional endovascular techniques. *AJNR Am J Neuroradiol* 2013;34:3–4
 35. Serbinenko FA. Balloon catheterization and occlusion of major cerebral vessels. *J Neurosurg* 1974;41:125–45
 36. American Society of Interventional and Therapeutic Neuroradiology. Carotid artery balloon test occlusion. *AJNR Am J Neuroradiol* 2001;22(8 suppl):S8–9
 37. Sorteberg A, Bakke SJ, Boysen M, et al. Angiographic balloon test occlusion and therapeutic sacrifice of major arteries to the brain. *Neurosurgery* 2008;63:651–60, discussion 660–61

Socioeconomic Disparities in the Utilization of Mechanical Thrombectomy for Acute Ischemic Stroke in US Hospitals

W. Brinjikji, A.A. Rabinstein, J.S. McDonald, and H.J. Cloft

ABSTRACT

BACKGROUND AND PURPOSE: Previous studies have demonstrated that socioeconomic disparities in the treatment of cerebrovascular diseases exist. We studied a large administrative data base to study disparities in the utilization of mechanical thrombectomy for acute ischemic stroke.

MATERIALS AND METHODS: With the utilization of the Perspective data base, we studied disparities in mechanical thrombectomy utilization between patient race and insurance status in 1) all patients presenting with acute ischemic stroke and 2) patients presenting with acute ischemic stroke at centers that performed mechanical thrombectomy. We examined utilization rates of mechanical thrombectomy by race/ethnicity (white, black, and Hispanic) and insurance status (Medicare, Medicaid, self-pay, and private). Multivariate logistic regression analysis adjusting for potential confounding variables was performed to study the association between race/insurance status and mechanical thrombectomy utilization.

RESULTS: The overall mechanical thrombectomy utilization rate was 0.15% (371/249,336); utilization rate at centers that performed mechanical thrombectomy was 1.0% (371/35,376). In the sample of all patients with acute ischemic stroke, multivariate logistic regression analysis demonstrated that uninsured patients had significantly lower odds of mechanical thrombectomy utilization compared with privately insured patients (OR = 0.52, 95% CI = 0.25–0.95, $P = .03$), as did Medicare patients (OR = 0.53, 95% CI = 0.41–0.70, $P < .0001$). Blacks had significantly lower odds of mechanical thrombectomy utilization compared with whites (OR = 0.35, 95% CI = 0.23–0.51, $P < .0001$). When considering only patients treated at centers performing mechanical thrombectomy, multivariate logistic regression analysis demonstrated that insurance was not associated with significant disparities in mechanical thrombectomy utilization; however, black patients had significantly lower odds of mechanical thrombectomy utilization compared with whites (OR = 0.41, 95% CI = 0.27–0.60, $P < .0001$).

CONCLUSIONS: Significant socioeconomic disparities exist in the utilization of mechanical thrombectomy in the United States.

Endovascular clot retrieval has become an increasingly utilized treatment for a select group of patients with acute ischemic stroke.¹ Previous studies have demonstrated that significant socioeconomic disparities exist in the utilization of treatments such as tPA for acute ischemic stroke.^{2,3} With the use of the Perspective data base, we sought to determine if any socioeconomic disparities exist in the utilization of mechanical thrombectomy for the treatment of acute ischemic stroke.

MATERIALS AND METHODS

Patient Population

The Perspective data base is a voluntary, fee-supported collection of data developed by Premier, Inc (Charlotte, North Carolina), to

assess quality and resource utilization. As of 2011, the Perspective data base consisted of approximately 15% of hospitalizations nationwide and represented more than 600 US hospitals. Detailed information of a patient's hospitalization, including patient demographics, hospital information, diagnoses, procedures, discharge status, payer, and all billed items, are recorded.

Patients who presented with acute ischemic stroke (ICD-9-CM diagnostic codes 433.x1 and 434.x1) from November 2005 through December 2011 were identified from the Perspective data base. Patients were only included if the stroke code was listed as the primary hospitalization diagnosis to avoid including patients with a history of stroke. Patients were stratified into 4 groups on the basis of insurance status: 1) uninsured, 2) Medicaid, 3) Medicare, and 4) private insurance, and 3 groups on the basis of race: 1) white, 2) black, and 3) Hispanic. Patients who received mechanical thrombectomy were identified by utilization of ICD-9 procedural code 39.74. We compared utilization rates of mechanical thrombectomy between insurance groups and racial groups. Other demographic variables and hospital characteristics

Received April 11, 2013; accepted after revision June 9.

From the Departments of Radiology (W.B., J.S.M., H.J.C.), Neurology (A.A.R.), and Neurosurgery (H.J.C.), Mayo Clinic, Rochester, Minnesota.

Please address correspondence to Waleed Brinjikji, MD, Mayo Clinic, OL 1-115, 200 First St SW, Rochester, MN 55905; e-mail: brinjikji.waleed@mayo.edu

<http://dx.doi.org/10.3174/ajnr.A3708>

Table 1: Demographic characteristics

	All Patients n (%)	Thrombectomy Patients n (%)	Non-Thrombectomy Patients n (%)	P
Total No. of patients	249,336	371 (0.2)	248,965 (99.8)	—
Mean age, y (SD)	71.6 (14.0)	66.6 (16.3)	71.6 (14.0)	<.0001
Sex				
Male	114,199 (45.8)	185 (49.9)	114,014 (45.8)	.29
Female	135,137 (54.2)	186 (50.1)	134,951 (54.2)	
Race				
White	159,673 (76.5)	270 (86.5)	159,403 (76.5)	<.0001
Black	38,342 (18.4)	27 (8.7)	38,315 (18.4)	
Hispanic	10,738 (5.1)	15 (4.8)	10,723 (5.1)	
Insurance status				
Private	38,741 (15.5)	95 (25.6)	38,646 (15.5)	<.0001
Medicare	181,995 (73.0)	224 (60.4)	181,771 (73.0)	
Medicaid	16,540 (6.6)	39 (10.5)	16,501 (6.6)	
Uninsured	12,060 (4.8)	13 (3.5)	12,047 (4.8)	
Hospital location				
Urban	222,497 (89.2)	361 (97.3)	222,136 (89.2)	<.0001
Rural	26,839 (10.8)	10 (2.7)	26,829 (10.8)	
Hospital teaching status				
Teaching	96,739 (38.8)	210 (56.6)	96,529 (38.8)	<.0001
Non-teaching	152,597 (61.2)	161 (43.4)	152,436 (61.2)	

included in this study were sex, age, hospital location, and hospital teaching status.

Separate analyses were performed to determine disparities in the utilization rate of mechanical thrombectomy among 1) all patients with a primary diagnosis of acute ischemic stroke and 2) patients with acute ischemic stroke treated at centers that performed mechanical thrombectomy in a given year.

Statistical Analysis

χ^2 tests were used to compare utilization rates of mechanical thrombectomy between insurance groups and race groups. For comparisons on the basis of insurance groups, the private insurance group was the reference group. For comparisons on the basis of race, white race was the reference. A multivariate logistic regression analysis was performed to study the association between insurance status and mechanical thrombectomy adjusting for patient age, race, sex, and hospital location and teaching status. A multivariate logistic regression analysis was performed to study the association between race and mechanical thrombectomy utilization, adjusting for patient age, insurance status, sex, hospital location, and teaching status. Multivariate logistic regression analyses were performed for the 2 separate samples 1) all patients with a primary diagnosis of acute ischemic stroke and 2) all patients with a primary diagnosis of acute ischemic stroke treated at centers offering thrombectomy. Multivariate outcomes are presented as odds ratios and 95% CIs. All statistical analysis was performed by use of the SAS-based software package JMP 9.0 (www.jmp.com).

RESULTS

Patient Population

A total of 249,336 patients were included in this study; 38,741 patients (15.5%) had private insurance, 181,995 patients (73.0%) had Medicare, 16,540 patients (6.6%) had Medicaid, and 12,060 patients (4.8%) were uninsured. Race data were available for

208,753 patients. Of these, 159,673 patients (76.5%) were white, 38,342 patients (18.4%) were black, and 10,738 patients (5.1%) were Hispanic. Mechanical thrombectomy utilization rate was 0.15% (371/249,336) in this sample. A total of 35,747 patients were treated at centers that performed mechanical thrombectomy. The utilization rate of mechanical thrombectomy at these centers was 1.0% (371/35,376). Demographic characteristics of the patients in this sample are summarized in Table 1.

Insurance Status and Utilization

When considering patients treated at all centers, mechanical thrombectomy utilization rates among private insurance patients was 0.24% (95/38,741). Mechanical thrombectomy utilization rate among Medicare patients was 0.12% (224/181,995), significantly lower than that of private insurance patients ($P < .0001$). Medicaid patients had a similar utilization rate of mechanical thrombectomy compared with private insurance patients (39/16,540, 0.24%, $P = .92$). Uninsured patients had significantly lower utilization rates of mechanical thrombectomy than private insurance patients (13/12,060, 0.11%, $P = .005$).

When we considered only patients treated at centers offering mechanical thrombectomy, mechanical thrombectomy utilization rates among private insurance patients was 1.4% (95/6947). Mechanical thrombectomy utilization rates among Medicare patients was 0.9% (224/24,756), significantly lower than that of private insurance patients ($P = .0008$). Medicaid patients had a similar utilization rate of mechanical thrombectomy compared with private insurance patients (39/2545, 1.5%, $P = .92$). Uninsured patients had similar rates of mechanical thrombectomy compared with private insurance patients (13/1499, 0.9%, $P = .13$). These data are summarized in Table 2.

Race and Utilization

When considering patients treated at all centers, mechanical thrombectomy utilization rate among white patients was 0.17% (293/159,673). Black patients had a significantly lower rate of mechanical thrombectomy utilization compared with white patients (30/38,342, 0.07%, $P < .0001$). Hispanic patients had a similar utilization rate of mechanical thrombectomy compared with whites (15/10,738, 0.13%, $P = .29$).

When we considered only patients treated at centers offering mechanical thrombectomy, mechanical thrombectomy utilization rates among white patients was 1.2% (293/24,988). Black patients had a significantly lower rate of mechanical thrombectomy utilization compared with white patients (30/4950, 0.6%, $P = .0006$). Hispanic patients had a similar utilization rate of mechanical thrombectomy compared with whites (15/1395, 1.1%, $P = .84$). These data are summarized in Table 2.

Table 2: Insurance status and race and mechanical thrombectomy utilization

	All Patients		Patients Treated at Thrombectomy Centers	
	n (%)	P	n (%)	P
Race				
White	293 (0.17)	Reference	293 (1.2)	Reference
Black	30 (0.07)	<.0001	30 (0.6)	.0006
Hispanic	15 (0.13)	.29	15 (1.1)	.84
Insurance				
Private	95 (0.24)	Reference	95 (1.4)	Reference
Medicare	224 (0.12)	<.0001	224 (0.9)	.0008
Medicaid	39 (0.24)	.92	39 (1.5)	.61
None	13 (0.11)	.005	13 (0.9)	.13

Table 3: Multivariate logistic regression analysis

	All Patients		Patients Treated at Thrombectomy Centers	
	OR (95% CI)	P	OR (95% CI)	P
Race ^a				
Black versus Hispanic	0.42 (0.23–0.81)	<.0001	0.50 (0.26–0.97)	.04
Black versus white	0.35 (0.23–0.51)	<.0001	0.41 (0.27–0.60)	<.0001
Hispanic versus white	0.78 (0.44–1.27)	.33	0.83 (0.46–1.36)	.47
Insurance ^b				
Medicare versus private	0.53 (0.41–0.70)	<.0001	1.12 (0.80–1.57)	.52
Medicaid versus private	1.09 (0.70–1.65)	.71	1.19 (0.76–1.82)	.43
None versus private	0.52 (0.25–0.95)	.03	0.63 (0.31–1.18)	.16
Medicaid versus Medicare	1.16 (0.73–1.82)	.52	1.07 (0.66–1.68)	.78
None versus Medicare	0.56 (0.27–1.05)	.07	0.57 (0.27–1.08)	.08
None versus Medicaid	0.48 (0.22–0.95)	.03	0.94 (0.60–1.51)	.78

^a Adjusted for insurance status, sex, age, hospital teaching status, and hospital location.

^b Adjusted for race, sex, age, hospital teaching status, and hospital location.

Multivariate Analysis: All Patients

After multivariate logistic regression analysis was performed, uninsured patients had a significantly lower odds of mechanical thrombectomy when compared with patients with private insurance (OR = 0.52, 95% CI = 0.25–0.95, $P = .03$). Medicare patients also had lower odds of mechanical thrombectomy utilization when compared with private insurance patients (OR = 0.53, 95% CI = 0.41–0.70, $P < .0001$). Medicaid patients had a similar odds of mechanical thrombectomy utilization when compared with private insurance patients (OR = 1.05, 95% CI = 0.67–1.59, $P = .83$).

After multivariate logistic regression analysis examining race and outcomes was performed, black patients had a significantly lower odds of mechanical thrombectomy utilization compared with white patients (OR = 0.35, 95% CI = 0.23–0.51, $P < .0001$). Hispanic patients had a similar utilization rate of mechanical thrombectomy compared with whites (OR = 0.78, 95% CI = 0.44–1.27, $P = .33$). These data are summarized in Table 3.

Multivariate Analysis: Patients Treated at Thrombectomy Centers

When examining patients treated at thrombectomy centers, there was no significant difference in thrombectomy utilization rates by insurance status. When examining odds of utilization by race, black patients had a significantly lower odds of mechanical thrombectomy utilization when compared with Hispanic patients (OR = 0.50, 95% CI = 0.26–0.97, $P = .04$). Blacks also had a significantly lower odds of receiving mechanical thrombectomy when compared with white patients (OR =

0.41, 95% CI = 0.27–0.60, $P < .0001$). There was no significant difference in mechanical thrombectomy utilization when comparing white and Hispanic patients. These data are summarized in Table 3.

DISCUSSION

Our study demonstrated that significant race- and insurance-based disparities exist in the utilization of mechanical thrombectomy for treatment of acute ischemic stroke. On our adjusted analyses, uninsured and Medicare patients had significantly lower odds of mechanical thrombectomy utilization when compared with their privately insured counterparts. Similarly, black patients had significantly lower odds of mechanical thrombectomy utilization when compared with white and Hispanic patients. When we performed our adjusted analysis only examining thrombectomy utilization of patients treated at hospitals offering thrombectomy, some of these disparities remained present. Although insurance status was no longer associated with thrombectomy utilization, black patients were significantly

less likely to receive mechanical thrombectomy than were their white and Hispanic counterparts. These findings suggest that disparities in mechanical thrombectomy utilization in the United States can be explained, in part, by lack of access to centers offering this treatment.

Studies examining racial and economic disparities in utilization of mechanical thrombectomy for acute ischemic stroke are scarce. One prior study of 602 patients found that blacks were significantly less likely to undergo endovascular interventions at stroke centers; however, when adjusted for the fact that African Americans had more delayed arrivals to the emergency department, they found no racial disparity.⁴ In general, socioeconomic status has been associated with significant disparities in the resource utilization for acute ischemic stroke. Patients of lower socioeconomic status have been shown to receive less emergent imaging, lower rates of hospital admission, and lower rates of poststroke care.^{3,5–7} Several prior studies have demonstrated significant socioeconomic disparities in the utilization of intravenous rtPA for the treatment of acute ischemic stroke.^{2,8–10} Nasr et al¹⁰ found that whites had significantly higher intravenous tPA treatment rates for acute ischemic stroke when compared with blacks and Hispanics in the United States. Johnston et al⁹ found that blacks were significantly less likely to receive intravenous tPA for acute ischemic stroke and demonstrated that contraindications to treatment did not account for the differences in tPA utilization rates. Prior studies in both the United States and Canada have demonstrated that neighborhood income is not associated with any significant differences in initial stroke care, but these

studies did not evaluate differences in mechanical thrombectomy utilization rates.^{11,12}

There are many potential factors that could account for these disparities. Prior studies have demonstrated that disparities in the treatment of acute ischemic stroke in general could be related to delays in treatment, education level, or differences in stroke etiology.^{2,13-15} Minority patients are more likely to present with higher severity of stroke symptoms than whites and also present with more small-vessel lacunar strokes, thus making them less amenable to mechanical thrombectomy.¹⁶⁻¹⁹ Lower rates of mechanical thrombectomy among Medicare recipients could be related to a less aggressive therapeutic approach in older patients rather than to any economic considerations.²⁰

Limitations

There are a number of limitations to our study. To maintain consistency with the Perspective data base, we used the same racial/ethnic terms defined in the data base (white, black, Hispanic); however, we acknowledge that the broad racial designations provided present a potential limitation. Other weaknesses of this study include the fact that we are unable to determine important variables such as stroke severity at presentation, time to presentation, patient eligibility for mechanical thrombectomy, and the presence of large-vessel occlusions. Because of our inability to differentiate between various stroke subtypes, and, given the fact that stroke subtypes vary significantly by race, the observed racial disparities in our study must be interpreted cautiously. We cannot exclude that a racial difference in the likelihood of consenting for endovascular therapy could have played a contributing role. Coding errors are also a potential limitation of this study, as they are with any study of a large administrative data base.^{21,22}

CONCLUSIONS

Our study demonstrated that significant socioeconomic disparities exist in the utilization of mechanical thrombectomy for the treatment of acute ischemic stroke. To ensure that all segments of the population have equal access to optimal stroke care, further studies are needed to study the underlying causes of these disparities.

Disclosures: Alejandro A. Rabinstein—UNRELATED: Royalties: Elsevier, Comments: For authorship rights; Other: Boston Scientific, Comments: Event adjudication board member for trial PREVAIL. Jennifer S. McDonald—UNRELATED: Grants/Grants Pending: GE Healthcare,* Comments: Investigator-initiated research grant. Harry J. Cloft—UNRELATED: Grants/Grants Pending: Cordis Endovascular,* Comments: Site PI at enrolling site for SAPHIRE (Stenting and Angioplasty with Protection in Patients at High Risk for Endarterectomy) registry (*money paid to institution).

REFERENCES

1. Hassan AE, Chaudhry SA, Grigoryan M, et al. **National trends in utilization and outcomes of endovascular treatment of acute ischemic stroke patients in the mechanical thrombectomy era.** *Stroke* 2012;43:3012-17
2. Cruz-Flores S, Rabinstein A, Biller J, et al. **Racial-ethnic disparities in stroke care: the American experience: a statement for healthcare professionals from the American Heart Association/American Stroke Association.** *Stroke* 2011;42:2091-116
3. Addo J, Ayerbe L, Mohan KM, et al. **Socioeconomic status and stroke: an updated review.** *Stroke* 2012;43:1186-91
4. Bhattacharya P, Mada F, Salowich-Palm L, et al. **Are racial disparities in stroke care still prevalent in certified stroke centers?** *J Stroke Cerebrovasc Dis* 2013;22:383-88
5. Langagergaard V, Palnum KH, Mehnert F, et al. **Socioeconomic differences in quality of care and clinical outcome after stroke: a nationwide population-based study.** *Stroke* 2011;42:2896-902
6. Lazzarino AI, Palmer W, Bottle A, et al. **Inequalities in stroke patients' management in English public hospitals: a survey on 200,000 patients.** *PLoS One* 2011;6:e17219
7. Sandel ME, Wang H, Terdiman J, et al. **Disparities in stroke rehabilitation: results of a study in an integrated health system in northern California.** *PM&R* 2009;1:29-40
8. Fang MC, Cutler DM, Rosen AB. **Trends in thrombolytic use for ischemic stroke in the United States.** *J Hosp Med* 2010;5:406-09
9. Johnston SC, Fung LH, Gillum LA, et al. **Utilization of intravenous tissue-type plasminogen activator for ischemic stroke at academic medical centers: the influence of ethnicity.** *Stroke* 2001;32:1061-68
10. Nasr DM, Brinjikji W, Cloft HJ, et al. **Racial and ethnic disparities in the use of intravenous recombinant tissue plasminogen activator and outcomes for acute ischemic stroke.** *J Stroke Cerebrovasc Dis* 2013;22:154-60
11. Brown AF, Liang LJ, Vassar SD, et al. **Neighborhood socioeconomic disadvantage and mortality after stroke.** *Neurology* 2013;80:520-27
12. Kapral MK, Fang J, Chan C, et al. **Neighborhood income and stroke care and outcomes.** *Neurology* 2012;79:1200-07
13. Sallar AM, Williams PB, Omishakin AM, et al. **Stroke prevention: awareness of risk factors for stroke among African American residents in the Mississippi delta region.** *J Natl Med Assoc* 2010;102:84-94
14. Schwamm LH, Reeves MJ, Pan W, et al. **Race/ethnicity, quality of care, and outcomes in ischemic stroke.** *Circulation* 2010;121:1492-501
15. Anderson BE, Rafferty AP, Lyon-Callo S, et al. **Knowledge of tissue plasminogen activator for acute stroke among Michigan adults.** *Stroke* 2009;40:2564-67
16. Frey JL, Jahnke HK, Bulfinch EW. **Differences in stroke between white, Hispanic, and Native American patients: the Barrow Neurological Institute stroke database.** *Stroke* 1998;29:29-33
17. Jones MR, Horner RD, Edwards LJ, et al. **Racial variation in initial stroke severity.** *Stroke* 2000;31:563-67
18. Pathak EB, Sloan MA. **Recent racial/ethnic disparities in stroke hospitalizations and outcomes for young adults in Florida, 2001-2006.** *Neuroepidemiology* 2009;32:302-11
19. White H, Boden-Albala B, Wang C, et al. **Ischemic stroke subtype incidence among whites, blacks, and Hispanics: the Northern Manhattan Study.** *Circulation* 2005;111:1327-31
20. Saposnik G, Cote R, Phillips S, et al. **Stroke outcome in those over 80: a multicenter cohort study across Canada.** *Stroke* 2008;39:2310-17
21. Tirschwell DL, Longstreth WT Jr. **Validating administrative data in stroke research.** *Stroke* 2002;33:2465-70
22. Woodworth GF, Baird CJ, Garces-Ambrossi G, et al. **Inaccuracy of the administrative database: comparative analysis of two databases for the diagnosis and treatment of intracranial aneurysms.** *Neurosurgery* 2009;65:251-56

Intraplaque High-Intensity Signal on 3D Time-of-Flight MR Angiography Is Strongly Associated with Symptomatic Carotid Artery Stenosis

A. Gupta, H. Baradaran, H. Kamel, A. Mangla, A. Pandya, V. Fodera, A. Dunning, and P.C. Sanelli

ABSTRACT

BACKGROUND AND PURPOSE: Intraplaque hemorrhage in carotid artery atherosclerotic plaque has been shown to be a marker of risk, associated with prior and future ischemic events, and has been associated with regions of intraplaque high-intensity signal on 3D-TOF MRA. We assessed the association of intraplaque high-intensity signal determined on 3D-TOF MRA with the incidence of prior ipsilateral stroke or TIA.

MATERIALS AND METHODS: We assessed intraplaque hemorrhage by evaluating for intraplaque high-intensity signal adapting a recently validated technique on 3D-TOF source images in participants with high-grade ($\geq 70\%$) extracranial carotid stenosis. Logistic regression analyses were used to assess the strength of association between the presence of intraplaque high-intensity signal on routine MRA sequences and prior stroke or TIA.

RESULTS: Intraplaque high-intensity signal was present in 22 (41.5%) of 53 carotid arteries studied in 51 patients. Ipsilateral ischemic events occurred in 15 (68.1%) of 22 in the intraplaque high-intensity signal–positive group (10 strokes, 5 TIAs) and in 4 (12.9%) of 31 in the intraplaque high-intensity signal–negative group (3 strokes, 1 TIA). Ischemic events occurred within the 6-month period preceding imaging in 18 (94.7%) of 19 cases. The univariate odds ratio of the association of intraplaque high-intensity signal with any prior ischemic event was 14.5 (95% CI, 3.6–57.6), and the multivariate age- and sex-adjusted odds ratio was 14.2 (95% CI, 3.3–60.5). The association remained present across 1.5T and 3T magnet field strengths.

CONCLUSIONS: Intraplaque high-intensity signal determined from MRA sequences already in place to measure luminal stenosis is strongly associated with prior ipsilateral ischemic events. Prospective validation of these findings to predict outcome in carotid artery stenosis could provide a valuable and widely accessible stroke risk stratification tool.

ABBREVIATIONS: IHIS = intraplaque high-intensity signal; IPH = intraplaque hemorrhage

Measurement of luminal diameter stenosis has been the mainstay of extracranial vascular imaging, with treatment guidelines from multicenter randomized controlled trials based largely on patient stratification by stenosis severity.^{1–3} However, with recent developments in MR imaging technology, it is possible to assess the composition of atherosclerotic carotid lesions to determine the presence of complicated or advanced plaque elements that are at greater risk to cause ischemic symptoms.^{4–6} One such component of carotid plaque that has been identified as a

component of advanced atherosclerotic lesions is intraplaque hemorrhage (IPH). When present in carotid atherosclerotic plaque, IPH has been associated with previous^{7,8} and future⁹ stroke and has been proposed as a possible marker of not only plaque inflammation¹⁰ but also of generalized cardiovascular risk.¹¹

MR imaging tools have allowed IPH to be detected with high diagnostic accuracy compared with histopathologic confirmation with most of the techniques that have been studied to date.⁴ However, a significant barrier to the widespread use of IPH assessment as a measure of embolic stroke risk has been that most studies have relied on high-resolution imaging by using specialized, dedicated MR imaging surface carotid coils¹² or black-blood coronal T1-weighted fat-suppressed MR imaging techniques.⁹ Neither of these techniques are part of the standard sequences routinely obtained in MRA examinations, which rely on TOF techniques to assess luminal diameter stenosis. Recent reports have suggested

Received May 14, 2013; accepted after revision July 8.

From the Departments of Radiology (A.G., H.B., V.F., P.C.S.), Neurology (H.K., A.M.), and Public Health (A.P., A.D., P.C.S.), Weill Cornell Medical College, New York, New York.

Dr. Gupta has been supported in part by the Association of University Radiologists General Electric Radiology Research Academic Fellowship.

Please address correspondence to Ajay Gupta, 525 East 68th St, Starr 8A, Box 141, New York, NY 10065; e-mail: ajg9004@med.cornell.edu

<http://dx.doi.org/10.3174/ajnr.A3732>

that routinely performed MRA techniques used to measure stenosis, including 3D-TOF imaging,^{13,14} can accurately predict IPH compared with histopathologic studies by the detection of intraplaque high-intensity signal (IHIS) relative to adjacent skeletal muscle. These studies, however, have been performed by use of dedicated carotid coils and not by standard quadrature neck array coils. Furthermore, it is also unknown whether IPH determined by 3D-TOF MRA neck images is associated with symptomatic carotid artery disease. The purpose of our study was to assess the association between IHIS determined on noncontrast 3D-TOF imaging and prior stroke or TIA in patients with high-grade carotid artery stenosis.

MATERIALS AND METHODS

Patients

Patients were screened for this institutional review board–approved retrospective study after review of consecutive MRA neck examinations performed from August 2009 through August 2012. Inclusion criteria included 1) high-grade extracranial internal carotid artery stenosis (70%–99%) identified on noncontrast 3D-TOF MRA, 2) detailed documentation of electronic medical records of whether stroke or TIA had occurred before the MRA, and 3) detailed medical record documentation of pre-existing vascular risk factors.

Imaging Technique

MRA neck studies were performed on either 1.5T or 3T Signa (GE Healthcare, Milwaukee, Wisconsin) scanners by use of standard quadrature neck array coils. No dedicated high-resolution surface coils were used, nor was gadolinium administered. 3D-TOF acquisition involved a 20-cm field of view centered at the carotid bifurcation, 1.4-mm section thickness, and a matrix of 320 × 192 and 320 × 224 on 1.5T and 3T, respectively. To assess the generalizability of this technique to clinical practice, we included in our analysis all studies with image quality sufficient to warrant a clinical interpretation at the time of original image acquisition.

Imaging Data Assessment

IHIS, a presumed marker for IPH, was determined by adaption of a method used by Qiao et al,¹³ in which hyperintense signal intensity on 3D-TOF source images in carotid plaque was assessed relative to adjacent muscle. Unlike the study by Qiao et al,¹³ our technique did not use data collected with a dedicated carotid coil. We used a quantitative cutoff value of signal intensity 50% greater than skeletal muscle based on region-of-interest analysis in the area of suspected IHIS.^{9,15} IHIS assessment was made blinded to clinical data by 2 independent board-certified neuroradiologists with disagreements resolved by a third neuroradiologist as a tiebreaker. We further analyzed the cases with discordant interpretations and specifically addressed the possibility that a decrease in image quality could be contributing to discordant IHIS interpretations by making a subjective assessment of the presence or absence of motion degradation or other MR imaging artifacts, limiting confident diagnosis of IHIS in these cases.

Stenosis was categorized as 70%–95% or > 95%–99% by use of a method adapted from a study of diagnostic accuracy of TOF MRA in high-grade carotid artery stenosis.¹⁶ We used MRA MIP

images to visually estimate the degree of stenosis, taking into account maximal luminal diameter stenosis relative to the caliber of normal-appearing distal ICA on MIP images, and used axial 3D-TOF source images to confirm stenosis measurements when MIP data did not provide unequivocal assessment of stenosis. Because measurements by use of the distal ICA as the denominator for stenosis measurements might underestimate the degree of stenosis in near-occlusion, as per North American Symptomatic Carotid Endarterectomy Trial guidelines,¹⁷ NASCET-type measurements were not used in such cases.

Clinical Data Assessment

The presence of ipsilateral TIA or stroke and coexisting vascular risk factors were determined by the consensus of 2 stroke neurologists after examination of the electronic medical record. The neurologists were blinded to the MRA IHIS assessments. Stroke and TIA were defined according to American Heart Association criteria,¹⁸ with a stroke and TIA defined as a permanent or transient episode, respectively, of neurologic dysfunction caused by focal brain or retinal ischemia. Only ipsilateral ischemic events referable to the stenotic ICA were considered positive events. The specific vascular risk factors collected in the cohort included the presence or absence of diabetes, hypertension, atrial fibrillation, hyperlipidemia, coronary artery disease, smoking history, chronic obstructive pulmonary disease, and chronic kidney disease.

Statistical Analysis

Statistical analysis was performed by use of logistic regression analysis to measure the strength of association between IHIS and ischemic events measured as an OR. A multivariate analysis was also performed, with calculation of an age- and sex-adjusted OR, as well as adjustment for covariate risk factors found to be statistically significant. Subset analyses were also performed stratifying test data from 1.5T or 3T MR imaging machines. We recorded the discrepancy rate for measurement of IHIS with interobserver agreement determined both by calculation of simple percent agreement and a Cohen κ coefficient statistic. Finally, to evaluate the possibility that interobserver interpretation differences were contributing significantly to the OR calculation, sensitivity analyses were performed with logistic regression analyses in 3 scenarios: 1) only with concordant IHIS interpretations, 2) treating all discordant interpretations as positive for IHIS, and 3) treating all discordant interpretations as negative for IHIS. All *P* values < .05 were considered statistically significant.

RESULTS

After the review of 4895 consecutive neck MRAs, 4648 studies were excluded because no high-grade stenosis was present. In the 247 of 4895 MRAs with high-grade stenosis or occlusion (5.0% of total MRA cases screened), after application of additional exclusion criteria, including exclusion of cases with occlusion or cases with primary vascular imaging done with a technique besides 3D-TOF, such as with contrast-enhanced MRA, our final cohort of 51 patients with 53 unique carotid arteries met inclusion criteria. Vascular risk factors were not significantly different between groups (Table 1), though more men had IHIS. IHIS was present in 22 (41.5%) of 53 carotid arteries studied (see representative case,

Fig 1). There was a 77% interobserver agreement rate (agreement in 41/53 cases), resulting in a κ coefficient of 0.50, suggesting moderate to good interobserver agreement. In the 12 cases with discordant interpretations, 10 of 12 studies were judged to have at least a moderate degree of motion degradation or other MR imaging artifacts limiting confident assessment of the presence or absence of IHIS.

Ipsilateral ischemic events occurred in 15 (68.1%) of 22 patients in the IHIS-positive group (10 strokes, 5 TIAs) and in 4 (12.9%) of 31 patients in the IHIS-negative group (3 strokes, 1 TIA) (Table 2). Ischemic events occurred within the 6 months preceding imaging in 18 (94.7%) of 19 cases, with the single outlier representing an ipsilateral stroke which occurred 10 years before imaging. In the univariate logistic regression analysis, the OR of the association of IHIS and prior ischemic events was 14.5 (95% CI, 3.6–57.6), whereas the age- and sex-adjusted OR was 14.2

(95% CI, 3.3–60.5). Excluding the 1 outlier ischemic event occurring 10 years before imaging, we found that the OR of the association of IPH and ischemic events within the prior 6 months was 13.5 (95% CI, 3.4–54.1). In addition, the association was preserved across magnet field strengths, as 32 arteries on a 1.5T magnet and 21 arteries on a 3T magnet had ORs of 17.8 (95% CI, 3.0–105.9) and 13.8 (95% CI, 1.2–156.6), respectively. OR data are summarized in Table 3. Finally, the strength of the association was between ischemic events, and IHIS was preserved across sensitivity analyses: 1) OR of 12.5 (95% CI, 2.53–61.8) in cases with only concordant interpretations analyzed, 2) OR of 5.46 (95% CI, 1.37–21.8) if the 12 discrepant cases were treated as IHIS negative, and 3) OR of 10.41 (95% CI, 2.73–39.8) if the 12 discrepant cases were treated as IHIS positive.

Table 1: Vascular risk factors in patients with and without IPH defined on MRA

Risk Factors	IPH-Positive (n = 22)	IPH-Negative (n = 31)	P Value
Age (mean years)	76.4 ± 9.46	77.6 ± 9.43	.6406
Sex: male, n (%)	13 (59)	9 (29)	.0286
Diabetes (%)	9 (41)	13 (42)	.9404
Hypertension (%)	18 (82)	30 (97)	.1474
Hyperlipidemia (%)	18 (82)	26 (84)	.8445
Atrial fibrillation (%)	4 (18)	3 (10)	.3676
Coronary artery disease (%)	9 (41)	14 (45)	.7583
Smoking (%)	15 (68)	19 (61)	.6062
Heart failure (%)	3 (14)	4 (13)	.9381
COPD (%)	2 (9)	4 (13)	.6660
Chronic kidney disease (%)	7 (32)	6 (19)	.2988
Stenosis severity: 95%–99% (%)	1 (5)	3 (10)	.6332

Note:—COPD indicates chronic obstructive pulmonary disease.

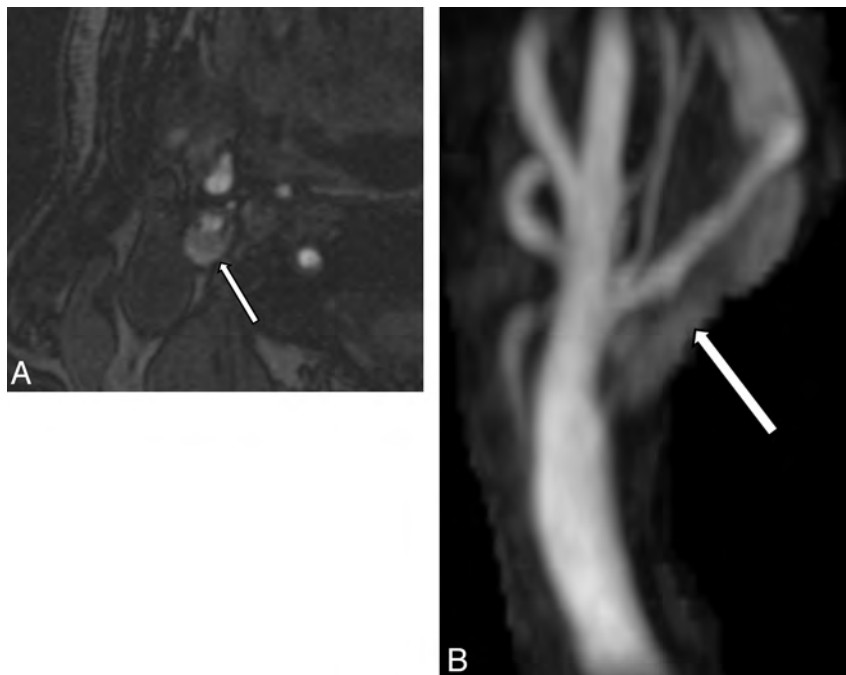


FIG 1. A, Axial 3D-TOF source image demonstrates signal hyperintensity in the plaque (arrow) of the high-grade right internal carotid artery stenosis. B, 3D-TOF maximum-intensity projection image of the same right carotid artery bifurcation illustrates a long-segment hyperintense signal (arrow) within the plaque of the right internal carotid artery consistent with IPH.

DISCUSSION

Our study demonstrates an association between IHIS, a potential marker of IPH, determined from routinely acquired 3D-TOF MRA source images and ischemic events. Specifically, our data suggest that patients with high-grade, extracranial carotid artery stenosis and IHIS are almost 14 times more likely to have had symptomatic disease compared with those with high-grade stenosis and no IHIS. Although several studies have characterized IPH or MR imaging by using black-blood, fat-suppressed T1-weighted sequences⁹ and high-resolution surface carotid coils,¹² these studies have thus far had limited clinical usefulness, as they have relied on specialized sequences or equipment not used in most MRA neck examinations done to characterize vessel stenosis. Previous studies have used source images from 3D-TOF studies to assess the presence of IPH,^{13,14,19} including a study comparing MR imaging–suspected IPH with histopathologic confirmation.⁸ In this study, Qiao et al⁸ found that source images from 3D-TOF MRA or from mask-phase images from contrast-enhanced MRA could detect IPH with high diagnostic accuracy and with excellent interobserver reliability, though the study did not measure the association of IPH from MRA images and ischemic events. In another similar study, Yamada et al¹⁴ used high signal intensity on 3D-TOF MRA MIP images as a surrogate for IPH but did not correlate these findings with the presence or absence of symptomatic carotid disease. Our study demonstrates a strong association between ischemic events and IPH, as determined on widely available, large field-of-view neck coils with a 4-minute MRA sequence (3D-TOF), which is nearly universally acquired during screening examinations of the extracranial vascular structures.

It is important to recognize that the studies reported in the prior literature assessing the association between 3D-TOF plaque high signal and IPH on histologic examinations have been per-

Table 2: Presence of symptomatic cerebrovascular ischemia with or without IPH on MRA

	IPH-Positive	IPH-Negative	P Value
History of any prior ipsilateral symptomatic disease, n (%)	15 (68)	4 (13)	<.0001
Median time since prior TIA/stroke, days	0 (IQR: 0–10)	0 (IQR: 0–7)	.7619
History of prior ipsilateral stroke, n (%)	10 (67)	3 (75)	.7500
Median time since prior stroke, days	0 (IQR: 0–7)	0 (IQR: 0–0)	.3605
History of prior TIA, n (%)	5 (33)	1 (25)	.7500
Median time since prior TIA, days	0 (IQR: 0–180)	14 (IQR: N/A)	.5338

Note:—IQR indicates interquartile range; N/A, not available.

Table 3: Summary of effect size and strength of association between IHIS and stroke or TIA

Type of Association	OR	95% CI
IHIS and any prior ischemic event	14.5	3.6–57.6
IHIS and prior ischemic event within 6 months	13.5	3.4–54.1
IHIS on 1.5T and prior ischemic event	17.8	3.0–105.9
IHIS on 3T and prior ischemic event	13.8	1.2–156.6

formed by use of dedicated surface carotid coils.^{13,14,19} As such, although it is likely that IHIS detected on 3D-TOF MRA performed with a standardized quadrature neck array coil will highly correspond with IPH on histologic examination, further radiologic-pathologic correlation studies are warranted to assess the diagnostic accuracy of the specific technique used in our study.

Two additional points regarding the MR imaging technique used for our study warrant further discussion. First, our study suggests that the association between IHIS and ischemic events is preserved across magnet field strengths. Because nearly all existing studies of IPH or IHIS have been performed on 1.5T magnets,^{9,11,12,20–22} and because the paramagnetic properties of IPH can potentially result in decreased signal hyperintensity on T1WI at 3T, our work supports the histopathologic correlation study by Qiao et al,⁸ suggesting a role for 3T imaging in IPH assessment by use of simple TOF techniques. Second, because TOF imaging has generally been used to assess for luminal diameter stenosis with limited data in the literature describing the use of this technique to assess the presence of IPH, we assessed the interobserver variability and found a κ coefficient suggesting moderate to good interobserver agreement. The logistic regression sensitivity analyses performed in our study demonstrate that our main results were robust to the interobserver variability present, and that 10 (83.3%) of 12 discrepant cases may have been related to motion-limited studies. Although we chose to analyze these motion-limited studies in our primary analysis to assess the generalizability of IHIS and IPH assessment in screening MRA studies, including studies occurring in critically ill patients or in patients unable to completely lie still for other reasons, future studies may be helpful to clarify how MR imaging quality influences the diagnostic accuracy of IPH assessment on 3D-TOF MRA vs histopathologic assessment. This is especially important regarding IPH assessment with standard field-of-view head and neck MR imaging coils because, despite the significant benefits of accessibility, speed, and ease of implementation, these coils provide less spatial resolution of the carotid artery than do multisequence, high-resolution techniques with dedicated surface carotid coils.

Our results are consistent with recent literature showing MR imaging of IPH to be associated with prior⁷ and future ischemic events.^{9,12} The magnitude of the strength of association between

IHIS in our study and prior stroke (OR, approximately 14) is in line with a meta-analysis of the strength of association between IPH and future ischemic events (OR, approximately 12).⁹ The rate of IPH in our cohort (41.5%) is similar to that reported in recent published studies.⁷ We noted IPH even in cases where imaging was performed outside of the immediate 24 hours after stroke or TIA.

In a recent study of IPH in symptomatic carotid disease by use of coronal T1-weighted fat-suppressed sequences to characterize IPH, Hosseini et al⁹ found that stroke risk with IPH was preserved for at least 5 years. The presence of IPH long after stroke and its ability to predict future stroke reinforce its potential value as a robust biomarker of plaque vulnerability in carotid atherosclerotic disease. Given the strong association between IPH and future events by use of specialized techniques, our findings raise the hope that routinely acquired imaging of the neck might play a role in predicting future events.

Our study had limitations that should be considered. First, our study was limited by a retrospective design, which could introduce significant patient heterogeneity into our analysis and the possibility that confounding vascular risk factors may be contributing to the differences present between groups. Despite this, detailed vascular risk factors were collected and were found to be similar between IHIS-positive and IHIS-negative groups, suggesting a low risk for confounding bias. In addition, we screened nearly 5000 MRA examinations to ensure a relatively homogeneous group of patients in stenosis severity (all $\geq 70\%$), in an effort to minimize the effect that differences in the degree of stenosis might have in a larger but more heterogeneous patient population. Second, a potential limitation was that IHIS could represent a combination of a lipid-rich necrotic core and IPH.¹⁴ The existing data suggest that this, however, is not a significant limitation because radiology-pathology correlation studies of 3D-TOF techniques have yielded a good diagnostic accuracy of MR imaging IPH classification compared with IPH determined from surgical specimens at carotid endarterectomy.¹³ Furthermore, because both a lipid-rich necrotic core and IPH are considered markers of plaque vulnerability,⁶ definitive differentiation may be of limited clinical relevance. Third, given the spatial resolution limits of 3D-TOF MRA by use of a quadrature neck array coil, confident differentiation of IHIS from an area of ulcerated plaque can be difficult. The effects of a quadrature neck array coil and its diagnostic accuracy in IPH determination vs histopathologic assessment are areas requiring further investigation. Fourth, our study assessed stroke or TIA that occurred before imaging, and as such, it remains unclear to what extent future events can be predicted by the use of this technique. We agree that validation of the use of 3D-TOF source images as a risk stratification tool for stroke will require a controlled prospective investigation. However, IPH detected by both coronal black-blood gradient-echo⁹ and dedicated carotid-coil-dependent, high-resolution techniques¹² has been shown to predict future stroke or TIA in independent studies in the literature. Because 3D-TOF source images have comparable accuracy in the identification of IPH relative to these other tech-

niques, it is reasonable to hypothesize that IHIS as determined on 3D-TOF MRA, a marker for IPH in our study, may have a similar predictive capacity.

CONCLUSIONS

Our study demonstrates that routinely acquired, screening MRA neck 3D-TOF source images, already widely used to measure luminal stenosis, can detect IHIS, which is strongly associated with prior ischemic events in patients with high-grade carotid artery stenosis. The prospective validation of our findings, as well as further histologic confirmation, may translate into regular reporting of IPH assessed by IHIS as a risk stratification tool to complement measures of luminal diameter stenosis on neck MRA.

Disclosures: Ajay Gupta—UNRELATED: Grants/Grants Pending: AUR GE Radiology Research and Academic Fellowship.* Comments: Salary support provided by this grant from 2012–2014. *Money paid to institution.

REFERENCES

1. Beneficial effect of carotid endarterectomy in symptomatic patients with high-grade carotid stenosis. North American Symptomatic Carotid Endarterectomy Trial Collaborators. *N Engl J Med* 1991;325:445–53
2. Halliday A, Harrison M, Hayter E, et al. 10-year stroke prevention after successful carotid endarterectomy for asymptomatic stenosis (ACST-1): a multicentre randomised trial. *Lancet* 2010;376:1074–84
3. Randomised trial of endarterectomy for recently symptomatic carotid stenosis: final results of the MRC European Carotid Surgery Trial (ECST). *Lancet* 1998;351:1379–87
4. den Hartog AG, Bovens SM, Koning W, et al. Current status of clinical magnetic resonance imaging for plaque characterisation in patients with carotid artery stenosis. *Eur J Vasc Endovasc Surg* 2013;45:7–21
5. Cai JM, Hatsukami TS, Ferguson MS, et al. Classification of human carotid atherosclerotic lesions with in vivo multicontrast magnetic resonance imaging. *Circulation* 2002;106:1368–73
6. Sary HC, Chandler AB, Dinsmore RE, et al. A definition of advanced types of atherosclerotic lesions and a histological classification of atherosclerosis. A report from the Committee on Vascular Lesions of the Council on Arteriosclerosis, American Heart Association. *Circulation* 1995;92:1355–74
7. Millon A, Mathevet JL, Boussel L, et al. High-resolution magnetic resonance imaging of carotid atherosclerosis identifies vulnerable carotid plaques. *J Vasc Surg* 2013;57:1046–51
8. Qiao Y, Etesami M, Astor BC, et al. Carotid plaque neovascularization and hemorrhage detected by MR imaging are associated with recent cerebrovascular ischemic events. *AJNR Am J Neuroradiol* 2012;33:755–60
9. Hosseini AA, Kandiyil N, Macsweeney ST, et al. Carotid plaque hemorrhage on MRI strongly predicts recurrent ischemia and stroke. *Ann Neurol* 2013;73:774–84
10. Altaf N, Akwei S, Auer DP, et al. Magnetic resonance detected carotid plaque hemorrhage is associated with inflammatory features in symptomatic carotid plaques. *Ann Vasc Surg* 2013;27:655–61
11. Singh N, Moody AR, Rochon-Terry G, et al. Identifying a high risk cardiovascular phenotype by carotid MRI-depicted intraplaque hemorrhage. *Int J Cardiovasc Imaging* 2013;29:1477–83
12. Takaya N, Yuan C, Chu B, et al. Association between carotid plaque characteristics and subsequent ischemic cerebrovascular events: a prospective assessment with MRI—initial results. *Stroke* 2006;37:818–23
13. Qiao Y, Etesami M, Malhotra S, et al. Identification of intraplaque hemorrhage on MR angiography images: a comparison of contrast-enhanced mask and time-of-flight techniques. *AJNR Am J Neuroradiol* 2011;32:454–59
14. Yamada K, Song Y, Hippe DS, et al. Quantitative evaluation of high intensity signal on MIP images of carotid atherosclerotic plaques from routine TOF-MRA reveals elevated volumes of intraplaque hemorrhage and lipid rich necrotic core. *J Cardiovasc Magn Reson* 2012;14:81
15. Singh N, Moody AR, Gladstone DJ, et al. Moderate carotid artery stenosis: MR imaging-depicted intraplaque hemorrhage predicts risk of cerebrovascular ischemic events in asymptomatic men. *Radiology* 2009;252:502–08
16. Babiarz LS, Romero JM, Murphy EK, et al. Contrast-enhanced MR angiography is not more accurate than unenhanced 2D time-of-flight MR angiography for determining > or = 70% internal carotid artery stenosis. *AJNR Am J Neuroradiol* 2009;30:761–68
17. Fox AJ. How to measure carotid stenosis. *Radiology* 1993;186:316–18
18. Easton JD, Saver JL, Albers GW, et al. Definition and evaluation of transient ischemic attack: a scientific statement for healthcare professionals from the American Heart Association/American Stroke Association Stroke Council; Council on Cardiovascular Surgery and Anesthesia; Council on Cardiovascular Radiology and Intervention; Council on Cardiovascular Nursing; and the Interdisciplinary Council on Peripheral Vascular Disease. The American Academy of Neurology affirms the value of this statement as an educational tool for neurologists. *Stroke* 2009;40:2276–93
19. Saam T, Ferguson MS, Yarnykh VL, et al. Quantitative evaluation of carotid plaque composition by in vivo MRI. *Arterioscler Thromb Vasc Biol* 2005;25:234–39
20. Yamada N, Higashi M, Otsubo R, et al. Association between signal hyperintensity on T1-weighted MR imaging of carotid plaques and ipsilateral ischemic events. *AJNR Am J Neuroradiol* 2007;28:287–92
21. Kurosaki Y, Yoshida K, Endo H, et al. Association between carotid atherosclerosis plaque with high signal intensity on T1-weighted imaging and subsequent ipsilateral ischemic events. *Neurosurgery* 2011;68:62–67; discussion 67
22. Kwee RM, van Oostenbrugge RJ, Mess WH, et al. MRI of carotid atherosclerosis to identify TIA and stroke patients who are at risk of a recurrence. *J Magn Reson Imaging* 2013;37:1189–94

CT Angiography Findings in Carotid Blowout Syndrome and Its Role as a Predictor of 1-Year Survival

C.-W. Lee, C.-Y. Yang, Y.-F. Chen, A. Huang, Y.-H. Wang, and H.-M. Liu



ABSTRACT

BACKGROUND AND PURPOSE: Carotid blowout is a serious late complication of prior treatment of advanced head and neck cancer. We evaluate the efficacy of CTA in the diagnosis of impending carotid blowout syndrome in patients with head and neck cancer, and its capability to predict clinical outcome.

MATERIALS AND METHODS: The clinical data of 29 patients with impending carotid blowout who underwent CTA were collected and analyzed. Imaging signs included tissue necrosis, exposed artery, viable perivascular tumor, pseudoaneurysm, and contrast extravasation. DSA was obtained in 20 patients. One-year outcomes were compared based on management.

RESULTS: The most common CTA finding was necrosis (94%), followed by exposed artery (73%), viable tumor (67%), pseudoaneurysm (58%), and contrast extravasation (30%). Exposed artery, pseudoaneurysm, and contrast extravasation were the 3 CTA findings related to outcomes. All of the pseudoaneurysm and contrast extravasation cases were associated with an exposed artery. An exposed artery was the most important prognostic predictor and could not be diagnosed on DSA. Patients without the 3 findings on CTA (group 1) had the best survival rate at 1-year follow-up, followed by patients with the 3 findings treated immediately by permanent artery occlusion (group 2). Patients with the 3 findings who had no immediate treatment (group 3) had the worst outcomes ($P < .001$ in group 1 vs group 3 and group 2 vs group 3; $P = .056$ group 1 vs group 2).

CONCLUSIONS: CTA, with its ability to diagnose an exposed artery compared with DSA, may offer important management and prognostic information in patients with impending carotid blowout.

ABBREVIATIONS: CBS = carotid blowout syndrome; PAO = permanent arterial occlusion

Carotid blowout syndrome (CBS) is defined as rupture of the carotid artery and its branches and is a serious complication after treatment of advanced head and neck cancer. Potential causes of CBS include radical resection, radiation therapy and radiation necrosis, carotid exposure, wound infection, pharyngocutaneous fistula, and recurrent or persistent carcinoma.¹ The overall incidence of carotid blowout after neck dissection has been reported to be as high as 4.3%, and the risk is increased another

7.6-fold with further radiation therapy.² CBS typically occurs 2–20 years after surgery or radiation therapy,^{3,4} and average estimates of cumulative neurologic morbidity and mortality are above 60% and 40%, respectively, in patients with CBS.⁵ CBS can be categorized into 1 of 3 categories: threatened, impending, and acute carotid blowout.¹ Threatened carotid blowout is defined as physical examination or imaging results that suggest inevitable hemorrhage from 1 of the carotid arteries or its branches if no action is taken. Impending carotid blowout (also called sentinel hemorrhage) is defined as transient hemorrhage that resolves spontaneously or with packing or pressure. Acute carotid blowout represents hemorrhage that cannot be controlled by packing or pressure.¹ Surgical management of carotid blowout is usually technically difficult and is associated with high morbidity and mortality rates.^{1,2,6,7} After surgical ligation or permanent arterial occlusion (PAO) of the carotid artery, the incidence of immediate or delayed cerebral ischemic complications can be as high as 15%–20%.^{7,8–12} The complication rate of a balloon occlusion test before PAO of the carotid artery is reported to be as high as 3.2%,

Received April 28, 2013; accepted after revision June 28, 2013.

From the Department of Medical Imaging and Radiology (C.-W.L., C.-Y.Y., Y.-F.C., Y.-H.W., H.-M.L.), Hospital and Medical College, National Taiwan University, Taipei, Taiwan; and Research Center for Adaptive Data Analysis (A.H.), National Central University, Jhongli City, Taiwan.

The work of A. Huang was supported by a grant from the National Science Council of Taiwan.

Please address correspondence to Hon-Man Liu, MD, Department of Medical Imaging, National Taiwan University Hospital, No. 7, Chung-Shan South Rd, Taipei, Taiwan, ROC 100; e-mail: hmliu@ntu.edu.tw

Indicates open access to non-subscribers at www.ajnr.org

<http://dx.doi.org/10.3174/ajnr.A3716>

and it may be even higher in fragile postirradiation vessels.¹³ Delayed ischemia after passing the balloon occlusion test is yet another concern.^{10,14,15} Stent-graft deployment, with or without coiling, is another endovascular treatment of CBS. Stent-grafting can preserve the affected carotid flow but has a high rate of early and delayed complications.¹⁶⁻¹⁹ No significant difference in short-term outcome between stent-graft deployment and PAO has been reported,²⁰ and long-term results have not been reported.¹⁷

CTA has become widely available and is sensitive and specific in the detection of hemorrhagic vascular disorders such as aneurysms, arteriovenous malformations, dural arteriovenous fistulas, and intracranial dissections. Contrast extravasation on CTA predicts hematoma expansion, mortality, and clinical outcome in primary intracerebral hemorrhage.²¹⁻²⁶ To our knowledge, there have been no past reports about the use of CTA in the diagnosis of CBS or as an outcome predictor. The aim of our study was to evaluate the efficacy of CTA in the diagnosis of impending CBS, and its capability to predict clinical outcome after management.

MATERIALS AND METHODS

This retrospective study was approved by our institutional review board. We retrieved and reviewed the records of patients with head and neck bleeding treated at our institution from July 2010–October 2011. Patients were included if they had a history of head and neck cancer and were treated with surgery and/or radiation and/or chemotherapy, and had acute hemorrhage controlled with pressure or packing (impending CBS).¹ Patients with bleeding that resolved spontaneously or with acute massive bleeding that needed immediate resuscitative therapy or embolization would not have undergone CTA at our institution and were excluded. Patients with bleeding that resolved spontaneously were closely observed for 24 hours, and CTA was performed if rebleeding occurred. The CTA findings, endovascular treatment, and outcomes were recorded and analyzed.

CTA Imaging and Evaluation

CTA was performed with a single 64-detector CT scanner (Light-Speed VCT; GE Healthcare, Milwaukee, Wisconsin). The routine CTA protocol for head and neck bleeding included scanning 3 phases: the precontrast phase, the arterial phase, and the venous phase. The scanning protocol was as follows: 64×0.625 collimation, 0.516 pitch, 0.4-second rotational time, and 100 kVp; 200 mA was used for precontrast studies, and 400 mA was used for arterial-phase and venous-phase studies. The coverage was from the aortic arch to the lateral ventricle level. Dual injectors were used. We measured the time of peak enhancement at the level of the aorta first with the bolus tracing method. A total of 12 mL of low-osmolarity contrast material was injected, followed by 16 mL of normal saline at a rate of 4 mL/s, which was scanned at a 2-second interval at the level of the ascending aorta. A total of 60 mL of contrast material followed by 35 mL of normal saline at a rate of 4 mL/s was injected for the arterial-phase scan after a delay. The venous phase was obtained 30 seconds after the arterial phase. The acquired images were reconstructed into axial, coronal, and sagittal images with 0.625-mm section thickness and stored. Maximal intensity projection images were reconstructed from sub-

tracted arterial-phase images. An experienced radiologist performed DSA with a biplane angiographic unit. When CTA indicated a treatment target, DSA was performed on the target vessel first. The vertebral arteries and contralateral common carotid artery were checked after PAO. Routinely, a 5F catheter and low-osmolarity contrast medium were used, and filming was performed at a frame rate of 4 per second. The DSA was used as the reference standard for the diagnosis of pseudoaneurysm and contrast extravasation in CBS. 3D rotational angiography was not performed in CBS in order to save time. All CTA images and DSA images were independently and retrospectively evaluated by 2 experienced neuroradiologists (C.-W.L. and H.-M.L. with 8 and 25 years of experience, respectively). The CTA and DSA interpretations were done separately, and readers were blinded to the result of the other study. The CTA and DSA images were evaluated for the following characteristics: 1) viable perivascular tumor, which was defined as any enhancing soft tissue on CTA or tumor blush anywhere on DSA; 2) tissue or tumor necrosis, which was defined as an area with lack of contrast enhancement in the soft tissues of the neck or tumor mass, adjacent to the suspect vessel; 3) contrast extravasation, which was defined as leakage of contrast medium, especially during the venous phase; 4) pseudoaneurysm, which was defined as a focal bulging of more than 30% of the parent arterial diameter; and 5) exposed artery, which was defined as more than half of the arterial circumference involved by necrotic tissue.

Interpretation was performed by use of the following sequence. MIP images were used to look for pseudoaneurysm and extravasation first. Once contrast extravasation was found, the bleeding point was detected by checking the sequential changes in the arterial- and venous-phase images. Checking the necrotic margin for identification of small pseudoaneurysms or exposed arteries was particularly important. Viable tumor and necrosis were reported as simply present or absent. Long segmental exposed arterial branches were defined as a single exposed artery. Pseudoaneurysms in a segmental exposed artery were counted as a single pseudoaneurysm. If there were multiple pseudoaneurysms or exposed arteries, they were reported separately. If there was disagreement between the 2 readers, a consensus decision was made after discussion.

Patient Treatment

At our institute, the choice of treatment for impending CBS was PAO without a balloon occlusion test. Platinum coils were the primary embolic material, and *n*-butyl-2-cyanoacrylate was used only in small external carotid artery branch lesions. To save time and avoid the danger of worse bleeding by using heparin, we did not perform the balloon occlusion test before PAO. We did not treat the impending CBS with stent-graft deployment. Long-term results of treatment with a stent graft in impending CBS have not been investigated and are therefore unknown.¹⁶⁻¹⁹ Perioperative use of antiplatelets and anticoagulants in patients undergoing stent-graft treatment was another concern. The timing of endovascular intervention was dependent on the clinical presentation, CTA findings, and patient and family decision. If a patient refused endovascular treatment, palliative treatment was given. Palliative treatment of patients with impending CBS who declined aggres-

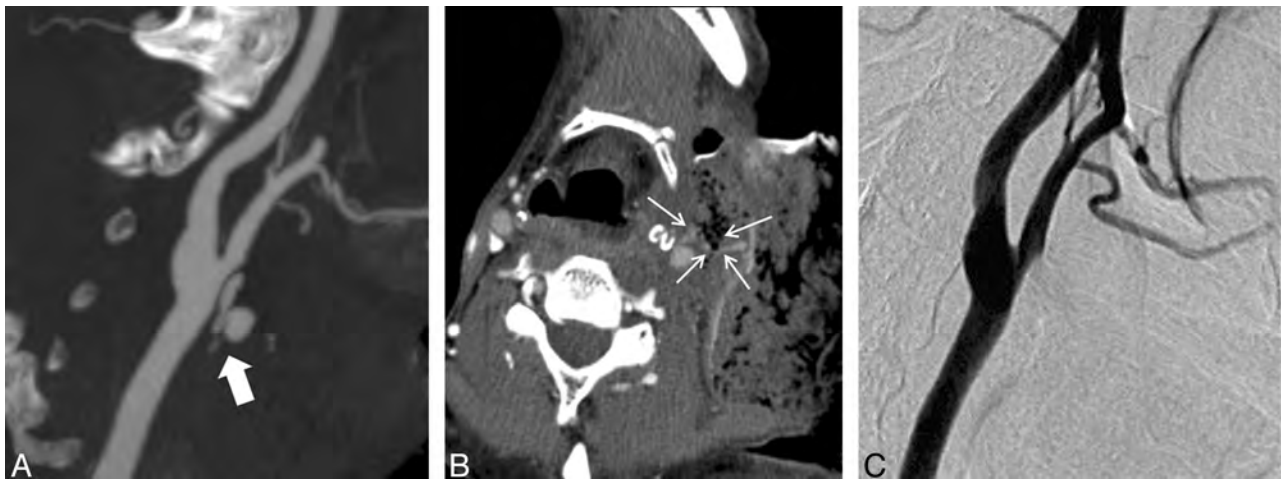


FIG 1. A 52-year-old man with a history of oropharyngeal cancer. *A*, MIP CTA imaging performed after bleeding was controlled by local packing shows contrast extravasation (arrow) from the common carotid artery near the bifurcation. *B*, Source image shows an exposed common carotid artery (arrows) surrounded by necrosis. *C*, DSA done immediately after CTA does not show contrast extravasation. However, the possibility of a further tamponade effect after CTA cannot be excluded in this case.

sive treatment included continuous pressure or packing, blood transfusion, fluid supplement, and tracheostomy if necessary.

Patient Outcomes

Patients were evaluated for at least 1 year after initial CTA or at the last hospital visit unless death occurred. We divided the patients into 3 groups according to the first CTA findings and treatment. Patients were categorized into group 1 if the CTA did not show pseudoaneurysm, extravasation, or an exposed artery, and they were treated conservatively. Patients were categorized as group 2 if the CTA demonstrated a pseudoaneurysm, extravasation, or an exposed artery, and they underwent immediate endovascular treatment. Patients were categorized as group 3 if the CTA demonstrated a pseudoaneurysm, extravasation, or an exposed artery, and they received no or delayed endovascular treatment.

Statistical Analysis

The adjusted Wald method was used to estimate the 95% CIs of the observed rates. The κ statistic was used to analyze the interobserver reliability. A value of 0.61–0.80 implied substantial agreement, and a value of 0.81–1.00 implied almost perfect agreement. The Kaplan-Meier survival curve with the pair-wise log-rank test was used to assess the difference of survival among the 3 groups. Survival was considered statistically different if $P < .05$.

RESULTS

From July 2010–October 2011, a total of 29 patients (2 women and 27 men) with a mean age of 53.5 years (age range, 38–76 years) were treated for impending CBS and were included in this study. Eighteen patients had received a radical neck dissection, 25 had received radiation therapy, 6 had received a second course of radiation therapy, 22 had received chemotherapy, and 1 had received photodynamic therapy. Four patients had a second CTA for another bleeding episode 52 to 162 days after the first CTA. Twenty patients had DSA after the first CTA, and 3 patients underwent DSA after the second CTA. In total, 33 CTA examinations were available for evaluation.

CTA Imaging and Evaluation

The most common CTA imaging finding was necrosis (94%), followed by an exposed artery (73%), viable tumor (67%), pseudoaneurysm (58%), and contrast extravasation (30%) (Figs 1 and 2). Contrast extravasation was more commonly found on the second CTA. The prevalence of image findings is listed in Table 1. Interobserver reliability showed almost perfect agreement regarding viable tumor, pseudoaneurysm, contrast extravasation, and exposed artery, and substantial agreement with respect to necrosis (Table 2). All pseudoaneurysms and contrast extravasation were associated with an exposed artery.

DSA and Management

Twenty-three DSA examinations were performed in 20 patients: 16 examinations were done within 6 hours after CTA, 6 were performed between 6 and 24 hours after CTA, and 1 was performed more than 24 hours after CTA. Two patients with a total of 3 pseudoaneurysms refused to undergo DSA after CTA. Three patients did not show evidence of pseudoaneurysm or extravasation on both the first CTA and DSA, but in 1 a pseudoaneurysm was identified on the second CTA and DSA that were performed 90 days later. The diagnostic performance of CTA compared with DSA in the detection of pseudoaneurysm and contrast extravasation was excellent. Comparison of both DSA and CTA results is shown in Table 3. Only 1 pseudoaneurysm was identified on DSA that was not seen on CTA; this occurred in a patient who had a delayed DSA performed after rebleeding.

Four patients had exposed arteries (including 1 patient with 2 exposed arteries) and refused endovascular management (3 patients at the first episode of bleeding and 1 patient at the second). One patient who received PAO died 63 days later as a result of rebleeding, at which time he declined further treatment. Two patients with exposed arteries on CTA did not undergo embolization immediately because their bleeding stopped before CTA, but massive bleeding subsequently occurred. Although embolizations were performed after resuscitation, they died at 7 and 18 days, respectively, after PAO. Another 2 patients had cardiac arrest be-

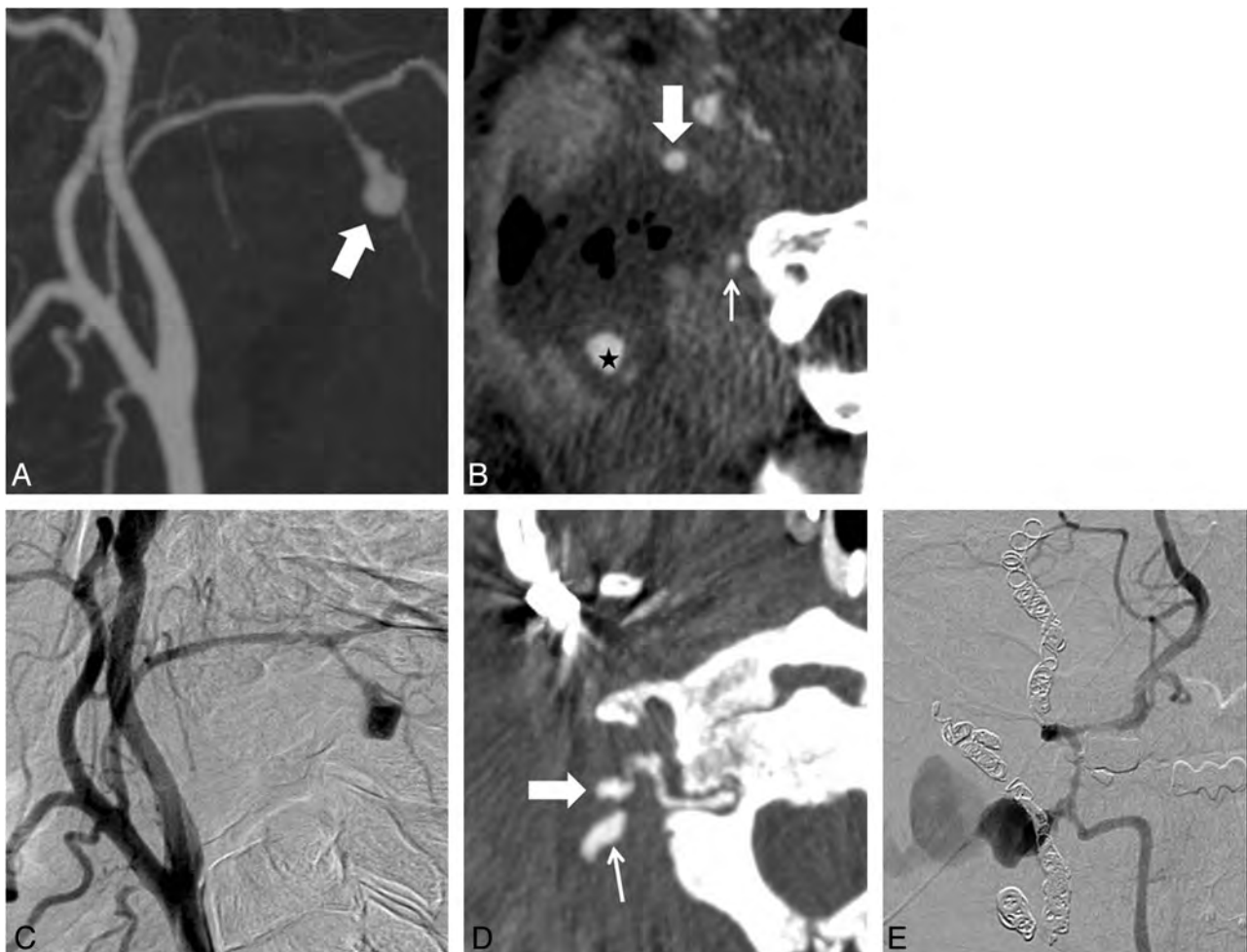


FIG 2. A 42-year-old man with a history of nasopharyngeal cancer. *A*, MIP CTA image shows a pseudoaneurysm (*arrow*) at the right occipital artery. *B*, Oblique reformatted image shows the pseudoaneurysm surrounded by necrotic tissue (*star*). Half of the circumference of the right internal carotid artery (*large arrow*) is exposed to the necrotic tissue, and the unexposed vertebral artery (*small arrow*) is close to the necrotic margin. *C*, DSA confirms the pseudoaneurysm of the occipital artery. The pseudoaneurysm is embolized with coils. At 64 days after treatment, another blowout occurs. *D*, Oblique reformatted CTA image shows a newly developed pseudoaneurysm (*large arrow*) with extravasation from the right vertebral artery (*small arrow*). *E*, DSA confirms the diagnosis.

Table 1: CTA findings in 29 patients with carotid blowout syndrome

Imaging Finding	All CTA	First CTA	Second CTA
Necrosis			
Percentage (ratio)	94% (31/33)	93% (27/29)	100% (4/4)
95% CI	0.79–0.99	0.77–0.99	0.54–1.00
Viable perivascular tumor			
Percentage (ratio)	67% (22/33)	66% (19/29)	75% (3/4)
95% CI	0.50–0.80	0.47–0.80	0.29–0.97
Pseudoaneurysm			
Percentage (ratio)	58% (19/33)	59% (17/29)	50% (2/4)
95% CI	0.41–0.73	0.40–0.75	0.15–0.85
Contrast extravasation			
Percentage (ratio)	30% (10/33)	24% (7/29)	75% (3/4)
95% CI	0.17–0.47	0.12–0.42	0.29–0.97
Exposed artery			
Percentage (ratio)	73% (24/33)	69% (20/29)	100% (4/4)
95% CI	0.56–0.85	0.51–0.83	0.54–1.00

fore CTA and died 1 and 11 days, respectively, after treatment. Two of the 4 patients who refused PAO died from hemorrhagic shock within 1 day, and the other 2 patients died 20 and 32 days, respectively, later. All patients had PAO according to the CTA

Table 2: Interobserver agreement of CTA findings in 29 patients with carotid blowout syndrome

Imaging Finding	κ	95% CI
Necrosis	0.785	0.38–1.00
Viable perivascular tumor	0.864	0.68–1.00
Pseudoaneurysm	0.942	0.83–1.00
Contrast extravasation	0.932	0.80–1.00
Exposed artery	0.807	0.60–1.00

findings, including even 1 patient with negative DSA findings. One patient had conservative treatment and was lost to follow-up after 190 days.

Patient Outcomes

Five (17.5%) of the 29 patients had rebleeding 52 to 162 days after the first CTA. Two had received conservative treatment, and 3 patients had received PAO after the first CBS. Four had CTA studies that showed new and different segmental exposed arteries. The survival curves of the 3 groups of patients with CBS are shown in Fig 3. The median survival time was more than 365 days in group 1 ($n = 9$), 141 days in group 2 ($n = 15$), and 18 days in

Table 3: Comparison of the diagnosis between the 23 studies of CTA and conventional angiography in 20 patients with carotid blowout syndrome

	CTA									
	Pseudoaneurysm		Contrast Extravasation		Viable Perivascular Tumor		Necrosis		Exposed Artery	
	Positive	Negative	Positive	Negative	Positive	Negative	Positive	Negative	Positive	Negative
Positive results on DSA	17	1	6	1	5	0	0	0	0	0
Negative results on DSA	0	5	4	12	11	7	23	0	20	3

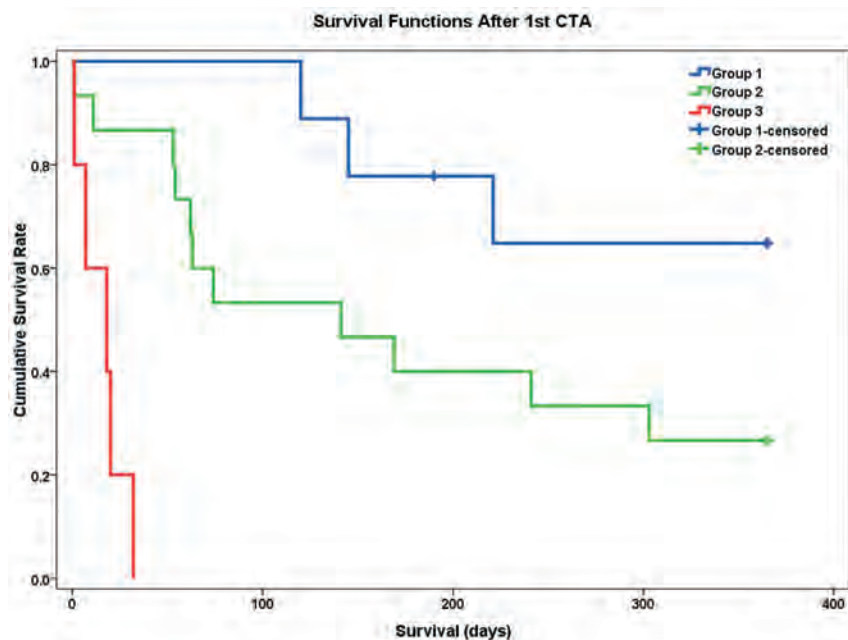


FIG 3. Kaplan-Meier survival curves with pair-wise log-rank test show group 1 (blue, no pseudoaneurysm/extravasation/exposed artery on CTA) has the best survival rate, followed by group 2 (green, with pseudoaneurysm/extravasation/exposed artery on CTA and treated by permanent artery occlusion), and the worst survival is noted in group 3 (red, with pseudoaneurysm/extravasation/exposed artery on CTA but not treated by permanent artery occlusion).

group 3 ($n = 5$). There were significant differences in survival time between group 1 and group 3 ($P < .001$) and between group 2 and group 3 ($P < .001$). The survival duration of group 1 tended to be better than in group 2 but did not reach statistical significance ($P = .056$). There was no significant difference in survival duration between patients with ($n = 19$; median survival duration, 145 days) and without ($n = 10$; median survival duration, 74 days) visible viable tumors ($P = .349$), between patients with ($n = 18$; median survival duration, 145 days) and without ($n = 11$; median survival duration, 74 days) radical neck dissection, between patients with ($n = 25$; median survival duration, 141 days) and without ($n = 4$; median survival duration > 365 days) irradiation ($P = .207$), and between patients with ($n = 22$; median survival duration, 120 days) and without ($n = 7$; median survival duration > 365 days) chemotherapy ($P = .247$). Only 2 patients had no necrosis, and they both survived for more than 1 year.

DISCUSSION

In our study, we found that CTA has a high accuracy for the diagnosis of impending CBS. Pseudoaneurysm, contrast extravasation, and exposed arteries on CTA were the 3 main indicators for aggressive treatment in patients with impending CBS. In patients with impending CBS with these 3 indicators, those treated

with urgent PAO usually had a better outcome than those who received no or delayed treatment.

In our series, only patients with impending CBS underwent CTA, and the percentage of those with contrast extravasation was not high (24.1% on initial CTA and 30% on all CTA). CTA showed contrast extravasation in 9 of 21 pseudoaneurysms and 10 of 26 exposed arteries. Among the 10 contrast extravasations that were shown on CTA, only 6 were identified on DSA, and 1 contrast extravasation was shown on DSA but not on CTA. This finding might be the result of intermittent bleeding and/or different timing of CTA vs DSA. Pseudoaneurysm was the most consistent finding between DSA and CTA. One pseudoaneurysm was shown on DSA but not on CTA, and this patient's DSA was done with delay. This result suggests that CTA is comparable to DSA in the detection of pseudoaneurysm in impending CBS. Necrosis and exposed arteries were the 2 most common CTA findings. An artery surrounded by necrotic tissue is prone to the development

of a pseudoaneurysm and bleeding.²⁶ DSA is essentially a study of the lumen of the vessel, and when extraluminal necrosis is present and is exposing the segmental artery, the lumen may appear angiographically normal. In our series, all pseudoaneurysms and extravasations were shown on an exposed arterial segment, and exposed arteries could only be detected by CTA, not by DSA. We suggest that an exposed artery is the most significant indicator on CTA for patients with CBS. DSA cannot detect an exposed artery and, in addition, might underestimate the extent of the lesion for PAO.

The overall incidence of recurrent CBS has been reported to be 26% and is mostly the result of progressive disease or treatment failure.²⁷ The incidence of recurrent CBS has been described as similar in patients who have undergone PAO or endovascular stent placement.^{16,17} In our series, the rate of recurrent CBS was approximately 17.5%, which is less than that in other published reports. We performed PAO according to CTA findings in the first CBS, and this might decrease the rate of treatment failure and occlude the vessel to a more accurate extent in our series. We recommend CTA to depict an exposed artery in patients with impending CBS, if possible.

CTA can noninvasively demonstrate the current status of diseased vessels without stroke risk in patients with episodic but clinically stable CBS, and prognostic information is rapidly avail-

able. CTA can define groups of patients who had bleeding but do not demonstrate the 3 indicators for urgent management (group 1). In this group, the outcome was relatively good even without PAO, and we believe that treatment of patients with impending CBS can be guided appropriately by CTA findings.

The survival duration was significantly better in group 1 than in group 3, indicating that patients without the 3 indicators on CTA had better outcomes than those with such indicators. The survival time was significantly better in group 2 than in group 3, indicating that the outcome in patients with impending CBS with these 3 indicators who received PAO was better than in those who received no or delayed treatment. The survival time was better in group 1 than in group 2, though the difference was not statistically significant. This finding indicates that PAO can improve the survival time in patients with these 3 indicators, or the progression of disease may cause new vascular lesions or death in both groups. A question that warrants further study is whether PAO of a normal-appearing artery very close to necrotic tissue can prevent bleeding in the future.

There were some limitations of our study that should be considered. This study was retrospective, and the number of patients was small because impending CBS is not a common disease. We did not perform 3D rotational angiography, which might have decreased the sensitivity of DSA. In addition, diagnosis of the subtle exposed arteries or small pseudoaneurysms on CTA is time consuming and experience dependent. Finally, we did not include patients with acute CBS who required immediate PAO; thus, the results can be only applied to patients who are relatively stable hemodynamically.

CONCLUSIONS

CTA demonstrates imaging findings not available with DSA that have potentially useful prognostic information for patients with impending CBS. Contrast extravasation, pseudoaneurysm, and exposed artery were all associated with poorer outcomes, with an exposed artery being the most significant predictor. Endovascular treatment should be performed as soon as possible in patients with impending CBS with these findings. If the above findings are absent, then conservative treatment can result in acceptable outcomes.

ACKNOWLEDGMENTS

Thanks to National Science Council (NSC) support for the Center for Dynamical Biomarkers and Translational Medicine, National Central University, Taiwan (NSC 101-2911-I-008-001).

Disclosures: Adam Huang—RELATED: Grant: National Science Council, Taiwan,* Comments: Government research funds; UNRELATED: Patents (planned, pending or issued): Pending patent applications: We have one U.S. patent application and 2 Taiwanese patent applications for removing bone from CT angiography imaging. *Money paid to institution.

REFERENCES

1. Chaloupka JC, Putman CM, Citardi MJ, et al. **Endovascular therapy for the carotid blowout syndrome in head and neck surgical patients: diagnosis and managerial considerations.** *AJNR Am J Neuroradiol* 1996;17:843–52
2. Maran AGD, Amin M, Wilson JA. **Radical neck dissection: a 19-year experience.** *J Laryngol Otol* 1989;103:760–64
3. Fonkalsrud EW, Sanchez M, Zerubavel R, et al. **Serial changes in arterial structure following radiation therapy.** *Surg Gynecol Obstet* 1977;145:395–400
4. Ernemann U, Herrmann C, Plontke S, et al. **Pseudoaneurysm of the superior thyroid artery following radiotherapy for hypopharyngeal cancer.** *Ann Otol Rhinol Laryngol* 2003;112:188–90
5. Chaloupka JC, Roth TC, Putman CM, et al. **Recurrent carotid blowout syndrome: diagnostic and therapeutic challenges in a newly recognized subgroup of patients.** *AJNR Am J Neuroradiol* 1999;20:1069–677
6. Moore OS, Klarlan M, Sigler LS. **Factors influencing the safety of carotid ligation.** *Am J Surg* 1969;118:666–68
7. Citardi MJ, Chaloupka JC, Son YH, et al. **Management of carotid artery rupture by monitored endovascular therapeutic occlusion (1988–1994).** *Laryngoscope* 1995;105:1086–92
8. Dandy WE. **Intracranial aneurysm of the internal carotid artery cured by operation.** *Ann Surg* 1938;107:654–59
9. Dandy WE. **Internal carotid arterial aneurysms in the carotid canal: diagnosis and treatment.** *Arch Surg* 1942;45:521–33
10. Fox AJ, Viñuela F, Pelz DM, et al. **Use of detachable balloons for proximal artery occlusion in the treatment of unclippable cerebral aneurysms.** *J Neurosurg* 1987;66:40–46
11. Chaloupka JC, Putman CM. **Endovascular therapy of surgical diseases of the cranial base.** *Clin Plast Surg* 1995;22:417–50
12. Lesley WS, Chaloupka JC, Weigle JB, et al. **Preliminary experience with endovascular reconstruction for the management of carotid blowout syndrome.** *AJNR Am J Neuroradiol* 2003;24:975–81
13. Mathis JM, Barr JD, Jungreis CA, et al. **Temporary balloon test occlusion of the internal carotid artery: experience in 500 cases.** *AJNR Am J Neuroradiol* 1995;16:749–54
14. Standard SC, Ahuja A, Guterman LR, et al. **Balloon test occlusion of the internal carotid artery with hypotensive challenge.** *AJNR Am J Neuroradiol* 1995;16:1453–58
15. Dare AO, Chaloupka JC, Putman CM, et al. **Failure of the hypotensive test during temporary balloon test occlusion of the internal carotid artery to predict delayed hemodynamic ischemia after therapeutic carotid occlusion.** *Surg Neurol* 1998;50:147–56
16. Warren FM, Cohen JJ, Nesbit GM, et al. **Management of carotid “blowout” with endovascular stent grafts.** *Laryngoscope* 2002;112:428–33
17. Simental A, Johnson JT, Horowitz M. **Delayed complications of endovascular stenting for carotid blowout.** *Am J Otolaryngol* 2003;24:417–19
18. Kim HS, Lee DH, Kim HJ, et al. **Life-threatening common carotid artery blowout: rescue treatment with a newly designed self-expanding covered nitinol stent.** *Br J Radiol* 2006;79:226–31
19. Gaba RC, West DL, Bui JT, et al. **Covered stent treatment of carotid blowout syndrome.** *Semin Intervent Radiol* 2007;24:47–52
20. Chang FC, Limg JF, Luo CB, et al. **Patients with head and neck cancers and associated postirradiated carotid blowout syndrome: endovascular therapeutic methods and outcomes.** *J Vasc Surg* 2008;47:936–45
21. Becker KJ, Baxter AB, Bybee HM, et al. **Extravasation of radiographic contrast is an independent predictor of death in primary intracerebral hemorrhage.** *Stroke* 1999;30:2025–32
22. Goldstein JN, Fazen LE, Snider R, et al. **Contrast extravasation on CT angiography predicts hematoma expansion in intracerebral hemorrhage.** *Neurology* 2007;68:889–94
23. Kim J, Smith A, Hemphill JC 3rd, et al. **Contrast extravasation on CT predicts mortality in primary intracerebral hemorrhage.** *AJNR Am J Neuroradiol* 2008;29:520–25
24. Li N, Wang Y, Wang W, et al. **Contrast extravasation on computed tomography angiography predicts clinical outcome in primary intracerebral hemorrhage: a prospective study of 139 cases.** *Stroke* 2011;42:3441–46
25. Demchuk AM, Dowlatshahi D, Rodriguez-Luna D, et al. **Prediction of haematoma growth and outcome in patients with intracerebral haemorrhage using the CT-angiography spot sign (PREDICT): a prospective observational study.** *Lancet Neurol* 2012;11:307–14
26. Chin SC, Jen YM, Chen CY, et al. **Necrotic nasopharyngeal mucosa: an ominous MR sign of a carotid artery pseudoaneurysm.** *AJNR Am J Neuroradiol* 2005;26:414–16
27. Chaloupka JC, Roth TC, Putman CM, et al. **Recurrent carotid blowout syndrome: diagnostic and therapeutic challenges in a newly recognized subgroup of patients.** *AJNR Am J Neuroradiol* 1999;20:1069–77

Multilevel Assessment of Atherosclerotic Extent Using a 40-Section Multidetector Scanner after Transient Ischemic Attack or Ischemic Stroke

L. Mechtouff, L. Boussel, S. Cakmak, J.-L. Lamboley, M. Bourhis, N. Boublay, A.-M. Schott, L. Derex, T.-H. Cho, N. Nighoghossian, and P.C. Douek

ABSTRACT

BACKGROUND AND PURPOSE: The first part of this study assessed the potential of MDCT with a CTA examination of the aorta and the coronary, cervical, and intracranial vessels in the etiologic work-up of TIA or ischemic stroke compared with established imaging methods. The objective of the second part of this study was to assess the atherosclerotic extent by use of MDCT in these patients.

MATERIALS AND METHODS: From August 2007 to August 2011, a total of 96 patients with ischemic stroke or TIA without an evident cardioembolic source were enrolled. All patients underwent MDCT. Atherosclerotic extent was classified in 0, 1, 2, 3, and 4 atherosclerotic levels according to the number of arterial territories (aortic arch, coronary, cervical, intracranial) affected by atherosclerosis defined as $\geq 50\%$ cervical, intracranial, or coronary stenosis or ≥ 4 -mm aortic arch plaque.

RESULTS: There were 91 patients who had an interpretable MDCT. Mean age was 67.4 years (± 11 years), and 75 patients (83.3%) were men. The prevalence of 0, 1, 2, 3, and 4 atherosclerotic levels was 48.3%, 35.2%, 12.1%, 4.4%, and 0%, respectively. Aortic arch atheroma was found in 47.6% of patients with 1 atherosclerotic level. The combination of aortic arch atheroma and cervical stenosis was found in 63.6% of patients with ≥ 2 atherosclerotic levels. Patients with ≥ 2 atherosclerotic levels were older than patients with < 2 atherosclerotic levels ($P = .04$) in univariate analysis.

CONCLUSIONS: MDCT might be useful to assess the extent of atherosclerosis. It could help to screen for high-risk patients who could benefit from a more aggressive preventive strategy.

ABBREVIATION: ECG = electrocardiogram

Assessment of atherosclerosis from the heart to the brain in patients with stroke may allow an optimal selection of high-risk patients who could benefit from a more aggressive preventive strategy. Several studies have evaluated the accuracy of MDCT

with CTA examination of the aorta and coronary, cervical, and intracranial vessels to detect atherosclerosis.¹⁻⁵

The first part of our study was a single-center, prospective, open-pilot study that was designed to assess MDCT with a CTA examination of the aorta and coronary, cervical, and intracranial vessels in the etiologic work-up of TIA and acute ischemic stroke compared with established imaging methods. Clinical and radiologic methods have been described elsewhere.⁶ In brief, patients 28–90 years old who were admitted to the hospital for a recent TIA or acute ischemic stroke without evident cardioembolic source in the Lyon Stroke Unit between August 1, 2007, and April 30, 2008, were included in this study. The period of inclusion was later extended to August 1, 2011. All patients had an MDCT examination with CTA of the aorta and coronary, cervical, and intracranial vessels compared with transthoracic echocardiography and transesophageal echocardiography, duplex ultrasonography of the cervical vessels, and MRA of the cervical and intracranial vessels. MDCT was not a part of the initial acute stroke assessment but was done within 7 days. We obtained approval from our local ethics committee and institutional review board and informed

Received February 21, 2013; accepted after revision April 25.

From the Stroke Unit (L.M., L.D., T.-H.C., N.N.), Hôpital Pierre Wertheimer, Hospices Civils de Lyon, Lyon, France; Radiology Department (L.B.), Hôpital de la Croix-Rousse, Hospices Civils de Lyon, Lyon, France; CNRS UMR 5220–INSERM U1044–Université Lyon 1, Villeurbanne, France (L.B., L.D., T.-H.C., N.N., P.C.D.); Stroke Unit (S.C.), Centre Hospitalier Villefranche-sur-Saône, France; Radiology Department (J.-L.L.), Hôpital d'instruction des Armées Desgenettes, Lyon, France; Cellule Recherche PAM Imagerie (M.B.), Hospices Civils de Lyon, Lyon, France; Pôle Information Médicale Evaluation Recherche (N.B.), Hospices Civils de Lyon, Lyon, France; Equipe d'Accueil 4129, Université Lyon 1, Villeurbanne, France; Hospices Civils de Lyon (A.-M.S.), Pôle Information Médicale Evaluation Recherche, RECIF, Université Lyon 1, Villeurbanne, France.

This work was supported by the Hospices Civils de Lyon.

Abstract previously presented at: 17th French Neurovascular Society meeting, European Stroke Conference 2012.

Please send correspondence to Laura Mechtouff, Stroke Unit, Hôpital Pierre Wertheimer, Hospices Civils de Lyon, 59 Boulevard Pinel, 69677 Lyon Bron CEDEX, France; e-mail: laura.mechtouff@chu-lyon.fr

<http://dx.doi.org/10.3174/ajnr.A3760>

consent from each patient. It has been demonstrated that MDCT is feasible and accurate for the identification of stroke causes though its sensitivity for the detection of minor cardiac sources is limited.

The objective of the second part of our study was to assess the global atherosclerotic extent by using MDCT in these patients.

MATERIALS AND METHODS

Research Design

In the second part of our study, we used data collected in the first part of the study.⁶

Imaging Protocols

We performed contrast-enhanced MDCT by using a Brilliance 40 scanner (Philips Healthcare, Best, the Netherlands), with iomeprol (Iomeron 400; Bracco Diagnostics, Milan, Italy) injected into the right cubital vein with an 18-gauge catheter. The patient was placed in the supine, head-first position. A 2-step protocol was performed: first, electrocardiogram (ECG)-gated aortic and heart acquisitions were performed in the head-to-feet direction, encompassing the aortic and heart area from the top of the aortic arch to the diaphragm. The following parameters were used: 40 detectors, individual detector width of 0.625 mm, retrospective ECG gating, tube voltage of 120 kV, tube current of 300 mAs, pitch of 0.2, and half-rotation reconstruction. Iomeprol 70 mL and then saline solution 60 mL were injected at 4 mL/s. A bolus-tracking method was used with an attenuation threshold of 200 Hounsfield units in the ascending aorta. Reconstruction parameters for the axial sections were a 1.5-mm effective section thickness, 1-mm increments, a reconstruction filter Cardiac B, and an adapted field of view. Retrospective ECG-gated reconstruction was performed at 40% and 75% of the R-R interval. Then, 2 minutes later, a non-ECG-gated acquisition from the aortic arch to the vertex (approximately 50 cm) was performed with the following parameters: feet-to-head direction, section thickness of 1.2 mm, pitch of 1.2, tube voltage of 120 kV, amperage of 300 mAs per section, reconstruction filter B, and the bolus tracker set on the aortic arch with an attenuation threshold at 200 Hounsfield units. Iomeprol 50 mL and then saline solution 60 mL were injected at 4 mL/s, for a total injected contrast material volume of 120 mL. The patient underwent imaging with the arms over the head during the aortic and heart acquisitions and with the arms at the sides during the second acquisition. General guidelines for ECG-gated cardiac MDCT were followed regarding the qualifications of the personnel, radiation dose monitoring, and the safety rules for contrast agent and β -blocker administration.⁷⁻⁹ β -Blockers (esmolol hydrochloride; Brevibloc; Baxter, Deerfield, Illinois) (0.5–1.0 mg per kilogram of body weight) were administered intravenously, if necessary, when the heart rate was higher than 80 beats per minute. CT was performed even in cases of atrial fibrillation. The total radiation dose and the heart rate of each patient during the examination were recorded. The thyroid gland was irradiated once during the acquisition from the aortic arch to the vertex.

Imaging Evaluation

The diagnostic work-up was focused on the following vascular abnormalities by use of MDCT with CTA:

- Atherosclerotic lesion of the carotid arteries leading to $\geq 50\%$ stenosis. The degree of carotid stenosis was measured with the North American Symptomatic Carotid Endarterectomy Trial (NASCET) criteria.¹⁰ A measure (measure 1) was taken of the diameter of the narrowest portion of the cervical ICA in the axial plane. This was compared with the maximal diameter (measure 2) of the cervical ICA distal to the carotid bulb at a location in which the imaging plane was orthogonal to the artery, the arterial walls were parallel, and where there was no arterial disease. The degree of cross-sectional stenosis was calculated in percent as: percent stenosis $(1 - [\text{measure 1}/\text{measure 2}]) \times 100\%$, analogous to the method used in NASCET. In cases of poststenotic dilation of the ICA, we used as a denominator for the ratio calculation the diameter of the internal carotid well beyond the bulb, where the walls are parallel. Near-occlusion cases were defined as the presence of notable stenosis of the ICA bulb and distal ICA caliber reduction, compared with 1) expected size, 2) the contralateral ICA, and 3) the ipsilateral external carotid artery). In these cases, we did not do a ratio calculation and arbitrarily assigned as 95% stenosis as established in NASCET.¹⁰⁻¹²
- Atherosclerotic lesion of the vertebral arteries leading to $\geq 50\%$ stenosis
- Aortic arch atheroma of > 4 mm
- Intracranial artery stenosis $\geq 50\%$
- Coronary artery stenosis $\geq 50\%$

Atherosclerotic extent was classified in 0, 1, 2, 3, and 4 atherosclerotic levels according to the number of arterial territories (aortic, coronary, cervical, intracranial) affected by at least 1 vascular abnormality as we described previously.

Statistical Analysis

Continuous variables were expressed as mean (standard deviation), and categorical variables were expressed as percentages. We compared continuous variables by using the *t* test or the Mann-Whitney test where appropriate, and categorical variables by using the Pearson χ^2 test or the Fisher exact test where appropriate. The associations between atherosclerotic extent (< 2 vs ≥ 2 atherosclerotic levels) and main vascular risk factors were measured by calculation of adjusted odds ratios and 95% confidence intervals by logistic regression analyses.

Multivariable models were adjusted for age, sex, diabetes, hypertension, dyslipidemia, and tobacco. The distribution of arterial disease combinations in patients with ≥ 2 atherosclerotic levels was compared by use of the Fisher exact test. A *P* value $< .05$ was considered statistically significant.

We performed statistical analysis by using STATA, version 11.0 (StataCorp, College Station, Texas) and R software, version 2.10.1 (<http://www.r-project.org/>).

RESULTS

Ninety-six patients were included. MDCT with CTA examination of the heart, aorta, and the cervical and intracranial vessels was not

Table 1: Demographic and medical data according to number of atherosclerotic levels in 91 patients

Number of atherosclerotic levels	0	1	2	3	All
Number of patients, <i>n</i> (%)	44 (48.3%)	32 (35.2%)	11 (12.1%)	4 (4.4%)	91
Age, y, mean (SD)	63.6 (10.6)	70.1 (10.3)	72.5 (10.8)	72.5 (10.0)	67.4 (11.0)
Male sex, <i>n</i> (%)	36 (83.7)	25 (78.1)	10 (90.9)	4 (100.0)	75 (83.3)
TIA, <i>n</i> (%)	27 (62.8)	17 (53.1)	6 (54.6)	3 (75.0)	53 (58.9)
Stroke					
Initial NIHSS, mean (SD)	5.2 (3.9)	7.7 (5.4)	6.5 (5.8)	0.3 (0.6)	6.1 (4.9)
Hypertension, <i>n</i> (%)	15 (34.9)	16 (50.0)	5 (45.5)	2 (50.0)	38 (42.2)
LDL cholesterol, g/L	1.23 (0.3)	1.20 (0.4)	1.14 (0.3)	1.50 (0.4)	1.22 (0.4)
Smoking, <i>n</i> (%)					
Former	7 (16.3)	8 (25.8)	3 (27.3)	1 (25.0)	19 (21.4)
Current	11 (25.6)	6 (19.3)	2 (18.2)	2 (50.0)	21 (23.6)
Never	25 (58.1)	17 (54.8)	6 (54.6)	1 (25.0)	49 (55.1)
CRP, mg/L (%)	10.0 (27.0)	6.1 (7.5)	4.5 (4.3)	3.0 (1.6)	7.7 (19.6)
Fibrinogen, g/L (%)	3.4 (1.0)	3.6 (0.8)	3.2 (1.1)	3.6 (0.3)	3.5 (1.0)
History of vascular disease (%)	9 (20.9)	11 (35.5)	6 (54.6)	0	26 (29.2)

Note:—CRP indicates C-reactive protein; LDL, low-density lipoprotein; SD, standard deviation.

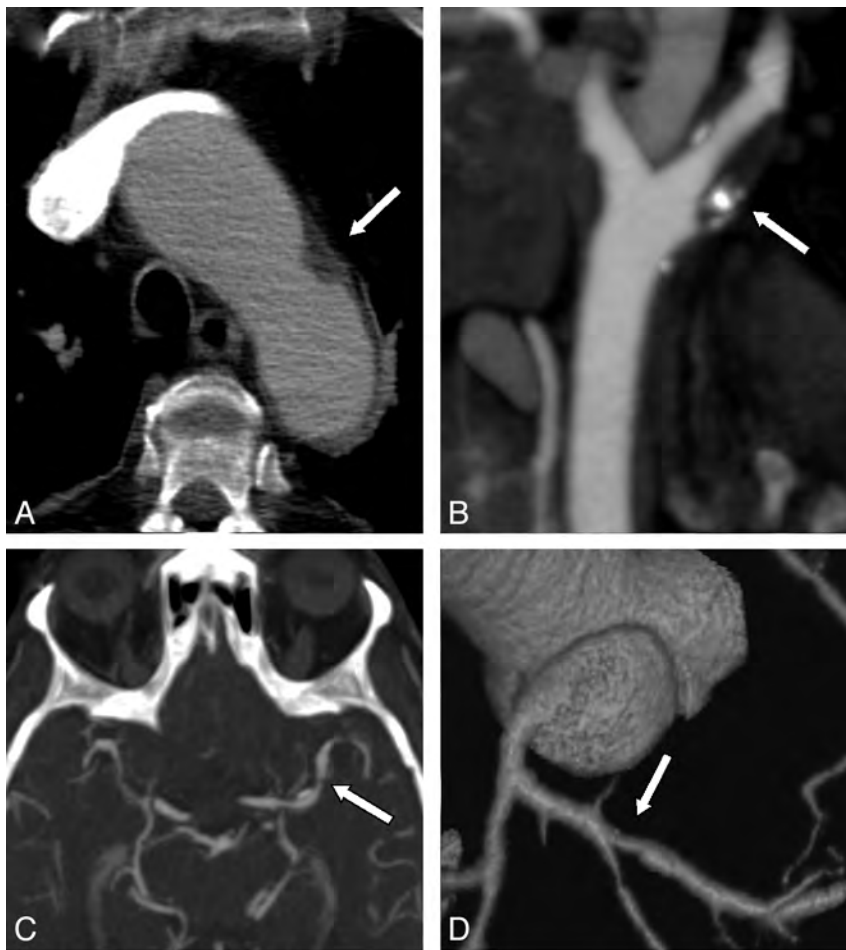


FIG 1. MDCT images (40 sections) show atherosclerosis of the aortic arch (A), internal carotid artery (B), left middle cerebral artery (C), and circumflex coronary artery (D).

done or was not interpretable in 5 patients. The characteristics of the remaining 91 patients are shown in Table 1. Mean age was 67.4 (\pm 11.0) years, 75 patients (83.3%) were men, 38 (41.1%) were diagnosed with ischemic stroke, and 53 (58.9%) were diagnosed with a TIA. The mean radiation dose to the patients was 18.7 (\pm 5.0) mSv.

The prevalence of \geq 4 mm aortic arch atheroma, \geq 50% coronary artery stenosis, \geq 50% cervical artery stenosis, and \geq 50% intracranial artery stenosis was 23.3%, 14.1%, 23.9%, and 13.6%, respectively (Fig 1).

Forty-four patients (48.3%) had no atherosclerotic level. The prevalence of 1, 2, 3, and 4 atherosclerotic levels was 35.2%, 12.1%, 4.4%, and 0%, respectively. Demographic and clinical data according to the number of atherosclerotic levels are detailed in Table 2. Results did not differ according to diagnosis (TIA vs ischemic stroke) ($P = .75$). The number of atherosclerotic levels was not associated with classic vascular risk factors besides age. Patients with \geq 2 atherosclerotic levels were older than patients with $<$ 2 atherosclerotic levels ($P = .04$). After adjustment for main confounding variables, this association was not found.

Among patients with 1 atherosclerotic level, 47.6% had \geq 4 mm aortic arch atheroma, 20.7% had \geq 50% coronary artery stenosis, 26.7% had \geq 50% cervical artery stenosis, and 26.7% had \geq 50% intracranial artery stenosis. Among patients with 2 atherosclerotic levels, 63.6% had both \geq 4 mm aortic arch atheroma and \geq 50% cervical artery stenosis. Among patients with 3 atherosclerotic levels, 50% had both \geq 4 mm aortic arch atheroma and \geq 50% cervical and coronary artery stenosis. The distribution of artery disease combinations in patients with \geq 2 atherosclerotic levels was significantly different ($P = .022$) (Fig 2). Aortic arch atheroma \geq 4 mm and \geq 50% cervical artery stenosis were most often associated.

DISCUSSION

We have shown that 16.5% of patients with stroke or TIA without evident cardioembolic source have \geq 2 atherosclerotic levels by use of MDCT. The combination of \geq 4-mm aortic arch atheroma and \geq 50% cervical stenosis was more often found.

The extent of atherosclerosis is heavier than in a previous study assessing 3 arterial levels (aorta, coronary, and cervical arteries) by use of a CTA protocol in patients with suspicion for TIA or stroke.¹³ In this previous study, among 79 patients, 26 (33%) had 1 atherosclerotic level, mainly a \geq 50% coronary artery stenosis. Only 7 patients (9%) had at least 2 atherosclerotic locations. The enrollment of patients with suspicion of TIA or stroke confirmed in only 60% of cases and the lack of assess-

Table 2: Number of atherosclerotic levels and risk factors

	Number of Atherosclerotic Levels		P Value
	< 2	≥2	
Number of patients	76	15	
Age, y, mean (SD)	66.4 (10.9)	72.5 (10.2)	.04
Sex			
Female, n (%)	14 (18.4)	1 (6.4)	.45
Male, n (%)	61 (81.3)	14 (93.3)	
Hypertension, n (%)	31 (41.3)	7 (46.7)	.77
Diabetes, n (%)	9 (12)	0	.34
LDL cholesterol (g/L), mean (SD)	1.22 (0.4)	1.23 (0.4)	.9
Smoking			
Former, n (%)	15 (20.3)	4 (26.7)	.75
Current, n (%)	17 (23.0)	4 (26.7)	
Never, n (%)	42 (56.8)	7 (46.7)	
CRP (mg/L), mean (SD)	8.4 (21.4)	4 (3.8)	.83
History of vascular disease, n (%)	20 (27.0)	6 (40)	.07

Note:—CRP indicates C-reactive protein; LDL, low-density lipoprotein; SD, standard deviation.

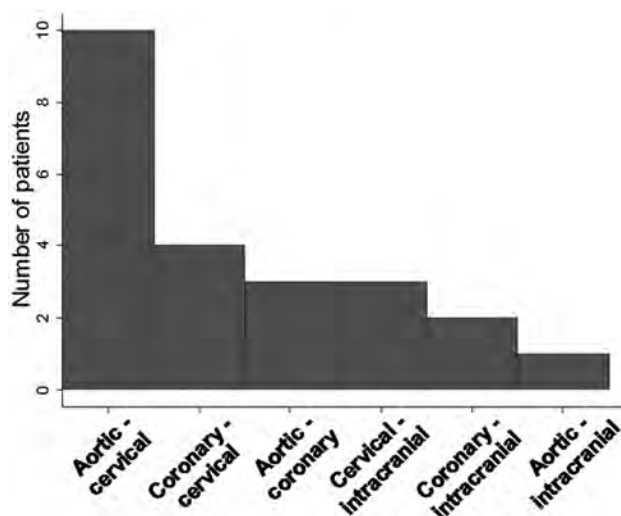


FIG 2. Arterial disease combinations in patients with ≥ 2 atherosclerotic levels.

ment of the intracranial arteries might account for this difference.

The association between aortic and cervical atherosclerosis was not found by MDCT in this previous study (Adraktas et al)¹³ but has been commonplace in studies using transesophageal echocardiography and carotid ultrasonography in patients with stroke.¹⁴⁻¹⁶ A prospective study and a case-control study have shown that aortic plaques were more likely detected in patients with stroke with $\geq 50\%$ carotid artery stenosis compared with $< 50\%$ carotid artery stenosis.^{14,15} Similar results have been shown with mobile thrombi. This association was also found in a third study.¹⁶

The distribution of atherosclerotic disease is in line with previous studies using MDCT in patients with stroke apart from cervical stenosis. Studies have detected $\geq 50\%$ intracranial artery stenosis in 10% of cases¹⁷ and ≥ 4 -mm aortic arch plaques in approximately 20% of cases,^{4,18} which could have contributed to stroke occurrence. Asymptomatic coronary artery disease has also

been detected in 18%–37.5% of cases.¹⁸⁻²² The prevalence of at least 1 $\geq 50\%$ cervical artery stenosis assessed by MDCT in patients with stroke is not available.

The main limitation of our CT protocol was the required radiation dose. Despite an attempt to lower the dose by decreasing the milliamper-second setting (from 300 mAs per section), the retrospective helical mode we used for cardiac examination led to high radiation exposure.

A MDCT protocol allows assessment of not only the aortic, cervical, and intracranial arteries as a usual etiologic work-up of TIA and stroke but also of the coronary arteries. The rate of cardiac mortality is twice as high as cerebrovascular mortality in patients with stroke.^{23,24} Detection of asymptomatic coronary artery stenosis could lead to optimized preventive strategies. Indeed, some anatomic patterns of coronary artery disease such as significant left main stenosis or multivessel disease are strong indications for revascularization.²⁵

CONCLUSIONS

According to the 2 parts of our study, MDCT might be used simultaneously for the etiologic work-up of TIA and ischemic stroke and for assessment of the extent of atherosclerosis. It could help to screen for high-risk patients who could benefit from more aggressive preventive strategies. More research is needed to assess whether the extent of atherosclerosis is associated with classic vascular risk factors and whether it could be an independent prognostic factor regarding vascular outcome in patients with stroke.

Disclosures: Philippe Charles Douek—UNRELATED: Consultancy: Genfit; Grants/Grants Pending: ANR*; Patents (planned, pending or issued): MR micro antenna (2002) not related to the work; Payment for Development of Educational Presentations: Philips; Comments: workshop on cardiac CT (image processing software in demonstration during workshop); Travel/Accommodations/Meeting Expenses Unrelated to Activities Listed: Philips; Comments: Funding for travel to Radiological Society of North America 2012. *Money paid to institution.

REFERENCES

- Nonent M, Serfaty JM, Nighoghossian N, et al. **Concordance rate differences of 3 noninvasive imaging techniques to measure carotid stenosis in clinical routine practice: results of the CARMEDAS multicenter study.** *Stroke* 2004;35:682–86
- Hamon M, Morello R, Riddell JW, et al. **Coronary arteries: diagnostic performance of 16- versus 64-section spiral CT compared with invasive coronary angiography—meta-analysis.** *Radiology* 2007;245:720–31
- Nguyen-Huynh MN, Wintermark M, English J, et al. **How accurate is CT angiography in evaluating intracranial atherosclerotic disease?** *Stroke* 2008;39:1184–88
- Ko Y, Park JH, Yang MH, et al. **Significance of aortic atherosclerotic disease in possibly embolic stroke: 64-multidetector row computed tomography study.** *J Neurol* 2010;257:699–705
- Wardlaw JM, Stevenson MD, Chappell F, et al. **Carotid artery imaging for secondary stroke prevention: both imaging modality and rapid access to imaging are important.** *Stroke* 2009;40:3511–17
- Boussel L, Cakmak S, Wintermark M, et al. **Ischemic stroke: etiologic work-up with multidetector CT of heart and extra- and intracranial arteries.** *Radiology* 2011;258:206–12
- Budoff MJ, Cohen MC, Garcia MJ, et al. **ACCF/AHA clinical competence statement on cardiac imaging with computed tomography and magnetic resonance.** *Circulation* 2005;112:598–617
- Schroeder S, Achenbach S, Bengel F, et al. **Cardiac computed tomography: indications, applications, limitations, and training requirements—report of a writing group deployed by the Working**

Group Nuclear Cardiology and Cardiac CT of the European Society of Cardiology and the European Council of Nuclear Cardiology. *Eur Heart J* 2008;29:531–56

9. Weinreb JC, Larson PA, Woodard PK, et al. **American College of Radiology clinical statement on noninvasive cardiac imaging.** *Radiology* 2005;235:723–27
10. North American Symptomatic Carotid Endarterectomy Trial (NASCET). **Methods, patient characteristics, and progress.** *Stroke* 1991;22:711–20
11. Bartlett ES, Walters TD, Symons SP, et al. **Diagnosing carotid stenosis near-occlusion by using CT angiography.** *AJNR Am J Neuroradiol* 2006;27:632–37
12. Fox AJ. **How to measure carotid stenosis.** *Radiology* 1993;186:316–18
13. Adraktas DD, Brasic N, Furtado AD, et al. **Carotid atherosclerosis does not predict coronary, vertebral, or aortic atherosclerosis in patients with acute stroke symptoms.** *Stroke* 2010;41:1604–09
14. Harloff A, Handke M, Geibel A, et al. **Do stroke patients with normal carotid arteries require TEE for exclusion of relevant aortic plaques?** *J Neurol Neurosurg Psychiatry* 2005;76:1654–58
15. Demopoulos LA, Tunick PA, Bernstein NE, et al. **Protruding atheromas of the aortic arch in symptomatic patients with carotid artery disease.** *Am Heart J* 1995;129:40–44
16. Amarenco P, Cohen A, Tzourio C, et al. **Atherosclerotic disease of the aortic arch and the risk of ischemic stroke.** *N Engl J Med* 1994;331:1474–79
17. Homburg PJ, Plas GJ, Rozie S, et al. **Prevalence and calcification of intracranial arterial stenotic lesions as assessed with multidetector computed tomography angiography.** *Stroke* 2011;42:1244–50
18. Cho HJ, Lee JH, Kim YJ, et al. **Comprehensive evaluation of coronary artery disease and aortic atherosclerosis in acute ischemic stroke patients: usefulness based on Framingham risk score and stroke subtype.** *Cerebrovasc Dis* 2011;31:592–600
19. Calvet D, Touzé E, Varenne O, et al. **Prevalence of asymptomatic coronary artery disease in ischemic stroke patients: the PRECORIS study.** *Circulation* 2010;121:1623–29
20. Hoshino A, Nakamura T, Enomoto S, et al. **Prevalence of coronary artery disease in Japanese patients with cerebral infarction: impact of metabolic syndrome and intracranial large artery atherosclerosis.** *Circ J* 2008;72:404–08
21. Yoon YE, Chang HJ, Cho I, et al. **Incidence of subclinical coronary atherosclerosis in patients with suspected embolic stroke using cardiac computed tomography.** *Int J Cardiovasc Imaging* 2011;27:1035–44
22. Seo WK, Yong HS, Koh SB, et al. **Correlation of coronary artery atherosclerosis with atherosclerosis of the intracranial cerebral artery and the extracranial carotid artery.** *Eur Neurol* 2008;59:292–98
23. Dharmoon MS, Sciacca RR, Rundek T, et al. **Recurrent stroke and cardiac risks after first ischemic stroke: the Northern Manhattan Study.** *Neurology* 2006;66:641–46
24. Touzé E, Varenne O, Chatellier G, et al. **Risk of myocardial infarction and vascular death after transient ischemic attack and ischemic stroke: a systematic review and meta-analysis.** *Stroke* 2005;36:2748–55
25. Wijns W, Kohl P, Danchin N, et al. **Guidelines on myocardial revascularization: Task Force on Myocardial Revascularization of the European Society of Cardiology (ESC) and the European Association for Cardio-Thoracic Surgery (EACTS).** *Eur Heart J* 2010;31:2501–55

Clinical Significance of Trochlear Calcifications in the Orbit

K. Buch, R.N. Nadgir, A.D. Tannenbaum, A. Ozonoff, A. Fujita, and O. Sakai

ABSTRACT

BACKGROUND AND PURPOSE: Trochlear calcification is frequently seen on CT scans that include the orbits, but prior studies linking this finding to diabetes mellitus were based on selected populations by using relatively thick sections. We assessed the relationship between trochlear calcification and diabetes mellitus and other chronic medical conditions in an unrestricted population by using thin-section CT.

MATERIALS AND METHODS: Noncontrast head CT studies performed consecutively on 1000 patients between January and February 2011 were retrospectively reviewed for the presence of trochlear calcifications. Axial 1.25-mm-thick images acquired by 64-detector row CT were reviewed. Medical records were reviewed for chronic medical conditions, including diabetes mellitus, chronic kidney disease, alcoholism, autoimmune conditions, endocrine disorders, serum calcium and alkaline phosphatase levels, and HIV status. Motion-limited studies and patients with limited clinical data were excluded. Statistical analyses were performed by using the Fisher exact test.

RESULTS: Thirty-two patients were excluded from analysis. Of the remaining 968 patients, 128 had trochlear calcification (13%). No significant association was observed between diabetes mellitus and trochlear calcifications in patients of any age ($P = .40$). There was no significant correlation between trochlear calcifications and chronic kidney disease, alcoholism, endocrine disorders, or HIV infection. Statistically significant associations among trochlear calcification, autoimmune conditions, and elevated alkaline phosphatase levels were observed ($P < .0001$ and $P < .0001$, respectively).

CONCLUSIONS: On the basis of a large unrestricted population with thin-section CT imaging of the orbit, no significant association was observed between trochlear calcifications and diabetes mellitus. A statistically significant association was observed between trochlear calcification and autoimmune disease and elevated alkaline phosphatase levels.

ABBREVIATIONS: ALP = alkaline phosphatase; CKD = chronic kidney disease; DM = diabetes mellitus; SLE = systemic lupus erythematosus

The trochlea is a cartilaginous structure within the superomedial orbit that permits unimpeded movement of the superior oblique tendon and sheath. Incidental calcification of the trochlea is frequently seen on routine CT scans through the orbit.¹⁻⁸ A prior study based on review of dedicated orbital CT imaging linked the presence of trochlear calcification with diabetes mellitus (DM), particularly in patients younger than 40 years of age.¹ In daily practice, however, review of medical

records in patients with trochlear calcification incidentally seen on CT usually failed to reveal evidence of glucose intolerance. While Ko and Kim² did not identify a similar association in a small review of orbital CT examinations, they observed an increased prevalence of trochlear calcifications in male patients. Cartilaginous and soft-tissue calcifications in other anatomic regions have been described in multiple prior studies in patients with autoimmune disorders and chronic renal insufficiency and among patients with dysregulations in calcium-phosphatase homeostasis.⁹

The purpose of this study was to examine the prevalence and demographics of trochlear calcification in a large unrestricted patient population by using thin-section CT images and to evaluate its clinical associations, if any. Specifically, we looked for a correlation between the presence of trochlear calcifications and common chronic medical conditions such as DM, chronic kidney disease (CKD), alcoholism, autoimmune conditions, endocrine disorders, and HIV infection.

Received May 1, 2013; accepted after revision June 7.

From the Departments of Radiology (K.B., R.N.N., A.D.T., A.F., O.S.) and Otolaryngology-Head and Neck Surgery (O.S.), Boston Medical Center, Boston University School of Medicine, Boston, Massachusetts; and Biostatistics Core (A.O.), Clinical Research Program, Children's Hospital Boston, Boston, Massachusetts.

Paper previously presented at: 98th Scientific Assembly and Annual Meeting of Radiological Society of North America, November 24-30, 2012; Chicago, Illinois.

Please address correspondence to Osamu Sakai, MD, PhD, Department of Radiology, Boston Medical Center, Boston University School of Medicine, Boston, FGH Building, 3rd Floor, 820 Harrison Ave, Boston, MA 02118; e-mail: osamu.sakai@bmc.org

<http://dx.doi.org/10.3174/ajnr.A3697>



FIG 1. Trochlear calcification. Axial CT images in soft-tissue (A) and bone (B) windows, and coronal CT image in a soft-tissue window (C) through the level of the trochlea demonstrate bilateral trochlear calcifications in a 45-year-old man who underwent CT after a motor vehicle collision and loss of consciousness.

MATERIALS AND METHODS

Following institutional review board approval, 1000 consecutive patients who underwent a noncontrast head CT at our tertiary health care center between January 2011 and February 2011 were reviewed for the presence of trochlear calcifications, regardless of the clinical indication prompting the CT examination. Reasons for the CT scans were very broad, with the most common clinical indications related to trauma, headache, and altered mental status.

Noncontrast head CT scans were axially acquired on 64-detector row CT scanners (LightSpeed VCT; GE Healthcare, Milwaukee, Wisconsin), and 5- and 1.25-mm-thick images were reconstructed per our institutional clinical protocol. The trochlea was included in all studies. The presence of trochlear calcifications was independently verified by 2 readers on the 1.25-mm axial images, and any discrepancies were resolved by consensus. Note was also made as to whether calcifications were unilateral or bilateral.

The electronic medical records were subsequently reviewed in all patients, and clinical parameters, including age, sex, presence or absence of DM, HIV infection, renal disease, alcoholism, autoimmune disorders, other endocrine disorders, and markers for abnormal calcium-phosphatase homeostasis by using serum markers including alkaline phosphatase (ALP) and serum calcium levels, were recorded. Electronic medical records were reviewed for at least 1 year before the date of the CT scan for the patients included in this study.

CKD was determined on the basis of review of patient medical records documenting a diagnosis of CKD or by using the National Kidney Foundation's clinical practice guidelines for a diagnosis of CKD.¹⁰ These parameters included abnormal serum creatinine or glomerular filtration rate levels for a period of >3 contiguous months. Patients presenting with acute renal failure were not included in this analysis. A diagnosis of alcoholism was determined by a review of the electronic medical records documenting a history of alcohol abuse. Determination of HIV status was made through review of electronic medical records, including serology data in addition to the primary care physician's notes recording a diagnosis of HIV infection. Autoimmune diseases were recorded on the basis of a review of the electronic medical records documenting a diagnosis of a rheumatologic condition in addition to serologic testing data. Endocrine disorders were also determined by a review of the electronic medical records containing a diagnosis of endocrine abnormality and laboratory data examining metabolic markers such as thyroid function tests and calcium and prolactin levels.

Severely motion-limited studies, follow-up examinations if performed in the same period, and patients with insufficient clinical data were excluded. The prevalence of comorbidities was compared across groups by using the Fisher exact test, and logistic regression models were used to control for age and sex.

RESULTS

A total of 968 patients who underwent technically adequate head CT imaging with corresponding medical records available were included. Eleven patient head CT scans were excluded on the basis of poor image quality due to motion artifacts, and 21 patients were excluded for insufficient electronic medical records. This study population consisted of 456 males and 512 females, ranging in age from 1 month to 100 years (mean age, 53 years). Trochlear calcifications were observed in 128 patients (Fig 1) and were bilateral in 56 patients and unilateral in 72 patients.

Prevalence

The prevalence of trochlear calcifications was 13.2% (128/968). The Table displays the prevalence of trochlear calcifications stratified by patient age. There was no association between trochlear calcifications and increasing patient age. Patients 11–20 years of age had the highest prevalence of trochlear calcifications (23.1%), followed by patients 31–40 years of age (20.2%). The youngest patient with trochlear calcifications was 15 years of age. There were 6 patients younger than 15 years of age, none of whom had trochlear calcifications. Trochlear calcifications were slightly more prevalent in male patients, occurring in 75 of the 128 patients with trochlear calcification (58.6%) compared with 53 female patients (41.4%). There was no statistically significant correlation between trochlear calcification and sex, however ($P = .06$).

Diabetes Mellitus

The prevalence of DM in this study population was 24.1% (234/968). Two hundred twenty-one of 234 patients (94.4%) had type 2 diabetes, compared with 14 patients (5.6%) with a diagnosis of type 1 DM. Of 128 patients with trochlear calcifications, 26 had a diagnosis of DM, of whom 23 had the diagnosis of DM type 2 and 3 had the diagnosis of DM type 1. Of the 840 patients without trochlear calcifications, 209 patients had a diagnosis of diabetes. After controlling for age and sex, there was no statistically significant association between DM and trochlear calcification ($P = .27$, OR = 0.76). Patient age of 54 years and older, but not patient sex, was strongly associated with the prevalence of DM.

Prevalence of patients with trochlear calcifications stratified by patient age

Patient Age (yr)	Total No. of Patients	Patients with Trochlear Calcifications	Prevalence of Trochlear Calcifications (95% CI)
0–10	23	0	0.0% (–, –)
11–20	26	6	23.1% (9.8–44.1)
21–30	109	17	15.6% (9.6–24.1)
31–40	104	21	20.2% (13.2–29.4)
41–50	168	24	14.3% (9.5–20.7)
51–60	206	25	12.1% (8.2–17.6)
61–70	128	15	11.7% (6.9–18.9)
71–80	114	9	7.8% (3.9–14.9)
81–90	65	9	13.8% (6.9–25.2)
Older than 91	24	2	8.3% (1.5–28.5)
Total	968	128	13.2% (11.2–15.6)

Alcoholism

The prevalence of documented alcoholism in this study population was 14.5% (140/968). Of 128 patients with trochlear calcifications, 21 had a diagnosis of alcoholism. After controlling for age and sex, there was no statistically significant correlation between trochlear calcifications and a diagnosis of alcoholism ($P = .50$, OR = 1.19). Male sex, but not age, was strongly associated with alcoholism.

HIV Infection

The prevalence of HIV infection in this study population was 3.6% (35/968). Of the 128 patients with trochlear calcifications, 4 had a diagnosis of HIV infection. After controlling for age and sex, there was no significant association between patients with trochlear calcifications and a diagnosis of HIV infection ($P = 1.00$, OR = 0.76). Male sex, but not age, was strongly associated with a diagnosis of HIV infection ($P = .002$).

Chronic Kidney Disease

The most common etiologies of CKD in this study population were hypertensive nephropathy and diabetic nephropathy. The prevalence of CKD in this study population was 8.4% (81/968). Of 128 patients with trochlear calcifications, 9 had a diagnosis of CKD. After controlling for age and sex, there was no significant association between CKD and the presence of trochlear calcification ($P = .73$, OR = 0.81). Increasing age, but not sex, was strongly associated with CKD ($P = .0001$).

Autoimmune Diseases

Autoimmune diseases in this patient population included rheumatoid arthritis, systemic lupus erythematosus (SLE), Crohn disease, Sjögren syndrome, and scleroderma. Forty-eight of 968 patients (5.0%) included in this investigation had a history of an autoimmune disease. The most common autoimmune disease identified in this population was rheumatoid arthritis, observed in 22 of 48 patients. Ten patients had SLE, 6 had Crohn disease, 5 had Sjögren syndrome, and 5 had scleroderma. Of the 128 patients with trochlear calcification, 17 had a diagnosis of an autoimmune disease, including 6 with a history of rheumatoid arthritis, 5 with SLE, 3 with Crohn disease, 1 with Sjögren syndrome, and 2 with scleroderma. After we controlled for age and sex, there was a statistically significant association between trochlear calcifications and a history of autoimmune disease ($P < .0001$, OR = 3.73). Given the relatively small number of patients included for

each type of autoimmune condition in this category, however, determination of significant associations with trochlear calcifications could not be reliably assessed.

Serum Calcium and ALP Levels

Elevated ALP levels were observed in 21.5% of patients (209/968). Of the 209 patients with elevated ALP levels, 42 had trochlear calcification. There was a strong statistically significant correlation between trochlear calcification and elevated ALP levels ($P < .0001$, OR =

1.87). Of the 128 patients with trochlear calcifications, none had elevated serum calcium levels.

Endocrine Disease

The most common endocrine disorders included in this study (excluding DM, which was analyzed separately) were hyperthyroidism, hypothyroidism, hyperparathyroidism, syndrome of inappropriate antidiuretic hormone, diabetes insipidus, and hyperprolactinemia.

Endocrinopathy other than diabetes was observed in 97 of 968 patients included in this investigation. Of these 97, thirty-eight patients had hypothyroidism, 14 had hyperthyroidism, 3 had acromegaly, 13 had hyperparathyroidism, 16 had hyperprolactinemia, 7 had syndrome of inappropriate antidiuretic hormone, and 6 had diabetes insipidus. Of the 128 patients with trochlear calcification, 10 had a diagnosis of endocrine disease, including 7 patients with hypothyroidism, 2 patients with hyperthyroidism, and 1 patient with acromegaly. No patient with hyperparathyroidism, hyperprolactinemia, syndrome of inappropriate antidiuretic hormone, or diabetes insipidus had trochlear calcifications. After we controlled for age and sex, there was no statistically significant correlation between trochlear calcifications and endocrine diseases ($P = .75$, OR = 1.44).

DISCUSSION

Trochlear calcifications have been reported in studies with conflicting data regarding the etiology and clinical association of these calcifications with common medical conditions.^{1,2} Prior studies postulated that calcification of the trochlea may be secondary to degenerative, inflammatory, metabolic, or posttraumatic etiologies.²

Hart et al¹ described a correlation between trochlear calcifications in patients younger than 40 years of age and DM.¹ Ko and Kim² subsequently found no correlation between trochlear calcifications and DM; however, they noted an increased prevalence of trochlear calcifications in male patients. These studies were performed by using thicker section CT images (3 mm in the study performed by Hart et al and 2 mm reported by Ko and Kim) and were performed in small, preselected populations of 159 and 216 patients, respectively, by using dedicated orbital CT studies in patients with orbital symptoms and pathology.^{1,2} Given that orbital symptoms and visual disturbances are common among patients with diabetes, these patient populations may be biased, with

a higher prevalence of patients with diabetes among the patient population compared with the general population.^{11,12}

In this investigation, the patient population consisted of consecutive patients who underwent noncontrast head CT imaging, thereby removing the possibility of bias among patients presenting with specific orbital symptoms. The larger patient population included in this study provides a broader assessment of trochlear calcifications compared with previously published reports. Furthermore, the thinner 1.25-mm CT sections allowed greater accuracy of trochlear calcification identification.

The prevalence of trochlear calcifications in our study was 13.2% compared with 12% cited by Hart et al¹ and 16%, by Ko and Kim.² No statistically significant correlation was observed between trochlear calcifications and increasing patient age or sex. A bimodal peak distribution was observed in patients with trochlear calcifications from 11 to 20 years of age and 31–40 years of age. The youngest patient with trochlear calcifications was 15 years of age. These observations imply that the presence of trochlear calcifications is probably not related to a degenerative process and is unlikely to be a congenital variant.

A statistically significant association was seen between a diagnosis of autoimmune disease and trochlear calcifications ($P < .0001$). The numbers for each type of autoimmune disease included in this study were small so that the evaluation of significant associations between trochlear calcifications and specific autoimmune diseases was limited, so autoimmune diseases were analyzed collectively. Calcification and systemic deposition of calcium salts have been described in multiple autoimmune diseases, including scleroderma, dermatomyositis, rheumatoid arthritis, Sjögren syndrome, and SLE, with a mean age of onset of 33.3 years.^{13,14} The deposition of calcification can be idiopathic, dystrophic, or due to calciphylaxis, and while the pathophysiology is unclear, it is thought to relate to circulating chronic inflammatory mediators.^{15–27}

Case reports describe both focal and extensive systemic deposition of calcification in patients with both rheumatoid arthritis and SLE, with calciphylaxis described as a rare complication of both diseases.^{16–23} SLE can lead to CKD, a well-known complication²²; however, CKD was not independently associated with trochlear calcifications. Widespread soft-tissue calcification in chronic inflammatory autoimmune disorders such as Sjögren syndrome, SLE, and rheumatoid arthritis has been described.^{20–23,25–27} Very few case reports describe focal calcifications within the soft tissues of the head and neck, with the exception of retropharyngeal calcific tendinitis and calcification of the longus colli muscle in a patient with rheumatoid arthritis.²⁸ On the basis of the results of this investigation, it appears that in addition to calcification within soft tissues previously described, trochlear calcifications may also be seen as an associated finding in patients with autoimmune conditions.

A statistically significant association between the presence of trochlear calcification and elevated ALP levels ($P < .0001$) was observed in this investigation. Alkaline phosphatase levels were evaluated in this patient population because they are an indirect marker for bone turnover and metabolism and calcium homeostasis. Increased vascular calcifications have been associated with elevated ALP levels in patients with disturbances in mineral-bone

metabolism.^{29–31} Aberrations in ALP levels have been seen in patients with chronic inflammatory and autoimmune diseases.^{29,30} It is unclear as to whether these aberrations are due to circulating inflammatory mediators directly related to the underlying disease process versus abnormal bone-mineral metabolism resulting from glucocorticoid therapy to treat these disorders.^{9,32,33} Most patients with elevated ALP levels did not have a coexistent autoimmune disorder or another condition to explain these levels, but nearly half (46.7%) of patients with an elevated ALP level and an autoimmune disorder had trochlear calcifications. Despite the statistically significant relationship between the presence of trochlear calcifications and elevated ALP levels, the specific reason for the relationship remains unclear because an isolated elevated ALP level is quite nonspecific.

There was no evidence that trochlear calcification is associated with other common medical conditions, including CKD, HIV infection, endocrine diseases, and history of alcohol abuse.

CONCLUSIONS

Trochlear calcifications are not uncommon, with a prevalence of 13% and no sex predilection; they also appear to be acquired, though not necessarily secondary to the aging process. On the basis of review of an unrestricted population undergoing thin-section CT imaging, we found no statistically significant association between the presence of trochlear calcifications and other common medical conditions, including DM, CKD, HIV infection, or a history of alcoholism. We did identify strong associations between the presence of trochlear calcifications and autoimmune disease and elevated ALP levels, but the reason for these associations remains elusive and requires further investigation.

Disclosures: Osamu Sakai—UNRELATED: Royalties: McGraw-Hill Companies.

REFERENCES

1. Hart BL, Spar JA, Orrison WW Jr. **Calcification of the trochlear apparatus of the orbit: CT appearance and association with diabetes and age.** *AJR Am J Roentgenol* 1992;159:1291–94
2. Ko S, Kim Y. **Incidence of calcification of the trochlear apparatus in the orbit.** *Korean J Ophthalmol* 2010;24:1–3
3. Murray JL, Hayman LA, Tang RA, et al. **Incidental asymptomatic orbital calcifications.** *J Neuroophthalmol* 1995;15:203–08
4. Helveston EM, Merriam WW, Ellis FD, et al. **The trochlea: a study of the anatomy and physiology.** *Ophthalmology* 1982;89:124–33
5. Sobel RK, Goldstein SM. **Trochlear calcification: a common entity.** *Orbit* 2012;31:94–96
6. Froula PD, Bartley GB, Garrity JA, et al. **The differential diagnosis of orbital calcification as detected on computed tomographic scans.** *Mayo Clin Proc* 1993;68:256–61
7. Xiao TL, Kalariya NM, Yan ZH, et al. **Trochlear calcification and intraorbital foreign body in ocular trauma patients.** *Chin J Traumatol* 2009;12:210–13
8. Shriver EM, McKeown CA, Johnson TE. **Trochlear calcification mimicking an orbital foreign body.** *Ophthalm Plast Reconstr Surg* 2011;27:e143–44
9. Nanke Y, Kotake S, Akama H, et al. **Alkaline phosphatase in rheumatoid arthritis patients: possible contribution of bone-type ALP to the raised activities of ALP in rheumatoid arthritis patients.** *Clin Rheumatol* 2002;21:198–202
10. **Kidney Disease Outcome Quality Initiative: Clinical Practice Guidelines for Chronic Kidney Disease: Evaluation, Classification, and Stratification.** National Kidney Foundation. Published January 2002.

Updated April 19, 2003. http://www.kidney.org/professionals/kdoqi/guidelines_ckd/toc.htm. Accessed July 14, 2013

11. Goldacre MJ, Wotton CJ, Keenan TD. **Risk of selected eye diseases in people admitted to hospital for hypertension or diabetes mellitus: record linkage studies.** *Br J Ophthalmol* 2012;96:872–76
12. Jeganathan VS, Wang JJ, Wong TY. **Ocular associations of diabetes other than diabetic retinopathy.** *Diabetes Care* 2008;31:1905–12
13. Okada J, Nomura M, Shirataka M, et al. **Prevalence of soft tissue calcifications in patients with SLE and effects of alfacalcidol.** *Lupus* 1999;8:456–61
14. Fairweather D, Frisancho-Kiss S, Rose N. **Sex differences in autoimmune disease from a pathological perspective.** *Am J Pathol* 2008;173:600–09
15. Shantsila E, Lip GY. **Systemic inflammation as a driver of vascular calcification: a proof of concept.** *J Intern Med* 2009;266:453–56
16. Masuda Y, Uchiyama Y, Hashimoto S, et al. **Symmetrica I progressive intracranial calcification in a patient with SLE.** *Intern Med* 2010;49:351
17. Yiu KH, Mok MY, Wang S, et al. **Prognostic role of coronary calcification in patients with rheumatoid arthritis and systemic lupus erythematosus.** *Clin Exp Rheumatol* 2012;30:345–50
18. Plazak W, Pasowicz M, Kostkiewicz M, et al. **Influence of chronic inflammation and autoimmunity on coronary calcifications and myocardial perfusion defects in systemic lupus erythematosus patients.** *Inflamm Res* 2011;60:973–80
19. Paccou J, Brazier M, Mentaverri R, et al. **Vascular calcification in rheumatoid arthritis: prevalence, pathophysiological aspects and potential targets.** *Atherosclerosis* 2012;224:283–90
20. Llamas-Velasco M, Eguren C, Santiago D, et al. **Calcinosis cutis and Sjögren's syndrome.** *Lupus* 2010;19:762–64
21. Ortiz A, Ceccato F, Roverano S, et al. **Calciophylaxis associated with rheumatoid arthritis: communication of the second case.** *Clin Rheumatol* 2009;28(suppl 1):S65–68
22. Igaki N, Moriguchi R, Hirota Y, et al. **Calciophylaxis in a patient with end-stage renal disease secondary to systemic lupus erythematosus associated with acral gangrene and mesenteric ischemia.** *Intern Med* 2001;40:1232–37
23. Sugimoto H, Hyodoh K, Kikuno M, et al. **Periarticular calcification in systemic lupus erythematosus.** *J Rheumatol* 1999;26:574–79
24. MacLean C, Brahn E. **Systemic lupus erythematosus: calciophylaxis induced cardiomyopathy.** *J Rheumatol* 1995;22:177–79
25. Minami A, Suda K, Kaneda K, et al. **Extensive subcutaneous calcification of the forearm in systemic lupus erythematosus.** *J Hand Surg Br* 1994;19:638–41
26. Mandelbrot DA, Santos PW, Burt RK, et al. **Resolution of SLE-related soft-tissue calcification following haematopoietic stem cell transplantation.** *Nephrol Dial Transplant* 2008;23:2679–84
27. Tristano AG, Villarreal JL, Rodríguez MA, et al. **Calcinosis cutis universalis in a patient with systemic lupus erythematosus.** *Clin Rheumatol* 2006;25:70–74
28. Lee S, Joo KB, Lee KH, et al. **Acute retropharyngeal calcific tenosynovitis in an unusual location: a case report in a patient with rheumatoid arthritis and atlantoaxial subluxation.** *Korean J Radiol* 2011;12:504–09
29. Kapustin AN, Davies JD, Reynolds JL, et al. **Calcium regulates key components of vascular smooth muscle cell-derived matrix vesicles to enhance mineralization.** *Circ Res* 2011;109:e1–12
30. Osorio A, Ortega E, Torres JM, et al. **Biochemical markers of vascular calcification in elderly hemodialysis patients.** *Mol Cell Biochem* 2013;374:212–17
31. Shroff RC, McNair R, Skepper JN, et al. **Chronic mineral dysregulation promotes vascular smooth muscle cell adaptation and extracellular matrix calcification.** *J Am Soc Nephrol* 2010;21:103–12
32. Jensen T, Hansen M, Madsen JC, et al. **Serum levels of parathyroid hormone and markers of bone metabolism in patients with rheumatoid arthritis. Relationship to disease activity and glucocorticoid treatment.** *Scand J Clin Lab Invest* 2001;61:491–501
33. Korczowska I, Łacki JK, Leszczyński P, et al. **Bone tissue metabolism in systematic lupus erythematosus patients treated with glucocorticosteroids [in Polish].** *Pol Arch Med Wewn* 2001;106:901–07

Prevalence of the Polar Vessel Sign in Parathyroid Adenomas on the Arterial Phase of 4D CT

M. Bahl, M. Muzaffar, G. Vij, J.A. Sosa, K. Roy Choudhury, and J.K. Hoang

ABSTRACT

BACKGROUND AND PURPOSE: The “polar vessel” sign has been previously described on sonography of parathyroid adenomas. We estimated the 4D CT prevalence of the polar vessel sign and determined features of parathyroid adenomas that are associated with this sign.

MATERIALS AND METHODS: Twenty-eight consecutive patients with parathyroid adenomas underwent 4D CT between 2008 and 2012 at 2 institutions. 4D CT images were reviewed for the presence of the polar vessel sign and a second vascular finding of an enlarged ipsilateral inferior thyroid artery. The polar vessel sign was correlated with adenoma weight and size and arterial phase CT attenuation.

RESULTS: Thirty-two parathyroid adenomas in 28 patients were studied, with a mean adenoma weight of 0.66 ± 0.65 g, a mean maximal CT diameter of 11.1 ± 4.9 mm, and a mean arterial attenuation of 148 ± 47 HU. The polar vessel sign was seen in 20/32 (63%) adenomas. Adenomas with a polar vessel had higher arterial phase attenuation than adenomas without a polar vessel (163 and 122 HU, respectively, $P < .01$). Size and weight were not significantly different for adenomas with and without polar vessels. An enlarged inferior thyroid artery was seen in only 2/28 (7%) patients with unilateral disease.

CONCLUSIONS: The polar vessel sign was present in nearly two-thirds of parathyroid adenomas on 4D CT and was more likely to be present in adenomas that had greater arterial phase enhancement. This sign can be used along with enhancement characteristics to increase the radiologist’s confidence that a visualized lesion is a parathyroid adenoma rather than a thyroid nodule or lymph node.

4D parathyroid CT is increasingly used for preoperative localization of parathyroid adenomas. 4D CT was first described in 2006 and involves ≥ 2 contrast phases with high-resolution multiplanar images of the neck and upper chest.¹ The characteristic features of parathyroid adenomas on 4D CT are low attenuation on noncontrast imaging, peak enhancement on the arterial phase, and washout of contrast on the venous phase.²⁻⁴ These allow differentiation between a parathyroid adenoma and its mimics, such as thyroid nodules and lymph nodes.

Characteristic enhancement may not be evident in all cases due to adenoma composition, small adenoma size, or suboptimal arterial timing. In these cases, the radiologist must rely on his or her knowledge of the expected locations of adenomas and morphologic findings. A morphologic feature that has been previously

described on sonography is a feeding artery (usually a branch of the inferior thyroid artery) to the adenoma.^{5,6} Small arteries cannot be seen on nuclear scintigraphy or MR imaging because of lower spatial resolution, and they have not been described on single venous phase CT, to our knowledge. In a recent review article, the authors noted the presence of a “polar vessel” sign on the arterial phase of 4D CT.⁴ The polar vessel sign can represent either an enlarged feeding artery or a draining vein seen on the arterial phase of imaging, and it is characterized by a vessel that terminates in a parathyroid adenoma and that is larger than contralateral neck vessels in a similar location.

The purpose of this study was to estimate the prevalence of the polar vessel sign on 4D CT and to determine features of parathyroid adenomas that are associated with this sign. We hypothesize that a polar vessel may be more commonly seen in adenomas that are larger or have more vivid arterial enhancement.

MATERIALS AND METHODS

Subjects

This was a retrospective study, from 2 institutions, of patients with primary hyperparathyroidism who underwent 4D CT between January 2008 and December 2012 as a localization study before parathyroid surgery. The study was approved by the institutional review

Received May 19, 2013; accepted after revision June 21.

From the Departments of Radiology (M.B., G.V., K.R.C., J.K.H.), Surgery, Division of Surgical Oncology (J.A.S.), and Radiation Oncology (J.K.H.), Duke University Medical Center, Durham, North Carolina; and Department of Radiology (M.M.), Carle Foundation Hospital, Urbana, Illinois.

Please address correspondence to Jenny K. Hoang, MD, Department of Radiology, Duke University Medical Center, Box 3808, Erwin Rd, Durham, NC 27710; e-mail: jennykh@gmail.com

<http://dx.doi.org/10.3174/ajnr.A3715>

board at both institutions and was compliant with the Health Insurance Portability and Accountability Act. We identified patients at both institutions by performing a radiology data base search of patients who had undergone 4D CT before surgery. Most 4D CT scans were ordered when sonography and scintigraphy findings were discordant or negative; but in 6 cases, 4D CT was the first investigation. Patients were excluded if the arterial phase scan was poorly timed (venous attenuation greater than arterial attenuation) because the polar vessel sign is only seen on arterial phase imaging. There were 34 patients with parathyroid adenomas. Six of the 34 were excluded due to the absence of optimal arterial phase imaging, with excluded cases more common in the first year of imaging due to development of the protocols.

Hospital electronic medical records were accessed to obtain the following information for each subject: basic demographics, operative reports, and surgical pathology reports.

4D CT Imaging Technique

4D CT scans at our institutions were obtained on different scanner types with different protocols. Studies at Duke University Medical Center were performed on 64-row multidetector CT scanners (750 HD and LightSpeed; GE Healthcare, Milwaukee, Wisconsin), and studies at Carle Foundation Hospital were performed on a 16-row multidetector CT scanner (LightSpeed; GE Healthcare). All CT scans included at least arterial and venous phase CT.

The current protocol at Duke University Medical Center consists of 3 imaging phases. The first phase is a noncontrast CT to include the thyroid gland; the z-axis is from the hyoid bone to the clavicular head. The next 2 phases are contrast phases from the angle of the mandible to the carina and are performed after intravenous administration of 75 mL of iopamidol (Isovue-300; Bracco, Princeton, New Jersey) via a 20-ga cannula in a right antecubital vein at a rate of 4 mL/s, followed by a 25-mL saline chaser. Arterial phase images are acquired 25 seconds after the start of the injection, and the delayed (venous) phase images are acquired 80 seconds from the start of the injection. The parameters for all 3 phases are the following: 0.625-mm section thickness; tube rotation time, 0.4 seconds; pitch factor, 0.516:1; FOV, 20 cm; 120 kV(peak); and automatic tube current modulation (Smart mA, GE Healthcare; with noise index, 10; minimum 100 mA and maximum 700 mA). One-millimeter-thick contiguous axial images in all 3 phases are sent to the PACS for interpretation and to allow manipulation of images on a 3D workstation. Reformatted images in the arterial phases are sent to the PACS as 2.5-mm-thick contiguous images in the axial, coronal, and sagittal planes.

CT scans at Carle Foundation Hospital consist of arterial and venous phases from the angle of the mandible to the carina and are obtained after intravenous administration of 100 mL of iopamidol (Isovue-300) via a 20-ga cannula in the right antecubital vein at a rate of 4 mL/s, followed by a 50-mL saline chaser. The arterial phase is acquired 20 seconds after the start of the injection, and the delayed (venous) phase is acquired 70 seconds from the start of the injection. The parameters for both phases are the following: 0.625-mm section thickness; tube rotation time, 0.5 seconds; pitch factor, 1.75:1, FOV, 20 cm; 120 kVp; and automatic tube current modulation (Smart mA with noise index 11; minimum 100 mA and maximum 440 mA). For interpretation,

1.25-mm reconstructed contiguous axial images and 1-mm-thick sagittal and coronal reformatted images in arterial and venous phases are sent to the PACS.

Image Interpretation

4D CT images were reviewed on a PACS workstation. Readers were an attending neuroradiologist, a neuroradiology fellow, and a diagnostic radiology resident with 11, 5, and 2 years of CT experience, respectively. Readers were given information about the location of the parathyroid adenoma based on the surgical findings and were asked to evaluate the CT scans for the presence of the polar vessel sign and a second vascular finding of an enlarged ipsilateral inferior thyroid artery on the arterial phase images. Readers were not assessed on their ability to detect the parathyroid adenoma because this was not a study on the performance of 4D CT for localization. The 2 junior readers were educated on how to recognize the vascular findings before starting the study. The polar vessel sign usually represents an enlarged feeding artery; but when followed to the origin, it can also represent a draining vein. It is characterized by a vessel that terminates in the parathyroid adenoma and is usually larger than contralateral neck vessels in a similar location (Figs 1 and 2). The polar vessel can be tortuous (Fig 1). An enlarged inferior thyroid artery was defined as increased enhancement or size of the artery on the side of the parathyroid adenoma compared with the artery in the contralateral neck (Fig 3). This was best assessed on axial and coronal images.

Note that Figs 1–3 are maximum-intensity-projection reconstructions to display the polar vessel on a single image. The images were not reviewed as maximum-intensity-projection images by the readers in the study or in the clinical setting. The polar vessel sign was assessed for all adenomas. The enlarged ipsilateral inferior thyroid artery was only evaluated in cases with unilateral disease (ie, not cases of bilateral multiglandular disease). The readers were not blinded to the location and number of parathyroid adenomas because the purpose of the study was not to determine the accuracy of 4D CT.

Other characteristics of the parathyroid adenomas, including location, dimensions, and arterial phase imaging attenuation, were also recorded. On arterial phase imaging, the mean attenuation was calculated on the basis of 3 region-of-interest measurements within the center of the parathyroid adenoma, avoiding cystic areas.

Data Analysis

The data were entered into an Excel spreadsheet (2007 Version; Microsoft, Redmond, Washington). Statistical analyses were performed by using SAS Enterprise (Version 4.2; SAS Institute, Cary, North Carolina) and the R package (www.r-project.org). Two-sample *t* tests were used to compare features of parathyroid adenomas with and without a polar vessel. The Fleiss κ was calculated to determine interrater agreement for the presence of a polar vessel and an enlarged ipsilateral thyroid artery. Agreement was regarded as poor with Fleiss $\kappa \leq 0.20$, as slight with 0.21–0.40, as moderate with 0.41–0.60, as substantial with 0.61–0.80, and as almost perfect with 0.81–1.00.⁷ *P* values < .05 were considered statistically significant.

RESULTS

Characteristics of Patients and Parathyroid Adenomas

The study population comprised 28 patients (24 females; mean age, 60 years; range, 15–83 years). All patients had parathyroid

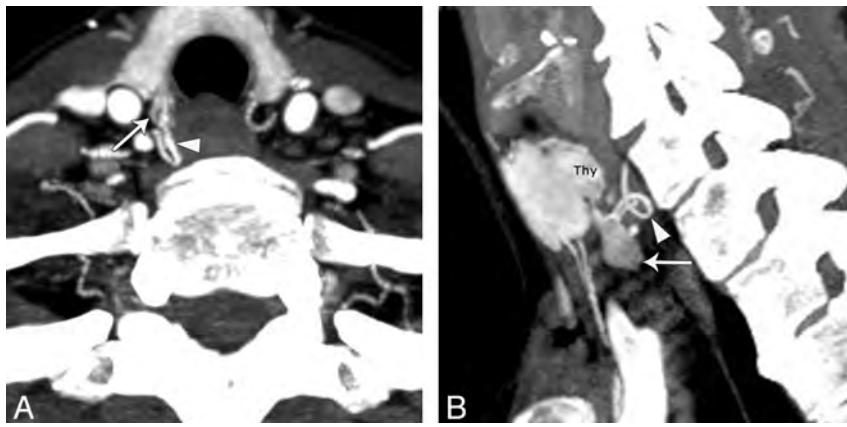


FIG 1. A 69-year-old woman with a right parathyroid adenoma. Axial (A) and sagittal (B) arterial phase images demonstrate an oval-shaped hyperenhancing adenoma posterior and inferior to the lower pole of the right thyroid gland (straight arrows). A characteristic tortuous feeding artery is seen at the superior aspect of the adenoma (arrowheads).



FIG 2. A 71-year-old woman with a left parathyroid adenoma. Coronal arterial phase image demonstrates a round hyperenhancing adenoma inferior to the lower pole of the left thyroid gland (straight arrow). A characteristic feeding artery (arrowhead) is seen at the superolateral aspect of the adenoma.

adenomas that could be identified on 4D CT in retrospect. Twenty-four of 32 (75%) parathyroid adenomas were reported prospectively in the radiology report. These cases represented the initial 4D CT scans at both institutions after introducing the protocol, and accuracy of localization was likely improved with experience. Four of 28 (14%) patients had double adenomas, and 2 of 28 (7%) had adenomas in ectopic locations (retropharynx and carotid space). The 32 adenomas in 28 patients had a mean weight of 0.66 ± 0.65 g, a mean maximal CT diameter of 11.1 ± 4.9 mm, and a mean arterial attenuation of 148 ± 47 HU.

Vascular Findings

The polar vessel sign was present in 23 (72%), 23 (72%), and 24 (75%) adenomas according to readers A, B, and C, respectively. All 3 readers agreed on the presence of a polar vessel sign in 20 of 32 (63%) adenomas. At least 2 of 3 readers agreed on the presence of a polar vessel sign in 24 of 32 (75%) adenomas. The Fleiss κ (an index of interrater agreement) was 0.68 (95% CI, 0.49–0.84), which indicates substantial agreement.

An enlarged inferior thyroid artery was present in 2 (7%), 6 (21%), and 3 (11%) adenomas according to readers A, B, and C, respectively. All 3 readers agreed on the presence of an enlarged inferior thyroid artery in 2 of 28 (7%) patients with unilateral disease. At least 2 of 3 readers agreed on the presence of an enlarged inferior thyroid artery in 3 of 28 (11%) patients. The Fleiss κ was 0.58 (95% CI, –0.04–0.84), which indicates moderate agreement.

Polar Vessel Sign and Parathyroid Adenoma Characteristics

For this analysis, an adenoma was considered to have a polar vessel only if all 3 readers agreed on its presence. Adenomas with a polar vessel had statistically significant higher arterial phase attenuation than adenomas without a polar vessel (163 and 122 HU, respectively; $P < .01$).

Adenomas with a polar vessel trended toward higher mean maximum diameters than adenomas without a polar vessel (12.4 and 9.0 mm, respectively), but this difference was not statistically significant ($P = .07$). There were no differences in gross pathologic weights of adenomas with or without the polar vessel (0.62 and 0.80 g, respectively; $P = .6$).

DISCUSSION

We report the prevalence of the polar vessel sign on parathyroid 4D CT, as well as the features of parathyroid adenomas associated with this sign. We found the polar vessel sign to be present in nearly two-thirds of parathyroid adenomas on 4D CT and to be more common in adenomas with greater arterial phase enhancement. The sign is common and can be used along with enhancement characteristics to increase the radiologist's confidence that a visualized lesion is a parathyroid adenoma.

Parathyroid adenomas can be difficult to differentiate from thyroid nodules, level VI lymph nodes, or ectopic thyroid tissue. Unlike parathyroid adenomas, lymph nodes and thyroid nodules are less likely to have prominent feeding arteries or draining veins that are visible on CT. We found the polar vessel sign to be confidently seen on 4D CT in 63% of adenomas by all readers and up to 75% of adenomas by 2 readers. Therefore, this sign can be regarded as common and useful. The polar vessel alone is not diagnostic of a parathyroid adenoma. In our clinical practice, the other signs of parathyroid adenoma, such as shape and enhancement, are used primarily to identify them. The presence of the polar vessel sign does, however, increase the confidence that the lesion is a parathyroid adenoma and may change the interpretation of “suspicious for parathyroid adenoma” to “in keeping with parathyroid adenoma.”

Our results are in accordance with findings of a polar vessel in the sonography literature. Lane et al⁶ reported sonographic findings of an extrathyroidal artery leading to a parathyroid adenoma in 35 of 42 (83%) adenomas and found that the presence of an extrathyroidal artery aided in the detection of an otherwise inconspicuous parathyroid gland in several patients. Wolf et al⁵ identi-

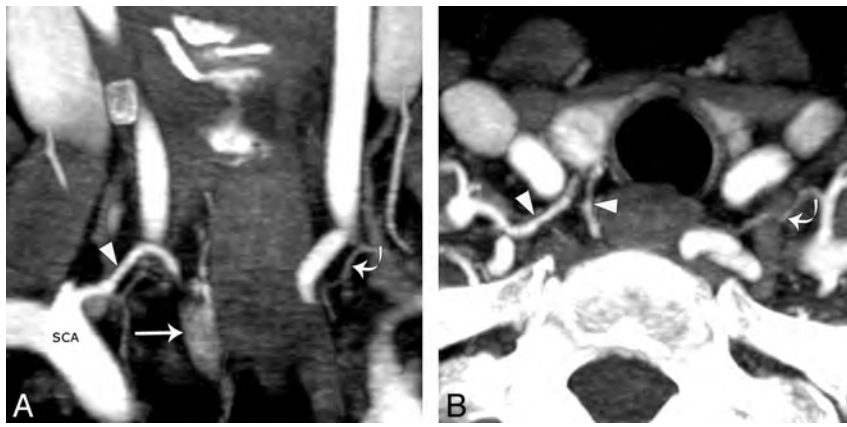


FIG 3. A 70-year-old woman with a right parathyroid adenoma. A, Coronal arterial phase image demonstrates an oval hyperenhancing adenoma in the right tracheoesophageal groove (straight arrow). Coronal (A) and axial (B) images show an enlarged inferior thyroid artery (arrowheads) arising from the right subclavian artery and terminating at the superior pole of the adenoma. Note the normal contralateral inferior thyroid artery (curved arrows).

fied the presence of a demonstrable blood supply from the inferior thyroid artery branches as a vascular arc surrounding the gland from 90° to 270°; in their series, 20 of 32 (63%) parathyroid adenomas had a color arc. Scheiner et al⁸ reported finding a vessel draping over an adenoma in 65% of cases. The arterial phase of 4D CT allows radiologists to see the CT correlate of this well-established sonographic vascular finding.

We attempted to identify adenomas that were more likely to have the polar vessel sign. The only characteristic that was significantly more likely to have the polar vessel sign was higher arterial phase attenuation. Higher CT attenuation or enhancement is a marker of the blood supply of a tissue. Hypersecreting parathyroid glands have increased blood supply.⁶ In fact, per adenomal vessels were described in the angiographic literature in the 1980s and accounted for the early experience with angiographic ablation for the treatment of parathyroid adenomas.^{9,10} These vessels are theorized to be enlarged normal vessels, parasitized by the parathyroid adenoma.¹⁰ Thus, adenomas that are more vascular and enhance more on CT are more likely to have a visible polar vessel. An alternate explanation for the polar vessel sign being present in adenomas with higher arterial attenuation is related to the CT technique; specifically, a CT scan with a more optimally timed arterial phase would be more likely to show higher arterial phase enhancement of a parathyroid adenoma along with its associated vessel.

There are several limitations to our study. The major limitation is that the radiologists reading the scans knew that the adenomas were present and therefore might be more likely to report the presence of a polar vessel. The alternative of asking the readers to find the adenoma and then the polar vessel sign would make the study significantly more complicated, however, because we would be assessing the accuracy of 4D CT for localization and the presence of the sign. This assessment could lead to an underestimation of the sensitivity of 4D CT because only 1 radiologist has the clinical experience to interpret 4D CT scans at the primary study institution. We thought readers of all levels were capable of reporting the presence or absence of a polar vessel sign in a known adenoma; thus, this study focuses on the prevalence of the polar vessel sign rather than its specificity and sensitivity

for diagnosing parathyroid adenoma. We agree that in future studies, readers should be blinded to the surgical results, and this will be the focus of our future work.

Second, this was a retrospective clinical series with a small study population. Small study size may affect the estimate of the prevalence of vascular findings and result in type II errors for the polar vessel associations, but it is reassuring to see that our prevalence estimates are similar to those in the sonography literature. Third, the CT scans were from 2 different institutions and were obtained with different protocols during the study period. The variation in scanning technique should not affect the data collected for adenoma diameter and arterial phase attenuation because all patients had arterial phase CT imaging.

CONCLUSIONS

The polar vessel sign is present in nearly two-thirds of surgically confirmed parathyroid adenomas on 4D CT and is more likely to be present in adenomas that have greater arterial phase enhancement. This sign may be used along with enhancement characteristics to potentially increase the radiologist's confidence that a visualized lesion is a parathyroid adenoma rather than a thyroid nodule or lymph node.

REFERENCES

- Rodgers SE, Hunter GJ, Hamberg LM, et al. **Improved preoperative planning for directed parathyroidectomy with 4-dimensional computed tomography.** *Surgery* 2006;140:932–40, discussion 940–41
- Beland MD, Mayo-Smith WW, Grand DJ, et al. **Dynamic MDCT for localization of occult parathyroid adenomas in 26 patients with primary hyperparathyroidism.** *AJR Am J Roentgenol* 2011;196:61–65
- Gafton AR, Glastonbury CM, Eastwood JD, et al. **Parathyroid lesions: characterization with dual-phase arterial and venous enhanced CT of the neck.** *AJNR Am J Neuroradiol* 2012;33:949–52
- Hoang JK, Sung WK, Bahl M, et al. **How to do parathyroid 4D-CT: tips and traps for technique and interpretation.** *Radiology* 2014;270:15–24
- Wolf RJ, Cronan JJ, Monchik JM. **Color Doppler sonography: an adjunctive technique in assessment of parathyroid adenomas.** *J Ultrasound Med* 1994;13:303–08
- Lane MJ, Desser TS, Weigel RJ, et al. **Use of color and power Doppler sonography to identify feeding arteries associated with parathyroid adenomas.** *AJR Am J Roentgenol* 1998;171:819–23
- Landis JR, Koch GG. **The measurement of observer agreement for categorical data.** *Biometrics* 1977;33:159–74
- Scheiner JD, Dupuy DE, Monchik JM, et al. **Pre-operative localization of parathyroid adenomas: a comparison of power and colour Doppler ultrasonography with nuclear medicine scintigraphy.** *Clin Radiol* 2001;56:984–88
- Miller DL, Doppman JL, Chang R, et al. **Angiographic ablation of parathyroid adenomas: lessons from a 10-year experience.** *Radiology* 1987;165:601–07
- Doppman JL, Brennan MF, Kahn CR, et al. **Circumscribing or per adenomal vessel: a helpful angiographic finding in certain islet cell and parathyroid adenomas.** *AJR Am J Roentgenol* 1981;136:163–65

Combination Therapy Consisting of Ethanol and Radiofrequency Ablation for Predominantly Cystic Thyroid Nodules

H.M. Yoon, J.H. Baek, J.H. Lee, E.J. Ha, J.K. Kim, J.H. Yoon, and W.B. Kim



ABSTRACT

SUMMARY: Predominantly cystic thyroid nodules are often aspirated before radiofrequency ablation to enhance its efficacy; however internal bleeding during the aspiration is a problem. We evaluated the feasibility and safety of ethanol ablation to control internal bleeding that occurred during preparatory aspiration. Between September 2010 and August 2011, 11 of 40 predominantly cystic nodules bled internally during fluid aspiration before radiofrequency ablation. To control the bleeding, 99% ethanol was injected. The efficacy of ethanol in controlling bleeding, final nodule volume and complications were assessed. Control of the bleeding by ethanol ablation and subsequent radiofrequency ablation was feasible in all patients. Ninety-one percent (10/11) could be treated in 1 session. The mean nodule volume dropped from 17.1 to 4.3 mL ($P < .018$). There were no major complications. Ethanol ablation and radiofrequency ablation combination therapy is a feasible and safe technique for treating predominantly cystic thyroid nodules that exhibit internal bleeding during preparatory aspiration.

ABBREVIATIONS: EA = ethanol ablation; RF = radio-frequency; US = ultrasound

Benign nodular thyroid disease is common, and 15%–25% of solitary nodules are cystic or predominantly cystic on sonography.¹ Most cystic lesions are considered caused by the hemorrhage and subsequent degeneration of pre-existing nodules.² In patients with cosmetic or symptomatic problems, the initial procedure is the simple aspiration of the cystic portion; this reduces the cyst volume and aids in specific diagnosis, but it is associated with a high recurrence rate of up to 80%.^{3,4} For recurrent cases after aspiration, ethanol ablation (EA) has been attempted with good results.^{5,6}

Recently, radiofrequency (RF) ablation has been used to treat benign thyroid nodules with a low complication rate,^{7–12} including thyroid nodules with a cystic portion^{6,8} and recurrent thyroid cancers.¹³ Although EA is effective for treating cystic and predominantly cystic nodules, 5%–25% of patients are refractory to EA.

For those refractory cases, EA has been re-attempted, but with a marked decline in subsequent efficacy.^{14,15} EA has been used as a first-line treatment for cystic thyroid nodules^{6,16}; however EA as a first-line treatment is debatable for predominantly cystic thyroid nodules^{15,17,18} because the recurrence rate is >50% in these nodules with solid components of >20%.

When treating predominantly cystic nodules by thermal ablation, it is recommended that the internal fluid content be aspirated before RF or laser ablation^{6,19} because it is easier to treat decompressed small nodules than larger ones.²⁰ Internal hemorrhage can develop during the aspiration, however, and this bleeding enlarges the nodule volume and has a heat sink effect that could affect the efficacy of RF ablation.

In our clinic, predominantly cystic thyroid nodules that bled internally after aspiration were injected with ethanol, after which they were subjected to RF ablation. The aim of this study was to evaluate the feasibility and safety of EA in controlling internal bleeding during aspiration of the internal fluid of predominantly cystic thyroid nodules before RF ablation.

MATERIALS AND METHODS

Patients

This retrospective study was approved by our institutional review board. Informed consent for procedures was obtained from all patients before each procedure.

Between September 2010 and August 2011, one hundred thirty-one RF ablations of benign thyroid nodules were per-

Received April 3, 2013; accepted after revision June 7.

From the Departments of Radiology and Research Institute of Radiology (H.M.Y., J.H.B., J.H.L., E.J.H.), Surgery (J.H.Y.), and Endocrinology and Metabolism (W.B.K.), University of Ulsan College of Medicine, Asan Medical Center, Seoul, Korea; and Department of Radiology (J.K.K.), Chung-Ang University College of Medicine, Seoul, Korea.

We declare that we have no proprietary, commercial, or financial interests that could be construed to have inappropriately influenced this study.

Please address correspondence to Jung Hwan Baek, MD, Department of Radiology and Research Institute of Radiology, University of Ulsan College of Medicine, Asan Medical Center, 86 Asanbyeongwon-Gil, Songpa-Gu, Seoul 138-736, Korea; e-mail address: radbaek@naver.com



Indicates article with supplemental on-line video.

<http://dx.doi.org/10.3174/ajnr.A3701>

formed in Asan Medical Center. Forty of these cases involved patients with predominantly cystic nodules whose internal fluid was aspirated before RF ablation. In 11 of these patients, each of whom had 1 nodule, the cysts bled internally during the aspiration of internal fluid, and they were enrolled in this study. We enrolled 3 men and 8 women with a mean age of 47.1 years (range, 30–69 years). All patients fulfilled the following criteria: 1) The cystic portion of the nodule exceeded 50% of the nodule volume, 2) there were thyroid nodule–related pressure symptoms or cosmetic problems, 3) the serum thyroid hormone and thyrotropin levels were within normal limits, 4) 2 separate ultrasound (US)-guided fine-needle aspirations led to a cytologically confirmed diagnosis of a benign lesion, and 5) there were no malignant features on the US examination.^{21–23}

Preablation Assessment

The US and US-guided fine-needle aspirations were performed by 2 radiologists (J.H.B. and J.H.L., who had 17 and 13 years of thyroid US experience, respectively). The US examinations were performed by using 1 of 2 US systems equipped with a linear high-frequency probe (5–14 MHz), namely, iU22 U (Philips Healthcare, Bothell, Washington) or EUB-7500 U (Hitachi Medical Systems, Tokyo, Japan). The size, volume, amount of solid component, and vascularity of each nodule were assessed. The 3 orthogonal diameters of each nodule (the largest diameter and the 2 diameters perpendicular to it) were measured, and the volume of each nodule was calculated by using the following equation: $V = \pi abc / 6$, where V is volume, a is the largest diameter, and b and c are the 2 perpendicular diameters.^{8,13,24} Under US guidance, 1 of the 2 radiologists performed fine-needle aspiration on the solid component of each nodule. At enrollment, the patients were asked to rate their symptom score on a 10-cm Visual Analog Scale (0–10). The physicians recorded a cosmetic grade (1, no palpable mass; 2, a palpable mass but no cosmetic problem; 3, cosmetic problem on swallowing only; and 4, readily detected cosmetic problem).^{6,25,26}

Procedure

All procedures were performed under US guidance. Intravenous sedatives or analgesics were not used before or during the procedure. The patients were placed in a supine position with mild neck extension. After skin sterilization and anesthesia with 2% lidocaine at the puncture site, a 16- or 18-ga needle was inserted into the cystic portion of the thyroid nodules through the isthmic area (this is the so-called transisthmic approach) to prevent leakage of fluid or ethanol.^{6,18,25} After the needle tip was placed into the cystic portion, as much of the internal fluid as possible was aspirated. If active bleeding was detected during the aspiration of the internal fluid, the aspiration was stopped and 99% ethanol was injected slowly into the cystic space to control the bleeding (On-line Video). The injected volume of ethanol corresponded to approximately 50% of the aspirated fluid volume. After 2 minutes of ethanol retention, as much of the injected ethanol as possible was removed.¹⁸ After real-time US confirmed that the bleeding had stopped, RF ablation was initiated. On the basis of previous experience, the RF ablation was performed by using a transisthmic approach and the moving-shot technique.

^{6–8,10,15,17,25–27} For this, an 18-ga 7-cm-long monopolar modified internally cooled electrode (Well-Point RF electrode; Taewoong Medical, Kimpo, Korea or VIVA; STARmed, Gyeonggi, Korea) with a 1- or 1.5-cm active tip and a 200-W RF generator (VIVA RF Generator; STARmed) was used.

When RF ablation was started with the 11 patients, echogenic bubbles developed much faster than would normally occur. This phenomenon was due to the remnants of ethanol in the nodule that had diffused into the septate cystic portion (On-line Video). The moving-shot technique used for thyroid RF ablation^{7,8,10,28–30} was first proposed by Baek et al,²⁶ who suggested that the thyroid nodule should be divided into multiple conceptual ablation units that would each undergo RF ablation; this was achieved by moving the electrode tip. Because the conceptual units are smaller at the periphery of the nodule and larger in the center of the nodule, the electrode tip was initially positioned in the deepest, most remote portion of the nodule where there were no disturbances caused by microbubbles; this positioning facilitated the monitoring of the electrode tip. RF ablation was terminated when all conceptual units of the targeted nodule had changed into a transient hyperechoic zone. Adverse events during and immediately after the procedure were recorded. After RF ablation, the patient was observed for 1–2 hours in the hospital.

Follow-Up and Analysis

At 1, 6, and 12 months after RF ablation and every 6–12 months thereafter, the clinical symptoms and cosmetic problems of all patients were re-evaluated. US examinations were also performed; changes in the amounts of the cystic portion, the internal vascularity, the echogenicity, the size, and the volume of the nodules were recorded. The efficacy of RF ablation was determined by measuring the volume reduction of the treated thyroid nodules and by assessing changes in the symptoms and cosmetic problems. Therapeutic success was defined as a nodule volume reduction >50%. Adverse events during the follow-up period were also recorded. Recurrence was defined as an increase in nodule volume by >50% relative to the volume recorded by US previously.²¹

Statistical Analysis

All statistical analyses were performed by using the Statistical Package for the Social Sciences for Windows (Version 18.0; IBM, Armonk, New York). The Wilcoxon signed rank test was used to evaluate the efficacy (changes in the largest diameter, the volume, and the cosmetic and symptom scores) of RF ablation at the 1-month, 6-month, and last follow-up visits.

RESULTS

After EA, the active bleeding stopped in all patients and US confirmed that there was no blood collection within the thyroid nodule. The efficacy of RF ablation is summarized in the Table. The mean follow-up period was 11.4 ± 6.7 months (range, 6–24 months). The mean largest diameter decreased from 4.1 ± 1.3 cm (range, 2.4–7.1 cm) before treatment to 2.3 ± 0.6 cm (range, 1.3–3.0 cm) at the last follow-up ($P = .003$), and the mean volume dropped from 17.1 ± 16.9 mL (range, 2.9–59.0 mL) to 2.6 ± 2.1

mL (range, 0.2–6.9 mL) at the last follow-up ($P = .005$). At the 1-month, 6-month, and last follow-up visits, the mean volume reduction percentages were 52.9%, 75.6%, and 81.0%, respectively. Therapeutic success was achieved in all patients. The mean cosmetic score decreased from 4.0 before treatment to 2.8 ± 1.0 (range, 1–4) at the last follow-up ($P = .01$). The mean symptom score dropped from 2.7 ± 1.5 (range, 1–5) before treatment to 1.1 ± 1.0 (range, 0–4) at the last follow-up ($P = .011$). The follow-up US examinations indicated well-treated nodules that no longer had a cystic portion and whose echogenicity of the solid portion and intranodular vascularity was decreasing (Fig 1).

The mean number of ablation sessions was 1.2 ± 0.6 (range, 1–3): Ten patients had 1 session, while the remaining patient had 3 sessions. The latter patient had a large initial thyroid nodule

Efficacy of ethanol and RF ablation combination therapy^a

	Initial	Last Follow-Up	P Value
Largest diameter (cm)	4.1 ± 1.3	2.3 ± 0.6	.003
Volume (mL)	17.1 ± 16.9	2.6 ± 2.1	.005
Cosmetic score	4.0 ± 0	2.8 ± 1.0	.01
Symptom score	2.7 ± 1.5	1.1 ± 1.0	.011
Volume reduction (%)	–	81	–
Therapeutic success (%) ^b	–	100	–

^a Values are means.

^b Therapeutic success is volume reduction >50%.

volume of 37.3 mL. The mean ablation time and power were 6.3 ± 3.0 minutes (range, 3–12 minutes) and 57.3 ± 24.9 W (range, 30–120 W), respectively. The mean total energy deposition was $21,218.2 \pm 11,523.7$ J (range, 7800–36,000 J). The mean energy delivered per milliliter of pretreatment nodule volume was 2013.3 ± 1228.3 J (range, 684.2–4230.8 J). The mean volume of aspirated internal fluid was 8.8 ± 9.3 mL (range, 2–35 mL), while the mean amount of ethanol that was injected was 5.1 ± 5.7 mL (range, 1–20 mL).

There were no major complications, such as voice changes, skin burn, hematoma, esophageal injury, tracheal injury, or infection, either during the procedure or in the follow-up period. During RF ablation, most patients reported pain and a sensation of heat in the neck that radiated to the head, shoulders, teeth, and chest. The symptoms were relieved by reducing the RF power or stopping the ablation for several seconds. All patients tolerated the RF ablation procedure well.

DISCUSSION

The present study showed that EA effectively controlled the post-aspiration hemorrhage in all patients. The RF ablation, after bleeding control was achieved, significantly reduced the nodule volume and relieved the symptomatic and cosmetic problems. In addition, 91% (10/11) of the patients could be treated by 1 RF session, and there were no recurrences during the follow-up pe-

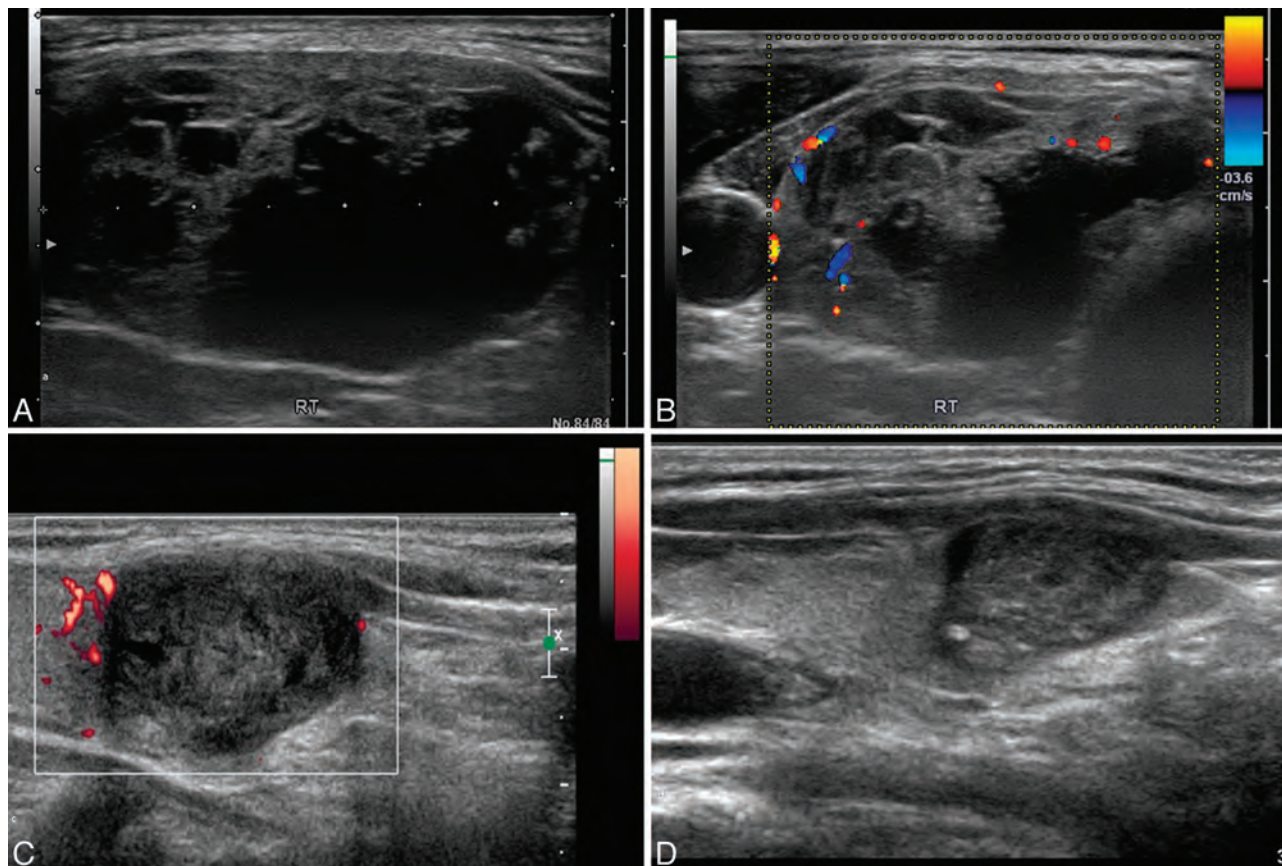


FIG 1. A 59-year-old female patient who presented with a bulge in the neck. *A*, Transverse US images at presentation show a thyroid nodule with a cystic portion in the right thyroid gland. The initial volume of the nodule was 11.4 mL. *B*, On Doppler US, increased vascularity in the solid portion of the nodule was also noted. *C* and *D*, After active bleeding was controlled by EA and RF ablation was performed, the volume of the ablated nodule decreased gradually to 2.8 and 0.9 mL at the 6- and 12-month follow-up US examinations, respectively. At the 12-month follow-up visit, the volume had been reduced by approximately 92%.

riod. There were also no complications that related to the EA or RF ablation.

Initial nodule volume can be a risk factor for poor volume reduction by RF and the need for additional RF treatment sessions. Huh et al²⁰ reported that an initial nodule volume larger than 20 mL required additional RF ablation to achieve satisfactory clinical results. Moreover, Jeong et al⁸ reported that thyroid nodules with a mean volume of 6.1 mL required an average of 1.4 treatment sessions, while Lim et al³¹ reported that thyroid nodules with a mean volume of 9.8 mL required 2.2 treatment sessions on average. These results indicate that smaller thyroid nodules can be treated with fewer sessions. In the present study, the mean nodule volume was larger (17.1 mL) than the mean volumes in the other RF studies (6.1–9.8 mL).^{8,31} Nevertheless, 91% (10/11) of patients could be treated in a single RF session; in addition, there were no recurrences during the mean follow-up period of 11.4 months. As a result, the mean treatment session number in this study was smaller (1.2) than the numbers in other studies (1.4–2.2). The present study differed from the preceding studies in that the internal fluid was aspirated to reduce the nodule volume with the aim of reducing the number of treatment sessions. The results indicate that this approach was successful. However, active bleeding can be triggered by the aspiration, and this can create an important technical problem: It can cause sudden enlargement of the thyroid nodule and the heat sink effect of the blood can make RF ablation ineffective. The present study showed that EA successfully controlled active bleeding during aspiration and that nodule volume was effectively reduced before RF ablation.

The reduction in nodule volume after RF ablation has been found to range from 33% to 58% at 1 month and from 51% to 92% at 6 months.²⁶ Jeong et al⁸ reported that after a mean follow-up period of 12 months, the mean volume reduction was 84.1% and that 70.2% of the nodules could be treated by a single treatment session. In the present study, the mean follow-up period was 11.4 ± 6.7 months, the mean volume reduction was 81.0%, and 91% (10/11) of the nodules could be treated by a single session. Therefore, our results are comparable with those of previous studies with fewer treatment sessions. In addition, there was 100% technical success and no major complications.

RF ablation combined with EA has been used for hepatocellular carcinomas in high-risk locations, and 2 studies have shown that this combination is more effective and safe than RF ablation alone.^{32,33} In these studies, the principal role of ethanol was to induce a larger necrotic area and to minimize complications.^{34,35} To our knowledge, the present study is the first to examine the efficacy of the combination of these 2 modalities in treating predominantly cystic thyroid nodules.

The present study has several limitations. First, it had a retrospective design, but a standard technique was used to control active bleeding during the RF ablation. Second, the number of cases was small, and the follow-up period was short. Third, there was no control group. Further prospective studies are required to verify the value of the current study.

CONCLUSIONS

EA is a feasible and safe technique for controlling the active bleeding of predominantly cystic thyroid nodules that can occur when internal fluid is aspirated before RF ablation, allowing RF ablation to proceed in a single session in most instances.

REFERENCES

1. Mazzaferri EL. **An overview of the management of papillary and follicular thyroid carcinoma.** *Thyroid* 1999;9:421–27
2. Yasuda K, Ozaki O, Sugino K, et al. **Treatment of cystic lesions of the thyroid by ethanol instillation.** *World J Surg* 1992;16:958–61
3. Cho YS, Lee HK, Ahn IM, et al. **Sonographically guided ethanol sclerotherapy for benign thyroid cysts: results in 22 patients.** *AJR Am J Roentgenol* 2000;174:213–16
4. Kim JH, Lee HK, Lee JH, et al. **Efficacy of sonographically guided percutaneous ethanol injection for treatment of thyroid cysts versus solid thyroid nodules.** *AJR Am J Roentgenol* 2003;180:1723–26
5. Zingrillo M, Torlontano M, Ghiggi MR, et al. **Percutaneous ethanol injection of large thyroid cystic nodules.** *Thyroid* 1996;6:403–08
6. Sung JY, Kim YS, Choi H, et al. **Optimum first-line treatment technique for benign cystic thyroid nodules: ethanol ablation or radiofrequency ablation?** *AJR Am J Roentgenol* 2011;196:W210–14
7. Baek JH, Moon WJ, Kim YS, et al. **Radiofrequency ablation for the treatment of autonomously functioning thyroid nodules.** *World J Surg* 2009;33:1971–77
8. Jeong WK, Baek JH, Rhim H, et al. **Radiofrequency ablation of benign thyroid nodules: safety and imaging follow-up in 236 patients.** *Eur Radiol* 2008;18:1244–50
9. Spiezia S, Garberoglio R, Milone F, et al. **Thyroid nodules and related symptoms are stably controlled two years after radiofrequency thermal ablation.** *Thyroid* 2009;19:219–25
10. Baek JH, Kim YS, Lee D, et al. **Benign predominantly solid thyroid nodules: prospective study of efficacy of sonographically guided radiofrequency ablation versus control condition.** *AJR Am J Roentgenol* 2010;194:1137–42
11. Deandrea M, Limone P, Basso E, et al. **US-guided percutaneous radiofrequency thermal ablation for the treatment of solid benign hyperfunctioning or compressive thyroid nodules.** *Ultrasound Med Biol* 2008;34:784–91
12. Baek JH, Lee JH, Sung JY, et al. **Complications encountered in the treatment of benign thyroid nodules with US-guided radiofrequency ablation: a multicenter study.** *Radiology* 2012;262:335–42
13. Baek JH, Kim YS, Sung JY, et al. **Locoregional control of metastatic well-differentiated thyroid cancer by ultrasound-guided radiofrequency ablation.** *AJR Am J Roentgenol* 2011;197:W331–36
14. Bennedbaek FN, Hegedus L. **Treatment of recurrent thyroid cysts with ethanol: a randomized double-blind controlled trial.** *J Clin Endocrinol Metab* 2003;88:5773–77
15. Lee JH, Kim YS, Lee D, et al. **Radiofrequency ablation (RFA) of benign thyroid nodules in patients with incompletely resolved clinical problems after ethanol ablation (EA).** *World J Surg* 2010;34:1488–93
16. Sung JY, Baek JH, Kim KS, et al. **Single-session treatment of benign cystic thyroid nodules with ethanol versus radiofrequency ablation: a prospective randomized study.** *Radiology* 2013;269:293–300
17. Jang SW, Baek JH, Kim JK, et al. **How to manage the patients with unsatisfactory results after ethanol ablation for thyroid nodules: role of radiofrequency ablation.** *Eur J Radiol* 2012;81:905–10
18. Kim YJ, Baek JH, Ha EJ, et al. **Cystic versus predominantly cystic thyroid nodules: efficacy of ethanol ablation and analysis of related factors.** *Eur Radiol* 2012;22:1573–78
19. Dossing H, Bennedbaek FN, Hegedus L. **Beneficial effect of combined aspiration and interstitial laser therapy in patients with benign cystic thyroid nodules: a pilot study.** *Br J Radiol* 2006;79:943–47
20. Huh JY, Baek JH, Choi H, et al. **Symptomatic benign thyroid nodules: efficacy of additional radiofrequency ablation treat-**

- ment session—prospective randomized study. *Radiology* 2012; 263:909–16
21. Moon WJ, Baek JH, Jung SL, et al. **Ultrasonography and the ultrasound-based management of thyroid nodules: consensus statement and recommendations.** *Korean J Radiol* 2011;12:1–14
 22. Moon WJ, Jung SL, Lee JH, et al. **Benign and malignant thyroid nodules: US differentiation—multicenter retrospective study.** *Radiology* 2008;247:762–70
 23. Park JM, Choi Y, Kwag HJ. **Partially cystic thyroid nodules: ultrasound findings of malignancy.** *Korean J Radiol* 2012;13:530–35
 24. Kim SM, Baek JH, Kim YS, et al. **Efficacy and safety of ethanol ablation for thyroglossal duct cysts.** *AJNR Am J Neuroradiol* 2011;32:306–09
 25. Sung JY, Baek JH, Kim YS, et al. **One-step ethanol ablation of viscous cystic thyroid nodules.** *AJR Am J Roentgenol* 2008;191:1730–33
 26. Baek JH, Lee JH, Valcavi R, et al. **Thermal ablation for benign thyroid nodules: radiofrequency and laser.** *Korean J Radiol* 2011;12:525–40
 27. Ha EJ, Baek JH, Lee JH. **The efficacy and complications of radiofrequency ablation of thyroid nodules.** *Curr Opin Endocrinol Diabetes Obes* 2011;18:310–14
 28. Ha EJ, Baek JH, Lee JH, et al. **Radiofrequency ablation of benign thyroid nodules does not affect thyroid function in patients with previous lobectomy.** *Thyroid* 2013;23:289–93
 29. Shin JE, Baek JH, Lee JH. **Radiofrequency and ethanol ablation for the treatment of recurrent thyroid cancers: current status and challenges.** *Curr Opin Oncol* 2013;25:14–19
 30. Na DG, Lee JH, Jung SL, et al. **Radiofrequency ablation of benign thyroid nodules and recurrent thyroid cancers: consensus statement and recommendations.** *Korean J Radiol* 2012;13:117–25
 31. Lim HK, Lee JH, Ha EJ, et al. **Radiofrequency ablation of benign non-functioning thyroid nodules: 4-year follow-up results for 111 patients.** *Eur Radiol* 2013;23:1044–49
 32. Zhang YJ, Liang HH, Chen MS, et al. **Hepatocellular carcinoma treated with radiofrequency ablation with or without ethanol injection: a prospective randomized trial.** *Radiology* 2007;244: 599–607
 33. Ren H, Liang P, Yu X, et al. **Treatment of liver tumours adjacent to hepatic hilum with percutaneous microwave ablation combined with ethanol injection: a pilot study.** *Int J Hyperthermia* 2011;27:249–54
 34. Wong SN, Lin CJ, Lin CC, et al. **Combined percutaneous radiofrequency ablation and ethanol injection for hepatocellular carcinoma in high-risk locations.** *AJR Am J Roentgenol* 2008; 190:W187–95
 35. Zhou P, Liu X, Li R, et al. **Percutaneous coagulation therapy of hepatocellular carcinoma by combining microwave coagulation therapy and ethanol injection.** *Eur J Radiol* 2009;71:338–42

Left Hemisphere Diffusivity of the Arcuate Fasciculus: Influences of Autism Spectrum Disorder and Language Impairment

T.P.L. Roberts, K. Heiken, D. Zarnow, J. Dell, L. Nagae, L. Blaskey, C. Solot, S.E. Levy, J.I. Berman, and J.C. Edgar



ABSTRACT

BACKGROUND AND PURPOSE: There has been much discussion whether brain abnormalities associated with specific language impairment and autism with language impairment are shared or are disorder specific. Although white matter tract abnormalities are observed in both specific language impairment and autism spectrum disorders, the similarities and differences in the white matter abnormalities in these 2 disorders have not been fully determined.

MATERIALS AND METHODS: Diffusion tensor imaging diffusion parameters of the arcuate fasciculus were measured in 14 children with specific language impairment as well as in 16 children with autism spectrum disorder with language impairment, 18 with autism spectrum disorder without language impairment, and 25 age-matched typically developing control participants.

RESULTS: Language impairment and autism spectrum disorder both had (elevating) main effects on mean diffusivity of the left arcuate fasciculus, initially suggesting a shared white matter substrate abnormality. Analysis of axial and radial diffusivity components, however, indicated that autism spectrum disorder and language impairment differentially affect white matter microstructural properties, with a main effect of autism spectrum disorder on axial diffusivity and a main effect of language impairment on radial diffusivity.

CONCLUSIONS: Although white matter abnormalities appear similar in language impairment and autism spectrum disorder when examining broad white matter measures, a more detailed analysis indicates different mechanisms for the white matter microstructural anomalies associated with language impairment and autism spectrum disorder.

ABBREVIATIONS: AD = axial diffusivity (λ_1) [where λ_1 , λ_2 , and λ_3 are the eigenvalues of the diffusion tensor]; ASD+LI = autism spectrum disorder with significant clinical language impairment; ASD-LI = autism spectrum disorder without language impairment; CELF-4 = Clinical Evaluation of Language—Fourth Edition; FA = fractional anisotropy; MD = mean diffusivity $(\lambda_1 + \lambda_2 + \lambda_3)/3$ [where λ_1 , λ_2 , and λ_3 are the eigenvalues of the diffusion tensor]; RD = radial diffusivity $(\lambda_2 + \lambda_3)/2$ [where λ_1 , λ_2 , and λ_3 are the eigenvalues of the diffusion tensor]; SLI = specific language impairment

Similarities and differences in the biologic “substrates” of language impairment (LI) in patients with specific language impairment (SLI) and in language-impaired patients with autism spectrum disorder (ASD) have been the subject of debate for nearly 30 years.¹ Some argue that the LI observed in both disorders is similar in nature.^{2,3} Supporting this view, adolescents with a history of SLI have a 10-fold increased risk for ASD.⁴ These 2 groups also share anatomic and electrophysiologic abnormalities. For example, patients with SLI and those with ASD with LI (ASD+LI) both have reversed asymmetry in frontal language-related cortex⁵ as well as delayed auditory-

evoked mismatch fields.⁶ Thus, part of the motivation of our present study is to identify neural substrates that support language and that are shared in SLI and ASD+LI.

Other evidence, however, suggests that the 2 disorders are distinct. For example, children with SLI make different types of errors than children with ASD+LI in nonword repetition tasks.⁷ Studies examining the superior longitudinal fasciculus, a major white matter pathway connecting the Broca and Wernicke areas and subserving language function, also suggest that SLI and ASD+LI are distinct. For example, in 2012 Verhoeven et al¹ found that whereas DTI fractional anisotropy (FA) measures of the superior longitudinal fasciculi were reduced in participants with SLI compared with age-matched control participants, FA differences were not observed between participants with ASD+LI and age-matched control participants (differences in ADC, a measure equivalent to mean diffusivity [MD], were also not found between any of the groups). This SLI and ASD+LI white matter difference might be interpreted as suggesting a neurobiologic abnormality unique to SLI.

Recently, our group demonstrated elevated MD of the left hemi-

Received April 23, 2013; accepted after revision June 24.

From the Lurie Family Foundations MEG Imaging Center, Department of Radiology, Children's Hospital of Philadelphia, Philadelphia, Pennsylvania.

This work was supported by NIH-R01DC008871 and NIH-P30HD026979 grants.

Please address correspondence to Timothy P.L. Roberts, PhD, Children's Hospital of Philadelphia, 34th and Civic Center Blvd, Neuroradiology, Suite 2115, Wood Building, Philadelphia, PA 19104.

Indicates open access to non-subscribers at www.ajnr.org

<http://dx.doi.org/10.3174/ajnr.A3754>

sphere superior longitudinal fasciculus in ASD vs typically developing control participants, with group differences exacerbated by the degree of LI in ASD participants.⁸ To further investigate the above issues, in our present study, diffusion parameters of the superior longitudinal fasciculus in SLI were compared with typically developing and both ASD groups examined in Nagae et al.⁸ Given that in the study by Nagae et al⁸ group differences were most pronounced in the arcuate fasciculus, an area that corresponds with the temporal aspect of the superior longitudinal fasciculus, analyses focused on DTI parameters in this superior longitudinal fasciculus subregion.

It has been hypothesized that similarities in left hemisphere MD elevation in ASD+LI and SLI would be revealed in a main effect of LI. However, given an elevation in MD, even without LI, as reported by Nagae et al,⁸ the possibility of a main effect of ASD per se was also considered. Although the MD results in the typically developing and ASD groups have been reported by Nagae et al,⁸ in our study, this previous work was extended by incorporating the SLI cohort. Furthermore, and importantly, to probe a mechanistic underpinning of MD observations, and to identify potential differences in the cause of MD elevation, closer examination of the axial diffusivities (ADs) and radial diffusivities (RDs) was attempted as functions of LI, and of a diagnosis of ASD.

MATERIALS AND METHODS

Some DTI analyses of the typically developing and ASD groups in our study have been reported previously.⁸ In addition, magnetoencephalography measures of the M100 auditory response and the magnetic mismatch field have been previously reported for all participants.^{6,9,10} All studies were performed with permission from our institutional review board, with the written informed consent of a parent and assent from participants.

Participants

Fourteen children with SLI (mean age, 9.73 ± 2.69 years; 8 boys) were recruited from the Center for Childhood Communication at the Children's Hospital of Philadelphia. Thirty-four participants with ASD were recruited through the Regional Autism Center at the Children's Hospital of Philadelphia: 16 with concomitant LI (mean age, 9.80 ± 2.57 years; 14 boys), and 18 without LI (mean age, 11.47 ± 3.25 ; 16 boys). A cohort of 25 age-matched control participants was also included (mean age, 11.42 ± 2.92 years, 16 boys). Groups did not differ in age ($P > .05$).

Speech-language pathologists and neuropsychologists completed diagnostic and language assessments. Details of the inclusion and exclusion criteria for each group are reported in previous studies.^{6,8-10} Language was assessed by use of tests including the Clinical Evaluation of Language Fundamentals—Fourth Edition (CELF-4)¹¹ and the Comprehensive Test of Phonological Processing.¹² All referred ASD participants had a prior diagnosis of ASD, which was confirmed by the Autism Diagnostic Observation Schedule,¹³ the Krug Asperger's Disorder Index,¹⁴ the Social Responsiveness Scale,¹⁵ and parent report on the Social Communication Questionnaire.¹⁶ Global intelligence and academic achievement were assessed by use of the Wechsler Intelligence Scale for Children—Fourth Edition¹⁷ and the Wechsler Individual Achievement Test—Second Edition.¹⁸ All participants had a score of at least 75 on either the Perceptual Reasoning Index or Verbal Comprehension Index of the Wechsler Intelligence Scale for Children—Fourth Edition.

Imaging

DTI acquisition and postprocessing has been detailed elsewhere.⁸ In brief, acquisition parameters were as follows: isotropic 2-mm-thick contiguous whole-brain acquisition performed on a 3T magnet (Verio; Siemens, Erlangen, Germany); FOV, 25.6 cm; matrix, 128×128 ; TR, 14,000 ms; TE, 70 ms; a scheme with 80 contiguous sections and 30 diffusion-encoding gradient directions; $b = 0$ (0 s/mm^2), $b_{\text{max}} = 1000 \text{ s/mm}^2$; generalized auto-calibrating partially parallel acquisition with an acceleration factor of 2.0. Postprocessing was performed by use of DTIStudio (Johns Hopkins University, Baltimore, Maryland).¹⁹ Streamline tractography of the right and left arcuate fasciculi was performed blind to the clinical group and following tractography protocol guidelines described by Wakana et al²⁰ and Nagae et al⁸ by use of the fiber assignment by continuous tractography algorithm and a multiple region-of-interest inclusion criterion, with an FA threshold of 0.25 and a turning angle cutoff value of 70° . Figure 1 depicts left and right arcuate fasciculi tractograms from a representative 10-year-old boy from each group. MD was integrated over the entire tract length as described by Nagae et al,⁸ as were magnitudes of each eigenvalue, allowing computation of axial and RDs. AD, equivalent to eigenvalue λ_1 , may be interpreted as diffusion along axon bundles. RD, defined as the mean of eigenvalues λ_2 and λ_3 , may be interpreted as that component of diffusion in a plane perpendicular to the primary orientation of axonal bundles.^{21,22}

Statistical Analysis

Statistical analyses included a 2×2 ANOVA (general linear model) with factors of ASD and LI. Age and Perceptual Reasoning Index were included as covariates in all analyses. Given findings showing typically developing and ASD group differences in the left, but not right, hemisphere,⁸ analyses were conducted separately for the left and right arcuate fasciculus tracts. Finally, regression analyses examined associations between clinical measures—language and symptom ratings—and diffusivity measures.

RESULTS

As expected, children with ASD (both \pm LI) scored higher on the Social Responsiveness Scale than children in the typically developing and SLI groups ($P < .001$). Social Responsiveness Scale scores did not differ between ASD–LI and ASD+LI ($P > .05$) but were higher in those with SLI than typically developing subjects ($P < .01$). CELF-4 Core Language Index scores were highest in the nonlanguage-impaired groups (ie, ASD–LI and typically developing, $P < .001$). The SLI cohort performed better on the CELF-4 Core Language Index than the ASD+LI group ($P = .01$). Typically developing and ASD–LI participants scored higher on the Full Scale Intelligence Quotient and Perceptual Reasoning Index than ASD+LI subjects ($P < .05$).

In the left hemisphere, main effects of ASD ($P = .03$) and LI ($P = .04$) were found on arcuate fasciculus MD (Fig 2). The interaction term was not significant ($P > .05$). Significance of findings remained the same when age and Perceptual Reasoning Index were not included as covariates. No differences in left arcuate fasciculus FA were found.

To further understand the left hemisphere diffusion abnormalities, we examined AD and RD. A main effect of ASD was

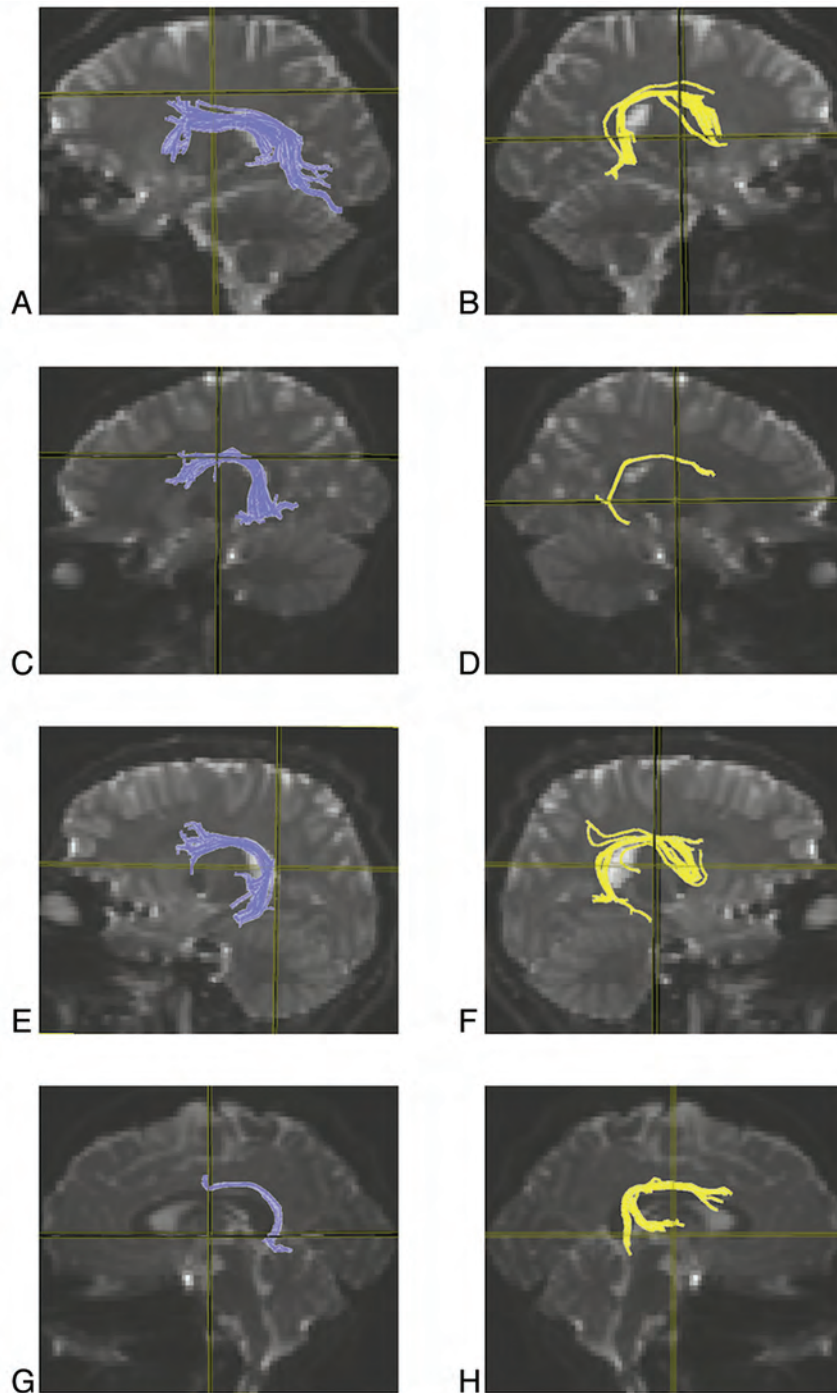


FIG 1. Streamline tractography of the arcuate fasciculus. Tractography of the left (left column; A,C,E,G) and right (right column; B,D,F,H) arcuate fasciculi in a 10-year-old male participant from each group (typically developing, A–B; ASD–LI, C–D; ASD+LI, E–F; SLI, G–H).

found on AD ($P < .001$) but not RD ($P = .61$) (Fig 3). Conversely, there was a main effect of LI on RD ($P = .02$) but not AD ($P = .55$) (Fig 4). There was also a significant ASD by LI interaction on AD ($P = .05$), revealing the highest AD in the ASD+LI group. The interaction term was not significant for RD ($P = .68$).

No group differences were observed in the right hemisphere arcuate fasciculus for any of the 4 DTI measures: MD, FA, RD, or AD. The Table shows age- and Perceptual Reasoning Index–corrected marginal means for MD, FA, AD, and RD for each hemisphere.

Hierarchical regression examined associations between clinical symptoms and diffusivity measures. Given the significant effects of age and Perceptual Reasoning Index on diffusivity, hierarchical regressions were performed with age entered first, Perceptual Reasoning Index second, and CELF-4 Core Language Index scores third, with left hemisphere arcuate fasciculus diffusivity parameters as the dependent measures (Table). CELF-4 Core Language Index scores predicted unique variance in left arcuate fasciculus MD [$F(1,68) = 7.83, P < .01$], RD [$F(1,68) = 5.00, P = .03$], and AD [$F(1,68) = 3.87, P = .05$]. Rerunning the above regressions for each subgroup, however, did not show relationships with CELF-4 Core Language Index for any of the individual groups. CELF-4 Core Language Index scores did not predict variance in FA [$F(1,68) = 1.09, P = .30$]. Pooling the 2 language impaired subgroups (SLI and ASD+LI), we observed a nonsignificant trend for an association between elevated MD and impaired language performance reflected in the CELF-4 Core Language Index [$F(1,25) = 3.29, P = .08$].

Regressions were also performed with age and Perceptual Reasoning Index entered into the first 2 blocks and Social Responsiveness Scale scores third. Social Responsiveness Scale scores predicted unique variance in MD [$F(1,67) = 3.92, P = .05$] and AD [$F(1,67) = 6.70, P = .01$]. Social Responsiveness Scale scores did not predict the variance in RD [$F(1,67) = 0.68, P = .41$] or FA [$F(1,67) = 0.25, p = 0.62$]. Similar to the CELF-4 Core Language Index analyses, regressions with Social Responsiveness Scale were not significant when groups were individually analyzed.

DISCUSSION

There were 2 main findings. First, main effects of both ASD and also LI were found on MD of the left hemisphere arcuate fasciculus, with both ASD and LI associated with elevated MD. At first, this finding appears to reflect a shared ASD

and LI biologic substrate. However, a second finding showed a main effect of ASD on the axial, but not radial, component of diffusivity, and a main effect of LI on the radial, but not axial, component of diffusivity. As both AD and RD elevations could contribute to the observed MD elevations, this trend suggests that though both ASD and LI are associated with microstructural abnormalities in the left hemisphere arcuate fasciculus, the nature of these microstructural abnormalities is somewhat distinct.

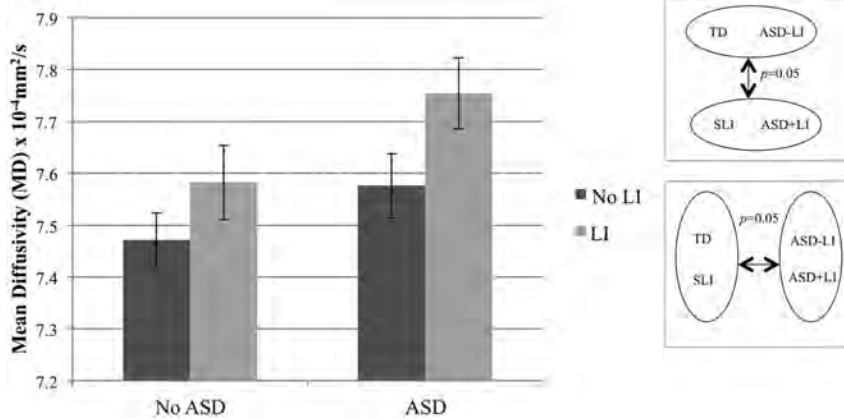


FIG 2. MD of the left arcuate fasciculus. ANOVA with factors of ASD (\pm) and LI (\pm), and covarying age and Perceptual Reasoning Index, revealed significant main effects of ASD ($P = .03$) and LI ($P = .04$).

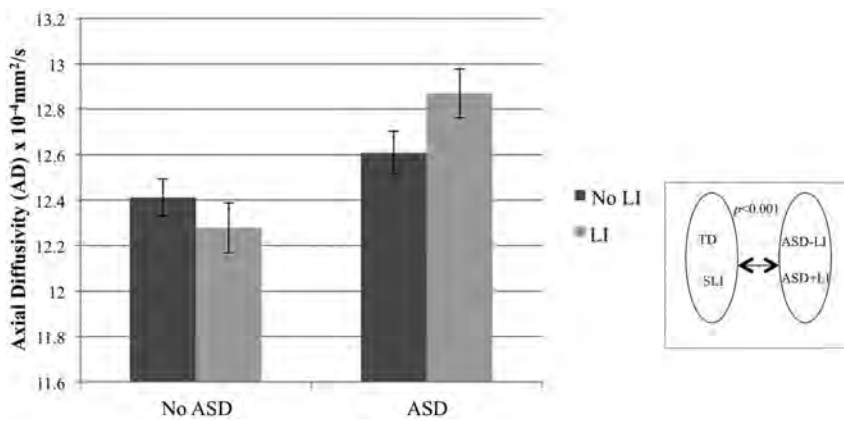


FIG 3. AD of the left arcuate fasciculus. ANOVA with factors of ASD (\pm) and LI (\pm), and covarying age and Perceptual Reasoning Index, revealed a main effect of ASD ($P < .001$). There was also a significant ASD by LI interaction ($P = .05$), revealing the greatest elevation in the ASD+LI group.

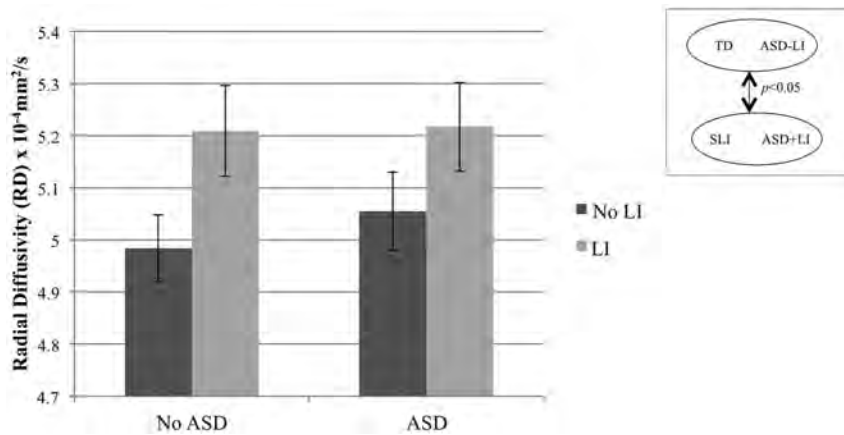


FIG 4. RD of the left arcuate fasciculus. ANOVA with factors of ASD (\pm) and LI (\pm), and covarying age and Perceptual Reasoning Index, revealed a significant main effect of LI ($P = .02$) on RD in the left arcuate fasciculus.

Diffusion imaging studies in ASD generally report elevated diffusivity and decreased FA in multiple brain areas, though the nature of arcuate fasciculus abnormalities is still in debate, as reviewed by Travers et al.²¹ Even less is known about the white

matter integrity of children with SLI. Verhoeven et al¹ compared DTI parameters of the superior longitudinal fasciculus in children with SLI and children with ASD+LI with healthy control participants. Contrary to present findings and previously reported ASD studies,^{8,21} the only significant finding in Verhoeven et al¹ was decreased FA in SLI. Discrepancies between this study and our present study may be related to the approach by Verhoeven et al,¹ namely to evaluate the entire superior longitudinal fasciculi tract rather than its subregions. Nonetheless, decreased FA is commonly associated with elevated MD; thus, apparent differences among studies may reflect differing sensitivities of these commonly used eigenvalue constructs rather than different underlying biologic processes. Furthermore, FA reflects a composite combination of eigenvalues perhaps obscuring opposing individual eigenvalue phenomena.

An additional finding emerges from attempting to understand the nature of the LI and ASD white matter abnormalities, with AD and RD analyzed separately (Figs 3–5). In our current study, AD was associated with ASD and RD with LI. That is, in both SLI and ASD+LI, elevated RD was observed, reinforcing the notion of similar anatomic substrates underlying LI in both populations. A main effect of ASD (and not LI) on AD, as well as the significant ASD by LI interaction in AD, however, suggests an additional contribution to a microstructural anomaly in ASD+LI (above and beyond that in SLI). Thus, in short, although ASD+LI and SLI may share a microstructural anomaly of elevated RD, they differ in AD. As Fig 5 illustrates, this mechanism leads to a “doubly” elevated MD in the ASD+LI cohort.

Consistent with the general linear model main effects, linguistic abilities (reflected in the CELF-4 Core Language Index) correlated with left hemisphere arcuate fasciculus RD when assessed across all participants. In addition, an association with AD was also resolved. However, this relationship between language skills and AD (not predicted by the general linear model analyses) was most likely driven by the fact that more than half of the LI participants also have ASD and, thus, elevated AD. Indeed, the relationship between CELF-4 Core Language Index scores and AD did not

Diffusion of the arcuate fasciculus

	TD		SLI		ASD-LI		ASD+LI	
	LH	RH	LH	RH	LH	RH	LH	RH
MD × 10 ⁻⁴ mm ² /s	7.472 ± 0.052 ^a	7.606 ± 0.059 ^a	7.582 ± 0.071	7.602 ± 0.078	7.576 ± 0.061 ^a	7.664 ± 0.070 ^a	7.754 ± 0.069 ^a	7.749 ± 0.079 ^a
FA	.542 ± 0.005 ^a	.528 ± 0.007 ^a	0.525 ± 0.007	.519 ± 0.009	.543 ± 0.006 ^a	.524 ± 0.008 ^a	.535 ± 0.007 ^a	.504 ± 0.009 ^a
RD	4.984 ± 0.064	5.140 ± 0.076	5.209 ± 0.087	5.233 ± 0.100	5.055 ± 0.075	5.255 ± 0.089	5.217 ± 0.085	5.404 ± 0.100
AD	12.412 ± 0.081	12.513 ± 0.085	12.278 ± 0.110	12.310 ± 0.112	12.609 ± 0.095	12.589 ± 0.100	12.870 ± 0.107	12.461 ± 0.113

Note:—All are marginal mean measures ± SEM projected to a mean age of 10.81 years and a Perceptual Reasoning Index (PRI) score of 101.92 in the left hemisphere; mean age was 10.75 years, and PRI score was 101.97 in the right hemisphere.

TD indicates typically developing; LH, left hemisphere; RH, right hemisphere.

^aPartially reported in Nagae et al.⁸

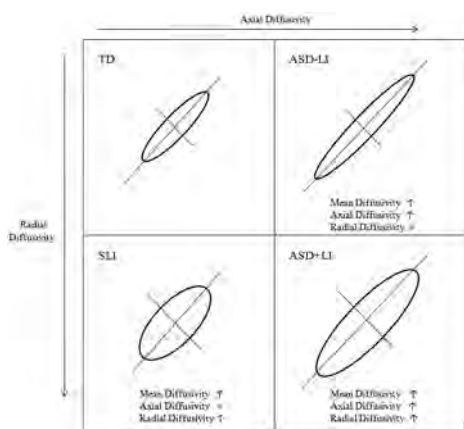


FIG 5. A schematic of the diffusion changes accompanying ASD and LI. Mean diffusivity was elevated in LI and ASD. Children with ASD had elevated AD (*right boxes*) and, thus, elevated MD. Patients with LI (*bottom boxes*) had elevated MD because of increased RD. Patients with ASD and LI had the highest MD values because of combined effects of both elevated RD and AD.

persist when ASD symptom severity was included in the model. Conversely, the relationship between linguistic skills and RD strengthened when measures of ASD were included in the model. However, none of the associations remained significant when individual subpopulations were considered, though there was a nonsignificant trend ($P = .08$) in the association between MD and CELF-4 Core Language Index when evaluated over all children with LI (SLI and ASD+LI groups pooled). As an analogy, Social Responsiveness Scale scores correlated positively with AD and were unrelated to RD when evaluated across all participants, but again, associations were not significant for individual subpopulations, perhaps reflecting the need for yet larger sample sizes in each group.

We encountered limitations comparing our current results with the previous literature. A review of DTI studies in ASD found that only approximately one-third of studies reported AD and RD findings.²¹ Fletcher et al²³ reported elevated MD and RD in the left arcuate fasciculus of 10 adolescents with ASD, and no differences in FA or AD. However, the wide range of participants' linguistic skills (composite CELF-3 scores ranged from 50–111 and were significantly lower than those of an age-matched control group) makes it difficult to distinguish the separate effects of ASD and LI on diffusivity. In a similar fashion, the limited data available on SLI offer limited insight into the effects of LI on white matter microstructural integrity. Verhoeven et al¹ did report a positive correlation between the Word Classes Receptive subtest

of the CELF-4 and mean FA in the superior longitudinal fasciculus of adolescents with SLI. However, no such correlations were found in the ASD+LI group, and the authors did not report AD or RD.

The biologic interpretation of these microstructural anomalies remains speculative. It is tempting to consider elevated RD as reflecting immaturely bundled axons (with greater interaxonal space for RD). Increases in AD are perhaps less intuitive. However, in white matter with fiber crossings, alterations to the pattern of these crossing fibers or, indeed, the RD of component fibers can both manifest as increased AD.²⁴ In mouse models, decreased AD and increased RD have been associated with acute axon and myelin damage, respectively.^{25–27} However, these findings may not directly translate to humans, particularly in cases of chronic white matter microstructural damage. Pathologic increases of AD have also been reported. In a small study of adults with acute optic neuritis, Naismith et al²⁸ reported decreased AD within 1 month of onset, but there was substantially increased AD relative to control participants 1 year later. Indeed, widespread increased AD has been demonstrated in Alzheimer disease,²⁹ and in the right frontal tracts of patients with Parkinson disease.³⁰ Moreover, RD and AD seem to be far less specific in areas of chronic microstructural damage. In a study of diffusion in the spinal cord of patients with multiple sclerosis, Klawiter et al³¹ reported associations between RD and both levels of demyelination and axonal damage, but no relationship between axonal damage and AD. Although DTI is sensitive to alterations to white matter microstructure, the technique alone cannot provide a specific mechanism for the observed changes.

Finally, although our present findings are intriguing, a limitation of our study was that small sample sizes prevented the inclusion of handedness and sex as factors or inclusion/exclusion criteria. Furthermore, although the sample size evaluated in our study is a non-meager 73, it is clear that fine-grained microstructural characterization of both ASD and LI substrates, common and distinct, will require much larger samples, perhaps a need served by emerging multi-institutional data sharing initiatives such as the National Database for Autism Research (<http://ndar.nih.gov/>).

CONCLUSIONS

Elevations in the MD of the left hemisphere arcuate fasciculus were associated with both ASD and LI, potentially suggesting a similar biologic substrate. Closer inspection of the microstruc-

tural anomalies, however, suggested that elevated AD was associated with ASD and elevated RD with LI. In comparing ASD+LI with SLI, it is clear that both are similar in that they share elevated RD, but that they are distinct in that only ASD+LI additionally manifests elevated AD, and thus ASD+LI shows the most profound elevations in MD.

ACKNOWLEDGMENTS

We acknowledge Rachel Golemski, Jamie Rundio, and Peter Lam for technical assistance. Dr. Roberts thanks the Oberkircher family for the Oberkircher Family Endowed Chair in Pediatric Radiology. The authors would like to thank Thorsten Feiweier of Siemens Medical Solutions for the diffusion imaging pulse sequence.

Disclosures: Timothy Roberts—RELATED: National Institutes of Health (NIH),* Nancy Lurie Marks Family Foundation (NLMFF),* Comments: R01DC008871, P30HD026979, a grant from NLMFF; UNRELATED: Consultancy: Elekta, Prism Clinical Imaging. Deborah Zarnow—RELATED: Grant: NIH R01DC008871,* Nancy Lurie Marks Family Foundation,* NIH P30HD026979.* Lidia Nagae—RELATED: Grant: NIH,* NLMFF,* Comments: NIH R01DC008871,* NLMFF,* NIH P30HD026979* (Dr. Roberts's grants); UNRELATED: Grants/Grants Pending: The Radiological Society of North America Fellow Grant Award.* Lisa Blaskey—RELATED: Grant: NIH,* Nancy Lurie Marks Family Foundation,* Comments: NIH grant R01DC008871 (TR), NLMFF. Cynthia Solot—RELATED: Grant: to Tim Roberts.* Susan Levy—RELATED: Grant: NIH,* Comments: Grants: R01DC008871, P30HD026979; Other: Nancy Lurie Marks Family Foundation,* Comments: Private foundation. Jeffrey Berman—UNRELATED: Consultancy: McGowan Associates, Comments: MR compatibility testing unrelated to manuscript. J. Christopher Edgar—RELATED: Grant: NIH,* Comments: Grant to Dr. Roberts to study auditory processes in autism.*Money paid to institution.

REFERENCES

- Verhoeven JS, Rommel N, Prodi E, et al. **Is there a common neuro-anatomical substrate of language deficit between autism spectrum disorder and specific language impairment?** *Cereb Cortex* 2012;22:2263–71
- Bishop DV. **Overlaps between autism and language impairment: phenomimicry or shared etiology?** *Behav Genet* 2010;40:618–29
- Tager-Flusberg H, Joseph RM. **Identifying neurocognitive phenotypes in autism.** *Philos Trans R Soc Lond B Biol Sci* 2003;358:303–14
- Conti-Ramsden G, Simkin Z, Botting N. **The prevalence of autistic spectrum disorders in adolescents with a history of specific language impairment (SLI).** *J Child Psychol Psychiatry* 2006;47:621–28
- De Fossé L, Hodge SM, Makris N, et al. **Language-association cortex asymmetry in autism and specific language impairment.** *Ann Neurol* 2004;56:757–66
- Roberts TP, Heiken K, Kahn SY, et al. **Delayed magnetic mismatch negativity field, but not auditory M100 response, in specific language impairment.** *Neuroreport* 2012;23:463–68
- Williams D, Payne H, Marshall C. **Non-word repetition impairment in autism and specific language impairment: evidence for distinct underlying cognitive causes.** *J Autism Dev Disord* 2013;43:404–17
- Nagae LM, Zarnow DM, Blaskey L, et al. **Elevated mean diffusivity in the left hemisphere superior longitudinal fasciculus in autism spectrum disorders increases with more profound language impairment.** *AJNR Am J Neuroradiol* 2012;33:1720–25
- Roberts TP, Khan SY, Rey M, et al. **MEG detection of delayed auditory evoked responses in autism spectrum disorders: towards an imaging biomarker for autism.** *Autism Res* 2010;3:8–18
- Roberts TP, Cannon KM, Tavabi K, et al. **Auditory magnetic mismatch field latency: a biomarker for language impairment in autism.** *Biol Psychiatry* 2011;70:263–69
- Semel EM, Wiig, EH, Secord, W. *Clinical Evaluation of Language Fundamentals (CELF-4)*. San Antonio, Texas: The Psychological Corporation; 2003
- Wagner RK, Torgesen JK, Rashotte CA, et al. *Comprehensive Test of Phonological Processing*. Austin, Texas: Pro-Ed; 1999
- Lord C, Risi S, Lambrecht L, et al. **The autism diagnostic observation schedule—generic: a standard measure of social and communication deficits associated with the spectrum of autism.** *J Autism Dev Disord* 2000;30:205–23
- Krug D, Arick, JR. *Krug Asperger's Disorder Index*. Los Angeles: Western Psychological Services; 2003
- Constantino J, Gruber, CP. *Social Responsiveness Scale (SRS)*. Los Angeles: Western Psychological Services; 2005
- Rutter M, Bailey, A., Lloyd, C. *SCQ: Social Communication Questionnaire*. Los Angeles: Western Psychological Services; 2003
- Wechsler D. *Wechsler Intelligence Scale for Children*. San Antonio, Texas: The Psychological Corporation; 2003
- Wechsler D. *Wechsler Individual Achievement Test*. San Antonio, Texas: The Psychological Corporation; 2001
- Jiang H, van Zijl PC, Kim J, et al. **DTIStudio: resource program for diffusion tensor computation and fiber bundle tracking.** *Comput Methods Programs Biomed* 2006;81:106–16
- Wakana S, Caprihan A, Panzenboeck MM, et al. **Reproducibility of quantitative tractography methods applied to cerebral white matter.** *Neuroimage* 2007;36:630–44
- Travers BG, Adluru N, Ennis C, et al. **Diffusion tensor imaging in autism spectrum disorder: a review.** *Autism Res* 2012;5:289–313
- Wozniak JR, Lim KO. **Advances in white matter imaging: a review of in vivo magnetic resonance methodologies and their applicability to the study of development and aging.** *Neurosci Biobehav Rev* 2006;30:762–74
- Fletcher PT, Whitaker RT, Tao R, et al. **Microstructural connectivity of the arcuate fasciculus in adolescents with high-functioning autism.** *Neuroimage* 2010;51:1117–25
- Wheeler-Kingshott CA, Cercignani M. **About “axial” and “radial” diffusivities.** *Magn Reson Med* 2009;61:1255–60
- Song SK, Yoshino J, Le TQ, et al. **Demyelination increases radial diffusivity in corpus callosum of mouse brain.** *Neuroimage* 2005;26:132–40
- Song SK, Sun SW, Ju WK, et al. **Diffusion tensor imaging detects and differentiates axon and myelin degeneration in mouse optic nerve after retinal ischemia.** *Neuroimage* 2003;20:1714–22
- Song SK, Sun SW, Ramsbottom MJ, et al. **Dysmyelination revealed through MRI as increased radial (but unchanged axial) diffusion of water.** *Neuroimage* 2002;17:1429–36
- Naismith RT, Xu J, Tutlam NT, et al. **Disability in optic neuritis correlates with diffusion tensor-derived directional diffusivities.** *Neurology* 2009;72:589–94
- Acosta-Cabronero J, Alley S, Williams GB, et al. **Diffusion tensor metrics as biomarkers in Alzheimer's disease.** *PLoS One* 2012;7:e49072
- Theilmann RJ, Reed JD, Song DD, et al. **White-matter changes correlate with cognitive functioning in Parkinson's disease.** *Front Neurol* 2013;4:37
- Klawiter EC, Schmidt RE, Trinkaus K, et al. **Radial diffusivity predicts demyelination in ex vivo multiple sclerosis spinal cords.** *Neuroimage* 2011;55:1454–60

Regional Cerebral Blood Flow in Children From 3 to 5 Months of Age

A.F. Duncan, A. Caprihan, E.Q. Montague, J. Lowe, R. Schrader, and J.P. Phillips



ABSTRACT

BACKGROUND AND PURPOSE: Understanding the relationship between brain and behavior in early childhood requires a probe of functional brain development. We report the first large study of regional CBF by use of arterial spin-labeling in young children.

MATERIALS AND METHODS: Cerebral blood flow by use of arterial spin-labeling was measured in 61 healthy children between the ages of 3 and 5 months. Blood flow maps were parcellated into 8 broadly defined anatomic regions of each cerebral hemisphere.

RESULTS: There was no sex effect; however, group analysis demonstrated significantly greater CBF in the sensorimotor and occipital regions compared with dorsolateral prefrontal, subgenual, and orbitofrontal areas ($P < .0001$). A significant age effect was also identified, with the largest increase in blood flow between 3 and 5 months occurring in the following regions: orbitofrontal ($P < .009$), subgenual ($P < .002$), and inferior occipital lobe ($P = .001$).

CONCLUSIONS: These results are consistent with prior histologic studies demonstrating regional variation in brain maturation and suggest that arterial spin-labeling is sensitive to regional as well as age-related differences in CBF in young children.

ABBREVIATION: ASL = arterial spin-labeling

Child development during the first year of life is dynamic and complex, with well-established clinical norms for monitoring behavioral development.¹ Brain structural development at this age is characterized by changing synaptic attenuation,² neuronal attenuation,³ and myelination.⁴ Less is known about functional brain development, which prevents a full understanding of the relationships between brain structure and the increasing cognitive and motor skills that characterize early childhood.

Brain function can be assessed with perfusion studies because

of the tight coupling of metabolism to blood flow. Regional metabolism can be directly measured by use of PET, which requires radioactively labeled water as an injected tracer. In children 3 months of age, PET demonstrates increased metabolism in the parietal, temporal and visual cortex, basal ganglia, and cerebellar hemispheres, with increased metabolism in the frontal lobes later in the first year.⁵ The radiation required for PET limits its feasibility for use in studies of typically developing children.⁶

Recent advances in MR technology provide a noninvasive method of assessing regional CBF by use of arterial spin-labeling (ASL).⁷ Because there is no radiation or injectable contrast agent, ASL is appropriate for longitudinal studies in children. Preliminary work suggests that it is sensitive to changes occurring during normal brain maturation^{7,8} as well as in clinical populations such as children with preclinical sickle cell disease.⁹ However, normal regional CBF has not been established by use of ASL. Although there is tremendous potential for ASL to provide early markers of disease or perhaps even therapeutic targets in young children with various clinical conditions, a necessary first step is identifying the range of normal CBF in healthy children.

The objectives of this study were to quantify normal regional CBF through the use of ASL in healthy term-born children 3–5 months of age and to determine whether age-related changes in CBF could be detected. At this age, tremendous developmental changes are occurring, which may be reflected in regional brain metabolism.

Received April 4, 2013; accepted after revision June 8.

From the Department of Pediatrics, Division of Neonatology (A.F.D., J.L.), Clinical and Translational Science Center (R.S.), and Department of Neurology (J.P.P.), University of New Mexico, Albuquerque, New Mexico; The MIND Research Network (A.C.), Albuquerque, New Mexico; and NeuroDevelopmental Science Center (E.Q.M.), Akron Children's Hospital, Akron, Ohio.

Primary funding was provided by Dr George Cowan and the Delle Foundation. This project was supported in part or in full by the National Center for Research Resources and the National Center for Advancing Translational Sciences of the National Institutes of Health through Grant No. 8UL1TR000041 and the University of New Mexico Clinical and Translational Science Center Translational Sciences of the National Institutes of Health through Grant No. 8UL1TR000041. Additional support included a grant from the Department of Energy DE-FG02-08ER64581.

Please address correspondence to Andrea Freeman Duncan, MD, The University of New Mexico, Department of Pediatrics, MSC10 5590, One University of New Mexico, Albuquerque, NM 87131-0001; e-mail: afduncan@salud.unm.edu

Indicates open access to non-subscribers at www.ajnr.org

<http://dx.doi.org/10.3174/ajnr.A3728>

MATERIALS AND METHODS

Subjects

This cross-sectional study was part of an ongoing longitudinal investigation of normal child development; 77 subjects were studied at 4 ± 1 month of age. Imaging occurred at the MIND Research Network in Albuquerque, New Mexico. Children were recruited from pediatric clinics and community advertisements. The study was approved by the University of New Mexico Institutional Review Board, and informed consent obtained from parents of all children before participation. Inclusion criteria included uncomplicated term delivery and no known medical or developmental disorders. Exclusion criteria included genetic disorders, visual or hearing impairment, or contraindication to MR imaging.

Data Acquisition

MRI was performed at night during natural sleep without sedative medication. Caregivers remained with children throughout. Once asleep, headphones were placed over the infants' ears for noise protection. Imaging was performed on a Trio 3T MR imaging scanner (Siemens, Erlangen, Germany) by use of the provided 12-channel radio frequency head coil.

T1-weighted images were collected along the sagittal plane with the use of a 5-echo 3D MPRAGE sequence: TR = 2530; TE = 1.64, 3.5, 5.36, 7.22, 9.08; TI = 1200, flip angle = 7°; FOV = 256 × 256 mm; matrix = 256 × 256, 1-mm-thick section, 192 sections; with generalized auto-calibrating partially parallel acquisition acceleration factor 2.

CBF was measured by means of the pulsed ASL method.^{10,11} Pulse sequence parameters were FOV = 220 mm, 64 × 64 matrix, and 4-mm section thickness with a 1-mm gap. Twenty-four axial sections were taken in ascending order along the anteroposterior commissure; TR = 4000 ms and TE = 12 ms. The sequence consisted of 105 volumes of interleaved global and section-selective inversion recovery acquisition with a saturation pulse applied to a slab inferior and superior to the imaging sections. The delay between the inversion pulse and saturation pulses were TI1 = 600 ms, and the delay between the inversion and excitation pulses was TI2 = 1600 ms. Total acquisition time was 7 minutes.

Data Processing

Because tissue contrast by use of T1 alone in children 4 months of age may be limited, we did not use an automatic segmentation algorithm such as FreeSurfer (<http://surfer.nmr.mgh.harvard.edu>).¹¹ We instead optimized the T1 parameters to give improved contrast in the acquired images and used a 9-month template.¹² The 9-month template was first separated into right and left hemispheres. Each hemisphere was parcellated into 8 regions by use of methods described by Limperopoulos et al.¹³ The axial plane was segmented through the anterior and posterior commissures. Three coronal planes were then manually drawn to divide each hemisphere into the following anatomic regions: dorsolateral prefrontal, premotor, sensorimotor, parieto-occipital, orbito-frontal, subgenual, midtemporal, and inferior-occipital (Fig 1B). The choice of the 3 coronal planes follows the locations used by Limperopoulos et al.¹³ The regions shown on one sagittal section in Fig 1B are volumes comprising the entirety of the cerebral volume. These regions were defined once on the 9-month tem-

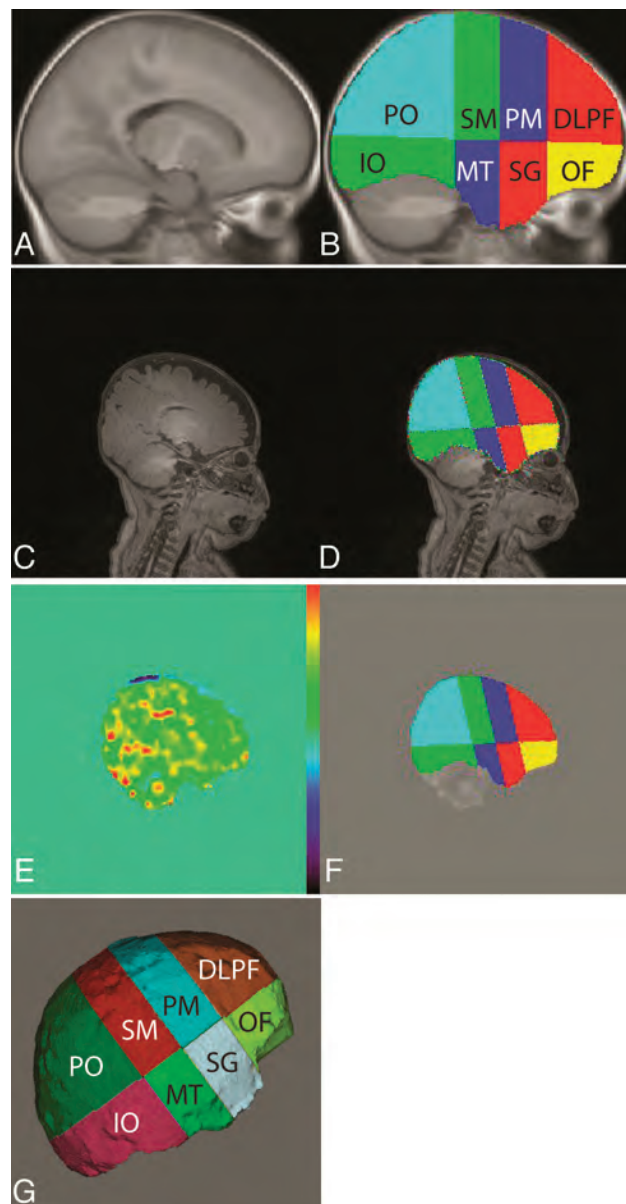


FIG 1. A and B, Brain segmentation process of the 9-month template is shown; C, 4-month T1 image; D, corresponding atlas after mathematica transformation. E, CBF image; F, CBF image with the atlas overlaid to demonstrate how well they are registered; G, the 8 segments projected onto the cortical surface.

plate and were then transformed on the T1 image obtained on each subject. Figure 1C shows a T1 image of the 4-month-old infant brain. The 4-month image was spatially normalized to the 9-month template by trimming the 4-month brain below the neck and extracting it by use of the Brain Extraction Tool program in the Functional MR Imaging of the Brain Software Library (<http://fsl.fmrib.ox.ac.uk/fsl>) package. The image was then spatially normalized by use of the FMRIB Linear Image Registration Tool program.

The 16 regions marked on the template (8 matching regions in each hemisphere) were transformed to the 4-month image by use of the inverse of the transformation found in the previous step. The resulting 8 regions of the right hemisphere mapped onto the 4-month brain are shown in Fig 1D. This method was repeated for

Demographic information for study subjects

	Total (n = 61)	Male (n = 37) (61%)	Female (n = 24) (39%)
Birth weight, g	3,294.95 ± 432.2	3,363.6 ± 408.8	3,190.5 ± 554.6
Gestational age, wk	39.2 ± 1.4	37.3 ± 9.1	38.9 ± 1.5
Age at scanning, d	123.6 ± 13	122.3 ± 12.6	125.5 ± 13.4 ^a
Sex, % girls ^a	39%		
Ethnicity ^a			
White	15 (24.59%)	8 (21.62%)	7 (29.16%)
Black	1 (1.64%)	1 (2.70%)	0 (0%)
Hispanic	34 (55.73%)	21 (56.75%)	13 (54.16%)
Native American	3 (4.92%)	2 (5.40%)	1 (4.16%)
Other	4 (6.55%)	3 (8.10%)	1 (4.16%)
Unknown	4 (6.55%)	2 (5.40%)	2 (8.33%)

Note:—Values are depicted as means ± standard deviations unless otherwise indicated.

^aP < .05.

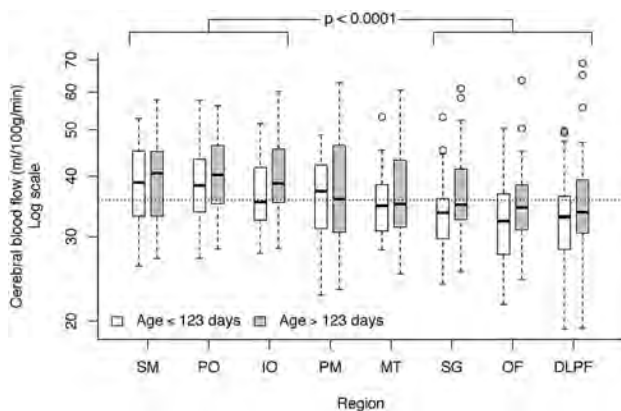


FIG 2. Regional differences in CBF. Although there were no significant differences within the 3 higher flow regions (sensorimotor, parieto-occipital, and inferior-occipital; $P = .43$) or within the 3 lower flow regions (subgenual, orbito-frontal, and dorsolateral prefrontal; $P = .15$), mean CBF between the high and low groups was highly significant. The mixed model fit age in a continuous manner, but, for illustrative purposes, age is split at the median. Horizontal dotted line is the median CBF value across all regions and ages.

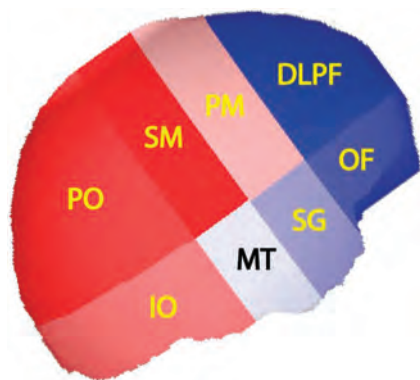


FIG 3. Regions with CBF above study population median are shown in shades of red and those regions with CBF below the median are shown in shades of blue. Darker color indicates greater deviation from the median flow. Thus, the sensorimotor (SM) region had the highest flow above the median and the dorsolateral prefrontal (DLPF) region had the lowest flow below the median.

all subjects. We proportionally divided each subject's brain into the 16 regions. Regions were labeled to identify the location in the brain. Thus, the dorsolateral prefrontal cortex is the superior-frontal region of the brain of identical proportional volume for each child.

The raw ASL images were motion-corrected by registering all the images to the first ASL image. The CBF image was created by use of methods described by Wang et al.¹⁰ Mean CBF was calculated for the each of the 16 regions defined on the T1 image (Fig 1D). Figure 1E demonstrates the CBF image spatially normalized to the T1 image, with overlaid regions of interest shown in Fig 1F. Figure 1G shows a cortical projection of the regions.

Statistical Analyses

Data for the repeated measures of mean total CBF on 8 regions (dorsolateral prefrontal, inferior-occipital, midtemporal, orbito-frontal, premotor, parieto-occipital, subgenual, sensorimotor) were plotted through the use of profile and boxplots to identify outliers. One subject was excluded because of extremely low mean CBF values across all regions. There were other isolated high outliers; none were removed, but data were analyzed on logarithmic scale to control their effect. No difference was found between mean CBF of left and right hemispheres for any region; therefore, right and left hemispheres were combined for analysis. Repeated measures were fit with linear mixed models in Proc Mixed in Statistical Analysis Software version 9.3 (SAS Institute, Cary, North Carolina) by use of a completely symmetric covariance structure within subjects. Fixed effects fit were region, age, and sex, with all possible 2-way interactions between them. Tukey-Kramer adjustments for multiple comparisons were used to identify groupings among regions. Estimated effects were exponentiated to return to original units.

RESULTS

Participants

Of 77 children scanned, 61 provided acceptable ASL data, for a success rate of 74%. There were significantly more boys than girls ($n = 37$ versus 24, $P < .001$). Ethnicities included Hispanic (56%), white (25%), Native American (5%), black (2%), and other (7%). Four children were of unknown ethnicity. Age at time of scanning ranged from 90–150 days (Table 1).

Figure 2 illustrates the regional distribution of CBF among the 8 regions. There were no significant 2-way interactions between sex, region, and age. Sex was not significant ($P = .70$), though region ($P < .0001$) and age ($P = .014$) were significant. Tukey comparisons found no significant differences within the 3 higher flow regions (sensorimotor, parieto-occipital, and inferior-occipital; $P = .43$) or within the 3 lower flow regions (subgenual, orbito-frontal, and dorsolateral prefrontal; $P = .15$). However, when comparing CBF between the higher and lower flow regions, all differences were significant. A contrast test for differences between average CBF in the high and low group was highly significant ($P < .0001$). There was no clear placement of premotor and midtemporal regions into one of these groups or into a separate group. Figure 3 shows the relative anatomic location and CBF of the regions. The median subject age was 123 days. At this age, the (geometric) mean for the high-flow regions was 38.9 mL/100 g/min (95% CI, 37.1, 40.8), and 34.2 mL/100 g/min (32.6, 35.9)

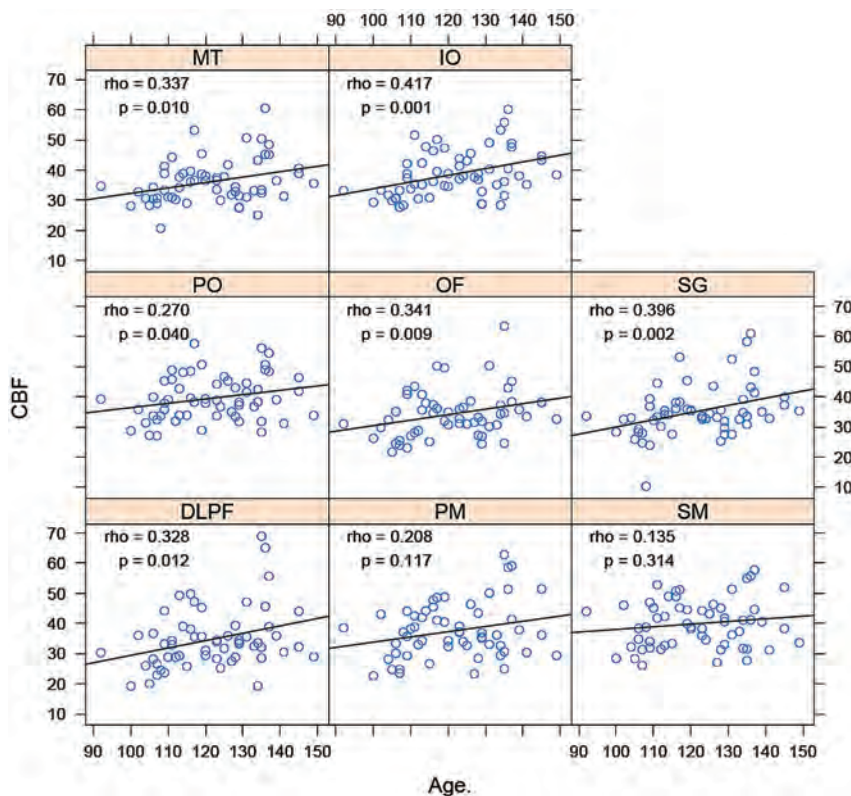


FIG 4. Cerebral blood flow versus age within each region; ρ is Spearman rank correlation coefficient.

for the low-flow regions. This corresponds to an average 13.8% (11.1%, 15.5%) difference between high- and low-flow regions.

An age effect was also noted. Average CBF increased 14.9% for each 30-day age increase; however, there was regional variation ranging from 3.0–28.1% (Fig 4). The relationship between age and CBF change was significant in all areas except premotor and sensorimotor. The strongest correlation between age and CBF was seen in the following areas: orbito-frontal ($P = .009$), inferior-occipital ($P = .001$), and subgenual ($P = .002$).

DISCUSSION

Understanding the relationship between brain and behavior in early childhood requires a probe of functional brain development. Because CBF reflects regional metabolism, ASL offers a noninvasive approach to studying brain function. In this report, we demonstrate the feasibility of the use of ASL in a group of healthy infants. Even within the narrow age range studied, ASL identifies significantly greater CBF in occipital and parietal lobes and the primary sensorimotor cortex compared with more anterior brain regions. In addition, we report significant age-related changes in CBF, which suggests that CBF change over time may be an important measure of functional brain development.

Histologic studies demonstrate the dynamic nature of early brain development, with rapid changes in neuronal³ and synaptic² attenuation occurring first in primary sensory (primary visual cortex, Heschl gyrus) and later in higher-order association regions (prefrontal). Recent MR imaging studies by use of high-resolution sequences show a similar pattern in early adolescence¹⁴ and as early as the first 2 months of life.¹⁵ More recent techniques,

such as DTI, characterize structural white matter development through childhood.¹⁶ These histologic and imaging studies provide powerful insights into the complex nature of early structural brain development.

Structure, however, does not equal function. Although our understanding of the rich tapestry of structural brain development has increased, the relation to brain function and behavior remains unclear. A study of functional brain development by use of PET to assess regional cerebral glucose metabolism^{5,17} found that the primary sensory and motor cortices, along with deeper cerebral areas, had the highest metabolic rates during the first months of life. Next, the parietal and temporal cortex developed increased glucose utilization. The frontal cortex demonstrated increased glucose metabolism by the end of the first year. These studies were ethically possible because of the sole inclusion of children requiring PET for clinical reasons that involve the substantial radiation exposure. PET is not feasible for the study of normal brain development. Other functional imaging modalities

require radiation (SPECT) or subject cooperation (stimulus-evoked fMRI). Recently, functional connectivity MR imaging has been used to identify network connectivity in children by assessment of the coherence of fluctuating levels of blood oxygenation at rest.¹⁸

Tight coupling of brain metabolism and blood flow¹⁹ suggests that CBF can be used as a marker of regional metabolic activity. With the use of magnetically labeled arterial water as a tracer, ASL quantifies CBF noninvasively.²⁰ ASL has been used for study of brain changes in disease states including vascular disease, dementia, and epilepsy.²⁰ Noguchi et al²¹ demonstrated that increased CBF measured by ASL may be related to increased microvascular attenuation in subjects with brain tumors. It is possible that in healthy children, increased CBF may be related to increased regional synaptogenesis, which, through neurovascular coupling, increases regional microvascular attenuation. Because ASL is noninvasive and requires no external tasks or exposure to radiation, it is well suited for use in pediatric samples. Wang et al¹⁰ were the first to use ASL in children, establishing feasibility at 1.5T. More recently, ASL has shown that preterm children have higher perfusion than term children.²² In healthy individuals from 4 years to adulthood, there is a decrease in CBF—most prominent in gray matter—by midadolescence.⁸ Taki and Kawashima²³ reported a nonlinear relationship between age and CBF from 5–18 years. They noted that these findings were similar to the reported gray matter volume increase in prepuberty followed by a postpuberty decrease.²⁴ Wang et al¹⁰ compared 8 children at 7 and 13 months of age. Regional CBF increased significantly at 13

months in the dorsolateral frontal lobes and decreased in the sensorimotor areas, consistent with the PET studies of Chugani.^{5,17}

We report the first large study of regional CBF by using ASL in young children. Lack of MR imaging contrast between gray and white matter at this age prohibited detailed regional segmentation, however by dividing the brain into broad anatomic areas¹³ we were able to demonstrate significantly greater CBF in the sensorimotor cortex and parietal/occipital lobes compared with dorsolateral prefrontal, orbitofrontal, and subgenual regions. Children were 3–5 months of age and therefore it is difficult to compare our findings with those of Limperopoulos et al¹³ However, our findings are consistent with the prior PET work of Chugani,⁵ who found increased cerebral metabolism at this age in the parietal and occipital regions and reduced frontal lobe metabolism. Our findings are also consistent with histologic studies demonstrating primary sensorimotor regions maturing earlier than higher association regions.^{2,3}

Our cohort included 61 subjects 3–5 months of age, allowing us to evaluate regional change in CBF over time. We found that CBF increased significantly with age in every region except the premotor and sensorimotor regions. Two of the regions in which there was the greatest age effect (orbital frontal and subgenual) had lower overall CBF. We speculate that this changing blood flow may reflect increasing metabolism that precedes a corresponding maturation of brain structure as occurs in the more anterior brain regions toward the end of the first year of life. Further studies are required to determine whether regional changes in CBF predict structural development, which could potentially serve as a marker of abnormal development before it becomes clinically evident.

Our findings are also consistent with normal clinical development. Clinical skills developing at 3–5 months include visual-motor tasks such as reaching, rolling over, and increasing control of movement.²⁵ Facial recognition and social interaction are highly visually dependent and are actively developing at this stage of childhood.²⁶ These skills involve the sensorimotor and occipital/parietal regions, which had the highest CBF in our subjects. The lowest flow was found in the anterior brain regions, which subserve later developing skills such as working memory, impulse inhibition, and self-regulation.^{27,28}

We did not find a sex difference in CBF at this age; however only 39% of our study cohort were girls. This is a limitation that may have been partially mitigated by our relatively large sample size, but the role of sex in early CBF requires further evaluation. Likewise, our cohort reflected the local demographics with a proportionally large Hispanic population. Although this may be a limitation, we are aware of no evidence that ethnicity affects regional CBF. Our unsuccessful scans were largely caused by excessive movement; thus, children who had difficulty sleeping in our MR imaging environment were not included in the data analysis. This is a difficult limitation to avoid. By use of an experienced scanning team and providing families with multiple options for aiding sleep, our success rate of 74% probably reflects a range of normally developing children. Though our sample size was substantial, individual variability in brain development at this age probably warrants a larger sample size to ensure power to detect all differences of clinical import. In addition, data obtained from

the cerebellum was markedly inconsistent, and therefore this region was not included in our study. Finally, this study is limited by the broadly defined regions studied, the inclusion of gray and white matter in the measurements, and the use of only T1 sequences. With additional data from a T2 sequence, a more physiologically meaningful segmentation may have been possible. These limitations must be considered in the interpretation of our results; however, the consistency of the findings across the study group strengthens the possibility that these differences may not have contributed importantly to the findings. However, it is impossible to know how these factors may bias our results. The validity of our findings is strengthened by their consistency with those found in a previous study of regional cerebral glucose utilization by use of PET scanning.^{5,17} This implies that ASL may provide a noninvasive means of determining regional brain functioning with the same accuracy as PET scanning without radiation exposure.

Our findings highlight the potential for use of ASL to assess functional brain development in early childhood. Future longitudinal studies including motor and cognitive measures may offer insights into early brain/behavioral relationships that have relevance for understanding normal and abnormal child development. Although these studies are inherently difficult, given the challenges of scanning children at this age without sedation, ASL offers the possibility of establishing early markers of abnormal development that may allow earlier, more effective treatment for children at risk for developmental disorders.

CONCLUSIONS

This study provides valuable information regarding neuroanatomic development in infants. The data begin to fill a large gap in the literature in the area of normal cerebral development. Knowledge of the normal development of the human brain is vital because without normative measures, it is impossible to truly characterize abnormalities of cerebral development. A better understanding of brain development will afford the medical community the opportunity to leverage the innate neuroplasticity involved in early brain development²⁹ by providing targeted developmental interventions at earlier ages to improve outcomes.

ACKNOWLEDGMENTS

We would like to acknowledge the work of our doctoral students and MIND Research Network staff: Susanne Duvall, Joy Van Meter, Lynette Silva, Judith Segall, Diana South, and Cathy Smith, who worked many nights performing MR imaging scanning on the children. We would also like to thank the families who traveled long distances to the University of New Mexico and persevered late into the night to get their children to sleep through the scans used to complete this study.

Disclosures: Arvind Caprihan—RELATED: Grant: Delle Foundation*; UNRELATED: Grants/Grants Pending: Other NIH grant support* (*money paid to institution).

The authors have no potential conflicts of interest with respect to the research, authorship, and/or publication of this article.

REFERENCES

1. Carey WB, Crocker AC, Coleman WL, et al. *Developmental-Behavioral Pediatrics*. 4th ed. Philadelphia: Elsevier; 2009:40–49

2. Huttenlocher PR, Dabholkar AS. **Regional differences in synaptogenesis in human cerebral cortex.** *J Comp Neurol* 1997;387:167–68
3. Shankle WR, Rafii MS, Landing BH, et al. **Approximate doubling of numbers of neurons in postnatal human cerebral cortex and in 35 specific cytoarchitectural areas from birth to 72 months.** *Pediatr Dev Pathol* 1999;2:244–59
4. Barkovich AJ. **Brain development: normal and abnormal.** In: Atlas SW, ed. *Magnetic Resonance Imaging of the Brain and Spine.* New York: Raven Press; 1991:129–75
5. Chugani HT. **A critical period of brain development: studies of cerebral glucose utilization with PET.** *Prev Med* 1998;27:184–88
6. Brix G, Lechel U, Glatting G, et al. **Radiation exposure of patients undergoing whole-body dual-modality 18F-FDG PET/CT examinations.** *J Nucl Med* 2005;46:608–13
7. Detre JA, Wang J, Wang Z, et al. **Arterial spin-labeled perfusion MRI in basic and clinical neuroscience.** *Curr Opin Neurol* 2009;22:348–55
8. Biagi L, Abbruzzese A, Bianchi MC, et al. **Age dependence of cerebral perfusion assessed by magnetic resonance continuous arterial spin labeling.** *J Magn Reson Imaging* 2007;25:696–702
9. Strouse JJ, Cox CS, Melhem ER, et al. **Inverse correlation between cerebral blood flow measured by continuous arterial spin-labeling (CASL) MRI and neurocognitive function in children with sickle cell anemia (SCA).** *Blood* 2006;108:379–81
10. Wang J, Licht DJ, Jahng GH, et al. **Pediatric perfusion imaging using pulsed arterial spin labeling.** *J Magn Reson Imaging* 2003;18:404–13
11. Fischl B, Salat DH, Busa E, et al. **Whole brain segmentation: automated labeling of neuroanatomical structures in the human brain.** *Neuron* 2002;33:341–55
12. Altaye M, Holland SK, Wilke M, et al. **Infant brain probability templates for MRI segmentation and normalization.** *Neuroimage* 2008;43:721–30
13. Limperopoulos C, Chilingaryan G, Guizard N, et al. **Cerebellar injury in the premature infant is associated with impaired growth of specific cerebral regions.** *Pediatr Res* 2010;68:145–50
14. Blakemore SJ. **Imaging brain development: the adolescent brain.** *Neuroimage* 2012;61:397–406
15. Gilmore JH, Shi F, Woolson SL, et al. **Longitudinal development of cortical and subcortical gray matter from birth to 2 years.** *Cereb Cortex* 2012;22:2478–85
16. Isaacson J, Provenzale J. **Diffusion tensor imaging for evaluation of the childhood brain and pediatric white matter disorders.** *Neuro-Imaging Clin North Am* 2011;21:179–89
17. Chugani HT, Phelps ME, Mazziotta JC. **Positron emission tomography study of human brain functional development.** *Ann Neurol* 1987;22:487–97
18. Smyser CD, Inder TE, Shimony JS, et al. **Longitudinal analysis of neural network development in preterm infants.** *Cereb Cortex* 2010;20:2852–62
19. Raichle ME. **Behind the scenes of functional brain imaging: a historical and physiological perspective.** *Proc Natl Acad Sci U S A* 1998;95:765–72
20. Detre JA, Rao H, Wang DJ, et al. **Applications of arterial spin labeled MRI in the brain.** *J Magn Reson Imaging* 2012;35:1026–37
21. Noguchi T, Yoshiura T, Hiwatashi A, et al. **Perfusion imaging of brain tumors using arterial spin-labeling: correlation with histopathologic vascular density.** *AJNR Am J Neuroradiol* 2008;29:688–93
22. Miranda MJ, Olofsson K, Sidaros K. **Noninvasive measurements of regional cerebral perfusion in preterm and term neonates by magnetic resonance arterial spin labeling.** *Pediatr Res* 2006;60:359–63
23. Taki Y, Kawashima R. **Brain development in childhood.** *Open Neuroimag J* 2012;6:103–10
24. Gogtay N, Giedd JN, Lusk L, et al. **Dynamic mapping of human cortical development during childhood through early adulthood.** *Proc Natl Acad Sci U S A* 2004;1:8174–79
25. Galletti C, Kutz DF, Gamberini M, et al. **Role of the medial parieto-occipital cortex in the control of reaching and grasping movements.** *Exp Brain Res* 2003;153:158–70
26. Piaget JP. *The Origins of Intelligence in Children.* New York: International Universities Press; 1952:153–236
27. Miller EK, Cohen JD. **An integrative theory of prefrontal cortex function.** *Annu Rev Neurosci* 2001;24:167–202
28. Braun K. **The prefrontal-limbic system: development, neuroanatomy, function, and implications for socioemotional development.** *Clin Perinatol* 2011;38:685–702
29. Francis JR, Song W. **Neuroplasticity of the sensorimotor cortex during learning.** *Neural Plast* 2011;2011:310737

Brain MRI Measurements at a Term-Equivalent Age and Their Relationship to Neurodevelopmental Outcomes

H.W. Park, H.-K. Yoon, S.B. Han, B.S. Lee, I.Y. Sung, K.S. Kim, and E.A. Kim

ABSTRACT

BACKGROUND AND PURPOSE: An increased prevalence of disabilities is being observed as more preterm infants survive. This study was conducted to evaluate correlations between brain MR imaging measurements taken at a term-equivalent age and neurodevelopmental outcome at 2 years' corrected age among very low–birth-weight infants.

MATERIALS AND METHODS: Of the various brain MR imaging measurements obtained at term-equivalent ages, reproducible measurements of the transcerebellar diameter and anteroposterior length of the corpus callosum on sagittal images were compared with neurodevelopmental outcomes evaluated by the Bayley Scales of Infant Development (II) at 2 years' corrected age (mean \pm standard deviation, 16.1 ± 6.4 months of age).

RESULTS: Ninety infants were enrolled. The mean gestational age at birth was 27 weeks and the mean birth weight was 805.5 g. A short corpus callosal length was associated with a Mental Developmental Index <70 ($P = .047$) and high-risk or diagnosed cerebral palsy ($P = .049$). A small transcerebellar diameter was associated with a Psychomotor Developmental Index <70 ($P = .003$), Mental Developmental Index <70 ($P = .004$), and major neurologic disability ($P = .006$).

CONCLUSIONS: A small transcerebellar diameter and short corpus callosal length on brain MR imaging at a term-equivalent age are related to adverse neurodevelopmental outcomes at a corrected age of 2 years and could be a useful adjunctive tool for counseling parents about future developmental outcomes.

ABBREVIATIONS: AED = antiepileptic drug; NICU = neonatal intensive care unit; MDI = Mental Developmental Index; PDI = Psychomotor Developmental Index; TCD = transcerebellar diameter

The survival rate of preterm infants has increased with the advances in neonatal care in recent decades. However, a higher prevalence of disabilities has also been observed in survivors of preterm birth at infancy and in childhood.^{1,2} Factors such as intraventricular hemorrhage,³ hypoxia, prematurity,³⁻⁵ and neonatal care^{3,6} have been reported to affect the developing brain; the mechanism of injury during the development of the cerebellum and corpus callosum in surviving premature infants may be caused by primary destruction or underdevelopment⁷ and axonal

injury,⁸ respectively. These factors in turn result in an altered brain volume or structure that can be seen as a reduced cerebral and/or cerebellar volume,^{3,9,10} subarachnoid space widening,^{3,6,11} corpus callosum thinning,¹²⁻¹⁴ and posthemorrhagic ventricular dilation on brain MR imaging.¹⁵ These findings have led to reports of various measurements of MR imaging as potential predictors of neurologic outcomes at infancy or in childhood.^{10,14,16,17}

We conducted a study in a single neonatal intensive care unit (NICU) to evaluate correlations between brain MR imaging measurements taken at term-equivalent age and the neurodevelopmental outcomes at 2 years' corrected age.

MATERIALS AND METHODS

Patients and Perinatal Data

Infants admitted to the NICU of Asan Medical Center Children's Hospital from January 2001 to December 2010 whose birth weight was <1 kg were included in the study cohort. Patients with a birth weight <1.5 kg who had clinical indications for brain MR imaging, such as a history of seizure or hypoxic events, or sus-

Received May 15, 2013; accepted after revision June 20.

From the Department of Pediatrics (H.W.P.), Division of Neonatology, Konkuk University Hospital, Konkuk University School of Medicine, Seoul, Korea; and Departments of Radiology (H.-K.Y.), Clinical Epidemiology and Biostatistics (S.B.H.), and Rehabilitation (I.Y.S.) and Department of Pediatrics, Division of Neonatology (B.S.L., K.S.K., E.A.K.), Asan Medical Center Children's Hospital, University of Ulsan, College of Medicine, Seoul, Korea.

Please address correspondence to Ellen Ai-Rhan Kim, MD, PhD, Department of Pediatrics, Division of Neonatology, Asan Medical Center Children's Hospital, University of Ulsan College of Medicine, 88, Olympic-ro 43-gil, Songpa-gu, Seoul 138-736 Korea; e-mail: hwwoman@naver.com

<http://dx.doi.org/10.3174/ajnr.A3720>

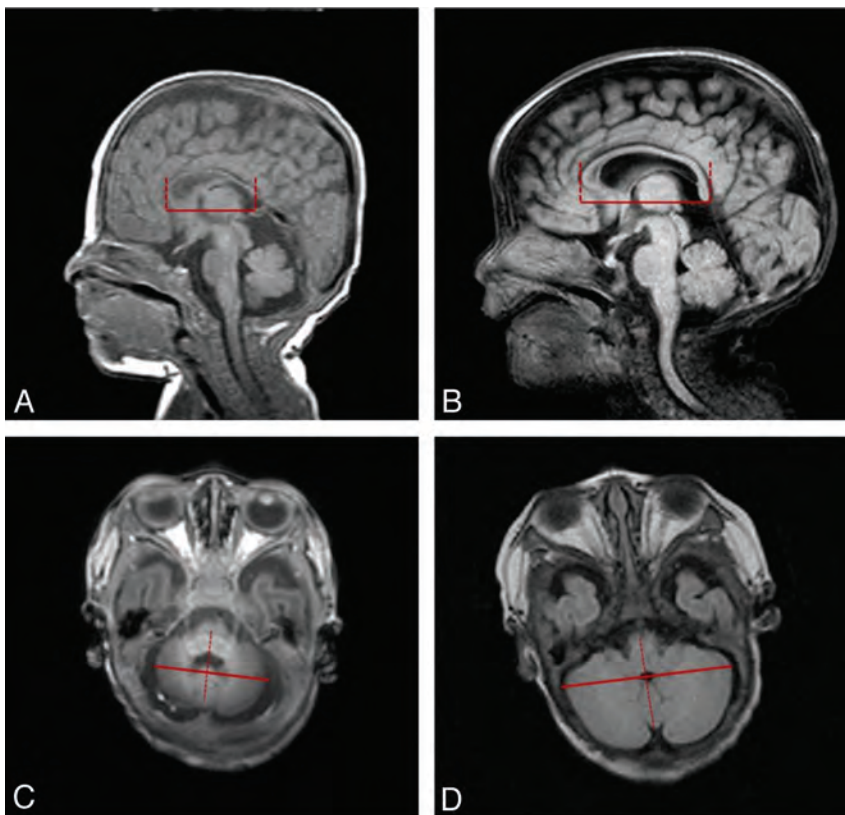


FIG 1. Linear measurements of anteroposterior length of corpus callosum (A and B) and transcerebellar diameter (C and D) and intraclass correlation coefficients (ICCs) for interobserver and intraobserver reliability. A, Short anteroposterior length of corpus callosum (34.1 mm); B, longer anteroposterior length of corpus callosum (44.4 mm); C, short transcerebellar diameter (36.2 mm); D, longer transcerebellar diameter (58.4 mm).

pected periventricular leukomalacia by head sonography were also included. The brain MR imaging was obtained at a term-equivalent age (37^{+0} to 41^{+6} weeks). All patients except for 2 (2.2%) underwent brain MR imaging before NICU discharge.

Exclusion criteria included infants who died before discharge and infants who had severe congenital anomalies such as chromosomal abnormalities or brain anomalies. The clinical charts of the subjects were retrospectively reviewed for various demographic and clinical data: antenatal steroids,¹⁸ necrotizing enterocolitis defined as modified Bell criteria greater than stage IIa, treatment of symptomatic patent ductus arteriosus¹⁹ either intravenously with indomethacin or by surgical ligation, laser operation for retinopathy of prematurity,²⁰ Papile classification of intraventricular hemorrhage, bronchopulmonary dysplasia (defined as oxygen dependence at 36 weeks' postmenstrual age), and treatment with antiepileptic drugs (AEDs) for electrographic and clinical seizure.

Oxygen requirement was defined as the supplementation of oxygen during hospitalization to maintain the target range of 88–93% saturation for infants born with a birth weight of ≤ 1.5 kg with bronchopulmonary dysplasia and $\geq 90\%$ for other infants.

Brain MR Imaging

The brain MR imaging was obtained with a 3T MR system (3T Achieva Nova Dual; Philips, Best, the Netherlands) around the term-equivalent age before discharge from the NICU. MR images

reviewed for this study consisted of spin-echo T1-weighted sagittal, T1-weighted axial, and T2-weighted axial images with parameters of 450/10/2 (TR/TE/excitations), 500/10/2, and 3000/80/2, with a field of view of 15 or 18 cm and a 256×256 matrix. Section thickness was 4 mm, with a 1-mm gap. Infants wearing ear protection devices were sedated with choral hydrate (25–50 mg/kg orally) or morphine (0.05 mg/kg intravenously).

Measurements of MR Imaging

Brain MR imaging measurements were taken by 2 different neonatologists under the supervision of 1 certified pediatric radiologist. The axial view of the transcerebellar diameter (TCD) and the anteroposterior length of the corpus callosum on sagittal view were measured (Fig 1) with the use of the entirely digital measuring system of the PACS of Asan Medical Center (PetaVision, version 2.1).²¹ The TCD was measured as the longest transverse diameter perpendicular to the cerebellar vermis on the axial view that showed both nasal septum and orbital area, and the corpus callosal length was measured as the anteroposterior length on the midline sagittal image in which the pituitary gland was seen (Fig 1).

Neurologic Outcomes

The neurodevelopmental outcomes were assessed at 2 years' corrected age with the Bayley Scales of Infant Development II by a certified neonatologist. The Mental Developmental Index (MDI) and the Psychomotor Developmental Index (PDI) were obtained. MDI or PDI scores < 70 were defined as significantly abnormal. Cerebral palsy was defined as a nonprogressive central nervous system disorder characterized by abnormal posture and abnormal muscular tone in at least 1 extremity; high-risk cerebral palsy was defined as the abnormal tone of extremities and delayed motor development during the first 2 years diagnosed by a certified medical doctor for pediatric rehabilitation. A major neurologic disability was defined as ≥ 1 of the following findings: MDI < 70 , PDI < 70 , cerebral palsy, sensorineural hearing loss, and/or seizure disorder.

Data Analysis and Statistics

Major neurologic disability was the primary outcome variable. A *P* value of $< .05$ was considered significant. Data were analyzed with the Student *t* test and logistic regression by use of SPSS 17.0 software (IBM, Armonk, New York). The intraclass correlation coefficients (ICC) for measurement consistency were calculated to analyze the intraobserver and interobserver agreement. In the multivariable regression, risk variables weakly associated with the outcomes in the univariate analysis ($P < .1$) were used as the candidate variables to identify independent predictors of adverse neurologic outcomes.

Table 1: General characteristics of the study population

Variables	Total (n = 90)
Gestational age, wk	27 ⁺¹ ± 2.3
Birth weight, g	805.5 ± 168.2
Sex, male	55.6% (M:F = 50:40)
Prenatal steroids	86 (95.6%)
PROM	18 (20%)
Delivery mode, C-section	67 (74.4%)
Presence of IUGR	36 (40%)
Apgar score, 1 min	4 ± 1.9
Apgar score, 5 min	7 ± 1.4
Duration of ventilator care, d	27 ± 25.3
Presence of BPD, O ₂ at 36 wk	22 (24.4%)
Postnatal steroids	45 (50%)
History of sepsis, culture-proven	28 (31.1%)
Peak level of CRP, mg/dL	2.83 ± 4.84
NEC	8 (8.9%)
ROP	48 (53.3%)
IVH grade 3–4	9 (10%)
Laser operation for ROP	21 (23.3%)
AED medication	8 (8.9%)

Note:—Data are reported as number (%) or as mean ± standard deviation. CRP indicates C-reactive protein; IUGR, intrauterine growth restriction; IVH, intraventricular hemorrhage; NEC, necrotizing enterocolitis; PROM, premature rupture of membrane; ROP, retinopathy of prematurity; BPD, bronchopulmonary dysplasia.

RESULTS

General Characteristics of Patients

The general characteristics of the 90 infants are shown in Table 1. Of the 90 patients, 80 (88.9%) were extremely low–birth weight infants.

Perinatal Factors Associated with Adverse Neurologic Outcomes

In total, 15 of 90 infants (16.7%) and 24 of 90 (26.7%) infants showed MDI and PDI values <70, respectively. Another 8 patients (8.9%) were diagnosed with cerebral palsy, and 33 (36.7%) showed major neurologic disabilities. Risk variables found to be significantly correlated with the outcomes in the univariate analysis were entered into multivariate analysis: AED medication (OR, 7.687; $P = .023$) and the duration of O₂ requirement (OR, 10.014; $P = .055$) were associated with a PDI <70; the duration of O₂ requirement (OR, 10.022; $P = .009$) and a history of sepsis (OR, 3.723; $P = .044$) were associated with an MDI <70. The use of prenatal steroids (OR, 0.065; $P = .028$) showed a protective effect on cognitive function (Table 2). The factors associated with a major neurologic disability included the use of AED medication (OR, 6.958; $P = .025$) and a history of sepsis (OR, 2.508; $P = .058$) (Table 2).

Association between Measurements of MR Imaging and Adverse Neurologic Outcomes

The linear measurement of the TCD and the anteroposterior length of the corpus callosum on MR imaging showed satisfactory ICCs for interobserver and intraobserver reliabilities (Fig 1). A short TCD was associated with poor motor and cognitive function, as indicated by a PDI <70 (OR, 0.780; $P = .003$), MDI <70 (OR, 0.785; $P = .004$), and major neurologic disability (OR, 0.815; $P = .006$). A short anteroposterior length of the corpus callosum was associated with an MDI <70 (OR, 0.876; $P = .047$) and high-risk or diagnosed cerebral palsy (OR, 0.915; $P = .049$) (Table 3).

Perinatal Factors Associated with TCD and Length of Corpus Callosum on Multivariate Analysis

Among several perinatal factors, birth weight (OR 0.005, $P = .043$), presence of bronchopulmonary dysplasia (OR, -2.358 ; $P = .007$), use of AED medication (OR, -3.347 ; $P = .010$), and a history of sepsis (OR, -1.642 ; $P = .034$) were associated with a short TCD. The factors associated with corpus callosal length included a small head circumference at the time of the MR imaging (OR, 3.947; $P < .001$), the use of prenatal steroids (OR, 10.141; $P = .002$), and AED medication (OR, -8.215 ; $P < .001$) (Table 4).

DISCUSSION

Many neonatologists counsel parents of very low–birth-weight infants about the long-term prognosis with the use of known antenatal^{22,23} and postnatal risk factors^{3,4,24,25} associated with neurodevelopmental outcomes. In-depth studies^{26–28} are in progress to better predict neurodevelopmental outcomes in this vulnerable population. The objective of this study was to evaluate correlations between brain MR imaging measurements taken at term-equivalent age before discharge from the NICU and the neurodevelopmental outcome at 2 years' corrected age among very low–birth-weight infants. We used the PACS system of the Asan Medical Center, which has been described in detail in Im et al²¹ to measure the different brain parameters. Other reports^{29–31} have shown the usefulness of this system, emphasizing its reproducibility and reliability as well as the convenient access to images. Unlike the other 9 MR imaging parameters that we also measured (data not shown), which included ventricle width, biparietal diameter, bifrontal diameter, subarachnoid space widening (axial and sagittal images), and corpus callosal thickness. Among them, only the TCD and corpus callosal length were found to have acceptable intraclass and interclass correlation coefficients for consistency (Fig 1). The measurement of TCD on the coronal plane was used before by Nguyen The Tich et al,¹⁶ but we measured TCD on the axial plane, which also could be applied on an axial CT image.

The rapid growth of the cerebellum that occurs from 28–40 weeks of gestation can be impeded by premature birth.^{7,32,33} Here, a smaller TCD, indicative of neuronal loss or impaired neuronal differentiation with a reduction in dendritic and axonal development that may be independent of immaturity,³ was associated with poor cognitive and psychomotor function. These results concur with those of the report of Tich et al³⁴ in preterm infants born at a gestational age <30 weeks or a weight of <1.25 kg. The cerebellar injury, mainly occurring in the external granular layer, possibly related to a disturbance of cerebellar growth caused by hemosiderin on the cerebellar surface or postnatal factors such as hypoxia-ischemia, infection, and steroids as well as direct cerebellar destructive injury.^{7,8} Impaired neuronal connection between cerebrum and cerebellum as a remote effect can also contribute to cerebellar underdevelopment.^{7,8}

We used phenobarbital as a primary medication in neonatal seizure when both clinical and electrical evidence of seizures was evident. Both the seizures and the AED medication may cause cerebellar atrophy—either synergistically³⁵ or independently³⁶—during the development of the cerebellum. Abnormalities of the cerebellum in mice after exposure to phenobarbital, such as a decrease in the number of Purkinje³⁷ and granular cells,³³ without

Table 2: Relationship between perinatal factors and adverse neurologic outcomes determined by multivariate logistic regression analysis

Neurologic Outcomes	Perinatal Factors	OR (95% CI)	P Value
PDI <70	Duration of O ₂ requirement	10.01 (0.999–10.028)	.055
	AED medication	7.69 (1.329–44.476)	.228
MDI <70	Duration of O ₂ requirement	10.02 (10.005–10.040)	.010
	Prenatal steroids	0.06 (0.005–0.747)	.028
	History of sepsis	3.72 (10.0337–13.363)	.044
Major neurologic outcomes	AED medication	6.96 (1.274–37.988)	.025
	History of sepsis	2.51 (0.970–6.485)	.058

Table 3: Association between MRI measurements and adverse neurologic outcomes determined by univariate logistic regression analysis

Measurements	Outcomes	OR (95% CI)	P Value
TCD	PDI <70	0.780 (0.662–0.919)	.003
	MDI <70	0.785 (0.665–0.927)	.004
	Major neurologic disability	0.815 (0.704–0.944)	.006
Corpus callosal length	MDI <70	0.876 (0.768–0.998)	.047
	High-risk or diagnosed CP	0.915 (0.838–0.999)	.049

Note:—CP indicates cerebral palsy.

Table 4: Perinatal factors associated with MRI measurements on multivariate analysis

Measurements	Perinatal Factors	Estimated Regression Coefficient (95% CI)	P Value
TCD	Birth weight	0.005 [0.001, 0.010]	.028
	Presence of BPD	–2.358 [–40.025, –0.692]	.007
	AED medication	–3.347 [–5.840, –0.853]	.010
	History of sepsis	–1.642 [–3.137, –0.146]	.034
Corpus callosal length	HC when MRI was taken	3.947 [1.915, 5.978]	<.001
	Prenatal steroids	10.141 [40.017, 16.264]	.002
	AED medication	–8.215 [–12.641, –3.790]	<.001

Note:—HC indicates head circumference; BPD, bronchopulmonary dysplasia.

an effect on the area of the cerebellum, have been reported. Sepsis, an independent risk factor for a poor neurologic outcome,^{25,34,38} could have exerted a detrimental effect on the growth of the cerebellum by diffuse white matter injury,²⁴ bacterial products and cytokines,^{39,40} arterial hypotension, and combined cerebral ischemia.²⁵ Bronchopulmonary dysplasia, a known risk factor for neurodevelopmental impairment, has also been reported to exert an effect on the granular cells of the cerebellum, as shown in a baboon model.³³ In the present study, however, bronchopulmonary dysplasia alone was not associated with severe cognitive and motor deficits, though the duration of O₂ requirement, which may have included a period of hyperoxia and hypoxia, was associated with poor cognitive and motor outcomes. Reports have shown that the use of either a high oxygen concentration, which affects the inner granular cell and Purkinje cell layer,³³ or a hypoxic insult, which affects neuronal migration,⁴¹ could influence the growth of the developing human cerebellum.

A premature transition from intrauterine to extrauterine life¹⁰ and stress or damage in the neonatal period could affect the development of the corpus callosum. The corpus callosum is known to have an intrinsic vulnerability to hypoxic-ischemic damage and hemorrhage.^{2,14} A decreased number or diameter of axons and myelin loss was observed in preterm infants with hypoxia or ischemia⁴² that could be explained with necrosis, apoptosis, astrogliosis, and microgliosis as well as injury of premyelinating oligodendrocytes in white matter, including the corpus callosum.^{7,43} In the development of the corpus callosum, the corpus callosum expands in the craniocaudal direction: genu first and then body to

splenium.¹² Thus, the development of the posterior part is an ongoing process that continues through the neonatal period after preterm birth, and an altered development of the corpus callosum such as a shortening and/or thinning persists into childhood.¹⁴ We assumed that the underdevelopment of the posterior part of the corpus callosum would result in a shorter length of the corpus callosum as well as a thinning of the splenium. Our attempt to measure the thickness of the corpus callosum was hampered by a poor consistency in the measurements (ICC = 0.133–0.418 in interobserver variability, ICC = 0.003–0.367 in intraobserver variability). Reports have shown a positive relationship between both the corpus callosal size and total white matter volume and a decreased area of the posterior or midposterior region corresponding to the splenium and poor verbal skill in preterm males.¹⁴ In our study, a short corpus callosal length was associated in univariate analysis with high-risk or diagnosed cerebral palsy and an MDI <70.

In contrast to the study of Wood et al,⁴⁴ which reported a relationship between the administration of antenatal steroids and a lower MDI, antenatal steroids showed a protective effect on the growth

of the corpus callosum in our study (Table 4), in accordance with the protective effect of antenatal steroids on white matter injury in very low–birth-weight infants reported by Leviton et al²³ and Agarwal et al.²² The effect of seizures, as evidenced by the use of AEDs in our study, might have caused the reduction in the corpus callosal volume, especially in the posterior region, as reported by Hermann et al.⁴⁵

There are limitations that must be addressed regarding the present study. We did not examine the association of the white or gray matter abnormalities, such as hemorrhage or leukomalacia, and other signal changes with brain measurements. The other limitation includes the short-term follow-up period and a lack of control group. Further research is required to determine whether the changes in brain structures in very preterm infants would persist into later life.

CONCLUSIONS

In this study, we were able to elucidate the usefulness of the axial measurement of the TCD and the length of the corpus callosum taken from brain MR imaging at term-corrected ages in predicting long-term neurologic outcome. Various perinatal factors, such as a lower birth weight, use of AEDs, sepsis, bronchopulmonary dysplasia, and a smaller head circumference, some of which are independently associated with poor cognitive and motor skills later in life, could affect the development of the cerebellum and corpus callosum during the most vulnerable period in NICU hospitalization.

REFERENCES

1. Inder TE, Warfield SK, Wang H, et al. **Abnormal cerebral structure is present at term in premature infants.** *Pediatrics* 2005;115:286–94
2. Back SA, Luo NL, Borenstein NS, et al. **Late oligodendrocyte progenitors coincide with the developmental window of vulnerability for human perinatal white matter injury.** *J Neurosci* 2001;21:1302–12
3. Neubauer AP, Voss W, Kattner E. **Outcome of extremely low birth weight survivors at school age: the influence of perinatal parameters on neurodevelopment.** *Eur J Pediatr* 2008;167:87–95
4. Shah DK, Doyle LW, Anderson PJ, et al. **Adverse neurodevelopment in preterm infants with postnatal sepsis or necrotizing enterocolitis is mediated by white matter abnormalities on magnetic resonance imaging at term.** *J Pediatr* 2008;153:170–75.e1
5. Wood NS, Marlow N, Costeloe K, et al. **Neurologic and developmental disability after extremely preterm birth: EPICure Study Group.** *N Engl J Med* 2000;343:378–84
6. Armstrong DL, Bagnall C, Harding JE, et al. **Measurement of the subarachnoid space by ultrasound in preterm infants.** *Arch Dis Child Fetal Neonatal Ed* 2002;86:F124–26
7. Volpe JJ. **Brain injury in premature infants: a complex amalgam of destructive and developmental disturbances.** *Lancet Neurol* 2009;8:110–24
8. Volpe JJ. **Cerebellum of the premature infant: rapidly developing, vulnerable, clinically important.** *J Child Neurol* 2009;24:1085–104
9. Sauerwein HC, Lassonde M. **Cognitive and sensori-motor functioning in the absence of the corpus callosum: neuropsychological studies in callosal agenesis and callosotomized patients.** *Behav Brain Res* 1994;64:229–40
10. Peterson BS, Anderson AW, Ehrenkranz R, et al. **Regional brain volumes and their later neurodevelopmental correlates in term and preterm infants.** *Pediatrics* 2003;111:939–48
11. Horsch S, Muentjes C, Franz A, et al. **Ultrasound diagnosis of brain atrophy is related to neurodevelopmental outcome in preterm infants.** *Acta Paediatr* 2005;94:1815–21
12. Rademaker KJ, Lam JN, Van Haastert IC, et al. **Larger corpus callosum size with better motor performance in prematurely born children.** *Semin Perinatol* 2004;28:279–87
13. Iai M, Tanabe Y, Goto M, et al. **A comparative magnetic resonance imaging study of the corpus callosum in neurologically normal children and children with spastic diplegia.** *Acta Paediatr* 1994;83:1086–90
14. Nosarti C, Rushe TM, Woodruff PW, et al. **Corpus callosum size and very preterm birth: relationship to neuropsychological outcome.** *Brain* 2004;127:2080–89
15. Dyet LE, Kennea N, Counsell SJ, et al. **Natural history of brain lesions in extremely preterm infants studied with serial magnetic resonance imaging from birth and neurodevelopmental assessment.** *Pediatrics* 2006;118:536–48
16. Nguyen The Tich S, Anderson PJ, Shimony JS, et al. **A novel quantitative simple brain metric using MR imaging for preterm infants.** *AJNR Am J Neuroradiol* 2009;30:125–31
17. Lind A, Parkkola R, Lehtonen L, et al. **Associations between regional brain volumes at term-equivalent age and development at 2 years of age in preterm children.** *Pediatr Radiol* 2011;41:953–61
18. **Effect of corticosteroids for fetal maturation on perinatal outcomes.** *NIH Consensus Statement* 1994;12:1–24
19. Hamrick SE, Hansmann G. **Patent ductus arteriosus of the preterm infant.** *Pediatrics* 2010;125:1020–30
20. Early Treatment for Retinopathy of Prematurity Cooperative Group. **Revised indications for the treatment of retinopathy of prematurity: results of the Early Treatment for Retinopathy of Prematurity Randomized Trial.** *Arch Ophthalmol* 2003;121:1684–94
21. Im KC, Choi IS, Ryu JS, et al. **PET/CT fusion viewing software for use with picture archiving and communication systems.** *J Digit Imaging* 2010;23:732–43
22. Agarwal R, Chiswick ML, Rimmer S, et al. **Antenatal steroids are associated with a reduction in the incidence of cerebral white matter lesions in very low birthweight infants.** *Arch Dis Child Fetal Neonatal Ed* 2002;86:F96–101
23. Leviton A, Dammann O, Allred EN, et al. **Antenatal corticosteroids and cranial ultrasonographic abnormalities.** *Am J Obstet Gynecol* 1999;181:1007–17
24. Stoll BJ, Hansen NI, Adams-Chapman I, et al. **Neurodevelopmental and growth impairment among extremely low-birth-weight infants with neonatal infection.** *JAMA* 2004;292:2357–65
25. Schlapbach LJ, Aebischer M, Adams M, et al. **Impact of sepsis on neurodevelopmental outcome in a Swiss national cohort of extremely premature infants.** *Pediatrics* 2012;128:e348–57
26. Hayashi-Kurahashi N, Kidokoro H, Kubota T, et al. **EEG for predicting early neurodevelopment in preterm infants: an observational cohort study.** *Pediatrics* 2012;130:e891–97
27. Sutton PS, Darmstadt GL. **Preterm birth and neurodevelopment: a review of outcomes and recommendations for early identification and cost-effective interventions.** *J Trop Pediatr* 2013;59:258–65
28. Harijan P, Beer C, Glazebrook C, et al. **Predicting developmental outcomes in very preterm infants: validity of a neonatal neurobehavioral assessment.** *Acta Paediatr* 2012;101:e275–81
29. Singh P, Davies TI. **A comparison of cephalometric measurements: a picture archiving and communication system versus the hand-tracing method: a preliminary study.** *Eur J Orthod* 2011;33:350–53
30. Monsky WL, Raptopoulos V, Keogan MT, et al. **Reproducibility of linear tumor measurements using PACS: comparison of caliper method with edge-tracing method.** *Eur Radiol* 2004;14:519–25
31. Khakharia S, Bigman D, Fragomen AT, et al. **Comparison of PACS and hard-copy 51-inch radiographs for measuring leg length and deformity.** *Clin Orthop Relat Res* 2011;469:244–50
32. Limperopoulos C, Soul JS, Gauvreau K, et al. **Late gestation cerebellar growth is rapid and impeded by premature birth.** *Pediatrics* 2005;115:688–95
33. Rees SM, Loeliger MM, Munro KM, et al. **Cerebellar development in a baboon model of preterm delivery: impact of specific ventilatory regimes.** *J Neuropathol Exp Neurol* 2009;68:605–15
34. Tich SNT, Anderson PJ, Hunt RW, et al. **Neurodevelopmental and perinatal correlates of simple brain metrics in very preterm infants.** *Arch Pediatr Adolesc Med* 2011;165:216–22
35. Ney GC, Lantos G, Barr WB, et al. **Cerebellar atrophy in patients with long-term phenytoin exposure and epilepsy.** *Arch Neurol* 1994;51:767–71
36. De Marcos FA, Ghizoni E, Kobayashi E, et al. **Cerebellar volume and long-term use of phenytoin.** *Seizure* 2003;12:312–15
37. Hannah RS, Roth SH, Spira AW. **Effect of phenobarbital on Purkinje cell growth patterns in the rat cerebellum.** *Exp Neurol* 1988;100:354–64
38. Shah DK, Anderson PJ, Carlin JB, et al. **Reduction in cerebellar volumes in preterm infants: relationship to white matter injury and neurodevelopment at two years of age.** *Pediatr Res* 2006;60:97–102
39. Schlapbach LJ, Aebischer M, Adams M, et al. **Impact of sepsis on neurodevelopmental outcome in a Swiss national cohort of extremely premature infants.** *Pediatrics* 2011;128:e348–57
40. Wu YW, Colford JM. **Chorioamnionitis as a risk factor for cerebral palsy.** *JAMA* 2000;284:1417–24
41. Rees S, Stringer M, Just Y, et al. **The vulnerability of the fetal sheep brain to hypoxemia at mid-gestation.** *Dev Brain Res* 1997;103:103–18
42. Nagy Z, Westerberg H, Skare S, et al. **Preterm children have disturbances of white matter at 11 years of age as shown by diffusion tensor imaging.** *Pediatr Res* 2003;54:672–79
43. Tekkok SB, Goldberg MP. **Ampa/kainate receptor activation mediates hypoxic oligodendrocyte death and axonal injury in cerebral white matter.** *J Neurosci* 2001;21:4237–48
44. Wood NS, Costeloe K, Gibson AT, et al. **The EPICure study: associations and antecedents of neurological and developmental disability at 30 months of age following extremely preterm birth.** *Arch Dis Child Fetal Neonatal Ed* 2005;90:F134–40
45. Hermann B, Hansen R, Seidenberg M, et al. **Neurodevelopmental vulnerability of the corpus callosum to childhood onset localization-related epilepsy.** *NeuroImage* 2003;18:284–92

CT and MRI of Pediatric Skull Lesions with Fluid-Fluid Levels

S.A. Nabavizadeh, L.T. Bilaniuk, T. Feygin, K.V. Shekdar, R.A. Zimmerman, and A. Vossough

ABSTRACT

SUMMARY: Fluid-fluid levels can occur whenever different fluid densities are contained within a cystic or compartmentalized lesion, usually related to the evolution of hematoma or necrosis. Review of the literature demonstrated that throughout the skeletal system, the most common etiology for fluid-fluid levels is aneurysmal bone cyst, but there are no dedicated studies of the pediatric calvaria, to our knowledge. In this report, we present clinicopathologic characteristics and CT and MR imaging of 11 patients with pediatric skull mass lesions demonstrating fluid-fluid levels. MR imaging demonstrated more fluid-fluid levels compared with CT in all cases. The etiologies of skull lesions with fluid-fluid levels were Langerhans cell histiocytosis in 4 (36.6%), aneurysmal bone cysts in 3 (27.2%), cephalohematoma in 3 (27.2%), and metastatic neuroblastoma in 1 (9%). Radiologists should be aware of the other etiologies of calvarial lesions with fluid-fluid levels in the pediatric skull.

ABBREVIATIONS: ABC = aneurysmal bone cyst; FFL = fluid-fluid level; LCH = Langerhans cell histiocytosis

Fluid-fluid levels (FFLs) may occur whenever different fluid densities are contained within a cystic or compartmentalized structure, usually related to hemorrhage or necrosis.^{1,2} Image acquisition near perpendicular to the plane of the FFL is required to optimally demonstrate it.^{1,2} FFLs in skeletal lesions have been a well-known imaging feature of aneurysmal bone cyst (ABC)^{3,4} for many decades. To our knowledge, there is no dedicated study focusing on the different etiologies of FFLs in the pediatric population and there is no study focused on fluid-fluid levels in calvarial lesions. However, 2 large studies primarily in adult patients have demonstrated that ABCs are the most common etiology of osseous lesions with FFLs throughout the body.^{5,6} Despite these data, the presence of FFLs remains a nonspecific finding and can be seen in a wide range of benign and malignant bone lesions, including fibrous dysplasia, telangiectatic osteosarcoma, osteoblastoma, simple bone cyst, lymphatic malformations, Ewing sarcoma, brown tumor, giant cell tumor, and chondroblastoma.⁵⁻⁹

In this study, head CT and MR imaging of pediatric patients having skull lesions with FFLs were retrospectively reviewed with the aim of characterizing these lesions.

CASE SERIES

Patients

The study was performed with approval of the institutional review board and was compliant with guidelines of the Health Insurance Portability and Accountability Act. We performed a retrospective review of records of pediatric patients with skull masses diagnosed between 2002 and 2012. Cases were ascertained from teaching files of the authors and a computerized search of the PACS for patients younger than 18 years of age who were diagnosed with a skull lesion showing fluid-fluid levels on CT or MR imaging. The search terms included various combinations and derivatives of “fluid-fluid,” “blood-fluid,” “fluid levels,” “skull,” and “calvarium.” Medical records were reviewed for patient age, sex, history of recent trauma to the lesion, history of coagulopathy, types of treatment, and histopathologic diagnosis. Patients with a history of surgery on the skull were excluded. The etiologic diagnosis was made by histopathologic examination of resected lesions in 6 patients and of biopsied specimens in 1 patient. In 3 patients who were classified as having cephalohematoma, the diagnosis was made on the basis of characteristic clinical presentation, history of traumatic vaginal delivery, and/or spontaneous resolution of the lesion by consensus of pediatric neuroradiologists and by review of medical records. Finally, 1 patient with primary neuroblastoma was diagnosed as having metastatic involvement of the skull on the basis of typical imaging findings of neuroblastoma both on CT and MR imaging and considerable improvement of the lesion after targeted chemotherapy.

Received May 10, 2013; accepted after revision June 20.

From the Department of Radiology, The Children's Hospital of Philadelphia, University of Pennsylvania, Philadelphia, Pennsylvania.

Please address correspondence to Seyed Ali Nabavizadeh, MD, Department of Radiology, The Children's Hospital of Philadelphia, University of Pennsylvania, 34th and Civic Center Blvd, Philadelphia, PA 19104; e-mail: nabavizadehs@email.chop.edu

<http://dx.doi.org/10.3174/ajnr.A3712>

Demographic, clinical, imaging, and histopathologic findings of pediatric patients with FFLs in skull lesions

Patient	Sex	Age (yr)	Location	CT	No. of FFLs on CT	MRI	No. of FFLs on MRI	History of Trauma	Histopathology	Final Diagnosis
1	M	4	Right parietal	NCCT	9	CE MRI	17	Minor head trauma	LCH	LCH
2	F	0.75	Occipital	—	N/A	CE MRI	2	—	LCH	LCH
3	F	13	Left temporal	CECT	3	CE MRI	19	—	ABC	ABC
4	F	10	Left parietal	NCCT	0	CE MRI	1	Forceps delivery	None	Cephalohematoma
5	M	0.25	Left parietal	—	N/A	CE MRI	4	—	None	Cephalohematoma
6	M	1.5	Sphenoid	—	N/A	CE MRI	2	—	None	Neuroblastoma
7	F	12	Left frontal	NCCT	3	CE MRI	5	Minor head trauma	LCH	LCH
8	M	11	Left temporal	CECT	2	CE MRI	6	—	ABC in the setting of fibrous dysplasia	ABC
9	M	0.5	Left orbit	CECT	1	CE MRI	14	—	LCH	LCH
10	M	0.02	Right parietal	—	N/A	CE MRI	3	+	None	Cephalohematoma
11	F	16	Right occipital and temporal	NCCT	7	CE MRI	29	—	ABC	ABC

Note:—CECT indicates contrast-enhanced CT; CE, contrast-enhanced; —, none; +, positive for trauma; N/A, not applicable.

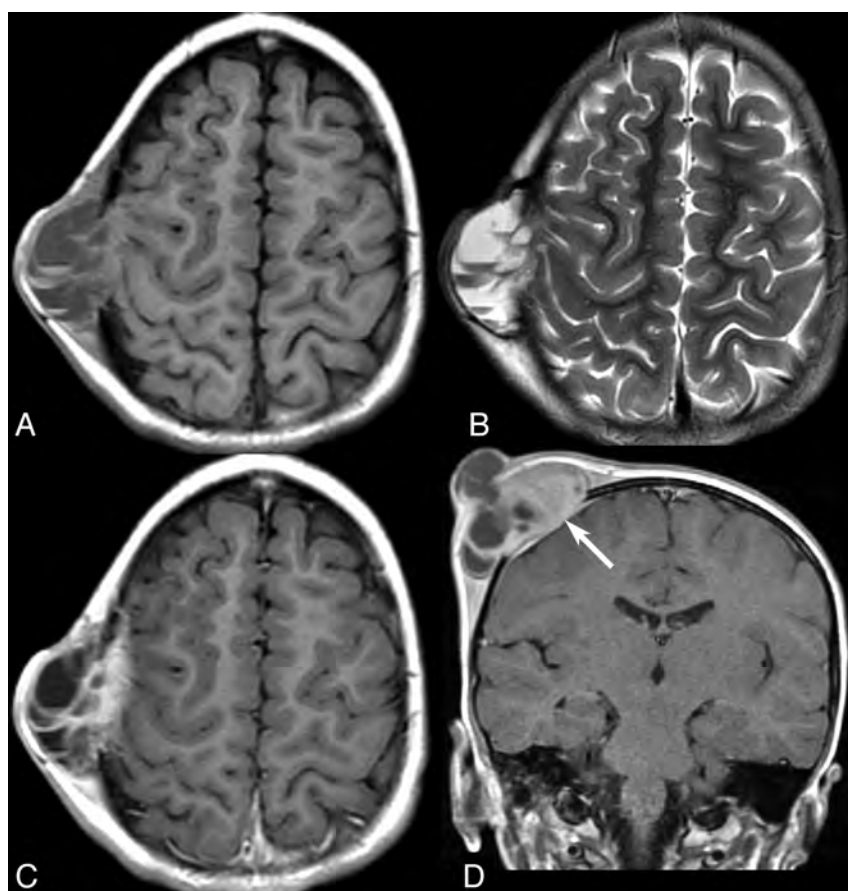


FIG 1. MR imaging in a patient with Langerhans cell histiocytosis. Axial T1- (A) and T2-weighted (B) images reveal multiple FFLs. An enhancing solid soft-tissue component is seen medially on postcontrast axial (C) and coronal (D) T1-weighted images.

CT and MR Imaging

CT was performed on various multidetector CT scanners (Siemens, Erlangen, Germany), and MR imaging was performed on 1.5T or 3T magnets (Siemens) with standard clinical protocols used at the time of the study. Axial CT sections were reconstructed at 3- or 5-mm thicknesses. MR imaging sequences varied among patients but generally included pre- and postcontrast T1-weighted, T2-weighted, fluid-attenuated inversion recovery, echo-planar spin-echo diffusion-weighted imaging, and either T2* gradient-echo susceptibility or susceptibility-weighted imaging.

The CT and MR imaging studies of these patients were re-

viewed by 2 pediatric neuroradiologists by consensus, and the findings were tabulated. For each scan, lesion location, number of fluid-fluid levels, and the presence or absence of soft-tissue components were evaluated. Diagnosis of hemorrhage was based on hyperattenuation on noncontrast CT or typical MR imaging findings (mainly hyperintensity on T1-weighted, hypointensity on T2-weighted, and/or susceptibility on gradient-echo or susceptibility-weighted images).

Clinicopathologic and Imaging Findings

Eleven patients (6 male, 5 female) with skull lesions showing fluid-fluid levels met the inclusion and exclusion criteria (Table). The mean age of patients at the time of primary diagnosis was 6.2 ± 6.1 years (range, 8 days to 16 years). The etiologies of the lesions included Langerhans cell histiocytosis (LCH) ($n = 4$ [36.6%]), aneurysmal bone cyst ($n = 3$ [27.2%]), cephalohematoma ($n = 3$ [27.2%]), and neuroblastoma ($n = 1$ [9%]).

In 7 patients, both CT (4 noncontrast, 3 contrast-enhanced) and MR imaging with and without contrast were performed. MR imaging with and without contrast was the only imaging technique in another 4 patients. In the 7 patients in whom a CT had been performed, FFLs were identified in 6 patients (85%). The mean number of fluid-

fluid levels detected on CT was 3.5 ± 3.2 (range, 1–9). FFLs were present on MR imaging in all 11 patients (100%). The mean number of detected fluid-fluid levels on MR imaging was 9.2 ± 9.1 (range, 1–29). The number of observed FFLs was significantly higher on MR imaging compared with CT ($Z = -2.36$, Wilcoxon signed-rank test, $P = .018$).

Three of 4 patients with LCH demonstrated prominent soft-tissue components (75%, Fig 1). The 3 patients with LCH who had undergone CT showed sharply marginated bone destruction. None of the patients with LCH showed substantial cystic bone expansion.

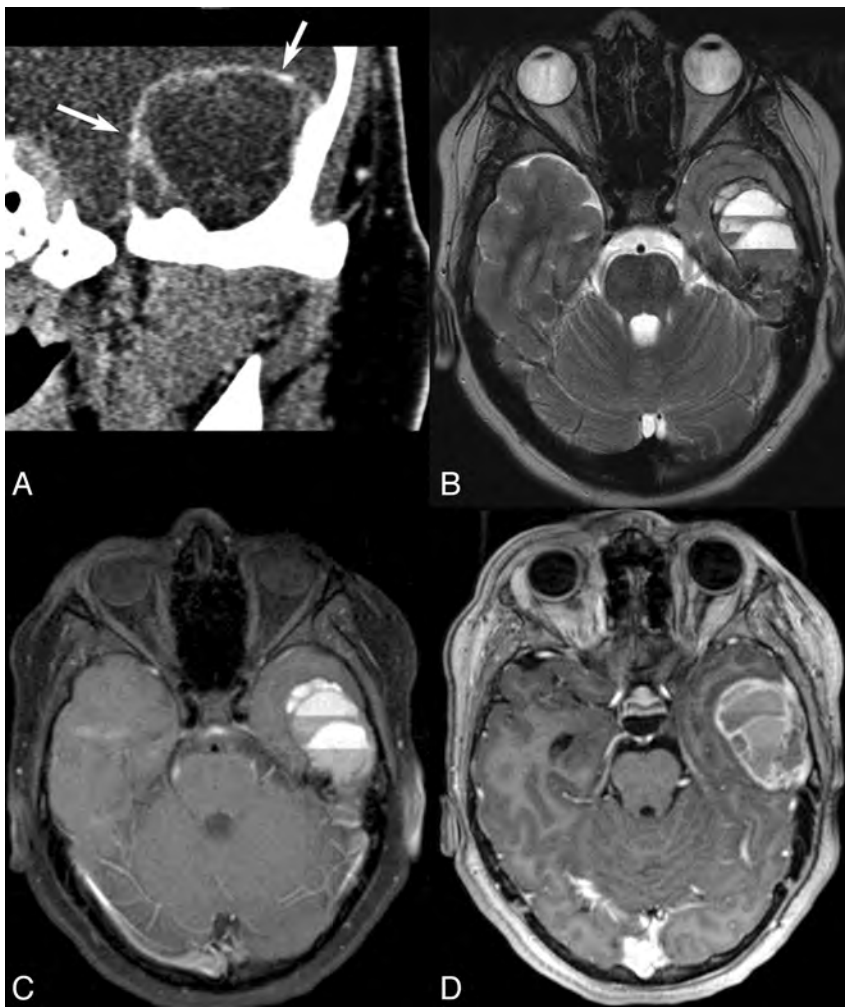


FIG 2. CT and MR imaging findings in a patient with an aneurysmal bone cyst. Coronal CT scan (A) reveals marked bone expansion by a well-defined cystic-appearing mass projecting into the left temporal fossa with very thin remnants of the bony cortex seen in the wall (*arrows*). T2-weighted (B) and precontrast T1-weighted (C) images reveal multiple FFLs. Peripheral and septal enhancement is noted on CT (A) and postcontrast T1-weighted images (D), but no large enhancing solid soft-tissue component is identified.

Two patients with LCH (patients 1 and 7) had a history of minor recent trauma to the lesion before imaging, having hit their head against a fish tank and television remote, respectively. There was no evidence of an abnormal coagulation profile in any of the patients. In patients with ABCs, 2 had primary ABCs and 1 had ABC in the setting of fibrous dysplasia. All patients with ABCs showed bone expansion (Fig 2).

All 3 patients with ABCs underwent surgical resection. Among the patients with LCH, 3 underwent surgical resection and 1 (patient 9) underwent chemotherapy after biopsy. Most interesting, follow-up imaging of this latter patient 3.5 months after completion of chemotherapy revealed a considerable increase in the number of FFLs, from 14 to >50 (Fig 3). The 1 patient with metastatic neuroblastoma also underwent treatment with chemotherapy, with a substantial decrease in the size of the lesion (Fig 4). None of the patients with cephalohematoma had a detectable solid or enhancing soft-tissue component at the time of the study, and no frank bone destruction was seen on CT or MR imaging (Fig 5). All patients with cephalohematoma were managed conservatively.

DISCUSSION

Generally, a bone lesion with FFLs is considered more likely to represent an ABC; therefore, it was surprising to us that our review of pediatric skull lesions revealed that LCH was the most common etiology of skull lesions with FFLs, followed by ABC. There is no dedicated study on the most common etiology of osseous lesions with FFLs in pediatric patients, to our knowledge. In addition, large studies that may have included some pediatric patients had not published their detailed results based on age groups,⁵⁻⁷ and the current literature is mainly limited to published case reports.⁹⁻¹⁴

There are only 2 case reports describing the presence of fluid-fluid level in LCH.^{12,14} In both of these cases, the FFL was demonstrated on both CT and MR imaging. The FFL in LCH represents hemorrhage, which may be triggered by trauma or may be spontaneous hemorrhage. Albadr et al¹² reported sudden spontaneous scalp swelling in a patient with LCH of the skull, which was then proved to be secondary to hemorrhage. Chen et al¹⁵ reported a patient with LCH of the skull complicated by a spontaneous epidural hematoma. Another potential hypothesis for hemorrhage in LCH is development of aneurysmal bone cyst features, which have been reported to be observed on histology in LCH.^{16,17} In our patients with LCH, 2 had a history of recent minor trauma, but the other 2 did not. Most interesting, the number of FFLs dramatically increased in 1 patient following chemotherapy (Fig 3), though the overall size of the lesions did decrease. Chemotherapy was used in this patient because there was orbital osseous involvement.¹⁸ No evidence of secondary ABC formation was demonstrated on histology in any of the 4 patients with LCH in this study.

We believe that several factors may contribute to the relatively high prevalence of LCH with FFL in this study. First, LCH is relatively more common in the pediatric population compared with adults, and the skull is the most frequently involved site in LCH.¹⁹ On the other hand, while ABCs can also occur in young patients, they are most often found in the metaphyses of long bones and rarely affect the skull.^{3,4,13} Despite the presence of FFLs, we believe that LCH may still potentially be differentiated from ABC on the basis of the presence of characteristic imaging findings such as sharp, nonsclerotic borders with a punched out appearance, lack of demonstrable bone expansion, and uneven destruction of the outer and inner cranial tables with a beveled edge contour on CT, though this may not be possible in all cases. The distinction may be more difficult on MR imaging. Another differentiating feature of LCH can be the presence of a prominent soft-tissue component, which was demonstrated in

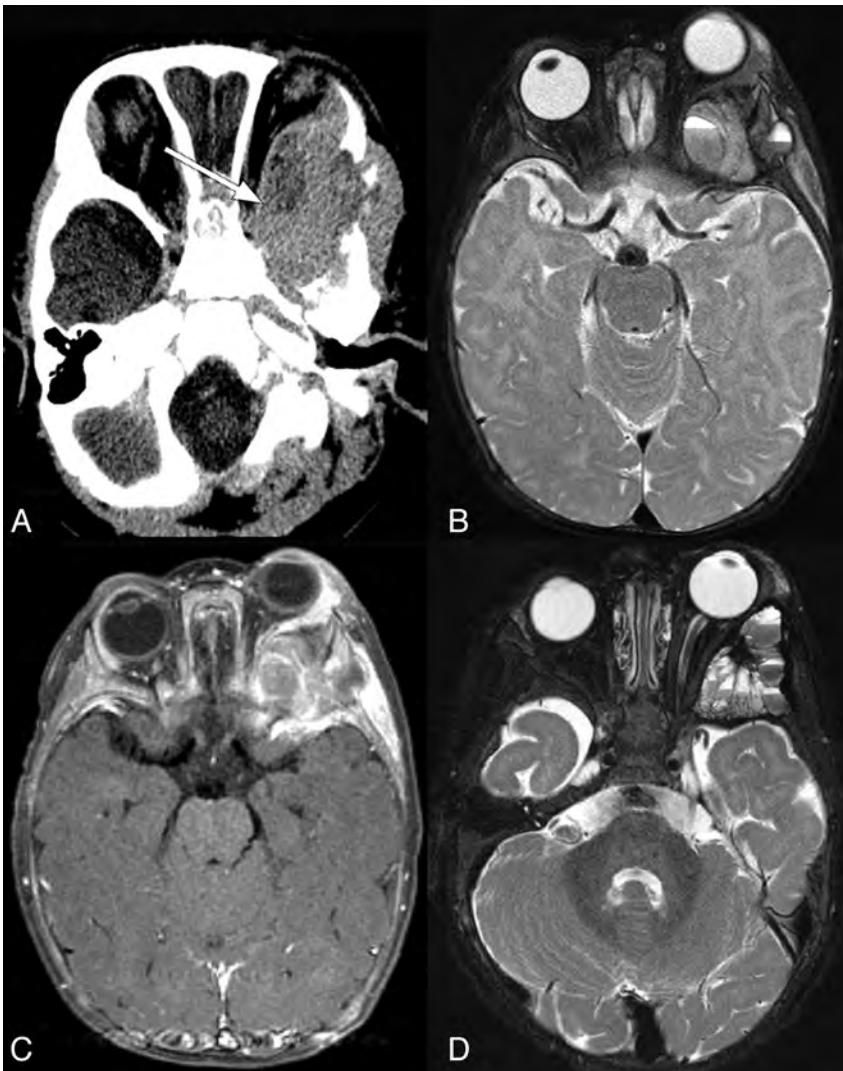


FIG 3. CT and MR imaging findings in a patient with Langerhans cell histiocytosis. Noncontrast CT (A) reveals a lytic lesion with a prominent soft-tissue component and well-defined bone destruction. An FFL is faintly seen (arrow). T2-weighted image (B) and postcontrast T1-weighted image (C) show a few FFLs and enhancement of soft-tissue components, respectively. Axial T2-weighted image (D) following chemotherapy now reveals an increase in the number of FFLs.

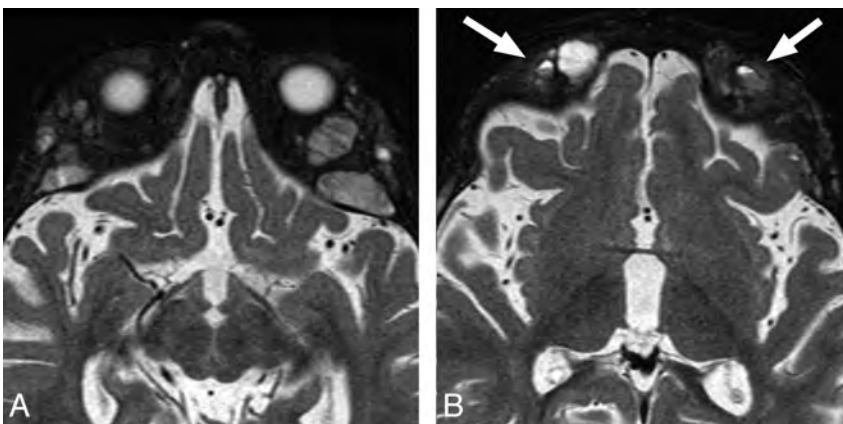


FIG 4. MR imaging findings in a patient with neuroblastoma demonstrate typical bone marrow infiltration and expansion by metastases (A). Multiple small FFLs are seen in the lesions (B).

most of the patients in this study, though occasionally an obvious soft-tissue component may not be present.

ABCs have been reported in many locations, including the orbit, occipital bone, frontal bone, temporal bone, parietal bone, and skull base.²⁰⁻²² In this study, we found 2 primary ABCs and a secondary ABC in the setting of fibrous dysplasia. The coexistence of an aneurysmal bone cyst and a companion lesion is well-known and is consistent with the concept of local hemodynamic changes secondary to precursor pathology. Trauma, benign lesions of the skeleton (eg, chondroblastoma, chondromyxoid fibroma, osteoblastoma, giant cell tumor, fibrous dysplasia), and even some malignant tumors (eg, osteosarcoma, chondrosarcoma, hemangioendothelioma) have been associated with development of aneurysmal bone cysts.^{10,17,23} In the setting of fibrous dysplasia, secondary ABC formation can occur in addition to the more common evolving fibrous dysplasia with lytic areas or cystic degeneration.²⁴

Cephalohematoma is a subperiosteal hemorrhage that results from tearing of delicate vessels that traverse through the bone into the scalp. It has been reported in 0.2%–3% of all births,²⁵⁻²⁷ though most are small and resolve spontaneously. Cephalohematomas are confined to suture borders where the periosteum is tightly adherent to the membranous tissue of the sutures.²⁸ The most common location is over the parietal bone followed by the occipital bone.²⁶

Multiple risk factors have been associated with the development of cephalohematoma, including birth trauma, fetal scalp monitors, instrumentation, greater birth weight, and nulliparity.^{25,29,30} Cephalohematoma is a benign condition, which usually does not require specific therapy. Most cephalohematomas resolve within a few weeks to months, depending on their size.^{29,31} Many patients with typical history and clinical examination for cephalohematoma will not be imaged. On the infrequent occasion when the hematoma fails to resorb, progressive subperiosteal osteogenesis results in a calcified cephalohematoma. The incidence of calcification has been reported to occur in 3%–5% of all cephalohematomas.³² In these cases, there is usually a history of a mass present since birth that is initially boggy and fluctuant and then gradually

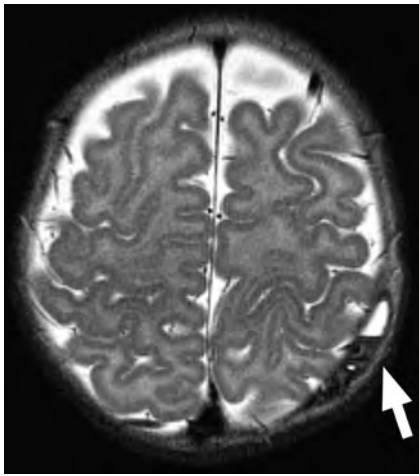


FIG 5. MR imaging of a 3-month-old patient found to have a bump on the head on physical examination. T2-weighted axial image shows an FFL within a cephalohematoma (arrow), confirmed to be within the bone on multiple planes and sequences (not shown).

hardens, typical of an ossifying cephalohematoma.³¹ In this series, we found 3 cases of cephalohematoma, one in a neonate, another in a young infant, and the other, a partially calcified cephalohematoma, in a 10-year-old patient. All of the lesions were in the parietal area, which is consistent with findings in the literature.²⁶

Neuroblastoma is the most common extracranial solid tumor. Metastatic involvement of the head and neck is common and manifests most often as osseous metastases with periosteal reactions involving the calvaria, orbit, or skull base^{33,34} and is also commonly seen both at presentation and at the time of tumor recurrence. One of the patients in this study had metastatic neuroblastoma involving the sphenoid bone. We are not aware of any report in the English literature describing FFLs in metastatic neuroblastoma to the skull.

The main limitation of our study is the relatively small number of patients, though there has been no focused study of osseous lesions of the skull with FFL, particularly in pediatric patients. Future larger studies may shed more light on the various etiologies of these lesions.

CONCLUSIONS

Radiologists should be aware that besides ABCs, there are other lesions in the pediatric skull that can demonstrate FFLs. In our series, LCH was the most common etiology followed by ABC. Cephalohematoma should also be considered in the appropriate clinical setting. As would be expected, MR imaging was more sensitive in detecting FFLs within the lesions.

REFERENCES

1. Tsai J, Dalinka M, Fallon M, et al. Fluid-fluid level: a non-specific finding in tumors of bone and soft tissue. *Radiology* 1990;175:779–82
2. Davies AM, Cassar-Pullicino VN, Grimer RJ. The incidence and significance of fluid-fluid levels on computed tomography of osseous lesions. *Br J Radiol* 1992;65:193–98
3. Hudson T. Fluid levels in aneurysmal bone cysts: a CT feature. *AJR Am J Roentgenol* 1984;141:1001–04
4. Hertzanu Y, Mendelsohn D, Gottschalk F. Aneurysmal bone cyst of the calcaneus. *Radiology* 1984;151:51–52
5. Van Dyck P, Vanhoenacker FM, Vogel J, et al. Prevalence, extension and characteristics of fluid-fluid levels in bone and soft tissue tumors. *Eur Radiol* 2006;16:2644–51
6. Alyas F, Saifuddin A. Fluid-fluid levels in bone neoplasms: variation of T1-weighted signal intensity of the superior to inferior layers—diagnostic significance on magnetic resonance imaging. *Eur Radiol* 2008;18:2642–51
7. O'Donnell P, Saifuddin A. The prevalence and diagnostic significance of fluid-fluid levels in focal lesions of bone. *Skeletal Radiol* 2004;33:330–36
8. Kobayashi Y, Murakami R, Toba M, et al. Chondroblastoma of the temporal bone. *Skeletal Radiol* 2001;30:714–18
9. Sharma A, Garg A, Mishra NK, et al. Primary Ewing's sarcoma of the sphenoid bone with unusual imaging features: a case report. *Clin Neurol Neurosurg* 2005;107:528–31
10. Haddad GF, Hambali F, Mufarrij A, et al. Concomitant fibrous dysplasia and aneurysmal bone cyst of the skull base: case report and review of the literature. *Pediatr Neurosurg* 1998;28:147–53
11. Wang YC, Huang JS, Wu CJ, et al. A huge osteoblastoma with aneurysmal bone cyst in skull base. *Clin Imaging* 2001;25:247–50
12. Albadr FB, Elgamel EA, Alorainy IA, et al. Fluid-fluid level in Langerhans cell histiocytosis of the skull. *Neurosciences* 2006;11:47–49
13. Sawin PD, Muhonen MG, Sato Y, et al. Aneurysmal bone cyst of the temporal bone presenting as hearing loss in a child. *Int J Pediatr Otorhinolaryngol* 1995;33:275–84
14. Hindman BW, Thomas RD, Young LW, et al. Langerhans' cell histiocytosis: unusual skeletal manifestations observed in thirty four cases. *Skeletal Radiol* 1998;27:177–81
15. Chen HC, Shen WC, Chou DY, et al. Langerhans cell histiocytosis of the skull complicated with an epidural hematoma. *AJNR Am J Neuroradiol* 2002;23:493–95
16. Mirra JM. *Bone Tumors: Clinical, Radiologic and Pathologic Correlations*. Philadelphia: Lea & Febiger; 1989:1269
17. Roncaroli F, Consales A, Galassi E, et al. Occipital aneurysmal bone cyst secondary to eosinophilic granuloma. *Pediatr Neurosurg* 2001;35:103–06
18. Langerhans Cell Histiocytosis Treatment. National Cancer Institute. <http://www.cancer.gov/cancertopics/pdq/treatment/lchistio/HealthProfessional/page7>. Accessed June 15, 2013
19. Bollini G, Jouve JL, Gentet JC, et al. Bone lesions in histiocytosis X. *J Pediatr Orthopaed* 1991;11:469–77
20. Calliauw L, Roels H, Caemaert J. Aneurysmal bone cysts in the cranial vault and base of skull. *Surg Neurol* 1985;23:193–98
21. Lichtenstein L. Aneurysmal bone cyst: observations on fifty cases. *Bone Joint Surg Am* 1957;39-A:873–82
22. Tillman BP, Dahlin DC, Lipscomb PR, et al. Aneurysmal bone cyst: an analysis of ninety-five cases. *Mayo Clin Proc* 1968;43:478–95
23. Ito H, Kizu O, Yamada K, et al. Secondary aneurysmal bone cyst derived from a giant-cell tumour of the skull base. *Neuroradiology* 2003;45:616–17
24. Faul S, Link J, Behrendt S, et al. MRI features of craniofacial fibrous dysplasia. *Orbit* 1998;17:125–32
25. Tan KL. Cephalohaematoma. *Aust N Z J Obstet Gynaecol* 1970;10:101–06
26. Ingram MD, Hamilton WM. Cephalohematoma in the newborn. *Radiology* 1950;55:502–07
27. LeBlanc CM, Allen UD, Ventureyra E. Cephalohematomas revisited: when should a diagnostic tap be performed? *Clin Pediatr (Phila)* 1995;34:86–89
28. Merlob P, Grunebaum M, Reisner SH. Crossed sagittal-suture cephalohaematoma. *Br J Radiol* 1985;58:1007–08
29. Hartley JB, Burnett CW. An inquiry into the causation and characteristics of cephalohematoma. *Br J Radiol* 1944;17:33–41
30. Petersen JD, Becker DB, Fundakowski JL, et al. A novel management for calcifying cephalohematoma. *Plast Reconstr Surg* 2004;113:1404–09
31. Morgan JE. Calcification in cephalohematomata of the newborn infant. *Am J Obstet Gynecol* 1944;48:702
32. Bruce DA. Cephalohematoma and subgaleal hematoma. In: Wilkins RH, Rengachary SS, eds. *Neurosurgery*. 2nd ed. New York: McGraw-Hill; 1995:2739–40
33. Chirathivat S, Post MJ. CT demonstration of dural metastases in neuroblastoma. *J Comput Assist Tomogr* 1980;4:316–19
34. Zimmerman RA, Bilaniuk L. CT of primary and secondary cranio-cerebral neuroblastoma. *AJR Am J Roentgenol* 1980;135:1239–42

Frequency of Discordance between Facet Joint Activity on Technetium Tc99m Methylene Diphosphonate SPECT/CT and Selection for Percutaneous Treatment at a Large Multispecialty Institution

V.T. Lehman, R.C. Murphy, T.J. Kaufmann, F.E. Diehn, N.S. Murthy, J.T. Wald, K.R. Thielen, K.K. Amrami, J.M. Morris, and T.P. Maus

ABSTRACT

BACKGROUND AND PURPOSE: The clinical impact of facet joint bone scan activity is not fully understood. The hypothesis of this study is that facet joints targeted for percutaneous treatment in clinical practice differ from those with reported activity on technetium Tc99m methylene diphosphonate SPECT/CT.

MATERIALS AND METHODS: All patients with a technetium Tc99m methylene diphosphonate SPECT/CT scan of the lumbar or cervical spine who underwent subsequent percutaneous facet joint steroid injection or comparative medial branch blocks at our institution between January 1, 2008, and February 19, 2013, were identified. Facet joints with increased activity were compared with those treated. A chart review characterized the clinical reasons for treatment discrepancies.

RESULTS: Of 74 patients meeting inclusion criteria, 52 (70%) had discrepant imaging findings and treatment selection of at least 1 facet joint, whereas 34 patients (46%) had a side (right vs left) discrepancy. Only 92 (70%) of 132 facet joints with increased activity were treated, whereas 103 (53%) of 195 of treated facet joints did not have increased activity. The most commonly documented clinical rationale for discrepancy was facet joint activity that was not thought to correlate with clinical findings, cited in 18 (35%) of 52 patients.

CONCLUSIONS: Facet joints undergoing targeted percutaneous treatment were frequently discordant with those demonstrating increased technetium Tc99m methylene diphosphonate activity identified by SPECT/CT at our institution, in many cases because the active facet joint(s) did not correlate with clinical findings. Further prospective double-blinded investigations of the clinical significance of facet joint activity by use of technetium Tc99m methylene diphosphonate SPECT/CT and comparative medial branch blocks are needed.

ABBREVIATIONS: ^{99m}Tc MDP = technetium Tc99m methylene diphosphonate; RF = radiofrequency

Clinical examination and anatomic imaging do not reliably identify specific painful facet joints.¹⁻³ Prior studies suggest that technetium Tc99m methylene diphosphonate (^{99m}Tc MDP) bone scan activity can predict if a facet joint is painful and if there will be a positive response to percutaneous intervention targeted specifically to active facet joints.⁴⁻⁶ These prior studies used strict treatment of every facet joint with increased radiotracer activity on bone scan,⁴⁻⁶ concluding that ^{99m}Tc MDP SPECT can decrease the number of treated facet joints.⁴ However, those results can only be applicable if this is used in clinical practice and is feasible. Moreover, these studies did not incorporate CT scan for facet joint localization, use comparative medial branch blocks for diagnosis, include clearly blinded patients and proceduralists, or ex-

amine the impact of ^{99m}Tc MDP bone scan results in actual clinical practice. Such shortcomings limit the conclusions of these prior reports and indicate the need for further examination of the clinical usefulness of ^{99m}Tc MDP facet joint activity. In addition, evaluation of the impact of imaging in actual practice is important because the efficacy demonstrated in clinical studies often does not translate into true clinical effectiveness when the ideal rigorous methods of the efficacy study are no longer applied.⁷ That is, the effect of real-life variables such as clinical findings suggesting facet joint pain on a specific side or level and the variability of physician experience and philosophy should be evaluated to confirm or refute the impact of controlled studies on actual clinical practice and to identify areas in need of future investigation.

In our anecdotal experience, the specific facet joints referred for percutaneous facet joint intervention are sometimes widely discordant from those with reported activity on ^{99m}Tc MDP SPECT/CT. Specifically, we have seen some patients with suspected facetogenic pain where the ^{99m}Tc MDP SPECT/CT scan does not seem to demonstrate concordant facet joint activity in

Received May 14, 2013; accepted after revision July 8.

From the Department of Radiology, Mayo Clinic College of Graduate Medical Education, Rochester, Minnesota.

Please address correspondence to: Vance T. Lehman, Department of Radiology, 200 First St SW, Rochester, MN 55905; e-mail: lehman.vance@mayo.edu

<http://dx.doi.org/10.3174/ajnr.A3731>

the location or even on the side of pain. We have also observed that many facet joints with bone scan activity do not seem to correlate with a clinical facet joint pain syndrome. However, the concordance of facet joint bone scan activity and targeted facet joint treatment in actual clinical practice is not well described. Furthermore, the clinical rationale for imaging-procedural discrepancy is not known.

The hypothesis of this study is that facet joints that are targeted for percutaneous treatment in clinical practice differ from those with reported activity on ^{99m}Tc MDP SPECT/CT scans.

MATERIALS AND METHODS

Patients

Approval for this Health Information Portability and Accountability compliant study was obtained from our institutional review board.

A chart review was performed of all patients who underwent both ^{99m}Tc MDP SPECT/CT imaging of the cervical or lumbar spine and percutaneous facet joint intervention (facet joint injection or medial branch block) between January 1, 2008, and February 19, 2013, at our institution.

Exclusion criteria were as follows: 1) cases in which the interval between the ^{99m}Tc MDP SPECT/CT examination and facet joint injection exceeded 100 days, and 2) cases in which facet joints with increased ^{99m}Tc MDP activity were not specifically named by level and side in the radiology report (eg, a statement such as “scattered facet joint activity” or “lower lumbar facet joint activity”).

^{99m}Tc MDP SPECT/CT Examinations

Patients underwent SPECT/CT of the cervical or lumbar spine 3–4 hours after injection with 20 mCi ($\pm 10\%$) ^{99m}Tc MDP. Examinations were performed on a Precedence 6-section or a 16-section scanner (Skylight SPECT system and Brilliance CT scanner; Philips Healthcare, Best, the Netherlands). SPECT parameters were as follows: 128 \times 128 word mode matrix, 128 views at 20 seconds per view, 1.46 zoom factor, step-and-shoot angular step of 3°, body contouring, and low-energy all-purpose collimator. CT parameters were as follows: 120 kVp, 60 mAs per section, 3-mm section thickness, and 3-mm increment. CT studies were acquired with helical scans with a pitch of 0.788 (6-section) or 0.813 (16-section) and a collimator thickness of 3 mm (6-section) and 1.5 mm (16-section).

Chart Review of SPECT/CT Reports and Treated Facet Joints

All relevant clinical notes between the time of ^{99m}Tc MDP SPECT/CT examinations and facet joint interventions, the ^{99m}Tc MDP SPECT/CT reports, the ^{99m}Tc MDP SPECT/CT images, the facet joint intervention procedure reports, and the procedural fluoroscopy images were reviewed in detail by a board-certified radiologist (V.T.L.) for side and level confirmation. All images were viewed on an Advantage workstation (GE Healthcare, Milwaukee, Wisconsin). Because the aim of our study was to characterize selection of treated facet joints in actual clinical practice rather than patient outcome, we did not perform de novo characterization of facet joint activity and success of facet joint injection (intra-articular vs periarticular). The specialty of the refer-

ring clinical provider was recorded. Cases in which the referring provider differed from the provider who ordered the ^{99m}Tc MDP SPECT/CT were noted; in these cases, the clinical notes of the referring provider were examined.

In the cervical spine, the bilateral C1–2 articulations through the C7–T1 facet joints were assessed (totaling 14 cervical facet joints for each patient). In the lumbar spine, the bilateral T12–L1 through the L5–S1 facet joints were assessed (totaling 12 facet joints for each patient). Because the number of lumbar vertebral bodies is variable, the lowest presacral lumbar-type vertebral body was designated L5 for the purposes of this analysis.

The facet joints targeted for percutaneous intervention, method of intervention (steroid injection or medial branch block), and type of image guidance were recorded. Although medial branch blocks are diagnostic procedures usually performed in 2 sessions to determine the appropriateness of subsequent radiofrequency (RF) ablation at our institution, the facet joints targeted with the first medial branch block were used for this portion of the analysis for consistency.

Patient Referral Practice Model

Our institution is a large, multispecialty, tertiary referral center and includes a dedicated spine center with a spine clinic and a spine interventional practice. The spine interventional practice is staffed by fellowship-trained musculoskeletal radiologists, neuro-radiologists, physical medicine and rehabilitation physicians, and anesthesiologists with subspecialty training in pain management. Specific facet joints targeted by the interventional practice are generally requested by referring clinicians. Occasionally, the proceduralist will choose different facet joints to target after conferring with the referring clinician. Referrals commonly come from pain medicine, though a wide variety of clinicians such as neurologists or primary care physicians also provide referrals. Facet joint interventions may be either steroid injections or RF ablation after dual comparative medial branch blocks, though facet joint injections are used more frequently at our institution. No specified criteria exist for selection of medial branch blocks with RF ablation; these are chosen based on clinical factors such as the preference of the specific referring provider and the expertise of the requested proceduralist. The specialty of the proceduralist for each intervention was recorded.

Data Analysis

A grouped data analysis was performed for all included patients. Subanalyses for the lumbar spine and cervical spine were also performed. The presence or absence of reported increased activity within each facet joint was compared with the presence or absence of targeted treatment of that facet joint. Facet joints were placed into 3 categories: 1) facet joints with reported ^{99m}Tc MDP activity and that were also treated (concordant), 2) facet joints with reported ^{99m}Tc MDP activity and that were not targeted for treatment (discordant), and 3) treated facet joints that were not reported as having ^{99m}Tc MDP activity (discordant). Patients were also categorized as either having 1) concordance of activity and injection for every facet joint or 2) at least 1 discordant facet joint. Facet joints without increased radiotracer activity that were not treated were also considered concordant, but further

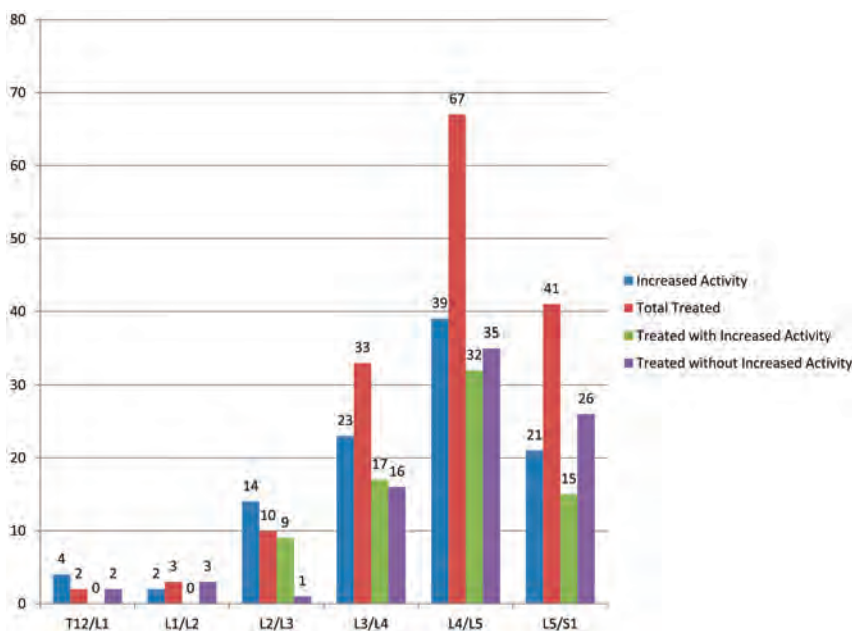


FIG 1. Number of lumbar facet joints per level with reported increased activity, total treated at that level with breakdown of those treated with and without activity. The left and right facet joints are grouped at each level.

detailed analysis of this category was not performed because a large number of facet joints that would not have been considered for treatment with or without imaging likely fall within this group.

The degree of left-right concordance of facet joint interventions and activity was recorded. Specifically, it was determined for each patient if 1) there was at least 1 injection on a side without a single facet joint with increased activity and/or, 2) there was a side with at least 1 facet joint with increased activity but without a single injection.

Categorization of Rationale for ^{99m}Tc MDP SPECT/CT-Procedural Discrepancy

In cases with requests for facet joint intervention that were discordant with the ^{99m}Tc SPECT/CT results in at least 1 facet joint, the clinical rationales for the discrepancies were categorized as follows: 1) facet joints with activity that did not correlate with clinical examination, 2) consideration of positive or negative response of some facet joints to prior intervention, 3) de-emphasis of facet joints with relatively low reported activity, 4) too many facet joints with activity to include each one for treatment, 5) targeted facet joints selected based on anatomic features of facet joint degenerative change or information obtained from other imaging test such as MR imaging, and 6) no documented clinical reasoning identified. Cases with multiple cited categories were grouped into the single predominant category cited in the medical record.

RESULTS

Patients, Referring Clinicians, and ^{99m}Tc MDP SPECT/CT Examinations

A total of 78 patients with a ^{99m}Tc MDP SPECT/CT and subsequent facet joint injection were identified. Overall, 4 were excluded for the following reasons: nonspecific reporting of facet joint activity in the radiology report ($n=3$), and > 100-day inter-

val between imaging and intervention ($n=1$). Therefore, 74 patients were included in this study, consisting of 43 women and 31 men with a mean age of 59 years (age range, 28–93 years). No included patient had a ^{99m}Tc MDP SPECT/CT and intervention of both the lumbar and cervical spine. Fifty-five patients (74%) underwent ^{99m}Tc MDP SPECT/CT and injection of the lumbar spine; 19 patients (26%), of the cervical spine. A total of 926 facet joints were assessed in this study: 660 in the lumbar spine and 266 in the cervical spine. The mean time between the ^{99m}Tc MDP SPECT/CT and the percutaneous intervention was 15.6 days (range, 0–99 days) overall, 13.4 days (range, 0–99 days) for the lumbar spine, and 22.1 days (range, 0–65 days) for the cervical spine.

The clinicians who ordered the ^{99m}Tc MDP SPECT/CT by specialty were physical medicine and rehabilitation ($n=48$; 65%), pain medicine ($n=10$; 14%), neurology ($n=7$; 9%), orthopedics ($n=4$; 5%), primary care ($n=3$; 4%), and rheumatology ($n=2$; 3%). Pain medicine includes physicians with either a physical medicine and rehabilitation or anesthesiology background. All 74 ^{99m}Tc MDP SPECT/CT examinations (100%) were originally performed with an indication to identify a pain generator rather than for a different category of diagnosis, such as metastatic disease or infection evaluation. Specifically, of the 74 examinations performed, 43 (58%) had an indication for facet joint evaluation, 23 (31%) were ordered to identify a pain generator with a general indication of “low back pain,” 6 (8%) were ordered to identify a pain generator with a general indication of “neck pain,” 1 (1%) was ordered to evaluate for possible fracture, and 1 (1%) was ordered to evaluate for a possible pars interarticularis defect.

Of 74 facet joint treatment referrals, 64 (86%) were requested directly from the physician who officially requested the ^{99m}Tc MDP SPECT/CT. Of the remaining 10 (14%) patients, facet joint injections were requested via an intermediary pain medicine specialist for 6 patients and an intermediary physical medicine and rehabilitation specialist in 4 patients.

Facet Joint Activity and Percutaneous Treatment

Overall, 132 facet joints (14%) had increased activity, 103 (16%) of 660 in the lumbar spine and 29 (11%) of 266 in the cervical spine. A total of 195 facet joints (21%) underwent percutaneous treatment under fluoroscopy: 156 (23%) in the lumbar spine and 39 (15%) in the cervical spine. The most common lumbar and cervical levels with both facet joint activity ($n=39$) and intervention were L4–5 ($n=67$) and C3–4 ($n=11$), respectively. Overall, 67 (91%) of 74 patients underwent steroid injection: 49 (89%) in the lumbar spine and 18 (95%) in the cervical spine. Seven patients (9%) underwent medial branch block: 6 (11%) in the lumbar spine and 1 (5%) in the cervical spine. The rate of reported concordant/discordant facet joint activity and treatment at each level is depicted in Figs 1 and 2.

On a per-patient basis, 52 patients (70%) had at least 1 discrepancy between reported facet joint activity and treatment, whereas 22 (30%) had no discrepancy, including 14 with lumbar spine intervention and 8 with cervical spine intervention. The rates of discrepancy per patient according to specialty of provider who directly ordered the facet joint injection were as follows: 1) physical medicine and rehabilitation (34 [69%] of 49), 2) pain medicine (10 [66%] of 16), 3) neurology (3 [100%] of 3), 4) adult primary care (2 [100%] of 2), 5) orthopedic surgery (2 [66%] of 3), and 6) rheumatology (1 [100%] of 1).

On a per-facet basis, 92 (47%) of 195 treated facet joints had increased activity on the ^{99m}Tc MDP SPECT/CT, whereas 103 targeted facet joints (53%) did not have increased activity. Therefore, of the 132 facet joints with increased activity, 92 (70%) were treated and 40 (30%) were not. The breakdown of the rate of facet joint intervention by activity and anatomic region is listed in Table 1.

Overall, 34 (46%) of 74 patients had a right-left side discrepancy. Specifically, 11 (15%) of 74 had activity on 1 side that was not treated, and 24 (32%) of 74 patients had treatment to at least 1 side that did not have increased activity. One patient was included in both of these groups. Clinical examples of patients with discordant treatment are depicted in Figs 3 and 4.

Clinical Reasons for ^{99m}Tc MDP SPECT/CT and Procedure Discordance

A total of 31 (60%) of 52 patients with a discrepancy had a documented clinical reason, whereas 21 (40%) did not. The most com-

mon cited reason was that the ^{99m}Tc MDP activity did not correspond with the clinical findings, documented in 18 (35%) of 52 patients. The reasons for discordance are detailed in Table 2.

DISCUSSION

The results of our study are that in the clinical practice at a large multispecialty institution, targeted percutaneous facet joint treatments were discrepant from ^{99m}Tc MDP SPECT/CT activity in most patients, many facet joints with increased activity were not targeted, many targeted facet joints did not demonstrate increased activity, and facet joint activity did not always correlate with clinically suspected painful facet joints or even the side of suspected painful facet arthropathy. These findings have implications for patient treatment and the need for further evaluation of the significance, accuracy, and predictive ability of ^{99m}Tc MDP SPECT/CT findings in evaluation of facet joint pain.

Prior reports have found that strictly targeting facet joints with increased ^{99m}Tc MDP activity is predictive of a positive response to percutaneous treatment⁴⁻⁶ and that use of bone scans can decrease the number of treated facet joints.⁴ However, in the current retrospective review of our institution, this association did not translate into actual clinical practice for patients in whom ^{99m}Tc MDP SPECT/CT examinations were ordered specifically to identify pain generators, mostly by pain physicians. The most commonly found documented reason was lack of correlation of facet joints with increased activity and clinical findings. Therefore, it is possible that the requesting providers were unable to reconcile

these apparent discrepancies and, when discordant, instead requested treatment of clinically implicated facet joints. For clinicians to reconcile widely discrepant imaging and clinical indicators, strong evidence guiding the usefulness, accuracy, and impact on patient outcomes is desirable. However, the lack of prior studies that fully meet current practice standards in conjunction with the results of our current study suggests that the significance of facet joint activity with ^{99m}Tc is not yet fully understood.

Prior studies were performed with ^{99m}Tc SPECT only,⁴⁻⁶ rather than ^{99m}Tc SPECT/CT for anatomic co-localization to definitively confirm the correct level of activity. Anatomic co-localization is important because facet joints are anatomically juxtaposed, the number of vertebral bodies is variable, and transitional lumbosacral vertebral bodies are present in 4%–30% of patients.⁸ Previously, criteria for active facet joints were either not

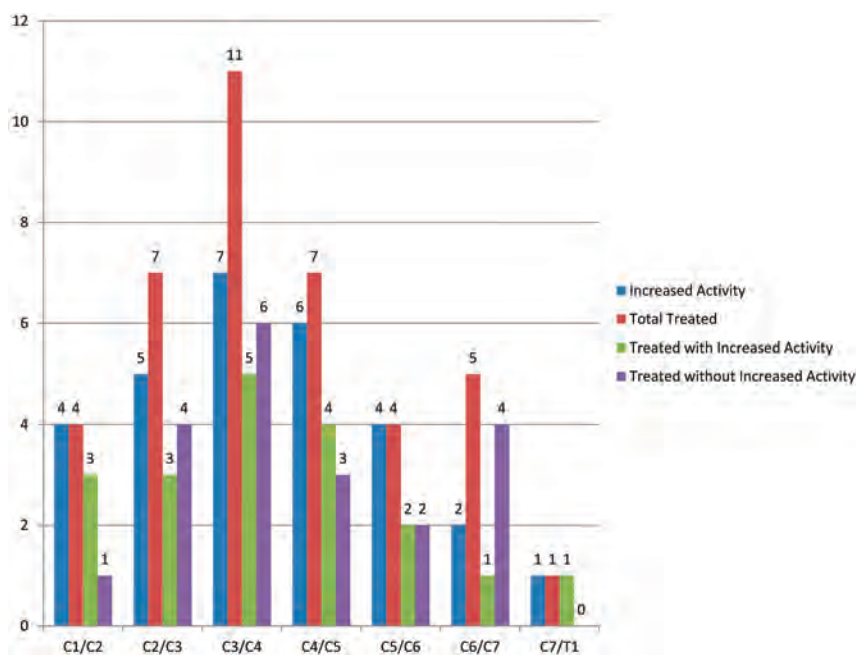


FIG 2. Number of cervical facet joints per level with reported increased activity, total treated at that level with breakdown of those treated with and without activity. The left and right facet joints are grouped at each level.

Table 1: Facet joint ^{99m}Tc MDP activity, percutaneous treatment, and anatomic region

	Facet Joints Treated Percutaneously			Facet Joints Not Treated Percutaneously		
	Lumbar (n = 156)	Cervical (n = 39)	Overall (n = 195)	Lumbar (n = 504)	Cervical (n = 227)	Overall (n = 731)
Activity present (%)	73 (47)	19 (49)	92 (47)	30 (6)	10 (4)	40 (5)
Activity absent (%)	83 (53)	20 (51)	103 (53)	474 (94)	217 (96)	691 (95)

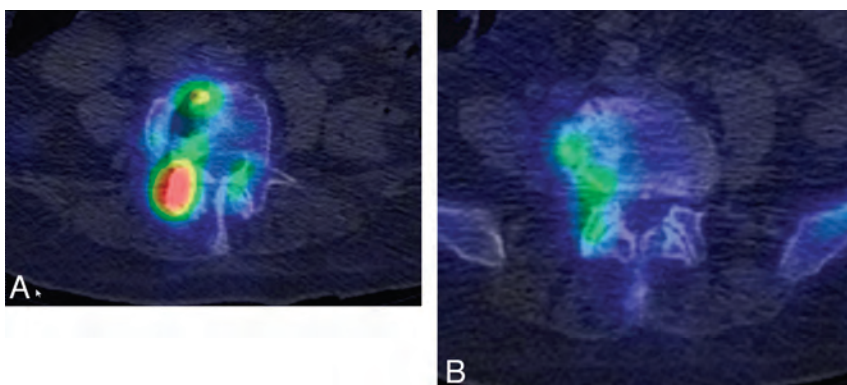


FIG 3. Left-right discordance with treatment of side with no reported activity in addition to a side with activity in a 90-year-old woman with bilateral low back pain. ^{99m}Tc MDP SPECT/CT demonstrates activity at the right, but not left, L3/L4 facet joint (A), and no reported increased activity at the bilateral L4/L5 facet joints (B) or other lumbar facet joints. Because of severe bilateral low back pain attributed to facet arthropathy, she underwent bilateral L3/L4 and L4/L5 facet joint injections.

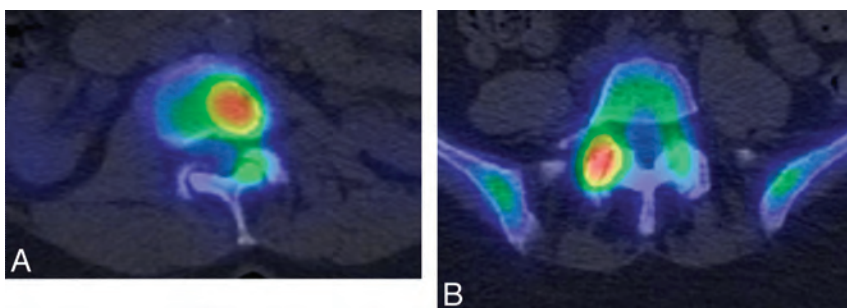


FIG 4. Left-right discordance with absent treatment on a side with activity as well as level discordance in a 60-year-old woman with back pain and clinical findings supporting a left upper facet joint pain generator. Mildly increased activity in the left L1–L2 facet joint (A) and marked increased activity in the right L4–L5 facet joint (B). Only the left L1–L2 facet joint underwent facet joint steroid injection.

Table 2: Reasons for discrepancy between facet joint activity and treatment

Reason	Patient Group		
	Lumbar (n = 41)	Cervical (n = 11)	Overall (n = 52)
Not documented (%)	18 (44)	3 (27)	21 (40)
Active facet joint not concordant with clinical findings (%)	13 (32)	5 (45)	18 (35)
Consideration of response (or lack of) to prior targeted treatment (%)	6 (15)	3 (27)	9 (17)
Relatively low reported activity (%)	2 (5)	0 (0)	2 (4)
Too many active facet joints to inject (%)	0 (0)	0 (0)	0 (0)
Information from other imaging (%)	2 (5)	0 (0)	2 (4)

clearly defined⁵⁻⁶ or were arbitrarily designated as those greater than the adjacent vertebral body,⁴ which could be problematic because vertebral body activity at the levels of degenerative spinal disease is highly variable in our experience. In addition, prior studies have included patients and proceduralists who were not clearly blinded,⁴⁻⁶ had widely overlapping statistical error measurements between treatment and control groups,⁴ and/or used facet joint injections/single medial branch blocks.⁴⁻⁶ A prior case series analysis describes a positive response to treatment of facet joints selected with ^{99m}Tc SPECT/CT where the patients and proceduralists were not clearly blinded, there was no control group, and comparative medial branch blocks were not used.⁹ Although

facet joint injections remain a treatment option in routine clinical practice, these have a 32% placebo rate.¹⁰ Comparative medial branch blocks are now considered the reference standard for diagnosis of painful facet joints and should be used for rigorous prospective study that will be fully accepted by the pain medicine community.¹¹

There are many possible explanations for the results of our study, though these are speculative given the retrospective study design. ^{99m}Tc MDP facet joint activity may not be necessary for or provide sufficient evidence of a painful facet joint. That is, facet joint activity is dependent on vascularity and chemisorption into bone mineral, particularly during osteoneogenesis,¹² and therefore has multiple potential causes such as active growth of an osteophyte¹³ or inflammation.^{4,14} These may not be equally associated with pain. In addition, the pathomechanism of facet joint pain is not fully understood and is likely multifactorial.¹⁵ It is possible that bone scan activity is present with some, but not all, causes or predisposing factors of facet joint pain. Clinicians may have also, knowingly or unknowingly, considered the reported prevalence of facet joint pain at specific spinal levels in decision making, which would be consistent with the finding that many facet joints without activity that were treated were at the L4–5 level.¹⁶ Because clinical localization of facet joint pain is challenging, it is possible that some cases had false assignment of discordant facet joint activity and clinical findings. However, the cases of complete side discrepancy indicate that false clinical localization is unlikely in all discordant cases; note that a prior study found no instances of contralateral facet joint pain referral.¹⁷ Finally, it is possible that patients who underwent ^{99m}Tc MDP SPECT/CT were a subgroup with confusing

or challenging clinical findings and were not fully representative of all patients with facetogenic back pain.

Because our institution did not collect outcome data in a consistent standardized format for all patients during the period of this retrospective study, lack of outcome assessment was a limitation. However, outcome data derived from patients treated primarily with steroid injections would have had limited usefulness because reliable determination of facet joint pain depends on consistent use of diagnostic comparative medial branch blocks.¹¹ Strict use of comparative medial branch blocks would likely require a prospective study design, ideally randomized and double blinded. Even with this limitation, the results of this study do enhance clinical equipoise for such a future

investigation because the effectiveness of ^{99m}Tc MDP SPECT/CT for prescription of treatment of specific facet joints in actual clinical practice was not high.

Our study had several other limitations. Because the patients were treated at a single institution, it is uncertain how generalizable these results were, and corroboration of results from other institutions would strengthen the findings. The retrospective study design precluded standardized patient recruitment, clinical assessment of all patients, consistent auditing of clinical decision making, and assessment of the efficacy of facet joint treatments. The included patients were assessed by a variety of clinicians who may have had different varying approaches to the use of bone scan activity in clinical decision making. The ^{99m}Tc MDP examinations were interpreted by a variety of nuclear medicine physicians who might have had varied practice patterns and varied thresholds for reporting or intervening on imaging findings. There is no commonly used clinical grading scale of facet joint activity, and our study dichotomized activity on the basis of only the radiology reports, reflecting actual clinical practice. A small number of facet joint injections were ordered by physicians who did not originally order or reference the bone scan.

In addition, future research could evaluate the significance of degree of facet joint activity and could evaluate if other clinical or radiographic findings are useful when used in conjunction with ^{99m}Tc MDP SPECT/CT results. It would also be useful to establish the prevalence of facet joint activity in patients without axial low back pain to assess specificity.

CONCLUSIONS

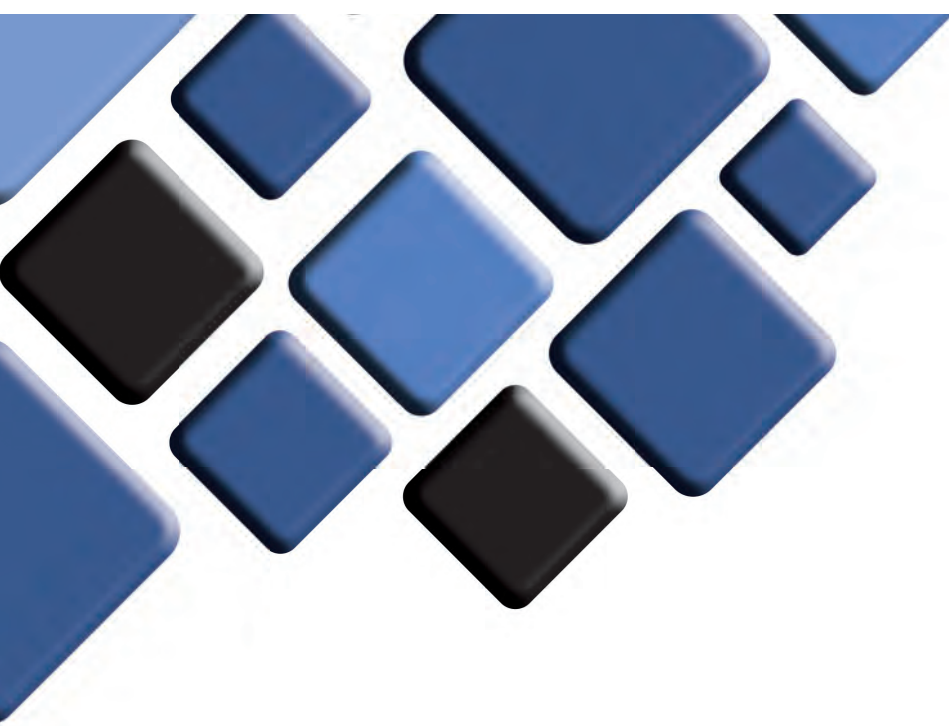
Facet joints undergoing targeted percutaneous treatment were frequently discordant with those demonstrating increased ^{99m}Tc MDP activity identified by SPECT/CT at our institution, often because the active facet joints did not seem to correlate with clinical findings. Further prospective, double-blinded investigation of the clinical significance of facet joint activity by use of ^{99m}Tc MDP SPECT/CT and comparative medial branch blocks is needed.

Disclosures: Kent Thielen—UNRELATED: Royalties: Nevro.* Timothy Maus—OTHER RELATIONSHIPS: Board of Directors, International Spine Intervention Society. *Money paid to institution.

REFERENCES

1. Bogduk N. Degenerative joint disease of the spine. *Radiol Clin North Am* 2012;50:613–28

2. Cohen SP, Raja SN. Pathogenesis, diagnosis, and treatment of lumbar zygapophysial (facet) joint pain. *Anesthesiology* 2007;106:591–614
3. Siegenthaler A, Eichenberger U, Schmidlin K, et al. What does local tenderness say about the origin of pain? An investigation of cervical zygapophysial joint pain. *Anesth Analg* 2010;110:923–27
4. Pneumaticos SP, Chatziioannou SN, Hipp JA, et al. Low back pain: prediction of short-term outcome of facet joint injection with bone scintigraphy. *Radiology* 2006;238:693–98
5. Dolan AL, Ryan PJ, Arden NK, et al. The value of SPECT scans in identifying back pain likely to benefit from facet joint injection. *Br J Rheumatol* 1996;35:1269–73
6. Koh WU, Kim SH, Hwang BY, et al. Value of bone scintigraphy and single photon emission tomography (SPECT) in lumbar facet disease and prediction of short-term outcome of ultrasound guided medial branch block with bone SPECT. *Korean J Pain* 2011;24:81–86
7. Sunshine JH, Applegate KE. Technology assessment for radiologists. *Radiology* 2004;230:309–14
8. Konin GP, Walz DM. Lumbosacral transitional vertebrae: classification, imaging findings, and clinical relevance. *AJNR Am J Neuroradiol* 2010;31:1778–86
9. McDonald M, Cooper R, Wang MY. Use of computed tomography-single-photon emission computed tomography fusion for diagnosing painful facet arthropathy. Technical note. *Neurosurg Focus* 2007;22:E2
10. Schwarzer AC, Wang S, Bogduk N, et al. Prevalence and clinical features of lumbar zygapophysial joint pain: a study in an Australian population with chronic low back pain. *Ann Rheum Dis* 1995;54:100–06
11. Bogduk N, ed. *Practice Guidelines for Spinal Diagnostic and Treatment Procedures*. 2nd ed. San Francisco: International Spine Intervention Society; 2004, pp. 559–63
12. Fogelman I. Skeletal uptake of disophosphonate: a review. *Eur J Nucl Med* 1980;5:473–76
13. Christensen SB. Localization of bone-seeking agents in developing experimentally induced osteoarthritis in the knee joint of the rabbit. *Scand J Rheumatol* 1983;12:343–49
14. Cavanaugh JM, Ozaktay C, Yamashita T, et al. Mechanisms of low back pain: a neurophysiologic and neuroanatomic study. *Clin Orthop Relat Res* 1997;335:166–80
15. Bogduk N. *Clinical and Radiological Anatomy of the Lumbar Spine*, 5th ed. St. Louis: Elsevier; 2012:183–86
16. Eubanks JD, Lee MJ, Cassinelli E, et al. Prevalence of lumbar facet arthrosis and its relationship to age, sex, and race: an anatomic study of cadaveric specimens. *Spine* 2007;32:2058–62
17. McCall IW, Park WM, O'Brien JP. Induced pain referral from posterior lumbar elements in normal subjects. *Spine* 1979;4:441–46



BARRICADETM COIL SYSTEM

PERFORMANCE AND VALUE DELIVERED



BLOCKADE
M E D I C A L

18 TECHNOLOGY DRIVE #169, IRVINE CA 92618 | P 949.788.1443
WWW.BLOCKADEMEDICAL.COM

 MADE IN AMERICA

CE
0297
MKTG-020 REV. B





Interventional Spine

Your **single source** for the latest in innovative **solutions.**

Introducing **the most complete and least invasive vertebral augmentation portfolio** on the market today. The **11g iVAS® Balloon System**, **TroFlex™ Curved Needle** and **iVAS Curette** may allow for streamlined access and improved procedural control when treating vertebral compression fractures. In addition, the **VertePort X4 Manifold™** provides an opportunity for quicker, more efficient procedures.

Stryker is proud to announce **a new paradigm in radiofrequency ablation**, the **Venom™ Cannula and Electrode** combination. This innovative design offers an alternative configuration at the distal end with a 'V' shape active tip, while maintaining the same gauge cannula as the standard configuration. The result is a **92% larger lesion** with the 20-gauge Venom Cannula and a 76% larger lesion with the 18-gauge Venom Cannula compared to the standard configuration. The optimized Venom Cannula also allows for efficient and precise anesthesia delivery to the targeted nerve through the side port design.

Visit **Stryker Booth #309** at SIR for a hands-on experience with our latest innovations.

